



TECHNISCHE  
UNIVERSITÄT  
DARMSTADT

# Demonstration and Optimization of the Chemical Looping Gasification Technology in 1 MW<sub>th</sub> Scale

Demonstration und Optimierung der Chemical Looping Vergasungstechnologie im 1 MW<sub>th</sub> Maßstab

Cumulative Dissertation of M. Sc. Paul Dieringer to Obtain the Degree of Dr.-Ing.

Technical University of Darmstadt, Department of Mechanical Engineering,  
Institute for Energy Systems and Technology

First Referee: Prof. Dr.-Ing. Bernd Epple

Co-Referee: Prof. Dr. habil. Andreas Dreizler

Date of Submission: 04.12.2023

Date of Disputation: 31.01.2024

Place: Darmstadt, Technical University of Darmstadt, Germany

---

This dissertation was carried out under the supervision of Prof. Dr.-Ing. Bernd Epple at the Institute for Energy Systems and Technology (EST) at Technical University of Darmstadt since March 2019.

---

# Demonstration and Optimization of the Chemical Looping Gasification Technology in 1 MW<sub>th</sub> Scale

Approved dissertation to obtain the degree of Dr.-Ing. by M.Sc. Paul Dieringer from Stuttgart

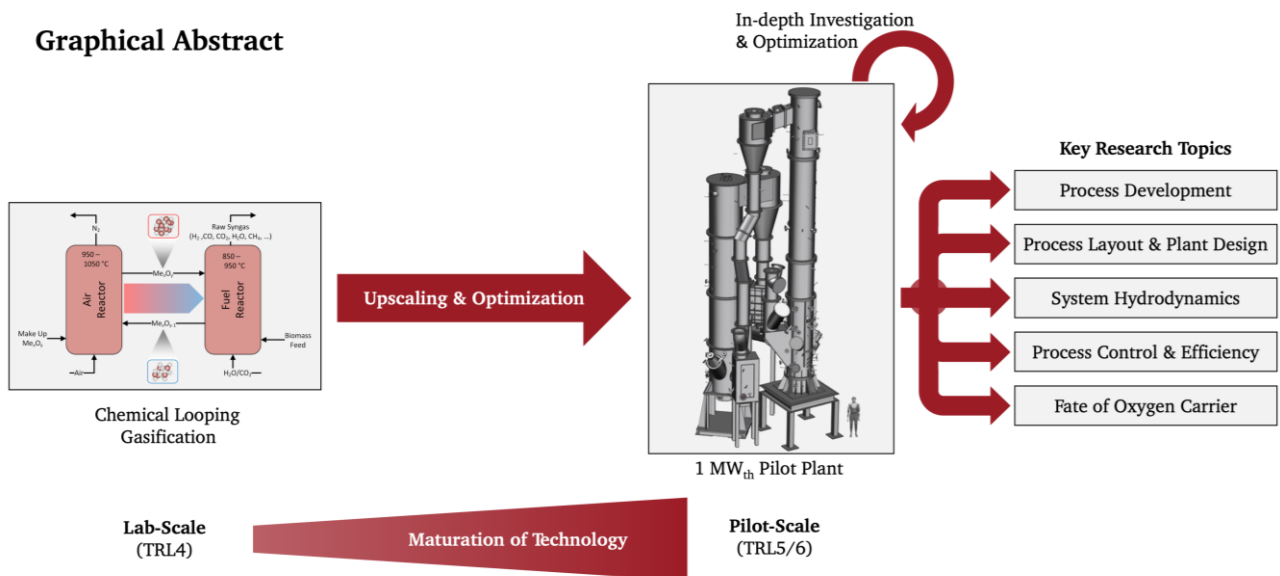
First Referee: Prof. Dr.-Ing. Bernd Epple  
Co-Referee: Prof. Dr. habil. Andreas Dreizler

Date of Submission: 04.12.2023  
Date of Disputation: 31.01.2024

Place: Darmstadt, Technical University of Darmstadt, Germany

---

## Graphical Abstract



This document is provided by *TUprints*,  
e-publishing service of the TU Darmstadt  
<http://tuprints.ulb.tu-darmstadt.de>  
[tuprints@ulb.tu-darmstadt.de](mailto:tuprints@ulb.tu-darmstadt.de)

URN: [urn:nbn:de:tuda-tuprints-266234](https://nbn-resolving.org/urn:nbn:de:tuda-tuprints-266234)  
URL: <https://tuprints.ulb.tu-darmstadt.de/id/eprint/26623>

Year of publication of the dissertation on *TUprints*: 2024

---

This dissertation is published under CC-BY 4.0 International  
<https://creativecommons.org/licenses/by/4.0>



---

The hope of a secure and livable world lies with disciplined nonconformists, who are dedicated to justice, peace, and brotherhood. The trailblazers in human, academic, scientific, and religious freedom have always been nonconformists. In any cause that concerns the progress of mankind, put your faith in the nonconformist!

*Martin Luther King Jr.*

---

---

## Abstract

---

Chemical looping gasification (CLG) is a novel thermochemical process allowing for the efficient conversion of different feedstocks (e.g. biomass, municipal waste) into a high-calorific synthesis gas ( $=\text{H}_2$  &  $\text{CO}$ ), which can subsequently be used for the synthesis of different marketable products, such as fuels or chemicals. While the CLG technology was successfully validated in lab scale using different reactor setups, feedstocks, and active materials, its demonstration in an industrially relevant environment remains a challenge. Overcoming this major technical hurdle on the pathway towards advancing the CLG technology to market maturity, thereby facilitating an efficient valorization of different waste streams in the future, signifies the main goal of this dissertation. To accomplish this, the existing  $1 \text{ MW}_{\text{th}}$  pilot plant at the Institute for Energy Systems and Technology (EST) was adapted and optimized in order to allow for long-term autothermal (i.e. without external energy input) chemical looping gasification. Here, the general steps of a standardized chemical engineering project, ranging from process definition and basic engineering to plant commissioning, operation, and optimization, were carried out between March 2019 and September 2023.

In the course of this venture, the general viability of autothermal chemical looping gasification in an industrially relevant environment was proven by ultimately achieving over 400 hours of CLG operation in the  $1 \text{ MW}_{\text{th}}$  pilot plant, utilizing three different biogenic materials as feedstock. This was facilitated by devising a novel process control concept as well as a holistic set of operational rules and principles, allowing for efficient autothermal CLG operation, with cold gas efficiencies up to 50 % being reached in  $1 \text{ MW}_{\text{th}}$  scale. On top of that, crucial findings for establishing a suitable process layout of an industrial-scale chemical looping gasifier were derived in the course of the adaptation and commissioning of the  $1 \text{ MW}_{\text{th}}$  pilot plant as well as the subsequent in-depth evaluation of the datasets gathered during autothermal CLG operation. Moreover, this evaluation allowed for a holistic investigation of relevant aspects for process up-scaling, covering the most auspicious routes for process optimization as well as potential technical bottlenecks one could encounter in industrial scale. Process simulations, using models validated with data gathered during autothermal CLG operation, show that when overcoming the technical hurdles faced in  $1 \text{ MW}_{\text{th}}$  scale, such as limited oxygen carrier (OC) lifetime and restricted OC circulation, cold gas efficiencies  $>80$  % and carbon conversions close to 90 % can be obtained in industrial scale. Hence, the technical competitiveness of the chemical looping gasification process was demonstrated within the scope of this work, thus encouraging future up-scaling activities, which could promote the CLG technology into a crucial building block for the aspired circular economy.

---

---

## Kurzfassung

---

Die *Chemical Looping* Vergasung (engl. chemical looping gasification, CLG) ist ein neuartiges thermochemisches Verfahren, das die effiziente Umwandlung verschiedener Einsatzstoffe (z. B. Biomasse, Abfälle) in ein hochkalorisches Synthesegas ( $=\text{H}_2$  & CO) ermöglicht, welches für die Synthese verschiedener marktgängiger Produkte wie z. B. Kraftstoffe oder Chemikalien verwendet werden kann. Während die CLG-Technologie im Labormaßstab, unter Verwendung verschiedener Reaktorkonfigurationen, Ausgangsstoffe und aktiver Materialien, erfolgreich validiert wurde, bleibt ihre Demonstration in einem industriell relevanten Umfeld eine Herausforderung. Die Überwindung dieser großen technischen Hürde auf dem Weg zur Marktreife der CLG-Technologie und die damit einhergehende Ermöglichung einer zukünftig effizienten Verwertung verschiedener Abfallströme ist das Hauptziel der vorliegenden Dissertation. Um dies zu erreichen wurde die bestehende  $1 \text{ MW}_{\text{th}}$  Pilotanlage am Institut für Energiesysteme und Technologie (EST) angepasst und optimiert, um die kontinuierliche autotherme (d.h. ohne externen Energieeintrag) *Chemical Looping* Vergasung zu demonstrieren. Dabei wurden von März 2019 bis September 2023 die standardisierten Schritte eines Chemieprojekts, beginnend mit der Prozessdefinition und dem Basic Engineering bis hin zur Inbetriebnahme, dem Betrieb und der Optimierung der Anlage, durchgeführt.

Im Verlauf dieses Projekts wurde die generelle Machbarkeit der autothermen *Chemical Looping* Vergasung in einer industriell relevanten Umgebung nachgewiesen, indem in der  $1 \text{ MW}_{\text{th}}$  Pilotanlage über 400 Stunden CLG-Betrieb mit drei verschiedenen biogenen Materialien als Einsatzstoff erreicht wurden. Ermöglicht wurde dies durch die Entwicklung eines neuartigen Prozesssteuerungskonzepts sowie die Erstellung von übergeordneten Betriebsregeln und -prinzipien, die einen effizienten autothermen CLG-Betrieb ermöglichen, sodass im  $1 \text{ MW}_{\text{th}}$ -Maßstab Kaltgaswirkungsgrade bis zu 50 % erzielt wurden. Darüber hinaus wurden sowohl bei der Anpassung und Inbetriebnahme der  $1 \text{ MW}_{\text{th}}$  Pilotanlage als auch bei der detaillierten Auswertung der während des autothermen CLG-Betriebs gesammelten Datensätze entscheidende Erkenntnisse für die geeignete Prozessauslegung eines industriellen *Chemical Looping* Vergasers gewonnen. Zudem ermöglichte diese Auswertung eine ganzheitliche Untersuchung relevanter Aspekte für eine Hochskalierung des Prozesses, welche neben den vorteilhaftesten Wegen für die Prozessoptimierung auch potenzielle technische Engpässe, die im industriellen Maßstab auftreten könnten, abdeckt. Simulationen mit validierten Prozessmodellen zeigen, dass bei Überwindung der im  $1 \text{ MW}_{\text{th}}$ -Maßstab ermittelten technischen Hürden, wie z. B. der begrenzten Lebensdauer des Sauerstoffträgers (engl. oxygen carrier, OC) und der eingeschränkten OC-Zirkulation, im industriellen Maßstab Kaltgaswirkungsgrade von mehr als 80 % und Kohlenstoffumsätze von nahezu 90 % erreicht werden können. Somit wurde im Rahmen dieser Arbeit die technische Wettbewerbsfähigkeit des *Chemical Looping* Vergasungsprozesses demonstriert, was zu zukünftigen Up-Scaling-Aktivitäten anregt, welche die CLG Technologie zu einem wichtigen Baustein der angestrebten Kreislaufwirtschaft avancieren lassen könnten.

---

---

## Acknowledgements

---

**Prof. Dr.-Ing. Bernd Epple:** Thank you for the opportunity to actively contribute to the important and pioneering research at the Institute for Energy Systems and Technology and for your trust in my capabilities and judgement.

**Prof. Dr. habil. Andreas Dreizler:** Thank you for your willingness to become the co-referee and for all your efforts going into the examination of my dissertation.

**Dr. Jochen Ströhle:** Thank you for your patience, endurance, and support, which were fundamental not only for the progress of my thesis, but also the success of the *CLARA* project. Special thanks for your mental acuity when correcting the countless reports, articles, letters, and presentations – I hope to never again forget an oxford comma whenever I will be writing.

**Falko Marx:** What at sometimes felt like having to make the impossible possible, was made manageable through your collaboration and support. Thank you for your pragmatism, advice, and loyalty and for letting me be the *good cop*, whenever emotions were running high in the technical workshop.

**Julia Karnetzke:** Thank you for being there when nobody was. Thank you for enduring and accepting all my moods and emotions. Thank you for letting me be myself, without forgetting to challenge my character and views.

This thesis would not have been possible without the help of others. Therefore, my special thanks goes to all **colleagues, cooperation partners, and co-authors.**

My special thanks also goes to **Harald Tremmel** and **Karl Voigtländer** for their support during the HAZOP analysis and the detail engineering of the 1 MW<sub>th</sub> CLG pilot plant.

Last but not least, I want to thank my friends and colleagues, **Jens Kaltenmorgen, Eric Langner, Jan May, Carina Hofmann, Jens Peters, Christian Heinze, Falah Alobaid, Susanne Tropp, Christof Bonk, Joachim Wagner, Pascal Reinig, Alex Hoh, Fabian Buchmann, Peter Ohlemüller, Coskun Yildiz, Marcel Richter, Dominik Wimmer, Martin Greco-Coppi, Dennis Hülsbruch, Pascal Koschwitz, Alexander Kuhn, Philipp Mohn, Fabiola Panitz, Marc Siodlaczek, Christoph Graf, and Adrian Marx** for their collaboration, support, guidance, and cooperation during my time at the Institute for Energy Systems and Technology.

---

---

## Preface

---

This cumulative thesis is organized into two main parts. In the **first part** (Part 1), being the Synopsis of this dissertation, an introduction to the research topic (Introduction) and a summary of the work (Synthesis) are presented. The Synopsis is followed by the **second part** (Part 2) of this dissertation, consisting of the five appended research papers (Research Paper I-V).



---

---

## Table of Contents

---

Abstract	v
Kurzfassung	vi
Acknowledgements	vii
Preface	viii
List of Publications	xi
Presentation of Own Contribution to the Publications	xv
Affidavit	xvii
Nomenclature	xix

---

### Part 1

---

<b>1 Introduction</b>	<b>1</b>
1.1 Research Background	1
1.2 Over-Arching Research Goal and Primary Research Questions	5
1.3 Classification of the Scope of the Individual Research Papers	8
1.4 Summary of Research Scope	19
<b>2 Synthesis</b>	<b>21</b>
2.1 Main Research Findings	21
2.2 Conclusion	33
2.3 Outlook	35
Appendix	37
A.1 Additional Information	37
A.2 Exemplary Engineering Documents	39
References	43

---

### Part 2

---

<b>Research Paper I</b>	<b>47</b>
<b>Research Paper II</b>	<b>75</b>
<b>Research Paper III</b>	<b>101</b>
<b>Research Paper IV</b>	<b>123</b>
<b>Research Paper V</b>	<b>171</b>

---

---

*This page is left blank intentionally*

---

---

## List of Publications

---

A full list of publications is given in Table I.<sup>†</sup> For reference, the type of the publication is also shown. Here, the following abbreviations for the publications types are used: Bachelor Thesis (BT), Semester Project (SP), Master Thesis (MT), Research Paper (RP), Conference Contribution (CoC), Patent (Pa).

The five research papers, making up the core of this cumulative thesis, **Research Paper I (RP-I)**, **Research Paper II (RP-II)**, **Research Paper III (RP-III)**, **Research Paper IV (RP-IV)**, and **Research Paper V (RP-V)**, are marked with grey shading in Table I.

Table I: List of publications.

Publication	Type
Paul Dieringer, “Influence of Solvent Selection on Solvent Exchange Kinetics from Hydrogels to Organogels“, <i>Bachelor Thesis</i> , TUHH 2015	BT
R. Subrahmanyam, P. Gurikov, P. Dieringer, M. Sun, and I. Smirnova, “On the Road to Biopolymer Aerogels—Dealing with the Solvent,” <i>Gels</i> , vol. 1, no. 2, pp. 291–313, Dec. 2015, doi: <a href="https://doi.org/10.3390/gels1020291">10.3390/gels1020291</a> .	RP
R. Subrahmanyam, P. Gurikov, P. Dieringer, M. Sun, and I. Smirnova, “Correction: Raman Subrahmanyam, <i>et al.</i> On the Road to Biopolymer Aerogels—Dealing with the Solvent. <i>Gels</i> 2015, 1, 291–313,” <i>Gels</i> , vol. 2, no. 3, p. 21, Aug. 2016, doi: <a href="https://doi.org/10.3390/gels2030021">10.3390/gels2030021</a> .	RP
Paul Dieringer, “Optimization of Ceria RPCs for Thermochemical Cycling“, <i>Semester Project</i> , ETH Zürich 2017	SP
Paul Dieringer, “Thermochemical Cycling of Reticulated Porous Ceria with CH <sub>4</sub> and CO <sub>2</sub> “, <i>Master Thesis</i> , ETH Zürich 2018	MT
Ackermann <i>et al.</i> , “Process for the production of syngas”, Patent <a href="https://patents.google.com/patent/WO2020058263A1">WO2020058263A1</a>	Pa
S. P. Raman <i>et al.</i> , “Alginate aerogels carrying calcium, zinc and silver cations for wound care: Fabrication and metal detection,” <i>The Journal of Supercritical Fluids</i> , vol. 153, p. 104545, Nov. 2019, doi: <a href="https://doi.org/10.1016/j.supflu.2019.104545">10.1016/j.supflu.2019.104545</a> .	RP
R. Subrahmanyam <i>et al.</i> , “A novel process for the hydrophobization of porous silica“, Patent <a href="https://patents.google.com/patent/WO2020193554">WO2020193554</a>	Pa

**Note:** Contributions to the publications listed above were made prior to the start of employment at the Institute for Energy Systems and Technology at TU Darmstadt. Hence, these publications do not cover the contents of this dissertation.

---

<sup>†</sup> It has to be noted that the first eight publications listed in Table I were not created within the scope of this dissertation. Nonetheless, these publications are listed here, because of the [special provisions of the department of Mechanical Engineering](#), stating that all publications including Bachelor and Master Theses have to be listed here.

Cont'd. **Table I:** List of publications.

Publication	Type
Paul Dieringer, Falko Marx, Jochen Ströhle, Bernd Epple, "CLARA – Chemical Looping Gasification for Sustainable Production of Biofuels", <i>2<sup>nd</sup> German Doctoral Colloquium Bioenergy</i> , Nürnberg, 09/2019	CoC
Falko Marx, Paul Dieringer, Jochen Ströhle, Bernd Epple, "The CLARA project: Chemical Looping Gasification for the Production of Biofuels", <i>8<sup>th</sup> High Temperature Solid Looping Cycles Network Meeting</i> , Geleen, 01/2020	CoC
Paul Dieringer, Falko Marx, Jochen Ströhle, Bernd Epple, "Chemical Looping Gasification – A Novel Process for the Sustainable Production of Biofuels", <i>6<sup>th</sup> Central European Biomass Conference (CEBC)</i> , Graz, 01/2020	CoC
P. Dieringer, F. Marx, F. Alobaid, J. Ströhle, and B. Epple, "Process Control Strategies in Chemical Looping Gasification—A Novel Process for the Production of Biofuels Allowing for Net Negative CO <sub>2</sub> Emissions," <i>Applied Sciences</i> , vol. 10, no. 12, p. 4271, Jun. 2020, doi: <a href="https://doi.org/10.3390/app10124271">10.3390/app10124271</a> .	RP-I
N. Detsios, K. Atsonios, P. Grammelis, P. Dieringer, C. Heinze, J. Ströhle, "Advanced Fischer-Tropsch biofuels production from syngas derived from Chemical Looping Gasification: A preliminary process simulation study", <i>eEUBCE2020</i> , Online, 07/2020	CoC
F. Marx, P. Dieringer, J. Ströhle, and B. Epple, "Design of a 1 MW <sub>th</sub> Pilot Plant for Chemical Looping Gasification of Biogenic Residues," <i>Energies</i> , vol. 14, no. 9, p. 2581, Apr. 2021, doi: <a href="https://doi.org/10.3390/en14092581">10.3390/en14092581</a> .	RP-II
N. M. Nguyen, F. Alobaid, P. Dieringer, and B. Epple, "Biomass-Based Chemical Looping Gasification: Overview and Recent Developments," <i>Applied Sciences</i> , vol. 11, no. 15, p. 7069, Jul. 2021, doi: <a href="https://doi.org/10.3390/app11157069">10.3390/app11157069</a> .	RP
F. Alobaid, P. Dieringer, and B. Epple, "Vorrichtung zur Zwischenspeicherung von Energie", Patent <a href="https://patents.google.com/patent/DE102021103883A1">DE102021103883A1</a>	Pa
Paul Dieringer, Falko Marx, Jochen Ströhle, Bernd Epple, "Design and Control Concept of a 1 MW <sub>th</sub> Chemical Looping Gasifier Allowing for Efficient Autothermal Syngas Production", <i>6<sup>th</sup> International Conference on Chemical Looping</i> , Zaragoza, 09/2022	CoC
Jochen Ströhle, Paul Dieringer, Amir Solemanisalim, Juan Adanez, Ibai Funcia, Andrea Di Giuliano, Florian Lebendig, Frank Buschsieweke, Konstantinos Atsonios, Nadine Gürer & Ye Huang, "Chemical Looping Gasification for Sustainable Production of Biofuels—The CLARA Project", <i>6<sup>th</sup> International Conference on Chemical Looping</i> , Zaragoza, 09/2022	CoC
Falko Marx, Paul Dieringer, Jochen Ströhle, Bernd Epple, "Solid Flux Measurement in Chemical Looping Gasification Based on Solid Samples", <i>24<sup>th</sup> Fluidized Bed Conversion Conference</i> , Göteborg, 05/2022	CoC

Cont'd. **Table I:** List of publications.

Publication	Type
Falko Marx, Paul Dieringer, Jochen Ströhle, “Autothermal Operation of a 1 MW <sub>th</sub> Chemical Looping Gasifier for Biogenic Residues”, 9 <sup>th</sup> <i>High Temperature Solid Looping Cycles Network Meeting</i> , Piacenza, 03/2023	CoC
Nikolaos Detsios <i>et al.</i> , “A comparative analysis and assessment of dual fluidized bed and chemical looping gasification”, 31 <sup>st</sup> <i>European Biomass Conference (EUBCE)</i> , Bologna, 06/2023	CoC
F. Marx, P. Dieringer, J. Ströhle, and B. Epple, “Solid Flux Measurement in Dual Fluidized Bed Processes Based on Solid Samples,” <i>Fuel</i> , vol. 341, p. 127589, Jun. 2023, doi: <a href="https://doi.org/10.1016/j.fuel.2023.127589">10.1016/j.fuel.2023.127589</a> .	RP
P. Dieringer, F. Marx, B. Michel, J. Ströhle, and B. Epple, “Design and control concept of a 1 MW <sub>th</sub> chemical looping gasifier allowing for efficient autothermal syngas production,” <i>International Journal of Greenhouse Gas Control</i> , vol. 127, p. 103929, Jul. 2023, doi: <a href="https://doi.org/10.1016/j.ijggc.2023.103929">10.1016/j.ijggc.2023.103929</a> .	RP-III
V. Gogulancea <i>et al.</i> , “Technoeconomic and Environmental Assessment of Biomass Chemical Looping Gasification for Advanced Biofuel Production,” <i>International Journal of Energy Research</i> , vol. 2023, pp. 1–17, Jul. 2023, doi: <a href="https://doi.org/10.1155/2023/6101270">10.1155/2023/6101270</a> .	RP
P. Dieringer, F. Marx, J. Ströhle, and B. Epple, “System Hydrodynamics of a 1 MW <sub>th</sub> Dual Circulating Fluidized Bed Chemical Looping Gasifier,” <i>Energies</i> , vol. 16, no. 15, p. 5630, Jul. 2023, doi: <a href="https://doi.org/10.3390/en16155630">10.3390/en16155630</a> .	RP-IV
F. Marx, P. Dieringer, J. Ströhle, and B. Epple, “Process efficiency and syngas quality from autothermal operation of a 1 MW <sub>th</sub> chemical looping gasifier with biogenic residues,” <i>Applications in Energy and Combustion Science</i> , vol. 16, p. 100217, 2023, doi: <a href="https://doi.org/10.1016/j.jaecs.2023.100217">10.1016/j.jaecs.2023.100217</a> .	RP
P. Dieringer <i>et al.</i> , “Fate of ilmenite as oxygen carrier during 1 MW <sub>th</sub> chemical looping gasification of biogenic residues,” <i>Applications in Energy and Combustion Science</i> , vol. 16, p. 100227, Dec. 2023, doi: <a href="https://doi.org/10.1016/j.jaecs.2023.100227">10.1016/j.jaecs.2023.100227</a> .	RP-V

---

*This page is left blank intentionally*

---

## Presentation of Own Contribution to the Publications

---

The present cumulative dissertation consists of five (I-V) research papers (see Part 2). The ten (1-10) researchers listed below have contributed to these research papers:

- 1) **Paul Dieringer (P.D.)**, Technical University of Darmstadt, Department of Mechanical Engineering, Institute for Energy Systems and Technology, Otto-Berndt-Str. 2, 64287 Darmstadt, Germany
- 2) **Falko Marx (F.M.)**, Technical University of Darmstadt, Department of Mechanical Engineering, Institute for Energy Systems and Technology, Otto-Berndt-Str. 2, 64287 Darmstadt, Germany
- 3) **Benjamin Michel (B.M.)**, Technical University of Darmstadt, Department of Mechanical Engineering, Institute for Energy Systems and Technology, Otto-Berndt-Str. 2, 64287 Darmstadt, Germany
- 4) **Falah Alobaid (F.A.)**, Technical University of Darmstadt, Department of Mechanical Engineering, Institute for Energy Systems and Technology, Otto-Berndt-Str. 2, 64287 Darmstadt, Germany
- 5) **Jochen Ströhle (J.S.)**, Technical University of Darmstadt, Department of Mechanical Engineering, Institute for Energy Systems and Technology, Otto-Berndt-Str. 2, 64287 Darmstadt, Germany
- 6) **Bernd Epple (B.E.)**, Technical University of Darmstadt, Department of Mechanical Engineering, Institute for Energy Systems and Technology, Otto-Berndt-Str. 2, 64287 Darmstadt, Germany
- 7) **Florian Lebendig (F.L.)**, Forschungszentrum Jülich GmbH, Institute for Energy and Climate Research (IEK-2), Wilhelm-Johnen-Straße, 52428 Jülich, Germany
- 8) **Michael Müller (M.M.)**, Forschungszentrum Jülich GmbH, Institute for Energy and Climate Research (IEK-2), Wilhelm-Johnen-Straße, 52428 Jülich, Germany
- 9) **Andrea Di Giuliano (A.D.G.)**, Department of Industrial and Information Engineering and Economics (DIIIE), University of L'Aquila, Piazzale E. Pontieri 1, Loc. Monteluco di Roio, 67100 L'Aquila, Italy
- 10) **Katia Gallucci (K.G.)**, Department of Industrial and Information Engineering and Economics (DIIIE), University of L'Aquila, Piazzale E. Pontieri 1, Loc. Monteluco di Roio, 67100 L'Aquila, Italy

For each of these papers, the author contributions are defined within the paper itself. These original author contributions are listed in Table II on the following page. Contributions by the author of this dissertation (P.D.) are marked in **bold font**. For term explanation, please refer to the [CRedit taxonomy](#).

Three of the five research papers (RP-I, RP-II, and RP-III) are also part of a second cumulative dissertation in preparation by Falko Marx.

---

**Table II:** Summary of author contributions for Research Papers I-V.

---

### **Research Paper I**

*Process Control Strategies in Chemical Looping Gasification—A Novel Process for the Production of Biofuels Allowing for Net Negative CO<sub>2</sub> Emissions*

Paul Dieringer, Falko Marx, Falah Alobaid, Jochen Ströhle and Bernd Eppele

Author Contributions: **Conceptualization**, J.S. and P.D.; **methodology**, P.D.; **writing—original draft preparation**, P.D.; writing—review and editing, F.M., J.S. and F.A.; **visualization**, P.D.; supervision, B.E.

---

### **Research Paper II**

*Design of a 1 MW<sub>th</sub> Pilot Plant for Chemical Looping Gasification of Biogenic Residues*

Falko Marx, Paul Dieringer, Jochen Ströhle and Bernd Eppele

Author Contributions: **conceptualization**, F.M., J.S. and P.D.; **simulation**, P.D. and F.M.; writing original draft preparation, F.M.; **writing—review and editing**, P.D., J.S. and F.M.; **visualization**, F.M. and P.D.; supervision, B.E.

---

### **Research Paper III**

*Design and Control Concept of a 1 MW<sub>th</sub> Chemical Looping Gasifier Allowing for Efficient Autothermal Syngas Production*

Paul Dieringer, Falko Marx, Benjamin Michel, Jochen Ströhle, Bernd Eppele

Author Contributions: P.D.: **Conceptualization, Methodology, Investigation, Data Curation, Writing – Original Draft, Visualization**. F.M.: Writing – Review & Editing, Methodology, Investigation, Data Curation. B.M.: Investigation. J.S.: Writing – Review & Editing, Supervision, Project Administration, Funding Acquisition. B.E.: Resources, Funding Acquisition.

---

### **Research Paper IV**

*System Hydrodynamics of a 1 MW<sub>th</sub> Dual Circulating Fluidized Bed Chemical Looping Gasifier*

Paul Dieringer, Falko Marx, Jochen Ströhle, Bernd Eppele

Author Contributions: P.D.: **Conceptualization, Methodology, Investigation, Data Curation, Writing – Original Draft, Visualization**. F.M.: Writing – Review & Editing, Methodology, Investigation, Data Curation. J.S.: Writing – Review & Editing, Supervision, Project Administration, Funding Acquisition. B.E.: Resources, Funding Acquisition.

---

### **Research Paper V**

*Fate of Oxygen Carrier during Continuous 1 MW<sub>th</sub> Chemical Looping Gasification of Biogenic Residues*

Paul Dieringer, Falko Marx, Florian Lebendig, Michael Müller, Andrea Di Giuliano, Katia Gallucci, Jochen Ströhle, Bernd Eppele

Author Contributions: P.D.: **Conceptualization, Methodology, Investigation, Data Curation, Writing – Original Draft, Visualization**. F.M.: Writing – Review & Editing, Methodology, Investigation, Data Curation. F.L.: Methodology, Investigation. M.M.: Methodology, Investigation, Writing – Original Draft, Funding Acquisition. A.D.G.: Methodology, Investigation, Writing – Original Draft, Funding Acquisition. K.G.: Methodology, Investigation, Writing – Original Draft, Funding Acquisition. J.S.: Writing – Review & Editing, Supervision, Project Administration, Funding Acquisition. B.E.: Resources, Funding Acquisition.

---



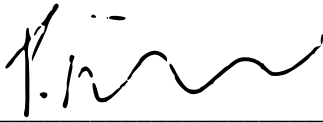
---

---

## Affidavit

---

I hereby declare in lieu of an oath that I have completed my dissertation independently and only with the aids indicated.



---

Paul Dieringer

---

*This page is left blank intentionally*

---



---

## Nomenclature

---

The nomenclature below refers to the symbols and abbreviations used in the Synopsis (Part 1) of this dissertation. While uniformity was pursued during drafting of the five research papers, some discrepancies and ambiguities in nomenclature could not be prevented. Therefore, please refer to the nomenclature of each individual research paper when referring to Part 2 of this dissertation.

---

### Latin Symbols

---

$d_{p,m}$	Mean particle diameter	$u$	Velocity
$\dot{m}$	Mass flow	$\dot{V}$	Volume flow
$P$	Power	$\dot{Q}$	Heat flow
$p$	Pressure	$x_i$	Volume fraction of species $i$
$RR_{AR}$	AR flue gas recirculation ratio	$X_s$	Oxidation degree of OC
$T$	Temperature		

---

### Greek Symbols

---

$\Delta H_R$	Reaction enthalpy	$\eta_{CG}$	Cold gas efficiency
$\Delta p$	Riser pressure drop	$\phi$	Oxygen carrier-to-fuel ratio
$\Delta X_s$	Change in OC oxidation degree	$\tau$	Residence time
$\lambda$	Air-to-fuel equivalence ratio		

---

### Acronyms/Abbreviations

---

AR	Air Reactor	ILMf	Ilmenite fine
BM	Biomass	K1/2/3	Campaign 1/2/3
CAD	Computer-aided Design	LS	Loop Seal
CCS	Carbon Capture & Storage	NASA	National Aeronautics and Space Administration
CFB	Circulating Fluidized Bed	OCAC	Oxygen-Carrier-Aided Combustion
CLC	Chemical Looping Combustion	OC	Oxygen Carrier
CLG	Chemical Looping Gasification	PCS	Process Control System
CS	Cooling System	PFD	Process Flow Diagram
DFBG	Dual Fluidized Bed Gasification	PFR	Pine Forest residue
FG	Flue Gas	PnID	Process & Instrumentation Diagram
FR	Fuel Reactor	RP	Research Paper
EU	European Union	WSP	Wheat Straw Pellets
GA	Gas Analysis	TU	Technical University
HAZOP	Hazard and Operability Study	SFB	Stationary Fluidized Bed
HV	Heating Value	TRL	Technological Readiness Level
IR	Internal (solid) Recirculation	TSL	To Safe Location
IWP	Industrial Wood Pellets		
ILMc	Ilmenite coarse		

---

### Indices

---

0	Reference state	in	Inlet
AR	Air Reactor	int.	Internal
circ.	Circulating	OC	Oxygen Carrier
calc.	Calculated	out	Outlet
eff.	Effective	RL	Refractory Lining
ent.	Entrainment	s	Solid
FR	Fuel Reactor	th	Thermal

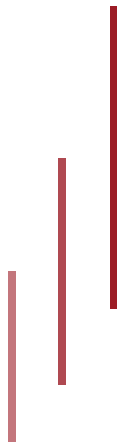
---



**Part 1**



***Synopsis***



---

## 1. Introduction

---

### 1.1. Research Background

With the average global surface temperature being on an unhalted rising trajectory [1] due to the constantly increasing anthropogenic greenhouse gas concentrations inside the earth's atmosphere [2], drastic changes in human activities, especially in the industrialized world, are crucial to avoid 'vast human misery' [3]. One industry sector for which CO<sub>2</sub> abatement has been negligible in the last decades, despite rapid technological progress and the introduction of a vast palette of political measures, is the transport sector. Even in the European Union (EU), being one of the most ambitious and influential communities of states worldwide when it comes to environmental policy, greenhouse gas emission from the transport sector have increased by more than 20 % (approx. 150 Mt CO<sub>2,equivalent</sub>) between 1990 and 2020 [4]. To counter this trend, the European Commission has set a target of achieving a share of 14 % renewable energy in the transport sector by 2030, while at the same time alleviating negative impacts on food availability and prices [5]. Here, biofuels are seen as a potential replacement for conventional fuels in the heavy freight transport and aviation industry, where electrification is currently not viable.

For the production of so-called 2<sup>nd</sup> generation biofuels, relying solely on non-food precursor materials, the thermochemical gasification pathway via a synthesis gas is an auspicious route. Generally, oxygen-blown gasifiers, which allow for the efficient production of a N<sub>2</sub>-free syngas and thus facilitate its direct deployment in various syntheses (e.g. methanol, Fischer-Tropsch), have been widely researched, going back to the start of the last century [6]. Recently, research interest in this field has gained renewed attention, due to current developments in terms of climate change and waste management, favoring the chemical valorization of residue materials (e.g. biomass, municipal waste, etc.) [7, 8]. Aside from their technical maturity, the benefits of oxygen-blown gasifiers arise from the direct utilization of molecular O<sub>2</sub> in the gasification chamber, facilitating high reaction temperatures and close to complete feedstock conversion. Therefore, cold gas efficiencies above 75 % can be obtained, depending on the gasifier type and the utilized feedstock [9]. An alternative approach to oxygen-blown gasifiers is the so-called dual fluidized bed gasification (DFBG) technology [10–12]. Here, feedstock gasification is achieved in two separate reactors between which a hot (inert) bed material is transferred. In the first reactor, the feedstock is gasified using steam as the gasification medium, resulting in the production of a hydrogen-rich synthesis gas. The heat required to drive the governing endothermic chemical reactions in this reactor is provided by a hot bed material coming from an exothermically operated second reactor, in which excess char is combusted with inlet air, resulting in a heating up of the bed material and the production of a CO<sub>2</sub>-containing flue gas. The DFBG technology has been successfully demonstrated in industrial applications with units exceeding a thermal load

of 100 MW<sub>th</sub>, thus making it another mature gasification technology [13]. A novel gasification technology closely related to the DFBG process is the chemical looping gasification (CLG) process illustrated in Figure 1. Its major advantage is that the oxygen necessary for efficient feedstock conversion is provided through the cyclic reduction and oxidation of an active oxygen carrier (OC) material, circulating between two reactors – the air reactor (AR), where the OC is being oxidized and the fuel reactor (FR), where the OC provides oxygen for (partial) feedstock oxidation. Consequently, CLG does not rely on a costly air separation unit, generally required for oxygen-driven gasification processes, yet allows for the efficient conversion of the utilized feedstock into a high-calorific syngas. Moreover, despite air being used as the oxygen source in the gasification process, CLG facilitates an efficient capturing of the CO<sub>2</sub> formed during the autothermal gasification step from the N<sub>2</sub>-free FR product gas in the downstream syngas purification unit. Thereby, a process exhibiting net negative CO<sub>2</sub> emissions can be attained, in case sustainably sourced biogenic feedstocks are used and the CO<sub>2</sub> captured from the raw product gas is stored (CCS) [14–16]. However, in comparison to oxygen-blown gasifiers, the CLG technology exhibits a relatively low technical maturity, so far mainly having been investigated in lab scale [17–20]. First studies carried out in small gasification pilots, reaching a thermal input up to 25 kW<sub>th</sub>, demonstrated that efficient continuous CLG operation is feasible [21–24]. However, when striving for industrial application in scales of several hundred megawatts [25, 26], investigations in larger pilots in the single-megawatt scale (1-5 MW<sub>th</sub>), where industry-like conditions prevail, are crucial in order to assess the impact of plant scale on crucial process characteristics such as reactor hydrodynamics, operability, and efficiency [27].

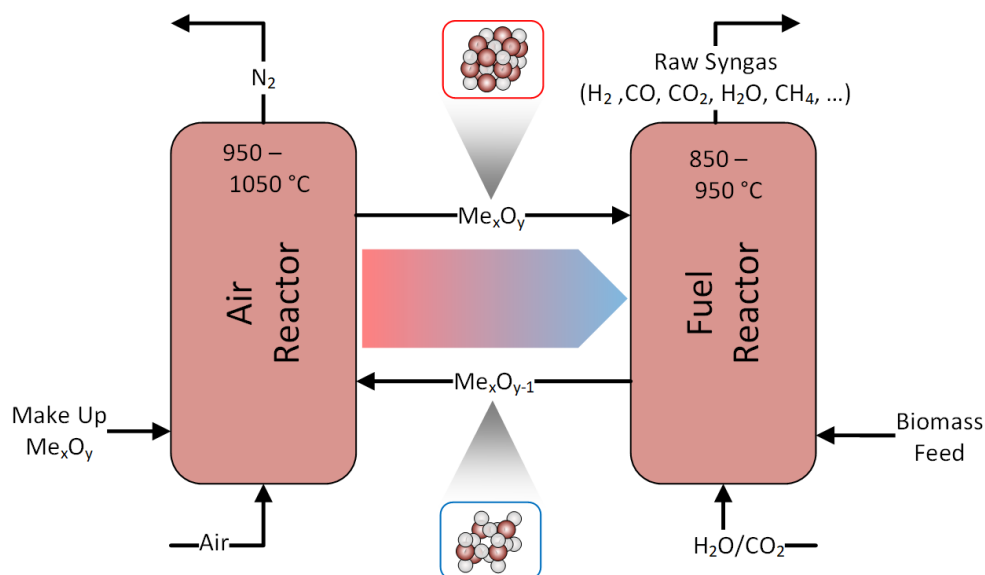


**Figure 1.** Schematic illustration of CLG process.

To quantify technological maturity, the European Union utilizes a technology readiness level (TRL) scale [28] (see Figure 2a), adapted from the one successfully deployed for space missions by the National Aeronautics and Space Administration (NASA) [29]. On the EU's TRL scale, the CLG technology was ranked at TRL 4 before 2019, with chemical looping gasification having been validated in lab scale, using different oxygen carriers [23, 30–32], reactor setups [31, 33–35], feedstocks [36–38], and operating conditions. A summary of these endeavors is presented in the extensive reviews by Nguyen *et al.* [14] and Goel *et al.* [39]. Overcoming the next crucial hurdle, i.e. promoting the TRL from 4 to 5-6 by validating and demonstrating the technology in a relevant environment, is a crucial step both from a technical as well as an economic perspective, especially for high temperature processes, where a certain scale is required to attain industrially relevant conditions.

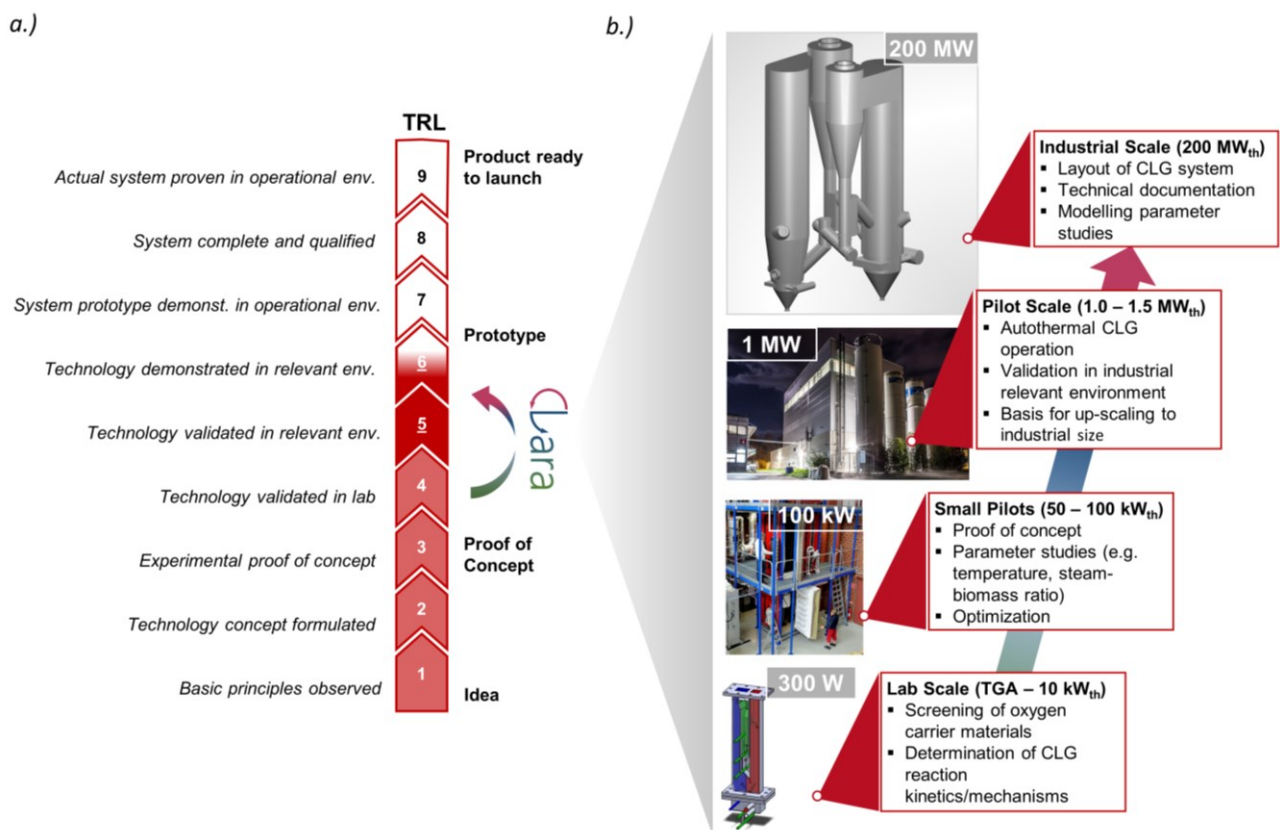


**Figure 2.** a.) European Union TRL scale [28], with indication of targeted TRL increase within the CLARA project. b.) Main efforts regarding the technical promotion of the CLG technology in different scales, defined for the CLARA project.

In an attempt to do so, the EU funded research project CLARA was initiated, aiming to demonstrate CLG in the MW-scale, making use of the existing 1 MW<sub>th</sub> facility at the Technical University (TU) of Darmstadt, previously used for carbonate looping [40, 41], chemical looping combustion (CLC) [42, 43], and High Temperature Winkler gasification [7, 8], amongst other

---

processes. In order to do so, the CLG technology was to be firstly refined in lab scale, making use of previous knowledge and focusing on topics crucial for technology up-scaling (e.g. investigation of OCs available in sufficient quantities). Based on these insights, the CLG technology was subsequently to be investigated in small pilot-scale units with thermal inputs ranging from 20 to 200 kW<sub>th</sub>. Ultimately, these efforts were to lead up to the investigation of the CLG technology in 1 MW<sub>th</sub> scale, thus promoting it to TRL 5-6 and allowing for important inferences for operation of a full-scale (200 MW<sub>th</sub>) plant, which was to be designed and modelled within the project. These foreseen steps of the *CLARA* project are illustrated in Figure 2b.



---

## 1.2. Over-Archiving Research Goal and Primary Research Questions

With this overarching aim in sight, the primary research goal of this dissertation can be formulated, namely advancing the CLG technology from lab and small pilot-scale to the 1 MW<sub>th</sub> scale, thereby demonstrating its technical competitiveness and allowing for future up-scaling endeavors. From this main research goal, the four primary scientific questions of this dissertation are derived:

- (i) Is autothermal CLG operation in industry-like conditions generally viable?*
- (ii) Which process control measures and operational practices are necessary to allow for efficient autothermal chemical looping gasification?*
- (iii) What is a suitable process design of an industrial chemical looping gasifier, allowing for efficient conversion of biomass residues into a high-quality syngas?*
- (iv) Which bottlenecks and optimization avenues should be considered when striving for the industrial application of CLG?*

To get to the core of these underlying questions, it was key to firstly define a route through which the sought-after answers can be obtained. With the 1 MW<sub>th</sub> pilot testing being at the core of the defined research questions, a methodology allowing for a successful investigation of the CLG technology in 1 MW<sub>th</sub> scale was identified at the outset.

Generally, the demonstration of CLG in 1 MW<sub>th</sub> scale can be defined as a chemical engineering project, requiring the successful completion of certain well-defined milestones. Here, Towler and Sinnott [44] provide an overview of a universal strategy which is being used to tackle projects of this sort (see Figure A-1 in Section A.1 in the Appendix), with the general steps being:

- Project specification,
- Process definition & evaluation,
- Basic process design (=basic engineering),
- Detailed process design (=detail engineering),
- Procurement & construction,
- Start-up & operation.

The main steps of this methodology, which aims at the successful commercialization of a product through the erection of a greenfield chemical plant, can also be used for the given endeavor. However, certain adaptations in the approach are necessary, to account for the project peculiarities. On the one hand, the goal of the project has to be shifted from the commercialization of a specific product to the technical advancement of the investigated process. Secondly, the approach has to be changed from a greenfield approach, where all infrastructure

---

and equipment is newly designed and procured for the specific task at hand, to a brownfield approach, as the CLG technology was to be demonstrated using the existing 1 MW<sub>th</sub> pilot plant.

To account for the former, the structure by Towler and Sinnott [44] was adapted as illustrated in Figure 3 (see blue box). Here, plant operation does not aim at the production of a marketable product, but serves the purpose of demonstrating the technical feasibility of the CLG technology in 1 MW<sub>th</sub> scale (=proof of concept), deriving refined operational rules and concepts, generating data for up-scaling purposes (e.g. process model building), as well as optimizing the technology. These goals thus require an in-depth evaluation of the process, ideally under varying operating conditions, as well as the acquisition of operational experience, preferably under stable and optimized operating conditions. Moreover, the goal of process optimization converts the overall structure into an iterative approach, where process design, boundary and operating conditions, or operational principles are adapted based on operational experience and insights gained during process operation and evaluation.

The adjustments in the procedure necessary for a brownfield endeavor are also highlighted in Figure 3 (see orange box). Firstly, the existing equipment has to be considered during the initial process evaluation. For example, the existing reactors of the 1 MW<sub>th</sub> pilot unit narrowed down the attainable boundary conditions (e.g. system heat losses) and operating conditions (e.g. thermal load, reactor gas velocities, etc.) during CLG. Secondly, it is clear that detail engineering is not required for the existing equipment (see grey boxes in Figure 3). However, specifications of existing equipment have to be closely considered during basic and detail engineering of all plant adaptations and extensions, to safeguard conformity and compatibility between new and existing plant components. Moreover, space constraints of the existing facilities have to be taken into account when designing new equipment and plant adaptations.

All activities leading up to the successful operation of the 1 MW<sub>th</sub> CLG system and ultimately to the preparation of this cumulative thesis fall along the structure visualized in Figure 3. In the subsequent Section 1.3, these activities will be elucidated in detail to provide an overview over the work upon which this dissertation is founded. Moreover, the five research papers, being the core of this cumulative thesis, are categorized along the progression of this structure (see cyan boxes in Figure 3), in order to highlight their relation to the primary research questions, connect them to the overarching goal of this cumulative thesis, and emphasize the specific aspects covered within each of them.

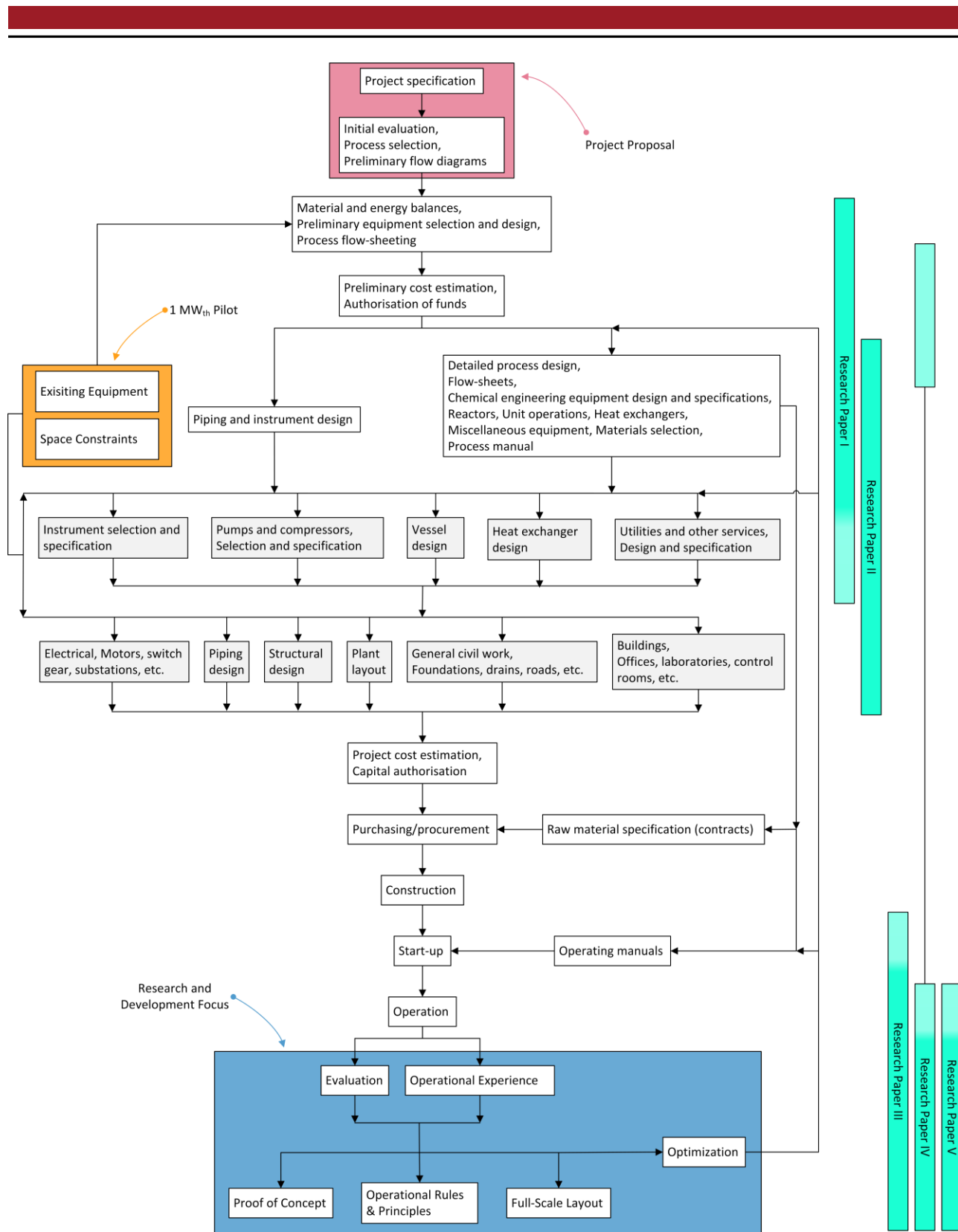


**Figure 3.** Structure of a chemical engineering project according to Towler and Sinnott [44]. Adapted for brownfield project (1 MW<sub>th</sub> pilot, see orange box) with research and development focus (see blue box). Grey shaded boxes indicate steps where only pilot plant adaptations and extensions had to be considered. The pink box indicates steps carried out during drafting of the project proposal (not scope of this dissertation). Cyan boxes indicate scope of the five research papers of this cumulative thesis.

---

### 1.3. Classification of the Scope of the Individual Research Papers

For the process definition, being the first step of the endeavor at hand, the project description and initial process evaluation were aligned with the *status quo* of the 1 MW<sub>th</sub> pilot plant, in order to establish the general boundary conditions of the project.<sup>1</sup> Using basic insights gained during detailed inspection and evaluation of the existing equipment of the 1 MW<sub>th</sub> pilot plant as well as simulation results obtained by deploying and adapting process models previously validated for CLC operation in 1 MW<sub>th</sub> scale [45], necessary plant adaptations and extensions were defined and an initial cost estimation of capital and operational expenditure was carried out. Subsequently, a first process flow diagram (PFD) was drafted, which is given in Figure 4. As indicated in this PFD in orange color, the following main adaptations and extensions were defined:

- Extension of the 1 MW<sub>th</sub> pilot plant with a syngas removal unit consisting of a hot gas filter, an induced draft fan, and a thermal oxidizer to allow for full conversion (=oxidation) and safe venting of the CLG product gas;
- Stream-lining of the reactor configuration of the 1 MW<sub>th</sub> unit to minimize heat losses during operation, thus enhancing overall process efficiency;
- Procurement of a new steam generator to safeguard sufficient steam supply during CLG operation and extension of the upstream water softening unit;
- Adaptation of the piping around the air reactor to allow for its fluidization with recirculated flue gas to enable control of the oxygen input into the CLG system;
- Adjustment & extension of analytic equipment to allow for meaningful process evaluation (e.g. tar measurement);
- Procurement of a new ash sluicing screw to allow for reliable material extraction from the AR during operation.

Apart from laying the foundation for the finalization of all basic engineering documents, drafting of the first layout of the 1 MW<sub>th</sub> CLG unit and calculation of the associated heat and mass balances provided meaningful insights into mechanics and fundamentals of an autothermal CLG process. While plant specific insights with regard to pilot plant adaptations and extensions were crucial for the advancement of the specific project, strategies allowing for autothermal CLG operation are of a universally applicable nature. Here, one important finding made during process simulation of the 1 MW<sub>th</sub> CLG system was that despite its closeness to the related chemical looping combustion process (CLC), alternative process control concepts are necessary for efficient CLG operation. This aspect, largely ignored in literature up to this point, was therefore established in a dedicated article, being the **first research paper** of this cumulative thesis. Here, it was shown

---

<sup>1</sup> As indicated in Figure 3 (pink box), the project specification and initial process evaluation were carried during the project application of the CLARA project and thus did not fall within the scope of this dissertation.

that in order to allow for efficient syngas production inside the CLG unit, heat and oxygen transport by the OC, circulating between AR and FR, have to be de-coupled. Building on this insight, different process control approaches to attain this de-coupling were introduced, thus paving the way for initial lab investigations under boundary and operating conditions meaningful for large-scale CLG systems (more details see Section 2.1-I). In order to do so, the first research paper of this cumulative thesis thus built on the information gathered during basic engineering of the process, i.e. the process definition, the calculation of the heat and mass balances, as well as the initial layout of the 1 MW<sub>th</sub> CLG system (see cyan box for RP-I in Figure 3) and formalized the most crucial findings to facilitate their consideration in all future studies.

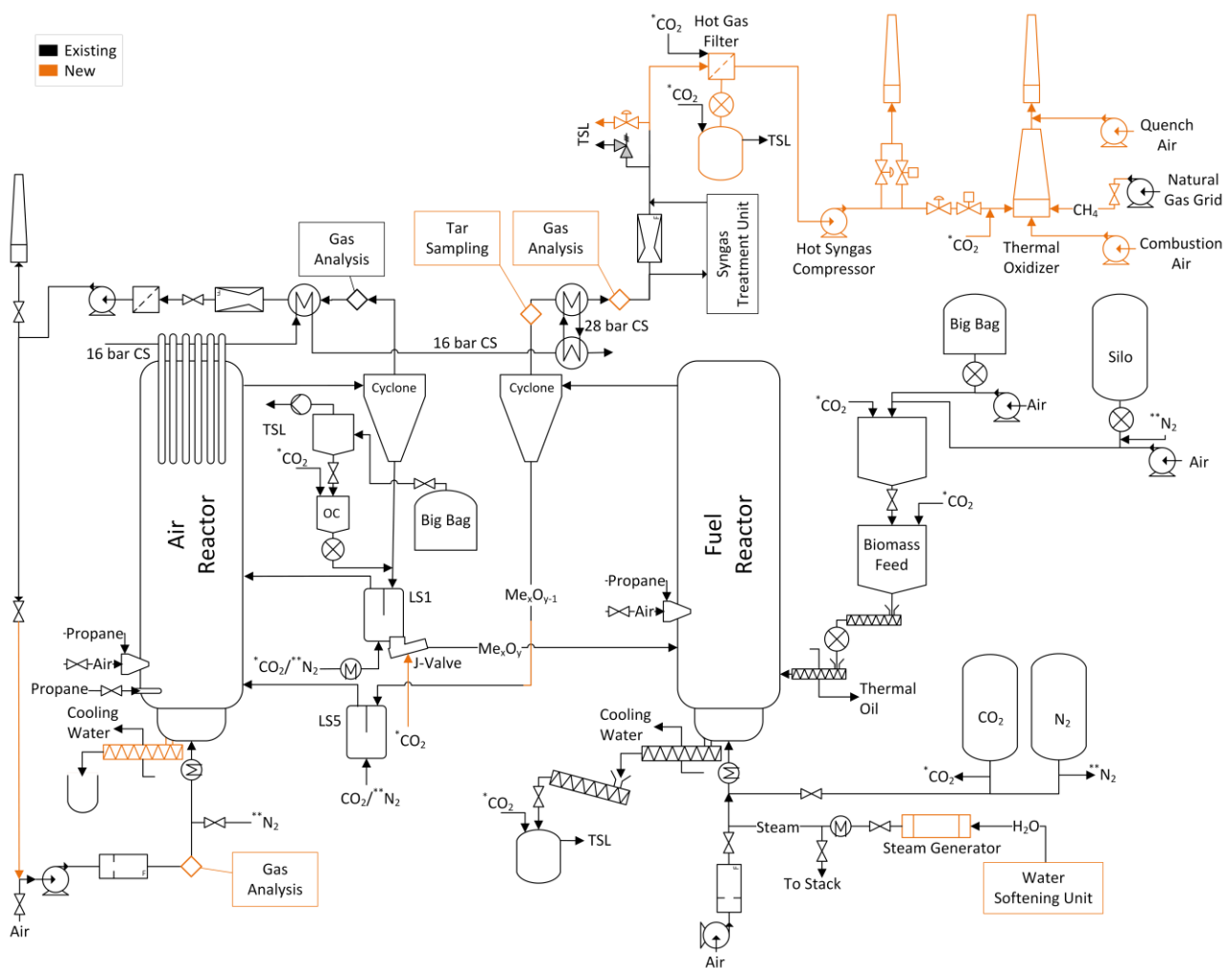


**Figure 4.** Plant configuration of the 1 MW<sub>th</sub> pilot plant for CLG operation. Pilot plant adaptations and extensions are marked in orange color. Abbreviations: CS=Cooling System, TSL=To Safe Location, OC/Me<sub>x</sub>O<sub>y</sub>=Oxygen Carrier. For explanation of the utilized symbols, please refer to Figure A-2 in Section A.1 in the Appendix.

---

On the basis of the previously derived basic engineering documents, the detail engineering of the 1 MW<sub>th</sub> CLG pilot plant was carried out. In a first step, all equipment was defined, allowing for the drafting of detailed PFDs for the entire pilot. Subsequently, a process manual was drafted, consisting of the following documents:

- Process description,
- Plant description,
- Description of pilot plant control (including safety measures),
- Layout and installation plan (including safety equipment).

Within these documents, the overall scheme of CLG operation in 1 MW<sub>th</sub> scale was defined, including information on start-up and shut-down sequences, process control, safety measures, and the general layout of the chemical looping gasifier. An example for this is provided in Figure A-4 in Section A.2 in the Appendix, showing a simplified schematic of the suggested operational procedure of the 1 MW<sub>th</sub> CLG unit. Apart from the illustrated process manual documents, process and instrumentation diagrams (PnID) for all relevant plant sections were drafted (see, e.g. Figure A-5 in Section A.2 in the Appendix), to define the final state of all vessels, piping, heat exchangers, process instrumentation, and actuators.

Based on these documents, an in-depth hazard and operability study (HAZOP) according to the international standard IEC 61882 was performed in cooperation with the company [Aichernig Engineering GmbH](#), to analyze deviations in technical systems that can result in operationally inhibiting or hazardous effects. For this purpose, the plant was divided into process-related subsystems and the effect of variations in all relevant process parameters (e.g. temperature too high, flow too low, etc.), also known as HAZOP ‘guidewords’, was analyzed. Based on the resulting failure scenarios, the existing measures for detecting, preventing, and controlling the ensuing effects were compared. Thereafter, additional measures were defined and documented in an action list, if the existing or documented measures were deemed insufficient to identify the cause of the deviation and/or to prevent the expected effects or to limit them to a tolerable level. In addition, any deficiencies in the documentation (PnID, operating manuals, etc.) were recorded in the action list so that they could be corrected later. The described review process during a HAZOP analysis is visualized in Figure A-3 in Section A.1 in the Appendix.

By incorporation of all items from the action list of the HAZOP analysis into the engineering documentation followed by the specification of all remaining plant characteristics (e.g. pipe isometries), the detail engineering of the 1 MW<sub>th</sub> CLG unit was finalized. The most relevant information on the design of the system was subsequently summarized in the **second research paper** of this dissertation, thereby not only showcasing the final plant layout, illustrated in

Figure 5, and the designated operational principle of the pilot, but also highlighting the operational range of the system in which process-wise investigations are facilitated. Through modelling the impacts of variations of different operating variables within this range, further insights into their postulated effect on process efficiency are highlighted in this work, thereby also illuminating crucial differences in system behavior in comparison to externally heated (lab-scale) CLG units. Moreover, potential bottlenecks of the implementation of the CLG process in 1 MW<sub>th</sub> scale were derived, providing room for optimization via adaptations of the underlying operating principles or the plant layout (more details see Section 2.1-II). Ultimately, the second research paper thus not only provides an overview over the plant layout, but also underlines the necessity for the investigation of the CLG technology in autothermal conditions in order to obtain a holistic understanding of the behavior of an industrial-scale chemical looping gasifier.

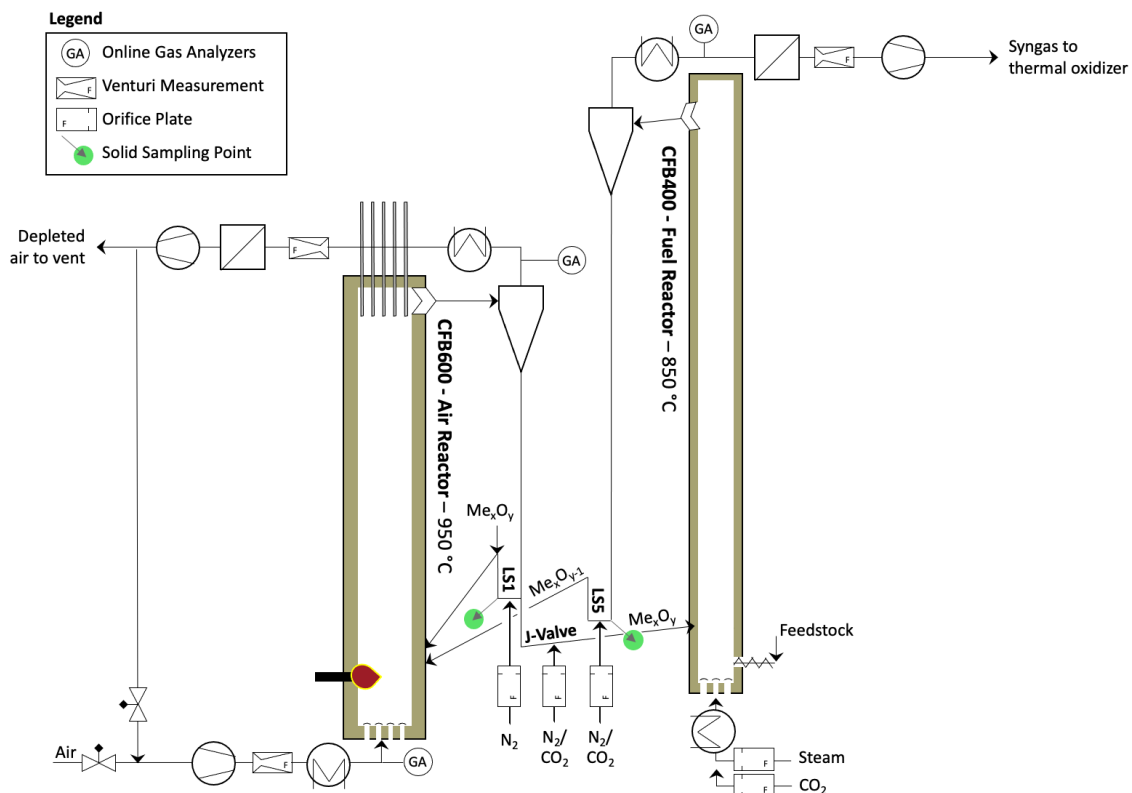


**Figure 5.** Simplified flow diagram of the 1 MW<sub>th</sub> CLG pilot plant. For explanation of the utilized symbols, please refer to Figure A-2 in Section A.1 in the Appendix.

Following the finalization of the detail engineering, procurement and construction of the pilot plant adaptations and extensions was pending. While the steps related to procurement and construction are not of a higher academic relevance, they constitute an integral part of any chemical engineering project (see Figure 3). Consequently, they can be considered to be a means to an end (i.e. 1 MW<sub>th</sub> CLG operation) and ultimately constitute an essential bridge between the primary research questions (i)-(iii), related to process definition and plant engineering, and

research question (iv), covering pilot plant operation and optimization, of this dissertation. Therefore, the general procedure pursued during procurement and construction is briefly exemplified for the syngas removal unit, being the most extensive implemented pilot plant adaption, hereinafter.

Using the technical requirements specified during detail engineering, orders for the individual components (e.g. hot gas filter, induced draft fan, thermal oxidizer) were placed, after techno-economic evaluation of the different available options. Once the final technical documentation from all suppliers was obtained, it was realized that erection of the syngas removal unit outside of the 1 MW<sub>th</sub> facility was necessary due to space constraints. Hence, a first layout for the given pilot plant adaption was created for the designated construction site (see Figure 6a) and a building permit was drafted at the responsible building authority. After receiving the positive notification from the authority, all sub-tasks related to construction (e.g. construction of the base plate, delivery and assembly of all main components, and manufacturing and fitting of all pipes) were outlined and scheduled. In parallel, the final layout of the syngas removal unit was defined (see Figure 6b), to be able to specify and plan all pending tasks. After successful construction of the bottom plate (see Figure 6c.1), the main components were delivered and assembled (see Figure 6c.2), before all connecting and auxiliary piping was installed. Finally, the measurement and control equipment was installed (see Figure 6c.3), signifying the completion of the dedicated construction project and the beginning of the subsequent commissioning phase.

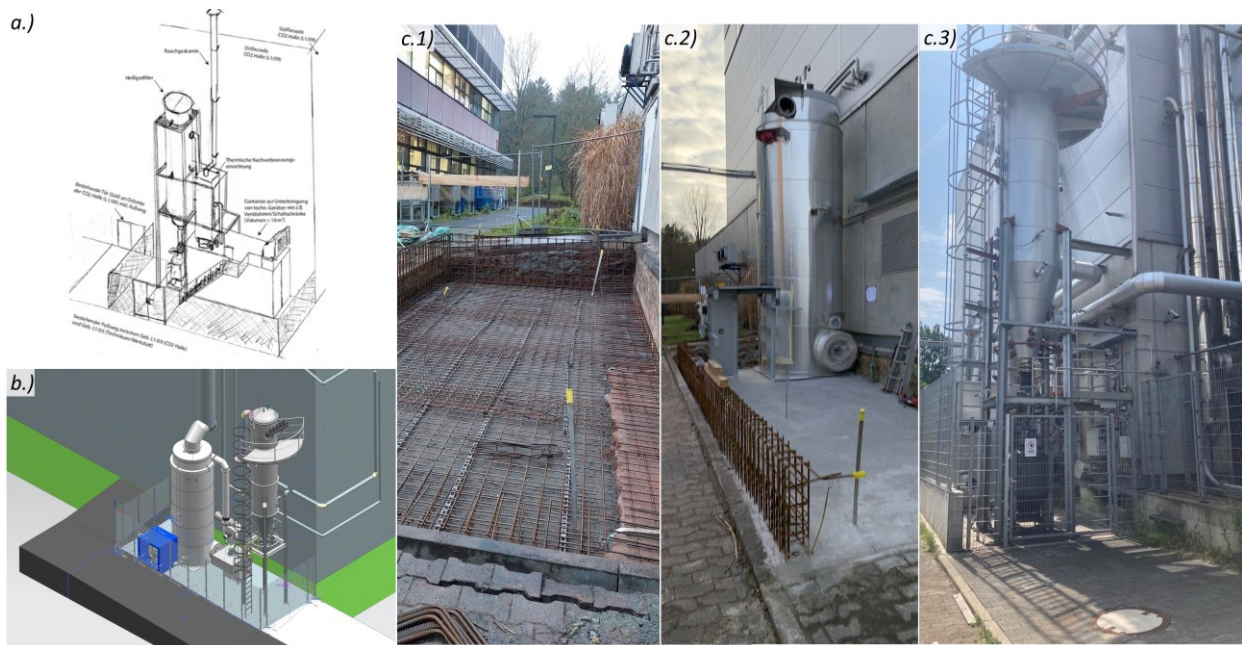


**Figure 6.** a.) Initial sketch of installation plan of syngas removal unit b.) CAD model of final installation plan of syngas removal unit. c.) Photographs of construction progress during erection of thermal oxidizer. 1.) Construction of bottom plate, 2.) Delivery and on-site assembly of equipment, 3.) Final syngas removal unit including all piping and measurement equipment.



Asides from new plant parts, existing equipment was also modified and/or adjusted according to the action list from the HAZOP analysis. Here, one crucial step was the reprogramming of the entire process control system (PCS) of the 1 MW<sub>th</sub> pilot plant, in order to allow for safe CLG operation. Apart from transferring the entire relevant measurement and automation equipment into a software environment with a sufficient safety integrity level, this meant implementing the refined safety logic matrix into the PCS. This safety matrix encompasses the associated safety shut-downs (see Figure 7a) and the automatic switch-overs between the available FR product gas routes (see Figure 7b), which transfer the pilot plant into a safe state in case of issues with different plant parts. This implementation was carried out using logic plans created by [Aichernig Engineering GmbH](#) on the basis of the results of the HAZOP analysis (see, e.g. Figure A-6 in Section A.2 in the Appendix).

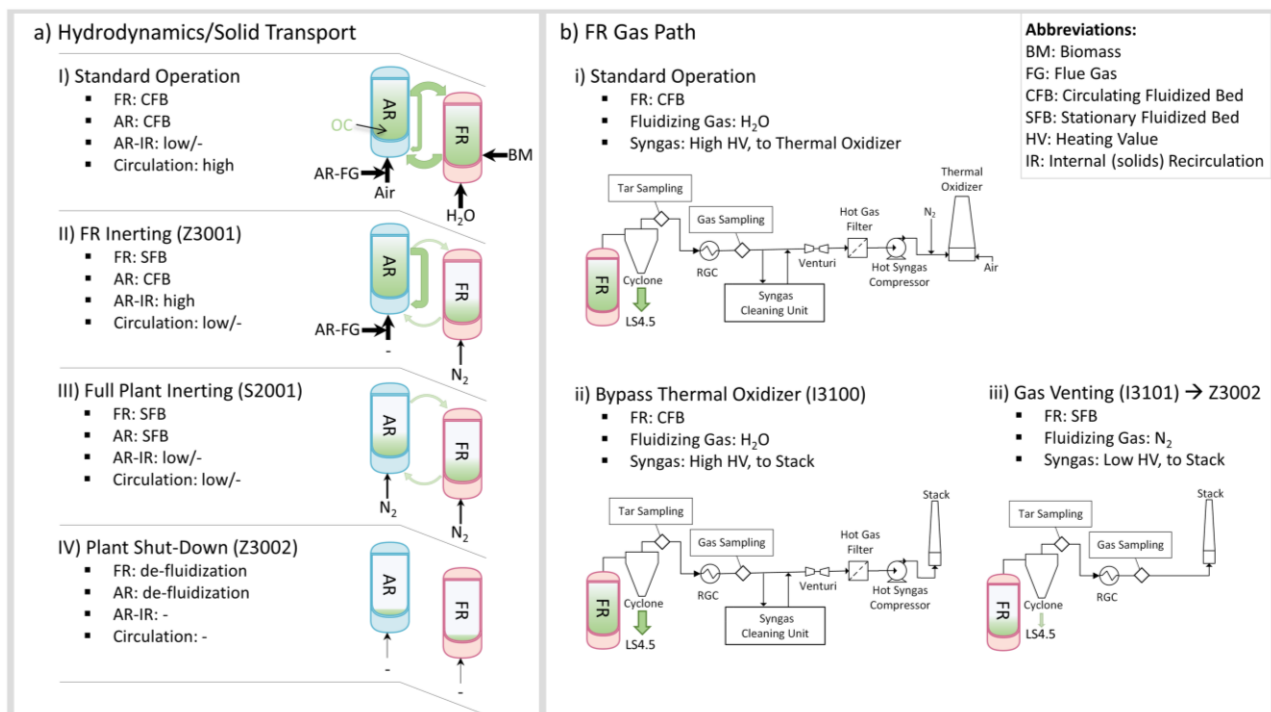


**Figure 7.** Overview of effect of dedicated shut-down sequences (Z-/S-/I-XXXX) on: a) Fluidizing modes (I-IV) in 1 MW<sub>th</sub> chemical looping gasifier and b) gas path of FR product gas (i & ii). For explanation of the utilized symbols, please refer to Figure A-2 in Section A.1 in the Appendix.

With the detail engineering of the 1 MW<sub>th</sub> CLG unit as well as the operational principles having been defined, the relevant operating manuals, consisting of the following documents, were drafted prior to system start-up:

- Training material for plant operators of the 1 MW<sub>th</sub> chemical looping gasifier,
- Experimental plan detailing the over-arching goal of pilot plant operation,
- Check-lists for start-up, operation, and shut-down of all relevant pilot plant sub-systems,
- Quick operational guide for the 1 MW<sub>th</sub> chemical looping gasifier for plant operators.

With the aid of these documents, the 1 MW<sub>th</sub> pilot plant was successfully operated in CLG mode within a two-week test campaign between March and April 2022. Here, approx. 110 h of CLG operation with industrial wood pellets (IWP) were achieved, thereby providing proof of concept for the feasibility of autothermal chemical looping gasification for the first time ever. Moreover, numerous crucial findings with regard to process and plant optimization, plant operability, process mechanics, and potential bottlenecks for process up-scaling were derived through subsequent process evaluation. One of these findings is related to the utilization of the novel process control concept, which was previously derived based on process simulations (more details see Section 2.1-I) and validated in lab [17, 35] and small pilot-scale [21, 46], in the 1 MW<sub>th</sub> scale. As illustrated in Figure 8, this process control concept allows for a de-coupling of heat and oxygen transfer between FR and AR and thus facilitates efficient CLG operation (i.e. high cold gas efficiency,  $\eta_{CG}$ ) by targeted exploitation of the dual-purpose of the OC (more details see Section 2.1-III).

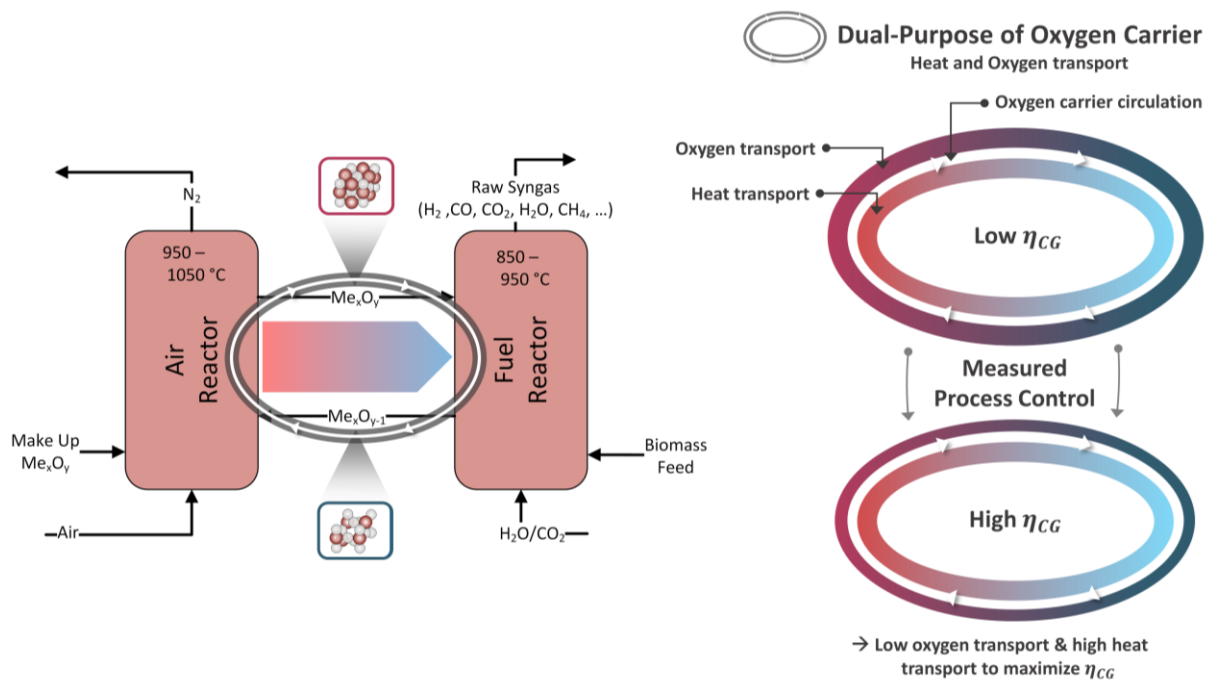


**Figure 8.** Graphical abstract of RP-III, illustrating the most important topic of the article, i.e. developing and demonstrating a process control concept for autothermal CLG in 1 MW<sub>th</sub> scale.

The first-ever utilization of this control concept in an autothermal setup did not only provide unique insights into its general viability, but also allowed for in-depth discernments regarding the governing mechanisms of an autothermal chemical looping gasifier, considering both internal process-wise interactions (e.g. effect of reactor temperature on reaction kinetics) as well as the interaction between the gasifier and its surroundings (e.g. heat losses). These findings are elaborated in detail in the **third research paper** of this dissertation. Discovery of these

---




interactions consequently significantly enhanced process understanding, on the one hand simplifying future up-scaling of the process, as novel full-scale plants can be designed to make use of these interactions most effectively, while minimizing negative feedback loops. On the other hand, the gained insights also provided novel avenues for optimizing process efficiency in 1 MW<sub>th</sub> scale, most substantially through fine-tuning of the operational principles used during pilot operation. Consequently, the scope of the third research paper stretches from the (re-)drafting of the operational manuals and system start-up to the final process evaluation, which is illustrated in Figure 3 (see cyan box for RP-III).

Using the insights gathered during the first 1 MW<sub>th</sub> test campaign (K1), minor optimizations and adaptations of the 1 MW<sub>th</sub> pilot were carried out. In combination with the enhanced operational principles, this led to the accomplishment of attaining more than 210 hours of chemical looping gasification operation with pine forest residue (PFR) pellets in June 2022. Apart from the enhanced stability and predictability of the process, process efficiency was also vastly improved, allowing for the production of a higher-quality syngas, with cold gas efficiencies up to 50 % being obtained [47]. Subsequent to this second test campaign (K2), further optimizing and refining of the 1 MW<sub>th</sub> plant ensued prior to the operation of the chemical looping gasifier with wheat straw pellets (WSP) during the third test campaign (K3) in August 2022. Here, the effect of the low-melting feedstock ash on CLG process efficiency was evaluated and the mechanism responsible for the observed agglomeration was defined based on an in-depth investigation of the governing process conditions and analysis of the formed agglomerates retrieved from the CLG system during operation. A summary of all three accomplished 1 MW<sub>th</sub> CLG test campaigns is given in Table 1.

After successful completion of the third and final CLG test campaign, yielding a total of more than 400 hours of chemical looping operation, the focus was shifted to the in-depth investigation of the generated data-set, consisting of recorded process live-data (e.g. pressure and temperature signals) as well as data from offline sampling (e.g. solid and tar samples). During process evaluation, the following focus points were set:

- Final optimization of the layout and operating principles of the 1 MW<sub>th</sub> chemical looping gasifier for future CLG pilot testing;
- Determination of the most crucial findings in terms of process efficiency, plant operability, and optimization avenues, universally applicable in any CLG setup, with special focus on autothermally operated large-scale (>50 MW<sub>th</sub>) CLG units;
- Establishing of a meaningful dataset from all three test campaigns, allowing for modelling of all crucial plant parts, to derive an auspicious full-scale reactor layout and optimized operating conditions;
- Determination of potential bottlenecks for process up-scaling and development of viable mitigation or overcoming strategies.

**Table 1:** Overview over main boundary conditions and findings from the three 1 MW<sub>th</sub> CLG test campaigns (KX). Euro coin in feedstock photographs for scale. Oxygen carriers: ilmenite fine (ILMf), ilmenite coarse (ILMc).

#	Feedstock Photograph	Feedstock Conversion	Oxygen Carrier	1 MW <sub>th</sub> Plant Operation	Main Findings
K1 - IWP		40 t (CLG: 20 t)	ILMf ( $d_{p,m}$ : 111 $\mu$ m)	20.03.22 - 16.04.22 (CLG: ~110 h)	<ul style="list-style-type: none"> <li>• Demonstration of autothermal CLG</li> <li>• Successful utilization of novel CLG control concept</li> </ul>
K2 - PFR		50 t (CLG: 40 t)	ILMf ( $d_{p,m}$ : 111 $\mu$ m) ILMc ( $d_{p,m}$ : 199 $\mu$ m)	15.06.22 - 30.06.22 (CLG: >210 h)	<ul style="list-style-type: none"> <li>• Stable multi-day CLG operation</li> <li>• Investigation of effect of CLG operating conditions</li> <li>• Optimization of CLG process efficiency</li> </ul>
K3 - WSP		30 t (CLG: 10 t)	ILMf ( $d_{p,m}$ : 111 $\mu$ m)	24.08.22 - 01.09.22 (CLG: ~80 h)	<ul style="list-style-type: none"> <li>• Assessment of effect of low-melting feedstock ashes on CLG efficiency</li> <li>• Investigation of OC-ash agglomeration phenomena in CLG systems</li> </ul>

During evaluation of all three test campaigns, it was found that controlling system hydrodynamics and especially solid entrainment from the two reactors is key when striving for efficient CLG operation. Therefore, these aspects were analyzed in detail making use of the dataset gathered during 1 MW<sub>th</sub> pilot testing, as well as data from preceding tests in a down-scaled cold flow model. Originally, the latter was used to define the underlying hydrodynamic operational principles of the reactor system during basic engineering (see top cyan box for RP-IV in Figure 3). These rules, specifying the hydrodynamic operational window of the dual-circulating fluidized bed system and allowing for tailored adjustment of hydrodynamic process conditions during CLG operation, were later found to be largely applicable in 1 MW<sub>th</sub> scale. Using the insights gathered during autothermal CLG operation in the 1 MW<sub>th</sub> pilot, they were further refined (see Figure 9), allowing for a targeted operation of the reactor system inside the entire defined operating window. The resulting formalized hydrodynamic operational rules are presented in the **fourth research paper** of this cumulative dissertation.

Additionally, it was found that accurate determination and prediction of the solid circulation between fuel and air reactor are necessary for meaningful process evaluations. Consequently, a

novel method for determining this process variable, relying on the collection of solid samples from both loop seals of the reactor system (see Figure 5), was developed [48]. Building on the dataset generated by this method and using the live-data obtained during 1 MW<sub>th</sub> pilot testing and operation of the down-scaled cold flow model, a novel easily-applicable approach for estimation of solid entrainment from any circulating fluidized bed (CFB) system, solely relying on readily-available live data, was developed. The derivation and application of this approach is also detailed in the fourth research paper (more details see Section 2.1-IV), allowing for its application in any CFB system, regardless of the underlying application purpose. Consequently, the fourth research paper encompasses all relevant findings in terms of system hydrodynamics, established during engineering and operation of the 1 MW<sub>th</sub> CLG unit, and thus signifies a crucial building block for the up-scaling of the technology to commercial scale.

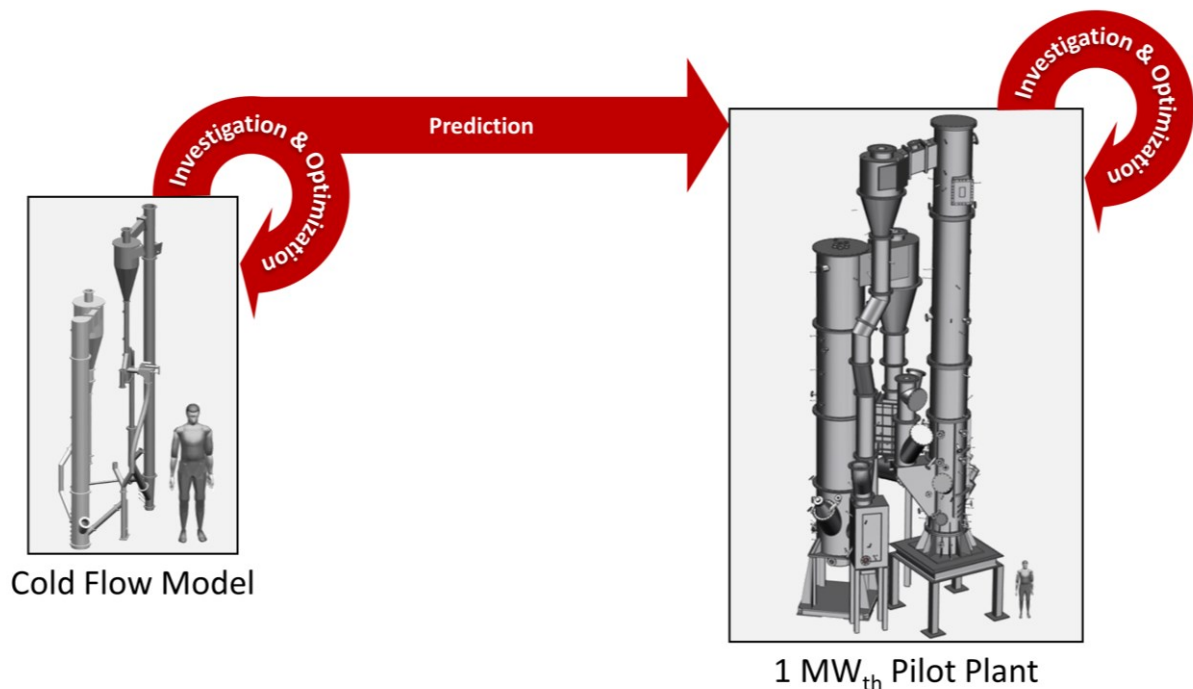


**Figure 9.** Graphical abstract of RP-IV, illustrating the most important topics of the article, i.e. investigating and optimizing system hydrodynamics of the 1 MW<sub>th</sub> CLG unit, using data from a down-scaled cold flow model and from autothermal 1 MW<sub>th</sub> CLG operation.

Another crucial aspect for process optimization and up-scaling is the performance and lifetime of the oxygen carrier, transporting heat and oxygen between the AR and FR during chemical looping gasification. With initial studies showing that the lifetime of the OC is lower for CLG in comparison to chemical looping combustion operation [17], OC consumption might become a hindrance in full-scale CLG units. To cast a light onto this aspect, the fate of ilmenite, used as oxygen carrier during all three 1 MW<sub>th</sub> CLG test campaigns (see Table 1), was investigated, using a variety of methods ranging from well-established laboratory analyses for OC characterization

(e.g. thermogravimetric analysis, scanning electron microscopy) [49, 50] to general observations and online data gathered during pilot testing. A representative selection of the more than 350 solid samples collected during 1 MW<sub>th</sub> CLG operation was analyzed using these methods, yielding a holistic picture of the fate of the oxygen carrier in industrially relevant process conditions. These results, which provide unique insights into the morphological, physical, and chemical changes the oxygen carrier undergoes during CLG operation in the 1 MW<sub>th</sub> scale are summarized in the **fifth research paper** of this cumulative dissertation. As illustrated in Figure 10, the effects of mechanical and chemical strain as well as the impact of feedstock interactions the OC is exposed to inside the CLG unit were investigated in order to determine the most important drivers of OC wastage. After identification of these drivers, approaches to decrease OC losses were established (more details see Section 2.1-V). Hence, important facets with regard to process optimization and up-scaling of the CLG technology were derived through these evaluations (see cyan box for RP-V in Figure 3). In summary, the fifth research paper thus not only provides insights into the fate of the OC during CLG operation in industry-like conditions, but also provides auspicious measures to improve OC lifetime and durability inside an industrial chemical looping system.

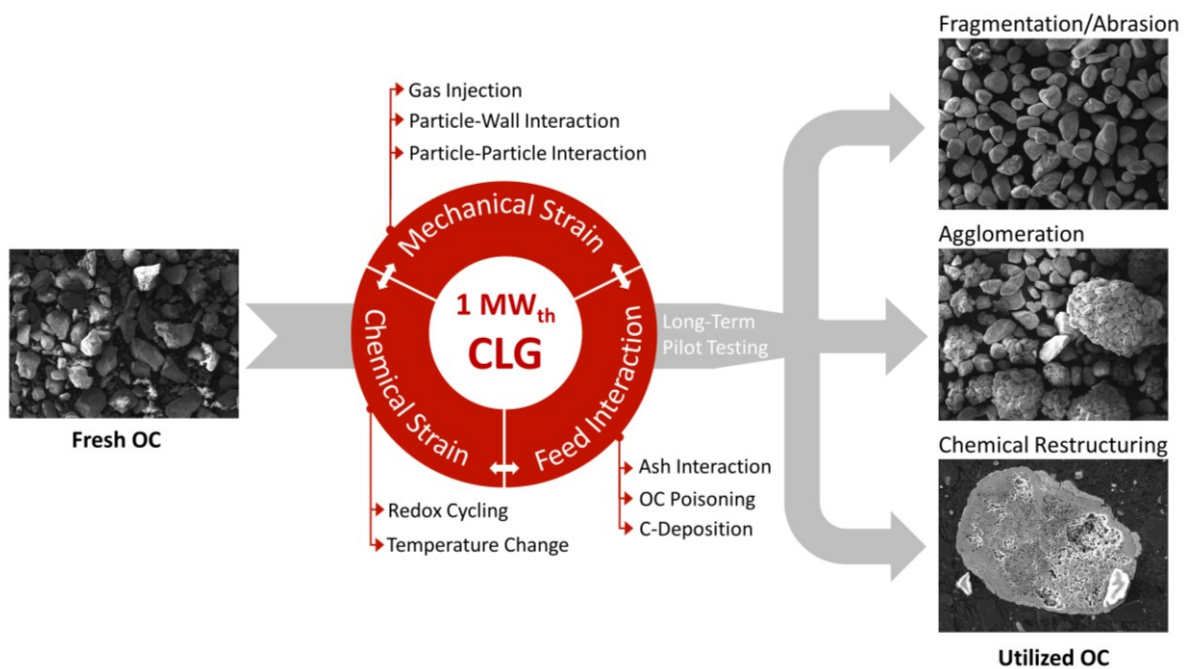


**Figure 10.** Graphical abstract of RP-V, illustrating the most important topics of the article, i.e. analyzing the fate of the OC during long-term pilot testing in 1 MW<sub>th</sub> scale.

## 1.4. Summary of Research Scope

All in all, the five research papers forming the core of this cumulative dissertation fall along the general structure of the underlying engineering project, illustrated in Figure 3, aiming to advance the CLG technology from small pilot to the 1 MW<sub>th</sub> scale. To achieve this over-arching goal connecting the five research papers, all tasks associated to this structure were successfully executed between April 2019 and September 2023. The basic steps of this structure are visualized in Figure 11 together with a temporal classification of the progress achieved within the project. As illustrated, the five research papers extend over the entire duration of this progress, incorporating the most crucial scientific findings, and thus cover all major aspects of the engineering project.<sup>2</sup>

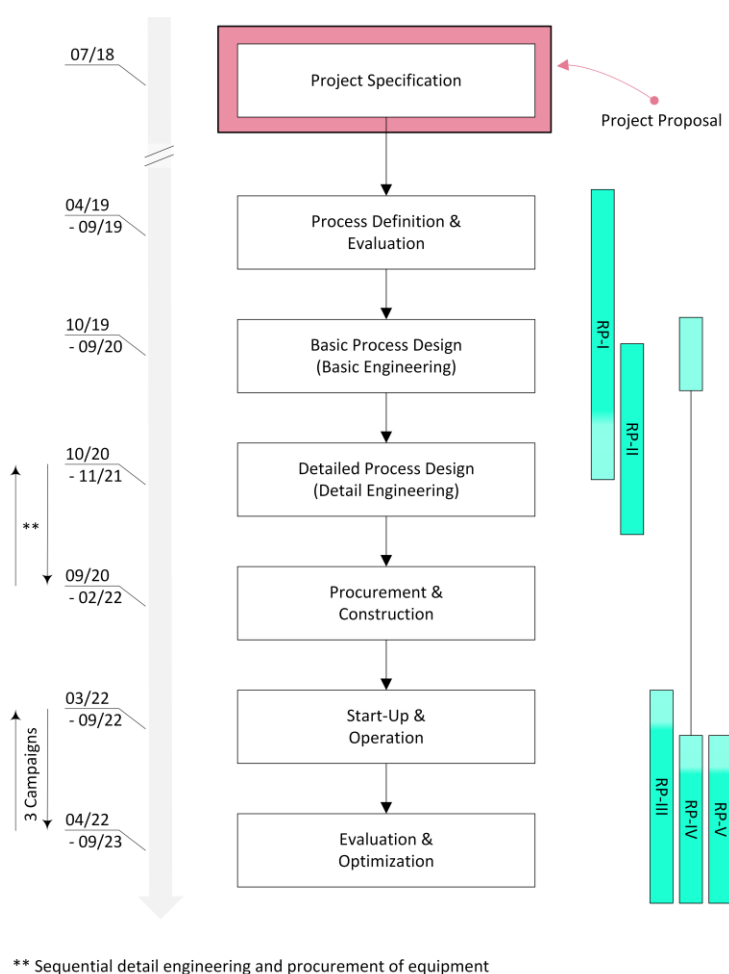


**Figure 11.** Basic steps of a chemical engineering project, with the timeline (grey arrow) followed for the validation of CLG in 1 MW<sub>th</sub> scale. The pink box indicates steps carried out during drafting of the project proposal (not scope of this dissertation). Cyan boxes indicate scope of the five research papers (RP) of this cumulative thesis.

<sup>2</sup> Aspects not covered within the research papers of this cumulative dissertation are the project specification, which was part of the project proposal drafted before the commencement of this dissertation (see pink box in Figure 11), as well as the procurement & construction step, not yielding any scientifically significant insights.

---

Through completing the relevant steps defined for this research project, all process fundamentals relevant for the implementation of the CLG technology in 1 MW<sub>th</sub> scale were defined, yielding a novel process control concept, which allows for efficient CLG operation (RP-I). Building on the resulting heat and mass balances and using the layout of the existing 1 MW<sub>th</sub> pilot plant, an optimized and dedicated CLG plant layout was devised during basic and detail engineering (RP-II). After successful commissioning of all plant components and subsequent system start-up, autothermal CLG operation was demonstrated, providing the first ever proof of concept of its technical viability in an industrially relevant scale and illustrating its governing process mechanics (RP-III). Finally, the datasets generated during three CLG test campaigns were utilized to analyze crucial aspects for optimization and process scale-up in detail, thus paving the way for further investigation of the CLG technology in large-scale (RP-IV & RP-V).

In the subsequent Synthesis of this dissertation (Chapter 2), the most important results from the five research papers of this dissertation, covering the above-stated topics, will be detailed, thus providing answers for the four primary research questions (i)-(iv), which were defined within this chapter.



---

## 2. Synthesis

---

### 2.1. Main Research Findings

After establishing the goal and primary research questions of this cumulative dissertation in the Introduction (Chapter 1), this chapter will conclusively illustrate how the main research findings from the five research papers answer those questions, hereinafter.

#### *Research Paper I*

The **first research paper** aimed at casting light onto the first (*i*) research question, related to the viability of CLG in industrial scale, by calculating the heat and mass balances of the CLG process in 1 MW<sub>th</sub> scale, using a simplified chemical equilibrium simulation approach. Here, the effect of different operating conditions (e.g. reactor temperatures, OC circulation, steam-to-biomass ratio) on process efficiency was evaluated. Within the scope of these endeavors, it was established that for OCs generally used for chemical looping purposes (e.g. ilmenite), a de-coupling of heat and oxygen transfer between the AR and FR is necessary to attain efficient CLG operation. This is the case as large heat fluxes between the two reactors are necessary to sustain the endothermic chemical reactions occurring in the FR, while excessive oxygen release in the FR has to be prevented to avoid full feedstock oxidation. Different process control measures allowing for this were evaluated, with results indicating that restricting the air supply in the AR, thereby decreasing the overall air-to-fuel equivalence ratio ( $\lambda$ ) of the process, is the most beneficial approach. Here, the underlying idea is that by decreasing  $\lambda$ , the circulating OC ( $\dot{m}_{oc}$ ) is not fully oxidized inside the AR, which means that its full heat transport capacity is exploited, while only a fraction of its oxygen transport capacity is utilized. These results are illustrated in Figure 12, showing simulation results for a 1 MW<sub>th</sub> CLG unit operated using this process control strategy. Figure 12a shows that the oxygen-carrier to fuel ratio ( $\phi$ ), relating the oxygen transported by the OC to the FR to the oxygen required for full feedstock conversion, is controlled by the air-to-fuel equivalence ratio for  $\lambda$ -values smaller than unity. This means that once the air input to the AR is reduced to attain  $\lambda < 1$ , the oxygen release in the FR is restricted and the feedstock is only partially oxidized. Due to the incurring decrease in exothermic full-oxidation reactions, FR temperatures decrease, yet they are maintained at elevated levels above 900 °C, due to the sustained OC circulation between AR and FR (see Figure 12b). Similar to FR temperatures, the net heat release of the process ( $\dot{Q}_{net}$ ) decreases with decreasing  $\lambda$ , as more endothermic gasification reactions occur inside the FR, which is illustrated in Figure 12c. To attain an autothermal process (i.e.  $\dot{Q}_{net}=0$ ), air-to-fuel equivalence ratios in the range of 0.35-0.4 are necessary, giving a first indication on suitable boundary and operating conditions for full-scale operation. Within this  $\lambda$ -range, cold gas efficiencies ( $\eta_{CG}$ ) between 60 and 65 % are attainable, which is illustrated in Figure 12d. Overall, the findings thus illustrate that autothermal CLG operation is viable in theory

by using the novel process control strategy developed within this work. Thereby, first advances towards answering the first **(i)** and second **(ii)** research question of this dissertation are presented in the first research paper, by demonstrating the general viability of CLG in industrial scale and presenting a suitable process control concept.

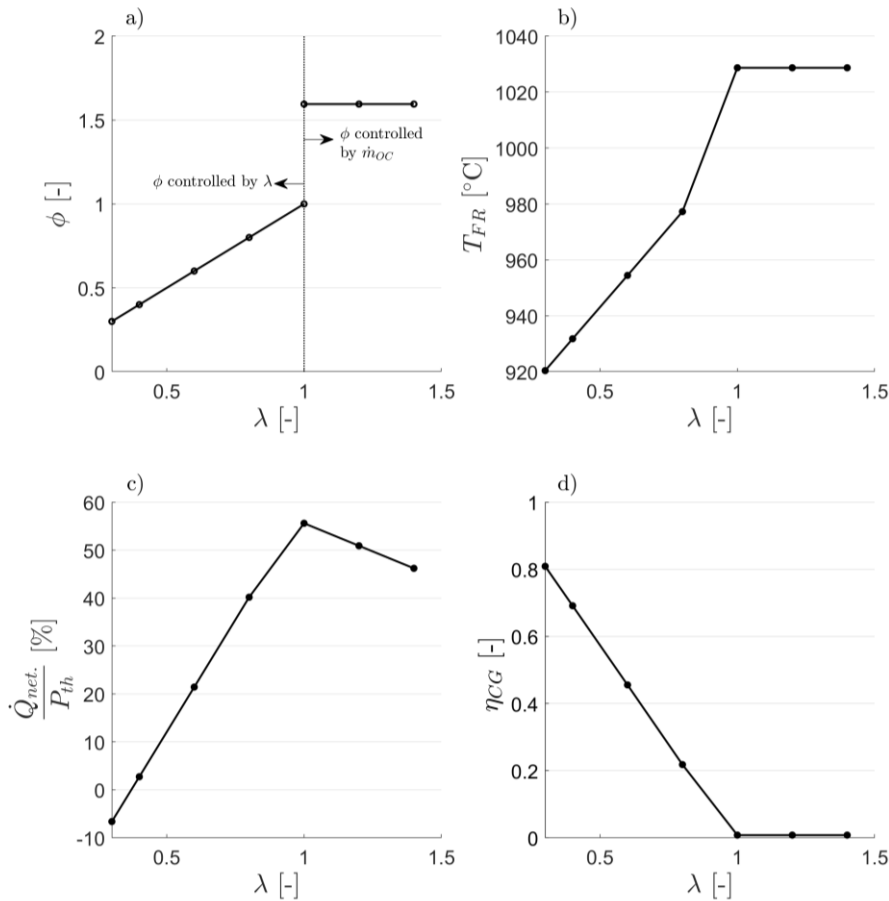


**Figure 12.** Simulation results for CLG operation through reducing  $\lambda$ . OC-to-fuel ratio as a function of the air-to-fuel equivalence ratio (a). Fuel reactor temperature (b), relative net process heat (c), and cold gas efficiency (d) for different values of  $\lambda$  ( $\dot{m}_{OC} = \text{const.}$ ). Adopted from RP-I.

Subsequently, the effects of variations in the most important operating conditions on process efficiency were simulated, to cast further light onto the process parameters and operational principles which should be pursued when using the novel process control concept during CLG in 1 MW<sub>th</sub> scale. The results of these endeavors are illustrated in Figure 13, showing that when assuming chemical equilibrium, cold gas efficiencies can be maximized by minimizing the steam-to-biomass ratio (see Figure 13a, b), minimizing the OC circulation rate<sup>3</sup> (see Figure 13c, d),

<sup>3</sup> This finding only is true if the OC circulation is sufficiently high to guarantee a stabilization of FR temperatures and the OC reactivity in the FR is high enough to allow for sufficient oxygen release driving the gasification reactions. The increase in process efficiency with decreasing OC circulation rate is mainly attributed to the utilized assumption that OC make-up rates increase with increasing OC circulation. Generally, large OC rates should be targeted in industrial CLG systems to boost process efficiency (see Section 2.2).

maximizing inlet temperatures of the fluidization gases (see Figure 13e, f), and limiting AR temperatures (see Figure 13g, h). When employing these approaches, process efficiency can be enhanced, as energy requirements for bringing inlet streams to reactor temperatures are reduced, yielding cold gas efficiencies exceeding 75 %. This means that by using the simplified simulation approach, first potential avenues for process optimization were also illuminated in RP-I, thus providing first insights towards answering research question (iv).

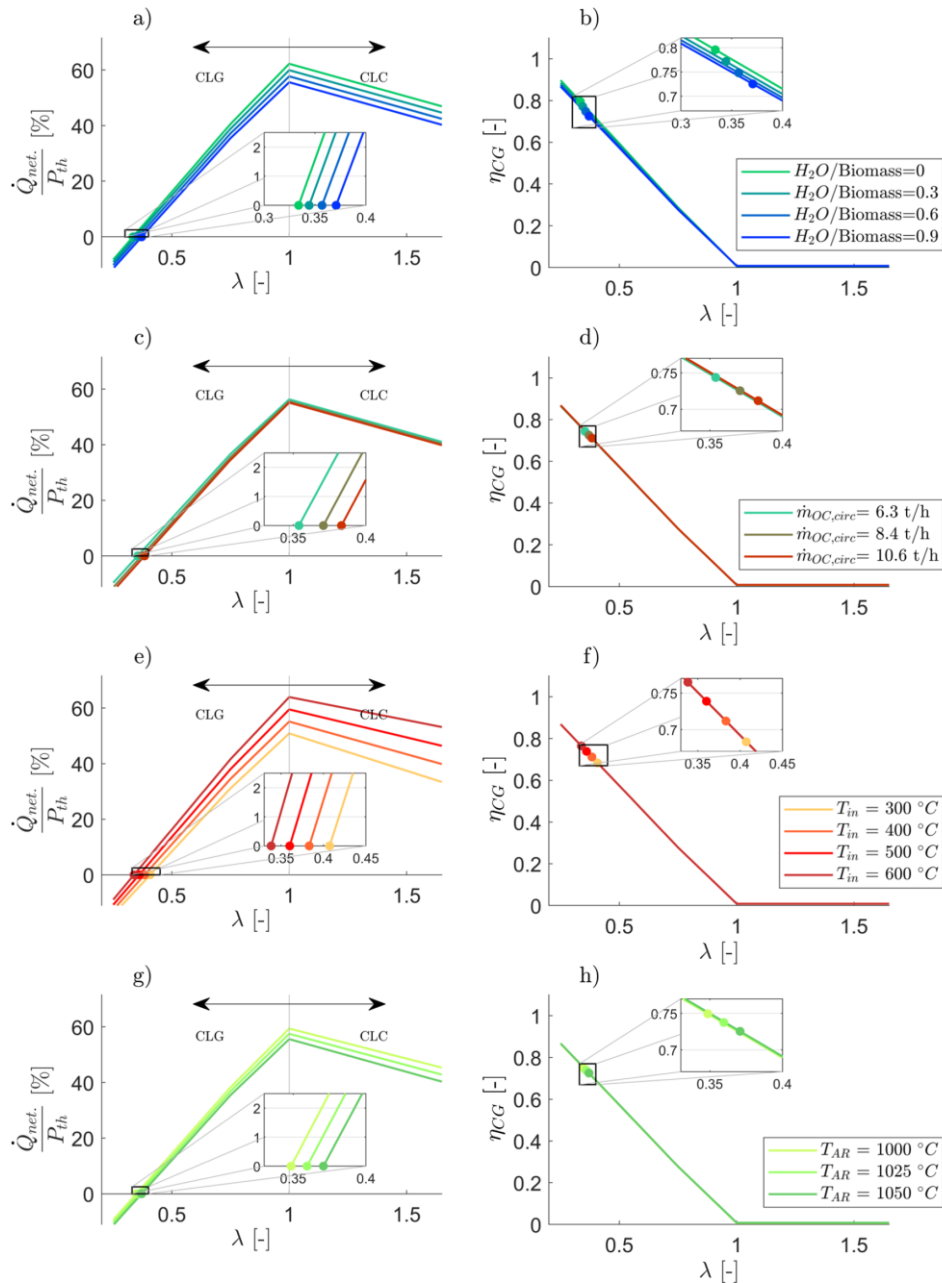


**Figure 13.** Net heat release and cold gas efficiency for CLC/CLG process as a function of the air to fuel equivalence ratio for different steam to biomass ratios (a,b), OC circulation rates (c,d), gas inlet temperatures (e,f), and air reactor temperatures (g,h). Circles mark the cold gas efficiency for autothermal CLG operation ( $\dot{m}_{OC} = \text{const.}$ , so  $\phi = \lambda$  for  $\lambda < 1$  and  $\phi = \text{const.} > 1$  for  $\lambda > 1$ ). Adopted from RP-I.

## Research Paper II

Making use of the calculated heat and mass balances, suitable adaptations of the existing 1 MW<sub>th</sub> pilot plant were formulated and implemented in order to allow for autothermal CLG operation (more details see Section 1.3), yielding the final layout of the 1 MW<sub>th</sub> chemical looping gasifier. This layout is presented in detail in the **second research paper**, marking a crucial milestone towards answering the third **(iii)** research question of this cumulative dissertation, i.e. the development of a suitable process design for industrial CLG operation. Apart from the general reactor configuration, shown in Figure 14, and the overall plant setup including auxiliaries (see Figure 5), all measurement equipment crucial for process supervision, control, and evaluation is also detailed in this article, facilitating future CLG up-scaling endeavors.

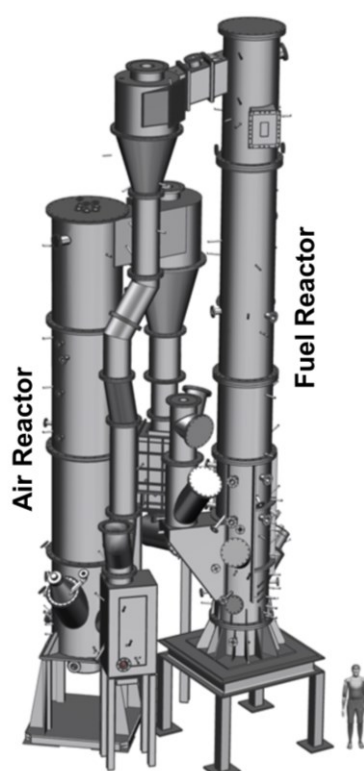


**Figure 14.** 1 MW<sub>th</sub> CLG reactor configuration including main coupling elements. Adopted from RP-II.

On the basis of the finalized plant layout as well as further refined process simulations, considering all its capabilities and limitations, the main adjustable operating variables in the 1 MW<sub>th</sub> unit were established, to cast further light onto the second **(ii)** research question, related to suitable process control concepts. Here, the following parameters, allowing for an optimization of process efficiency, were defined:

- Thermal load of the CLG system, adjusted via feedstock supply to the FR,
- Oxygen transport to the FR, controlled via air supply and flue gas recirculation in the AR,
- OC circulation, adjusted via the hydrodynamic operating conditions (esp. fluidization velocities, more details see RP-IV),

- 
- AR and FR reactor inventories, adjusted via OC make-up rates as well as the distribution of solids within the system (controlled by system hydrodynamics),
  - Staging of fluidization medium for the FR, directly controlled via dedicated control systems.

In doing so, the overall scope of the operating manual, clearly specifying the process control measures and operational practices used during subsequent CLG operation inside the 1 MW<sub>th</sub> pilot, was defined, paving the way for the first ever demonstration of autothermal CLG operation.

### *Research Paper III*

Application of these during the first CLG test campaign (K1), allowed for stable operation of the 1 MW<sub>th</sub> chemical looping gasifier with industrial wood pellets (IWP, see Table 1), confirming the theoretical findings made before and thereby validating that autothermal CLG operation in industrially relevant conditions is possible. Thus a conclusive answer for the first *(i)* research question, related to the viability of CLG in industrial conditions, was found. These findings are summarized in the **third research paper** of this dissertation, where, apart from delivering proof of concept for autothermal CLG operation, initial findings regarding the attainable key performance indicators of the CLG process, such as cold gas efficiency and carbon conversion as well as their inherent trade-offs, are provided. For example, it was shown that cold gas efficiencies up to 35 % can be attained in the 1 MW<sub>th</sub> CLG unit by restricting the air supply to the AR accordingly. Yet, it was demonstrated that in doing so carbon conversions in the FR decrease to values as low as 80 %, due to the ensuing more reducing atmosphere and lower temperatures inside the FR, inhibiting char gasification kinetics.<sup>4</sup> Based on these observations, first experimentally founded avenues shedding light onto optimization of CLG process efficiencies are presented, thereby illuminating one aspect raised by the fourth *(iv)* research question. Most importantly, the application of the novel CLG process control concept in the 1 MW<sub>th</sub> pilot, allowed for deeper insights into the governing phenomena of the CLG process. Due to the presence of industry-like conditions inside the 1 MW<sub>th</sub> CLG unit, the inherent acting mechanism of the novel process control concept, shown in Figure 15, could be derived, using live as well as offline data collected during operation. Thereby, a quantum leap towards answering the second *(ii)* research question of this thesis was attained.

---

<sup>4</sup> The key performance indicators given here fall below the values obtainable in a full-scale industrial system due to the peculiarities of the 1 MW<sub>th</sub> pilot plant (e.g. relatively high heat losses) and the utilization of non-optimized operating conditions (e.g. thermal load) during K1. Vast improvements in process efficiency, with cold gas efficiencies reaching values up to 50 %, were already attained by initial process optimizations during the second 1 MW<sub>th</sub> test campaign (K2) [47]. For a full-scale CLG system, cold gas efficiencies >80 % and FR carbon conversions up to 90 % have been predicted [51].

As shown in Figure 15, it was found that air input into the AR could be decreased by initiating flue gas recirculation ( $RR_{AR} \uparrow$ ), which subsequently results in a decrease in the oxygen content in the AR product gas ( $x_{O_2,AR,out} \downarrow$ ) without disturbing system hydrodynamics. Due to this decrease in oxygen availability in the AR, the oxygen carrier leaves the AR in a less oxidized state ( $X_{S,AR} \downarrow$ ), entailing a decrease in oxygen release in the FR ( $\lambda_{eff} \downarrow$ ,  $\Delta X_S \downarrow$ ). As postulated by the preceding process simulations, this decrease in oxygen release inside the FR leads to a net decrease in reaction enthalpy inside the FR ( $\Delta H_R \downarrow$ ), entailing a drop-off in system temperatures ( $T_{AR} \downarrow$ ,  $T_{FR} \downarrow$ ). In the absence of external heating, the interaction with the system surroundings is also affected by this measure, with refractory lining temperatures ( $T_{RL}$ ), being crucial for overall heat losses, interacting with reactor temperatures.

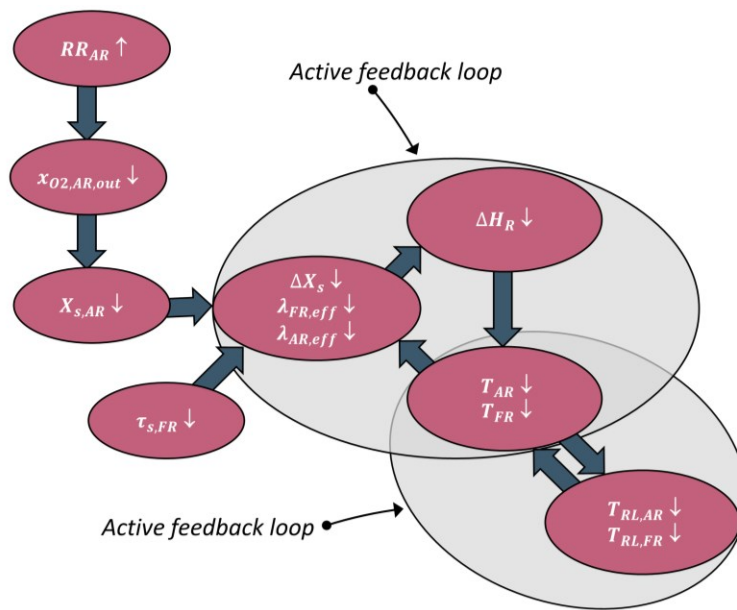


**Figure 15.** Schematic illustration of the suggested mechanism of action of the novel CLG process control concept – Effect of an increase in the AR recycling ratio ( $RR_{AR} \uparrow$ ) on important process variables. Adopted from RP-III.

Due to the similarity of the 1 MW<sub>th</sub> pilot plant with a full-scale setup, the described interconnectivity of the different process variables leading to the observed behavior will also prevail in an industrial chemical looping gasifier. Therefore, the novel process control concept and its observed effect on process behavior and efficiency as well as the general operational principles of the 1 MW<sub>th</sub> CLG unit are expected to also be applicable for a full-scale system.

#### Research Paper IV

Through achieving over 400 h of continuous chemical looping operation in 1 MW<sub>th</sub> scale by using the novel concept and operational principles, crucial CLG operational experience was gathered. One central finding of the 1 MW<sub>th</sub> CLG experiments being that system hydrodynamics and OC circulation between AR and FR are a vital and at the same time sensitive factor in large-scale

chemical looping systems. Consequently, system hydrodynamics, forming the back-bone of the CLG technology, were further investigated by also incorporating data from a down-scaled cold flow model. Combination of these two related data sets illuminated the fundamentals of the system's hydrodynamic behavior, with the most important results being presented in the **fourth research paper**. Here, it was found that within certain boundaries (e.g. operating range of a fluidized bed), the hydrodynamics of the dual-circulating fluidized bed (CFB) system, illustrated in Figure 16, constitute a self-regulating system. This means that although a change in one variable (e.g. riser gas velocity) affects multiple other variables (e.g. riser mass inventory, solid entrainment rate), a new stable operating point is found. Consequently, a free variation of each process variable is possible within a given range. However, when doing so, certain process risks related to changes in selected operating variables have to be considered.

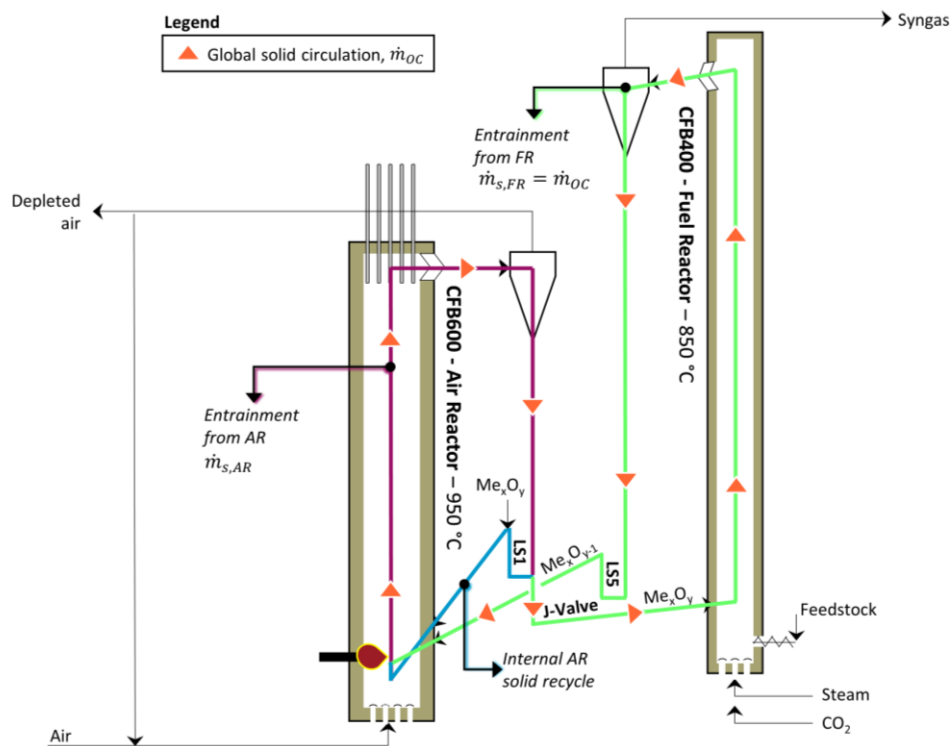


**Figure 16.** Layout of reactor system of the 1 MW<sub>th</sub> CLG pilot plant with an indication of different solid streams cycling through the system. Orange=global solid circulation, green=solid entrainment from FR and J-valve, purple=solid entrainment from AR, blue=AR internal solid circulation. Adopted from RP-IV.

One example for such a characteristic hydrodynamic variable variation is a decrease in the AR gas velocity ( $u_{0,AR} \downarrow$ ), which entails a redistribution of the reactor inventory between AR and FR, with the inventory in the latter decreasing ( $\Delta p_{AR} \uparrow$ ,  $\Delta p_{FR} \downarrow$ ).<sup>5</sup> Furthermore, the acting pressure of the J-valve also decreases slightly ( $\Delta p_{J-valve} \downarrow$ ), entailing a decrease in the material transport

<sup>5</sup> In a fluidized bed system, the CFB riser pressure drop is directly proportional to the mass inventory in the riser.

through it ( $\dot{m}_{s,J-valve} \downarrow$ ). Due to the decrease in FR reactor inventory, solid entrainment from the FR also decreases slightly ( $\dot{m}_{s,FR} \downarrow$ ), yielding a new steady state for the FR ( $\dot{m}_{s,in} = \dot{m}_{s,out}$ ). On the other hand, the solid entrainment from the AR strongly decreases ( $\dot{m}_{s,AR} \downarrow \downarrow$ ) despite the increase in reactor inventory, due to the reduction in AR gas velocity. In summary, one thus obtains a new operating point for which the solid circulation between AR and FR is reduced, while the internal solid circulation for the AR, stabilizing the hydrodynamic system, is also diminished ( $\dot{m}_{s,AR,int.} \downarrow$ ). This means that a certain process risk is associated to this variation, as the AR loop seal (LS1, see Figure 16) is emptied once the internal solid circulation ceases and more material is extracted from it than enters it via entrainment from the AR riser. Hence, the AR gas velocity has to be adapted gently to avoid major disturbances in system hydrodynamics. Moreover, significant reductions in this parameter can also entail a de-fluidization of the bed material inside the AR. However, as both reactors are operated beyond the entrainment velocity of the bed material, the risk of  $u_{0,AR}$  falling below the minimum fluidization velocity of the OC particles is low. Equivalent cause-and-effect scenarios were derived for all major hydrodynamic process variables, yielding a ground set of operational rules, crucial for stable hydrodynamic behavior of the 1 MW<sub>th</sub> pilot plant, which is provided in Table 2. Adherence to this set of hydrodynamic operating principles ensures efficient control and operation of the chemical looping gasifier, thus further illuminating the second (ii) research question of this dissertation.

**Table 2:** Overview over ground-set of rules to adapt hydrodynamic conditions in the dual-circulating fluidized bed CLG reactor system. Adopted from RP-IV.

Process Variable	Effect						Risks				
	$\Delta p_{FR}$	$\Delta p_{AR}$	$\Delta p_{J-valve}$	$\dot{m}_{s,FR}$	$\dot{m}_{s,AR}$	$\dot{m}_{s,AR,int.}$	Emptying LS4.1	Overfilling System	Emptying System	Defluidization	Pneum. Transport
$u_{0,FR}$	↑	Light Blue	Light Blue	Light Blue	Light Blue	Light Blue	Yellow	Green	Green	Green	Yellow
$u_{0,AR}$	↑	Light Blue	Light Blue	Light Blue	Light Blue	Light Blue	Green	Green	Green	Green	Yellow
$\dot{V}_{J-valve}$	↑	Dark Blue	Dark Blue	Dark Blue	Dark Blue	Dark Blue	Red	Green	Green	Green	Green
$p_{FR}$	↑	Light Blue	Light Blue	Light Blue	Light Blue	Light Blue	Green	Green	Green	Green	Green
$p_{AR}$	↑	Light Blue	Light Blue	Light Blue	Light Blue	Light Blue	Green	Green	Green	Green	Green
$\dot{m}_{MU,OC}$	↑	Dark Blue	Dark Blue	Dark Blue	Dark Blue	Dark Blue	Green	Red	Green	Green	Green
	↓	Light Blue	Light Blue	Light Blue	Light Blue	Light Blue	Green	Green	Red	Green	Green

**Legend**

- Strong increase
- Slight Increase
- Unchanged
- Slight decrease
- Strong decrease
- No Risk
- Low Risk
- High Risk

\* The top freeboard pressure is regulated via the rotational speed of the off-gas ventilators for the 1 MW<sub>th</sub> pilot plant, whereas it can be adjusted by repositioning the gas flap upstream of the filter for the CFM.



With solid entrainment ( $\dot{m}_{s,ent.}$ ) being the driving force for OC circulation between the AR and the FR, the latter having been identified as a crucial operating parameter during process simulation and autothermal 1 MW<sub>th</sub> pilot operation, the effect of different hydrodynamic operating conditions on solid entrainment from both reactors was also evaluated in detail in RP-IV. Here, it was found that CFB riser gas velocities ( $u_0$ ) as well as pressure drops ( $\Delta p$ ) positively influence solid entrainment (see also Table 2). Using the data generated during the operation of a down-scaled cold flow model, a novel method to predict solid entrainment by solely using live-data was developed to allow for fast and universal evaluation of this process parameter. This method was subsequently validated for the 1 MW<sub>th</sub> scale by using solid circulation rates determined via the approach previously developed by Marx *et al.* [48]. Application of this novel method to the data from all three 1 MW<sub>th</sub> test campaigns showed that it can be successfully applied to any CFB system, with the calculated data for both reactors of the 1 MW<sub>th</sub> CLG system given in Figure 17.

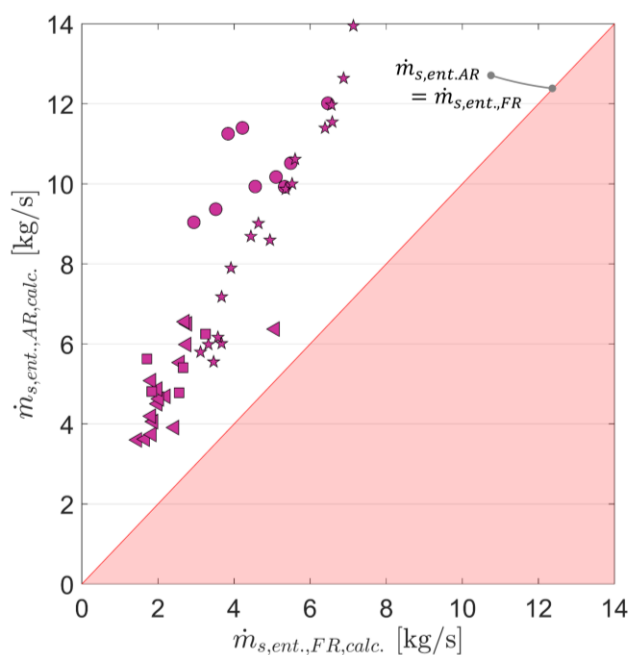


**Figure 17.** Calculated entrainment rates for the AR as a function of calculated entrainment rates for the FR for 1 MW<sub>th</sub> pilot plant for operating periods for which solid samples were collected. K1 (circles), K2 (coarse ilmenite-triangles, fine ilmenite-pentagrams), and K3 (squares). Adopted from RP-IV.

Analysis of this data provided further insights into the system's hydrodynamics during CLG operation. For example, it was found that throughout the majority of operating periods investigated within the three test campaigns, the AR was operated with significantly higher solid entrainment rates than the FR, which is illustrated in Figure 17.<sup>6</sup> This finding thus suggests that

<sup>6</sup> For the given reactor setup, material entrained from the AR but not transported to the FR is channeled directly back to the AR, thus constituting an excess solid stream not participating in heat and oxygen transport between AR and FR (see blue line in Figure 16).

---

the AR could have been operated with lower gas velocities, which would have led to higher overall process efficiencies, as the heating demand for the AR inlet gas stream would have been reduced (more details see RP-I). Moreover, it was shown that utilization of a coarser ilmenite granulation (ILMc) as OC in the 1 MW<sub>th</sub> CLG unit restricted the maximum attainable solid circulation to values <3 kg/s for the majority of operating points (see triangles in Figure 17), providing a sound explanation for the observed impaired process efficiency, since both heat and oxygen transport to the FR were restricted by OC circulation. As illustrated with these examples, the novel determination method for solid entrainment from the two CFB reactors simplifies future optimization approaches with regard to reactor hydrodynamics for any reactor configuration.

In summary, the fourth research paper therefore does not only present how stable hydrodynamics can be attained during CLG operation, but also allows for optimization of the hydrodynamic operating conditions (e.g. solid circulation) of the (full-scale) CLG reactor layout through application of the novel method for determining solid entrainment. Consequently, the following important insights towards the answering of research questions *(ii)*, *(iii)*, and *(iv)* were attained:

- *(ii)*: Development of operating principles to attain stable hydrodynamics in a CLG system;
- *(iii)*: Demonstration of the suitability of the layout of the 1 MW<sub>th</sub> system for efficient CLG operation from a hydrodynamic perspective, while providing suitable adaptations in reactor geometry and layout promising an enhancement of hydrodynamic system behavior;
- *(iv)*: Verification that solid circulation between AR and FR can become a bottleneck in CLG applications and elaboration of process-wise optimization avenues allowing for the overcoming of this obstacle (e.g. optimized J-valve or FR riser outlet geometry, tailored OC granulation).

#### *Research Paper V*

Another finding made during 1 MW<sub>th</sub> CLG pilot testing is that the fate of the OC, being central for heat and oxygen transfer between the two reactors of the CLG system, is crucial for the conversion of the feedstock fed into the gasifier and thus for the overall process efficiency. By investigating three different biomass feedstocks and two ilmenite types with different granulations (ILMf & ILMc) as OC under varying operating conditions in an industry-like environment (see Table 1), unique insights into the evolvement of morphological, physical and, chemical changes occurring in the OC during 1 MW<sub>th</sub> CLG operation were gathered. Based on these findings, bottlenecks related to OC lifetime and agglomeration were detected. To prevent these bottlenecks from becoming ‘show-stoppers’ in future large-scale CLG systems, solution and alleviation strategies, mitigating negative effects on the OC during CLG operation, were derived within the **fifth research paper** of this cumulative dissertation.

---

By investigating ilmenite OC samples originating from different plant locations, using a wide variety of lab techniques (e.g. thermogravimetric analysis, pycnometry, scanning electron microscopy, etc.), it was found that in the absence of agglomeration, the combination of abrasion and fine losses primarily determines the lifetime of the OC inside the 1 MW<sub>th</sub> CLG unit. For the optimized CLG operating conditions, an average OC lifetime inside the chemical looping gasifier of approx. 70 hours was determined, which is significantly lower than the ones determined in small pilots [17]. Hence, possible explanations for this decrease in OC lifetime with increasing scale as well as measures to enhance OC lifetime were established. On the other hand, the chemical properties of the spent OC materials were analyzed. Here it was found that chemical deactivation and chemical poisoning of the OC do not occur to detrimental extents, with utilized samples exhibiting redox reaction rates exceeding those of the fresh OC material. This means that in an industrial-size CLG unit, OC make-up rates will be primarily driven by fine losses from the reactor system and not by OC deactivation. Yet, these fine losses can be drastically reduced in comparison to the 1 MW<sub>th</sub> setup, e.g. by utilizing cyclones with higher separation efficiencies or by adapting the plant in such a way that recovered fines can be reintroduced into the system, meaning that substantially longer OC lifetimes should be attainable.

Another potential technical bottleneck was observed during gasification of wheat straw pellets (WSP), containing ashes tending towards melting at elevated temperatures [52, 53], inside the 1 MW<sub>th</sub> chemical looping gasifier. Here, bed agglomeration was observed inside the AR of the 1 MW<sub>th</sub> reactor system, with agglomerates measuring up to 20 cm being recovered from the pilot plant after shut-down (see photograph in Figure 18). Through the combination of observations made during CLG operation, inspection of the 1 MW<sub>th</sub> pilot after operation, and in-depth analyses of collected agglomerate samples, a mechanism for the observed behavior was derived, which is given in Figure 18. Due to the ash composition of the utilized wheat straw, rich in silicates and alkali salts, low-melting eutectic phases liquefy inside the AR ( $T_{AR} > 900$  °C) [53–55], which is illustrated in Figure 18b. These molten ash particles then facilitate the formation of OC agglomerates inside the reactor system according to the melt-induced agglomeration mechanism [52], as OC particles are bound together by the molten ash, which eventually re-solidifies (see Figure 18c). In zones of low turbulence (e.g. reactor outlet, stand-pipes), the growth of these agglomerates is not hindered through the abrasive forces prevailing inside the riser of the CFB, leading to a continuous growth in agglomerate size, as shown in Figure 18d.

To avoid the occurrence of agglomeration-related issues in a full-scale CLG unit, preventive measures were formulated. While these are primarily related to tailored feedstock pre-treatment methods, such as additivation or washing to modify ash chemistry and thereby reduce the ash melt fraction at process temperatures [56], dedicated operational measures to limit agglomerate

formation and minimize the negative impact of it on process efficiency were also derived. Here, an example is the safeguarding of high solid circulation rates between AR and FR, reducing the temperature gradient between the two reactors and thus leading to comparably low AR and high FR temperatures. While the former alleviates the risk of temperature-induced melt formation occurring inside the AR, the latter allows for a more complete feedstock conversion inside the FR and thus reduces char and ash carryover to the AR [47], thereby diminishing negative effects of potential ash melting.

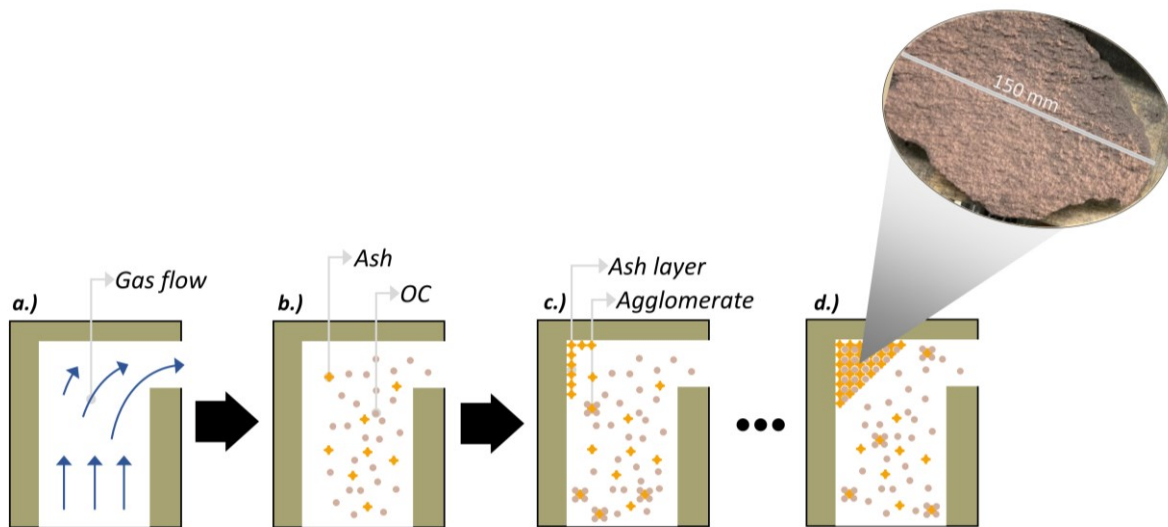


**Figure 18.** Postulated mechanism for formation of large agglomerate slabs inside AR: a.) Empty AR with indication of gas flow, b.) AR with ilmenite (=OC) and ash particles, c.) formation of first agglomerates and sticky ash layer on AR refractory lining in zones of low turbulence, d.) adherence of ilmenite particles on ash layer leading to growth of ash/OC layer on refractory lining and ultimately to fully formed agglomerate slabs (photograph of agglomerate slab see inset). Adopted from RP-V.

Overall, the fifth research paper thus showcases two crucial bottlenecks of the CLG technology having to be considered during up-scaling endeavors (OC consumption and bed agglomeration) and presents alleviating measures suitable for large-scale systems. Thereby, important findings related to the fourth (iv) research question were derived, thus promoting the technical maturity of the CLG technology.

---

## 2.2. Conclusion

Within the process of achieving the over-arching research goal of this dissertation, i.e. the demonstration and optimization of CLG in 1 MW<sub>th</sub> scale, the following progress in answering the four primary research questions was made:

*(i) Is autothermal CLG operation in industry-like conditions generally viable?*

Using different process modelling approaches, it was firstly demonstrated that autothermal CLG operation is viable in theory, before validating the CLG technology during more than 400 h of operation under industrially relevant conditions in 1 MW<sub>th</sub> scale, thus providing an unambiguous positive answer for the first research question.

*(ii) Which process control measures and operational practices are necessary to allow for efficient autothermal chemical looping gasification?*

On the basis of the calculated heat and mass balances and the existing 1 MW<sub>th</sub> pilot plant, a novel plant layout allowing for CLG operation was derived. Subsequently, a process control concept (incl. safety measures) and all relevant operating procedures were developed. This process control concept, relying on AR flue gas recirculation to control the oxygen transport from the AR to the FR, was successfully deployed for 240 h in 1 MW<sub>th</sub> scale, yielding cold gas efficiencies up to 50 %. To allow for further efficiency enhancements, the underlying operating procedures were updated and optimized based on operational experience gained during the three different 1 MW<sub>th</sub> CLG test campaigns, resulting in an elaborate knowledge base containing all relevant process (control) parameters and operational procedures relevant for efficient autothermal CLG operation.

*(iii) What is a suitable process design of an industrial chemical looping gasifier, allowing for efficient conversion of biomass residues into a high-quality syngas?*

CLG operation in the specifically adapted 1 MW<sub>th</sub> pilot plant showed that the derived process design fulfills its designated purpose. Hence, it can be summarized that a similar setup would also be suitable for an industrial CLG system. Important insights gained during 1 MW<sub>th</sub> operation allowed for the development of possible optimization avenues in terms of reactor geometry and configuration, available for future up-scaling endeavors, such as an adaption of the FR riser or J-valve geometry to boost solid circulation between the two reactors. Using the layout of the novel 1 MW<sub>th</sub> chemical looping gasifier as a basis, a design of a full-scale (200 MW<sub>th</sub>) CLG system was derived in the CLARA project. This design was further investigated through different process models validated using data from the CLG experiments conducted in 1 MW<sub>th</sub> scale, yielding an optimized reactor layout and operational window. In doing so, the technical competitiveness of the CLG

---

technology in comparison to other gasification technologies (e.g. DFBG) was underpinned, with cold gas efficiencies >80 % and carbon conversions close to 90 % having been determined via process simulations [51]. Therefore, the layout of the 1 MW<sub>th</sub> CLG system as well as the operational experience gained during its operation are deemed crucial in answering how a suitable layout of a full-scale CLG system would look like and which process efficiencies can be attained in industrial scale.

*(iv) Which bottlenecks and optimization avenues should be considered when striving for the industrial application of CLG?*

A holistic consideration of all relevant aspects in terms of optimization of the autothermal CLG process was provided using both simulation approaches as well as data from continuous CLG operation in the MW-scale. Here, unique insights related to process optimization and the alleviation of bottlenecks, which were derived based on operational experience gained during operation of the 1 MW<sub>th</sub> pilot plant, are most noteworthy. These include specific aspects in terms of OC utilization and system hydrodynamics, which were found to be crucial during 1 MW<sub>th</sub> CLG operation, allowing for important inferences for a full-scale CLG system. For one, it was established that adaptations and/or optimizations in the employed OC material, the underlying process conditions, or the process layout are required to enhance the OC lifetime inside the CLG system, which was determined to be as low as 70 h in 1 MW<sub>th</sub> scale, thus posing a potential techno-economic obstacle for process up-scaling. Furthermore, OC circulation between the AR and FR was found to be a limiting factor in the 1 MW<sub>th</sub> system, especially when employing coarser OC material, suggesting that full-scale systems should enable OC circulation rates >3 kg/s MW through a suitable reactor layout (see *(iii)*) and adequate OC selection to optimize process efficiency. It is expected that consideration of these findings during future erection and operation of an industrial-scale CLG system will prove to be invaluable.

Consequently, this dissertation demonstrated the technical competitiveness of the CLG technology through the erection and operation of an autothermal 1 MW<sub>th</sub> chemical looping gasifier, with the main findings from the underlying endeavors facilitating and encouraging future up-scaling activities. Therefore, the CLG process is deemed to be an auspicious technology for the future valorization of various biogenic waste streams, thus allowing for their chemical recycling during production of carbon-neutral or carbon-negative end-products.<sup>7</sup>

---

<sup>7</sup> End products produced via CLG-driven process chains can exhibit a negative carbon footprint in case CCS is deployed and a sustainably sourced biogenic feedstock is utilized.

---

### 2.3. Outlook

With the groundwork for future utilization of the CLG technology in waste-to-value process chains having been laid within this dissertation, the following aspects should be covered in future research on this topic:

- Although the general viability of the adapted 1 MW<sub>th</sub> pilot plant for CLG operation was validated, subsequent process evaluation showed that certain adaptations in plant design, such as a redesign of the J-valve, transporting material between AR and FR, or a modification of the FR riser exit geometry, could significantly enhance the overall process efficiency. The pursuit of these endeavors during future CLG operation will elucidate their promise in optimizing CLG efficiency in industrial scale.
- While feedstock selection was restricted to three different biomasses in this dissertation, CLG operation with other waste-based feedstocks (e.g. sewage sludge or municipal/ industrial waste) will elucidate whether the CLG technology is a viable option for waste-to-value chains aiming at the valorization of waste streams going beyond biomasses. In case of successful validation, chemical looping gasification can develop into a crucial building block in future circular economies, converting a wide array of waste streams into useful end-products.
- Along those lines, the suitability of alternative OC materials to ilmenite, being a material oftentimes used in chemical looping applications [57, 58], should be investigated. Here, special focus should be placed on waste materials to improve overall process economics and reduce the environmental footprint of the CLG technology. One such material having shown great promise in initial small-scale CLG tests is steel converter slag [30, 35].
- After providing proof-of-concept that continuous multi-week CLG operation is possible, its demonstration over longer durations (>2 weeks), using a single set of optimized operating conditions, will cast further light onto the general plant efficiency and operability. Long-term investigations of this sort will bring further aspects relevant for technology up-scaling to light (e.g. effect of feedstock variability on process efficiency or potential OC de-activation with increasing operating time), thereby further increasing the technological maturity of the CLG technology.
- With the primary goal of any waste-to-value process chain being the production of a marketable end-product, subsequent endeavors should lay their focus on the successful demonstration of the production of these products (e.g. methanol, Fischer-Tropsch products) from the synthesis gas produced via CLG in sizeable amounts. Although first operational experience in the 1 MW<sub>th</sub> full-chain configuration, encompassing gasification, gas cleaning, and fuel synthesis, was gained in the *CLARA* project, further advances are

---

required. By building on the key findings presented in this dissertation, continuous long-term CLG operation at optimized conditions can be attained (see point above), thus facilitating in-depth investigations of the entire process-chain, including the analysis, quality control, and utilization of the final product.

- The endeavors elucidated above should finally lead towards the demonstration of the CLG technology in a system prototype (5-10 MW<sub>th</sub>) running in an operational environment (=TRL 7), thus paving the way for full system qualification and operation (TRL 8/9).

Pursuit of these research avenues will ultimately allow for a conclusive assessment regarding the technical suitability of the CLG technology for waste-to-value process chains in industrial-scale circular economy setups.



## Appendix

### A.1 Additional Information

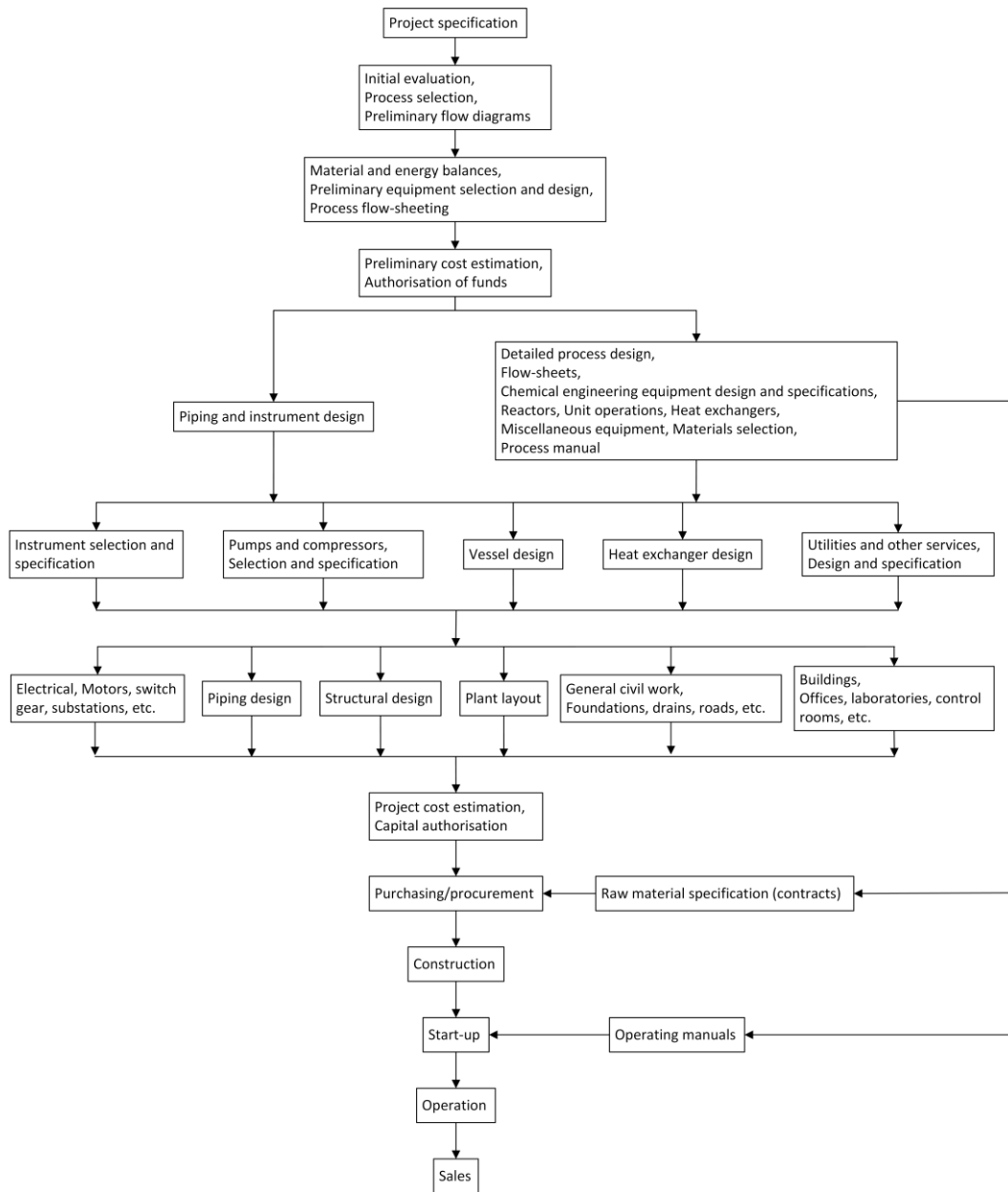


Figure A-1. Structure of a chemical engineering project, adopted from Towler and Sinnott [44].

	Closed vessel/ reactor		Blower/fan		Lance (for cooling or gas injection)
	Open vessel/barell		Heat exchanger		Sampling port
	Cyclone		Pump		Big Bag
	Loop Seal		Valve		Holding vessel
	J-valve		Rotary valve		Burner
	Filter		Pressure relief valve		Orifice measurement
	Stack		Feeding screw		Venturi Measurement

Figure A-2. Explanation of symbols utilized in process flow diagrams.

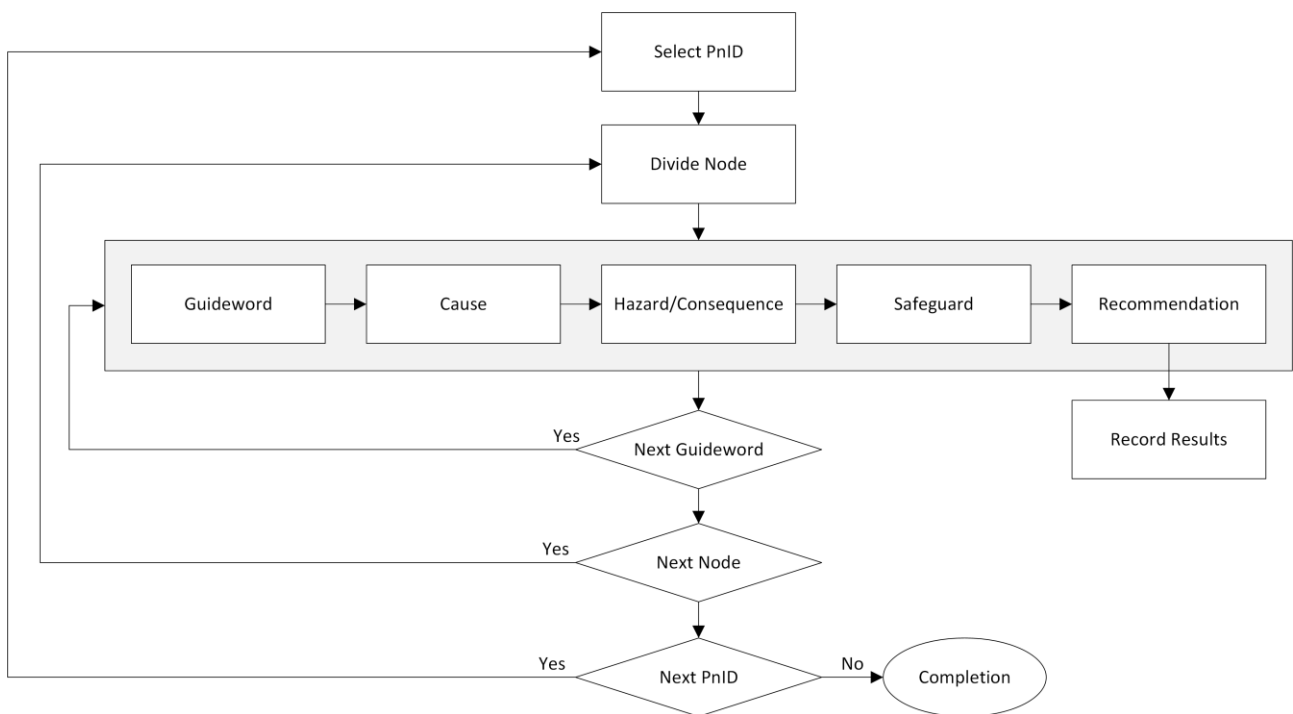
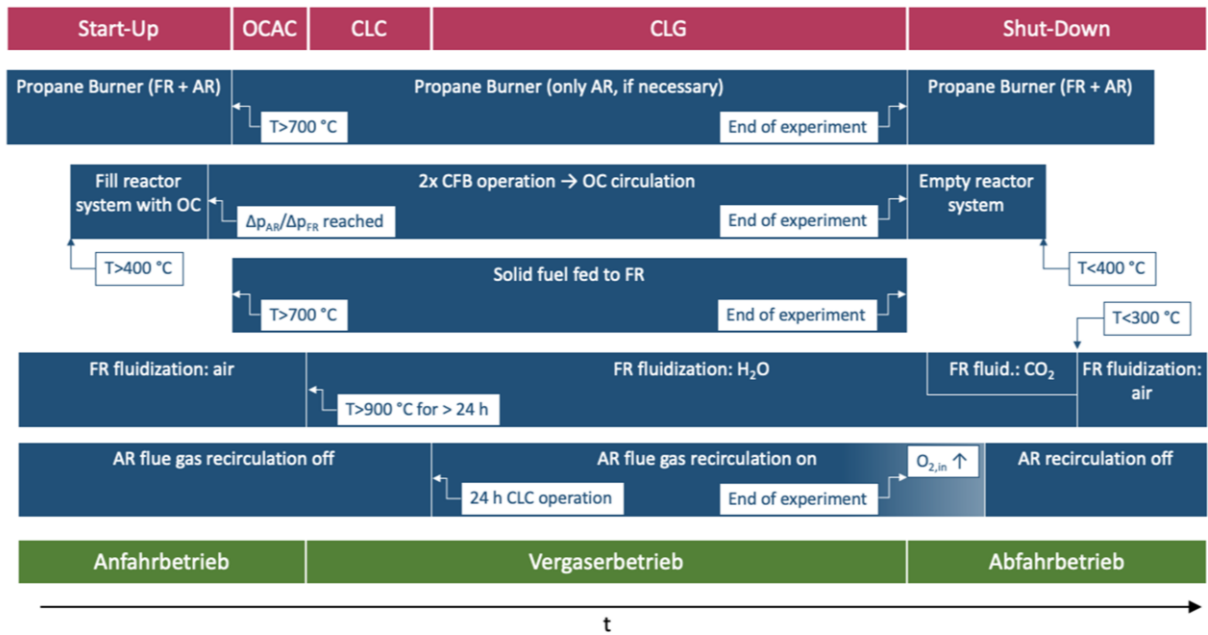


Figure A-3. Flow process of a HAZOP analysis for each guideword according to Nolan [59] (grey box), embedded into the overall HAZOP flow chart according to Guo *et al.* [60].

## A.2 Exemplary Engineering Documents



**Figure A-4.** Schematic illustration of the suggested operational sequence for CLG with indications of the sub-processes (pink), main operating conditions (blue), and different operational states (green), adopted from the process manual of the 1 MW<sub>th</sub> chemical looping gasifier.

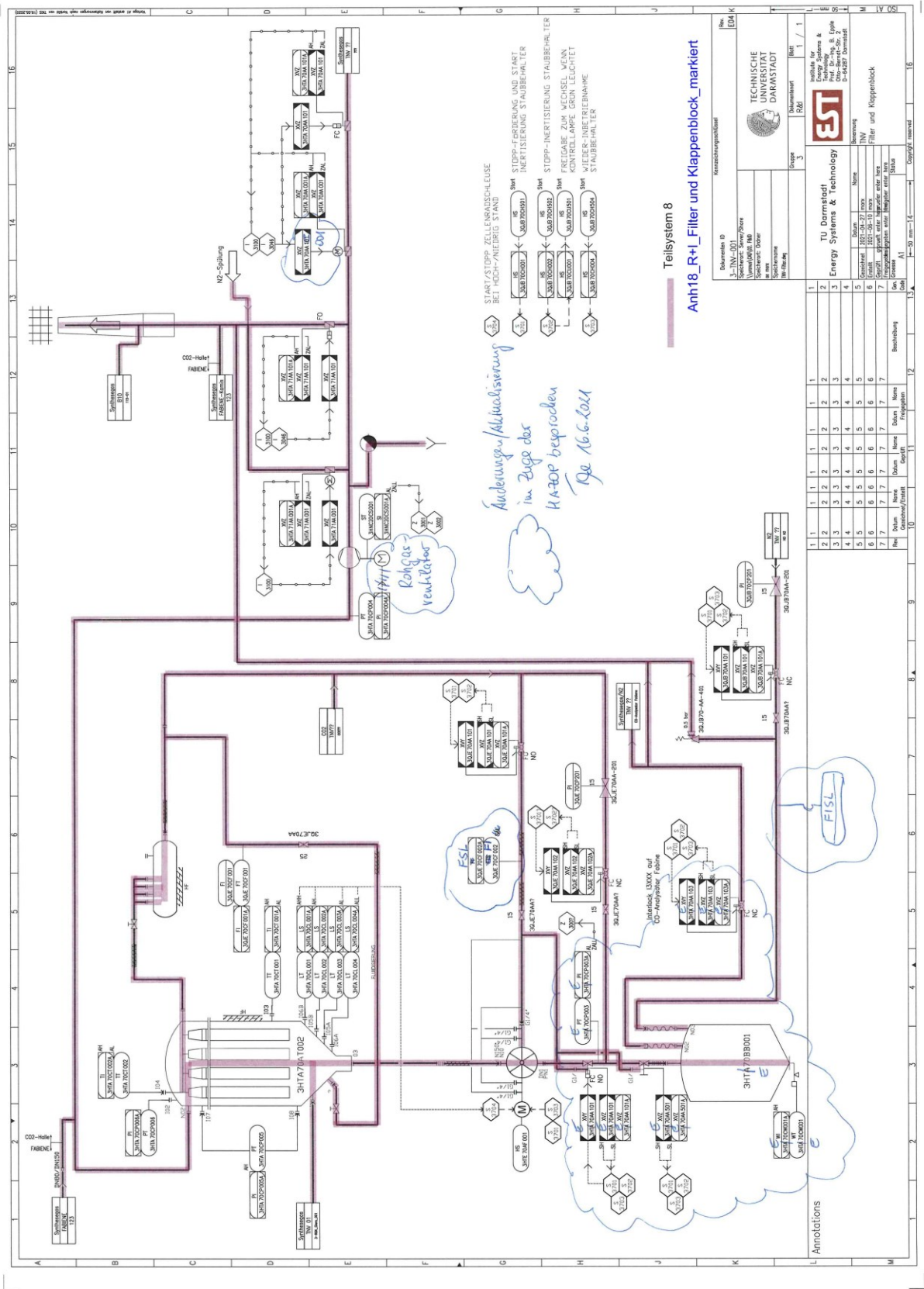


Figure A-5. Example of a PnID used and annotated during HAZOP analysis of 1 MW<sub>th</sub> CLG unit.

#### 4 Schutz Z3001 10CJF00EE001

Im Folgenden wird die Schutzlogik der Anlage beschrieben. Der Anlagenschutz stoppt den Energie- und Stoffstrominput in die Anlage.

Es ist eine Erstwerterfassung zu programmieren um den auslösenden Faktor eindeutig identifizieren zu können. Es wird auch ein nicht fehlersicheres Schutzsignal gebildet, dass dann in der Normallogik angewendet wird.

Die Darstellung erfolgt hier aus Platzgründen in mehreren Teilen.

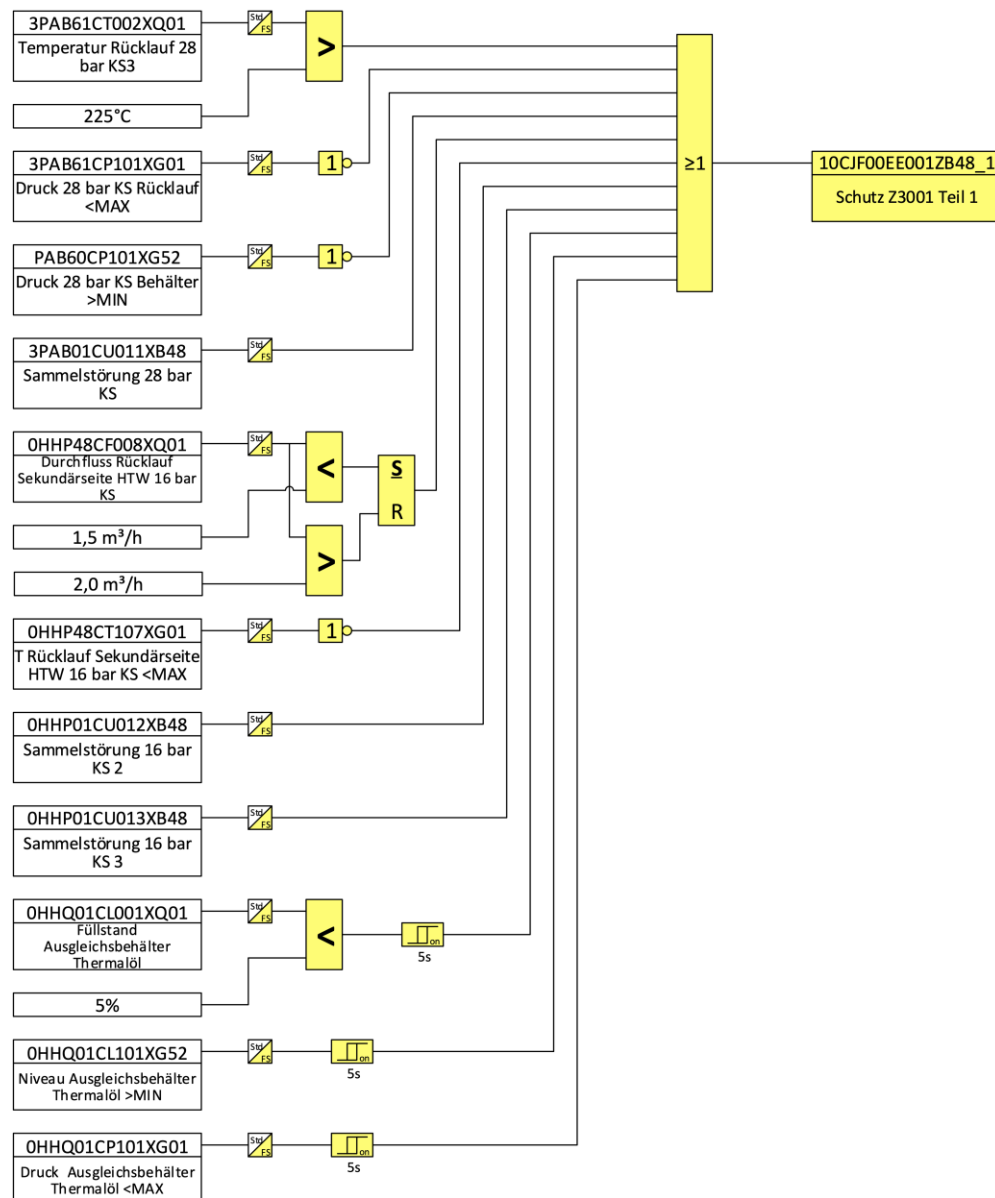


Figure A-6. Example of logic plan used to program the safety matrix of the PLS of the 1 MW<sub>th</sub> CLG pilot plant.

---

*This page is left blank intentionally*

---

---

## References

---

1. World Meteorological Organization (WMO) (2023) WMO Global Annual to Decadal Climate Update (Target years: 2023-2027). 24
2. Global Monitoring Laboratory (GML), National Oceanic and Atmospheric Administration (NOAA) Monthly Average Mauna Loa CO<sub>2</sub>. In: Carbon Cycle Greenhouse Gases. <https://gml.noaa.gov/ccgg/trends/>. Accessed 10 Mar 2023
3. Ripple WJ, Wolf C, Newsome TM, Galetti M, Alamgir M, Crist E, Mahmoud MI, Laurance WF, 15,364 scientist signatories from 184 countries (2017) World Scientists' Warning to Humanity: A Second Notice. *BioScience* 67:1026–1028
4. European Environmental Agency (EEA) Greenhouse gas emissions from transport in Europe. In: EEA Indicators. <https://www.eea.europa.eu/ims/greenhouse-gas-emissions-from-transport>. Accessed 10 Mar 2023
5. (2018) DIRECTIVE (EU) 2018/ 2001 OF THE EUROPEAN PARLIAMENT AND OF THE COUNCIL - of 11 December 2018 - on the promotion of the use of energy from renewable sources. Official Journal of the European Union 128
6. Higman C, Burgt M van der (2008) Gasification, 2nd ed. Gulf Professional Pub./Elsevier Science, Amsterdam ; Boston
7. Heinze C, May J, Langner E, Ströhle J, Epple B (2023) High Temperature Winkler gasification of Rhenish lignite in an optimized 500 kWth pilot plant. *Fuel* 333:126289
8. Langner E, Kaltenmorgen J, Heinze C, Ströhle J, Epple B (2023) Fluidized bed gasification of solid recovered fuels in a 500 kWth pilot plant. *Fuel* 344:127901
9. Higman C (2008) Gasification. In: Combustion Engineering Issues for Solid Fuel Systems. Elsevier, pp 423–468
10. Kirnbauer F, Hofbauer H (2011) Investigations on Bed Material Changes in a Dual Fluidized Bed Steam Gasification Plant in Güssing, Austria. *Energy Fuels* 25:3793–3798
11. Ripfel-Nitsche K, Hofbauer H, Rauch R, Goritschnig M (2007) BTL – BIOMASS TO LIQUID (FISCHER TROPSCH PROCESS AT THE BIOMASS GASIFIER IN GÜSSING). Proceedings of the 15th European Biomass Conference & Exhibition 4
12. Hermann H, Reinhard R, Klaus B, Reinhard K, Christian A Biomass CHP Plant Güssing – A Success Story. 13
13. Hanchate N, Ramani S, Mathpati CS, Dalvi VH (2021) Biomass gasification using dual fluidized bed gasification systems: A review. *Journal of Cleaner Production* 280:123148
14. Nguyen NM, Alobaid F, Dieringer P, Epple B (2021) Biomass-Based Chemical Looping Gasification: Overview and Recent Developments. *Applied Sciences* 11:7069
15. Huang Z, Zhang Y, Fu J, et al (2016) Chemical looping gasification of biomass char using iron ore as an oxygen carrier. *International Journal of Hydrogen Energy* 41:17871–17883
16. Guo Q, Cheng Y, Liu Y, Jia W, Ryu H-J (2014) Coal Chemical Looping Gasification for Syngas Generation Using an Iron-Based Oxygen Carrier. *Ind Eng Chem Res* 53:78–86
17. Condori O, García-Labiano F, de Diego LF, Izquierdo MT, Abad A, Adánez J (2021) Biomass chemical looping gasification for syngas production using ilmenite as oxygen carrier in a 1.5 kWth unit. *Chemical Engineering Journal* 405:126679
18. Zhao H, Guo L, Zou X (2015) Chemical-looping auto-thermal reforming of biomass using Cu-based oxygen carrier. *Applied Energy* 157:408–415
19. Huang Z, He F, Feng Y, Zhao K, Zheng A, Chang S, Li H (2013) Synthesis gas production through biomass direct chemical looping conversion with natural hematite as an oxygen carrier. *Bioresource Technology* 140:138–145
20. Hedayati A, Soleimanisalim AH, Mattisson T, Lyngfelt A (2022) Thermochemical conversion of biomass volatiles via chemical looping: Comparison of ilmenite and steel converter waste materials as oxygen carriers. *Fuel* 313:122638

21. Condori O, Abad A, Izquierdo MT, de Diego LF, García-Labiano F, Adánez J (2023) Assessment of the chemical looping gasification of wheat straw pellets at the 20 kW<sub>th</sub> scale. *Fuel* 344:128059
22. Wei G, He F, Huang Z, Zheng A, Zhao K, Li H (2015) Continuous Operation of a 10 kW<sub>th</sub> Chemical Looping Integrated Fluidized Bed Reactor for Gasifying Biomass Using an Iron-Based Oxygen Carrier. *Energy Fuels* 29:233–241
23. Ge H, Guo W, Shen L, Song T, Xiao J (2016) Biomass gasification using chemical looping in a 25 kW<sub>th</sub> reactor with natural hematite as oxygen carrier. *Chemical Engineering Journal* 286:174–183
24. Gogolev I, Soleimanisalim AH, Mei D, Lyngfelt A (2022) Effects of Temperature, Operation Mode, and Steam Concentration on Alkali Release in Chemical Looping Conversion of Biomass—Experimental Investigation in a 10 kW<sub>th</sub> Pilot. *Energy Fuels* 36:9551–9570
25. Xu D, Tong A, Fan L-S (2022) State of Scale-Up Development in Chemical Looping Technology for Biomass Conversions: A Review and Perspectives. *Waste Biomass Valor* 13:1363–1383
26. Lyngfelt A, Leckner B (2015) A 1000 MW<sub>th</sub> boiler for chemical-looping combustion of solid fuels – Discussion of design and costs. *Applied Energy* 157:475–487
27. Bolhar-Nordenkampf M, Bosch K, Rauch R, Kaiser S, Tremmel H, Aichernig C, Hofbauer H (2002) Scale-up of a 100kW<sub>th</sub> pilot FICFB-gasifier to a 8 MW<sub>th</sub> FICFB-gasifier demonstration plant in Güssing (Austria).
28. Apache POI (2020) EN Horizon 2020 Work Programme 2018-2020 10. Secure, clean and efficient energy. European Union Agency for Asylum, Malta
29. Tzinis I (2021) Technology Readiness Level | NASA. In: Technology Readiness Level. [https://www.nasa.gov/directorates/heo/scan/engineering/technology/technology\\_readiness\\_level/](https://www.nasa.gov/directorates/heo/scan/engineering/technology/technology_readiness_level/). Accessed 23 Jun 2023
30. Hildor F, Leion H, Linderholm CJ, Mattisson T (2020) Steel converter slag as an oxygen carrier for chemical-looping gasification. *Fuel Processing Technology* 210:106576
31. Liu Q, Hu C, Peng B, Liu C, Li Z, Wu K, Zhang H, Xiao R (2019) High H<sub>2</sub>/CO ratio syngas production from chemical looping co-gasification of biomass and polyethylene with CaO/Fe<sub>2</sub>O<sub>3</sub> oxygen carrier. *Energy Conversion and Management* 199:111951
32. Wei G, He F, Zhao Z, Huang Z, Zheng A, Zhao K, Li H (2015) Performance of Fe–Ni bimetallic oxygen carriers for chemical looping gasification of biomass in a 10 kW<sub>th</sub> interconnected circulating fluidized bed reactor. *International Journal of Hydrogen Energy* 40:16021–16032
33. Yan J, Sun R, Shen L, Bai H, Jiang S, Xiao Y, Song T (2020) Hydrogen-rich syngas production with tar elimination via biomass chemical looping gasification (BCLG) using BaFe<sub>2</sub>O<sub>4</sub>/Al<sub>2</sub>O<sub>3</sub> as oxygen carrier. *Chemical Engineering Journal* 387:124107
34. Huseyin S, Wei G, Li H, He F, Huang Z (2014) Chemical-looping gasification of biomass in a 10 kW<sub>th</sub> interconnected fluidized bed reactor using Fe<sub>2</sub>O<sub>3</sub>/Al<sub>2</sub>O<sub>3</sub> oxygen carrier. *Journal of Fuel Chemistry and Technology* 42:922–931
35. Condori O, García-Labiano F, de Diego LF, Izquierdo MT, Abad A, Adánez J (2021) Biomass chemical looping gasification for syngas production using LD Slag as oxygen carrier in a 1.5 kW<sub>th</sub> unit. *Fuel Processing Technology* 222:106963
36. Abdalazeez A, Tianle L, Cao Y, Wang W, Abuelgasim S, Liu C (2022) Syngas production from chemical looping gasification of rice husk-derived biochar using BaFe<sub>2</sub>O<sub>4</sub> as an oxygen carrier. *Journal of the Energy Institute* 105:376–387
37. He F, Huang Z, Li H, Zhao Z (2011) Biomass Direct Chemical Looping Conversion in a Fluidized Bed Reactor with Natural Hematite as an Oxygen Carrier. In: 2011 Asia-Pacific Power and Energy Engineering Conference. IEEE, Wuhan, China, pp 1–7
38. Moldenhauer P, Linderholm C, Rydén M et al (2018) Experimental investigation of chemical-looping combustion and chemical-looping gasification of biomass-based fuels using steel converter slag as oxygen carrier. *Proceedings of the International Conference on Negative CO<sub>2</sub> Emissions* 18
39. Goel A, Moghaddam EM, Liu W, He C, Kontinen J (2022) Biomass chemical looping gasification for high-quality syngas: A critical review and technological outlooks. *Energy Conversion and Management* 268:116020



40. Hilz J, Helbig M, Haaf M, Daikeler A, Ströhle J, Epple B (2018) Investigation of the fuel influence on the carbonate looping process in 1 MWth scale. *Fuel Processing Technology* 169:170–177
41. Hilz J, Helbig M, Haaf M, Daikeler A, Ströhle J, Epple B (2017) Long-term pilot testing of the carbonate looping process in 1 MWth scale. *Fuel* 210:892–899
42. Ohlemüller P, Ströhle J, Epple B (2017) Chemical looping combustion of hard coal and torrefied biomass in a 1 MW th pilot plant. *International Journal of Greenhouse Gas Control* 65:149–159
43. Ohlemüller P, Busch J-P, Reitz M, Ströhle J, Epple B (2016) Chemical-Looping Combustion of Hard Coal: Autothermal Operation of a 1 MWth Pilot Plant. *Journal of Energy Resources Technology* 138:042203
44. Towler GP, Sinnott RK (2008) *Chemical engineering design: principles, practice and economics of plant and process design*. Elsevier/Butterworth-Heinemann, Amsterdam ; Boston
45. Ohlemüller P, Alobaid F, Abad A, Adanez J, Ströhle J, Epple B (2018) Development and validation of a 1D process model with autothermal operation of a 1 MW th chemical looping pilot plant. *International Journal of Greenhouse Gas Control* 73:29–41
46. Condori O, García-Labiano F, de Diego LF, Izquierdo MT, Abad A, Adánez J (2022) Syngas production via Biomass Chemical Looping Gasification (BCLG) in a 50 kWth unit using ilmenite as oxygen carrier. *Proceedings of the Fluidized Bed Conversion Conference 2022* 10
47. Marx F, Dieringer P, Ströhle J, Epple B (2023) Process efficiency and syngas quality from autothermal operation of a 1 MWth chemical looping gasifier with biogenic residues. *Applications in Energy and Combustion Science* 16:100217
48. Marx F, Dieringer P, Ströhle J, Epple B (2023) Solid Flux Measurement in Dual Fluidized Bed Processes Based on Solid Samples. *Fuel* 341:127589
49. Cuadrat A, Abad A, Adánez J, de Diego LF, García-Labiano F, Gayán P (2012) Behavior of ilmenite as oxygen carrier in chemical-looping combustion. *Fuel Processing Technology* 94:101–112
50. Adánez J, Cuadrat A, Abad A, Gayán P, de Diego LF, García-Labiano F (2010) Ilmenite Activation during Consecutive Redox Cycles in Chemical-Looping Combustion. *Energy Fuels* 24:1402–1413
51. Detsios N, Atsonios K, Grammelis P, Dieringer P, Ströhle J, Nikkanen V, Orfanoudakis NG (2023) A Comparative Analysis and Assessment of Dual Fluidized Bed and Chemical Looping Gasification: Design Considerations for Commercial Use and Applicability in BTL Schemes. *Proceedings of the 31st European Biomass Conference and Exhibition 5-8 June 2023*:6 Pages
52. Miao Z, Jiang E, Hu Z (2022) Review of agglomeration in biomass chemical looping technology. *Fuel* 309:122199
53. Lebendig F, Funcia I, Pérez-Vega R, Müller M (2022) Investigations on the Effect of Pre-Treatment of Wheat Straw on Ash-Related Issues in Chemical Looping Gasification (CLG) in Comparison with Woody Biomass. *Energies* 15:3422
54. Lindström E, Öhman M, Backman R, Boström D (2008) Influence of Sand Contamination on Slag Formation during Combustion of Wood Derived Fuels. *Energy Fuels* 22:2216–2220
55. Mlonka-Mędrała A, Magdziarz A, Gajek M, Nowińska K, Nowak W (2020) Alkali metals association in biomass and their impact on ash melting behaviour. *Fuel* 261:116421
56. Lebendig F, Müller M (2022) Effect of pre-treatment of herbaceous feedstocks on behavior of inorganic constituents under chemical looping gasification (CLG) conditions. *Green Chem* 24:9643–9658
57. Adanez J, Abad A, Garcia-Labiano F, Gayan P, de Diego LF (2012) Progress in Chemical-Looping Combustion and Reforming technologies. *Progress in Energy and Combustion Science* 38:215–282
58. Leion H, Lyngfelt A, Johansson M, Jerndal E, Mattisson T (2008) The use of ilmenite as an oxygen carrier in chemical-looping combustion. *Chemical Engineering Research and Design* 86:1017–1026
59. Nolan DP (2011) *Safety and security review for the process industries: application of HAZOP, PHA and What-If and SVA reviews*, 3rd ed. Elsevier/GPP, Oxford
60. Guo Z, Zou S, Ma W, Dai H (2021) HAZOP Analysis and Research of Temporary Acid Adding System for High-Discharge Waste Liquid. *Science and Technology of Nuclear Installations* 2021:1–6

---



## Part 2

—

## *Research Papers*



---

**Research Paper I**

---

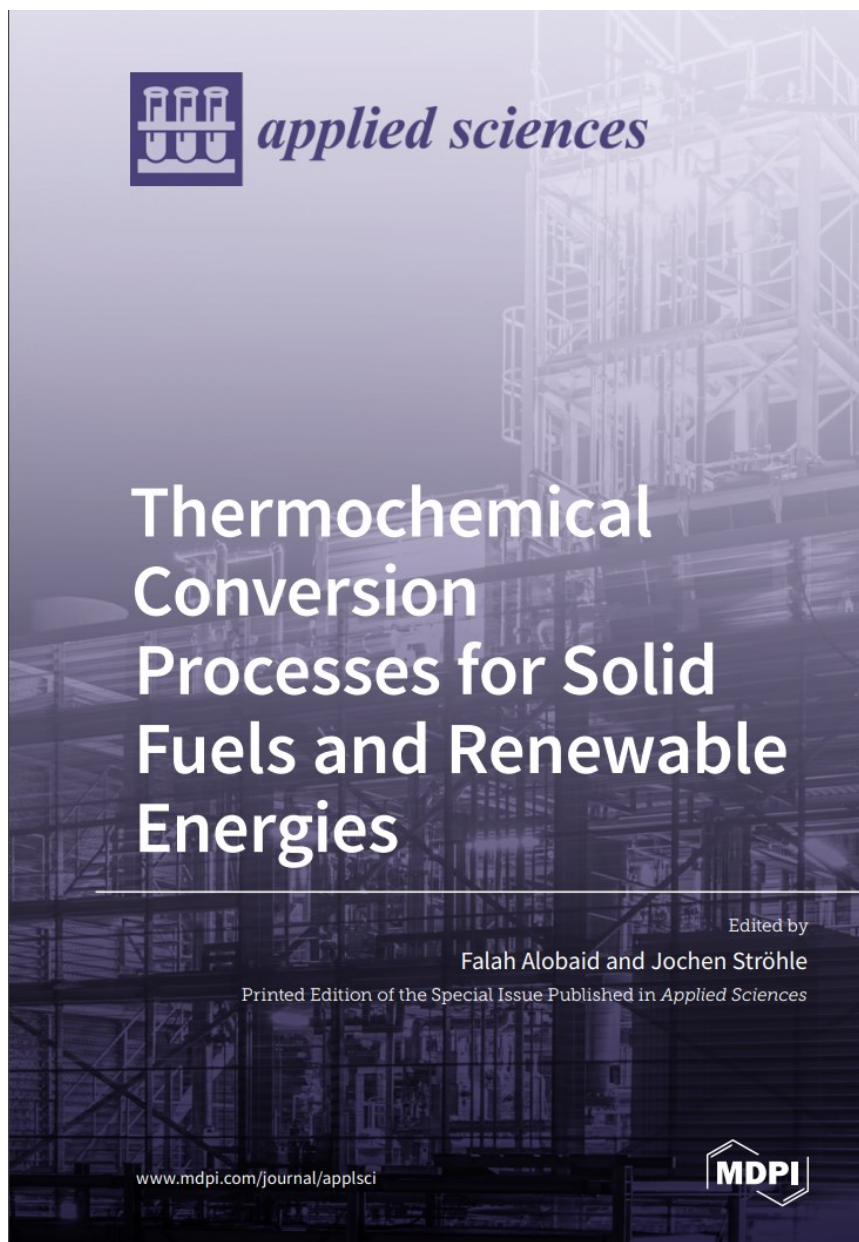
*Process Control Strategies in Chemical Looping Gasification—A Novel Process for the Production of Biofuels Allowing for Net Negative CO<sub>2</sub> Emissions*

Paul Dieringer, Falko Marx, Falah Alobaid, Jochen Ströhle, Bernd Epple

---

**Journal:** Applied Sciences, Vol. 10  
**Date:** 06/2020  
**DOI:** [10.3390/app10124271](https://doi.org/10.3390/app10124271)  
**ISSN:** 2076-3417  
**Copyright:** Open Access License: CC BY 4.0

---



Article

# Process Control Strategies in Chemical Looping Gasification—A Novel Process for the Production of Biofuels Allowing for Net Negative CO<sub>2</sub> Emissions

Paul Dieringer <sup>\*</sup>, Falko Marx, Falah Alobaid, Jochen Ströhle  and Bernd Epple

Institute for Energy Systems & Technology, Technical University Darmstadt, Otto-Berndt-Str. 2, 64287 Darmstadt, Germany; falko.marx@est.tu-darmstadt.de (F.M.); falah.alobaid@est.tu-darmstadt.de (F.A.); jochen.stroehle@est.tu-darmstadt.de (J.S.); bernd.epple@est.tu-darmstadt.de (B.E.)

\* Correspondence: paul.dieringer@est.tu-darmstadt.de; Tel.: +49-6151-16-22692

Received: 20 May 2020; Accepted: 12 June 2020; Published: 22 June 2020



**Abstract:** Chemical looping gasification (CLG) is a novel gasification technique, allowing for the production of a nitrogen-free high calorific synthesis gas from solid hydrocarbon feedstocks, without requiring a costly air separation unit. Initial advances to better understand the CLG technology were made during first studies in lab and bench scale units and through basic process simulations. Yet, tailored process control strategies are required for larger CLG units, which are not equipped with auxiliary heating. Here, it becomes a demanding task to achieve autothermal CLG operation, for which stable reactor temperatures are obtained. This study presents two avenues to attain autothermal CLG behavior, established through equilibrium based process simulations. As a first approach, the dilution of active oxygen carrier materials with inert heat carriers to limit oxygen transport to the fuel reactor has been investigated. Secondly, the suitability of restricting the air flow to the air reactor in order to control the oxygen availability in the fuel reactor was examined. Process simulations show that both process control approaches facilitate controlled and de-coupled heat and oxygen transport between the two reactors of the chemical looping gasifier, thus allowing for efficient autothermal CLG operation. With the aim of inferring general guidelines on how CLG units have to be operated in order to achieve decent synthesis gas yields, different advantages and disadvantages associated to the two suggested process control strategies are discussed in detail and optimization avenues are presented.

**Keywords:** chemical looping; biomass gasification; process control; process simulation

## 1. Introduction

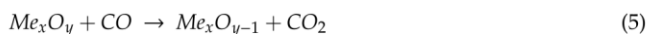
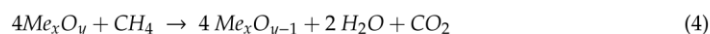
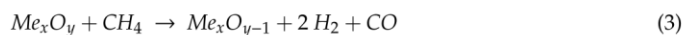
The reduction of greenhouse gas emissions (GHGE) in order to reach the unilateral goals agreed upon in the UNFCCC Paris Agreement is one of the major challenges of civilization in the 21st century. While notable advances in the energy sector have been achieved in recent years [1,2], the de-carbonization of the transport sector, which is responsible for almost one quarter of the European GHGE emissions [3] and consumes 36% of the global final energy [1], signifies a key issue on the path to a closed carbon cycle. Especially the replacement of conventional fuels in the heavy freight transport and aviation industry, where electrification is currently not viable, remains a major hurdle. When considering the European Union's Renewable Energy Directive (RED II) [4], which set a target of a share of 14% renewable energy in the transport sector by 2030, while at the same time alleviating negative impacts on food availability and prices, it is clear that significant advances in renewable fuel generation are required.

The production of so-called advanced or second-generation biofuels through thermochemical conversion of biomass-based residues is an auspicious pathway to achieve these goals. Gasification is

a mature thermochemical biomass conversion process, although its primary use is the generation of heat and electricity, while the synthesis of advanced biofuels through the gasification route has not been implemented in an industrial scale, yet [5].

Commonly, biomass gasification is achieved through utilizing air or pure oxygen in the gasifier. Albeit, pure oxygen is typically used in gasification processes embedded in biomass-to-biofuel process chains, since a nitrogen-free, high calorific value syngas is required for fuel synthesis [6]. The provision of this oxygen requires an air separation unit (ASU), which is associated with high capital and operational costs, hence adversely affecting the energetic plant efficiency and process economics [6,7]. Alternatively, steam [8–10] or carbon dioxide [10–12] can be deployed as the gasification medium. Yet, either of the two suffers from slow gasification kinetics [6,13,14] and strong process endothermicity [6,15], limiting the process efficiency. To circumvent this, the dual fluidized bed gasification (DFBG) technology achieves feedstock gasification in two connected reactors; a gasifier in which steam gasification of the deployed feedstock is attained, and a combustor in which the residual char is combusted facilitating full char conversion and the provision of heat, which is transported to the gasifier using an inert circulating bed material [16–18].

A similar gasification concept allowing for decent fuel conversions, without requiring an ASU is the chemical looping gasification (CLG) process, where biomass gasification is also carried out in two separate reactors (see Figure 1) [15,19–22]. Just as the related chemical looping combustion (CLC) process, CLG is realized using two coupled fluidized bed reactors, in order to attain good heat and mass transport characteristics [21,23,24]. Here, steam or carbon dioxide provide bed fluidization and gasification (see Equations (1) and (2)) of the feedstock in the fuel reactor (FR) [15,24]. Additional oxygen for the partial (see Equation (3)) or full (see Equations (4)–(6)) oxidation of gaseous hydrocarbon species, enhancing gasification kinetics and reducing the process endothermicity, is supplied through a circulating oxygen carrier (OC,  $Me_xO_y$ ) [19,21,24]. Furthermore, the homogeneous water gas shift (WGS) reaction (Equation (7)) takes place inside the gas phase.



The required oxygen transport to the FR is facilitated through a repeated regeneration of the OC (see. Equation (8)) in the air reactor (AR) with oxygen contained in the inlet air [15,20,24]. Moreover, unconverted char is combusted in the air reactor (see. Equation (9)), leading to a full conversion of the deployed feedstock [23,25].



The latter reaction is generally undesired, as a high carbon conversion is targeted inside the FR, in order to maximize the carbon capture efficiency of the process [23,26,27]. In literature, carbon capture efficiencies in the range of 90–99% are reported for CLC [26,28,29]. As approximately one third of the carbon contained in the feedstock is transferred into the valorized end-product (e.g., liquid Fischer-Tropsch fuels) in process chains employing CLG for syngas generation, this means that up to 65% of the carbon contained in the feedstock can be captured and stored, constituting negative

emissions in case biogenic feedstocks are being employed. Yet, in reality figures falling short of this value can be expected, as a fraction of the feedstock carbon will be lost in the AR in the form of  $\text{CO}_2$ .

Apart from the oxygen transport, the continuous solid circulation between the two reactors provides the required heat transport from the AR, in which the exothermic re-oxidation of the OC occurs, to the FR, where the endothermic gasification reactions take place [15,19,23], thus allowing for stable elevated reactor temperatures.

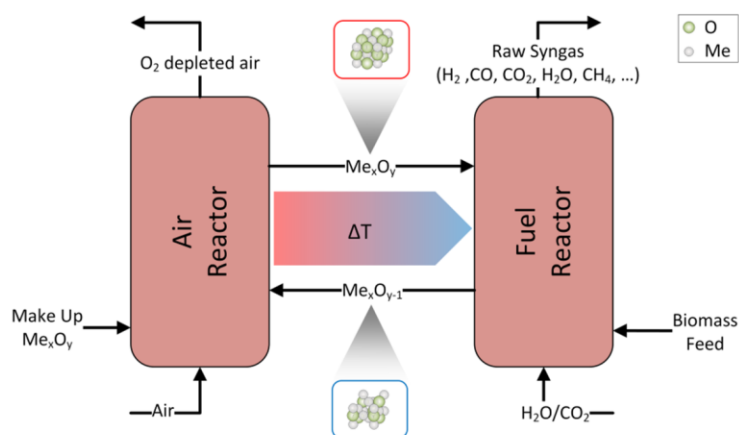


Figure 1. Schematic of chemical looping gasification (CLG) process.

CLG not only offers excellent characteristics in terms of feedstock flexibility [24], but is especially well suited for biomass-based feedstocks [30,31], commonly exhibiting a reactive char and containing a large fraction of volatiles. This means that high char conversions can be achieved through the gasification reaction with steam or  $\text{CO}_2$ , while volatiles are converted to the desired syngas species through their partial oxidation on the OC surface (see Equation (3)). Furthermore, it is reported that iron containing materials [32–35] can facilitate the cracking and oxidation of tars, which are known to be formed in significant amounts during biomass gasification [36].

While the role of the gasification agent is similar in CLC and CLG (i.e., char gasification), the oxygen carrier is meant to only partially oxidize the gaseous species in CLG, yielding a raw product gas with a high heating value [23,37], instead of a heat release from the AR, which is used for heat and power generation in CLC [24,38,39]. This shift from CLC to CLG is achieved through lowering the oxygen-to-fuel equivalence ratio in the FR to values below unity. An autothermal CLG process, maximizing the chemical energy contained in the raw syngas without relying on external heating, is obtained when the net heat release from the process equals zero (neglecting heat losses).

Although one might hence deduce that the transition from CLC to CLG is straightforward, there are major differences between the two processes. While large OC circulation rates are favorable in CLC, as they allow for a high oxygen availability in the FR, which favors fuel combustion [40–43] and provide for a large heat transport from the AR to the FR [41,44,45], the former is not desired in CLG. Here, the oxygen availability in the FR has to be limited in order to prevent the full oxidation of the employed feedstock. However, even more so than in CLC, CLG requires large heat transportation rates from the AR and FR due to the less pronounced occurrence of full oxidation reactions (Equations (4)–(6)), at the cost of highly endothermic partial oxidation reactions (Equation (3)) in the FR. This leads to a fundamental challenge in terms of process control, as both, heat and oxygen transfer between the two reactors, have to be controlled independently in order to attain an autothermal CLG process. Initial advances to reach this target were made by Ge et al. [37], diluting an active OC material with an inert, thus obtaining stable reactor temperatures for a lab-scale CLG unit. Yet, due to the significance of this inherent challenge, an in-depth analysis of this issue is required. Therefore, this work takes a holistic

approach to this matter, employing process simulations in order to establish suitable process control measures to attain an autothermal CLG process. In the following, the developed process model will be introduced in Section 2, before general process control and optimization strategies are presented and discussed in detail in Section 3. To round off these elucidations, the most crucial findings and an outlook on future research topics are given in Section 4 of this article.

## 2. Modelling Methods

### 2.1. Description of the Process Model

The deployed Aspen Plus™ model, shown in Figure 2, is largely adopted from a previous study by Ohlemüller et al. [25]. Here, the chemical reactions occurring in the AR and FR are modelled in two separate reactors, whereas gas-solid and solid-solid separation is achieved through cyclones and separators, respectively. In order to reduce model complexity, the AR and FR were modelled as equilibrium RGIBBS reactors in this work, as this simplification allows for a basic description of the most crucial phenomena required for process control and obviates the necessity of accurate kinetic data. To account for the solid circulation in chemical looping processes, a constant mass stream of solids continuously cycles through the system (OCR-TOAR/OCO-TOFR), after being added to the system after initiation of the simulation (INIT).

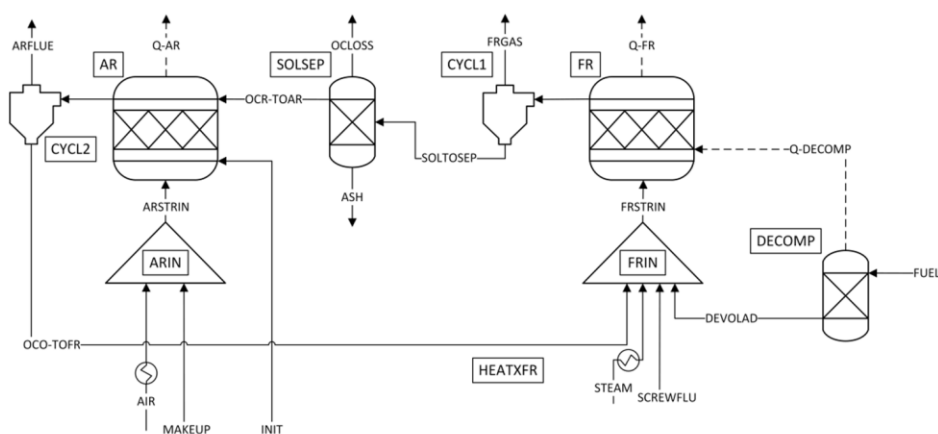


Figure 2. Flow sheet of the Aspen Plus™ CLG process model.

For completeness and comprehensibility reasons, all components and streams are briefly described in the following:

- Prior to any calculation, an initial solid mass flow is given into the system (INIT), to model the circulating solid OC mass. Instead of estimating the actual solid loss, the approach of Ohlemüller et al. [25], setting the total OC loss (OCLLOSS) to 1% of the circulating mass to achieve fast flowsheet conversion, was adopted. The same amount of fresh solids was constantly fed to the AR (MAKEUP), to achieve constant solid circulation.
- For both reactors, cyclones are employed to achieve solid-gas separation. The FR products are separated into a gas (FRGAS) and solid (SOLTOSEP) stream, via CYCL1 (separation efficiency 100%). Similarly, the AR products are separated into a gas (ARFLUE) and solid stream (OCO-TOFR) in CYCL2 (separation efficiency 100%).
- All streams entering the process are fed at ambient temperature ( $T_0 = 25\text{ °C}$ ), except for the stream STEAM, which is fed as saturated steam ( $120\text{ °C}$ ).

- The steam and the air entering the FR/AR are preheated to a designated inlet temperature ( $T_{air,AR}$ ,  $T_{H_2O,FR}$ ). If not stated otherwise, the inlet temperature of both streams (STEAM, AIR) when entering the FR/AR is set to 400 °C.
- As Aspen Plus™ is not equipped to handle solid fuels, the biomass feedstock (FUEL) is fed to the decomposer (DECOMP), where it is decomposed into its pyrolysis products (DEVOLAD). The heat of pyrolysis (Q-DECOMP) is transferred to the fuel reactor. A detailed description of the decomposer block is given in Section 2.2.
- The pyrolysis products (DEVOLAD), the gasification agent (STEAMX), the OC recycled from the AR (OCO-TOFR), and the CO<sub>2</sub> required for solid feeding and loop seal fluidization (SCREWFLU) are mixed (FRIN) before entering the fuel reactor.
- Subsequently, the educts entering the fuel reactor (FR) are converted into reaction products according to the chemical equilibrium at the given boundary conditions ( $T_{FR}$ ,  $P_{FR} = 1$  atm).
- The solids leaving CYCL1 are separated into the OC fed to the AR (OCR-TOAR) and a stream containing carbon and ash (SOL) in the solids separation (SOLSEP). This separation signifies the removal of bed material (i.e., OC, ash and unconverted feedstock) from the FR via sluicing during operation. Additionally, a fraction of the oxygen carrier material is removed from the system (OCLOSS), to model OC losses via sluicing and attrition.
- The OC makeup stream (MAKEUP) and the inlet air (AIRX) are mixed (ARIN) before being fed to the AR.
- Inside the air reactor (AR) the reduced OC and the unreacted char react with the oxygen contained in the air according to the chemical equilibrium at the given boundary conditions ( $T_{AR}$ ,  $P_{AR} = 1$  atm).

## 2.2. Decomposer

Generally, the conversion of a fuel during gasification is described by three subsequent mechanisms: drying, pyrolysis and gasification [6]. While the gasification step is modelled in the FR, the former two mechanisms are modelled in the decomposer block in this study. As drying solely encompasses the release of moisture from the fuel [6,46], the main focus of this section is placed on fuel pyrolysis. Ohlemüller et al. [25] applied the pyrolysis model of Matthesius et al. [47] to predict the pyrolysis product composition from coal proximate and ultimate analysis parameters. Although it is reported that the basic mechanism of coal and biomass pyrolysis are similar [6,7], it was decided to employ a pyrolysis model specifically tailored for biomass feedstocks, as this study is focused on the conversion of biomass-based fuels. Neves et al. [48] devised a pyrolysis model for biomass feedstock built on the basis of an extensive experimental database. Similar to the pyrolysis model by Matthesius et al. [47], this model solely requires information on the feedstock composition (C, H, O and char content) to estimate the final chemical composition of the organics after pyrolysis, allowing for its straight forward implementation into the existing Aspen Plus™ model. Cuadrat et al. [49] found that the formation of tar and larger hydrocarbons (>C1) is negligible in the presence of ilmenite and steam/CO<sub>2</sub>. Therefore, the assumption by Ohlemüller et al. [25] and Mendiara et al. [50] that tars and larger hydrocarbons are directly converted to methane and carbon monoxide was also adopted in this study. Moreover, oxygen and hydrogen contained in the char were converted to syngas, resulting in a char solely consisting of carbon. As the FR is modelled based on chemical equilibrium, these simplifications do not have an impact on the final simulation results.

By applying these assumptions, the product compositions after pyrolysis were calculated on the basis of the proximate and ultimate analysis of wood pellets, being the model feedstock for all subsequent considerations (see Table 1).



**Table 1.** Summary of the Ultimate and Proximate analysis for industrial wood pellets.

Ultimate Analysis	wt-%	Proximate Analysis	wt-%
C (d.a.f.)	50.8	Moisture	6.5
H (d.a.f.)	6	Ash (d.b.)	0.7
N (d.a.f.)	0.07	Volatile matter (d.b.)	85.1
O (d.a.f.)	43.2	Fixed carbon (d.b.)	14.2
S (d.a.f.)	0.008		
Cl (d.a.f.)	0.006		
Net calorific value [MJ/kg]	17.96		

Since the pyrolysis product composition is highly temperature dependent [6,7,48], a constant temperature representing the FR temperature during CLG was selected as the input for the pyrolysis model ( $T_{devol.} = 900$  °C). A summary of the final product composition after de-volatilization, which was implemented into the process model, is given in Table 2.

**Table 2.** Mass yields [wt-%] for DECOMP Aspen Plus<sup>®</sup> block for industrial wood pellets according to pyrolysis model of Neves et al. [48] ( $T = 900$  °C).

Component	wt-%	Component	wt-%
ASH	0.65	H <sub>2</sub> O	14.06
CO	55.20	N <sub>2</sub>	0.06
C	11.92	CO <sub>2</sub>	3.11
CH <sub>4</sub>	13.55	H <sub>2</sub> S	0.01
H <sub>2</sub>	1.43		

### 2.3. Boundary Conditions

For all subsequent simulations, the biomass input was selected in such a way, that the thermal load,  $P_{th}$ , of the chemical looping gasifier amounted to 1 MW. In terms of the circulating solid materials, the deployed oxygen carrier material is ilmenite, for which it has been established that the major redox stages are FeO + TiO<sub>2</sub>, Fe<sub>3</sub>O<sub>4</sub>, TiO<sub>2</sub> and Fe<sub>2</sub>TiO<sub>5</sub> [51]. These redox stages were modelled as FeTiO<sub>3</sub> (for FeO + TiO<sub>2</sub>), Fe<sub>3</sub>O<sub>4</sub>, TiO<sub>2</sub>, and Fe<sub>2</sub>O<sub>3</sub> + TiO<sub>2</sub> (for Fe<sub>2</sub>TiO<sub>5</sub>). Deeper redox stages (e.g., FeO) were also considered in the process model, yet were not found to be formed in notable amounts. The inert solid sand was modelled through pure SiO<sub>2</sub>. The FR and AR are operated under atmospheric pressure. Moreover, the air reactor temperature was set to 1050 °C, if not stated otherwise. The fuel reactor temperature results from the energy balance of the process, requiring that both reactors are in heat balance ( $\dot{Q}_{FR} = 0$ ,  $\dot{Q}_{AR} \geq 0$ ). As the kinetic syngas inhibition of char gasification reactions [8,12] is not considered in the RGIBBS equilibrium calculation, full char conversion is attained inside the FR for all temperatures considered in this study. Although this simplification signifies a deviation from reality, it does not impact the general inferences which will be elaborated on hereinafter. For the steam to biomass ratio in the FR a value of 0.9, reported for a 2–4 MW<sub>th</sub> chemical looping gasifier in literature [52], was selected if not stated otherwise. During CLC/CLG operation CO<sub>2</sub> is required for fuel feeding and inerting. This stream of CO<sub>2</sub>, entering the fuel reactor, was selected in such a way that the CO<sub>2</sub> to biomass ratio amounts to 0.2, to take into account that the CO<sub>2</sub> input through the feeding section increases with increased thermal load. The two remaining process variables, the air mass flow entering the AR and the circulating oxygen carrier mass, were adjusted in such a way that autothermal CLG operation was achieved. A summary of all boundary conditions is given in Table A1 in Appendix A.

### 3. Results and Discussion

#### 3.1. Attaining CLG Behavior

Generally, shifting from a combustion to a gasification process is achieved through lowering the air/oxygen-to-fuel ratio of the process, thereby decreasing the ratio of fully to partially oxidized gas species leaving the process and hence increasing the heating value of the product gas [6,53,54]. Here, the critical parameter is the so called air-to-fuel equivalence ratio given by the ratio of oxygen fed to the AR,  $\dot{m}_{O,AR}$ , and the oxygen required for full feedstock combustion,  $\dot{m}_{O,stoich}$ :

$$\lambda = \frac{\dot{m}_{O,AR}}{\dot{m}_{O,stoich}}. \quad (10)$$

According to this definition, (close to) full combustion of the feedstock is attained for air-to-fuel equivalence ratios larger than unity ( $\lambda > 1$ ), while gasification processes require sub-stoichiometric oxygen feeding (i.e.,  $\lambda < 1$ ).

Due to the dissection of the gasification/combustion reaction into two separate reactors in chemical looping processes, there is no direct contact between the air entering the AR and the fuel entering the FR. Hence, the application of an alternative parameter, the oxygen-carrier-to-fuel equivalence ratio,  $\phi'$ , relating the amount of oxygen carried by the OC to the FR to the oxygen required for stoichiometric combustion, has been suggested [43]:

$$\phi' = \frac{R_{OC} \cdot \dot{m}_{OC}}{\dot{m}_{O,stoich}}. \quad (11)$$

Here,  $R_{OC}$  denotes the oxygen transport capacity of the given oxygen carrier material. While this parameter accurately relates the two quantities for CLC, where the OC always leaves the AR in a (close to) fully oxidized state, this is not necessarily the case in CLG. Therefore, a slightly altered oxygen-carrier-to-fuel equivalence ratio,  $\phi$ , considering the possibility of a partially reduced OC leaving the AR, has been proposed for gasification applications [35]:

$$\phi = \frac{R_{OC} \cdot \dot{m}_{OC} \cdot X_{s,AR}}{\dot{m}_{O,stoich}}, \quad (12)$$

where  $X_{s,AR}$  signifies the oxidation degree of the oxygen carrier at the AR outlet, given by [24,35]:

$$X_{s,AR} = \frac{m_{OC,AR} - m_{OC,red}}{R_{OC} \cdot m_{OC,ox}}. \quad (13)$$

Here,  $m_{OC,red}$  and  $m_{OC,ox}$  are the mass of an OC sample in a fully reduced and oxidized state respectively, while  $m_{OC,AR}$  is the mass of the OC sample leaving the AR. For ilmenite the fully reduced oxygen carrier is approximated by  $\text{FeTiO}_3$ , the fully oxidized state is approximated by  $\text{Fe}_2\text{O}_3 + 2\text{TiO}_2$ , and  $\text{Fe}_3\text{O}_4 + 3\text{TiO}_2$  denotes an intermediate redox state ( $X_s = 0.67$ ).

In order to assess how  $\lambda$  and  $\phi$  have to be adjusted in order to obtain an efficient CLG process, one should first assess the general impact of these two parameters on the process. Due to the relative fast kinetics of the OC re-oxidation [55–57], the oxygen carrier is often assumed to leave the AR in a (close to) fully oxidized state for  $\lambda > 1$  in chemical looping processes. In contrast, sub-stoichiometric air-to-fuel equivalence ratios ( $\lambda < 1$ ) only lead to a partial re-oxidation of the OC in the AR. Following the same logic, the OC material can be assumed to leave the FR in a (close to) fully reduced state in case  $\phi < 1$ , whereas partial reduction is attained for  $\phi > 1$ . From these deductions, it becomes clear that “standard” CLC operation is attained for  $\lambda > 1$  and  $\phi > 1$ , [42,43]. Here, a highly oxidized OC leaves the AR, before being partially reduced in the FR, which is illustrated in Figure 3a.

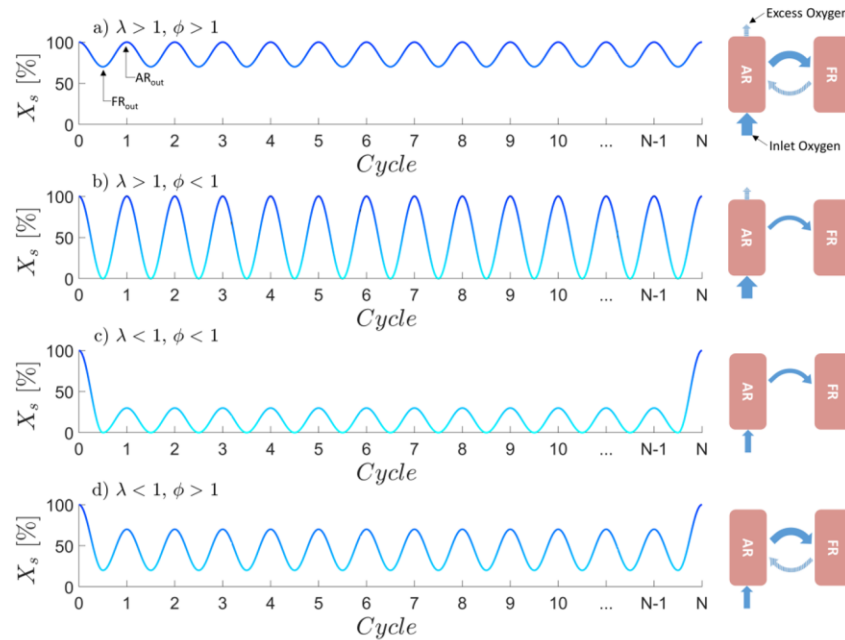


**Figure 3.** Different chemical looping modes (a–d) dependent on the air-to-fuel equivalence ratio  $\lambda$  and the oxygen-carrier-to-fuel equivalence ratio  $\phi$ .

When targeting pronounced syngas formation, the oxygen release in the FR has to be limited, so that full feedstock oxidation is prevented [35,52]. The most obvious avenue that can be pursued to achieve this is lowering  $\phi$  below unity. When doing so, the employed air-to-fuel equivalence ratio  $\lambda$  determines how much oxygen is transported between the two reactors per gram of OC. In case of  $\lambda > 1$ , which is illustrated in Figure 3b, the oxygen carrier undergoes a full redox cycle and hence the full oxygen transport capacity of the OC material (i.e.,  $R_{OC}$ ) is exploited. On the other hand,  $\lambda < 1$  means that in equilibrium the OC leaves the AR in a partially reduced state, hence also reducing the mass specific oxygen transport of the OC (see Figure 3c). Lastly, one might also consider a process with  $\lambda < 1$  and  $\phi > 1$ , as shown Figure 3d. In order to attain a steady-state process exhibiting these characteristics, full reduction of the oxygen carrier has to be prevented in the FR (e.g., kinetically), so that a fraction of oxygen is transported back to the AR. This means that in contrast to the former approaches, this case cannot be attained in equilibrium-like conditions. While this approach might also be feasible for CLG operation in theory, straight forward measures allowing for a controlled oxygen release in the FR are not at hand. Consequently, lowering the oxygen-to-fuel-ratio in the FR (i.e.,  $\phi < 1$ ) is the most promising avenue to attain CLG behavior. When aiming for large syngas yields,  $\phi$  has to assume values below unity, while values exceeding unity are targeted in CLC [42,43]. In the following, different effective control strategies to achieve this reduction in  $\phi$ , required for pronounced syngas formation in the FR, while at the same time achieving an autothermal process, will be investigated.

In order to simplify the subsequent considerations, a standard parameter to describe gasification processes, the cold gas efficiency (CGE),  $\eta_{CG}$ , will be deployed hereinafter. It describes which amount of chemical energy from the fuel is transferred to the gaseous FR product gas during gasification [6,7].

$$\eta_{CG} = \frac{\dot{n}_{gas,FR} \cdot (x_{CH_4,FR} \cdot LHV_{CH_4} + x_{CO,FR} \cdot LHV_{CO,FR} + x_{H_2,FR} \cdot LHV_{H_2})}{\dot{m}_{fuel} \cdot LHV_{fuel}} \quad (14)$$

Here,  $\dot{n}_{gas,FR}$  and  $\dot{m}_{fuel}$  denote the mole flow of the product gas stream and the fuel input into the FR, respectively.  $LHV$  is the lower heating value of the fuel (mass basis) and the gas species (molar basis) and  $x_i$  is the mole fraction of the gas species.

### 3.2. Reduction of OC Circulation

One approach to obtain CLG behavior, which has been suggested by Pissot et al. [52], is reducing the amount of OC cycled through the system ( $\dot{m}_{OC}$ ), hence reducing  $\phi$ . This approach can be deduced directly from Equation (12). Due to the resulting lower oxygen transport to the FR, syngas formation is favored, as less oxygen for full oxidation of the feedstock is provided by the OC. The simulation results for this approach are given in Figure 4. When considering the gas composition (Figure 4a) of the streams leaving the air and fuel reactor, various trends are visible. As expected, the syngas content in the gaseous FR products increases with decreasing OC circulation rate, which can directly be attributed to the lower oxygen/fuel ratio in the FR. Consequently, steam and  $CO_2$  formation decrease. Yet, it has to be noted that substantial syngas concentrations are only attained for  $\phi < 1$ , which requires significant reductions in the OC circulation rate, when compared to CLC, where OC-to-fuel equivalence ratios as high as 8 [27] and 25 [40] are reported in literature for solid and gaseous fuels, respectively. For the gas concentrations leaving the AR, a strong impact of  $\phi$  on the effluent oxygen is visible. As the inlet air mass flow was not varied ( $\lambda = 1.2$ ), this observation is clear, as less  $O_2$  is removed from the gas stream due to the lower OC circulation for  $\phi < 1$ . Furthermore, the  $CO_2$  content in the AR product is predicted to be insignificant, indicating a complete char conversion, which is expected in chemical equilibrium. When considering Figure 4b, showing the solid composition after the fuel and air reactor, it can be seen that the OC leaves the AR and FR in a fully oxidized ( $Fe_2O_3 + TiO_2$ ) and reduced ( $FeTiO_3$ ) state, respectively for  $\phi < 1$ , whereas the OC is only partially reduced (indicated through the presence of  $Fe_3O_4$ ) in the FR in case  $\phi$  exceeds unity. Hence, the fraction of  $FeTiO_3$  leaving the FR strongly increases with decreasing OC circulation, signifying a higher degree of reduction of the OC, due to the lower oxygen availability. As expected one consequently obtains chemical looping combustion behavior (see Figure 3a) for oxygen-carrier-to-fuel equivalence ratios greater than unity ( $\phi > 1$ ), whereas chemical looping gasification behavior (see Figure 3b) is attained for  $\phi < 1$ .

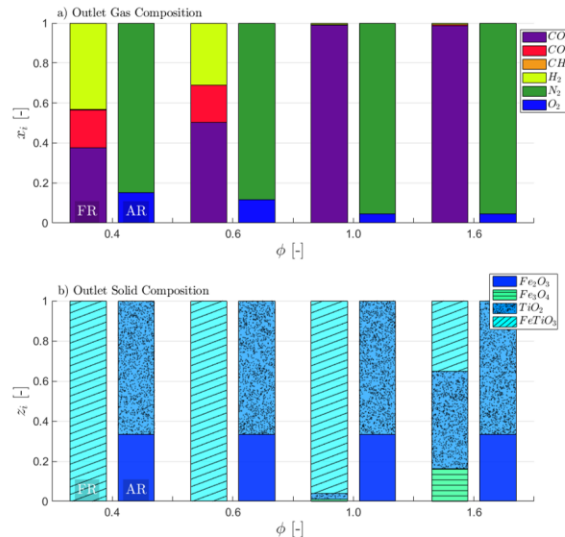


**Figure 4.** Simulation results for CLG operation through reduced oxygen carrier (OC) circulation. Dry molar gas composition (a) and molar solid composition (b) as a function of  $\phi$  for varying OC circulation rates ( $\lambda = 1.2$ ).

Based on these findings, one can conclude that a successful shifting from CLC to CLG for a given air-to-fuel ratio can be attained through a reduction in the OC circulation, which can also be seen in Figure 5a, showing a linear dependence between the two parameters. This means that for a change of  $\phi$  from 1.0 to 0.5, the OC circulation rate has to be halved. However, lower solid circulation rates also result in a proportional decrease in the heat transport from the AR to the FR and hence a drop-off in FR temperatures [35,58]. While a moderate decrease in fuel reactor temperatures with decreasing OC circulation rate is visible for  $\phi > 1$ , for which complete feedstock conversion is attained in the FR, this decrease becomes more prominent for  $\phi < 1$ , where gasification reactions in the FR are dominant, hence increasing the endothermicity of reactions occurring in the FR. Consequently, FR temperatures fall below 800 °C for  $\phi < 0.5$ , where the availability of circulating OC material for sensible heat transport between the FR and AR is halved, when compared to  $\phi = 1$  and more importantly the syngas content in the FR products is significant (see Figure 4a). This increase in syngas content also goes in hand with a decrease in the total net heat release from the CLG process ( $\dot{Q}_{net}$ ), which can be calculated from the difference in the enthalpies of the streams entering ( $in$ ) and leaving ( $out$ ) the air and fuel reactor (see Equation (15)), as the enthalpy of the FR products increases.

$$\dot{Q}_{net} = \sum_{FR,in} \dot{m}_i \cdot h_i - \sum_{FR,out} \dot{m}_i \cdot h_i + \sum_{AR,in} \dot{m}_i \cdot h_i - \sum_{AR,out} \dot{m}_i \cdot h_i \quad (15)$$

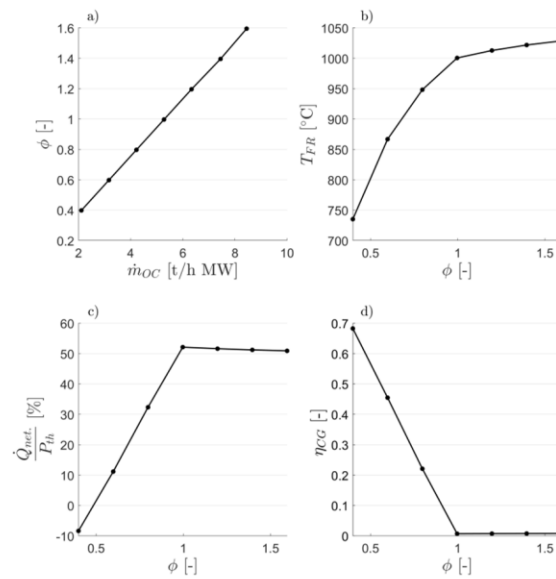


**Figure 5.** Simulation results for CLG operation through reduced OC circulation. OC-to-fuel ratio as a function of the OC circulation rate (a). Fuel reactor temperature (b), relative net process heat (c), and cold gas efficiency (d) for different values of  $\phi$  ( $\lambda = 1.2$ ).

The decrease in net process heat release with decreasing  $\phi$ , indicating the retaining of chemical energy in the FR products, also becomes visible upon consideration of Figure 5c, depicting the relative net heat release of the process for the different OC-to-fuel ratios. For the given boundary conditions, an autothermal process, for which syngas yields are maximized without relying on external heat addition ( $\dot{Q}_{net} = 0$ ) is attained for an OC to fuel ratio of approx. 0.5. The resulting cold gas efficiency for this operating point amounts to approx. 60% (see Figure 5d) at a FR temperature of 775 °C. Although the equilibrium model predicts full char and volatile conversions for these temperatures (see Figures 4a

and 5d), char, volatile, and tar conversion are known to be kinetically governed processes in chemical looping systems [25,55,56,59], leading to product compositions deviating strongly from equilibrium composition [35,52]. Due to this reason, temperature differences in the range of 50 to 100 °C are generally targeted in dual fluidized bed gasification [16], in order to obtain sufficiently high gasifier temperatures, allowing for decent char, volatile, and tar conversions. Accordingly, FR temperatures in the range of 850–950 °C are desired in CLG, in order to attain high carbon capture efficiencies and cold gas efficiencies as well as low syngas tar loads [20,23,37,60,61].

These considerations underline that, although the desired reduction in  $\phi$  is possible, attaining an efficient autothermal CLG process through a reduction in the OC circulation rate is not a recommendable strategy as it entails low fuel reactor temperatures, due to the dual-purpose of the OC circulation (i.e., oxygen and heat transport). Consequently, alternative approaches, allowing for a decoupling of oxygen and heat transport between the AR and FR and hence increased FR temperatures are required, in order to attain a CLG process exhibiting the desired characteristics.

### 3.3. Dilution of OC with Inert Bed Material

One strategy allowing for a decoupling of oxygen and heat transport between air and fuel reactor, which has been discussed in literature, is employing a mixture of an active OC material and a solid inert species (e.g., sand) [35,37,52]. Here, the inert fraction serves purely as a heat carrier, transferring sensible heat between the two reactors, without participating in the occurring reactions, while the active OC fraction fulfills its dual purpose of oxygen and heat transport. Consequently, this approach is a combination of CLG and dual fluidized bed gasification, which solely employs inert bed materials for heat transport. Following this logic, Ge et al. [37] found that through accurately tailoring the mixing ratio of inert silica sand and hematite, serving as an OC, FR temperatures can be stabilized at elevated levels (i.e., >900 °C), while at the same time ensuring a controlled oxygen transport to the FR, resulting in large syngas yields.

In terms of the impact of the variation in OC-to-fuel ratio on gas compositions achieved through this dilution of the OC material with an inert, similar observations are obtained (see Figure 6a). This means syngas formation increases steadily for  $\phi < 1$ . Moreover, the OC carrier composition, shown in Figure 3b, follows similar trends as observed for a plain reduction in the OC circulation rate (see Section 3.2), with a fully reduced OC leaving the FR for  $\phi < 1$  (see Figure 3b), whereas only partial reduction is observed for  $\phi > 1$  (see Figure 3a). Yet, the fraction of active OC material clearly decreases with decreasing  $\phi$ , due to the dilution with silica sand.

As the total amount of circulating solids is kept constant, the mass of circulating OC material is inversely proportional to the dilution factor. This means that there exists a linear relationship between the solid fraction of the inert material ( $z_{SiO_2}$ ) and  $\phi$ , which is visible in Figure 7a. Hence, for a given solid circulation rate, shifting from CLC to CLG can be attained through increased inert dilution. The positive effect of inert addition on FR temperatures becomes apparent upon consideration of Figure 7b. In contrast to a direct reduction in the OC circulation rate, the substitution of a fraction of the active metal oxide with an inert heat carrier allows for a sustaining of FR temperatures above 980 °C even for OC to fuel ratios as low as 0.5. Due to this increase in FR temperatures, the average temperature of the CLG process increases, leading to a slightly increased  $\phi$  of approx. 0.55 for which autothermal operation is attained (see Figure 7c) (Higher process temperatures increase the heating demands of the educts entering the FR and AR and hence reduce the OC-to-fuel ratios for which autothermal operation can be obtained). Therefore, the cold gas efficiency obtained for autothermal operation for the given approach is also marginally reduced (see Figure 7d), when compared to the approach discussed in Section 3.2. Yet, it has to be noted that due to the intensified heat transport between the AR and FR, significantly smaller reactor temperature gradients are required for the given approach. Consequently, AR temperatures can be lowered without jeopardizing char conversions in the FR, thus reducing average process temperatures and allowing for strongly increased cold gas efficiencies (see also Section 3.5). Another advantage of this approach is that a catalytic material,

not participating in oxygen transport (e.g., olivine), could be employed for OC dilution instead of sand, allowing for improved syngas characteristics with regard to tar content.

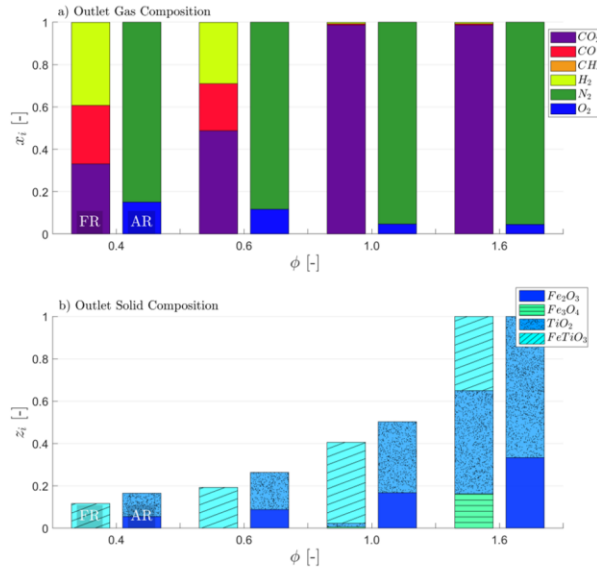


**Figure 6.** Simulation results for CLG operation through OC dilution with inert  $SiO_2$  sand. Dry molar gas composition (a) and molar solid composition (b) as a function of  $\phi$  for varying OC circulation rates ( $\lambda = 1.2, \dot{m}_{OC} + \dot{m}_{SiO_2} = const.$ ).

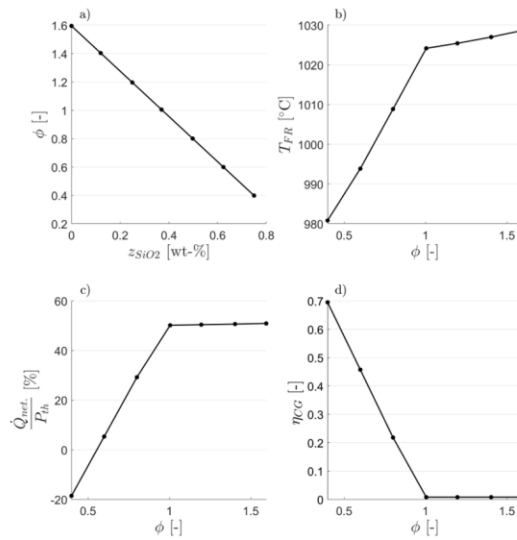


**Figure 7.** Simulation results for CLG operation through OC dilution with inert  $SiO_2$  sand. OC-to-fuel ratio as a function of the inert concentration of the circulating solid mixture (a). Fuel reactor temperature (b), relative net process heat (c), and cold gas efficiency (d) for different values of  $\phi$  ( $\lambda = 1.2, \dot{m}_{OC} + \dot{m}_{SiO_2} = const.$ ).

Despite the presented advantages, Larsson et al. [35] found that, albeit slightly reducing tar loads, the addition of an active OC (ilmenite) to an inert circulating bed material in a dual-fluidized bed gasifier (for  $\phi < 0.2$ ), entails a continuous drop in cold gas efficiency. This was explained by the fact that ilmenite addition does not enhance char conversion significantly, while its presence leads to a partial oxidation of the product gas. On the other hand, Pissot et al. [52] found that dilution of an active OC bed with up to 90% of an inert material does not entail visible enhancements in the cold gas efficiency of the CLG process, while it has a visible negative impact on carbon conversion. This shows that the mixing of an inert and an active OC material can have different effects on the process depending on the governing boundary conditions. Another drawback of this approach is that, albeit the addition of solids allows for an adjustment of  $\phi$  during operation, it leads to a large system inertia, making it an arduous task to quickly react to disturbances. Moreover, a fraction of the solid material has to be removed from the system for ash removal in a continuously operated CLG unit. Economic considerations require a separation of these materials for further processing, recycling, and disposal. Clearly, the presence of a third component (i.e., sand, olivine) further complicates this task. Lastly, it is known that the operation of a fluidized bed with multiple bed materials of different characteristics brings about additional challenges in terms of material fluidization, entrainment, and attrition, as well as bed segregation [62]. Due to these reasons it was also suggested to employ materials of a low oxygen transport capability ( $R_O$ ), such as LD-slag, containing a large inactive fraction not participating in the oxygen transport, which fulfills the purpose of the inert heat carrier [52]. Through this, oxygen carrier circulation rates providing sufficient heat transport between the reactors can be targeted, without obtaining OC-to-fuel equivalence ratios above unity. Yet, for this approach the main challenge is finding suitable OC materials exhibiting an oxygen transport capability in the desired range, high activity towards hydrocarbon conversion, and good chemical and mechanical stability.

### 3.4. Reduction of Air-to-Fuel Equivalence Ratio

To allow for a less restricted material selection and avoid solid inert addition, an alternative strategy to decouple oxygen and heat transport between the AR and FR is required. In order to achieve this, Larson et al. [35] suggested the deployment of a secondary system in which the OC is pre-reduced before entering the FR. This means that, as shown in Figure 3c, a partially reduced OC enters the FR ( $X_s < 1$ ), thus entailing a lower OC-to-fuel ratio (see Equation (12)). Instead of employing a secondary reactor to accomplish this, one can also operate the AR in a sub-stoichiometric fashion ( $\lambda < 1$ ), thereby preventing full re-oxidation of the OC in the AR. This means that in order to attain CLG conditions, the amount of air fed into the air reactor can be reduced, while retaining a constant OC circulation. As a consequence, the OC steadily reaches a lower degree of oxidation, hence lowering its oxygen release in the FR, until steady state is reached (more details see Appendix B). This approach has already been pursued in a 140 kW<sub>th</sub> chemical looping reforming unit, employing methane as a fuel [44]. The suggested concept becomes more lucid when considering the simulation results shown in Figure 8. Clearly, the amount of fully reduced ilmenite leaving the air and fuel reactor increases when decreasing the air input into the AR for  $\phi < 1$  (see Figure 8b). While the same is true for the solids leaving the FR for all presented CLG approaches, a strong increase in the FeTiO<sub>3</sub> and Fe<sub>3</sub>O<sub>4</sub> content in the AR products is obtained when reducing  $\lambda$  below unity. This can be explained by the fact that the oxygen available in the air reactor is insufficient to fully re-oxidize the OC, signified through an O<sub>2</sub>-free product gas from the AR for  $\phi < 1$  (see Figure 8a). Consequently, a pure stream of N<sub>2</sub> containing small concentrations of Argon and other minor compounds is produced in the AR [44]. Since substantial quantities of OC are cycled through the system in a fully reduced state, they effectively act as an inert, meaning that they transfer sensible heat, but do not participate in the occurring chemical reactions through oxygen release and uptake. However, in practice the reduced OC could potentially function as a catalytic site for tar cracking and methane reforming and favor the formation of syngas [32–35], thereby enhancing the process characteristics. Another advantage of the given approach is that an undiluted OC can be employed, which simplifies the required solid-gas and solid-solid (ash-OC-char) separation and the



operation of the CLG unit with regard to the fluidization behavior. Moreover, the net heat duty of the process can be tailored promptly and easily through an adjustment of the air flow to the AR, allowing for quick responses to disturbances (e.g., variations in feedstock composition).

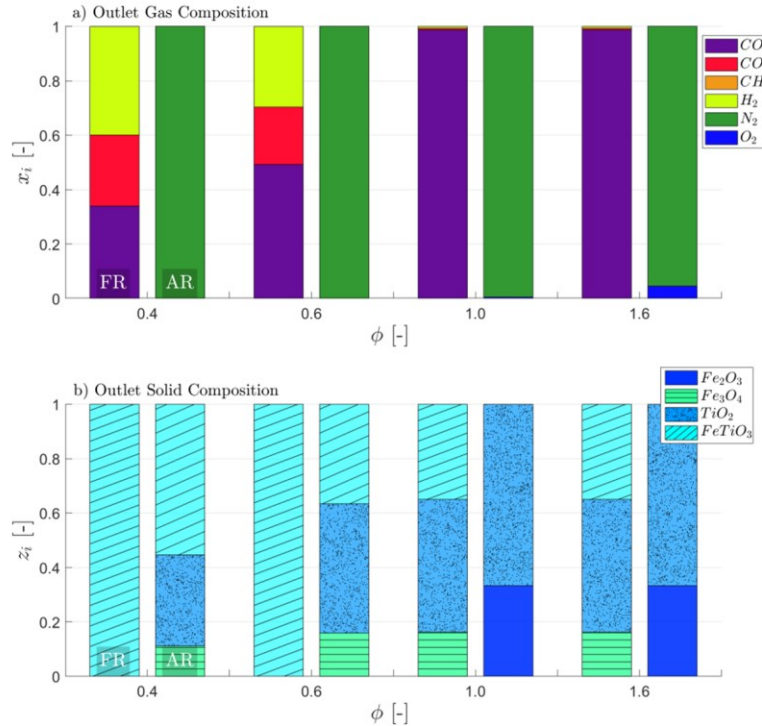


**Figure 8.** Simulation results for CLG operation through reducing  $\lambda$ . Dry molar gas composition (a) and molar solid composition (b) as a function of  $\phi$  ( $\dot{m}_{OC} = const.$ ).

The impact of the air-to-fuel equivalence ratio ( $\lambda$ ) on  $\phi$  is shown in Figure 9a. In CLC mode ( $\lambda > 1$ ), where full OC oxidation is achieved in the AR (i.e.,  $X_{s,AR} = 1$ ),  $\phi$  assumes a constant value, given by the amount of oxygen which is transported by a fully oxidized OC for a given circulation rate, regardless of the deployed air-to-fuel ratio (see Equation (12)). In contrast, lowering  $\lambda$  to values below unity to attain CLG operation means that  $\phi$  and  $\lambda$  are equal, as the oxygen transport to the FR is limited by the oxygen availability in the AR:

$$\phi = \begin{cases} \lambda & \text{for } \lambda < 1 \\ \frac{R_{OC} \dot{m}_{OC}}{m_{O,stoich}} = const. & \text{for } \lambda \geq 1 \end{cases} \quad (16)$$

The discontinuity of this relation for  $\lambda = 1$  can be explained by the fact that when surpassing this value, a transient shift from CLC (see Figure 3a) to CLG (see Figure 3c) behavior (or vice versa) occurs, which goes in hand with a continuous decrease (resp. increase) in the oxidation degree of the oxygen carrier, before steady state sets in (more details see Appendix B).

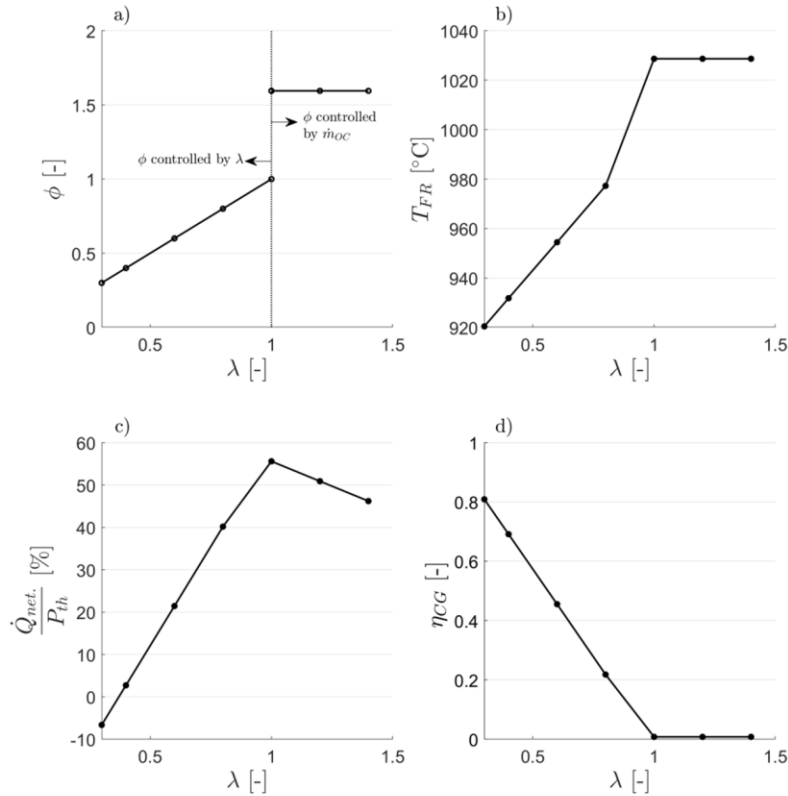


**Figure 9.** Simulation results for CLG operation through reducing  $\lambda$ . OC-to-fuel ratio as a function of the air-to-fuel equivalence ratio  $\lambda$  (a). Fuel reactor temperature (b), relative net process heat (c), and cold gas efficiency (d) for different values of  $\lambda$  ( $\dot{m}_{OC} = const.$ ).

In terms of FR temperatures, Figure 9b shows that the given approach leads to a successful retaining of FR temperatures above 900 °C, even for  $\phi$ -values as low as 0.4, due to the transportation of sensible heat by the OC. Moreover, the given approach yields more beneficial results in terms of the process heat balance, which can be seen in Figure 9c. Clearly, autothermal CLG operation is attained for  $\phi = 0.37$ , which means cold gas efficiencies exceeding 70% can be achieved (see Figure 9d). This is the case as in contrast to the previous approaches (see Sections 3.2 and 3.3), the AR is not operated in air excess during CLG operation, reducing the loss of sensible heat through the AR off-gases. This means that if one would reduce the air feed to the AR to the minimum extent required for full OC re-oxidation for the CLG approach employing inert dilution (see Section 3.3), enhanced cold gas efficiencies could be attained. Nonetheless, the given approach clearly shows advantages in terms of process control due to its flexibility, the possibility of freely selecting a suitable OC material (i.e., no specific limits on  $R_O$ ), without having to consider material mixtures, and the availability of a catalytically active reduced OC material, instead of an inert solid, cycling through the system. Moreover, the chemical strain on the OC material is reduced as the change in oxidation degree for each redox cycle is lower, when compared to the former approaches, relying on full reduction and oxidation in the FR and AR, respectively (see Figure 3b,c), which should have beneficial effects on the OC lifetime.

However, one issue that might arise due to the operation of the AR in a sub-stoichiometric fashion is related to the fact that during operation a fraction of the feedstock char leaves the FR unconverted and hence travels to the AR with the circulating OC material [23,26,27]. This so called “carbon slip”

leads to competing reactions between the OC material and the residual char, in case the AR is operated with  $\lambda < 1$ . Yet, simulations show that in an oxygen deficient atmosphere carbon conversion is favored to OC re-oxidation in chemical equilibrium. Moreover, CO formation shows to be negligible (more details see Appendix C). Due to the fast kinetics of both char conversion and OC re-oxidation, it can be expected that equilibrium-like conditions are attained in the AR and hence all residual char is fully oxidized to CO<sub>2</sub> in the AR. This hypothesis is also supported by chemical looping experiments in small scale fixed bed reactors, during which it was established that in the beginning of the re-oxidation stage oxygen preferentially reacts with deposited carbon before re-oxidizing the OC [21,63,64]. Nonetheless, experiments showing that this is also the case in a continuously operated CLG unit and that CO formation is negligible are required to establish that full char conversion without substantial CO formation in the AR can be attained for this approach. Another issue related to this approach is the potential deep reduction of the OC, which could potentially entail problems related to intensified OC attrition or bed agglomeration. Although the process model does not predict substantial formation of deeper reduction stages (e.g., FeO) in the FR, such phases, related to bed agglomeration, have been found to be formed in CLC under highly reducing conditions [51,65,66]. Therefore, the gravity of this issue should be further investigated in experimental studies.

### 3.5. Optimizing CLG Efficiency

In the previous section it was established that OC-to-fuel equivalence ratios smaller than unity are required in the FR. Moreover, it was demonstrated only when decoupling heat and oxygen transfer between the AR and FR,  $\phi < 1$  and FR temperatures above 850 °C can be obtained for an autothermal CLG process. Thermodynamically speaking, it does not make a difference how this decoupling of heat and oxygen transport is attained, which is why the following considerations will focus on the CLG approach presented in Section 3.4, employing a reduction in the air-to-fuel equivalence ratio to achieve CLG behavior.

When optimizing gasification processes, the trade-off between maximizing the carbon conversion in the gasifier and at the same time attaining high cold gas efficiencies is at the core of many optimization strategies. This is also the case in CLG, where  $\eta_{CGE} = 1$  and complete char conversion is desired, yet not attainable. While large carbon capture efficiencies are obtained in cases where the char is gasified in the fuel reactor to a large extent, which is promoted by high FR temperatures [20,23,37], large steam/biomass ratios [20,37], and high OC-to-fuel ratios (if sufficient char residence times are provided) [27,52], cold gas efficiencies are maximized by the minimization of the oxidation of H<sub>2</sub> and hydrocarbons in the FR [35]. Although full oxidation of syngas in the FR should be limited to achieve large CGEs, formation of steam and CO<sub>2</sub> in the FR is required to a certain extent to obtain autothermal CLG conditions. The degree to which this formation of fully oxidized gas species is required is determined by the criterion of the CLG process being in heat balance ( $\dot{Q}_{net} = 0$ ). This means that the heat release attained through full feedstock oxidation has to balance the heat demand of pre-heating of all inlet streams to the given reactor temperatures, the heat of reaction for endothermic gasification reactions, and the heat losses of the CLG unit. This has also been shown in the previous sections where despite assuming chemical equilibrium (i.e., full feedstock conversion), cold gas efficiencies deviating strongly from unity were obtained for autothermal boundary conditions (see Figures 5, 7 and 9).

Therefore, one approach to enhance the cold gas efficiency in CLG is a reduction in the inlet gas flows entering the air and fuel reactor. Since the air mass flow entering the AR is required to control  $\phi$ , this leaves the steam mass flow entering the FR as a free variable which can be altered to enhance cold gas efficiencies. The effect of a reduction in the steam to biomass ratio on the net heat release of the process is shown in Figure 10a. It is visible that, with a decreasing steam to biomass ratio, the air-to-fuel equivalence ratio for which an autothermal process is attained decreases. Due to the direct correlation between the oxygen availability and cold gas efficiency in CLG (see Figure 10b), this also means that the CGE obtained for autothermal operation increases with decreasing steam/biomass ratio, so that the CGE is raised from 72.5 to 77.1%, when decreasing the steam/biomass ratio from 0.9 to 0.3. However,

it is obvious that the reduction of the steam to biomass ratio would also entail a drop in carbon capture efficiencies of the process, as less steam is available for char gasification and the kinetic inhibition effect of syngas increases with decreasing steam concentrations (entailing larger syngas partial pressures) in the FR [8,12,67,68]. This becomes most obvious for a steam to biomass ratio of 0, for which char conversions in the FR would be diminutive in a real gasifier, due to the slow kinetics of heterogeneous solid-solid OC-feedstock reactions [67–69]. As this drop in char conversion is not predicted by the equilibrium model, the negative effect on process efficiency with decreasing steam to biomass ratio cannot be evaluated in this study. However, sufficient steam availability clearly is a prerequisite in CLG, when targeting large char conversions and hence carbon capture efficiencies.

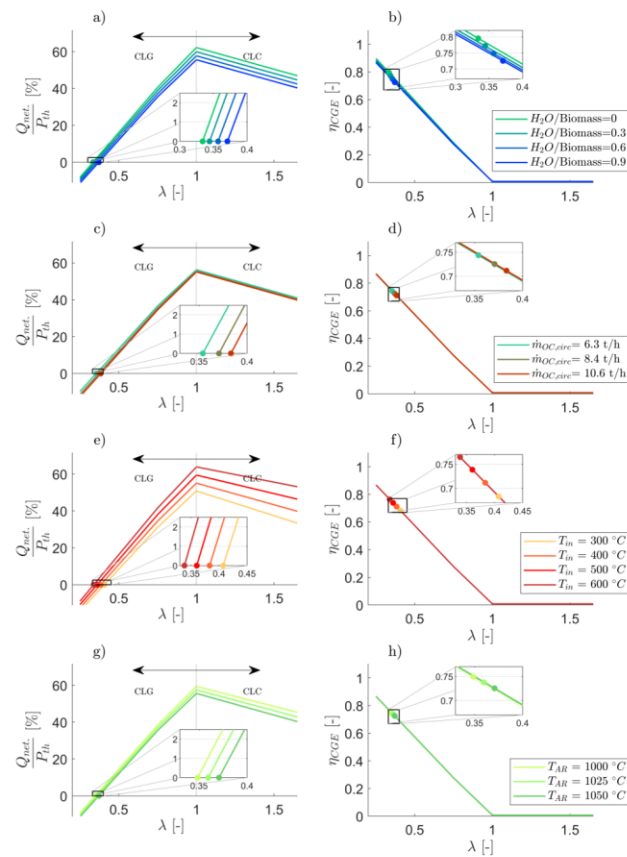


**Figure 10.** Net heat release and cold gas efficiency for CLC/CLG process as a function of the air to fuel equivalence ratio for different steam to biomass ratios (a,b), OC circulation rates (c,d), gas inlet temperatures (e,f), and air reactor temperatures (g,h). Circles mark the cold gas efficiency for autothermal CLG operation ( $\dot{m}_{OC} = const.$ , so  $\phi = \lambda$  for  $\lambda < 1$  and  $\phi = const. > 1$  for  $\lambda > 1$ ).

Another possible measure to enhance CGEs are variations in the circulation rate of the OC, which is shown in Figure 10c,d. Clearly, larger solid circulation rates enhance the heat transport between the reactors and hence entail higher FR temperatures [16]. However, due to material attrition, solid loss, which necessitates continuous make-up feeding, also scales with the circulation rate. As shown in Figure 10d, the effect of this material loss on the process heat balance is comparatively small, thus its effect on the cold gas efficiency is low. However, the model predicts an increase in FR temperatures

from 892 to 951 °C, when increasing the circulation rate from 6.3 to 10.6 t/h. This means that generally, large solid circulation rates are desired in CLG units, as large FR temperatures are beneficial for volatile and char conversion [20,23,37]. Yet, it has to be kept in mind that the solid circulation in dual fluidized bed systems requires solid entrainment from the fluidized bed riser, which can be increased through an increase in gas velocities (i.e., increase in steam/biomass ratio), smaller particle diameters or smaller reactor diameters [16]. Moreover, intensified solid circulation also increases the occurrence of a “carbon slip” to the AR, due to the lower residence times of the char particles in the FR [27,28,70]. This means that the OC circulation rate can only be varied within a given range.

Increasing the inlet temperature of the steam and air entering the FR and AR respectively, thereby decreasing the heat demand for heating up of the gases inside the reactor, is a further strategy to boost cold gas efficiencies. As shown in Figure 10e, this approach allows for a reduction of the air-to-fuel equivalence ratio from 0.38 to 0.34 when increasing inlet temperatures from 400 °C to 600 °C. Hence, maximizing inlet gas temperatures through heat recuperation is a key task in CLG in order to optimize the process efficiency, which is illustrated by the increase in the CGE from 68.3 to 76.5%, when increasing gas inlet temperatures from 300 to 600 °C (see Figure 10f). Due to the absence of corrosive compounds and the high process temperatures, the hot off-gases leaving the AR are ideal for steam generation and heat recuperation. On the other hand, special syngas coolers are being used to recuperate sensible heat from syngas streams for steam production [71–73], highlighting that efficient gas pre-heating using heat from process off-gases is possible in CLG.

Furthermore, variations in the AR temperatures can be considered, in order to enhance CLG process efficiencies. Generally speaking, a reduction in average process temperatures is beneficial for the process heat release, as pre-heating demands for all educts (i.e., inlet gases & feedstock material) are being reduced as a consequence, thus allowing for intensified heat extraction for a given air-to-fuel ratio (see Figure 10g). As visible in Figure 10h, a slight increase in the CGE by 2.4 percentage points can be attained for autothermal CLG operation when lowering AR temperatures from 1050 to 1000 °C. Yet, it has to be kept in mind that in chemical looping processes, air and fuel reactor temperatures are coupled, which means that a drop in FR temperatures is an inevitable effect of reduced AR temperatures. For the given boundary conditions, FR temperatures are projected to directly correlate with AR temperatures, which means that for the given reduction in AR temperatures from 1050 to 1000 °C, a corresponding drop in FR temperatures from 928 to 880 °C entails. This means that when attempting to prevent the ensuing drop in FR temperatures, related to negative effects on volatile and carbon conversion, OC circulation rates have to be increased accordingly as a counter-measure.

Although these insights allow for a first glimpse on process optimization approaches, it becomes clear that a detailed consideration of reaction kinetics and reactor hydrodynamics is quintessential, when aiming for a holistic optimization of the CLG process, as both phenomena have a pronounced effect on the process parameters. As it is well known that the conversion of char and other hydrocarbons is kinetically governed [25,55,56,59], the impact of reactor temperature, residence time, and gas concentrations on reaction kinetics need to be established in detail, allowing for accurate predictions of the governing reactions in a realistic environment. Moreover, reactor hydrodynamics are a crucial factor in chemical looping systems [74,75], making it a pre-requisite to consider them in advanced CLG process models. Through considering these phenomena, it thus becomes feasible to assess to which extent the preceding approaches can be utilized to obtain a CLG process exhibiting not only a high cold gas efficiency, but also excellent carbon capture efficiencies. Nonetheless, the preceding explanations offer valuable insights on the fundamental challenges associated with the autothermal CLG process, which require catering to, when implementing the technology in large scale.

#### 4. Conclusions

In the course of this study, an equilibrium process model for the chemical looping gasification of biomass, using ilmenite ore as the oxygen carrier, was deployed to establish adequate process control techniques to attain autothermal behavior for gasifiers of any scale. It was shown that

pursuing continuous CLG operation leads to unique challenges in terms of the OC circulation, which is responsible for both, oxygen and heat transport between the air and fuel reactor. While high OC circulation is generally beneficial in CLC to achieve complete fuel conversion in the FR and prevent a drop in FR temperatures, CLG faces an essential dilemma. Here, large OC circulation rates are necessary to fulfill the process heat balance (i.e., retain constant temperatures in the FR), whereas significantly lower circulation rates are required in terms of the necessary oxygen transport. Hence, heat and oxygen transport have to be de-coupled. Based on model calculations, two strategies to achieve autothermal CLG behavior through a de-coupling of oxygen and heat transport were presented. One eligible option is the dilution of the OC with an inert solid (e.g., sand), allowing for an accurate tailoring of the mixture's heat capacity and oxygen transport capability through its composition. As an alternative, the oxygen transport to the FR can be controlled through the oxygen availability (i.e., air supply) in the AR, leading to a deeply reduced oxygen carrier cycling through the system, not being fully re-oxidized in the AR. While both approaches lead to stable autothermal CLG behavior with sufficiently high FR temperatures, the latter strategy possesses certain advantages in terms of process control and fuel reactor chemistry, based on which it was deemed more suitable for large-scale operation. Regardless of the deployed approach, it was shown that restricting oxygen release in the FR is key in controlling CLG operation, where large cold gas efficiencies are desired. As partial oxidation of the feedstock is necessary in order to fulfill the heat balance of an autothermal process, this means that heat losses and heat sinks in the chemical looping gasifier have to be minimized, so that the oxygen input into the FR can be reduced, thus boosting syngas yields. Possible strategies to achieve this are gas pre-heating, variations in the OC circulation, alterations in the average CLG process temperature, and a reduction in the H<sub>2</sub>O/biomass ratio in the FR.

Certainly, the presented findings encourage a deeper investigation of the chemical looping gasification of biomass on a numerical level, as only through the deployment of elaborate models considering hydrodynamics and reaction kinetics in-depth inferences regarding the process efficiency are facilitated. Moreover, they also call for experimental investigations of the suggested process control strategies. Especially the suggested continuous CLG operation with a deeply reduced OC, not being fully re-oxidized in the AR, means setting foot on a new terrain. Here, the suitability of the presented approach is decided by the fact whether positive (e.g., pronounced methane reforming ability, increased syngas selectivity & tar cracking) or negative effects (e.g., intensified attrition, reactivity loss, particle agglomerations) prevail.

**Author Contributions:** Conceptualization, J.S. and P.D.; methodology, P.D.; writing—original draft preparation, P.D.; writing—review and editing, F.M., J.S. and F.A.; visualization, P.D.; supervision, B.E. All authors have read and agreed to the published version of the manuscript.

**Funding:** This work has received funding of the European Union's Horizon 2020-Research and Innovation Framework Programme under grant agreement No. 817841 (Chemical Looping gasification for sustainable production of biofuels-CLARA).

**Acknowledgments:** The authors would like to thank the Technical University of Darmstadt, enabling the open-access publication of this paper.

**Conflicts of Interest:** The authors declare no conflict of interest. The funders had no role in the design of the study; in the collection, analyses, or interpretation of data; in the writing of the manuscript, or in the decision to publish the results.

**Nomenclature**

Symbol	Explanation	Unit
$h_i$	Enthalpy of stream $i$	kJ/kg
$\dot{m}_i$	Mass flow of component/element $i$	kg/h
$M_i$	Molar mass of component/element $i$	g/mole
$\dot{n}_i$	Mole flow of component/element $i$	kmole/h
$P$	Power	kW
$p$	Pressure	bar
$R_{OC}$	Oxygen transport capacity of oxygen carrier	-
$\dot{m}_{air,AR}$	Mass flow of air entering the AR	kg/h
$T$	Temperature	°C
$x_i$	Mass/mole fraction in gas phase	-
$X_i$	Conversion of component $i$	-
$Y_{i,j}$	Mass yield of component/element $i$ from substance $j$	-
$z_i$	Mass/mole fraction in solid phase	-
$\eta_{CC}$	Carbon capture efficiency	-
$\eta_{CGE}$	Cold gas efficiency	-
$\lambda$	Air-to-fuel equivalence ratio	-
$\phi$	Oxygen carrier-to-fuel equivalence ratio	-

Subscript	Explanation
AR	Air reactor
devol.	Devolatilization.
FR	Fuel reactor
init	Initial
net	net
O	Oxygen
OC	Oxygen Carrier
ox	Oxidation
red	Reduction
s	Solid
stoich	Stoichiometric
th	Thermal

Abbreviation	Explanation
AR	Air Reactor
ASU	Air Separation Unit
CGE	Cold Gas Efficiency
CLC	Chemical Looping Combustion
CLG	Chemical Looping Gasification
FR	Fuel Reactor
GHGE	Greenhouse Gas Emissions
LHV	Lower Heating Value
OC	Oxygen Carrier
RED II	European Union Renewable Energy Directive
WGS	Water-Gas-Shift

**Appendix A. Boundary Conditions for CLG Process Model**

A summary of all model boundary conditions employed for the simulations presented in Section 3.2, Section 3.3 and Section 3.4 is given in Table A1.

**Table A1.** Boundary conditions for 1 MW<sub>th</sub> CLC/CLG process model for different CLG approaches.

Parameter	Approach 1 *	Approach 2 *	Approach 3 *	Unit
$T_{FR}$	730–1030	980–1030	930–1030	°C
$T_{AR}$	1050	1050	1050	°C
$p_{FR}/p_{AR}$	1.013	1.013	1.013	bar
$\dot{m}_{fuel}$	200.4	200.4	200.4	kg/h
$\dot{m}_{H_2O,FR}$	180.4	180.4	180.4	kg/h
$\dot{m}_{CO_2,FR}$	40.1	40.1	40.1	kg/h
$\dot{m}_{air,AR}$	1362.6	1362.6	454–1590	kg/h
$T_{CO_2,FR}$	25	25	25	°C
$T_{H_2O,FR}/T_{air,AR}$	400	400	400	°C
$\dot{m}_{OC,init}$	2.11–8.45	8.45	8.45	t/h
$z_{SiO_2}$	0	0–75	0	wt-%

\* CLG approach 1: Reduction in OC circulation rate (see Section 3.2), CLG approach 2: Dilution with solid inert (see Section 3.3), CLG approach 3: Reduction of air inlet into AR (see Section 3.4).

### Appendix B. Shifting from CLC to CLG Operation through Variations in the Air-to-Fuel Equivalence Ratio

As described in Section 3.4, the oxygen availability in the FR is solely dependent on the circulation rate of the OC and the oxygen transport capability of the OC material ( $R_O$ ), when operating the AR in air excess ( $\lambda > 1$ ) in CLC, as the OC material is fully oxidized inside the AR. When subsequently reducing  $\lambda$  to values below unity from a steady state CLC operating point (see Figure A1a), the limited air availability in the AR leads to a transient phase during which the OC undergoes a continuous drop in the oxidation degree with each redox cycle, as more oxygen is consumed in the FR (combustion conditions) than is being supplied in the AR. As soon as the oxidation degree in the FR approaches 0, the oxygen availability in the subsequent redox cycle is determined by the oxygen supply in the AR. Hence,  $\phi$  is equal to  $\lambda$  from this point onwards. As indicated in Figure A1a, this means that steady state CLG conditions are attained as a consequence. When on the other hand starting off with steady state CLG operation ( $\lambda < 1$ ) before increasing  $\lambda$  beyond unity, the OC undergoes a transient phase during which its oxidation degree increases with each redox cycle, since more oxygen is supplied in the AR than is being consumed in the FR. As soon as the amount of oxygen transported by the OC is sufficient to fully oxidize the deployed feedstock, CLC conditions are attained. It has to be noted that this can be the case before steady state is reached (see Figure A1b). This means that despite the described discontinuity in the relation between  $\lambda$  and  $\phi$  for  $\lambda = 1$ , a rapid switch in the OC-to-fuel ratio will not occur during operation, as the transition from CLC to CLG or vice versa will occur smoothly via a transient phase during which the oxidation degree of the OC adapts to the newly set boundary conditions.

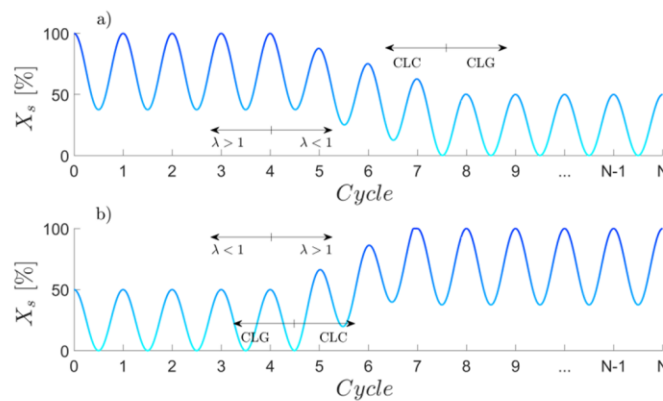


**Figure A1.** Progression of the OC oxidation degree when shifting from CLC ( $\lambda > 1$ ) to CLG ( $\lambda < 1$ ) mode through variations of the air-to-fuel equivalence ratio. (a) Shift from CLC to CLG, (b) shift from CLG to CLG.



### Appendix C. Char Conversion in an Sub-Stoichiometrically Operated AR

In order to establish how a mixture of unconverted char and a fully reduced OC behaves in an sub-stoichiometric oxygen containing atmosphere in the AR, a mixture of char (5 mole-%) and a reduced OC (78 mole-%  $\text{FeTiO}_3$ , 6 mole-%  $\text{Fe}_2\text{O}_3$  and 11 mole-%  $\text{TiO}_2$ ) were reacted with different amounts of air in an RGIBBS reactor of varying temperature (900–1100 °C). The results for an AR temperature of 1000 °C are shown in Figure A2. It is visible that char conversion occurs prior to OC re-oxidation, as the char fraction is zero regardless of the deployed air-to-fuel ratio. Moreover, the chemical equilibrium predicts a further reduction of the OC in case the amount of oxygen contained in the inlet air is insufficient for char conversion. Certainly, this behavior can only be observed in case of sufficiently long reaction times (rarely given in a fluidized bed), since solid-solid reactions between OC and char particles are known to exhibit slow kinetics [67–69]. This means that when attempting full char conversion, the inlet air entering the AR has to be sufficient to provide full carbon combustion. When this is the case, it can be assumed that full char conversion is attained inside the AR. In terms of the CO content at the reactor outlet it can be seen that full CO conversion to  $\text{CO}_2$  is achieved regardless of the utilized air-to-fuel ratio, indicated by negligible concentrations of CO in the AR outlet (see Figure A2).

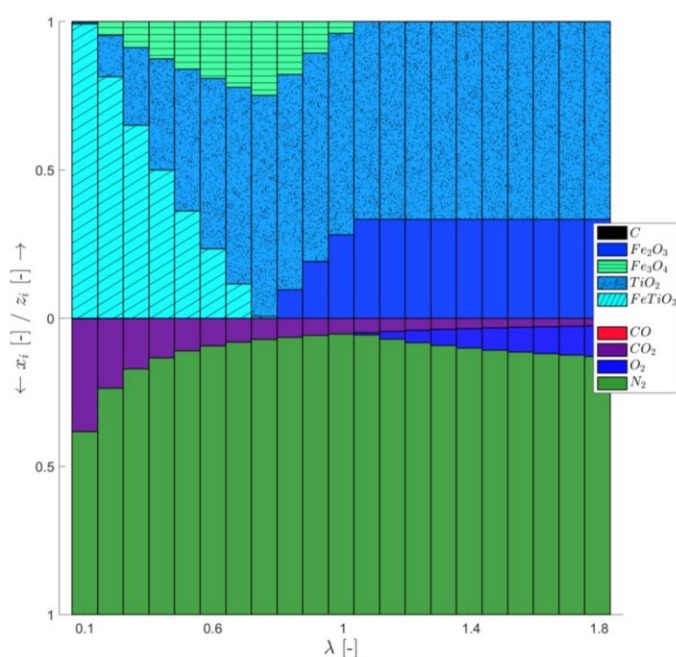


**Figure A2.** Solid and gas composition at chemical equilibrium for TAR = 1000 °C at varying air-to-fuel equivalence ratio  $\lambda$  (Inlet solid composition: 78 mole-%  $\text{FeTiO}_3$ , 6 mole-%  $\text{Fe}_2\text{O}_3$  and 11 mole-%  $\text{TiO}_2$ ).

### References

1. International Energy Agency (IEA). *Key World Energy Statistics 2018*; International Energy Agency: Paris, France, 2018.
2. Energy Information Administration. Statistics Data Browser—Electricity Generation from Renewables by Source. Available online: <https://www.iea.org/statistics/> (accessed on 23 August 2019).
3. European Commission. Transport Emissions—A European Strategy for Low-Emission Mobility. Available online: [https://ec.europa.eu/clima/policies/transport\\_en](https://ec.europa.eu/clima/policies/transport_en) (accessed on 23 August 2019).
4. EUR-Lex. Directive (EU) 2018/2001 of the European Parliament and of the Council of 11 December 2018 on the Promotion of the Use of Energy from Renewable Sources (Text with EEA Relevance). Available online: <https://eur-lex.europa.eu/legal-content/en/TXT/?uri=CELEX:32018L2001> (accessed on 12 June 2020).
5. Carrasco, J.E.; Monti, A.; Tayeb, J.; Kiel, J.; Giro, F.; Matas, B.; Santos Jorge, R. *Strategic Research and Innovation Agenda 2020*; EERA: Brussels, Belgium, 2020; p. 82.

6. De, S.; Agarwal, A.K.; Moholkar, V.S.; Thallada, B. *Coal and Biomass Gasification: Recent Advances and Future Challenges*; Springer: Berlin/Heidelberg, Germany, 2018.
7. Higman, C.; Van der Burgt, M. *Gasification*, 2nd ed.; Gulf Professional Publishing: Houston, TX, USA; Elsevier Science: Amsterdam, The Netherlands, 2008.
8. Barrio, M.; Gbel, B.; Rimes, H.; Henriksen, U.; Hustad, J.E.; Srensen, L.H. Steam gasification of wood char and the effect of hydrogen inhibition on the chemical kinetics. In *Progress in Thermochemical Biomass Conversion*; Bridgwater, A.V., Ed.; Blackwell Science Ltd.: Oxford, UK, 2001; pp. 32–46.
9. Hansen, L.K.; Rathmann, O.; Olsen, A.; Poulsen, K. *Steam Gasification of Wheat Straw, Barley Straw, Willow and Giganthus*; Risø National Laboratory: Roskilde, Denmark, 1997.
10. Klose, W.; Wolki, M. On the intrinsic reaction rate of biomass char gasification with carbon dioxide and steam. *Fuel* **2005**, *84*, 885–892. [[CrossRef](#)]
11. Ollero, P.; Serrera, A.; Arjona, R.; Alcantarilla, S. The CO<sub>2</sub> gasification kinetics of olive residue. *Biomass Bioenergy* **2003**, *24*, 151–161. [[CrossRef](#)]
12. Barrio, M.; Hustad, J.E. CO<sub>2</sub> Gasification of birch char and the effect of CO inhibition on the calculation of chemical kinetics. In *Progress in Thermochemical Biomass Conversion*; Bridgwater, A.V., Ed.; Blackwell Science Ltd.: Oxford, UK, 2001; pp. 47–60.
13. Basu, P. *Biomass Gasification and Pyrolysis*; Elsevier: Amsterdam, The Netherlands, 2010.
14. Ge, H.; Zhang, H.; Guo, W.; Song, T.; Shen, L. System simulation and experimental verification: Biomass-based integrated gasification combined cycle (BIGCC) coupling with chemical looping gasification (CLG) for power generation. *Fuel* **2019**, *241*, 118–128. [[CrossRef](#)]
15. Huang, Z.; Zhang, Y.; Fu, J.; Yu, L.; Chen, M.; Liu, S.; He, F.; Chen, D.; Wei, G.; Zhao, K.; et al. Chemical looping gasification of biomass char using iron ore as an oxygen carrier. *Int. J. Hydrogen Energy* **2016**, *41*, 17871–17883. [[CrossRef](#)]
16. Karl, J.; Pröll, T. Steam gasification of biomass in dual fluidized bed gasifiers: A review. *Renew. Sust. Energ. Rev.* **2018**, *98*, 64–78. [[CrossRef](#)]
17. Xu, G.; Murakami, T.; Suda, T.; Matsuzawa, Y.; Tani, H. The superior technical choice for dual fluidized bed gasification. *Ind. Eng. Chem. Res.* **2006**, *45*, 2281–2286. [[CrossRef](#)]
18. Aigner, I.; Pfeifer, C.; Hofbauer, H. Co-gasification of coal and wood in a dual fluidized bed gasifier. *Fuel* **2011**, *90*, 2404–2412. [[CrossRef](#)]
19. Huang, Z.; He, F.; Feng, Y.; Zhao, K.; Zheng, A.; Chang, S.; Wei, G.; Zhao, Z.; Li, H. biomass char direct chemical looping gasification using NiO-modified iron ore as an oxygen carrier. *Energy Fuels* **2014**, *28*, 183–191. [[CrossRef](#)]
20. Ge, H.; Guo, W.; Shen, L.; Song, T.; Xiao, J. Biomass gasification using chemical looping in a 25 kW<sub>th</sub> reactor with natural hematite as oxygen carrier. *Chem. Eng. J.* **2016**, *286*, 174–183. [[CrossRef](#)]
21. Guo, Q.; Cheng, Y.; Liu, Y.; Jia, W.; Ryu, H.-J. Coal chemical looping gasification for syngas generation using an iron-based oxygen carrier. *Ind. Eng. Chem. Res.* **2014**, *53*, 78–86. [[CrossRef](#)]
22. Huang, Z.; He, F.; Feng, Y.; Zhao, K.; Zheng, A.; Chang, S.; Li, H. Synthesis gas production through biomass direct chemical looping conversion with natural hematite as an oxygen carrier. *Bioresour. Technol.* **2013**, *140*, 138–145. [[CrossRef](#)] [[PubMed](#)]
23. Huseyin, S.; Wei, G.; Li, H.; He, F.; Huang, Z. Chemical-looping gasification of biomass in a 10 kW<sub>th</sub> interconnected fluidized bed reactor using Fe<sub>2</sub>O<sub>3</sub>/Al<sub>2</sub>O<sub>3</sub> oxygen carrier. *J. Fuel Chem. Technol.* **2014**, *42*, 922–931. [[CrossRef](#)]
24. Adanez, J.; Abad, A.; Garcia-Labiano, F.; Gayan, P.; De Diego, L.F. Progress in chemical-looping combustion and reforming technologies. *Prog. Energy Combust. Sci.* **2012**, *38*, 215–282. [[CrossRef](#)]
25. Ohlemüller, P.; Alobaid, F.; Abad, A.; Adanez, J.; Ströhle, J.; Epple, B. Development and validation of a 1D process model with autothermal operation of a 1 MW<sub>th</sub> chemical looping pilot plant. *Int. J. Greenh. Gas Control* **2018**, *73*, 29–41. [[CrossRef](#)]
26. Markström, P.; Linderholm, C.; Lyngfelt, A. Chemical-looping combustion of solid fuels—Design and operation of a 100 kW unit with bituminous coal. *Int. J. Greenh. Gas Control* **2013**, *15*, 150–162. [[CrossRef](#)]
27. Cuadrat, A.; Abad, A.; García-Labiano, F.; Gayán, P.; De Diego, L.F.; Adánez, J. Effect of operating conditions in Chemical-Looping Combustion of coal in a 500 W<sub>th</sub> unit. *Int. J. Greenh. Gas Control* **2012**, *6*, 153–163. [[CrossRef](#)]

28. Pérez-Vega, R.; Abad, A.; García-Labiano, F.; Gayán, P.; De Diego, L.F.; Adánez, J. Coal combustion in a 50 kW<sub>th</sub> chemical looping combustion unit: Seeking operating conditions to maximize CO<sub>2</sub> capture and combustion efficiency. *Int. J. Greenh. Gas Control* **2016**, *50*, 80–92. [[CrossRef](#)]
29. Ströhle, J.; Orth, M.; Epple, B. Chemical looping combustion of hard coal in a 1 MW<sub>th</sub> pilot plant using ilmenite as oxygen carrier. *Appl. Energy* **2015**, *157*, 288–294. [[CrossRef](#)]
30. Cao, Y.; Casenas, B.; Pan, W.-P. Investigation of chemical looping combustion by solid fuels. 2. Redox reaction kinetics and product characterization with coal, biomass, and solid waste as solid fuels and CuO as an oxygen carrier. *Energy Fuels* **2006**, *20*, 1845–1854. [[CrossRef](#)]
31. Leion, H.; Mattisson, T.; Lyngfelt, A. Solid fuels in chemical-looping combustion. *Int. J. Greenh. Gas Control* **2008**, *2*, 180–193. [[CrossRef](#)]
32. Virginie, M.; Adánez, J.; Courson, C.; De Diego, L.F.; García-Labiano, F.; Niznansky, D.; Kiennemann, A.; Gayán, P.; Abad, A. Effect of Fe–olivine on the tar content during biomass gasification in a dual fluidized bed. *Appl. Catal. B Environ.* **2012**, *121–122*, 214–222. [[CrossRef](#)]
33. Kuhn, J.N.; Zhao, Z.; Felix, L.G.; Slimane, R.B.; Choi, C.W.; Ozkan, U.S. Olivine catalysts for methane and tar-steam reforming. *Appl. Catal. B Environ.* **2008**, *81*, 14–26. [[CrossRef](#)]
34. Mendiara, T.; Johansen, J.M.; Utrilla, R.; Geraldo, P.; Jensen, A.D.; Glarborg, P. Evaluation of different oxygen carriers for biomass tar reforming (I): Carbon deposition in experiments with toluene. *Fuel* **2011**, *90*, 1049–1060. [[CrossRef](#)]
35. Larsson, A.; Israelsson, M.; Lind, F.; Seemann, M.; Thunman, H. Using ilmenite to reduce the tar yield in a dual fluidized bed gasification system. *Energy Fuels* **2014**, *28*, 2632–2644. [[CrossRef](#)]
36. Milne, T.A.; Evans, R.J.; Abatzoglou, N. *Biomass Gasifier “Tars”: Their Nature, Formation, and Conversion*; National Renewable Energy Laboratory: Golden, CO, USA, 1998.
37. Ge, H.; Guo, W.; Shen, L.; Song, T.; Xiao, J. Experimental investigation on biomass gasification using chemical looping in a batch reactor and a continuous dual reactor. *Chem. Eng. J.* **2016**, *286*, 689–700. [[CrossRef](#)]
38. Leion, H.; Jerndal, E.; Steenari, B.-M.; Hermansson, S.; Israelsson, M.; Jansson, E.; Johnsson, M.; Thunberg, R.; Vadenbo, A.; Mattisson, T.; et al. Solid fuels in chemical-looping combustion using oxide scale and unprocessed iron ore as oxygen carriers. *Fuel* **2009**, *88*, 1945–1954. [[CrossRef](#)]
39. Fan, L.-S. *Chemical Looping Systems for Fossil Energy Conversions*; Wiley-AIChE: Hoboken, NJ, USA, 2010.
40. Mayer, K.; Penthor, S.; Pröll, T.; Hofbauer, H. The different demands of oxygen carriers on the reactor system of a CLC plant—Results of oxygen carrier testing in a 120 kW<sub>th</sub> pilot plant. *Appl. Energy* **2015**, *157*, 323–329. [[CrossRef](#)]
41. Ohlemüller, P.G. *Untersuchung von Chemical-Looping-Combustion im Megawatt-Maßstab*; Cuvillier: Göttingen, Germany, 2019.
42. De Diego, L.F.; García-Labiano, F.; Gayán, P.; Celaya, J.; Palacios, J.M.; Adánez, J. Operation of a 10 kW<sub>th</sub> chemical-looping combustor during 200h with a CuO–Al<sub>2</sub>O<sub>3</sub> oxygen carrier. *Fuel* **2007**, *86*, 1036–1045. [[CrossRef](#)]
43. Adánez, J.; Gayán, P.; Celaya, J.; De Diego, L.F.; García-Labiano, F.; Abad, A. Chemical Looping Combustion in a 10 kW<sub>th</sub> Prototype Using a CuO/Al<sub>2</sub>O<sub>3</sub> Oxygen Carrier: Effect of Operating Conditions on Methane Combustion. *Ind. Eng. Chem. Res.* **2006**, *45*, 6075–6080. [[CrossRef](#)]
44. Pröll, T.; Bolhär-Nordenkampf, J.; Kolbitsch, P.; Hofbauer, H. Syngas and a separate nitrogen/argon stream via chemical looping reforming—A 140 kW pilot plant study. *Fuel* **2010**, *89*, 1249–1256. [[CrossRef](#)]
45. Ohlemüller, P.; Busch, J.-P.; Reitz, M.; Ströhle, J.; Epple, B. Chemical-Looping Combustion of Hard Coal: Autothermal Operation of a 1 MW<sub>th</sub> Pilot Plant. *J. Energy Resour. Technol.* **2016**, *138*, 042203. [[CrossRef](#)]
46. Mallick, D.; Mahanta, P.; Moholkar, V.S. Co-gasification of coal and biomass blends: Chemistry and engineering. *Fuel* **2017**, *204*, 106–128. [[CrossRef](#)]
47. Matthesius, G.A.; Morris, R.M.; Desai, M.J. Prediction of the volatile matter in coal from ultimate and proximate analyses. *J. S. Afr. Inst. Min. Metall.* **1987**, *5*, 157–161.
48. Neves, D.; Thunman, H.; Matos, A.; Tarelho, L.; Gómez-Barea, A. Characterization and prediction of biomass pyrolysis products. *Prog. Energy Combust. Sci.* **2011**, *37*, 611–630. [[CrossRef](#)]
49. Cuadrat, A.; Abad, A.; Gayán, P.; De Diego, L.F.; García-Labiano, F.; Adánez, J. Theoretical approach on the CLC performance with solid fuels: Optimizing the solids inventory. *Fuel* **2012**, *97*, 536–551. [[CrossRef](#)]

50. Mendiara, T.; Pérez-Astray, A.; Izquierdo, M.T.; Abad, A.; De Diego, L.F.; García-Labiano, F.; Gayán, P.; Adánez, J. Chemical Looping Combustion of different types of biomass in a 0.5 kW<sub>th</sub> unit. *Fuel* **2018**, *211*, 868–875. [\[CrossRef\]](#)
51. Leion, H.; Lyngfelt, A.; Johansson, M.; Jerndal, E.; Mattisson, T. The use of ilmenite as an oxygen carrier in chemical-looping combustion. *Chem. Eng. Res. Des.* **2008**, *86*, 1017–1026. [\[CrossRef\]](#)
52. Pissot, S.; Vilches, T.B.; Maric, J.; Seemann, M. Chemical looping gasification in a 2–4 MW<sub>th</sub> dual fluidized bed gasifier. In Proceedings of the 23rd International Conference on Fluidized Bed Conversion, Seoul, South Korea, 13 May 2018.
53. Li, K.; Zhang, R.; Bi, J. Experimental study on syngas production by co-gasification of coal and biomass in a fluidized bed. *Int. J. Hydrogen Energy* **2010**, *35*, 2722–2726. [\[CrossRef\]](#)
54. Narváez, I.; Orío, A.; Aznar, M.P.; Corella, J. Biomass gasification with air in an atmospheric bubbling fluidized bed. effect of six operational variables on the quality of the produced raw gas. *Ind. Eng. Chem. Res.* **1996**, *35*, 2110–2120. [\[CrossRef\]](#)
55. Abad, A.; Adánez, J.; Cuadrat, A.; García-Labiano, F.; Gayán, P.; De Diego, L.F. Kinetics of redox reactions of ilmenite for chemical-looping combustion. *Chem. Eng. Sci.* **2011**, *66*, 689–702. [\[CrossRef\]](#)
56. Zafar, Q.; Abad, A.; Mattisson, T.; Gevert, B. Reaction kinetics of freeze-granulated NiO/MgAl<sub>2</sub>O<sub>4</sub> oxygen carrier particles for chemical-looping combustion. *Energy Fuels* **2007**, *21*, 610–618. [\[CrossRef\]](#)
57. Mattisson, T.; Lyngfelt, A.; Cho, P. The use of iron oxide as an oxygen carrier in chemical-looping combustion of methane with inherent separation of CO<sub>2</sub>. *Fuel* **2001**, *80*, 1953–1962. [\[CrossRef\]](#)
58. Ohlemüller, P.; Ströhle, J.; Epple, B. Chemical looping combustion of hard coal and torrefied biomass in a 1 MW<sub>th</sub> pilot plant. *Int. J. Greenh. Gas Control* **2017**, *65*, 149–159. [\[CrossRef\]](#)
59. Dennis, J.S.; Scott, S.A. In situ gasification of a lignite coal and CO<sub>2</sub> separation using chemical looping with a Cu-based oxygen carrier. *Fuel* **2010**, *89*, 1623–1640. [\[CrossRef\]](#)
60. He, F.; Huang, Z.; Li, H.; Zhao, Z. Biomass Direct Chemical Looping Conversion in a Fluidized Bed Reactor with Natural Hematite as an Oxygen Carrier. In Proceedings of the Asia-Pacific Power and Energy Engineering Conference (IEEE), Wuhan, China, 28–31 March 2011; pp. 1–7.
61. Zhao, H.; Guo, L.; Zou, X. Chemical-looping auto-thermal reforming of biomass using Cu-based oxygen carrier. *Appl. Energy* **2015**, *157*, 408–415. [\[CrossRef\]](#)
62. Kunii, D.; Levenspiel, O. *Fluidization Engineering*, 2nd ed.; Butterworth-Heinemann: Boston, MA, USA, 1991.
63. Song, Q.; Xiao, R.; Deng, Z.; Zhang, H.; Shen, L.; Xiao, J.; Zhang, M. Chemical-looping combustion of methane with CaSO<sub>4</sub> oxygen carrier in a fixed bed reactor. *Energy Convers. Manag.* **2008**, *49*, 3178–3187. [\[CrossRef\]](#)
64. Ryu, H.-J.; Bae, D.-H.; Jin, G.-T. Effect of temperature on reduction reactivity of oxygen carrier particles in a fixed bed chemical-looping combustor. *Korean J. Chem. Eng.* **2003**, *20*, 960–966. [\[CrossRef\]](#)
65. Cuadrat, A.; Abad, A.; Adánez, J.; De Diego, L.F.; García-Labiano, F.; Gayán, P. Behavior of ilmenite as oxygen carrier in chemical-looping combustion. *Fuel Process. Technol.* **2012**, *94*, 101–112. [\[CrossRef\]](#)
66. Cho, P.; Mattisson, T.; Lyngfelt, A. Carbon Formation on Nickel and Iron Oxide-Containing Oxygen Carriers for Chemical-Looping Combustion. *Ind. Eng. Chem. Res.* **2005**, *44*, 668–676. [\[CrossRef\]](#)
67. Leion, H.; Lyngfelt, A.; Mattisson, T. Effects of Steam and CO<sub>2</sub> in the Fluidizing Gas when Using Bituminous Coal in Chemical-Looping Combustion. In Proceedings of the 20th International Conference on Fluidized Bed Combustion, Xi'an, China, 18–21 May 2009; pp. 608–611.
68. Leion, H.; Mattisson, T.; Lyngfelt, A. The use of petroleum coke as fuel in chemical-looping combustion. *Fuel* **2007**, *86*, 1947–1958. [\[CrossRef\]](#)
69. Brown, T.A.; Dennis, J.S.; Scott, S.A.; Davidson, J.F.; Hayhurst, A.N. Gasification and chemical-looping combustion of a lignite char in a fluidized bed of iron oxide. *Energy Fuels* **2010**, *24*, 3034–3048. [\[CrossRef\]](#)
70. Mendiara, T.; De Diego, L.F.; García-Labiano, F.; Gayán, P.; Abad, A.; Adánez, J. Behaviour of a bauxite waste material as oxygen carrier in a 500 W<sub>th</sub> CLC unit with coal. *Int. J. Greenh. Gas Control* **2013**, *17*, 170–182. [\[CrossRef\]](#)
71. Herdel, P.; Krause, D.; Peters, J.; Kolmorgen, B.; Ströhle, J.; Epple, B. Experimental investigations in a demonstration plant for fluidized bed gasification of multiple feedstock's in 0.5 MW<sub>th</sub> scale. *Fuel* **2017**, *205*, 286–296. [\[CrossRef\]](#)
72. Weidenfeller, D.J.; Kulik, R.; Rothenpieler, K.; Stückrath, K.; Hetzer, J. Design, Simulation and Practical Experience of the Largest Syngas Cooler in Operation for Coal Gasification. In Proceedings of the 8th International Freiberg Conference, Cologne, Germany, 12–16 June 2016.

73. Schmidtsche Schack, ARVOS GmbH. *Schmidtsche Schack@Solutions for Gasification Plants*. Available online: <https://www.schmidtsche-schack.com/products/syngas-cooler#c255> (accessed on 17 June 2020).
74. Bischi, A.; Langørgen, Ø.; Morin, J.-X.; Bakken, J.; Ghorbaniyan, M.; Bysveen, M.; Bolland, O. Hydrodynamic viability of chemical looping processes by means of cold flow model investigation. *Appl. Energy* **2012**, *97*, 201–216. [[CrossRef](#)]
75. Markström, P.; Lyngfelt, A. Designing and operating a cold-flow model of a 100 kW chemical-looping combustor. *Powder Technol.* **2012**, *222*, 182–192. [[CrossRef](#)]



© 2020 by the authors. Licensee MDPI, Basel, Switzerland. This article is an open access article distributed under the terms and conditions of the Creative Commons Attribution (CC BY) license (<http://creativecommons.org/licenses/by/4.0/>).



*This page is left blank intentionally*

---

## Research Paper II

---

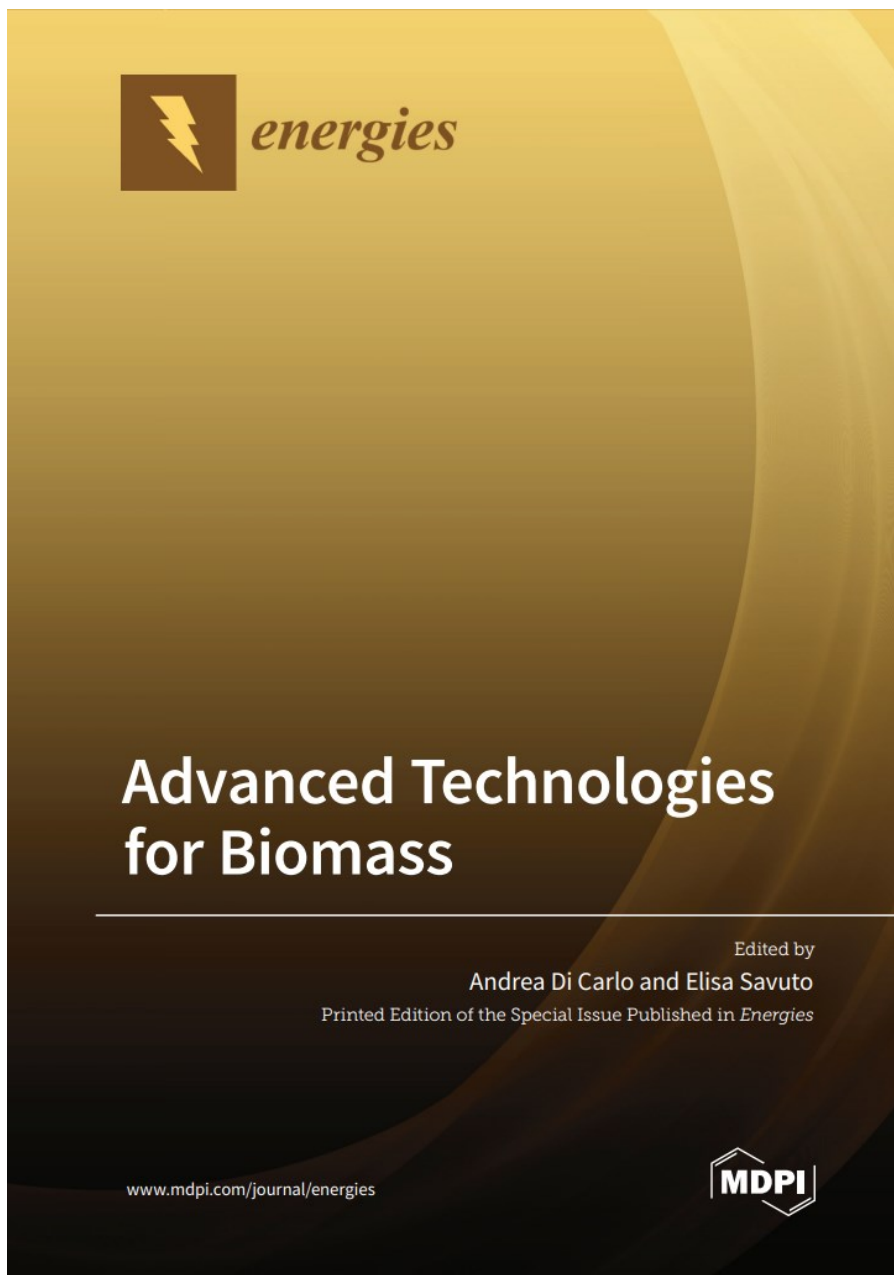
*Design of a 1 MW<sub>th</sub> Pilot Plant for Chemical Looping Gasification of Biogenic Residues*

Falko Marx, Paul Dieringer, Jochen Ströhle, Bernd Epple

---

**Journal:** Energies, Vol. 14  
**Date:** 04/2021  
**DOI:** [10.3390/en14092581](https://doi.org/10.3390/en14092581)  
**ISSN:** 1996-1073  
**Copyright:** Open Access License: CC BY 4.0

---



Article

# Design of a 1 MW<sub>th</sub> Pilot Plant for Chemical Looping Gasification of Biogenic Residues

Falko Marx <sup>\*</sup>, Paul Dieringer, Jochen Ströhle and Bernd Epple

Institute for Energy Systems & Technology, Technische Universität Darmstadt, Otto-Berndt-Str. 2, 64287 Darmstadt, Germany; paul.dieringer@est.tu-darmstadt.de (P.D.); jochen.stroehle@est.tu-darmstadt.de (J.S.); bernd.epple@est.tu-darmstadt.de (B.E.)  
\* Correspondence: falko.marx@est.tu-darmstadt.de; Tel.: +49-6151-16-23002

**Abstract:** Chemical looping gasification (CLG) is a promising process for the thermochemical solid to liquid conversion route using lattice oxygen, provided by a solid oxygen carrier material, to produce a nitrogen free synthesis gas. Recent advances in lab-scale experiments show that CLG with biomass has the possibility to produce a carbon neutral synthesis gas. However, all experiments have been conducted in externally heated units, not enabling autothermal operation. In this study, the modification of an existing pilot plant for demonstrating autothermal operation of CLG is described. Energy and mass balances are calculated using a validated chemical looping combustion process model extended for biomass gasification. Based on six operational cases, adaptations of the pilot plant are designed and changes discussed. A reactor configuration using two circulating fluidized bed reactors with internal solid circulation in the air reactor is proposed and a suitable operating strategy devised. The resulting experimental unit enables a reasonable range of operational parameters within restrictions imposed from autothermal operation.

**Keywords:** chemical looping; biomass; gasification; fluidized bed; autothermal; pilot plant



**Citation:** Marx, F.; Dieringer, P.; Ströhle, J.; Epple, B. Design of a 1 MW<sub>th</sub> Pilot Plant for Chemical Looping Gasification of Biogenic Residues. *Energies* **2021**, *14*, 2581. <https://doi.org/10.3390/en14092581>

Academic Editor: Andrea Di Carlo

Received: 31 March 2021

Accepted: 28 April 2021

Published: 30 April 2021

**Publisher's Note:** MDPI stays neutral with regard to jurisdictional claims in published maps and institutional affiliations.



**Copyright:** © 2021 by the authors. Licensee MDPI, Basel, Switzerland. This article is an open access article distributed under the terms and conditions of the Creative Commons Attribution (CC BY) license (<https://creativecommons.org/licenses/by/4.0/>).

## 1. Introduction

The reduction of greenhouse gas emissions is one of the major challenges in the 21st century. The European Commission sets a minimum share of 14% as a goal for renewable transport fuels produced from non food or feed sources in 2030 [1] in order to combat global warming according to the UNFCCC Paris Agreement. This is a major increase from the less than 0.1% share of renewable transport fuels in 2018 in the European Union (including food grade sources) [2] and necessitates the development of second generation biofuels. Moreover, first generation biofuels mostly utilize biochemical conversion from sugar and starch or physicochemical conversion from plant oil or fat for the production of drop in fuels [3]. However, these processes cannot be used efficiently for the production of second generation biofuels from EU approved biogenic sources—as they are low in sugar, starch, oil and fat and high in cellulose and lignin—so new production processes are needed.

However, efficient technological pathways for the production of second generation exist only partially and not in an entire process chain, in the form of thermochemical conversion through gasification, methanol or Fischer–Tropsch synthesis and subsequent refining. Gasification, the starting point of the process chain for solid to liquid conversion, is presently used for the generation of heat and electricity [4] and very little for the production of liquid biofuels [5]. It is a well known process which converts solid feedstock into a high caloric syngas and is considered to have a high potential for the decarbonization of hard to electrify aviation and maritime transport sectors. Additionally, the energy required for the conversion is provided by the biomass feedstock giving the potential of a total carbon neutral drop-in fuel.



As the feedstocks considered by the European Union [1] include seasonally varying types of biomass like husk and straw, as well as more continually sourceable foresting residue, sewage sludge, and biogenic household waste, fluidized bed gasification with its good feedstock flexibility seems a suitable process. Moreover, the good heat and mass transfer characteristics of fluidized bed facilitate complete conversion of the feedstock into syngas, thus achieving a high carbon conversion [6,7] and process efficiency [7,8]. Furthermore, as fuel synthesis requires an N<sub>2</sub>-free syngas and thus gasification without the presence of N<sub>2</sub> [9], the subsequent syngas cleaning gives rise to easy carbon capture with storage or utilization making the carbon footprint of the product negative. The N<sub>2</sub>-free gasification environment is usually created by the provision of pure oxygen provided by an air separation unit (ASU) [9,10], but in fluidized bed gasification another possibility exists to create an N<sub>2</sub>-free atmosphere: dual fluidized bed gasification (DFBG) utilizes two reactors to split the gasification process from the oxidation or combustion process used to generate the necessary heat while avoiding the expensive ASU. Nonetheless, as heated solid bed material circulating between the two reactors is used to transfer the energy for the process, the transport of some amounts of carbon from the feedstock to the gasification reactor is necessary for the combustion reactor to generate the required heat, giving a substantial amount of CO<sub>2</sub>-emission from the process.

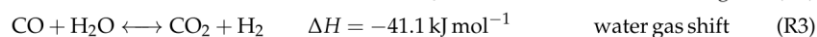
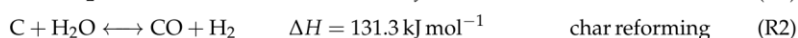
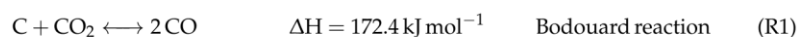
The chemical looping gasification (CLG) process operates in a similar manner using two coupled fluidized bed reactors. However, instead of transporting residual feedstock from the gasification reactor to one operated with air, it employs a metal oxide to transport oxygen from a reactor operated with air towards the gasification, thus giving the benefit of a process with virtually no CO<sub>2</sub> emission. So far all experiments with continuous operation of the process were conducted in lab and pilot scale with external heating [11–15] and a maximum thermal load of 25 kW [16,17]. Furthermore, autothermal operation has not been demonstrated and problems of process scale up have not been identified and alleviated. Therefore the existing 1 MW chemical looping combustion (CLC) pilot plant located at Technische Universität Darmstadt is modified for the operation and investigation of the CLG process with biomass.

In this work, the design and modifications of the 1 MW pilot plant are described. Starting from the underlying, fundamental gasification process, the existing infrastructural restrictions, and the planned operation range, mass and energy balances are calculated and required adjustments identified and implemented.

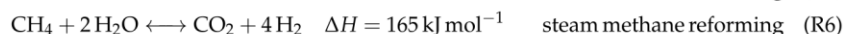
## 2. Theory

### 2.1. Gasification Fundamentals

Fluidized bed CLG of solid feedstocks comprises, after initial drying and devolatilization, the following main reactions:



Further important reactions between the commonly used gasification agent H<sub>2</sub>O [9] and the formed methane is the steam methane reforming reaction:



where reaction (R6) is the combination of reactions (R3) and (R5).

The influence of reactions (R5) and (R6) largely depends on the formed methane from devolatilization and reaction (R4). These reactions require a high amount of heat, as indicated by the reaction enthalpies, thus greatly contributing to the overall endothermic re-

action inside the fuel reactor (FR). Moreover, it is clear that higher gasification temperatures lead to lower amounts of CH<sub>4</sub>.

Reactions (R1) and (R2) necessitate a high amount of heat which cannot be balanced by the exothermic reactions (R3) and (R4) and has to be supplied for the gasification process. This heat can either be provided in situ through the oxidation of part of the feedstock (syngas species, volatiles and char) or externally e.g., through supply of a bed material heated in a second reactor enabling an autothermal process. The CLG process, schematically shown in Figure 1, employs both routes to supply the gasification energy. The solid oxygen carrier (OC) material supplies sensible heat to the fuel reactor (FR) while also providing lattice oxygen for the oxidation of part of the feedstock.

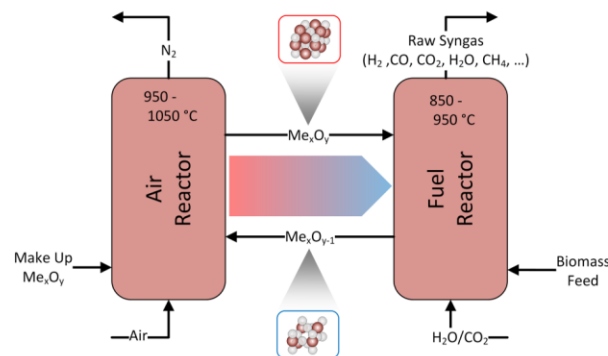
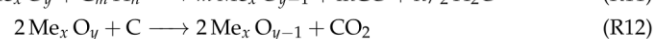
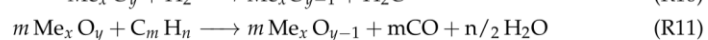
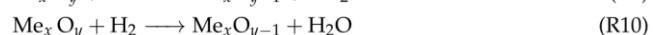
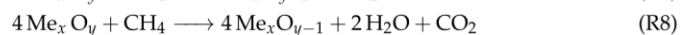
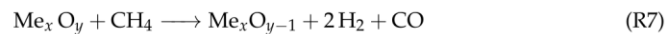
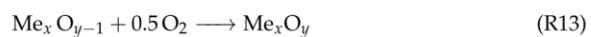


**Figure 1.** Schematic of the CLG process showing the cyclic reduction and oxidation of an OC material which is oxidized in the air reactor (AR) and reduced in the fuel reactor (FR).

However, additional reactions have to be considered when the bed material is a chemically active part of the feedstock conversion. In the FR where the OC material is reduced the reactions are:



Solid–solid reactions between char and OC (R12) are generally slower than the heterogeneous gas solid reactions (R7) to (R10) and can therefore be neglected [18,19] except for very high reaction temperatures [20]. The reduced OC is then transported to the air reactor (AR), where it is oxidized with air in an exothermic reaction:



Inside the AR the combustion of char, reaction (R14) is favored above the oxidation of OC through reaction (R13) [20–22], so residual char transported with the OC from the FR to the AR will be combusted before the oxidation of the OC, adding to the full feedstock conversion and supplying additional heat to the exothermic re-oxidation, (R13). However, (R14) is undesired during CLG, as it reduces the major advantage of a virtually CO<sub>2</sub>-free flue gas stream from the AR when compared to DFBC.

CLG has been demonstrated to work as a continuous process in externally heated bench and lab-scale units up to 25 kW [17]. Large-scale experiments at Chalmers

University [23] suffer from the necessity of the AR to supply hot water for building heating and thus the requirement of significant fuel feeding to the AR. Therefore, exhibiting a severe mismatch of reactor dimension of factor 3 to 6 [24] while not depending on (R13) for heat release inside the AR. Hence, these experiments cannot be considered autothermal or even CLG, creating a need for experiments in a bigger scale to confirm the possibility and investigate the performance of autothermal CLG.

Process parameters considered important during the design are the cold gas efficiency:

$$\eta_{CG} = \frac{\dot{n}_{FR,out}(X_{CH_4} \cdot LHV_{CH_4} + X_{CO} \cdot LHV_{CO} + X_{H_2} \cdot LHV_{H_2})}{\dot{m}_{FS} \cdot LHV_{FS}} \quad (1)$$

with  $X_i$  being the mole fraction of species  $i$ ,  $LHV$  the lower heating value, and  $\dot{n}_{FR,out}$  and  $\dot{m}_{FS}$  being the product gas output and the feedstock input, respectively. The oxygen carrier to fuel equivalence ratio is defined by [25]:

$$\phi = \frac{R_{OC} \cdot \dot{m}_{OC} \cdot X_{s,AR}}{\dot{m}_{O,stoich}} \quad (2)$$

$$X_{s,AR} = \frac{m_{OC,AR} - m_{OC,red}}{R_{OC} \cdot m_{OC,ox}} \quad (3)$$

In this definition the oxygen required for full feedstock conversion is  $m_{O,stoich}$ ,  $R_{OC}$  is the oxygen transport capacity of the OC material,  $X_{s,AR}$  is the oxidation degree of the OC,  $m_{OC,red}$  and  $m_{OC,ox}$  are the mass of the fully reduced and oxidized state respectively, while the mass of the OC leaving the AR is  $m_{OC,AR}$ . For gasification  $\phi$  has to be smaller than unity to prevent the full oxidation of the feedstock [25,26]. However, syngas formation is observed even for values of  $\phi > 1$  [27]. Values of  $\phi < 1$  can be achieved by reducing the mass flow  $\dot{m}_{OC}$  or the OC oxidation, i.e.,  $m_{OC,AR} - m_{OC,red}$ . The first option has the disadvantage of also influencing the heat transport  $\dot{Q}$  between the reactors:

$$\dot{Q} = \dot{m}_{OC} \cdot c_p \cdot \Delta T \quad (4)$$

with  $c_p$ , the heat capacity of the OC and  $\Delta T$ , the temperature difference of OC particles entering and leaving the FR. The influence of the OC oxidation on  $c_p$  is small and can be compensated by adjustments of  $\dot{m}_{OC}$  during practical application of option two.

Additionally the fraction of syngas in the dry product gas is defined as:

$$x_{SG} = \frac{X_{CO} + X_{H_2}}{X_{CH_4} + X_{CO} + X_{H_2} + X_{CO_2} + X_{H_2S} + X_{N_2}} \quad (5)$$

## 2.2. Bed Materials for Chemical Looping Gasification

The selection and testing of bed materials is a crucial task when designing a CLG process. Eight criteria for CLC are given by Adanez et al. [28] and repeated here with notes on how they apply to CLG:

1. Oxygen transport capacity: as gasification processes limit the supply of oxygen below the stoichiometric ratio required for full feedstock conversion, a high oxygen transport capacity is not so important as the process is limited by the sensible heat transported and not the oxygen [16,26]. For CLC the supply of excess oxygen is not critical, for CLG it must be limited without impairing the transport of sensible heat as otherwise, the temperature in the FR would drop, negatively influencing the gasification [26].
2. Thermodynamic suitability: the bed material must be able to oxidise the feedstock at least partially while not releasing molecular oxygen. Thus chemical looping with oxygen uncoupling (CLOU) materials cannot be used for CLG.
3. High reactivity over multiple reduction-oxidation cycles: activation over multiple cycles can increase or decrease reactivity.

4. **Stability:** the expected lifetime of the bed material should be as long as possible, as losses through attrition need to be compensated by a make-up stream. This make-up stream requires heating to process temperature, thus always leading to an efficiency drop. Measurement and calculation of OC lifetime is not straightforward and can vary by a factor of 3.2 for one experiment depending on the method used [29].
5. **Carbon deposition:** carbon transport towards the AR with subsequent combustion negatively impacts carbon utilization and capture efficiency. However, Adanez et al. [28] note that no carbon deposition has been found in relevant studies.
6. **Fluidization properties:** formation of agglomerates or low melting compounds with parts of the feedstock must be avoided. This becomes difficult if a herbaceous feedstock—high in ash and alkali metals—is used and might require mitigation measures like pre-treatment [30,31] or feedstock mixing [32].
7. **Cost:** the current production cost for synthetic materials make them non competitive when compared to naturally occurring minerals or waste materials.
8. **Toxicity:** deployment of environmental friendly and non-toxic OC material avoids special and costly requirements during handling and disposal of deactivated OC material.

Moreover, the design for pilot and demonstration plants need to consider an additional point:

9. **Availability:** the selected material must be available in the required quantity. Synthesized OC materials are not available on a commercial scale yet. So a natural ore or a waste material must be used.

Especially OC materials which are categorized as materials for syngas production [33–35] are problematic as they are either synthetic materials not available in the required quantities, expensive or toxic to humans and the environment. However, even materials with full oxidation capability for combustion can be used for the production of high calorific syngas when suitable control concepts are employed [11,16,26]. While lots of operating experience with bed materials for DFBG in the range above 1 MW exists [36], there is little experience with OC materials in the same power range [23,25]. However, even those experiments do not give a good indication of their process performance, as the AR—or rather combustor, as it is always fed with fuel—used is oversized by a factor of 3 to 6 [24], effectively creating a reservoir of OC and sensible heat more dependent on the required energy for heating supply than the CLG process. Moreover, higher attrition rates of e.g., ilmenite are reported for CLG when compared with CLC [11] but if the effects are the same in a bigger CLG plant is still an open question. Due to the small size of lab-scale reactors, the OC material undergoes more oxidation/reduction cycles per hour, thus giving higher stress from chemical conversion when compared to the mechanical stress from the transport through the reactors and coupling elements.

Depending on the requirements of the targeted application for the syngas, a last point is to be considered when selecting the OC bed material:

10. **Catalytic properties:** selecting a material (or additive) which catalytically reduces the formation of unwanted components like tars [37,38] and CH<sub>4</sub> [39] or binds elements to the solid fraction (e.g., sulphur in form of gypsum) as a primary method. Secondary gas cleaning methods might therefore not be necessary or can be designed much smaller.

Tar production is of major concern for subsequent syngas treatment especially for biomass gasification where tar production is high [40]. Bed height, bed material, temperatures, velocities, feedstock, and feedstock feeding location [37] have an influence on the production of tars. Existing kinetic models for the prediction of tar production are not applicable as they are developed for a very specific process and reactor size [15], need fitting against the actual reactor performance [41], or are not reliable in the prediction of tars formed [42–44]. Furthermore, no model was developed for CLG yet.

### 3. Process Design

In the following, the CLG technology fundamentals described in Section 2 are combined with boundary conditions from the existing pilot plant as well as feedstock properties and hydrodynamic characteristics yielding a process design suitable for the demonstration of autothermal CLG in the existing 1 MW<sub>th</sub> pilot plant.

#### 3.1. Existing Pilot Plant

The heart of the CLG pilot plant consists of two refractory lined circulating fluidized bed (CFB) reactors which are coupled using two loop seals and one J-valve and have properties indicated in Table 1. The CFB400-reactor of the pilot plant has been used as gasifier for High Temperature Winkler (HTW<sup>TM</sup>) gasification [45,46] and as FR in the CLG-related processes for chemical looping combustion, while the CFB600-reactor has been used as AR [47–51]. Thus major components can be reused for CLG by combining elements from the CLC and the HTW<sup>TM</sup> process configurations. Nonetheless, major adaptations are made, as the HTW<sup>TM</sup> configuration is build for lower fluidization velocities and with 0.5 MW<sub>th</sub> [45] also for lower thermal input.

**Table 1.** Reactor properties of the 1 MW CLG pilot plant.

Reactor	AR—CFB600	FR—CFB400	Unit
Height	8.66	11.35	m
Inner diameter	0.59	0.28 to 0.4	m
Outer diameter	1.3	1.0	m
Temperature	1050	950	°C
Fuel feeding	in bed (propane lance), return leg of LS 4.5 (solids)	in bed via screw (solids)	

Furthermore, as electrical preheating temperatures of fluidization media are limited to 400 °C, process stream heating has to be done inside the reactors, negatively impacting cold gas efficiency which would be optimized in an industrial plant using heat integration. The cooling system sets a limit of 1 MW<sub>th</sub> which can be safely handled for CLC. However, as a major part of the energy of the feedstock remains as heating value in the product gas, feedstock input above the 1 MW<sub>th</sub> is possible for CLG.

Therefore the following case has been set as design specifications for the investigations of CLG for which mass and energy balances were calculated, required changes to the pilot plant identified and modifications designed.

- As the cooling system is designed to handle a thermal load of 1 MW safely, the design power of the pilot plant is set to 1 MW<sub>th</sub>.
- Ilmenite as OC: For the selected thermal power, a total inventory of about 1000 kg was used during CLC experiments in the pilot plant [50], and the same can be expected for CLG. Thus, of the points listed in Section 2.2, the availability is a major concern for experiments in that scale, and a natural ore or a widely available waste material had to be selected. Recent studies show promising results for ilmenite in continuous units [11], and operating experience with ilmenite in the pilot plant exists [49,50]. Moreover, ilmenite has been shown to catalytically reduce tars [25,52].
- Temperatures for the AR of 1050 °C and 950 °C are considered the maximum viable temperatures. Higher FR temperatures will yield a higher H<sub>2</sub>/CO ratio at the expense of lower cold gas efficiency. So slightly lower FR temperatures might be desired in industrial application. Moreover, as OC ash interaction may lead to problems at high temperatures [31] and the temperature difference between the reactors is an important parameter for process control [26], the FR temperature is not fixed and considered an important variable in the planned experiments.
- Industrial wood pellets as feedstock as described in Section 3.2.

### 3.2. Feedstocks

As model feedstock for the calculation of the heat and mass balances and the design of modifications, industrial wood pellets have been selected, as they are widely available and allow for easy comparison with existing gasification technologies in pilot and demonstration scale where wood based materials are gasified [36]. Additionally, wheat straw, as a seasonal varying biomass source, and pine forest residue, as a more constant source, are selected as feedstocks from the EU-approved list [1] for experimental investigations.

Initial investigations of wheat straw by Di Giuliano et al. [31] indicate that it is a difficult feedstock for CLG, due to its low ash softening point and the possibility to cause agglomerates and bed defluidization, so that it requires at least some pre-treatment. However, as fluidization velocities in the CFB reactors are two magnitudes higher than the investigated fluidization velocities, the required pre-treatment cannot be directly inferred, but a higher fluidization velocity seems to lower the required pre-treatment effort [31]. Moreover, reaction kinetics for pelletized wheat straw in various bed materials are similar to pellets of pine forest residue [53] opening up possibilities to switch between these feedstocks during gasifier operation. Nevertheless, additional investigations on the pre-treatment of wheat straw are needed to be able to give accurate information on the fuel properties—which are indicated in Table 2 for the planned feedstocks—as they vary with pre-treatment. It is assumed that pre-treatment of wheat straw will make handling and gasification easier, as it reduces agglomeration tendencies (additivation, torrefaction) and water content (drying, torrefaction). Thus, raw wheat straw is the most difficult to gasify and can be used as a lower end in feedstock quality.

**Table 2.** Proximate and ultimate analysis of feedstocks.

	Component	Wood Pellets	Pine Forest Residue	Wheat Straw
<b>Proximate Analysis</b> in wt. – %	Moisture	6.5	7	7
	Ash (d.b.)	0.7	1.86	7.5
	Volatiles (d.b.)	85.1	78.86	81.5
	Fixed carbon (d.b.)	14.2	12.28	11
<b>Ultimate Analysis</b> in wt. – %	C (d.a.f.)	50.8	52.7	48.2
	H (d.a.f.)	6	6.4	6.5
	N (d.a.f.)	0.07	0.39	0.43
	O (d.a.f.)	43.2	40.5	44.9
	S (d.a.f.)	0.008	0.05	0.11
	Cl (d.a.f.)	0.006	0.007	0.05
<b>Net calorific value</b> in MJ kg <sup>−1</sup>		17.96	18.41	17.12

### 3.3. Heat and Mass Balances

Heat and mass balances for the pilot plant were calculated considering reaction kinetics of ilmenite and reactor hydrodynamics using a validated Aspen Plus™ model for CLC [51] extended to cover biomass gasification via a Langmuir–Hinschelwood mechanism [26]. However, instead of an equilibrium model used by Dieringer et al. [26], the more realistic original reaction kinetics for ilmenite were used for the OC gas reaction. As a starting point, the CLC case was selected in terms of reactor dimensions, temperatures, solid inventories, pressure, and loop seal (LS) fluidization. The feedstock flow  $\dot{m}_{FS}$  (industrial wood pellets) was selected as 1 MW<sub>th</sub>, and the heat losses were assumed to be 110 kW which falls in the reported range of 60 kW to 200 kW [48,50]. Furthermore, heat losses are considered to be dependent on reactor temperature and independent of feedstock input. LS fluidization with CO<sub>2</sub> is set to 84.2 kg h<sup>−1</sup> based on previous operating experience [49,50]. To obtain autothermal operation at these conditions, the oxygen availability inside the AR was varied through the inlet feed rate of air into the AR, while the heat transport between both reactors was controlled through the global metal oxide solid circulation rate ( $\dot{m}_{OC,AR,out}$ ,  $\dot{m}_{OC,FR,out}$ ), until both reactors were in heat balance. The hydrodynamic constraints related

to the required solid entrainment (calculated as suggested by Kunii and Levenspiel [54], described in detail elsewhere [51,55]) from each reactor were achieved by varying the steam inlet flow  $\dot{m}_{\text{H}_2\text{O}}$  and flue gas recirculation inlet flow  $\dot{m}_{\text{AR},\text{reci}}$  for the FR and AR, respectively, while setting internal solid circulation to zero. All boundary conditions are listed in Table 3, and the corresponding results are in Table 4. The listed streams are visualized in the reactor configuration in Figure 2.

**Table 3.** Boundary conditions for the simulation of autothermal CLG operations of the 1 MW pilot plant.

Property	Value	Unit	Property	Value	Unit
$d_{p,50}$	154	$\mu\text{m}$	$T_{\text{Gas},\text{in}}$	400	$^{\circ}\text{C}$
$\Delta p_{\text{FR}}$	61	mbar	$\Delta p_{\text{AR}}$	90	mbar
$p_{\text{FR}}$	1	bar	$p_{\text{AR}}$	1	bar
$d_{\text{FR}}$	0.28 to 0.4	m	$d_{\text{AR}}$	0.59	m
$h_{\text{FR}}$	11.35	m	$h_{\text{AR}}$	8.66	m

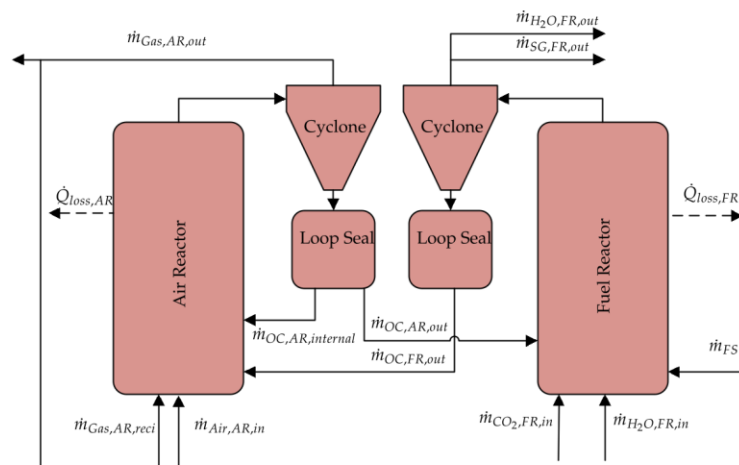


**Figure 2.** Streams for the calculation of mass and energy balances of the CLG process.

In small scale units where the energy is supplied via furnace heating, the oxygen supply can be controlled via the circulation. However, in the 1 MW pilot plant the heat is supplied only via the circulation of the bed material. From the results of the Reference case, it can be seen that the transport of oxygen must be limited in order to obtain a good gasification process, while the solid circulation must remain high as indicated by the substantial amount of recirculated gas fed to the reactor. Thus, a new control method for the oxygen transport must be realised, decoupling the transport of oxygen from the transport of sensible heat as described by Dieringer et al. [26]. Moreover, the superficial gas velocity  $u_0$  in the AR is below the range of a CFB, as shown in Figure 3, while the calculated solid flux  $G_S$  is also below the range commonly observed in commercial CFB units [56]. Indeed, past operation of the AR showed good performance with superficial gas velocities of approximately  $3.5 \text{ m s}^{-1}$  to  $5 \text{ m s}^{-1}$ . In the pilot plant, the installation of a (partial) flue gas recirculation for the AR is used to increase  $u_0$  while also supplying the inert fluidization medium required for the process control. Increasing the solids discharge from the AR—while keeping the global solids circulation constant—creates the need for an internal solid circulation in the AR—where material not transported through the J-valve is returned via the LS—which is not common in smaller units. In fact, most lab- and bench-scale units have internal solids recirculation for the FR to enhance carbon conversion [57] or no solids recirculation at all [11,17]. Nonetheless, this solution comes with a penalty, as additional

fluidization medium is needed and has to be heated to process temperature. However, reducing the diameter of an existing, refractory lined reactor is costly and time consuming, so the efficiency penalty has to be accepted; yet it also opens the possibility to use the start-up burner for fast temperature adjustments in-between experimental set points without severe impact on reactor hydrodynamics. In a commercial unit, the diameter would be designed according to process specification and corresponding hydrodynamics, requiring the flue gas recirculation only for process control. Nonetheless, this initial estimation shows that CLG is possible in the existing 1 MW pilot plant.

**Table 4.** Simulation results for autothermal CLG operations of the 1 MW pilot plant. Stream names correspond to Figure 2. Boundary conditions deviating from the reference case are underlined. The first block contains the thermodynamic and hydrodynamic constraints and results, the second block contains the process streams (in some cases with composition). The third block gives information on solid composition for the FR, while the last block shows general process performance parameters.

Stream	Reference	HT1	HT2	HF	HP1	HP2	Unit
$T_{AR}$	1025	<u>1050</u>	<u>1050</u>	1025	1025	1025	°C
$T_{FR}$	900	900	<u>950</u>	900	900	900	°C
$\dot{m}_{FS}$	200.4	200.4	200.4	200.4	<u>240.48</u>	<u>280.56</u>	kg h <sup>-1</sup>
$u_{0,AR}$	3.42	3.12	3.97	<u>5.03</u>	<u>5.01</u>	<u>5.01</u>	m s <sup>-1</sup>
$u_{0,FR}$	6.25	5.46	7.64	5.67	6.23	6.75	m s <sup>-1</sup>
$\dot{Q}_{loss,AR}$	48.5	49.4	49.9	49.3	50.5	49.6	kW
$\dot{Q}_{loss,FR}$	59.8	61.8	59.8	61.3	59.4	61.2	kW
$\dot{m}_{OC,AR,out}$	7180	5690	9979	6244	7257	8285	kg h <sup>-1</sup>
$\dot{m}_{OC,FR,out}$	7130	5649	9906	6175	7199	8236	kg h <sup>-1</sup>
$\dot{m}_{OC,AR,internal}$	0	0	0	12,120	10,994	9971	kg h <sup>-1</sup>
$\dot{m}_{Air,AR,in}$	640	600	745	730	760	802	kg h <sup>-1</sup>
$\dot{m}_{Gas,AR,out}$	950.6	854.6	1062.7	1404.3	1413.6	1425.5	kg h <sup>-1</sup>
— $X_{CO_2,AR}$	0.111	0.117	0.096	0.098	0.111	0.122	
— $X_{O_2,AR}$	0.004	0.003	0.005	0.005	0.004	0.003	
$\dot{m}_{AR,reci}$	360.7	296.3	391.2	744.3	708.2	672.8	kg h <sup>-1</sup>
$\dot{m}_{H_2O,FR,in}$	301.53	237.04	383.83	247.14	263.4	276.94	kg h <sup>-1</sup>
$\dot{m}_{CO_2,FR,in}$	84.2	84.2	84.2	84.2	84.2	84.2	kg h <sup>-1</sup>
$\dot{m}_{H_2O,FR,out}$	362.9	294.5	451.5	318.8	337.9	354.0	kg h <sup>-1</sup>
$\dot{m}_{Syngas,FR,out}$	271.1	267.0	287.8	280.5	307.3	334.3	kg h <sup>-1</sup>
— $X_{CO_2,FR}$	0.466	0.439	0.543	0.531	0.440	0.377	
— $X_{CO,FR}$	0.304	0.317	0.240	0.277	0.324	0.354	
— $X_{CH_4,FR}$	0.092	0.099	0.057	0.072	0.095	0.113	
— $X_{H_2,FR}$	0.139	0.145	0.160	0.119	0.141	0.156	
— $X_{H_2S,FR}$	$5.26 \times 10^{-5}$	$5.22 \times 10^{-5}$	$5.13 \times 10^{-5}$	$5.38 \times 10^{-5}$	$5.48 \times 10^{-5}$	$5.56 \times 10^{-5}$	
$\dot{n}_{Solid,FR,out}$	14.84	11.54	20.60	13.38	15.09	16.90	mol h <sup>-1</sup>
— $X_{C,out}$	0.04	0.05	0.03	0.05	0.05	0.05	
— $X_{Fe_2O_3,out}$	0.09	0.06	0.10	0.13	0.09	0.07	
— $X_{FeTiO_3,out}$	0.68	0.76	0.66	0.57	0.68	0.74	
— $X_{TiO_2,out}$	0.18	0.12	0.21	0.25	0.18	0.14	
$\dot{n}_{Solid,FR,in}$	15.55	12.11	21.70	14.43	15.93	17.54	mol h <sup>-1</sup>
— $X_{Fe_2O_3,in}$	0.17	0.16	0.18	0.23	0.19	0.15	
— $X_{FeTiO_3,in}$	0.48	0.53	0.47	0.30	0.44	0.55	
— $X_{TiO_2,in}$	0.35	0.31	0.35	0.46	0.37	0.30	
— $X_{Fe_3O_4,in}$	0.00	0.00	0.00	0.00	0.00	0.00	
$\eta_{CG}$	0.474	0.505	0.384	0.396	0.475	0.531	
$x_{SG}$	0.443	0.462	0.400	0.396	0.465	0.511	
$\phi$	0.585	0.412	0.836	0.729	0.537	0.412	



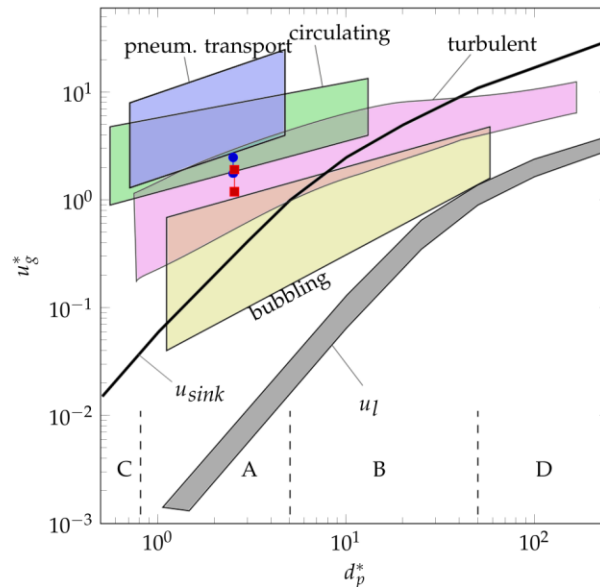


Figure 3. Grace diagram indicating the operation regimes of the FR —●— and AR —■—.

In order to assess the exact limits and to find the corresponding bottle necks where adaptations are needed, some variations on the boundary conditions have been made to be able to decide on equipment alteration and to generate data for the subsequent detailed design. While the simulation of the reference case yields a cold gas efficiency  $\eta_{CG}$  of 0.474, values above 0.8 are reported for externally heated continuous units with a slight increase of  $\eta_{CG}$  with increasing FR temperature [11]. Thus, two additional points with increased AR temperature (HT1) and increase of both reactor temperatures (HT2) were considered to test the feasibility of higher temperatures in the 1 MW pilot plant. The low superficial gas velocity for the AR was raised to  $u_{0,AR} = 5 \text{ m s}^{-1}$  by increasing the flow of fluidization medium (HF) to see the effect and possibility at higher inlet and outlet streams. This case was also used as a basis for an increase in fuel input to 1.2 MW (HP1) and 1.4 MW (HP2) to reduce the relative impact of heat loss and test the limits of the syngas handling equipment. During experimental operation, the AR superficial velocity would be targeted at slightly above the minimum discharge needed for either stable operation or required by the process—whichever is higher—in order to keep the negative impact of heat demand by fluidization medium low. However, for design purposes, the upper end of the range has to be considered.

From the variation of the reactor temperatures, it is clear that increasing the AR temperature is beneficial to process efficiency, while also increasing the FR, negatively impacts the process performance. For HT1 the increased heating demand in the AR is counteracted by the reduced solids circulation ( $\dot{m}_{OC,FR,out}$  and  $\dot{m}_{OC,AR,out}$ ) needed to supply the heat for the gasification process and thus reducing the overall amount of required fluidization medium ( $\dot{m}_{Air,AR,in}$ ,  $\dot{m}_{AR,reci}$  and  $\dot{m}_{H_2O,FR,in}$ ) to achieve this lowered solids circulation. The higher FR temperature in HT2 leads to a syngas composition higher in  $H_2$  and lower in  $CH_4$  which is desired, but also requiring significantly higher solids circulation. The corresponding heating requirement of fluidization medium negatively impacts process efficiency. The influence on the syngas quality is caused not only by the raise in gasification temperature, but also in the added steam content from fluidization, influencing reactions (R3), (R5) and (R6). The biggest effect has the increase of the oxygen carrier to fuel equivalence ratio  $\phi$  which raises the relative contribution of oxidation reactions (R8) to (R12).

The increase in AR solids entrainment through higher fluidization velocity (HF) essentially decouples the reactor hydrodynamics of both reactors. Here the model constraint of no internal solids circulation  $\dot{m}_{OC,AR,internal}$  is omitted. Instead, the superficial gas velocity  $u_{0,AR}$  is targeted at  $5 \text{ m s}^{-1}$ . The higher heat demand for the fluidization medium here has to be supplied by exothermic reaction (R13) leading to a higher degree of OC oxidation as indicated by the increase in  $\phi$ . Consequently, the solids circulation between the reactors is lowered as more oxygen is supplied per OC mass. This leads to lower fluidization requirements and heat demand in the FR reducing the negative impact of the higher fluidization velocity in the AR. Increasing the feedstock input  $\dot{m}_{FS}$  while keeping the AR hydrodynamic constant (HP1 and HP2) positively influences process efficiency, as the relative increase in FR fluidization medium required for solids discharge is only about half of the relative increase in feedstock. Thus, only a relatively small part of the additional feedstock is used to cover the energy requirement of the additional fluidization medium, while most of the additional feedstock energy is available for the conversion into syngas making a positive impact on syngas content and cold gas efficiency. This positive influence is mostly caused by more beneficial reactor hydrodynamics and lower relative heat losses of the reactors.

The simulated cases shed light on the process range the reactors can be operated without major modifications, and also highlights the huge impact of heat loss and heat demand in this scale of experiments. It shows that higher FR temperatures in case HT2 require higher fluidization and bigger size of downstream syngas equipment than significant increases in feedstock input (HP2) making this the more critical case to be considered during design. Although the syngas quality increases with higher FR temperature, the cold gas efficiency is drastically reduced, which is in contrast to the observations from Condori et al. [11]. This discrepancy can be explained by the external heating in the lab-scale plant, which can thus compensate the higher heating demands of the process streams. The positive effect of high temperatures for process streams entering the reactors has been shown [26], highlighting the need of good heat recovery and integration for the process. Moreover, the simulated process conditions make clear that individual variations of process parameters like steam to biomass ratio, or oxygen carrier to fuel equivalence ratio  $\phi$  as done by Condori et al. [11] are not possible if no external heating is available. Instead, the CFB mode and the defined solid discharge required for the heat transport also lower the steam to biomass ratio and oxygen carrier to fuel equivalence ratio, as can be seen by the feedstock increase (HP1, HP2). Furthermore, the predicted influence of these combined changes is not necessarily the same as the one observed in small-scale experiments. This can be seen by the increase of  $X_{CH_4}$  with increasing feedstock input, where the accompanying changes in steam to biomass ratio and oxygen carrier to fuel equivalence ratio lead to lower  $CH_4$  in the experiments described by Condori et al. [11].

Confirmation or refutation of either the trends experimentally observed in small scale units or simulated for the existing pilot plant necessitates experiments in the  $1 \text{ MW}_{th}$  range where autothermal operation—instead of external electrical heating—becomes necessary. Here, the requirements imposed by autothermal operation of the process limit the range of applicable parameter variation as they are interdependent. Therefore, the existing pilot plant is modified to provide the experimental data needed.

#### 4. Plant Design

The flow sheet in Figure 4 shows a simplified configuration of the designed pilot plant, including major components and important subsystems. Some of the components already available from CLC and HTW<sup>TM</sup> can be reused, while other subsystems are new or altered. For all subsystems affected by the new CLG process and the alterations a HAZOP analysis has been performed to ensure safe operation.

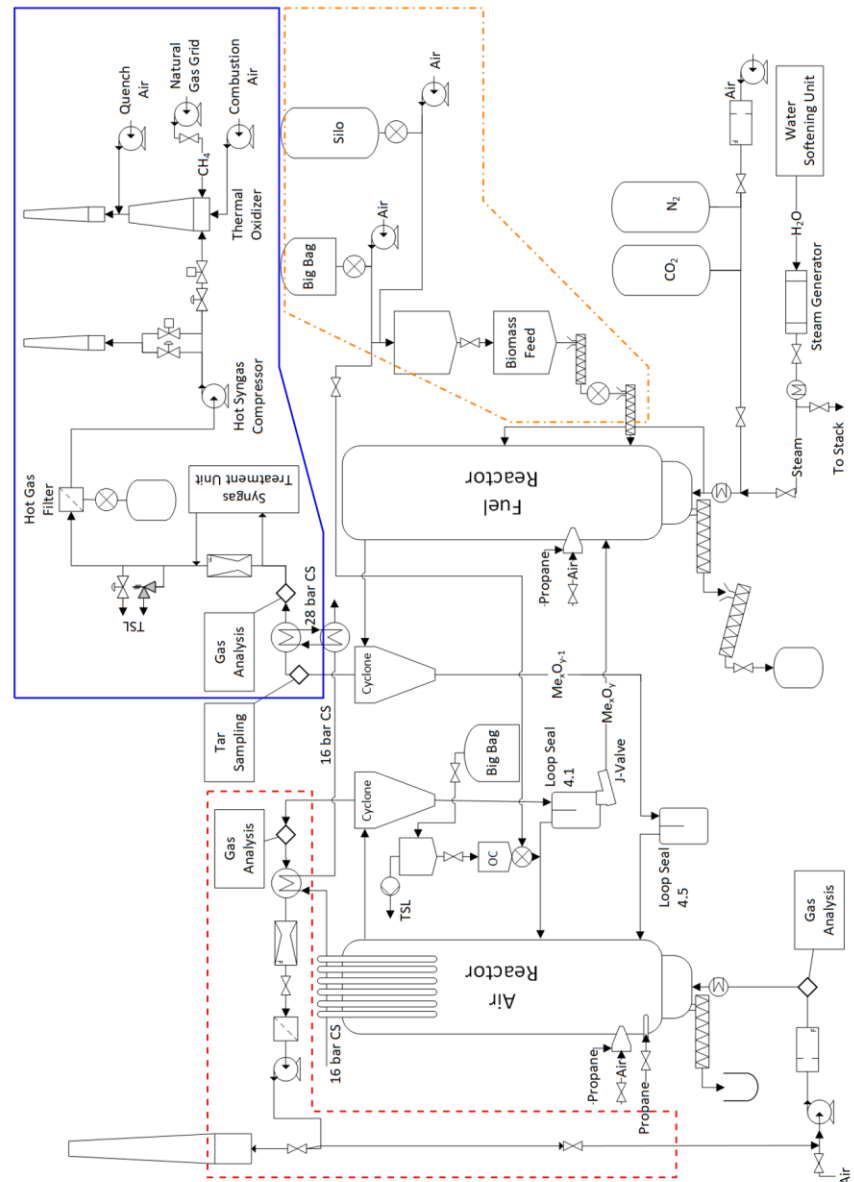


**Figure 4.** Schematic of the CLG pilot plant showing the main subsystems. CS: cooling system, OC: oxygen carrier, TSL: to safe location. syngas handling: —, flue gas handling: - - -, biomass feeding: - · - · -

#### 4.1. Reactor System

The reactor system (Figure 5) comprises of the two CFB reactors, two LS and a J-Valve as coupling elements. The total inventory of bed material during CLG operation with ilmenite is about 1000 kg with approximately 250 kg in the AR, 80 kg in the FR, and the rest in the coupling elements. Transport of sensible heat to the FR is not facilitated by internal solid circulation and additional fluidization medium would be required, cooling down the reactor and negatively impacting on process efficiency. Thus, no internal circulation is implemented for the FR. Moreover, process simulations show only reduced OC leaving

the reactor [26] giving no benefit of returning it from the cyclone to the reactor. However, the Gibbs reactor model employed in this study leads to full conversion, while in reality a mixture of different phases will always be present. Nonetheless, the prevalence of highly reduced phases in both FR and AR has been confirmed in continuous experiments [11].

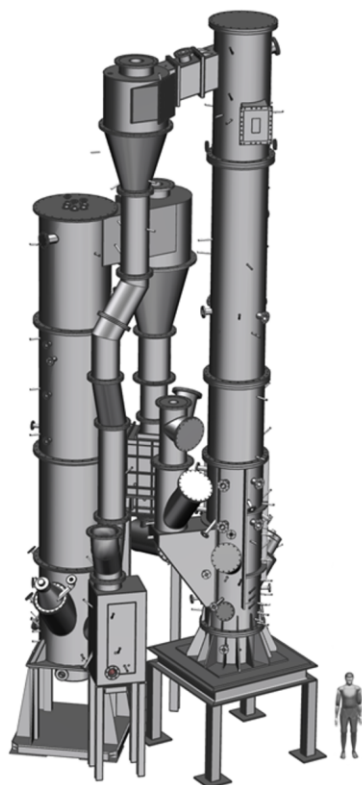


**Figure 5.** CLG reactor configuration including the main coupling elements.

Although many lab-scale reactor designs feature a FR operating in bubbling mode (e.g., [11,14,17,58]), the used CFB mode of the FR has the advantage of improved gas-solid mixing and thus featuring higher rates of carbon conversion [57], while the requirement ranges for the size and shape of the feedstock is wider [10] opening up possibilities for more feedstocks. Furthermore, the higher solids concentration in the freeboard may enhance tar cracking and methane reforming by supply of additional oxygen and catalytic sites in this region. However, increasing superficial velocities too much will lead to pneumatic transport in the FR (Figure 3) and unstable reactor hydrodynamics.

The disadvantage of having no internal solid recirculation for the FR is the transport of all discharged feedstock particles towards the AR. Furthermore, for the pilot plant, the minimization of heat losses is considered more important than the minimization of carbon slip towards the AR as relative heat losses for the pilot plant are in the range of 0.1 to 0.2. So minimization of coupling elements is used instead of carbon recovery via a carbon stripper. However, carbon slip is assumed to be a minor problem as the biomasses considered for the experiments contain low amounts of fixed carbon [9]. The feeding location is lowered into the dense region of the bed when compared to previous CLC experiments [49] where high carbon slip for hard coal was experienced, which should reduce the carbon slip as char gasification in the densest region is enhanced. Moreover,

carbon slip is more pronounced in small reactors and the sometimes utilized carbon strippers might not be required in bigger units [59]. Nonetheless, to maximize residence time of char particles inside the dense region, a variable amount of fluidization medium can be rerouted directly before the wind box of the FR to a second stage fluidization located at approx. one fifth of the reactor height. This increases bed density in the lower region and residence time of OC particles while keeping a high solids discharge in the CFB operation is possible by increasing the reactor inventory. The exact influence must be determined via experimental operation.

Investigations in the FR are the most crucial, as the formation of tars make the process and reactor design more critical to subsequent equipment than the re-oxidation in the AR. Therefore, it is advantageous for experimental operation to handle imbalances of solids discharge between the reactors inside the AR instead of the FR where it would negatively impact temperature and possibly lead to poorer syngas quality. The feedstock input directly in the dense zone of the bed should also reduce the amount of tars formed during initial devolatilization [37].

#### 4.2. Flue Gas Handling

The flue gas composition from the AR is measured by an on-line gas analysis before the flue gas is cooled down in a heat exchanger to approx. 230 °C (Figure 4, red box). The flow rate is measured using a venturi before the fines passing the cyclone are separated by a filter giving a dust-free flue gas. The following induced draft fan is used to control the pressure in the reactor and vents the flue gas via a stack. Part of the flue gas can be recirculated via a controlled butterfly valve to adjust the inlet of the AR fluidization. The variation of flue gas recirculation allows to adjust the superficial gas velocity  $u_{0,AR}$  and thereby the entrainment of particles from the AR while keeping the OC to fuel equivalence ratio  $\phi$  constant. This is a small but significant adjustment in converting from a CLC plant to a CLG plant as it allows to control the overall process as described in [26].

#### 4.3. Syngas Handling

Major modifications are needed for the FR off-gases (Figure 4, blue box) when converting a CLC unit into a CLG unit, as all parts need to be designed with the consideration of explosive atmospheres. Moreover, commonly used heat exchangers are either prone to clogging with tars on cold surfaces or the syngas cooling rate is too low, allowing for recombination of syngas species. The process simulation from Section 3.3 shows high syngas streams that need to be safely handled and greatly exceed the capacity of the syngas removal deployed for HTW<sup>TM</sup> gasification [45,46]. The only component reusable is the cooler, a patented tube-in-tube gas liquid heat exchanger from SCHMIDT'SCHE SCHACK consisting of four tubes cooling the gas to approx. 380 °C very fast and without recirculation zones [60] avoiding the recombination of syngas to longer hydro-carbons. The cooling water is pressurised to 28 bar to be able to raise temperature levels to 200 °C in order to avoid excessive condensation of tars inside the tubes of the raw gas cooler.

After the cooler the syngas is available for cleaning. Here part of the syngas can be routed to a syngas treatment unit for cleaning and separation of CO<sub>2</sub>, so that it is subsequently available for synthesis. Moreover, test rigs for the fine cleaning of the syngas and the synthesis of higher hydro-carbons are added, creating the unique possibility to investigate the whole solid to liquid value chain.

The return line from the syngas treatment unit consisting of all streams not used for synthesis is merged back, and the gas is routed to a hot gas filter for the removal of solids, resulting in a dust free syngas stream to the hot syngas compressor used to control the pressure in the FR. From here the syngas is transported to a thermal oxidizer for safe venting. The option of a second stack where the FR off gas can be vented is included for start up, shut down and to allow for a restart of the thermal oxidizer in case of failures without the full shut down of the pilot plant. The additional valves before the hot gas filter

are installed for safety pressure relief in case the switching between the thermal oxidizer and the second stack fails.

The described syngas line differs substantially from the ones deployed in either industrial scale or lab-scale. While in industrial plants all produced syngas would be cleaned, only the amount of syngas needed for research in gas cleaning is processed in the pilot plant to reduce the cost of the deployed gas cleaning equipment. In lab-scale the small quantities of formed syngas allow for untreated release to a safe location in the environment, which is not possible for streams in the size of the pilot plant, entailing the need for the thermal oxidizer.

All properties of the syngas stream leaving the FR are of major importance for further process development. Thus, sample and measurement sites consisting of an isokinetic dust and tar sampling port, a psychrometric water content measurement, and an on-line gas analysis are integrated into the syngas line. The isokinetic sampling of dust and tars is done before the raw syngas is cooled while ports for the measurement of the water content and gas composition are located before and after the cooler and can be connected as required.

#### 4.4. Solid Feeding

##### 4.4.1. Feedstock

The pilot plant is equipped with various entry points for solid feedstocks (Figure 4, orange box) like a big bag station, a container station (not shown on Figure 4) and a silo capable of introducing pulverized and pelletized feedstocks which are transported pneumatically to a fuel container purged with CO<sub>2</sub>. This container discontinuously feeds fuel to a second, weighted container from which the fuel is fed continuously, controlled via screws and a hopper directly in to the bed of the FR. Both containers are pressurised to the bed pressure of the FR at the location of the feed screw to avoid the back flow of syngas into the fuel feeding system. The screw feeder is cooled with thermal oil to ensure that gasification temperatures are only reached in the bed and no gasification occurs inside the screw.

##### 4.4.2. Oxygen Carrier

Initial filling of loop seals with OC is done via a weighted dosing container, a hopper, a screw conveyor, and a series of tubs connected to the stand-pipes. OC material is fed into the return leg of LS 4.1 for reactor filling and make-up dosing to compensate losses caused by agglomeration and attrition.

#### 4.5. Cooling and Preheating

The cooling system is designed to handle the full 1 MW of heat released during CLC and therefore has enough capacity for further increase of feedstock as discussed previously. However, for bigger units, where process heat would be used to generate steam and preheat the input streams, changes might be required when compared to CLC to optimize the heat integration. Nonetheless, this is no concern for the pilot plant, where steam generation and preheating is done via independently powered systems. Yet, it limits also the operation range of the pilot plant—seen on simulated case HT2—where higher outlet stream temperatures always lead to a severe process penalty. For the pilot plant, this penalty cannot be alleviated by heat recovery for the preheating of inlet streams. Here the option of higher preheating temperatures would require a substantial increase of heat exchanger surface, for which no space is available at the existing site. Furthermore, the existing electrical infrastructure is already at its limit, so increasing the electrical preheating power is not feasible.

Increasing the fuel input necessitates deeper investigation of the limitation of safe operation in terms of the cooling system, especially when considering that most of the 1000 kg OC material is in a highly reduced state during operation. Here the safety relevant quantity is not the total amount of feedstock input or the reduced OC, but the possible amount of oxygen input to the AR. The oxygen input will first fully oxidise the OC inside the AR, possibly with much higher power than the nominal feedstock input which will set a limit only after full oxidation inside the AR has been reached. Here mitigation measures are an over design of the cooling system and a limitation of oxygen input to safely handable amounts.

#### 4.6. On Line Measurements

##### 4.6.1. Gas Analysis

The main product of the gasification process, the synthesis gas from the FR, is extracted and analyzed continuously as shown in Figure 6 via a heated probe which includes a filter (1), that can be back flushed with CO<sub>2</sub> to prevent blockage.

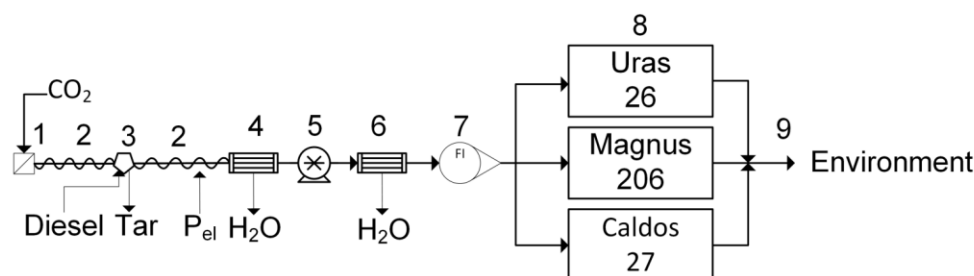


**Figure 6.** Schematic of the gas analysis equipment: (1) heated probe with filter, (2) heated tube, (3) tar removal (only for FR), (4) condenser for water removal, (5) pump, (6) condenser for water removal, (7) rotameter, (8) measurement equipment, (9) safe location in the environment.

The gas then passes in a heated tube (2)—to prevent the condensation of remaining tars—to a tar removal unit with diesel as solvent (3) and a first condenser unit (4) where the majority of the water and higher hydro-carbons are removed. The measurement gas pump (5) transports the gas through a second condenser unit to remove the rest of the water (6) which is followed by a rotameter (7) measuring the sampling gas flow. The sampling gas is distributed to the commercially available gas analysing equipment from ABB (8) given in Table 5 before being released to a safe location in the environment (9).

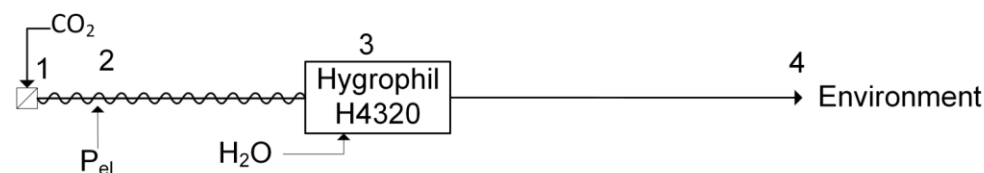
O<sub>2</sub> is measured via its paramagnetic quality in an Magnus 206 analyzer while H<sub>2</sub> is determined via thermal conductivity in a Caldos 27 unit. The components CO<sub>2</sub>, CO, CH<sub>4</sub>, SO<sub>2</sub> and NO are measured by an spectroscopic non-dispersive infra red (NDIR) sensor in an Uras 26 analyzer.

For the AR both gas analysis lines differ in the heated probe which does not include a tar removal unit. The measurement ranges of the equipment is different, as can be seen in Table 5 and H<sub>2</sub> and CH<sub>4</sub> is not measured. At the inlet of the AR, the composition is of interest to control the oxygen feed to the process and the amount of recirculated flue gas.

The water content is measured in both reactor outlets via a psychrometric Hygrophil H4320 unit from Bartec with the sampling gas extraction as shown in Figure 7. The gas is extracted via a heated probe (1) and transported in an electrically heated tube (2) to the analyzer (3) which includes a CO<sub>2</sub>-driven ejector pump to facilitate the gas transport. The gas is released to the environment afterwards (4).

**Table 5.** Listing of gas analysis equipment for all reactors.

Reactor	Equipment	Measurement Principle	Component	Range	Error	Unit
FR	Magnos 206	paramagnetic	O <sub>2</sub>	0 to 25	0.9	vol. – %
	Caldos 27	thermal conductivity	H <sub>2</sub>	0 to 40	1.8	vol. – %
	Uras 26	NDIR	CO <sub>2</sub>	0 to 100	3.0	vol. – %
	Uras 26	NDIR	CO	0 to 40	1.2	vol. – %
	Uras 26	NDIR	CH <sub>4</sub>	0 to 20	0.6	vol. – %
	Uras 26	NDIR	SO <sub>2</sub>	0 to 5	0.15	vol. – %
	Uras 26	NDIR	NO	0 to 1000	30	ppm
	Hygrophil H4320	psychrometric	H <sub>2</sub> O	2 to 100	0.3	vol. – %
AR outlet	Magnos 206	paramagnetic	O <sub>2</sub>	0 to 25	0.9	vol. – %
	Uras 26	NDIR	CO <sub>2</sub>	0 to 30	0.9	vol. – %
	Uras 26	NDIR	CO	0 to 5	0.15	vol. – %
	Uras 26	NDIR	SO <sub>2</sub>	0 to 4000	120	ppm
	Uras 26	NDIR	NO	0 to 1000	30	ppm
	Hygrophil H4320	psychrometric	H <sub>2</sub> O	2 to 100	0.3	vol. – %
AR inlet	Magnos 206	paramagnetic	O <sub>2</sub>	0 to 25	0.9	vol. – %
	Uras 26	NDIR	CO <sub>2</sub>	0 to 100	3.0	vol. – %
	Uras 26	NDIR	CO	0 to 5	0.15	vol. – %
	Uras 26	NDIR	SO <sub>2</sub>	0 to 5	0.15	vol. – %
	Uras 26	NDIR	NO	0 to 1000	30	ppm

**Figure 7.** Schematic of the water content analysis equipment: (1) heated probe with filter, (2) heated tube, (3) psychrometric analyzer, (4) safe location in the environment.

Both water content measurements and the three gas analysis are integrated in the process control system of the pilot plant with all measurements available in real time and as trend lines.

#### 4.6.2. Temperature and Pressure

The pilot is equipped with temperature and pressure in all inlet and outlet streams of the reactors including the LS fluidization. Multiple additional measurement sites for pressure and temperature are installed along the reactor height to acquire more insight in the reactor state during operation. The pressure sensors for the AR are differential pressure transducers with the other side open to atmosphere while at the FR all pressure measurements are purged with CO<sub>2</sub> and are mostly differential pressure transducers measuring between different reactor heights. This allows us to control the bed height and density and to control the influence of the second stage fluidization.

#### 4.6.3. Flow Measurements

The flow rates of all streams entering the reactors and coupling elements are measured either with an orifice plate, a rotameter or are controlled via a mass flow controller. The main streams leaving the reactors are measured via two venturi with side streams for off-line analysis, process control or the syngas treatment unit measured inside the respective analysis or control equipment. The mass flow of solids entering the system is measured via load cells and the corresponding trend line gradients.



#### 4.7. Off-Line Sampling

##### 4.7.1. Solid Sampling

The bottom product removal of the AR transfers the material to an open barrel and is immediately accessible for inspection and sampling, while for the FR it is transferred to a sealed and CO<sub>2</sub>-purged container which can be replaced periodically during operation to allow for the collection of samples. The same is implemented for filter dust sampling. The AR filter is equipped with a hopper and an open barrel, while the FR filter has an additional CO<sub>2</sub> purge and the container is sealed.

Both loop seals allow for the collection of solid samples for off-line analysis. The OC samples enable the determination of the exact phase composition of the circulating OC and to balance the reactors individually. Moreover, knowledge of the oxidation level before and after the reactors allows for an additional method for the quantification of solid circulation.

##### 4.7.2. Gas and Tar Sampling

More gas species like COS and higher hydrocarbons can be measured using Fourier transform infrared (FTIR) spectroscopy which can be connected at different locations. These measurements are not considered important during pilot plant operation but are important for the evaluation of the process. At the FTIR a port for gas sample bags and gas mice exists to enable off-line gas analysis.

Additionally, isokinetic sampling is possible in the synthesis gas line allowing for dust and tar sample collection according to tar protocol/CEN TS 15439. Velocity is measured by an S-Pitot tube 550 mm downstream of the sampling lance, both located in the center line of a refractory lined tube. The dust loaded syngas sample stream is transferred via a heated lance towards a heated filter and through six impinger bottles where five are filled with isopropanol as solvent and the last is empty. The impinger bottles are tempered to 40 °C (impinger 1, 2 and 4) and −20 °C (impinger 2, 5 and 6). The sample volume is measured inside a commercially available ST5 isokinetic sampler from Dado lab, which also adjusts the sample volume flow based on the pitot measurement.

## 5. Plant Operation

The simulations from Section 3.3 show that autothermal CLG experiments are needed to obtain further insights into the process, which are of high relevance for industrial deployment. The modified pilot plant (Section 4) renders these experiments feasible allowing for the generation of the following, required information:

- 5.1. Literature, describing the demonstration of autothermal operation of the CLG process, is not yet available. While autothermal CLC has been successfully demonstrated [49,51] the higher prevalence of endothermic reactions impose the need for higher heat transfer to the FR and different control strategies [26].
- 5.2. Continuous CLG of residual biomass has been successfully demonstrated in lab-scale [11,15,16]. Nonetheless, upscaling to higher thermal loads is necessary to obtain data for reliable simulations and design of industrial scale units.
- 5.3. Due to their interdependence, the key performance indicators achievable in autothermal operation are unknown. This affects the cold gas efficiency  $\eta_{CG}$ , the carbon conversion  $\eta_{CC}$ , the syngas yield  $x_{SG}$  and the syngas quality (tars, CH<sub>4</sub>, etc.). For example, in electrically heated systems the cold gas efficiency  $\eta_{CG}$  can be theoretically driven to 100% by supplying enough heat through the furnace. However, the exact amount of external heat supplied is seldom reported. The carbon slip depends amongst other on reactor size [59] and data for bigger scale units is not existent.
- 5.4. Tar production can presently not be accurately predicted as no model was developed for CLG yet. Especially bed height and feeding location are also dependent on reactor size and their influence cannot be quantified [37]. The pilot plant experiments will give important insight on this matter in industrial like conditions, allowing for inferences for future upscaling endeavours.

- 5.5. OC life time is difficult to assess with currently available data, as the time of circulation and thus of re-oxidation cycles increases with increasing reactor size while the mechanical erosion is dependent on the transport velocity only. The exact contribution of the two effects is unknown and thus it is likely that the size of the reactor will have an influence on the OC life time.
- 5.6. Assessment of economic feasibility of the CLG process requires data from bigger scale units to make accurate predictions for e.g., sizing of components and process performance.

For the demonstration of autothermal CLG (item 5.1.) a suitable control concept for the oxygen carrier to fuel equivalence ratio  $\phi$  based on a sub-stoichiometric AR operation (reduced OC oxidation, see Equations (2) and (3)) according to Dieringer et al. [26] is implemented. The corresponding operating strategy considering pilot plant limitations is described in the following.

#### *Chemical Looping Gasification Operation*

The start-up sequence of the pilot plant is preheating with electrically heated air, preheating with propane burner, OC filling plus propane burner, CFB combustion, CLC as described in [47]. Afterwards the switch to CLG is achieved by a reduction of air input to the AR while increasing flue gas recirculation, thus reducing  $\phi$  to values smaller than unity. After stable CLG operation is attained, optimization of individual key performance indicators is targeted during experiments. The devised experimental operation of the pilot plant (described hereafter) allows to directly obtain data for items 5.2. and 5.3. while information for items 5.4. and 5.5. can be inferred from additional off-line analysis. Item 5.6. builds on this data but needs additional information, e.g., component and material pricing, which cannot be generated in the pilot plant. The main operation variables through which the process can be controlled are:

- Thermal load: Increasing the thermal load above 1 MW<sub>th</sub> decreases the relative heat loss as it depends on reactor temperature and not on thermal load. Therefore, a higher fraction of the feedstock input,  $\dot{m}_{FS}$ , can be converted into syngas increasing process efficiency. The feedstock input rate  $\dot{m}_{FS}$  is directly proportional to the thermal load, but an adjustment requires corresponding changes in fluidization imposed by reactor hydrodynamics and heat balance influencing the steam to biomass ratio. Nonetheless, the simulations in Section 3.3 show also an increase of CH<sub>4</sub> production with increasing thermal load, indicating a tendency to form hydrocarbons including tars. The limit for the thermal input is set by the maximum possible feedstock input and the syngas handling and cooling, as higher loads result in a higher amount of product gas which has to be handled safely. During operation a high thermal load is targeted at all operation points to obtain high  $\eta_{CG}$ .
- The OC to fuel equivalence ratio  $\phi$  determines the net heat release from the process. A higher value of  $\phi$  (while keeping everything else constant) results in a higher temperature inside AR and FR. However, the cold gas efficiency  $\eta_{CG}$  will decrease with higher  $\phi$  as does the production of CH<sub>4</sub> and tars. The control of  $\phi$  is straightforward through the control of the oxygen availability inside the AR.

For experimental investigation the variation of temperatures is important. However, higher temperatures increase the load on the cooling system. Here the limits have to be considered during operation, and a reduction in thermal load (leading to smaller process streams and further decreasing  $\eta_{CG}$ ) may be required in order to be able to reach higher gasification temperatures. Moreover, the refractory lining of the AR and/or the ash melting behaviour of the feedstock inside the FR limit the maximum admissible reactor temperatures.

Actual control of  $\phi$  is achieved via the variable amounts of air and recirculated AR flue gas fed to the AR to obtain a sub-stoichiometric environment inside the AR as it is the most suitable method for large scale operation described in detail by Dieringer et al. [26].

- The global solids circulation  $\dot{m}_{OC}$  can be controlled via adjustment of J-valve and FR fluidization and transports sensible heat required in the FR. Depending on the operating state of the AR internal solids recirculation, fluidization of the AR needs adjustment as well to obtain hydrodynamic equilibrium between the reactors. Yet,  $\dot{m}_{OC}$  is not directly accessible during pilot plant operation but can be inferred qualitatively from the temperature difference between the reactors. Higher solids circulation reduces the temperature difference  $\Delta T$  between AR and FR. An accurate determination of  $\dot{m}_{OC}$  is possible only indirectly via the oxygen content in the solid samples taken from the loop seals.

Increasing global solids circulation reduces not only  $\Delta T$  but also  $\eta_{CG}$  as more fluidization medium and corresponding heating is required. Furthermore, OC residence time inside the reactors is reduced when the solids circulation increases and as higher superficial gas velocities are employed, carbon slip towards the AR might increase. The variable to be controlled is the gasification temperature inside the FR while the limit of the AR temperature might require adjustment via  $\phi$ .

The OC to fuel equivalence ratio  $\phi$  and the global solids circulation  $\dot{m}_{OC}$  are used to investigate the inevitable trade-off between cold gas efficiency and syngas quality in the form of produced  $CH_4$ , higher hydrocarbons, and tar. In contrast, the maximization of the thermal load is used to boost the process performance  $\eta_{CG}$  for all operation points by allowing for a smaller value of  $\phi$  while at the same time guaranteeing autothermal operation.

While the variables above are used to adjust and stabilize the process and to investigate general trends, two more adjustable parameters exist which can be used to influence the syngas quality:

- Bed pressure drop  $\Delta p$ : The simulations in Section 3.3 are done with a fixed pressure drop  $\Delta p$  for both reactors. However, during operation of the pilot plant,  $\Delta p$  can be varied and is dependent on the exact distribution of bed material between the reactors (controlled by the governing hydrodynamic boundary conditions) as well as the total amount of bed material inside the reactor system. Increasing the pressure drop inside the FR will increase OC particle residence time inside the reactor (and the amount of OC per feedstock input). This will also increase the entrainment from the FR and thereby the solid circulation. However, increasing  $\Delta p$  allows for the reduction of fluidization medium, while keeping the entrainment constant, thus improving process efficiency. Reduction of tar and  $CH_4$  content in syngas is facilitated by the increased availability of catalytic sites for conversion.  
The OC make up stream is used to control the overall amount of OC inside the reactor system, while its distribution is influenced by small adjustments to fluidization medium. The required changes in fluidization are small compared to the changes needed for the operation variables discussed above. The range of  $\Delta p$  is limited by the reactor hydrodynamics and the characteristics of corresponding peripheral equipment (e.g., maximum load of AR primary air fan).
- Second stage fluidization can be varied to enhance the residence time of the feedstock inside the dense zone of the FR as describes in Section 4.1. Rerouting part of the fluidization medium to the second stage fluidization will reduce entrainment and solid circulation, if the total amount of steam is kept constant and can be counteracted by additional bed material. Qualitative effects on synthesis gas are the same as for the bed pressure drop  $\Delta p$ , however, the quantitative influence may vary.

The feedstock types given in Table 2 are an additional parameter for experimental variation. However, the feedstock is not usable as process control variable and is therefore not included in the list above. Furthermore, the other variables must be used to adjust for feedstock variation to keep the process stable.

## 6. Conclusions

In this article, the design pathway of a 1 MW<sub>th</sub> chemical looping gasification (CLG) pilot plant, allowing for autothermal, semi-industrial process investigation, has been described in detail. Starting from a process model, considering fundamental CLG characteristics, a suitable operational mode and associated necessary adaptations for an existing 1 MW<sub>th</sub> chemical looping combustion (CLC) pilot plant have been established. Subsequently, it has been illustrated which inherent interconnections and trade-offs associated to CLG can be further analyzed in such an experimental setup and which strategies towards an optimized process setup, replicable in industry scale, can be pursued with it. These are:

- Calculation of heat and mass balances for autothermal CLG show a significantly reduced range of freely selectable operation parameters (operation temperatures, steam to biomass feed ratio, and oxygen carrier to fuel equivalence ratio), when compared to externally heated lab-scale units, due to the requirements of autothermal operation.
- Process control under autothermal condition can be achieved via three parameters: thermal load, oxygen carrier to fuel equivalence ratio, and global solid circulation. However, due to restrictions imposed by reactor hydrodynamics and autothermal operation, changes in one parameter must be balanced by changes in at least one of the other two. Moreover, the global solids circulation is adjusted indirectly via fluidization velocities and can only be inferred qualitatively from the reactor temperature difference during operation.
- Attempting to attain high cold gas efficiency and good syngas quality through higher gasification temperature inevitably results in high relative heat losses, as heat integration is not reasonably achievable in the 1 MW<sub>th</sub> scale and the existing unit. This leads to an unavoidable trade-off between cold gas efficiency and syngas quality, e.g., CH<sub>4</sub> and tar content which has to be accepted during experiments.
- Data which are not reliably obtainable from simulation, like tar formation or oxygen carrier (OC) life time, yet are fundamental for scale-up and economic considerations becomes available by conducting experiments in an industry relevant scale in the designed pilot plant.

In summary, future endeavours aiming towards industrial application of CLG are facilitated, through the described design of a 1 MW<sub>th</sub> CLG pilot plant. Here, the experimental facility lays the foundation to generate a unique robust dataset containing essential information required for up-scaling of CLG to industry size, thus propelling the technology towards market maturity.

**Author Contributions:** conceptualization, F.M., J.S. and P.D.; simulation, P.D. and F.M.; writing—original draft preparation, F.M.; writing—review and editing, P.D., J.S. and F.M.; visualization, F.M. and P.D.; supervision, B.E. All authors have read and agreed to the published version of the manuscript.

**Funding:** This work has received funding of the European Union’s Horizon 2020—Research and Innovation Framework Programme under grant agreement No. 817841 (Chemical Looping gasification for sustainAble production of biofuels—CLARA).

**Acknowledgments:** The authors gratefully acknowledge the support given by Harald Tremmel and Karl Voigtländer from AICHERNIG Engineering GmbH during HAZOP analysis.

**Conflicts of Interest:** The authors declare no conflict of interest.

### Abbreviations

The following abbreviations are used in this manuscript:

AR	air reactor
ASU	air separation unit
CFB	circulating fluidized bed
CLC	chemical looping combustion
CLG	chemical looping gasification
CLOU	chemical looping with oxygen uncoupling
DFBG	dual fluidized bed gasification
FR	fuel reactor
FTIR	Fourier transform infrared
HTW <sup>TM</sup>	High Temperature Winkler
LS	loop seal
NDIR	non-dispersive infra red
OC	oxygen carrier

### Symbols

$LHV$	$\text{MJ kg}^{-1}, \text{MJ mol}^{-1}$	lower heating value
$R_{OC}$		oxygen transport capacity
$T$	K, °C	temperature
$X$		mole fraction
$\Delta H$	$\text{J mol}^{-1}$	reaction enthalpy
$\Delta p$	Pa, bar	differential pressure
$\phi$		oxygen carrier to fuel equivalence ratio
$\dot{Q}$	W	heat flow
$\dot{m}$	$\text{kg s}^{-1}$	mass flow
$\dot{n}$	$\text{mol s}^{-1}$	molar flow
$\eta_{CG}$		cold gas efficiency
$c_p$	$\text{J kg}^{-1} \text{K}^{-1}$	specific heat
$d_{p,50}$	m	mean particle diameter
$d$	m	diameter
$h$	m	height
$m$	kg	mass
$p$	Pa, bar	pressure
$u$	$\text{m s}^{-1}$	velocity
$x_{SG}$		syngas content

### Subscripts

AR	Air Reactor
FR	Fuel Reactor
FS	Feed Stock
OC	Oxygen Carrier
O	Oxygen
<i>internal</i>	internal recirculation
<i>in</i>	stream entering reactor
<i>loss</i>	loss
<i>out</i>	stream leaving reactor
<i>ox</i>	oxidized
<i>reci</i>	recirculation
<i>red</i>	reduced
<i>stoich</i>	stoichiometric

### References

1. Directive (EU) 2018/2001 of the European Parliament and of the Council of 11 December 2018 on the Promotion of the Use of Energy from Renewable Sources. p. 128. Available online: <https://eurovent.eu/?q=articles/review-directive-eu-20182001-promotion-use-energy-renewable-sources-gen-115400> (accessed on 19 December 2020).

2. International Energy Agency. Data & Statistics. 2020. Available online: <https://www.iea.org/data-and-statistics?country=EU28&fuel=Energy20transition20indicators&indicator=Biotrans> (accessed on 19 December 2020).
3. Kaltschmitt, M. (Ed.) *Energy from Organic Materials (Biomass): A Volume in the Encyclopedia of Sustainability Science and Technology*, 2nd ed.; Springer: New York, NY, USA, 2019. [CrossRef]
4. Carrasco, J.E.; Monti, A.; Tayeb, J.; Kiel, J.; Girio, F.; Matas, B.; Santos Jorge, R. Strategic Research and Innovation Agenda 2020. EERA Technical Report. 2020. Available online: <http://www.eera-bioenergy.eu/wp-content/uploads/pdf/EERABioenergySRIA2020.pdf=AOvVaw012VUhnaiUbL-yP76cz6s> (accessed on 19 December 2020).
5. Molino, A.; Larocca, V.; Chianese, S.; Musmarra, D. Biofuels Production by Biomass Gasification: A Review. *Energies* **2018**, *11*, 811. [CrossRef]
6. Gómez-Barea, A.; Leckner, B. Estimation of Gas Composition and Char Conversion in a Fluidized Bed Biomass Gasifier. *Fuel* **2013**, *107*, 419–431. [CrossRef]
7. Thomsen, T.P.; Sárossy, Z.; Göbel, B.; Stoholm, P.; Ahrenfeldt, J.; Frandsen, F.J.; Henriksen, U.B. Low Temperature Circulating Fluidized Bed Gasification and Co-Gasification of Municipal Sewage Sludge. Part 1: Process Performance and Gas Product Characterization. *Waste Manag.* **2017**, *66*, 123–133. [CrossRef]
8. Arena, U.; Zaccariello, L.; Mastellone, M.L. Fluidized Bed Gasification of Waste-Derived Fuels. *Waste Manag.* **2010**, *30*, 1212–1219. [CrossRef]
9. De, S.; Agarwal, A.K.; Moholkar, V.S.; Thallada, B. (Eds.) *Coal and Biomass Gasification: Recent Advances and Future Challenges; Energy, Environment, and Sustainability*; Springer: Singapore, 2018. [CrossRef]
10. Higman, C.; van der Burgt, M. *Gasification*, 2nd ed.; Gulf Professional Pub.: Boston, MA, USA; Elsevier: Amsterdam, The Netherlands, 2008.
11. Condori, O.; García-Labiano, F.; de Diego, L.F.; Izquierdo, M.T.; Abad, A.; Adánez, J. Biomass Chemical Looping Gasification for Syngas Production Using Ilmenite as Oxygen Carrier in a 1.5 kW<sub>th</sub> Unit. *Chem. Eng. J.* **2021**, *405*, 126679. [CrossRef]
12. Huseyin, S.; Wei, G.Q.; Li, H.B.; He, F.; Huang, Z. Chemical-Looping Gasification of Biomass in a 10 kW<sub>th</sub> Interconnected Fluidized Bed Reactor Using Fe<sub>2</sub>O<sub>3</sub>/Al<sub>2</sub>O<sub>3</sub> Oxygen Carrier. *J. Fuel Chem. Technol.* **2014**, *42*, 922–931. [CrossRef]
13. Guo, Q.; Cheng, Y.; Liu, Y.; Jia, W.; Ryu, H.J. Coal Chemical Looping Gasification for Syngas Generation Using an Iron-Based Oxygen Carrier. *Ind. Eng. Chem. Res.* **2014**, *53*, 78–86. [CrossRef]
14. Wei, G.; He, F.; Huang, Z.; Zheng, A.; Zhao, K.; Li, H. Continuous Operation of a 10 kW<sub>th</sub> Chemical Looping Integrated Fluidized Bed Reactor for Gasifying Biomass Using an Iron-Based Oxygen Carrier. *Energy Fuels* **2015**, *29*, 233–241. [CrossRef]
15. Samprón, I.; de Diego, L.F.; García-Labiano, F.; Izquierdo, M.T.; Abad, A.; Adánez, J. Biomass Chemical Looping Gasification of Pine Wood Using a Synthetic Fe<sub>2</sub>O<sub>3</sub>/Al<sub>2</sub>O<sub>3</sub> Oxygen Carrier in a Continuous Unit. *Bioresour. Technol.* **2020**, *316*, 123908. [CrossRef] [PubMed]
16. Ge, H.; Guo, W.; Shen, L.; Song, T.; Xiao, J. Experimental Investigation on Biomass Gasification Using Chemical Looping in a Batch Reactor and a Continuous Dual Reactor. *Chem. Eng. J.* **2016**, *286*, 689–700. [CrossRef]
17. Ge, H.; Guo, W.; Shen, L.; Song, T.; Xiao, J. Biomass Gasification Using Chemical Looping in a 25 kW<sub>th</sub> Reactor with Natural Hematite as Oxygen Carrier. *Chem. Eng. J.* **2016**, *286*, 174–183. [CrossRef]
18. Brown, T.A.; Dennis, J.S.; Scott, S.A.; Davidson, J.F.; Hayhurst, A.N. Gasification and Chemical-Looping Combustion of a Lignite Char in a Fluidized Bed of Iron Oxide. *Energy Fuels* **2010**, *24*, 3034–3048. [CrossRef]
19. Leion, H.; Mattisson, T.; Lyngfelt, A. The Use of Petroleum Coke as Fuel in Chemical-Looping Combustion. *Fuel* **2007**, *86*, 1947–1958. [CrossRef]
20. Chen, L. The Direct Solid-Solid Reaction between Coal Char and Iron-Based Oxygen Carrier and Its Contribution to Solid-Fueled Chemical Looping Combustion. *Appl. Energy* **2016**, *184*, 9–18. [CrossRef]
21. Leion, H.; Mattisson, T.; Lyngfelt, A. Solid Fuels in Chemical-Looping Combustion. *Int. J. Greenh. Gas Control* **2008**, *2*, 180–193. [CrossRef]
22. Song, Q.; Xiao, R.; Deng, Z.; Zhang, H.; Shen, L.; Xiao, J.; Zhang, M. Chemical-Looping Combustion of Methane with CaSO<sub>4</sub> Oxygen Carrier in a Fixed Bed Reactor. *Energy Convers. Manag.* **2008**, *49*, 3178–3187. [CrossRef]
23. Pissot, S.; Vilches, T.B.; Maric, J.; Seemann, M. Chemical Looping Gasification in a 2–4 MW<sub>th</sub> Dual Fluidized Bed Gasifier. In Proceedings of the 23rd International Conference on Fluidized Bed Conversion, Seoul, Korea, 13–17 May 2018; p. 10.
24. Larsson, A.; Seemann, M.; Neves, D.; Thunman, H. Evaluation of Performance of Industrial-Scale Dual Fluidized Bed Gasifiers Using the Chalmers 2–4-MW<sub>th</sub> Gasifier. *Energy Fuels* **2013**, *27*, 6665–6680. [CrossRef]
25. Larsson, A.; Israelsson, M.; Lind, F.; Seemann, M.; Thunman, H. Using Ilmenite to Reduce the Tar Yield in a Dual Fluidized Bed Gasification System. *Energy Fuels* **2014**, *28*, 2632–2644. [CrossRef]
26. Dieringer, P.; Marx, F.; Alobaid, F.; Ströhle, J.; Eppler, B. Process Control Strategies in Chemical Looping Gasification—A Novel Process for the Production of Biofuels Allowing for Net Negative CO<sub>2</sub> Emissions. *Appl. Sci.* **2020**, *10*, 4271. [CrossRef]
27. Yin, S.; Shen, L.; Dosta, M.; Hartge, E.U.; Heinrich, S.; Lu, P.; Werther, J.; Song, T. Chemical Looping Gasification of a Biomass Pellet with a Manganese Ore as an Oxygen Carrier in the Fluidized Bed. *Energy Fuels* **2018**, *32*, 11.
28. Adanez, J.; Abad, A.; García-Labiano, F.; Gayán, P.; de Diego, L.F. Progress in Chemical-Looping Combustion and Reforming Technologies. *Prog. Energy Combust. Sci.* **2012**, *38*, 215–282. [CrossRef]
29. Linderholm, C.; Knutsson, P.; Schmitz, M.; Markström, P.; Lyngfelt, A. Material Balances of Carbon, Sulfur, Nitrogen and Ilmenite in a 100 kW CLC Reactor System. *Int. J. Greenh. Gas Control* **2014**, *27*, 188–202. [CrossRef]

30. Alabdrabameer, H.A.; Taylor, M.J.; Kauppinen, J.; Soini, T.; Pikkarainen, T.; Skoulou, V. Big Problem, Little Answer: Overcoming Bed Agglomeration and Reactor Slagging during the Gasification of Barley Straw under Continuous Operation. *Sustain. Energy Fuels* **2020**, *4*, 3764–3772. [\[CrossRef\]](#)
31. Di Giuliano, A.; Funcia, I.; Pérez-Vega, R.; Gil, J.; Gallucci, K. Novel Application of Pretreatment and Diagnostic Method Using Dynamic Pressure Fluctuations to Resolve and Detect Issues Related to Biogenic Residue Ash in Chemical Looping Gasification. *Processes* **2020**, *8*, 1137. [\[CrossRef\]](#)
32. Fernández, M.J. Sintering reduction of herbaceous biomass when blended with woody biomass: Predictive and combustion tests. *Fuel* **2019**, *239*, 1115–1124. [\[CrossRef\]](#)
33. Luo, S.; Zeng, L.; Fan, L.S. Chemical Looping Technology: Oxygen Carrier Characteristics. *Annu. Rev. Chem. Biomol. Eng.* **2015**, *6*, 53–75. [\[CrossRef\]](#) [\[PubMed\]](#)
34. Fan, L.S.; Zeng, L.; Luo, S. Chemical-Looping Technology Platform. *AIChE J.* **2015**, *61*, 2–22. [\[CrossRef\]](#)
35. Zhao, X.; Zhou, H.; Sikarwar, V.S.; Zhao, M.; Park, A.H.A.; Fennell, P.S.; Shen, L.; Fan, L.S. Biomass-Based Chemical Looping Technologies: The Good, the Bad and the Future. *Energy Environ. Sci.* **2017**, *10*, 1885–1910. [\[CrossRef\]](#)
36. Larsson, A.; Kuba, M.; Berdugo Vilches, T.; Seemann, M.; Hofbauer, H.; Thunman, H. Steam Gasification of Biomass—Typical Gas Quality and Operational Strategies Derived from Industrial-Scale Plants. *Fuel Process. Technol.* **2021**, *212*, 106609. [\[CrossRef\]](#)
37. Gómez-Barea, A.; Ollero, P.; Leckner, B. Optimization of Char and Tar Conversion in Fluidized Bed Biomass Gasifiers. *Fuel* **2013**, *103*, 42–52. [\[CrossRef\]](#)
38. Devi, L.; Ptasiński, K.J.; Janssen, F.J. Pretreated Olivine as Tar Removal Catalyst for Biomass Gasifiers: Investigation Using Naphthalene as Model Biomass Tar. *Fuel Process. Technol.* **2005**, *86*, 707–730. [\[CrossRef\]](#)
39. Amin, A.M.; Croiset, E.; Epling, W. Review of Methane Catalytic Cracking for Hydrogen Production. *Int. J. Hydrogen Energy* **2011**, *36*, 2904–2935. [\[CrossRef\]](#)
40. Milne, T.A.; Evans, R.J.; Abatzoglou, N. *Biomass Gasifier “Tars”: Their Nature, Formation, and Conversion*; Technical Report NREL/TP-570-25357; United States Department of Energy: Washington, DC, USA, 1998. [\[CrossRef\]](#)
41. Benedikt, F.; Kuba, M.; Schmid, J.C.; Müller, S.; Hofbauer, H. Assessment of Correlations between Tar and Product Gas Composition in Dual Fluidized Bed Steam Gasification for Online Tar Prediction. *Appl. Energy* **2019**, *238*, 1138–1149. [\[CrossRef\]](#)
42. Palma, C.F. Model for Biomass Gasification Including Tar Formation and Evolution. *Energy Fuels* **2013**, *27*, 5. [\[CrossRef\]](#)
43. Wojnicka, B.; Ściażko, M.; Schmid, J.C. Modelling of Biomass Gasification with Steam. *Biomass Conv. Bioref.* **2019**. [\[CrossRef\]](#)
44. Stark, A.K.; Bates, R.B.; Zhao, Z.; Ghoniem, A.F. Prediction and Validation of Major Gas and Tar Species from a Reactor Network Model of Air-Blown Fluidized Bed Biomass Gasification. *Energy Fuels* **2015**, *29*, 2437–2452. [\[CrossRef\]](#)
45. Herdel, P.; Krause, D.; Peters, J.; Kolmorgen, B.; Ströhle, J.; Epple, B. Experimental Investigations in a Demonstration Plant for Fluidized Bed Gasification of Multiple Feedstock’s in 0.5 MW Th Scale. *Fuel* **2017**, *205*, 286–296. [\[CrossRef\]](#)
46. Krause, D.; Herdel, P.; Ströhle, J.; Epple, B. HTW™-Gasification of High Volatile Bituminous Coal in a 500 kWth Pilot Plant. *Fuel* **2019**, *250*, 306–314. [\[CrossRef\]](#)
47. Ströhle, J.; Orth, M.; Epple, B. Design and Operation of a 1 MWth Chemical Looping Plant. *Appl. Energy* **2014**, *113*, 1490–1495. [\[CrossRef\]](#)
48. Ströhle, J.; Orth, M.; Epple, B. Chemical Looping Combustion of Hard Coal in a 1 MWth Pilot Plant Using Ilmenite as Oxygen Carrier. *Appl. Energy* **2015**, *157*, 288–294. [\[CrossRef\]](#)
49. Ohlemüller, P.; Busch, J.P.; Reitz, M.; Ströhle, J.; Epple, B. Chemical-Looping Combustion of Hard Coal: Autothermal Operation of a 1 MWth Pilot Plant. *J. Energy Resour. Technol.* **2016**, *138*, 042203. [\[CrossRef\]](#)
50. Ohlemüller, P.; Ströhle, J.; Epple, B. Chemical Looping Combustion of Hard Coal and Torrefied Biomass in a 1 MW Th Pilot Plant. *Int. J. Greenh. Gas Control* **2017**, *65*, 149–159. [\[CrossRef\]](#)
51. Ohlemüller, P.; Alobaid, F.; Abad, A.; Adanez, J.; Ströhle, J.; Epple, B. Development and Validation of a 1D Process Model with Autothermal Operation of a 1 MW Th Chemical Looping Pilot Plant. *Int. J. Greenh. Gas Control* **2018**, *73*, 29–41. [\[CrossRef\]](#)
52. Min, Z.; Asadullah, M.; Yimsiri, P.; Zhang, S.; Wu, H.; Li, C.Z. Catalytic Reforming of Tar during Gasification. Part I. Steam Reforming of Biomass Tar Using Ilmenite as a Catalyst. *Fuel* **2011**, *90*, 1847–1854. [\[CrossRef\]](#)
53. Di Giuliano, A.; Lucantonio, S.; Gallucci, K. Devolatilization of Residual Biomasses for Chemical Looping Gasification in Fluidized Beds Made up of Oxygen-Carriers. *Energies* **2021**, *14*, 311. [\[CrossRef\]](#)
54. Kunii, D.; Levenspiel, O. *Fluidization Engineering*, 2nd ed.; Butterworth-Heinemann Series in Chemical Engineering; Butterworth-Heinemann: Boston, MA, USA, 1991.
55. Ohlemüller, P.; Alobaid, F.; Gunnarsson, A.; Ströhle, J.; Epple, B. Development of a Process Model for Coal Chemical Looping Combustion and Validation against 100 kWth Tests. *Appl. Energy* **2015**, *157*, 433–448. [\[CrossRef\]](#)
56. Grace, J.R.; Avidan, A.A.; Knowlton, T.M. (Eds.) *Circulating Fluidized Beds*, 1st ed.; Blackie Academic & Professional: London, UK; New York, NY, USA, 1997.
57. Schmid, J.C.; Pfeifer, C.; Kitzler, H.; Pröll, T.; Hofbauer, H. A New Dual Fluidized Bed Gasifier Design for Improved in Situ Conversion of Hydrocarbons. In Proceedings of the International Conference on Polygeneration Strategies (ICPS), Vienna, Austria, 30 August–1 September 2011; p. 10.
58. Kronberger, B.; Johansson, E.; Löffler, G.; Mattisson, T.; Lyngfelt, A.; Hofbauer, H. A Two-Compartment Fluidized Bed Reactor for CO<sub>2</sub> Capture by Chemical-Looping Combustion. *Chem. Eng. Technol.* **2004**, *27*, 1318–1326. [\[CrossRef\]](#)

59. Lyngfelt, A.; Leckner, B. A 1000 MWth Boiler for Chemical-Looping Combustion of Solid Fuels—Discussion of Design and Costs. *Appl. Energy* **2015**, *157*, 475–487. [[CrossRef](#)]
60. Hetzer, J.; Kulik, R.; Rothenpieler, K.; Stückrath, K.; Weidenfeller, D.J. Design, Simulation and Practical Experience of the Largest Syngas Cooler in Operation for Coal Gasification. In Proceedings of the 8th International Freiberg Conference, Cologne, Germany, 12–16 June 2016.



---

**Research Paper III**

---

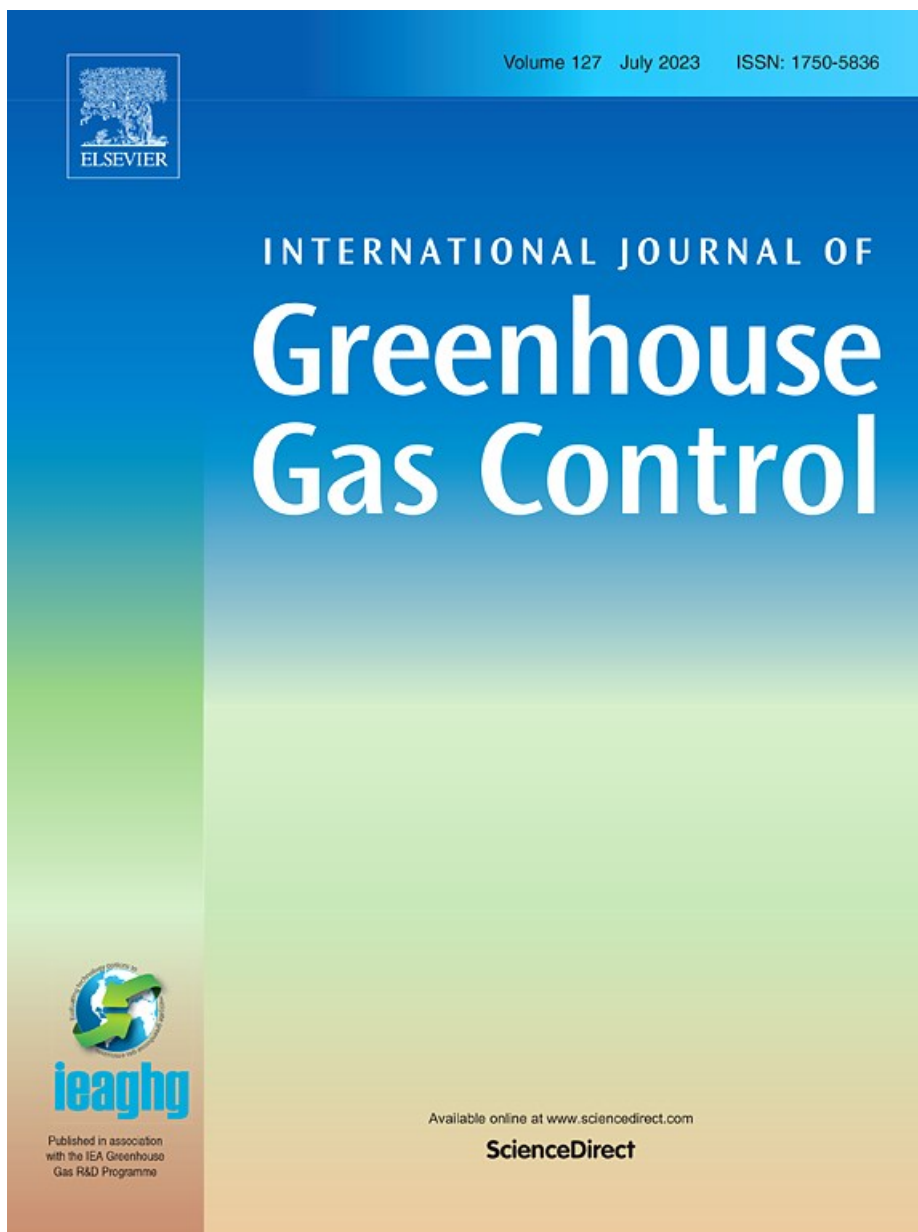
*Design and Control Concept of a 1 MW<sub>th</sub> Chemical Looping Gasifier Allowing for Efficient Autothermal Syngas Production*

Paul Dieringer, Falko Marx, Benjamin Michel, Jochen Ströhle, Bernd Epple

---

**Journal:** International Journal of Greenhouse Gas Control, Vol. 127  
**Date:** 07/2023  
**DOI:** [10.1016/j.ijggc.2023.103929](https://doi.org/10.1016/j.ijggc.2023.103929)  
**ISSN:** 1750-5836  
**Copyright:** Open Access License: CC BY 4.0

---





Contents lists available at ScienceDirect

## International Journal of Greenhouse Gas Control

journal homepage: [www.elsevier.com/locate/ijggc](http://www.elsevier.com/locate/ijggc)

## Design and control concept of a 1 MW<sub>th</sub> chemical looping gasifier allowing for efficient autothermal syngas production

Paul Dieringer<sup>\*</sup>, Falko Marx, Benjamin Michel, Jochen Ströhle, Bernd Epple

*Institute for Energy Systems and Technology, Technical University Darmstadt, Otto-Berndt-Str. 2, 64287 Darmstadt, Germany*

## ARTICLE INFO

## Keywords:

Chemical looping  
Biomass  
Gasification  
Process control  
Pilot scale  
Autothermal

## ABSTRACT

Chemical looping gasification (CLG) is a novel gasification concept, allowing for the efficient production of a high calorific, N<sub>2</sub>-free syngas with low tar content. Previous studies showed that the inherent process characteristics require a dedicated process control concept in order to allow for sufficient solid and thus heat transport between the two reactors (air and fuel reactor) of the gasification unit, while at the same time being able to accurately tailor the air-to-fuel equivalence ratio ( $\lambda$ ), thus obtaining stable gasification conditions. To demonstrate its viability, a suitable control concept was implemented in the 1 MW<sub>th</sub> modular pilot plant located at the Technical University Darmstadt. In this paper, results obtained during the first ever autothermal CLG operation, achieved in this unit using biomass pellets as the feedstock, are presented, highlighting important process fundamentals. It is demonstrated that the novel process control concept allows for an accurate control of  $\lambda$  in semi-industrial scale, while at the same time guaranteeing stable hydrodynamics and thus solid and heat transport between the air and fuel reactor, making it a suitable control concept for large-scale implementation. Moreover, it is demonstrated that the underlying phenomena of the CLG process lead to substantial system inertia, as the solid bed inventory of the gasifier acts as an oxygen storage during transient periods, evoked by changes in the air-to-fuel equivalence ratio.

## 1. Introduction

In light of the current challenges in terms of climate protection and energy transition, novel, sustainable and yet competitive processes and technologies in the energy, transport, and industry sector are urgently needed. Thus, innovative carbon-negative process chains for the production of 2<sup>nd</sup> generation biofuels are required (DIRECTIVE (EU) 2018). Here, one option under broad consideration is converting biogenic residues into a high-calorific syngas, before further treatment and fuel synthesis (Atsonios et al., 2020; Roshan Kumar et al., 2022).

Oxygen-blown gasifiers, allowing for the efficient production of a N<sub>2</sub>-free syngas, thus facilitating its direct utilization in syntheses, have been widely researched, going back to the start of the last century (Higman and van der Burgt, 2008). With recent developments encouraging routes of valorizing residues (e.g. biomass, municipal waste, etc.) chemically, research interest in this field has been revived (Heinze et al., 2023; Langner et al., 2023). Apart from their maturity, the advantages of oxygen-blown gasifiers arise from the direct utilization of molecular oxygen in the gasification chamber, thus facilitating high reaction temperatures and excellent feedstock conversion. Therefore, cold gas

efficiencies above 75% can be obtained, depending on the gasifier type and the utilized feedstock (Higman and van der Burgt, 2008).

A novel gasification technology, allowing for an efficient conversion of biomass residues into a high-calorific syngas, is the chemical looping gasification (CLG) process, illustrated in Fig. 1. Its major advantage is that the oxygen required for efficient feedstock conversion is supplied through the cyclic reduction and oxidation of an oxygen carrier (OC). Hence, CLG does not rely on a costly air separation unit, commonly required for oxygen-driven gasification processes. Moreover, despite air being used as the oxygen source in the gasification process, CLG allows for an efficient capturing of the CO<sub>2</sub> formed during the autothermal gasification step from the N<sub>2</sub>-free product gas in the downstream syngas purification unit, thus allowing for net negative CO<sub>2</sub> emissions of the biomass-to-biofuel process chain (Nguyen et al., 2021; Huang et al., Oct. 2016; Huang et al., Jan. 2014; Ge et al., 2016a; Guo et al., 2014; Huang et al., Jul. 2013).

Initial advances in the CLG were mainly restricted to lab-scale investigations. Here, the CLG technology was investigated in batch (Huang et al., Jan. 2014; Huang et al., Jul. 2013; Xu et al., Nov. 2021) as well as continuous reactor setups (Huseyin et al., 2014; Acharya et al., 2009), operated as fixed bed (Yan et al., May 2020; Liu et al., Nov. 2019)

<sup>\*</sup> Corresponding author.

E-mail address: [paul.dieringer@est.tu-darmstadt.de](mailto:paul.dieringer@est.tu-darmstadt.de) (P. Dieringer).

<https://doi.org/10.1016/j.ijggc.2023.103929>

Received 19 January 2023; Received in revised form 27 April 2023; Accepted 8 June 2023

Available online 19 June 2023

1750-5836/© 2023 The Author(s). Published by Elsevier Ltd. This is an open access article under the CC BY license (<http://creativecommons.org/licenses/by/4.0/>).

Nomenclature		Abbreviations/Acronyms	
<b>Latin Symbols</b>		AR	Air Reactor
$d$	Diameter	BP	Operating Period
$l$	length	CFB	Circulating Fluidized Bed Reactor
$LHV$	Lower heating value	CGE	Cold Gas Efficiency
$m_i$	Mass of species $i$	CLG	Chemical Looping Gasification
$\dot{m}_i$	Mass Flow of species $i$	CLC	Chemical Looping Combustion
$\dot{n}_i$	Mole Flow of species $i$	DFBG	Dual Fluidized Bed Gasification
$P$	Power	FR	Fuel Reactor
$\dot{Q}_{cool}$	Cooling Duty	LS	Loop Seal
$RR$	Recycling Ratio	MSR	Measurement and Control
$R_{OC}$	Oxygen transport capability	OC	Oxygen Carrier
$R_{Feed}$	Oxygen requirement of feedstock	TP	Transient Period
$R_{C3H8}$	Oxygen requirement of Propane		
$T$	Temperature		
$u_0$	Gas Velocity		
$\dot{V}_{Rec.}$	Volume flow of recycled AR flue gas	<b>Indices</b>	
$\dot{V}_{Air}$	Volume flow of fresh air	AR	Air Reactor
$w_i$	Mass fraction of species $i$	C	Carbon
$x_i$	Mole fraction of species $i$	eff	Effective
$X_i$	Conversion of species $i$	gas	Gas
		Feed	Feedstock
		FR	Fuel Reactor
		fine	Fine fraction
		in	Inlet
		o	Oxygen
<b>Greek Symbols</b>		OC	Oxygen Carrier
$\Delta X_s$	Difference in oxidation degree of OC	out	Outlet
$\Delta H_R$	Reaction enthalpy	ox	Oxidized
$\lambda$	Air-to-fuel equivalence ratio	red	Reduced
$\eta_{CGE}$	Cold gas efficiency	RL	Refractory Lining
$\phi_\lambda$	Ratio of effective air-to-fuel equivalence ratios for FR and AR	S	Solid
$\tau_s$	Solids residence time	tot	Total
		th	Thermal

or fluidized bed reactors (Huseyin et al., 2014; Condori et al., 2021a; Condori et al., 2021b), using oxygen carriers of different nature (Huang et al., Jan. 2014; Hildor et al., 2020; Moldenhauer et al., 2018; He et al., 2011; Zhao et al., 2015; Abdalazeez et al., 2022). Moreover, the suitability of various biomass-based feedstocks, such as rice husks (Ge et al., 2016a; Abdalazeez et al., 2022; Ge et al., 2016b), rice straw (Hu et al., Feb. 2019), sawdust (Xu et al., Nov. 2021; He et al., 2011), and wood pellets (Condori et al., 2021b; Hildor et al., 2020; Moldenhauer et al., 2018) has been established for CLG operation. In their review, Goel

et al. (2022) present a comprehensive overview over those endeavors, highlighting the most important variables affecting the efficiency of the CLG system, such as FR temperature, gasification agent, or properties of the utilized OC. More recent advances, conducted in larger pilot plants, aim towards the large-scale implementation of the CLG technology (Ge et al., 2016a; Pissot et al., 2018; Condori et al., 2022), thus tackling fundamental questions with regard to process stability, operability, and efficiency.

One aspect that has been found to be crucial for up-scaling of the CLG

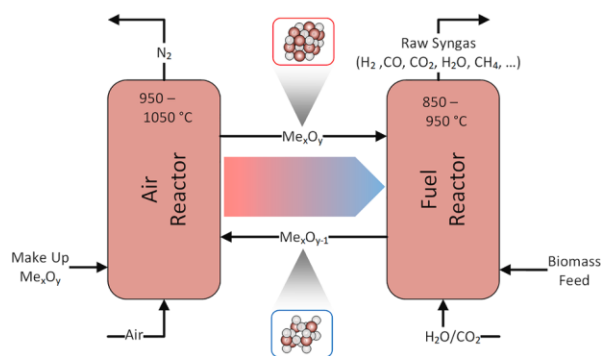


Fig. 1. Illustration of CLG process.

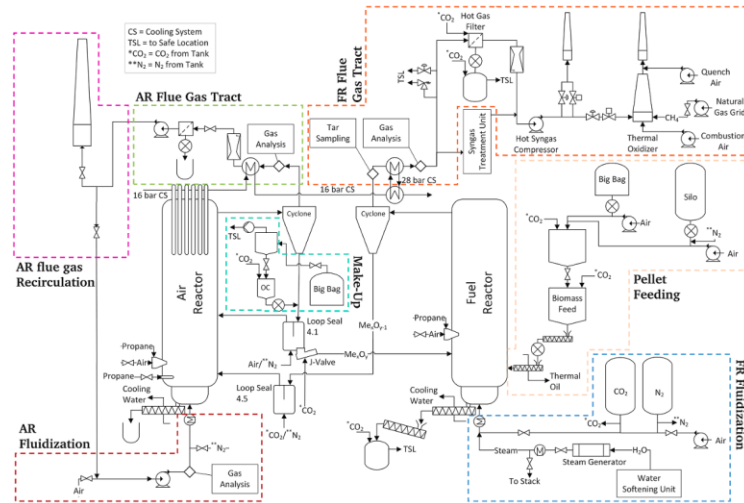


Fig. 2. Simplified process flow diagram of the 1 MW<sub>th</sub> CLG pilot plant.

technology is related to the dual-purpose of the OC material, circulating between AR and FR (Dieringer et al., 2020; Samprón et al., 2021). As it does not only transport O<sub>2</sub> from the air reactor (AR) to the fuel reactor (FR), but is also responsible for the transport of sensible heat between the two reactors (Ohlemüller et al., 2016; Pröll et al., 2010), it allows for a N<sub>2</sub>-free oxidation of the feedstock inside the FR and facilitates a stabilization of FR temperatures at the desired levels (i.e. >800 °C). In contrast to chemical looping combustion, partial oxidation of the feedstock is desired inside the FR in CLG (Huseyin et al., 2014; Ge et al., 2016b). This means that the oxygen availability in the FR has to be limited, while large heat fluxes to the FR are required, in order to maintain a stable fuel reactor temperature despite the pronounced occurrence of endothermic gasification reactions (Dieringer et al., 2020; Samprón et al., 2021). Therefore, novel process control strategies and plant designs, allowing for a de-coupling of oxygen and heat transport between the AR and FR are required in CLG (Dieringer et al., 2020; Samprón et al., 2021). In theory, a number of process control concepts are viable to achieve autothermal (i.e. without external heating) CLG operation. Yet, modeling approaches (Dieringer et al., 2020; Samprón et al., 2021) as well as initial test runs in small (Condori et al., 2021a,b) and medium-sized pilots (Condori et al., 2022) showed that restricting the air supply in the AR to reduce the overall air-to-fuel ratio to values below unity, hence obtaining gasification conditions, is the most promising approach. Therefore, the 1 MW<sub>th</sub> pilot plant located at the Technical University Darmstadt, was adapted accordingly, to allow for autothermal CLG operation in an industrially relevant environment.

The aim of this study was to demonstrate that the production of a high-grade synthesis gas is feasible via autothermal CLG, using the adapted 1 MW<sub>th</sub> pilot plant in combination with a tailored novel process control concept. The presented work comprises overarching results of the first-ever successful autothermal CLG operation, including a comprehensive set of live-data for the most important system variables, as well as characterization of OC samples collected throughout the continuous 14 days of operation. On the basis of these data-sets, a holistic acting mechanism for the CLG technology is proposed, laying the ground-work for the systemic understanding of an industrially operated chemical looping gasifier. Moreover, the presented results show that using the suggested process control strategy allows for the

production of a high-calorific syngas in semi-industrial scale, underlining the competitiveness of the CLG technology.

## 2. Experimental

### 2.1. 1 MW<sub>th</sub> pilot plant layout

The layout of the 1 MW<sub>th</sub> CLG pilot plant is described in detail elsewhere (Marx et al., 2021). Therefore, only the main features of the pilot, schematically shown in Fig. 2, are elaborated hereinafter.

The reactor system, consisting of an air reactor (0.59 m inner diameter, 8.66 m height), a fuel reactor (0.4 m inner diameter, 11.35 m height), and three coupling elements (two loop seals and a J-valve), is refractory lined to minimize heat losses, allowing for autothermal operation (i.e. without electrical heating). Both reactors are designed as circulating fluidized bed (CFB) reactors and are equipped with water-cooled ash sluicing screws for continuous or batch-wise material extraction from the bed. Moreover, each reactor can be additionally heated with propane, using a start-up burner or a bed lance. The AR has a design temperature of 1050 °C and can be fluidized with air or a mixture of air and recycled AR flue gas, which can be electrically pre-heated to temperatures up to 375 °C. For process control reasons, the inlet gas composition (O<sub>2</sub>, CO<sub>2</sub>) is measured for the AR (see Section 2.3.2).<sup>1</sup> The fuel reactor has a design temperature of 970 °C and can be fluidized with air, steam, a mixture of steam and CO<sub>2</sub>, or a mixture of air and CO<sub>2</sub>. The fluidization media can be electrically pre-heated to temperatures up to 450 °C. Each reactor is equipped with a cyclone for gas solid separation and a loop seal to prevent bypassing of gasses. Global solid circulation between the two reactors is achieved with a J-valve, connecting the loop seal (LS) of the AR (LS4.1) with the fuel reactor. The circulating mass flow between both reactors can be adjusted by changing the fluidization flow of the J-Valve, which can be fluidized with nitrogen or CO<sub>2</sub>. For the fuel reactor, all entrained material leaving the

<sup>1</sup> CO<sub>2</sub> is measured inside the AR primary air line as CO<sub>2</sub> formed inside the AR through the combustion of residual char coming from the FR can be recycled back to the primary air line when AR flue gas recirculation is initiated.

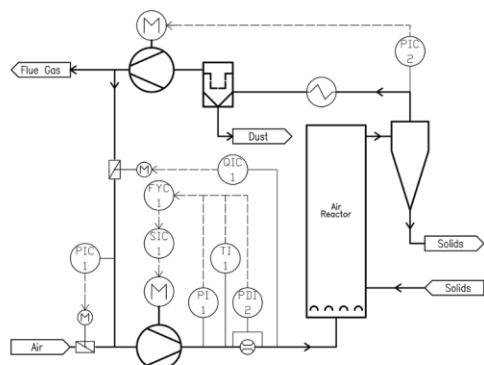


Fig. 3. Illustration of CLG control concept utilized in 1 MW<sub>th</sub> pilot plant.

riser is directly transferred into the AR via LS4.5, which is fluidized with nitrogen or CO<sub>2</sub>. On the other hand, the option of internal solid circulation via LS4.1, fluidized with nitrogen,<sup>2</sup> exists for the AR. This internal solid circulation stabilizes the hydrodynamics of the overall system. A solid fuel flow up to 250 kg/h corresponding to a thermal power of about 1.24 MW is introduced into the dense bed of the FR via an oil-cooled feeding screw. Fuel supply is either achieved from a fuel silo or via big bags through a weighted container equipped with a dosing screw, allowing for an exact control of the fuel mass flow. The fuel reactor off-gasses first pass a syngas cooler, where it is cooled to a temperature of approx. 350 °C. Subsequently, the gas composition (CO, CO<sub>2</sub>, O<sub>2</sub>, H<sub>2</sub>, CH<sub>4</sub>) is measured online. To allow for safe venting to the environment, the FR product gas is then transferred through a hot gas filter, operated at up to 250 °C, using a hot syngas compressor, before it enters a thermal oxidizer, required for full conversion of all hydrocarbon species to CO<sub>2</sub> and H<sub>2</sub>O. After online gas sampling (CO, CO<sub>2</sub>, O<sub>2</sub>, SO<sub>2</sub>, NO), the off-gasses from the AR are cooled in a heat exchanger, to a temperature <250 °C. Thereafter, the gas enters a fabric filter for dedusting. Downstream of the induced draft fan controlling the freeboard pressure of the AR (see PIC2 in Fig. 3), the AR flue gasses can be vented to the environment through a stack or can be partly recycled back to the AR airbox via the primary-air fan. In order to maintain constant reactor inventories throughout operation, the pilot is equipped with a pneumatically fed, make-up feeding system, allowing for the controlled introduction of up to 200 kg/h of the OC ilmenite into the standpipe of LS4.1.

## 2.2. Materials

### 2.2.1. OC bed material - ilmenite

Ilmenite from the Norwegian Company Titania AS, which was successfully deployed during previous chemical looping experiments in the 1 MW<sub>th</sub> pilot (Ohlemüller et al., 2016; Ströhle et al., 2015; Ohlemüller et al., 2017), was used as OC for the CLG experiments presented in this study. For the fresh material, a bulk density of 2550 kg/m<sup>3</sup>, a particle density of 4486 kg/m<sup>3</sup>, and a mean particle diameter of 111 μm ( $d_{p,10} = 31 \mu\text{m}$ ,  $d_{p,90} = 224 \mu\text{m}$ ) was determined.

### 2.2.2. Feedstock

The feedstock used for pilot testing are industrial wood pellets conforming to the Norm ENPlus A1, purchased from Eckard GmbH, Germany.

<sup>2</sup> Fluidization with air is also possible for LS4.1, however this option is neglected due to safety reasons (risk of air bypassing to FR).

Table 1

Proximate and Ultimate analysis for industrial wood pellets.

Component	wt.-% (d.a.f.)	Component	wt.-% (a.r.)
C	50.8	C-fix	13.3
H	6	Volatiles	79.6
O	43.2	Ash	0.65
N	0.07	Moisture	6.5
S	0.008		
Cl	0.006		

The pellets exhibit a cylindrical shape ( $l \sim 10\text{--}25 \text{ mm}$ ,  $d \sim 6 \text{ mm}$ ), a bulk density of 650 kg/m<sup>3</sup>, and a lower heating value of 17.96 MJ/kg. Proximate and Ultimate analysis for the pellets are given in Table 1.

## 2.3. Process control concept

### 2.3.1. Process control alternatives

Previous studies concluded that restricting the air supply in the AR, thus lowering the air-to-fuel equivalence ratio ( $\lambda$ ) of the entire process below unity, is the most auspicious approach to obtain gasification conditions in chemical looping (Dieringer et al., 2020; Samprón et al., 2021). Yet, as the air supplied in the AR is not only responsible for providing the oxygen driving the chemical looping process, but is also crucial for obtaining sufficient solid circulation between the two reactors (Dieringer et al., 2020; Samprón et al., 2021), there are three conceivable options to achieve the desired gas velocity in the AR ( $u_{0,AR}$ ) and the reduction in  $\lambda$  simultaneously:

- Designing the AR specifically for CLG operation (i.e. with a smaller inner diameter than for CLC operation) to reduce the amount of fluidization medium required.
- Recycling AR flue gasses to the AR air box and mixing it with the inlet air.
- Diluting the inlet air to the AR with an inert (e.g. N<sub>2</sub>).

The last option signifies a straight-forward as well as easy to implement and validated (Condori et al., 2021a,b, 2022) option, however leads to significant operational costs due to the constant consumption of inerts. Hence, this option should be neglected for units of substantial thermal load (>50–100 kW<sub>th</sub>). The second option leads to starkly reduced operational costs, when compared to (iii), yet comes with additional process complexity, requiring additional measurement and control (MSR) equipment for process control. Moreover, the recycled AR flue gas leads to increased compression demands for the AR primary-air fan and has to be brought to reactor temperatures, requiring additional heat. In contrast, the first approach allows for a direct process control in CLG without additional operational costs for inerts and pre-heating of recycled AR flue gas or equipment requirements, owing to its direct tailoring to the required process conditions. However, it is clear that this approach is only viable for greenfield plants, as variations in reactor dimensions are not easily attainable for existing units. Moreover, when using this approach, the plant layout does not allow for meaningful variations in  $\lambda$  (e.g. in case of significant changes in the composition of the supplied feedstock, requiring more or less heat supply in the gasifier), as  $\lambda$  and  $u_{0,AR}$  are directly coupled. Therefore, the plant flexibility is reduced.

Based on this brief evaluation, it becomes obvious that only the second option, i.e. the extension of the existing 1 MW<sub>th</sub> pilot plant with an AR flue gas recirculation line, signifies a viable option for its adaption for chemical looping gasification, allowing for meaningful parameter variations. On top of this, the suggested process control concept could

also be considered for a full-scale CLG setup, in which feedstock of varying quality, source, or nature is to be converted, necessitating operation at varying  $\lambda$  to fulfill the heat balance. The implementation of this concept is described in detail in the subsequent chapter.

### 2.3.2. Implementation of process control concept

For the independent control of two parameters, the AR gas velocity  $u_{O,AR}$  and the air-to-fuel equivalence ratio  $\lambda$ , two separate control loops are necessary. The process control concept described below, relying on three independent control loops, is illustrated in Fig. 3.

Firstly, the gas velocity in the AR is controlled indirectly via the total inlet volume flow into the AR (FY1 from FYC1). The volume flow is measured with an aperture measurement, consisting of an orifice plate, a pressure measurement (PI1), a differential pressure measurement (PDI2), and a temperature measurement (TI1) inside the primary-air line of the AR. The calculated value for the inlet volume flow is then controlled through a speed controller (SIC1), controlling the rotary speed of the primary-air fan via a frequency converter. This control loop thus allows for an independent control of  $u_{O,AR}$  via the total volume flow by the operator through either setting a fixed rotational speed for the primary-air fan or selecting the desired volume flow for the controller (FYC1). In order to control the oxygen input into the reactor and hence the air-to-fuel equivalence ratio  $\lambda$  of the CLG process, the primary-air line is equipped with an online oxygen measurement (QI1 from QIC1). To determine the oxygen input, the oxygen concentration (QI1 from QIC1) is multiplied with the volume flow entering the AR (FY1). With this knowledge, the oxygen input can then be controlled via a regulating flap in the AR flue gas recycle, which is opened automatically by a dedicated controller (QIC1) to increase the flue gas recycle, thus decreasing the air input and vice versa. Consequently, the operator can set a desired oxygen input and hence a fixed value for  $\lambda$  by either selecting the desired oxygen concentration inside the primary-air line or by manually positioning the regulating flap to a designated position. In theory, these two control loops are sufficient for the desired purpose. However, to further increase system stability, a third control loop was implemented. This control loop regulates the pressure upstream of the primary-air fan through a second gas flap located inside the air intake line. Here, the pressure controller (PIC1) opens the regulating flap to reduce the pressure and closes it to increase the pressure. By setting a fixed value for the pressure upstream of the primary-air fan, it is guaranteed that the primary-air fan runs at a constant rotational speed for a given volume flow even when the AR flue gas recirculation is adjusted to control the air-to-fuel equivalence ratio of the process.

### 2.4. Operating conditions

In March and April 2022, several periods of stable multi-hour CLG operation were obtained within a two-week test campaign, during which the 1 MW<sub>th</sub> pilot unit was continuously operated 24 h/day. In total, the pilot was operated for ~100 h in chemical looping mode during this period. To allow for meaningful comparisons and illustrations of important trends, thirty Operating periods (BP) were selected for analysis, during each of which the most important boundary conditions, summarized in Table 4 in the appendix, were kept constant. All thirty Operating periods were split into 20-minutes sub-periods, yielding a total of 177 sub-periods for subsequent analysis, which also facilitates the investigation of potential changes occurring within the individual operating points. Moreover, three transient periods (denoted as TP-1, TP-2, and TP-3) with a duration of approx. 5–8 hours, leading up to stable CLG operation, are described in detail in this paper. These transient periods are characterized by a transient sub-period induced through a targeted adaption of the AR recycling ratio by the operator, entailing a characteristic switch towards gasification conditions. The boundary conditions for these periods are given in Table 5 in the appendix.

### 2.5. Evaluation parameters

To evaluate the merit of the novel CLG control concept, several evaluation parameters are introduced. Firstly, the air-to-fuel equivalence ratio, given by the ratio between the available oxygen for solid feedstock conversion and the oxygen required for full feedstock combustion, is used to quantify the oxygen input into the gasifier system. Here, the numerator constitutes the difference of the oxygen fed to the AR,  $\dot{m}_{O,AR,in}$ , and the amount of oxygen required for combustion of the additional propane fed to the AR via the propane lance:

$$\lambda = \frac{\dot{m}_{O,AR,in} - \dot{m}_{C_{3H_8},AR} \cdot R_{C_{3H_8}}}{\dot{m}_{Feed} \cdot R_{Feed}} \quad (1)$$

In Eq. (1),  $R_{C_{3H_8}}$  (3.628 kg<sub>O</sub>/kg) and  $R_{Feed}$  (1.306 kg<sub>O</sub>/kg) signify the oxygen demand for full conversion of propane and the biomass feedstock, estimated from the elemental composition, respectively. According to this definition, (close to) full combustion of the feedstock is attained for air-to-fuel equivalence ratios larger than unity ( $\lambda > 1$ ), while gasification processes require sub-stoichiometric oxygen feeding (i.e.  $\lambda < 1$ ). However, it has to be noted that in chemical looping processes incomplete feedstock conversion is generally obtained for  $\lambda \geq 1$  (Adánez et al., 2006; Pérez-Vega et al., 2016; Ohlemüller, 2019), as the oxidation of volatiles by the OC in the FR is limited by kinetics (Fossdal et al., May 2011; Liu et al., Oct. 2013) as well as gas/solid mixing.

As for some Operating periods, not all oxygen fed to the AR is consumed in it, the effective air-to-fuel equivalence ratio, considering the difference between the input and output of elemental oxygen for the AR ( $\dot{m}_{O,AR,in}$ ,  $\dot{m}_{O,AR,out}$ ), is a useful tool to evaluate how much oxygen is taken up by the OC inside the AR (Condori et al., 2022):<sup>3</sup>

$$\lambda_{AR,eff} = \frac{\dot{m}_{O,AR,in} - \dot{m}_{O,AR,out}}{\dot{m}_{Feed} \cdot R_{Feed}} \quad (2)$$

Similarly, the effective air-to-fuel equivalence ratio in the FR can be calculated considering the input and output of elemental oxygen for the FR, thereby constituting how much oxygen is released inside the FR by the OC (Condori et al., 2022):

$$\lambda_{FR,eff} = \frac{\dot{m}_{O,FR,out} - \dot{m}_{O,FR,in}}{\dot{m}_{Feed} \cdot R_{Feed}} \quad (3)$$

Clearly, the system is in steady state if  $\lambda_{AR,eff} = \lambda_{FR,eff}$ , which means that the OC takes up and releases the same amount of oxygen in the AR and FR, respectively. Hence, the quotient of the effective air-to-fuel equivalence ratios of the AR and FR ( $\phi_\lambda$ ) can be utilized to evaluate the state of the CLG unit (Condori et al., 2022):

$$\phi_\lambda = \frac{\lambda_{FR,eff}}{\lambda_{AR,eff}} \begin{cases} < 1 & \text{Oxygen accumulation in OC} \\ = 1 & \text{System in steady state} \\ > 1 & \text{Oxygen depletion from OC} \end{cases} \quad (4)$$

As described in Section 2.3.2,  $\lambda$  is controlled through a recycling of AR flue gasses for AR fluidization. To quantify the extent of recirculation, the AR flue gas recycling ratio is introduced:

$$RR_{AR} = \frac{\dot{V}_{Rec,AR}}{\dot{V}_{Rec,AR} + \dot{V}_{Air,AR}} \quad (5)$$

Here  $RR_{AR}=0$  signifies operation with pure air, while  $RR_{AR}=1$  signifies operation with pure AR flue gas. The recirculation rate can easily be calculated by a mass balance around the primary-air line (more details, see derivation in Chapter A.1 in the appendix):

$$RR_{AR} = \frac{x_{O_2,AR,in} - 21 \text{ vol.}\%}{x_{O_2,AR,out} - 21 \text{ vol.}\%} = \frac{x_{CO_2,AR,in}}{x_{CO_2,AR,out}} \quad (6)$$

<sup>3</sup> In Eq. (1), (2) and (3), the oxygen inlet and outlet into the AR/FR are evaluated by using the respective volume flow measurements (venturi nozzles and orifice plates) and online gas analyzers (see Fig. 2).

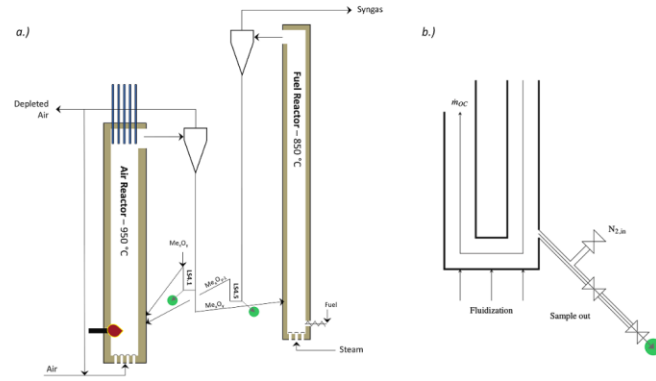


Fig. 4. a) Illustration of reactor system with indication of solid sampling points. b) Schematical detail view of solid sampling setup.

$$X_{C,AR} = \frac{\dot{m}_{gas,AR} \cdot \left( \frac{w_{CO,AR}}{M_{CO}} + \frac{w_{CO_2,AR}}{M_{CO_2}} \right) \cdot M_C - \dot{m}_{C_{3H_8,AR}} \cdot w_{C,C_{3H_8,AR}} - \frac{x_{CO_2,AR,fil}}{M_{CO_2}} \cdot (\dot{m}_{Rec,AR} + \dot{m}_{Air,AR}) \cdot M_C}{\dot{m}_{Feed} \cdot w_{C,Feed}} \quad (9)$$

In order to simplify the subsequent considerations, the cold gas efficiency (CGE),  $\eta_{CGE}$ , relating the energy content of the produced syngas at the FR outlet to the energy input through the solid feedstock (Higman and van der Burgt, 2008; De et al., 2018), is used to describe the efficiency of the gasification processes:

$$\eta_{CGE} = \frac{\dot{n}_{gas,FR,out} \cdot (x_{CH_4,FR,out} \cdot LHV_{CH_4} + x_{CO,FR,out} \cdot LHV_{CO,FR} + x_{H_2,FR,out} \cdot LHV_{H_2})}{\dot{m}_{Feed} \cdot LHV_{Feed} + \dot{m}_{C_{3H_8,AR}} \cdot LHV_{C_{3H_8}} - \dot{Q}_{cool,AR}} \quad (7)$$

Here the propane input ( $P_{th,C_{3H_8}} = \dot{m}_{C_{3H_8,AR}} \cdot LHV_{C_{3H_8}}$ ) and the cooling duty ( $\dot{Q}_{cool,AR}$ ) of the AR cooling lances<sup>4</sup> are considered, to obtain a meaningful value.

Another important parameter for the CLG unit is the amount of carbon converted in the FR, which is given by:

$$X_{C,FR} = \frac{\dot{n}_{gas,FR,out} \cdot \left( x_{CH_4,FR,out} \cdot \frac{M_C}{M_{CH_4}} + x_{CO,FR,out} \cdot \frac{M_C}{M_{CO}} + x_{CO_2,FR,out} \cdot \frac{M_C}{M_{CO_2}} \right) \cdot M_C}{\dot{m}_{Feed} \cdot w_{C,Feed}} \quad (8)$$

Char travelling to the AR together with the circulating solid is converted to CO<sub>2</sub> there. In case of  $\lambda \ll 1$ , CO can also be formed in minor amounts inside the AR, so that the carbon conversion inside the AR is given by:

<sup>4</sup> Generally, cooling in the AR is not desired during CLG operation. However, due to constructional reasons, the cooling lances of the AR in the 1 MW<sub>th</sub> unit cannot be fully extracted from the reactor and hence lead to heat extraction during operation.

The total carbon conversion inside the CLG unit is the sum of the AR and FR char conversion and should be close to 1, as the only way for carbon to “escape” the unit is in particulate form towards the FR or AR filter.

$$X_{C,tot} = X_{C,FR} + X_{C,AR} \leq 1 \quad (10)$$

## 2.6. Solid sampling and analysis

A detailed elaboration of the sampling and analysis procedure of the OC samples is presented by Marx et al. (2023). To further expand analysis, this methodology is also applied in this study. Here, solid samples were taken from the standpipe of the two loop seals during CLG operation (see Fig. 4a), using a dedicated sampling setup illustrated in Fig. 4b. In order to ensure samples representing the current process state, the sampling tube was flushed with nitrogen to remove all material in the sampling tube and replace it with fresh material. The process was observed via infra-red thermometer and was deemed successful when temperatures 300 °C on the outside were reached, signifying that “fresh”, hot material had entered the sampling line. The sample (300–700 g) was then discharged from the loop seal via ball valves into a sealed vessel where it was left for cool down for approx. two hours in order to prevent reaction with ambient air. Afterwards the sample was removed from the system.

For analysis of the carbon content, the samples were first classified into two particle fractions using a 400 μm sieve. The coarse fraction (containing the majority of the transported char) was not considered further, as due to the particle size of the raw material (see Chapter 2.2.1) it can be assumed that ilmenite particles are not present inside the coarse fraction. The fine fraction was processed in a commercially available elemental analysis system (Elementar vario MACRO cube in CHNS

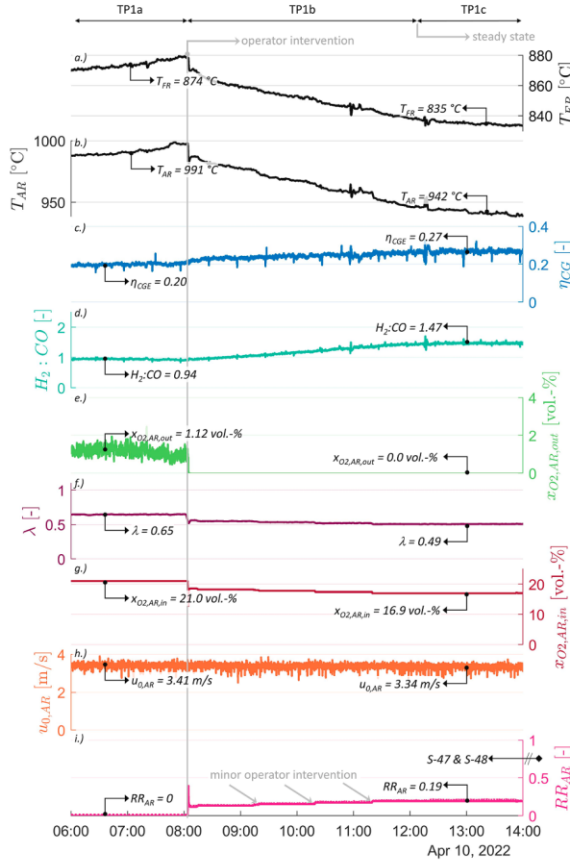


Fig. 5. Progression of important process and evaluation parameters over time for TP-1.

From top to bottom: a.) FR and b.) AR temperature, c.) cold gas efficiency ( $\eta_{CGE}$ ), d.)  $H_2/CO$ -ratio in FR product gas, e.) oxygen concentration at AR outlet ( $x_{O_2,AR,out}$ ), f.) air-to-fuel equivalence ratio ( $\lambda$ ), g.) oxygen concentration at AR inlet ( $x_{O_2,AR,in}$ ), h.) AR gas velocity, and i.) AR flue gas recycling ratio ( $RR_{AR}$ ), calculated from  $O_2$  (-) and  $CO_2$  (-) balance. Arrows with diamonds at the end signify the sampling time of a given solid sample.

setup). Each fraction was analyzed in triplicate with a sample mass of 50 mg, using a method providing oxygen according to the approximate carbon content and oxygen uptake. To determine the oxidation degree ( $X_s$ ) of the samples, their weight change in an oxidizing atmosphere was subsequently determined by oxidizing a sample mass of approx. 5 g in a laboratory oven at 900 °C with the mass being determined before ( $m_{LS,1}$ ) and after ( $m_{LS,2}$ ) oxidation.

In chemical looping, the oxidation degree of the OC is generally given by Adanez et al. (2012); Larsson et al. (2014):

$$X_{s,i} = \frac{m_{OC,i} - m_{OC,red}}{R_{OC} \cdot m_{OC,ox}} \quad (11)$$

Here,  $m_{OC,red}$  and  $m_{OC,ox}$  are the mass of an OC sample in a fully reduced and oxidized state respectively, while  $m_{OC,i}$  is the mass of the OC sample in its current state. Using the mass of loop seal samples before and after oxidation and assuming that the latter signifies a fully oxidized OC sample (i.e.  $m_{OC,ox} = m_{LS,2}$ ), one can thus calculate the oxidation degree:

$$\begin{aligned} X_{s,i} &= \frac{m_{LS,1} \cdot (1 - w_{CLS, fine}) - m_{LS,2} \cdot (1 - R_{OC})}{R_{OC} \cdot m_{LS,2}} \\ &= 1 - \frac{m_{LS,2} - m_{LS,1} \cdot (1 - w_{CLS, fine})}{R_{OC} \cdot m_{LS,2}} \end{aligned} \quad (12)$$

To arrive at Eq. (12), the following assumptions are used:

i The extent to which the OC sample can be reduced is given by the oxygen transport capacity ( $R_{OC}$ ). For the utilized ilmenite, an oxygen transport capacity of 3.7 wt.-% was determined (Condori et al., 2021b). This value falls slightly below the theoretical oxygen transport capacity for the redox couple  $Fe_2TiO_5/FeTiO_3$  (Adanez et al., 2012). With the given value of  $R_{OC}$  the samples' reduced mass can be calculated by:

$$m_{OC,red} = m_{OC,ox} \cdot (1 - R_{OC}) = m_{LS,2} \cdot (1 - R_{OC}) \quad (13)$$

ii Since the fresh loop seal sample contains small fraction of char, originating from the carbon slip occurring between AR and FR (Huseyin et al., 2014; Markström et al., 2013; Cuadrat et al., 2012), the carbon content of the LS samples has to be considered for the calculation of the oxidation degree. As the char can be assumed to be fully burned-off inside the laboratory oven, the "real" loop seal mass ( $m_{OC,i}$ ), can be calculated by:

$$m_{OC,i} = m_{LS,1} - m_{c, fine} = m_{LS,1} \cdot (1 - w_{CLS, fine}) \quad (14)$$

iii Due to the low content of ash for the raw feedstock (see Table 1), it can be assumed that the ash content inside the LS samples is negligible.



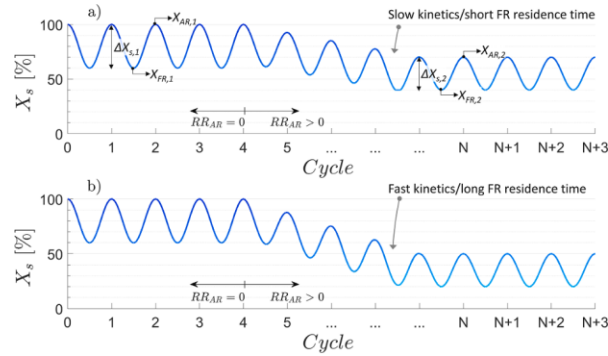


Fig. 6. Progression OC oxidation degree when increasing the air reactor recycling ratio ( $RR_{AR}$ ). The reduction extent at the FR outlet is determined by FR reaction kinetics and the FR residence time. a) Minor decrease in oxidation degree at FR outlet ( $X_{s,FR,1}$ ), b) Significant decrease in oxidation degree at FR outlet. Adapted from Dieringer et al. (2020).

### 3. Results and discussion

During application of the novel process control concept in the 1 MW<sub>th</sub> scale, it was observed that the CLG unit displays a characteristic transient system response to changes in the AR recycling ratio, giving meaningful insights into the mechanics of the CLG process. This behavior is explained on the basis of three different transient periods in Chapter 3.1. Subsequently, Chapter 3.2 illustrates how the new process control concept affects process efficiency in steady-state.

#### 3.1. Transient system response to application of novel process control concept

##### 3.1.1. System response of 1 MW<sub>th</sub> CLG unit during transient periods

The progression of the most important process parameters for the first transient period under consideration (TP-1) is illustrated in Fig. 5. It includes three distinct sub-periods on April 10th, 2022. Between 6:00 and approx. 8:00 h, the pilot plant was operated in steady state without AR flue gas recirculation (TP-1a). Thereafter, operators started AR flue gas recirculation at approx. 8:00 h, initiating the transient sub-period of the process stretching until approx. 12:00 h (TP-1b). During this sub-period, minor adaptations with regard to the AR flue gas recycling were carried out by the operator to reach the destined operating period. Between 12:00 h and 14:00 h the process reached steady state and did not show any major variations in the operating and evaluation parameters (TP-1c).

When considering Fig. 5, the interventions by the operator are best visible in the AR recycling ratio (Fig. 5i). By repositioning the flue gas recirculation flap, the recirculation rate of the process was sharply increased from 0 to 0.15 at 8:00 h.<sup>5</sup> As a consequence, the inlet oxygen concentration to the AR decreased from 21 to 16.9 vol.-% (see Fig. 5g). Due to the process control concept, described in detail in Section 2.3.2, the gas velocity  $u_{0,AR}$  was maintained at a constant value of 3.3–3.4 m/s (see Fig. 5h), leading to stable hydrodynamics for the CLG process throughout the entire transient period under consideration.<sup>6</sup> However, as the air-input into the system was reduced, while the thermal load of the gasifier was kept constant throughout the entire transient period, the air-to-fuel equivalence ratio dropped from a value of 0.65 to 0.49 (see Fig. 5f).

<sup>5</sup> Minor operator adaptations at later stages lead to an increase of this value to 0.19 over the considered period.

<sup>6</sup> Apart from  $u_{0,AR}=\text{const.}$ , this requires a constant reactor inventory, a constant gas velocity in the FR ( $u_{0,FR}$ ) and constant volume flows for both loop seals and the J-Valve, which was the case here.

The first notable observation which can be made is that due to this decrease in  $\lambda$ , the oxygen concentration at the AR outlet immediately dropped to a value of 0 vol.-% (see Fig. 5e), meaning that all oxygen is fully consumed inside the AR. This means that the inlet oxygen is fully required for the re-oxidation of the OC, the combustion of the propane input into the AR and the combustion of char coming from the FR, denoted as carbon slip (Huseyin et al., 2014; Markström et al., 2013; Cuadrat et al., 2012). As the oxygen concentration remains at 0 vol.-% after this change in recirculation rate, it can be postulated that the OC is not fully oxidized inside the AR, as the oxygen availability is reduced. Yet, the oxygen release inside the FR is not altered instantly (see below), as the boundary conditions in the FR are not altered directly. Consequently, it can be assumed that the oxidation degree of the OC ( $X_s$ ), given by the Eq. (11), is periodically decreased during each cycle, as postulated in a previous study (Dieringer et al., 2020), until new steady-state conditions are found.

To cast further light on this behavior, the theoretical progression of the oxidation degree of the oxygen carrier is illustrated in

Fig. 6. Clearly, not only the oxidation degree at the AR outlet, but also the change in oxidation degree between FR and AR ( $\Delta X_s$ , see Eq. (15)) has to decrease for the new steady-state conditions (see Fig. 6,  $\Delta X_{s,1} > \Delta X_{s,2}$ ), as the OC circulation rate between the FR and AR is kept constant, yet less oxygen is being transported from the AR to the FR, due to the decrease in air input (Samprón et al., 2021):

$$\Delta X_s = X_{s,AR} - X_{s,FR} = \frac{m_{OC,AR} - m_{OC,FR}}{R_{OC} \cdot m_{OC,ox}} \quad (15)$$

Depending on the interplay of the kinetics of the different occurring reactions and the OC residence time in the FR, determining to which extent the OC is reduced in the FR (Liu et al., Oct. 2013), the oxidation degree at the outlet of the AR and FR can either decrease slightly (see Fig. 6a) or sharply (see Fig. 6b) until steady state conditions are attained.<sup>7</sup>

The above elucidations on the ensuing shift in the oxidation degree of the OC are supported, when considering the progression of the H<sub>2</sub>/CO ratio (see Fig. 5d), and the cold gas efficiency (see Fig. 5c), over time. Clearly, the hydrogen to carbon monoxide ratio in the FR product gas increases continuously after the increase in the AR recycling ratio during sub-period TP-1b. This can be explained by the fact, that due to its more favorable reaction kinetics when compared to CO, hydrogen is preferentially oxidized on the oxygen carrier (Abad et al., 2011). As less oxygen is available from the OC with decreasing  $X_{s,AR}$ , oxidation of syngas

<sup>7</sup> For long residence times and high FR temperatures values close to zero can also be obtained for  $X_{s,FR}$  (Condori et al., Feb. 2021).

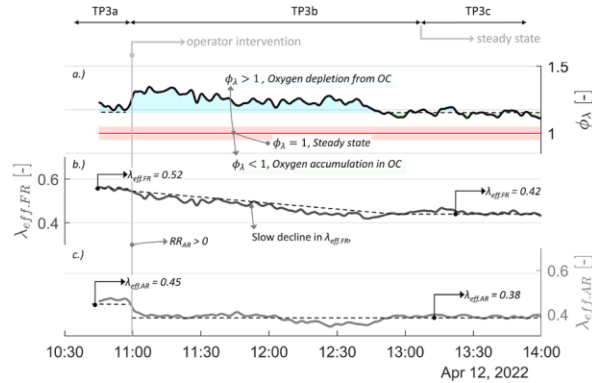


Fig. 7. Progression of effective air-to-fuel equivalence ratio of FR (b) and AR (c) and their ratio (a) over time for TP-3. The red shaded area in (c) denotes steady state conditions with  $\phi_x = 1 \pm 0.05$ .

Table 2

Oxidation degree ( $X_S$ ) in% for OC samples collected from LS4.1 and LS4.5 during the transient periods TP-1, TP-2, and TP-3. Sampling times for each sample are indicated in Fig. 5 (TP-1), Fig. 17 (TP-2), and Fig. 18 (TP-3) and are listed in Table 3 in the Appendix.

Period	TP-1		TP-2		TP-3	
Loop Seal	LS4.1	LS4.5	LS4.1	LS4.5	LS4.1	LS4.5
Sub-Period	TP-1a		TP-2b		–	–
Sample-#	S-42	S-43	S-60	S-59	–	–
$X_S$ [%]	$94.6 \pm 0.1$	$74.7 \pm 0.5$	$81.2 \pm 0.3$	$60.9 \pm 0.2$	–	–
$\Delta X_S$ [%]	$19.9 \pm 0.3$		$20.4 \pm 0.2$		–	–
Sub-Period	–		TP-2c		TP-3c	
Sample-#	–	–	S-61	S-62	S-66	S-65
$X_S$ [%]	–	–	$81.8 \pm 0.1$	$65.8 \pm 0.4$	$83.7 \pm 1.1$	$64.4 \pm 0.6$
$\Delta X_S$ [%]	–	–	$16.0 \pm 0.3$		$19.3 \pm 0.8$	

species on the oxygen carrier occurs less pronouncedly and as hydrogen was previously oxidized to greater extents, the  $H_2/CO$  ratio increases from 0.94 to 1.47.<sup>8</sup> Following the same logic, the cold gas efficiency of the process steadily increases from a value of 0.20 to 0.27, as less oxygen is released by the OC inside the FR and hence more chemical energy is maintained in the FR product gasses. Yet, in contrast to the other variables previously discussed, the change in  $H_2/CO$ -ratio and the cold gas efficiency does not occur instantly, but over a duration of approx. four hours. Firstly, this system inertia can be explained by the fact that each OC particle has to gradually reach new steady-state conditions (e.g. getting reduced from  $X_{S,FR,1}$  to  $X_{S,FR,2}$ ). Secondly, it can be explained by the fact that in order to reach steady-state conditions, the entire reactor inventory, (800–1000 kg), has to be reduced to lower oxidation degrees until equilibrium is reached. Thus, this chemical inertia of the system has to be considered, when adapting process variables affecting the air-to-fuel equivalence ratio of the process.

When considering the reactor temperatures measured during the transient period TP-1 (see Fig. 5a & Fig. 5b), it becomes visible, that all reactor temperatures decrease as soon as the AR flue gas recirculation is switched on, with average AR temperatures dropping from 991 to 942 °C, while FR temperatures decrease from 874 to 835 °C over the duration of the transient period. This can be explained by the fact, that less oxidizing reactions occur and hence reaction exothermicity decreases. Similar to the  $H_2/CO$  ratio and the cold gas efficiency, reactor temperatures require approx. four hours to reach stable values. Again, this can be explained by the fact that as the oxygen release from the OC inside the

FR is diminished during sub-period TP-1b, the total reaction exothermicity decreases. Consequently, the heat release from the CLG unit decreases and system temperatures drop along with the decrease in oxygen transport from the AR to the FR. Moreover, this finding suggests that the transient behavior of the reactor system might in part also be related to the refractory lining of the reactor system, slowly reacting to the changes occurring inside the reactor and hence cushioning a rapid drop in reactor temperatures. As reactor temperatures are also dependent on the temperature of the refractory lining, with the temperature gradient between gas phase and refractory wall determining the heat flux to the surroundings, this means that there exists a feedback loop between the reactor temperature, determined by the chemical reactions occurring inside the reactor system, and the refractory lining temperature. Therefore, larger CLG units, for which the surface-to-volume ratio is much smaller than for the 1 MW<sub>th</sub> unit, might show a more rapid system response than what has been observed here, depending on which effect is the more dominant (i.e. the slow reduction of the OC or the thermal inertia of the refractory lining). Another important finding that can be derived from the temperature profiles shown in Fig. 5a and Fig. 5b is that the temperature difference between both reactors stays constant during the entire transient period, starting at a value of 117 K and ending at a 107 K. This again shows that throughout the entire period, solid circulation was maintained constant, underlining the effectivity of the novel process control concept.

A similar behavior was observed for all parameters and variables highlighted above for the other two transient periods under consideration (TP-2 & TP-3), meaning that the observed behavior occurs in a comparable fashion, when the AR flue gas recirculation is initiated (see Chapter A.2 in the appendix). This means that although slight differences in terms of the transient switch-over times or the extent to which the evaluation parameters change are visible, the governing phenomena

<sup>8</sup> Another reason for this could be the decrease in FR temperature, going in hand with the increase in  $RR_{AR}$ , which leads to shift in the WGS equilibrium and a decrease in char conversion.

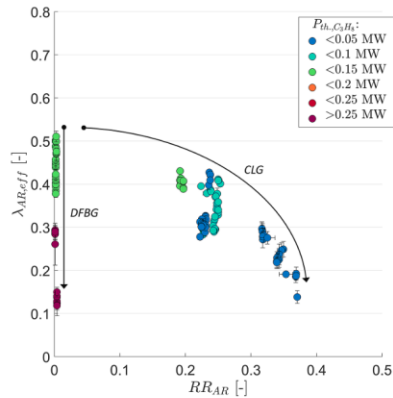


Fig. 8. Effective air-to-fuel equivalence ratio in the AR as a function of the flue gas recycling ratio in the AR for different thermal loads of propane firing for all operating periods given in Table 4.

for the observed behavior are the same.

### 3.1.2. Oxygen balancing during transient periods

As mentioned before, it is postulated that by reducing the oxygen input into the AR through initiating AR flue gas recycling, the extent to which the OC is oxidized inside the AR reduces with each cycle (see Fig. 6). If this is the case, it should also be visible in the oxygen balance of the CLG system, as the oxygen carrier should be depleted of oxygen during the transient period (i.e.  $\phi_2 > 1$ , see Eq. (4)). Fig. 7 shows that the expected behavior was observed during the transient periods, showing the effective air-to-fuel equivalence ratios as well as their quotient for the period TP-3. Fig. 7c shows that as soon as the recycling ratio is started by the operator at 11:00 on 12th April 2022, initiating the transient sub-period TP-3b, the effective air-to-fuel equivalence ratio in the AR immediately drops from a value of 0.45 to a value of 0.38. This indicates that less oxygen is taken up by the OC inside the AR instantly, due to the limitation in oxygen availability. On the other hand, the effective air-to-fuel equivalence ratio inside the FR declines slowly over the entire duration of TP-3b (see Fig. 7b). For one, this shows that the OC releases less and less oxygen inside the FR until a new steady-state is obtained, indicating that its oxygen release inside the FR is slowly restricted and the control concept yields the desired results. When considering the transient response, Fig. 7b suggests that the lowered oxygen release inside the FR results from gradual changes taking place within the OC throughout the entire transient period. Again, this points to the fact that for each cycle the OC gets more reduced and hence its oxygen release kinetics decelerate inside the FR (Abad et al., 2011; Ohlemüller et al., 2018), leading to lower oxygen release rates. The ensuing oxygen depletion of the OC is visually highlighted in blue shading in Fig. 7a, showing that  $\phi_2$  increases to an elevated level throughout the entire transient sub-period TP-3b, indicating that oxygen is “consumed” by the occurring chemical reactions within the transient period, before it drops to its initial value as soon as steady state conditions are reached in sub-period TP-3c.<sup>9</sup> Consequently, it can be

<sup>9</sup> As visible from Eq. (4) oxygen depletion occurs for  $\phi_2 > 1$ . However, in Fig. 7c the baseline for oxygen depletion is set at a value of 1.15 for which  $\phi_2$  stagnates for the steady-state conditions TP-3a and TP-3c. Although mass and component (C, H, O) balances could be closed with an accuracy of  $\pm 5\%$  for all operating points under consideration, it is believed that this upwards skew in  $\phi_2$  in Fig. 7c by 15% in the data can be accredited to measurement inaccuracy (e.g. venturi/aperture flow measurements, moisture measurement).

summarized that the OC inventory of the CLG unit serves as an oxygen storage, slowly releasing oxygen until a new steady state is reached, thereby playing an important role in the transient system response.

### 3.1.3. Behavior of the oxygen carrier inventory during transient periods

To further cast light onto the system’s behavior during the transient periods, analyses of solid samples at the AR and FR outlet can be considered, in order to enhance process understanding. One important question is which oxidation degree is reached at the FR and AR outlet in steady state. Moreover, it remains open whether each particle requires multiple cycles to reach this steady state, or if the length of the transient period is primarily dominated by the size of the reactor inventory (i.e. individual particles reach steady state conditions within  $< 1-2$  cycles, yet multiple hours are required for a unit of the considered size until all particles have been cycled through the system). To cast light onto this, the oxidation degree of samples taken from both loop seals at different stages of the transient period TP-1, TP-2, and TP-3 are listed in Table 2. As expected, the higher oxidation degrees ( $X_s$ ) are obtained for LS4.1 prior to the onset of AR flue gas recirculation (e.g. TP-1a: S-42:  $X_s = 94.6$

$\pm 0.1\%$  vs. TP-3c S-66:  $X_s = 83.7 \pm 1.1$ ) which can again be explained by the fact that while close to full oxidation of the OC is achieved in the AR when sufficient amounts of oxygen are supplied (i.e.  $RR_{AR}=0$ ), only partial oxidation of the OC is attained in an oxygen deficient AR atmosphere. Consequently, as illustrated in Fig. 6, AR flue gas recirculation leads to a general drop in  $X_s$  for the entire CLG system (i.e. for AR & FR). While this observation supports the general mechanics of the process control concept, it does not directly explain how its application leads to a higher CLG process efficiency (i.e. higher CGEs). As stated before, cold gas efficiencies correlate with the amount of oxygen released inside the FR, leading to more or less complete feedstock conversion. The oxygen released in the FR is the one transported to it via the OC from the AR given by:

$$\dot{m}_{O,AR \rightarrow FR} = \dot{m}_{OC} \cdot R_{OC} \cdot \Delta X_s \quad (16)$$

Hence, for a constant global solid circulation ( $\dot{m}_{OC}$ ), which can be assumed here as the hydrodynamic boundary conditions were not altered within each transient period, the change in the oxidation degree between AR and FR ( $\Delta X_s$ ) should decrease when  $RR_{AR}$  is increased. Again, this is corroborated by the data listed in Table 2 (e.g. TP-2b: S-59/60:  $\Delta X_s = 20.4 \pm 0.2\%$  vs. TP-2c S-61/62:  $\Delta X_s = 16.0 \pm 0.3\%$ ). The observed decrease in  $\Delta X_s$  thus means due to its incomplete oxidation in the AR, the OC is less “keen” to release oxygen inside the FR, leading to a lower overall oxygen transport to the FR and hence higher cold gas efficiencies. This observation is also supported by kinetic studies performed with ilmenite, showing that OC reaction kinetics generally decrease with decreasing oxidation degree (Abad et al., 2011; Ohlemüller et al., 2018). In summary, the mechanics of the suggested process control concept can thus also be verified on the basis of solid samples collected from both loop seals during operation. Here, it can be observed that while the restriction of oxygen supply in the AR leads to a direct drop in  $X_s$ , this drop then leads to a subsequent decrease in  $\Delta X_s$  and hence oxygen transport due to kinetic reasons. Moreover, it can be seen that all values obtained for oxidation degrees of the solid samples from LS4.5 listed in Table 2 are larger than 50%. Therefore, it can be postulated that the oxygen release inside the FR is restricted kinetically, preventing a full reduction ( $X_s=0\%$ , i.e. bulk of particle in  $FeTiO_3$  phase) of the OC inside the FR. In a 1.5 kWth unit, exhibiting a dissimilar layout to the 1 MW<sub>th</sub> unit (i.e. FR in bubbling regime), allowing for distinctly larger solid residence times inside the FR, oxidation degrees  $0\% < X_s, FR < 20\%$  were determined for  $\lambda < 0.3$  at temperatures between 820 and 940 °C (Condori et al., 2021b). This shows that in case of more favorable kinetics (higher FR temperatures) (Abad et al., 2011; Ohlemüller et al., 2018) and longer residence times (Liu et al., Oct. 2013), the OC is reduced to lower oxidation degrees inside the FR. Yet, even at these conditions, full reduction is not attained due to kinetic reasons. In case

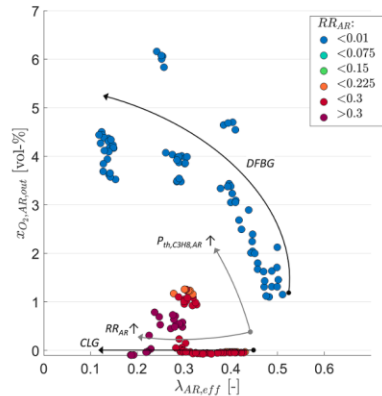


Fig. 9. Outlet AR O<sub>2</sub> concentration as a function of the effective air-to-fuel equivalence ratio in the AR as a function of the flue gas recycling ratio in the AR for different oxygen concentrations at AR outlet for all operating periods given in Table 4. Gray arrows denote the progression of x<sub>O<sub>2</sub>,AR,out</sub> with increasing RR<sub>AR</sub> (CLG) and P<sub>th,C3H8,AR</sub> (DFBG), respectively.

this kinetic barrier is overcome (e.g. through higher FR temperatures) and the oxygen release inside the FR is restricted due to thermodynamic reasons (i.e. X<sub>s,FR</sub>=0), the time required to reach steady state conditions after changes in RR<sub>AR</sub> would decrease, as steady state conditions are reached inside the FR as soon as X<sub>s,FR</sub>=0 is attained. Nonetheless, the system would still require a certain stabilization time for the entire OC inventory to reach its fully reduced state.

3.2. Steady-state system response to application of novel process control concept

While the investigation of the transient system response of the CLG unit to changes in the air supply provides insights into the underlying phenomena, comparisons of steady-state operating periods with different boundary conditions allow for a holistic analysis of the merit of the process control concept to optimize CLG process efficiency. During the 60 h of steady-state chemical looping operation investigated within this work, the process control concept was successfully applied for a total duration of ~35 h. Results of these endeavors are summarized in Fig. 8, showing the dependency of the AR recycling ratio and the effective air-to-fuel equivalence ratio in the AR. Here, two regions can clearly be observed. On the y-axis of Fig. 8, 78 operating sub-periods, for which flue gas recirculation in the AR were switched off, are visible. For the remaining 99 operating sub-periods, AR recycling ratios larger than zero were employed. Before AR flue gas recirculation was initiated (RR<sub>AR</sub>=0), the pilot was operated with propane firing at different thermal loads in the AR for given operating periods. While propane injection was used to counter the high relative heat losses of the 1 MW<sub>th</sub> pilot (10–15% of thermal input) for selected operating periods, (gaseous) fuel injection is commonly applied in DFBG applications as a mean of temperature control in both reactors (Ripfel-Nitsche et al., 2007; Bolhar-Nordenkamp et al., 2002; Bolhar-Nordenkamp et al., 2003), meaning that the deeper investigation of this measure on CLG efficiency provides further important insights.

3.2.1. Effect of process control concept on oxygen transport from AR to FR

Evaluation of all 177 operating sub-periods showed that for the given plant layout two options to control the oxygen transport to the FR exist. For the sub-periods, located on the y-axis of Fig. 8 (i.e. RR<sub>AR</sub>=0), a clear dependency between λ<sub>AR,eff</sub> and the propane input is visible. This indicates that in the case of significant propane injection in the AR, oxygen

uptake by the OC is impaired leading to lower values of λ<sub>AR,eff</sub>. Since oxygen concentrations larger than 1 vol.-% were measured at the outlet of the AR for all operating periods with RR<sub>AR</sub>=0 (see Fig. 9), the drop in the effective air-to-fuel equivalence ratio in the AR cannot be associated to thermodynamic constraints (i.e. enough oxygen for full-reoxidation of the OC was available inside the AR for all operating periods with RR<sub>AR</sub>=0). This suggests that the injection of propane into the dense bed of the AR impairs the oxygen uptake of the OC kinetically (e.g. by leading to a reducing atmosphere in the dense bed, where gas-solid contacting is high), which is also supported by the fact that for RR<sub>AR</sub>=0, the outlet AR O<sub>2</sub> concentration increases with decreasing λ<sub>AR,eff</sub>. Regardless of the mechanism, this means that through propane injection, the OC behaves more and more as an “inert” inside the FR, as the OC enters the FR in a more reduced state, thus impairing reaction kinetics inside the FR. Ultimately, the control concept enforced by propane injection can thus be seen as a form of dual-fluidized bed

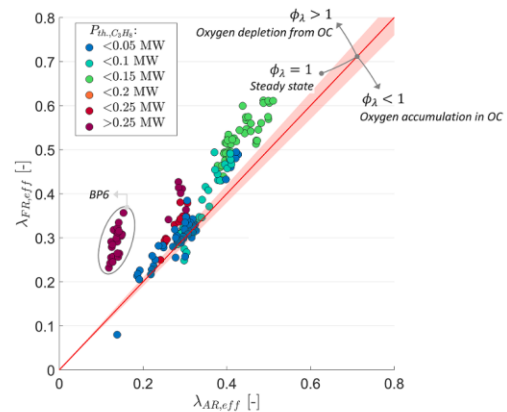


Fig. 10. Effective air-to-fuel equivalence ratio in FR as a function of air-to-fuel equivalence ratio in AR for varying propane loads for all operating periods given in Table 4. The red shaded area indicates a deviation of 5% from the angle bisector.

Table 3  
Oxidation degree (X<sub>s</sub>) in% for all OC samples collected from LS4.1 and LS4.5 during operation.

Sample-#	Location	X <sub>s</sub> [%]	ΔX <sub>s</sub> [%]	Sampling Time
CLA1-S-10	LS4.1	104.4 ± 1.2	–	15:38 02.04.2022
CLA1-S-13	LS4.1	15.2 ± 0.6	–	05:30 03.04.2022
CLA1-S-42	LS4.1	94.6 ± 0.1	19.9 ± 0.3	03:30 10.04.2022
CLA1-S-43	LS4.5	74.7 ± 0.5	–	–
CLA1-S-49	LS4.1	86.7 ± 0.0	–	15:30 10.04.2022
CLA1-S-59	LS4.5	60.9 ± 0.2	20.4 ± 0.2	21:30 11.04.2022
CLA1-S-60	LS4.1	81.2 ± 0.3	–	–
CLA1-S-61	LS4.1	81.8 ± 0.1	16.0 ± 0.3	03:20 12.04.2022
CLA1-S-62	LS4.5	65.8 ± 0.4	–	–
CLA1-S-65	LS4.5	64.4 ± 0.6	19.3 ± 0.8	14:30 12.04.2022
CLA1-S-66	LS4.1	83.7 ± 1.1	–	–
CLA1-S-69	LS4.5	75.4 ± 0.9	14.9 ± 0.8	17:05 13.04.2022
CLA1-S-70	LS4.1	90.3 ± 0.8	–	–
CLA1-S-73	LS4.5	73.8 ± 0.9	17.3 ± 0.4	20:30 13.04.2022
CLA1-S-74	LS4.1	91.1 ± 0.0	–	–
CLA1-S-75	LS4.1	93.5 ± 0.1	14.8 ± 0.1	20:30 13.04.2022
CLA1-S-76	LS4.5	78.7 ± 0.1	–	–
CLA1-S-78	LS4.1	90.5 ± 0.2	13.7 ± 0.4	11:15 14.04.2022
CLA1-S-79	LS4.5	76.8 ± 0.7	–	–
CLA1-S-84	LS4.5	77.1 ± 0.5	13.1 ± 0.4	11:15 14.04.2022
CLA1-S-85	LS4.1	90.2 ± 0.4	–	–
CLA1-S-86	LS4.5	76.7 ± 0.1	10.3 ± 0.2	18:10 14.04.2022
CLA1-S-87	LS4.1	87.0 ± 0.2	–	–

gasification (DFBG), for which fuel introduction in the AR is used to drive up AR temperatures and thus obtain a driving force for the chemical reactions in the FR and an inert bed material is used to transport the reaction heat between the two reactors (Ripfel-Nitsche et al., 2007; Bolhar-Nordenkampf et al., 2002; Bolh ar-Nordenkampf et al., 2003).

On the other hand, the desired effect on  $\lambda_{AR,eff}$  is obtained by using the suggested process control concept, manipulating the AR recycling ratio at low propane input. For the given operating periods this translates into a drop of  $\lambda_{AR,eff}$  from  $\sim 0.5$  to  $\sim 0.2$  as the AR recycling ratio is increased from 0 to 0.38. As elucidated in detail in Chapter 3.1, this can be explained by the fact that the oxygen uptake by the OC in the AR is diminished as the oxygen availability in the AR decreases. This lack in oxygen availability in the AR for  $RR_{AR} > 0$  is also seen in Fig. 9, as outlet  $O_2$  concentrations  $< 2$  vol-% (generally  $< 1$  vol-%) were measured for the AR, when the AR flue gas recirculation was switched-on ( $RR_{AR} > 0.1$ ).

Efficient CLG operation is only obtained if the decrease in  $\lambda_{AR,eff}$  with increasing  $RR_{AR}$ , also translates into a drop in the effective air-to-fuel equivalence ratio inside the FR. This is the case as  $\lambda_{FR,eff}$  primarily governs the CLG process efficiency, by determining how much oxygen is released inside the FR, leading to a given degree of feedstock oxidation. To determine the correlation between the two effective air-to-fuel equivalence ratios,  $\lambda_{FR,eff}$  and  $\lambda_{AR,eff}$  are shown in Fig. 10 for all 177 operating sub-periods under investigation. It becomes clear that in case of low amounts of propane firing, all values fall onto or close to the angle bisector, signifying  $\phi_i = 1$ .<sup>10</sup> Thus, the CLG unit is in steady state for those operating conditions, and oxygen release in the FR is equal to the oxygen uptake in the AR, meaning that given sufficient stabilization times (see Chapter 3.1), a decrease in  $\lambda_{AR,eff}$  also translates into an equivalent decrease in  $\lambda_{FR,eff}$ . However, as soon as propane loads exceed 150 kW, a clear upwards deviation from the angle bisector is visible, signifying that more oxygen is released in the FR than is taken up in the AR. This again underlines the previous hypothesis (see above), that in case of strong propane firing, oxygen uptake in the AR might be the rate-limiting step. This means when operating the CLG unit for long times with propane firing, the entire OC inventory slowly becomes more and more reduced until a new steady state is reached.<sup>11</sup> A finding supporting this hypothesis is that a solid sample taken from LS4.1 towards the end of BP6 (highlighted in Fig. 10) showed a strong degree of reduction (S-13:  $X_{s,AR} = 15.2\%$ , see Table 3 in the Appendix), when its oxidation degree was determined. Therefore, co-firing of propane or any other feedstock in the AR has to be considered undesired for CLG operation as it prevents meaningful oxygen transport from the AR to the FR. On the other hand, when striving for DFBG operation (i.e. no/limited oxygen transport) it yields the option to obtain a strongly reduced OC entering the FR, releasing low amounts of oxygen and potentially catalyzing certain chemical reactions (e.g. tar or methane reforming) (Zhou et al., 2022; Min et al., 2011). However, this approach is not considered further here, as efficient CLG operation, signified by meaningful oxygen transport between AR and FR, is targeted.

### 3.2.2. Acting mechanism of novel process control concept

Further insights into the underlying phenomena of the novel process control concept can be obtained when considering the oxidation degree of solid samples collected during different operating periods. As elaborated in Chapter 3.1, the pursued measure to obtain a more deeply reduced OC entering the FR is the restriction of air supply in the AR.

<sup>10</sup> As explained above (see Chapter 3.1.2), measurement inaccuracy leads to minor deviations from  $\phi_i = 1$  for some operating points, although mass and component (C, H, O) balances could be closed with an accuracy of  $\pm 5\%$  for all operating points.

<sup>11</sup> Within the entire duration of BP6 ( $> 7$  h), steady-state conditions were not reached, meaning that the OC was further reduced throughout the entire duration.

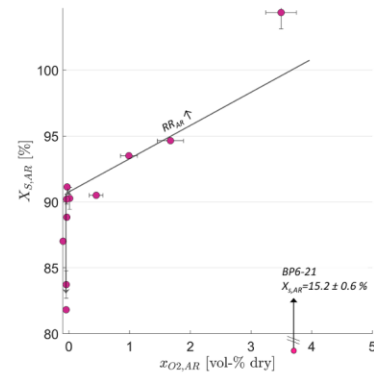


Fig. 11. Oxidation degree of samples collected from LS4.1 as a function of the oxygen content at the AR outlet (for sampling times for the respective samples please refer to Table 3). Gray arrows denote the progression of  $X_{s,AR}$  as  $RR_{AR}$  is increased.

Fig. 11, showing the dependency of the oxidation degree of samples collected from LS4.1 with the oxygen content at the AR outlet, displays a clear correlation between the two parameters. In case of oxygen excess ( $x_{O_2,AR} > 3$  vol-%), full oxidation of the OC is achieved in the AR (for low amounts of propane firing). Yet, with decreasing oxygen content at the AR outlet,  $X_{s,AR}$  drops to a value of approx. 90% at  $x_{O_2,AR} = 0$  vol-%, indicating that OC oxidation kinetics play a crucial role inside the AR at low oxygen concentrations. When further decreasing the oxygen input at  $x_{O_2,AR} = 0$  vol-% through increasing  $RR_{AR}$ , the oxidation degree of the OC further decreases, as its oxidation is hindered through thermodynamic constraints. Consequently, the application of flue gas recirculation for the AR is an efficient measure to prevent full OC oxidation in the AR. As mentioned before, another approach to achieve this is the injection of significant amounts of propane into the AR, as practiced during BP6. Fig. 15 shows that as an effect of continuous propane-induced oxygen depletion of the OC during BP6 (see also Fig. 10), the OC sample collected from LS4.1 towards the end of BP6 exhibited a close to fully reduced state. Therefore, the solid sample corroborates the previous hypothesis that propane injection hinders oxygen uptake inside the AR. Moreover, it can be postulated that the OC was further reduced with each redox cycle, as more oxygen was released inside the FR than taken up inside the AR during BP6 (see Fig. 10), requiring a given time until the entire OC inventory was reduced to  $X_{s,AR} < 20\%$ . This would also explain why the 21 sub-periods of BP6 fall onto a line rather than an individual point in Fig. 10 and Fig. 15 (see Chapter 3.2.3) as the OC was continuously reduced further throughout the entire length of BP6 ( $> 7$  h). This finding makes another strong point for using the suggested process control strategy, relying on AR flue gas recirculation, to control the degree of oxidation of the OC at the AR outlet, as opposed to propane injection - while rapid and tailored adjustments of the system are attainable for the former, extensive stabilization times are necessary for the latter.

Ultimately, the decrease in  $X_{s,AR}$  obtained for either approach only yields the desired result (i.e. an increase in the CGE), if oxygen release in the FR is reduced. As explained before, this means that the change in oxidation degree between AR and FR and thus the effective air-to-fuel equivalence ratio have to be reduced for a given solid circulation rate (see Eq. (16)). It is known that as  $X_{s,AR}$  is reduced (e.g. through oxygen restriction in the AR), the propensity of the OC to release oxygen inside the FR is reduced (Abad et al., 2011; Ohlem uller et al., 2018). The ensuing slower reaction kinetics, thus ultimately lead to an increase in the CGE, as the feedstock is oxidized to lesser extents inside the FR. This

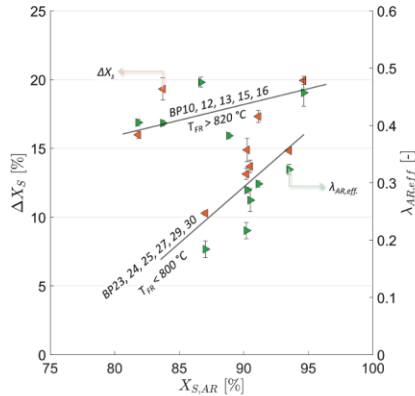


Fig. 12. Change in oxidation degree between AR and FR determined for samples collected from LS4.1 & LS4.5 and efficient AR air-to-fuel equivalence ratio as a function of AR oxidation degree (for sampling times for the respective solid samples refer to Table 3).

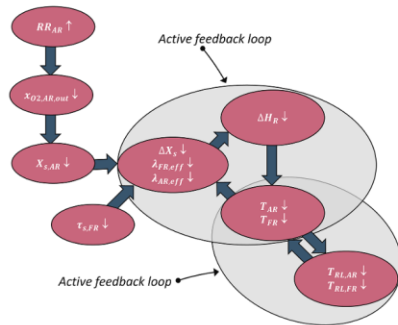


Fig. 13. Schematic illustration of the suggested mechanism of action of the CLG process control concept - Effect of an increase in the AR recycling ratio ( $RR_{AR} \uparrow$ ) on important process variables.

correlation is illustrated in Fig. 12, showing a distinct impact of  $X_{s,AR}$  on  $\Delta X_s$  and  $\lambda_{AR,eff}$ . However, it becomes visible, that the oxidation degree at the AR outlet is not the only variable affecting the oxygen release inside the FR. For BP10, 12, 13, 15, and 16 for which FR temperatures fell into the range of 820–890 °C, significantly higher values were obtained for  $\Delta X_s$  and  $\lambda_{AR,eff}$  for a given value of  $X_{s,AR}$  than for BP23, 24, 25, 27, 29, and 30, for which FR temperatures were below 800 °C. This can be related to the fact, that apart from  $X_s$ , the FR temperature is another crucial parameter affecting OC reaction kinetics (Abad et al., 2011; Ohlemüller et al., 2018). Consequently, one has to consider this active feedback loop between  $X_{s,AR}$ ,  $\Delta X_s$ , and  $T_{FR}$ , when attempting to explain the behavior of the CLG unit during the transient switch-over periods.

To further understand this, the entire mechanism of action proposed for the CLG process control concept, which is illustrated in Fig. 13, has to be considered. As explained above, the oxygen release inside the FR is kinetically limited for the 1 MW<sub>th</sub> unit, and is thus dependent on the oxidation degree of the OC entering the FR ( $X_{s,AR}$ ), FR temperatures, and the solids residence time inside the FR ( $\tau_{s,FR}$ ). Subsequent to the increase in  $RR_{AR}$ , entailing a decrease in the oxygen content in the AR,  $X_{s,AR}$  decreases. This parameter being one factor impacting OC kinetics, thus

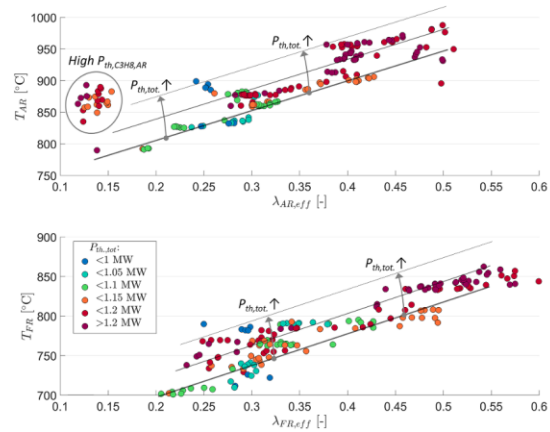


Fig. 14. AR (top) and FR (bottom) reactor temperatures as a function of the effective air-to-fuel equivalence ratio for different thermal loads for all operating periods given in Table 4. Gray markup to guide the eye: Straight lines mark the effect of  $\lambda_{eff}$  on reactor temperatures, whereas arrows mark the effect of increasing total thermal loads.

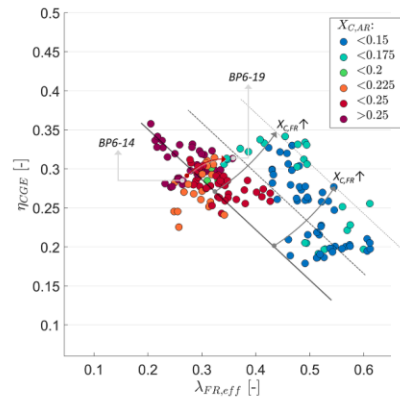


Fig. 15. Cold gas efficiency as a function of the effective air-to-fuel equivalence ratio in the FR for varying AR carbon conversions for all operating periods given in Table 4. Gray markup to guide the eye: Straight lines mark the effect of  $\lambda_{FR,eff}$  on the cold gas efficiency, whereas arrows mark the effect of increasing  $X_{c,FR}$  (=decreasing  $X_{c,AR}$ ).

leads to a drop in the oxygen release in the FR (i.e.  $\Delta X_s$ ,  $\lambda_{FR,eff}$  and  $\lambda_{AR,eff}$  decrease<sup>12</sup>). Due to this, the enthalpy of reaction (i.e.  $\Delta H_r$ ) of the entire system decreases, as exothermic oxidation reactions occur to lesser extents inside the FR and AR. As a result of this, reactor temperatures decrease (see Fig. 5 in Chapter 3.1.1 and Fig. 14 in Chapter 3.2.3), which again leads to slower OC reaction kinetics and thus a decrease in oxygen release inside the FR. The time required for this active feedback loop between OC reaction kinetics, reactor enthalpies, and reactor temperatures to stabilize, can be named as another factor playing into the

<sup>12</sup> Fig. 12 and Fig. 19 (see appendix) show a close correlation between  $\Delta X_s$  and  $\lambda_{AR,eff}$ , demonstrating that the decrease in oxygen release in the FR and uptake in the AR ( $\lambda_{FR,eff}$  and  $\lambda_{AR,eff}$ ), which can be derived from the FR and AR product gas composition, is also clearly visible in the solids composition ( $\Delta X_s$ ).

transient behavior of the CLG unit after changes of  $RR_{AR}$ . Clearly, the duration required for this feedback loop to stabilize depends on several factors, such as the size of the reactor inventory (i.e. total OC mass), the interplay of gas-phase and refractory temperatures ( $T_{RL}$ ),<sup>13</sup> as well as the extent to which the oxygen availability inside the AR is reduced, explaining why the duration required to reach steady state varied for TP-1, TP-2, and TP-3 (2–4 h).

On the one hand, the inclusion of data collected from the solid samples thus corroborate all fundamental hypotheses derived from on-line data, such as the fact that changes in the oxidation degree of the OC, induced through reduced oxygen availability in the AR, are responsible for the increased CGE of the CLG unit. On the other hand, the combined analysis of online and offline data collected for different steady state CLG operating periods allowed for deeper insights into the mechanisms occurring inside the CLG unit, further promoting the understanding of the novel gasification technology.

### 3.2.3. Effect of novel process control concept on CLG process efficiency

After presenting the acting mechanism of the novel process control concept, the question is how it affects the overall efficiency of the process. When evaluating CLG efficiency in the 1 MW<sub>th</sub> scale, it has to be kept in mind that in contrast to other units, a free variation of individual parameters is not possible, due to the entanglement of hydrodynamics, product and educt compositions, reaction kinetics, temperatures, etc. One important example for this is given in Fig. 14. Here, it becomes obvious that in chemical looping mode the effective air-to-fuel equivalence ratios primarily determine reactor temperatures.<sup>14</sup> This can be related to the fact that depending on the oxygen release (FR) and uptake (AR), the exothermicity of the chemical reactions vary, leading to changes in reactor temperatures, which was already observed in Chapter 3.1. As it is known that changes in FR temperatures affect the CLG efficiency (Condori et al., 2021a,b, 2022), this means that altering  $\lambda_{FR,eff}$  impacts CLG efficiency directly (i.e. through reduced oxygen release) as well as indirectly (i.e. via decreasing FR temperatures). Another effect visible in Fig. 14 is that higher reactor temperatures are generally attainable for given air-to-fuel equivalence ratios by increasing the total thermal input. Again this observation can be explained by considering the heat balance of the system, as for higher thermal loads, the relative impact of heat losses from the reactor walls as well as the cooling effect of the cooling lances decreases and hence higher reactor temperatures can be sustained.

These observations ultimately underline an inherent trade-off also faced in full-scale units: Although higher reactor temperatures are generally preferable (esp. for reaction kinetics), they also mean that higher air-to-fuel equivalence ratios are required, lowering key performance indicators such as the cold gas efficiency of the process. Therefore, there exists a “sweet spot” for which reactor temperatures are sufficiently high to drive the underlying chemical reactions, yet air-to-fuel equivalence ratios are low enough to obtain meaningful CGEs (see below). However, when extrapolating these results to a full-scale gasifier, the following peculiarities of the 1 MW<sub>th</sub> pilot have to be factored-in:

- i Because of the high surface-to-volume ratio of the pilot plant, heat losses amount to approx. 10–15% of the thermal input, reducing the amount of energy available for the chemical reactions.

<sup>13</sup> As elaborated in Chapter 3.1, the interplay between reactor gas phase temperatures and refractory lining temperatures decelerates rapid temperature drops/increases, esp. for reactors with a high surface-to-volume ratio.

<sup>14</sup> In an autothermal setup reactor temperatures are dependent on the entire set of boundary conditions (see also Fig. 13). Apart from the efficient air-to-fuel equivalence ratio and the thermal load highlighted in Fig. 14, this includes solid circulation, the amount of gas used for fluidization, and heat losses, amongst others (Dieringer et al., Jun. 2020).

- ii Due to the setup of the reactor system, the cooling lances in the AR cannot be fully removed from the pilot plant and hence continuously extract heat from the reactor system. For the given operating periods, heat extraction via those cooling lances amounts to 7–11% of the thermal input, further reducing the energy available for chemical reactions.<sup>15</sup>
- iii Due to i. and ii., reactor temperatures in the 1 MW<sub>th</sub> unit are lower than in an industrial setup for a given set of boundary conditions. Hence, reaction kinetics are slower, leading to lower feedstock conversions inside the FR and ultimately to lower overall efficiencies.
- iv The calculation of the cold gas efficiency (see Eq. (7)) neglects all hydrocarbons except for methane (i.e.  $C \geq 2$ ). This means the energy contained in these species is not represented in the cold gas efficiency.

Therefore, when operating an industry-scale chemical looping gasifier autothermally and when considering the full heating value of the FR product gas, process simulations show that cold gas efficiencies well above 60% can be expected at FR temperatures above 850 °C and air-to-fuel equivalence ratios around 0.3 (Dieringer et al., 2020; Samprón et al., 2021). Due to the peculiarities of the 1 MW<sub>th</sub> unit, values for the CGE obtained here fall short of this value. Nonetheless, the analysis of the impact of important process variables on the cold gas efficiency in the 1 MW<sub>th</sub> unit yields unique insights, regardless of the absolute value obtained, due to the industry-like setup of the CLG system.

Previous studies found that for externally heated CLG units, the most important variable affecting the CGE is the efficient FR air-to-fuel equivalence ratio (Condori et al., 2021a; Condori et al., 2022). The dependency for those two parameters obtained for the 1 MW<sub>th</sub> pilot plant is shown in Fig. 15. As expected, the cold gas efficiency increases with decreasing  $\lambda_{FR,eff}$  as less oxygen is released in the FR, leading to an increase in the heating value of the FR product gasses, supporting the findings made in Chapter 3.1. For the operating periods under investigation, the cold gas efficiency increases from 20% to above 35% when decreasing  $\lambda_{FR,eff}$  from 0.4 to 0.2 by using AR flue gas recirculation.

A second trend visible in Fig. 15 is that  $\eta_{CGE}$  increases with decreasing carbon conversion in the AR. This means that as the feedstock is converted to a greater degree inside the FR ( $X_{C,AR}$  &  $X_{C,FR}$ , see Eq. (10)), more gas or gas with a higher heating value is obtained from the FR. Strategies to increase char conversion inside the FR are for example increased FR temperatures [(Cetin et al., 2005; Barrio and Hustad, 2001; Barrio et al., 2001; Keller et al., 2011; DIRECTIVE (EU) 1997; Ollero et al., 2003)], an increase in residence times of all solids in the FR (e.g. higher reactor inventories or alternative FR layout) (Condori et al., 2022; Pérez-Vega et al., 2016), or an exclusive increase in char residence times in the FR, e.g. via intermediate char separation and reintroduction in a so-called carbon stripper (Pérez-Vega et al., 2016; Abad et al., 2013; Abad et al., 2015). Yet, for a given reactor layout, optimizing char conversion inside the FR without jeopardizing the cold gas efficiency is not easily done, due to the system’s entanglement. One example for this being that higher FR char conversions were generally obtained at higher FR temperatures. However, as shown in Fig. 14, these are obtained for higher values of  $\lambda_{FR,eff}$ , for which lower CGEs are obtained (see Fig. 15), thus signifying an additional trade-off, which needs to be optimized to increase process efficiency. Another interesting trend visible in Fig. 15, which was observed towards the end of BP-6, where large amounts of propane were fired (see Fig. 10), is that the cold gas efficiency increases slightly as the effective air-to-fuel equivalence ratio increases between BP6–14 and BP6–19. To this point, it is unclear why

<sup>15</sup> This circumstance is accounted for in the calculation of the CGE, yet clearly still impacts reactor temperatures.

this behavior was observed. Yet, this again indicates that at very low OC oxidation degrees,<sup>16</sup> the OC could catalyze endothermic gas phase reactions (e.g. tar/methane reforming), thereby increasing the energy content of the FR product gas. The catalytic effect of reduced ilmenite on different reactions has also been observed in literature (Zhou et al., 2022; Min et al., 2011). Hence, the results presented in Fig. 15 suggest that lower air-to-fuel equivalence ratios in the FR could enhance cold gas efficiencies of the CLG process not only by lowering the oxygen release in the FR, but also by catalyzing endothermic gas-phase reactions, favoring the formation of syngas species, through the presence of a more reduced OC inside the FR at lower values of  $\lambda_{FR,eff}$ . This hypothesis needs to be confirmed by further studies, e.g. measurements of higher hydrocarbons.

#### 4. Conclusions

One crucial aspect in up-scaling the CLG technology is the demonstration of a viable process control concept, allowing for autothermal operation. In the course of this work, it has been shown that the suggested process control concept, utilizing AR flue gas recirculation to restrict the air supply in the AR, allows for an independent control of reactor hydrodynamics and the air-to-fuel equivalence ratio of the CLG process, forming the basis for efficient CLG operation. Based on experimental results gathered in 1 MW<sub>th</sub> scale, the following conclusions can be made:

- The presented CLG concept satisfies all relevant criteria, i.e. facilitating the production of a high-calorific raw synthesis gas through guaranteeing sufficiently high temperatures in the FR, without jeopardizing the chemical energy contained in the feedstock.
- The selected route of implementation, i.e. flue gas recycling for the AR, showed promising results during the 1 MW<sub>th</sub> test campaigns, as the oxygen input was controlled accurately, without disturbing reactor hydrodynamics on thus, solid and heat transport between the reactors.
- Other process-wise implementation options, such as diluting the inlet air for the AR with an inert (e.g. N<sub>2</sub>) or tailoring AR dimensions, briefly described in this paper, should show similar results and can be employed, depending on their suitability for the given plant layout. Hence, the general control concept of reducing the air-to-fuel equivalence ratio ( $\lambda$ ) is suitable for large-scale (>100 MW<sub>th</sub>) CLG units.
- Experimental data shows, that changes in  $\lambda$  propagate slowly into the system. This considerable inertia of the system is caused by the fact that the OC inventory of the gasifier effectively acts as an oxygen storage, releasing surplus oxygen during the transient adjustment process. Moreover, the interplay of reactor temperatures, OC reaction kinetics and reaction enthalpies is deemed to play a crucial role in the system's transient response. For the 1 MW<sub>th</sub> unit, switch-over times of up to 4 h were observed when reducing  $\lambda$  through initiating flue gas recycling inside the AR. Consequently, this system inertia has to be considered, when operating CLG units of substantial size.
- Qualitative and quantitative comparisons between different transient switch-over periods showed that the observed behavior occurs consistently regardless of the exact boundary conditions, indicating that the observed transient behavior is a key aspect in operation of large-scale CLG units.

- Through analysis of solid OC samples extracted from both loop seals during operation, the postulated progression of the oxidation degree of the OC during the transient switch-over periods was verified. With the inclusion of this data set, a detailed mechanism of action of the CLG process control concept was formulated.

In summary, the results presented in this paper provide a comprehensive understanding of the CLG technology and its governing phenomena and thus can be considered to be a crucial building block in advancing it towards market maturity. To further extend process understanding and to be able to further refine the process control concept, it is foreseen to apply it to concept to reach lower  $\lambda$  (0.35–0.45) at thermal loads up to 1.5 MW<sub>th</sub>, to increase the cold gas efficiency in semi-industrial scale, further underlining the competitiveness of the CLG technology.

#### Author contribution

**Paul Dieringer:** Conceptualization, Methodology, Investigation, Data Curation, Writing – Original Draft, Visualization. **Falko Marx:** Writing – Review & Editing, Methodology, Investigation, Data Curation. **Benjamin Michel:** Investigation. **Jochen Ströhle:** Writing – Review & Editing, Supervision, Project Administration, Funding Acquisition. **Bernd Eppe:** Resources, Funding Acquisition.

All authors have read and agreed to the published version of the manuscript.

#### Funding

This work has received funding of the European Union's Horizon 2020-Research and Innovation Framework Programme under grant agreement No. 817841 (Chemical Looping gasification foR sustainAble production of biofuels-CLARA).

The content of this work reflects only the author's view, and the European Commission is not responsible for any use that may be made of the information it contains.

The funders had no role in the design of the study; in the collection, analyses, or interpretation of data; in the writing of the manuscript, or in the decision to publish the results.

#### Declaration of Competing Interest

The authors declare that they have no known competing financial interests or personal relationships that could have appeared to influence the work reported in this paper.

#### Data availability

Data will be made available on request.

#### Acknowledgements

The authors would like to thank Aichernig Engineering GmbH, Austria for their support in the design and safety analysis of the 1 MW<sub>th</sub> CLG unit.

<sup>16</sup> As stated in Chapter 3.2.2, low values for X<sub>S</sub> were found to be present toward the end of BP-6, associated to the prolonged duration of oxygen depletion during BP-6, see Fig. 10 & Fig. 11.



## Annex 1. Additional Information

### A.1. Derivation of calculation for AR recycling ratio ( $RR_{AR}$ )

The calculation of  $RR_{AR}$  is achieved by calculating a component balance (C or O) around the primary-air line (system boundaries, see Fig. 16).

As the only unit operation taking place inside these system boundaries is the mixing of the recycled AR flue gas and fresh air, the total mass and thus volume flow stays constant:

$$\dot{V}_{in,AR} = \dot{V}_{Rec,AR} + \dot{V}_{Air,AR} \quad (17)$$

#### i) Oxygen Balance

The oxygen balance around the primary-air line thus can be formulated as:

$$\dot{V}_{in,AR} \cdot x_{O_2,AR,in} = \dot{V}_{Rec,AR} \cdot x_{O_2,AR,out} + \dot{V}_{Air,AR} \cdot 21 \text{ vol.}\% \quad (18)$$

With consideration of Eq. (17), Eq. (18) can be formulated as:

$$\dot{V}_{in,AR} \cdot x_{O_2,AR,in} = (\dot{V}_{in,AR} - \dot{V}_{Air,AR}) \cdot x_{O_2,AR,out} + \dot{V}_{Air,AR} \cdot 21 \text{ vol.}\% \quad (19)$$

Reordering of Eq. (19) yields:

$$\dot{V}_{Air,AR} = \dot{V}_{in,AR} \cdot \frac{x_{O_2,AR,in} - x_{O_2,AR,out}}{21 \text{ vol.}\% - x_{O_2,AR,out}} \quad (20)$$

Combination of Eq. (5), Eq. (17), and Eq. (18) thus results in:

$$RR_{AR} = \frac{\dot{V}_{Rec,AR}}{\dot{V}_{Rec,AR} + \dot{V}_{Air,AR}} = \frac{\dot{V}_{in,AR} - \dot{V}_{in,AR} \cdot \frac{x_{O_2,AR,in} - x_{O_2,AR,out}}{21 \text{ vol.}\% - x_{O_2,AR,out}}}{\dot{V}_{in,AR}} = \frac{x_{O_2,AR,in} - 21 \text{ vol.}\%}{x_{O_2,AR,out} - 21 \text{ vol.}\%} \quad (21)$$

If the desired CLG operation is achieved, the outlet  $O_2$  concentration for the AR drops to 0 vol.-%, and Eq. (21), simplifies to:

$$RR_{AR} = \frac{x_{O_2,AR,in} - 21 \text{ vol.}\%}{-21 \text{ vol.}\%} \quad (22)$$

#### ii) Carbon Balance

For the carbon balance, it is assumed that the  $CO_2$  content of ambient air can be neglected:

$$\dot{V}_{in,AR} \cdot x_{CO_2,AR,in} = \dot{V}_{Rec,AR} \cdot x_{CO_2,AR,out} \quad (23)$$

Combination of Eq. (5), and Eq. (23) thus results in:

$$RR_{AR} = \frac{x_{CO_2,AR,in}}{x_{CO_2,AR,out}} \quad (24)$$

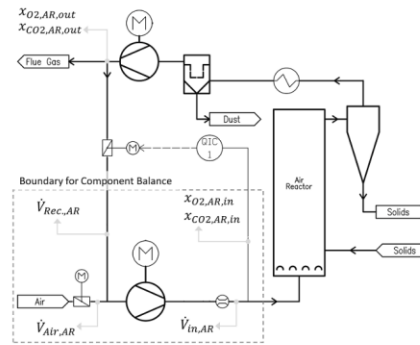


Fig. 16. Illustration of CLG control concept utilized in 1 MW<sub>th</sub> pilot plant with system boundary (dashed line) and all variables (grey arrows) used for derivation of AR recycling.

A.2. Progression of Evaluation Parameters during TP-2 & TP-3

Fig. 17 and Fig. 18 show the progression of the most important evaluation parameters for the transient periods TP-2 and TP-3, respectively. It is visible that for all three transient periods similar observations can be made. These are presented in detail in Chapter 3.1.

A.3. Oxidation degree of OC samples collected during 1 MW<sub>th</sub> operation

Table 3 shows a summary of the oxidation degrees ( $X_S$ ) of all loop seal samples collected during CLG operation, with the corresponding sampling location and time. The change in oxidation degree between AR and FR ( $\Delta X_S$ ) for those solid samples is visualized as a function of the efficient AR air-to-fuel equivalence ratio in Fig. 19.

A.4. Boundary conditions of operating periods under consideration

The boundary conditions for each steady-state operating point under consideration are listed in Table 4, while boundary conditions for the transient periods are given in Table 5.

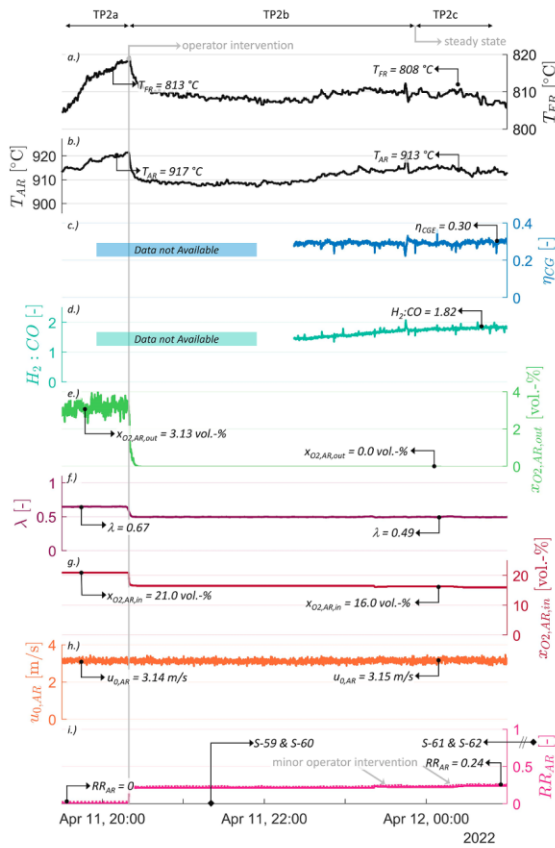
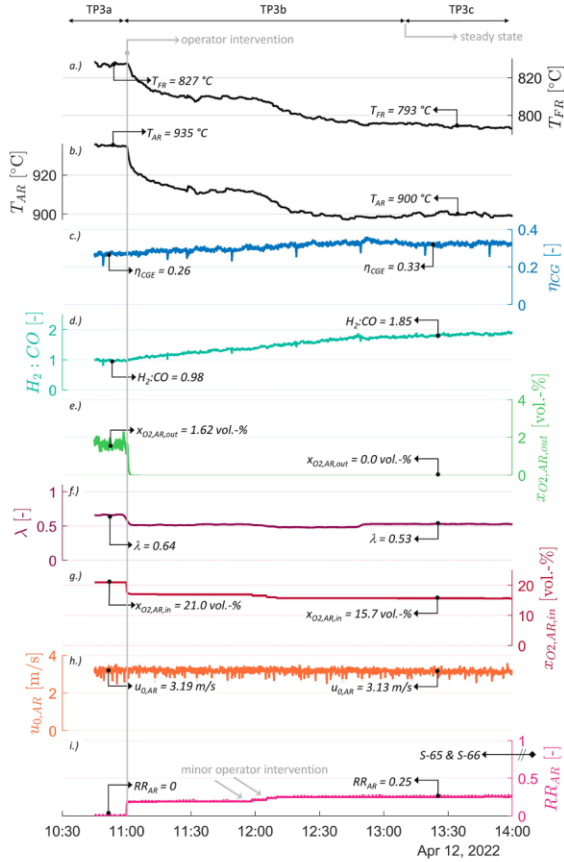
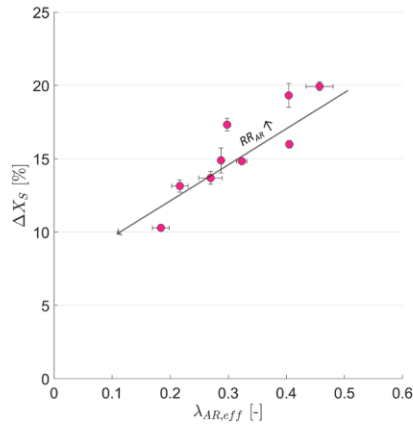


Fig. 17. Progression of important process and evaluation parameters over time for TP-2. From top to bottom: a.) FR and b.) AR temperature, c.) cold gas efficiency ( $\eta_{CGE}$ ), d.)  $H_2/CO$ -ratio in FR product gas, e.) oxygen concentration at AR outlet ( $x_{O_2,AR,out}$ ), f.) air-to-fuel equivalence ratio ( $\lambda$ ), g.) oxygen concentration at AR inlet ( $x_{O_2,AR,in}$ ), h.) AR gas velocity, and i.) AR flue gas recycling ratio ( $RR_{AR}$ ), calculated from  $O_2$  (-) and  $CO_2$  (-) balance. Arrows with diamonds at the end signify the sampling time of a given solid sample.



**Fig. 18.** Progression of important process and evaluation parameters over time for TP-3.

From top to bottom: a.) FR and b.) AR temperature, c.) cold gas efficiency ( $\eta_{CGE}$ ), d.)  $H_2/CO$ -ratio in FR product gas, e.) oxygen concentration at AR outlet ( $x_{O_2,AR,out}$ ), f.) air-to-fuel equivalence ratio ( $\lambda$ ), g.) oxygen concentration at AR inlet ( $x_{O_2,AR,in}$ ), h.) AR gas velocity, and i.) AR flue gas recycling ratio ( $RR_{AR}$ ), calculated from  $O_2$  (-) and  $CO_2$  (:) balance. Arrows with diamonds at the end signify the sampling time of a given solid sample.



**Fig. 19.** Correlation between the measured efficient AR air-to-fuel equivalence ratio and the oxidation degree between AR and FR determined for samples collected from LS4.1 & LS4.5.

**Table 4**  
Operating conditions for steady-state operating periods under investigation. BPX (steady-state operating period).

Variable	Description	BP1	BP2	BP3	BP4	BP5	BP6	BP7	Unit
$m_{Feedstock}$	Mass flow of biomass pellets to FR	156.1	167.5	163.4	175.4	190.3	191.5	223.2	kg/h
$m_{Make-Up}$	Mass flow of OC to LS4.1	34.7	88.4	68.2	56.6	0.0	41.9	0.0	kg/h
$T_{AR}$	AR max. temperature	898.6	885.2	879.3	884.8	843.6	877.2	958.6	°C
$T_{FR}$	FR max. temperature	812.2	820.9	821.7	821.9	756.7	772.9	858.9	°C
$\Delta P_{AR}$	AR pressure drop (inventory)	21.5	32.9	44.4	39.5	29.0	32.8	41.7	mbar
$P_{AR,Cyclone}$	Pressure downstream of AR cyclone	-3.1	-3.1	-3.1	-3.1	-3.1	-3.1	-1.0	mbar
$\Delta P_{FR}$	FR pressure drop (inventory)	37.5	45.9	49.5	50.3	65.1	65.8	70.6	mbar
$P_{FR,Cyclone}$	Pressure downstream of FR cyclone	5.5	5.4	5.5	5.6	5.1	5.2	7.4	mbar
$m_{FM,FR}$	Mass flow of FR fluidization (H <sub>2</sub> O)	304.8	306.0	301.6	297.2	249.8	253.7	237.7	kg/h
$m_{FM,AR}^*$	Mass flow of AR fluidization*	953.7	952.3	952.1	953.9	932.5	921.7	1004.8	kg/h
$m_{C3H8,AR}$	Mass flow of propane entering AR	16.6	18.3	19.4	19.4	19.4	19.4	8.6	kg/h
$m_{FM,LS4.1}$	Vol. flow of LS4.1 fluidization	19.2 (N <sub>2</sub> )	19.3 (N <sub>2</sub> )	19.2 (N <sub>2</sub> )	19.4 (N <sub>2</sub> )	20.5 (N <sub>2</sub> )	22 (N <sub>2</sub> )	16 (N <sub>2</sub> )	Nm <sup>3</sup> /h
$m_{FM,LS4.5}$	Vol. flow of LS4.5 fluidization	26.7 (N <sub>2</sub> )	29.2 (N <sub>2</sub> )	29.9 (N <sub>2</sub> )	30.8 (N <sub>2</sub> )	30.4 (N <sub>2</sub> )	31 (N <sub>2</sub> )	20.6 (CO <sub>2</sub> )	Nm <sup>3</sup> /h
$m_{FM,J-Valve}$	Vol. flow of J-Valve fluidization	13.4 (N <sub>2</sub> )	15.7 (N <sub>2</sub> )	16.8 (N <sub>2</sub> )	16.9 (N <sub>2</sub> )	18.3 (N <sub>2</sub> )	18.1 (CO <sub>2</sub> )	18.4 (N <sub>2</sub> )	Nm <sup>3</sup> /h
$RR_{AR}$	AR flue gas recycling ratio	0.00	0.00	0.00	0.00	0.00	0.00	0.00	-

Variable	Description	BP8	BP9	BP10	BP11	BP12	BP13	BP14	BP15	Unit
$m_{Feedstock}$	Mass flow of biomass pellets to FR	222.8	223.6	226.4	220.8	231.8	226.4	235.0	229.1	kg/h
$m_{Make-Up}$	Mass flow of OC to LS4.1	0.0	33.2	35.3	24.9	46.1	53.8	0.0	50.9	kg/h
$T_{AR}$	AR max. temperature	957.9	963.1	974.5	992.6	943.3	948.0	919.8	911.6	°C
$T_{FR}$	FR max. temperature	858.7	869.0	892.3	908.7	864.6	881.4	839.5	833.6	°C
$\Delta P_{AR}$	AR pressure drop (inventory)	37.8	45.0	52.0	48.7	47.3	39.8	55.4	53.7	mbar
$P_{AR,Cyclone}$	Pressure downstream of AR cyclone	-1.0	-1.0	-1.0	-1.0	-1.1	-1.1	-0.9	-0.9	mbar
$\Delta P_{FR}$	FR pressure drop (inventory)	69.6	61.4	68.0	66.4	70.6	69.3	75.9	73.4	mbar
$P_{FR,Cyclone}$	Pressure downstream of FR cyclone	7.8	7.2	7.6	5.8	6.8	7.2	5.1	5.2	mbar
$m_{FM,FR}$	Mass flow of FR fluidization (H <sub>2</sub> O)	239.1	232.1	227.0	229.9	230.9	235.7	216.8	217.9	kg/h
$m_{FM,AR}^*$	Mass flow of AR fluidization*	1005.7	965.6	965.6	966.2	970.2	1000.6	969.4	971.0	kg/h
$m_{C3H8,AR}$	Mass flow of propane entering AR	8.6	10.1	10.1	10.1	10.1	10.1	6.8	3.6	kg/h
$m_{FM,LS4.1}$	Vol. flow of LS4.1 fluidization	15.9 (N <sub>2</sub> )	15.7 (N <sub>2</sub> )	15.1 (N <sub>2</sub> )	14.9 (N <sub>2</sub> )	15.6 (N <sub>2</sub> )	15.2 (N <sub>2</sub> )	15.7 (N <sub>2</sub> )	15.6 (N <sub>2</sub> )	Nm <sup>3</sup> /h
$m_{FM,LS4.5}$	Vol. flow of LS4.5 fluidization	19.6 (CO <sub>2</sub> )	18.8 (CO <sub>2</sub> )	19.5 (CO <sub>2</sub> )	19.1 (CO <sub>2</sub> )	19.3 (CO <sub>2</sub> )	16.5 (CO <sub>2</sub> )	14.9 (CO <sub>2</sub> )	15.3 (CO <sub>2</sub> )	Nm <sup>3</sup> /h
$m_{FM,J-Valve}$	Vol. flow of J-Valve fluidization	20.9 (CO <sub>2</sub> )	21.8 (CO <sub>2</sub> )	22 (CO <sub>2</sub> )	22 (CO <sub>2</sub> )	22.9 (CO <sub>2</sub> )	23.7 (CO <sub>2</sub> )	19.5 (CO <sub>2</sub> )	18.9 (CO <sub>2</sub> )	Nm <sup>3</sup> /h
$RR_{AR}$	AR flue gas recycling ratio	0.00	0.00	0.00	0.00	0.19	0.00	0.23	0.24	-

Variable	Description	BP16	BP17	BP18	BP19	BP20	BP21	BP22	BP23	Unit
$m_{Feedstock}$	Mass flow of biomass pellets to FR	221.3	223.7	221.5	228.9	228.9	230.2	226.6	232.5	kg/h
$m_{Make-Up}$	Mass flow of OC to LS4.1	0.0	1.7	0.0	0.0	23.2	91.8	0.0	13.0	kg/h
$T_{AR}$	AR max. temperature	906.2	904.0	903.3	902.2	893.8	884.4	883.7	882.1	°C
$T_{FR}$	FR max. temperature	821.7	821.3	816.0	814.2	808.8	806.6	800.5	792.9	°C
$\Delta P_{AR}$	AR pressure drop (inventory)	44.0	42.3	47.2	45.2	47.6	56.5	64.4	63.8	mbar
$P_{AR,Cyclone}$	Pressure downstream of AR cyclone	-1.1	-1.1	-1.1	-1.1	-1.1	-1.1	-1.2	-1.2	mbar
$\Delta P_{FR}$	FR pressure drop (inventory)	90.0	91.0	77.8	74.7	74.2	73.5	65.2	63.5	mbar
$P_{FR,Cyclone}$	Pressure downstream of FR cyclone	7.4	6.9	7.0	8.1	6.4	7.3	7.2	7.1	mbar
$m_{FM,FR}$	Mass flow of FR fluidization (H <sub>2</sub> O)	186.5	183.7	164.7	181.8	183.8	193.8	195.8	197.3	kg/h
$m_{FM,AR}^*$	Mass flow of AR fluidization*	972.8	968.2	928.2	929.3	928.2	969.3	933.1	927.2	kg/h
$m_{C3H8,AR}$	Mass flow of propane entering AR	5.4	5.4	5.4	5.4	5.4	7.2	5.4	5.4	kg/h
$m_{FM,LS4.1}$	Vol. flow of LS4.1 fluidization	15 (N <sub>2</sub> )	15 (N <sub>2</sub> )	15.2 (N <sub>2</sub> )	15.3 (N <sub>2</sub> )	15.2 (N <sub>2</sub> )	16 (N <sub>2</sub> )	16 (N <sub>2</sub> )	16.1 (N <sub>2</sub> )	Nm <sup>3</sup> /h
$m_{FM,LS4.5}$	Vol. flow of LS4.5 fluidization	14.9 (CO <sub>2</sub> )	14.8 (CO <sub>2</sub> )	15.7 (CO <sub>2</sub> )	15.5 (CO <sub>2</sub> )	15.8 (CO <sub>2</sub> )	20.3 (N <sub>2</sub> )	20.6 (N <sub>2</sub> )	20.5 (N <sub>2</sub> )	Nm <sup>3</sup> /h
$m_{FM,J-Valve}$	Vol. flow of J-Valve fluidization	11.8 (CO <sub>2</sub> )	11.6 (CO <sub>2</sub> )	11.6 (CO <sub>2</sub> )	11.6 (CO <sub>2</sub> )	12.4 (CO <sub>2</sub> )	14.7 (CO <sub>2</sub> )	13.3 (CO <sub>2</sub> )	12.5 (CO <sub>2</sub> )	Nm <sup>3</sup> /h
$RR_{AR}$	AR flue gas recycling ratio	0.25	0.25	0.25	0.25	0.25	0.24	0.24	0.24	-

Variable	Description	BP24	BP25	BP26	BP27	BP28	BP29	BP30	Unit
$m_{Feedstock}$	Mass flow of biomass pellets to FR	229.8	228.9	213.7	209.5	209.6	221.9	238.8	kg/h
$m_{Make-Up}$	Mass flow of OC to LS4.1	0.0	10.6	20.9	0.0	0.0	0.0	5.5	kg/h
$T_{AR}$	AR max. temperature	882.5	868.6	844.0	840.7	834.0	833.0	797.3	°C
$T_{FR}$	FR max. temperature	794.4	788.9	757.7	746.0	730.3	725.4	722.8	°C
$\Delta P_{AR}$	AR pressure drop (inventory)	64.5	64.0	63.4	56.0	50.8	49.0	74.3	mbar
$P_{AR,Cyclone}$	Pressure downstream of AR cyclone	-1.1	-1.0	-1.0	-1.0	-1.0	-1.0	-0.8	mbar
$\Delta P_{FR}$	FR pressure drop (inventory)	65.5	76.8	106.7	124.7	134.3	135.6	65.0	mbar
$P_{FR,Cyclone}$	Pressure downstream of FR cyclone	7.6	7.2	7.4	7.1	7.0	7.1	7.0	mbar
$m_{FM,FR}$	Mass flow of FR fluidization (H <sub>2</sub> O)	196.4	200.6	200.9	203.0	203.2	204.3	251.1	kg/h
$m_{FM,AR}^*$	Mass flow of AR fluidization*	927.2	944.7	952.1	953.5	956.5	957.3	960.4	kg/h
$m_{C3H8,AR}$	Mass flow of propane entering AR	5.4	0.9	0.9	0.9	0.9	0.9	0.9	kg/h
$m_{FM,LS4.1}$	Vol. flow of LS4.1 fluidization	16.1 (N <sub>2</sub> )	16.5 (N <sub>2</sub> )	16.7 (N <sub>2</sub> )	16.7 (N <sub>2</sub> )	16.8 (N <sub>2</sub> )	16.9 (N <sub>2</sub> )	17.7 (N <sub>2</sub> )	Nm <sup>3</sup> /h
$m_{FM,LS4.5}$	Vol. flow of LS4.5 fluidization	20.1 (N <sub>2</sub> )	18.9 (N <sub>2</sub> )	16.1 (CO <sub>2</sub> )	16.3 (CO <sub>2</sub> )	16.1 (CO <sub>2</sub> )	16.4 (CO <sub>2</sub> )	16.8 (CO <sub>2</sub> )	Nm <sup>3</sup> /h
$m_{FM,J-Valve}$	Vol. flow of J-Valve fluidization	12.5 (CO <sub>2</sub> )	18.4 (CO <sub>2</sub> )	19.4 (CO <sub>2</sub> )	19.8 (CO <sub>2</sub> )	20.1 (CO <sub>2</sub> )	20.9 (CO <sub>2</sub> )	21.8 (CO <sub>2</sub> )	Nm <sup>3</sup> /h
$RR_{AR}$	AR flue gas recycling ratio	0.23	0.23	0.32	0.32	0.35	0.34	0.37	-

\* AR fluidization medium: pure air or mixture of air & AR recycled flue gas.

**Table 5**  
Operating conditions for the transient operating periods under investigation. TP-X (Transient Period).

Variable	Description	TP-1	TP-2	TP-3	Unit
$\dot{m}_{Feedstock}$	Mass flow of biomass pellets to FR	227.6	234.9	223.3	kg/h
$\dot{m}_{Make-Up}$	Mass flow of OC to LS4.1	44.4	37.4	10.8	kg/h
$T_{AR}$	AR max. temperature	973.1	918.5	914.1	°C
$T_{FR}$	FR max. temperature	889.9	842.2	835.2	°C
$\Delta P_{AR}$	AR pressure drop (inventory)	48.6	56.1	46.8	mbar
$P_{AR,Cyclone}$	Pressure downstream of AR cyclone	-1.0	-1.0	-1.1	mbar
$\Delta P_{FR}$	FR pressure drop (inventory)	68.0	70.3	87.6	mbar
$P_{FR,Cyclone}$	Pressure downstream of FR cyclone	7.2	5.2	7.1	mbar
$\dot{m}_{FM,FR}$	Mass flow of FR fluidization (H <sub>2</sub> O)	239.5	239.7	217.1	kg/h
$\dot{m}_{FM,AR}^*$	Mass flow of AR fluidization <sup>a</sup>	968.4	950.3	971.3	kg/h
$\dot{m}_{C3H8,AR}$	Mass flow of propane entering AR	10.1	6.8	7.7	kg/h
$\dot{m}_{FM,LS4.1}$	Vol. flow of LS4.1 fluidization	15.2 (N <sub>2</sub> )	15.4 (N <sub>2</sub> )	14.8 (N <sub>2</sub> )	Nm <sup>3</sup> /h
$\dot{m}_{FM,LS4.5}$	Vol. flow of LS4.5 fluidization	22.4 (CO <sub>2</sub> )	14.8 (CO <sub>2</sub> )	16.5 (CO <sub>2</sub> )	Nm <sup>3</sup> /h
$\dot{m}_{FM,J-Valve}$	Vol. flow of J-Valve fluidization	19.6 (CO <sub>2</sub> )	19.8 (CO <sub>2</sub> )	15.6 (CO <sub>2</sub> )	Nm <sup>3</sup> /h

<sup>a</sup> AR fluidization medium: pure air or mixture of air & recycled AR flue gas.

## References

- Abad, A., Adánez, J., Cuadrat, A., García-Labiano, F., Gayán, P., de Diego, L.F., Feb. 2011. Kinetics of redox reactions of ilmenite for chemical-looping combustion. *Chem. Eng. Sci.* 66 (4), 689–702. <https://doi.org/10.1016/j.ces.2010.11.010>.
- Abad, A., Adánez, J., de Diego, L.F., Gayán, P., García-Labiano, F., Lyngfelt, A., Nov. 2013. Fuel reactor model validation: assessment of the key parameters affecting the chemical-looping combustion of coal. *Int. J. Greenhouse Gas Control* 19, 541–551. <https://doi.org/10.1016/j.ijggc.2013.10.020>.
- Abad, A., Adánez, J., Gayán, P., de Diego, L.F., García-Labiano, F., Sprachmann, G., Nov. 2015. Conceptual design of a 100 MWth CLC unit for solid fuel combustion. *Appl. Energy* 157, 462–474. <https://doi.org/10.1016/j.apenergy.2015.04.043>.
- Abdalazeez, A., Tianle, L., Cao, Y., Wang, W., Abuelgasim, S., Liu, C., Dec. 2022. Syngas production from chemical looping gasification of rice husk-derived biochar using BaFe<sub>2</sub>O<sub>4</sub> as an oxygen carrier. *J. Energy Inst.* 105, 376–387. <https://doi.org/10.1016/j.joei.2022.10.009>.
- Acharya, B., Dutta, A., Basu, P., Oct. 2009. Chemical-looping gasification of biomass for hydrogen-enriched gas production with in-process carbon dioxide capture. *Energy Fuels* 23 (10), 5077–5083. <https://doi.org/10.1021/ef9003889>.
- Adánez, J., Abad, A., García-Labiano, F., Gayán, P., de Diego, L.F., Apr. 2012. Progress in chemical-looping combustion and reforming technologies. *Prog. Energy Combust. Sci.* 38 (2), 215–282. <https://doi.org/10.1016/j.peccs.2011.09.001>.
- Adánez, J., Gayán, P., Celaya, J., de Diego, L.F., García-Labiano, F., Abad, A., Aug. 2006. Chemical looping combustion in a 10kW<sub>th</sub> prototype using a CuO/Al<sub>2</sub>O<sub>3</sub> oxygen carrier: effect of operating conditions on methane combustion. *Ind. Eng. Chem. Res.* 45 (17), 6075–6080. <https://doi.org/10.1021/ie060364l>.
- Atsonios, K., Nesiadis, A., Detsios, N., Koutita, K., Nikolopoulos, N., Grammelis, P., Jan. 2020. Review on dynamic process modeling of gasification based biorefineries and bio-based heat & power plants. *Fuel Process. Technol.* 197, 106188 <https://doi.org/10.1016/j.fuproc.2019.106188>.
- Barrio, M., Gbel, B., Rimes, H., Henriksen, U., H.ustad, J.E., S.rensen, L.H., 2001. Steam gasification of wood char and the effect of hydrogen inhibition on the chemical kinetics. In: Bridgwater, A.V. (Ed.), *Progress in Thermochemical Biomass Conversion*. Blackwell Science Ltd, Oxford, UK, pp. 32–46. <https://doi.org/10.1002/9780470694954.ch2>.
- Barrio, M., H.ustad, J.E., 2001. CO<sub>2</sub> gasification of birch char and the effect of CO inhibition on the calculation of chemical kinetics. In: Bridgwater, A.V. (Ed.), *Progress in Thermochemical Biomass Conversion*. Blackwell Science Ltd, Oxford, UK, pp. 47–60. <https://doi.org/10.1002/9780470694954.ch3>.
- Bolhar-Nordenkamp, M., et al., 2002. Scale-up of a 100kWth pilot FICFB-gasifier to a 8 MWth FICFB-gasifier demonstration plant in Güssing (Austria). presented at the: *Proc. 1st International Ukrainian Conference on Biomass For Energy*. Kyiv, Ukraine.
- Bolhar-Nordenkamp, M., Rauch, R., Bosch, K., Aichernig, C., 2003. Biomass CHP plant Güssing – using gasification for power generation. In: *Proceeding of the 2nd Regional Conference on Energy Technology Towards a Clean Environment*, p. 7.
- Cetin, E., Moghtaderi, B., Gupta, R., Wall, T.F., Apr. 2005. Biomass gasification kinetics: influences of pressure and char structure. *Combust. Sci. Technol.* 177 (4), 765–791. <https://doi.org/10.1080/00102200590917266>.
- Condori, O., García-Labiano, F., de Diego, L.F., Izquierdo, M.T., Abad, A., Adánez, J., 2022. Syngas production via Biomass Chemical Looping Gasification (BCLG) in a 50 kWth unit using ilmenite as oxygen carrier. In: *Proceedings of the Fluidized Bed Conversion Conference 2022*, p. 10.
- Condori, O., García-Labiano, F., de Diego, L.F., Izquierdo, M.T., Abad, A., Adánez, J., 2021b. Biomass chemical looping gasification for syngas production using ilmenite as oxygen carrier in a 1.5 kWth unit. *Chem. Eng. J.* 405, 126679 <https://doi.org/10.1016/j.cej.2020.126679>.
- Condori, O., García-Labiano, F., de Diego, L.F., Izquierdo, M.T., Abad, A., Adánez, J., 2021a. Biomass chemical looping gasification for syngas production using LD Slag as oxygen carrier in a 1.5 kWth unit. *Fuel Process. Technol.* 222, 106963 <https://doi.org/10.1016/j.fuproc.2021.106963>.
- Cuadrat, A., Abad, A., García-Labiano, F., Gayán, P., de Diego, L.F., Adánez, J., Jan. 2012. Effect of operating conditions in Chemical-Looping Combustion of coal in a 500Wth unit. *Int. J. Greenhouse Gas Control* 6, 153–163. <https://doi.org/10.1016/j.ijggc.2011.10.013>.
- De, S., A.garwal, A.K., M.oholkar, V.S., Thallada, B., 2018. *Coal and Biomass Gasification: Recent Advances and Future Challenges*.
- Dieringer, P., Marx, F., Alobaid, F., Ströhle, J., Epple, B., Jun. 2020. Process control strategies in chemical looping gasification—a novel process for the production of biofuels allowing for net negative CO<sub>2</sub> emissions. *Appl. Sci.* 10 (12), 4271. <https://doi.org/10.3390/app10124271>.
- “DIRECTIVE (EU) 2018/2001 OF THE EUROPEAN PARLIAMENT AND OF THE COUNCIL - of 11 December 2018 - on the promotion of the use of energy from renewable sources,” p. 128.
- Fossdal, A., et al., May 2011. Study of inexpensive oxygen carriers for chemical looping combustion. *Int. J. Greenhouse Gas Control* 5 (3), 483–488. <https://doi.org/10.1016/j.ijggc.2010.08.001>.
- Ge, H., Guo, W., Shen, L., Song, T., Xiao, J., 2016a. Biomass gasification using chemical looping in a 25kW<sub>th</sub> reactor with natural hematite as oxygen carrier. *Chem. Eng. J.* 286, 174–183. <https://doi.org/10.1016/j.cej.2015.10.092>.
- Ge, H., Guo, W., Shen, L., Song, T., Xiao, J., 2016b. Experimental investigation on biomass gasification using chemical looping in a batch reactor and a continuous dual reactor. *Chem. Eng. J.* 286, 689–700. <https://doi.org/10.1016/j.cej.2015.11.008>.
- Goel, A., M.oghaddam, E.M., Liu, W., He, C., Kontinen, J., Sep. 2022. Biomass chemical looping gasification for high-quality syngas: a critical review and technological outlooks. *Energy Convers. Manage.* 268, 116020 <https://doi.org/10.1016/j.enconman.2022.116020>.
- Guo, Q., Cheng, Y., Liu, Y., Jia, W., Ryu, H.-J., Jan. 2014. Coal chemical looping gasification for syngas generation using an iron-based oxygen carrier. *Ind. Eng. Chem. Res.* 53 (1), 78–86. <https://doi.org/10.1021/ie401568x>.
- Hansen, L.K. (Ed.), 1997. *Steam Gasification of Wheat Straw, Barley straw, Willow and Giganteus*. Risø National Laboratory, Roskilde in Risø-R, no. 944.
- He, F., Huang, Z., Li, H., Zhao, Z., Mar. 2011. Biomass direct chemical looping conversion in a fluidized bed reactor with natural hematite as an oxygen carrier. In: *2011 Asia-Pacific Power and Energy Engineering Conference. IEE, Wuhan, China*, pp. 1–7. <https://doi.org/10.1109/APPEEC.2011.5748486>.
- Heinze, C., May, J., Langner, E., Ströhle, J., Epple, B., Feb. 2023. High Temperature Winkler gasification of Rhenish lignite in an optimized 500 kWth pilot plant. *Fuel* 333, 126289. <https://doi.org/10.1016/j.fuel.2022.126289>.
- Higman, C., van der Burgt, M., 2008. *Gasification*, 2nd ed. Gulf Professional Pub./ Elsevier Science, Amsterdam ; Boston.
- Hildor, F., Leon, H., Linderholm, C.J., Mattisson, T., Dec. 2020. Steel converter slag as an oxygen carrier for chemical-looping gasification. *Fuel Process. Technol.* 210, 106576 <https://doi.org/10.1016/j.fuproc.2020.106576>.
- Hu, J., et al., Feb. 2019. Using chemical looping gasification with Fe<sub>2</sub>O<sub>3</sub>/Al<sub>2</sub>O<sub>3</sub> oxygen carrier to produce syngas (H<sub>2</sub>+CO) from rice straw. *Int. J. Hydrogen Energy* 44 (6), 3382–3386. <https://doi.org/10.1016/j.ijhydene.2018.06.147>.
- Huang, Z., et al., Jan. 2014. Biomass char direct chemical looping gasification using NiO-modified iron ore as an oxygen carrier. *Energy Fuels* 28 (1), 183–191. <https://doi.org/10.1021/ef401528k>.
- Huang, Z., et al., Jul. 2013. Synthesis gas production through biomass direct chemical looping conversion with natural hematite as an oxygen carrier. *Bioresour. Technol.* 140, 138–145. <https://doi.org/10.1016/j.biortech.2013.04.055>.
- Huang, Z., et al., Oct. 2016. Chemical looping gasification of biomass char using iron ore as an oxygen carrier. *Int. J. Hydrogen Energy* 41 (40), 17871–17883. <https://doi.org/10.1016/j.ijhydene.2016.07.089>.
- Huseyin, S., Wei, G., Li, H., He, F., Huang, Z., Aug. 2014. Chemical-looping gasification of biomass in a 10 kWth interconnected fluidized bed reactor using Fe<sub>2</sub>O<sub>3</sub>/Al<sub>2</sub>O<sub>3</sub> oxygen carrier. *J. Fuel Chem. Technol.* 42 (8), 922–931. [https://doi.org/10.1016/S1872-5813\(14\)60039-6](https://doi.org/10.1016/S1872-5813(14)60039-6).
- Keller, M., Leon, H., Mattisson, T., Lyngfelt, A., Mar. 2011. Gasification inhibition in chemical-looping combustion with solid fuels. *Combust. Flame* 158 (3), 393–400. <https://doi.org/10.1016/j.combustflame.2010.09.009>.

- Langner, E., Kaltenmorgen, J., Heinze, C., Ströhle, J., Eppe, B., Jul. 2023. Fluidized bed gasification of solid recovered fuels in a 500 kWth pilot plant. *Fuel* 344, 127901. <https://doi.org/10.1016/j.fuel.2023.127901>.
- Larsson, A., Israelsson, M., Lind, F., Seemann, M., Thunman, H., Apr. 2014. Using Ilmenite to reduce the tar yield in a dual fluidized bed gasification system. *Energy Fuels* 28 (4), 2632–2644. <https://doi.org/10.1021/ef500132p>.
- Liu, F., et al., Oct. 2013. Investigation of a Canadian Ilmenite as an oxygen carrier for chemical looping combustion. *Energy Fuels* 27 (10), 5987–5995. <https://doi.org/10.1021/ef401513p>.
- Liu, Q., et al., Nov. 2019. High H<sub>2</sub>/CO ratio syngas production from chemical looping co-gasification of biomass and polyethylene with CaO/Fe<sub>2</sub>O<sub>3</sub> oxygen carrier. *Energy Convers. Manage.* 199, 111951 <https://doi.org/10.1016/j.enconman.2019.111951>.
- Markström, P., Linderholm, C., Lyngfelt, A., Jul. 2013. Chemical-looping combustion of solid fuels – design and operation of a 100kW unit with bituminous coal. *Int. J. Greenhouse Gas Control* 15, 150–162. <https://doi.org/10.1016/j.ijggc.2013.01.048>.
- Marx, F., Dieringer, P., Ströhle, J., Eppe, B., Apr. 2021. Design of a 1 MWth pilot plant for chemical looping gasification of biogenic residues. *Energies* 14 (9), 2581. <https://doi.org/10.3390/en14092581>.
- Marx, F., Dieringer, P., Ströhle, J., Eppe, B., Jun. 2023. Solid flux measurement in dual fluidized bed processes based on solid samples. *Fuel* 341, 127589. <https://doi.org/10.1016/j.fuel.2023.127589>.
- Min, Z., Asadullah, M., Yimsiri, P., Zhang, S., Wu, H., Li, C.-Z., 2011. Catalytic reforming of tar during gasification. Part I. Steam reforming of biomass tar using ilmenite as a catalyst. *Fuel* 90 (5), 1847–1854. <https://doi.org/10.1016/j.fuel.2010.12.039>.
- Moldenhauer, P., Linderholm, C., Rydén, M., et al., 2018. Experimental investigation of chemical-looping combustion and chemical-looping gasification of biomass-based fuels using steel converter slag as oxygen carrier. In: *Proceedings of the International Conference on Negative CO<sub>2</sub> Emissions*, p. 18.
- N. guyen, N.M., Alobaid, F., Dieringer, P., Eppe, B., Jul. 2021. Biomass-based chemical looping gasification: overview and recent developments. *Appl. Sci.* 11 (15), 7069. <https://doi.org/10.3390/app11157069>.
- O.hlemüller, P.G., 2019. *Untersuchung Von Chemical-Looping-Combustion im Megawatt-Maßstab*, 1. Auflage. Cuvillier Verlag, Göttingen.
- Ohlemüller, P., Alobaid, F., Abad, A., Adanez, J., Ströhle, J., Eppe, B., Jun. 2018. Development and validation of a 1D process model with autothermal operation of a 1 MW th chemical looping pilot plant. *Int. J. Greenhouse Gas Control* 73, 29–41. <https://doi.org/10.1016/j.ijggc.2018.03.013>.
- Ohlemüller, P., Busch, J.-P., Reitz, M., Ströhle, J., Eppe, B., Jul. 2016. Chemical-looping combustion of hard coal: autothermal operation of a 1 MWth pilot plant. *J. Energy Resour. Technol.* 138 (4), 042203 <https://doi.org/10.1115/1.4032357>.
- Ohlemüller, P., Ströhle, J., Eppe, B., Oct. 2017. Chemical looping combustion of hard coal and torrefied biomass in a 1 MW th pilot plant. *Int. J. Greenhouse Gas Control* 65, 149–159. <https://doi.org/10.1016/j.ijggc.2017.08.013>.
- Ollero, P., Serrera, A., Arjona, R., Alcantarilla, S., 2003. The CO<sub>2</sub> gasification kinetics of olive residue. *Biomass Bioenergy* 11.
- Pérez-Vega, R., Abad, A., García-Labiano, F., Gayán, P., de Diego, L.F., Adánez, J., Jul. 2016. Coal combustion in a 50kWth chemical looping combustion unit: seeking operating conditions to maximize CO<sub>2</sub> capture and combustion efficiency. *Int. J. Greenhouse Gas Control* 50, 80–92. <https://doi.org/10.1016/j.ijggc.2016.04.006>.
- Pissot, S., Vilches, T.B., Maric, J., Seemann, M., May 2018. Chemical looping gasification in a 2-4 MWth dual fluidized bed gasifier. In: *Proceedings of the 23rd International Conference on Fluidized Bed Conversion*. Seoul, South Korea, p. 10.
- Pröll, T., Bolhär-Nordenkamp, J., Kolbitsch, P., Hofbauer, H., Jun. 2010. Syngas and a separate nitrogen/argon stream via chemical looping reforming – a 140kW pilot plant study. *Fuel* 89 (6), 1249–1256. <https://doi.org/10.1016/j.fuel.2009.09.033>.
- Ripfel-Nitsche, K., Hofbauer, H., Rauch, R., Goritschnig, M., 2007. BTL – biomass to liquid (Fischer Tropsch process at the biomass gasifier in Güssing). In: *Proceedings of the 15th European Biomass Conference & Exhibition*, p. 4.
- Roshan Kumar, T., Mattisson, T., Rydén, M., Stenberg, V., 2022. Process analysis of chemical looping gasification of biomass for Fischer-Tropsch crude production with net-negative CO<sub>2</sub> emissions: part 1. *Energy Fuels*. <https://doi.org/10.1021/acs.energyfuels.2c00819> p. acs.energyfuels.2c00819, Jun.
- Samprón, I., de Diego, L.F., García-Labiano, F., Izquierdo, M.T., Jul. 2021. Optimization of synthesis gas production in the biomass chemical looping gasification process operating under auto-thermal conditions. *Energy* 226, 120317. <https://doi.org/10.1016/j.energy.2021.120317>.
- Ströhle, J., Orth, M., Eppe, B., Nov. 2015. Chemical looping combustion of hard coal in a 1 MW th pilot plant using ilmenite as oxygen carrier. *Appl. Energy* 157, 288–294. <https://doi.org/10.1016/j.apenergy.2015.06.035>.
- Xu, F., et al., Nov. 2021. Direct chemical looping gasification of pine sawdust using Fe<sub>2</sub>O<sub>3</sub>-rich sludge ash as an oxygen carrier: thermal conversion characteristics, product distributions, and gasification performances. *Fuel* 304, 121499. <https://doi.org/10.1016/j.fuel.2021.121499>.
- Yan, J., et al., May 2020. Hydrogen-rich syngas production with tar elimination via biomass chemical looping gasification (BCLG) using BaFe<sub>2</sub>O<sub>4</sub>/Al<sub>2</sub>O<sub>3</sub> as oxygen carrier. *Chem. Eng. J.* 387, 124107 <https://doi.org/10.1016/j.cej.2020.124107>.
- Zhao, H., Guo, L., Zou, X., Nov. 2015. Chemical-looping auto-thermal reforming of biomass using Cu-based oxygen carrier. *Appl. Energy* 157, 408–415. <https://doi.org/10.1016/j.apenergy.2015.04.093>.
- Zhou, Z., Li, L., Liu, X., Zhou, Z., Sun, Z., Duan, L., 2022. Accelerated syngas generation from chemical looping CH<sub>4</sub> reforming by using reduced ilmenite ore as catalyst. *Fuel Process. Technol.* 232, 107270 <https://doi.org/10.1016/j.fuproc.2022.107270>.

---

## Research Paper IV

---

### *System Hydrodynamics of a 1 MW<sub>th</sub> Dual Circulating Fluidized Bed Chemical Looping Gasifier*

Paul Dieringer, Falko Marx, Jochen Ströhle, Bernd Epple

---

**Journal:** Energies, Vol. 16  
**Date:** 07/2023  
**DOI:** [10.3390/en16155630](https://doi.org/10.3390/en16155630)  
**ISSN:** 1996-1073  
**Copyright:** Open Access License: CC BY 4.0

---



Article

# System Hydrodynamics of a 1 MW<sub>th</sub> Dual Circulating Fluidized Bed Chemical Looping Gasifier

Paul Dieringer \*, Falko Marx , Jochen Ströhle \* and Bernd Epple

Institute for Energy Systems and Technology, Otto-Berndt-Str. 2, 64287 Darmstadt, Germany; falko.marx@est.tu-darmstadt.de (F.M.); bernd.epple@est.tu-darmstadt.de (B.E.)

\* Correspondence: paul.dieringer@est.tu-darmstadt.de (P.D.); jochen.stroehle@est.tu-darmstadt.de (J.S.)

## Highlights:

What are the main findings?

- A holistic dataset covering the hydrodynamic behavior of a 1 MW<sub>th</sub> coupled dual-fluidized bed reactor system, encompassing more than 100 h of hot chemical looping gasification operation, is presented.
- Using data collected during more than 50 h of operation of a downscaled cold flow model (CFM), the hydrodynamic behavior of the hot 1 MW<sub>th</sub> setup is predicted and further evaluated.
- A novel and robust method to calculate solids entrainment from a circulating fluidized bed (CFB) system, relying solely on pressure and temperature measurements, developed using the CFM data and validated using live data from the 1 MW<sub>th</sub> chemical looping gasifier, is presented.

What is the implication of the main finding?

- Data from the cold flow model and the 1 MW<sub>th</sub> pilot plant show that free variations of all underlying hydrodynamic boundary conditions are viable in a given range, each resulting in a characteristic response of the dual-fluidized bed reactor system. These findings are formalized in a set of operating ground rules, applicable to similar dual-fluidized bed systems of any scale.
- The novel calculation approach for the solid entrainment from the CFB(s) can be applied to any fluidized bed setup, allowing for accurate determination of this crucial parameter in any process configuration.



**Citation:** Dieringer, P.; Marx, F.; Ströhle, J.; Epple, B. System Hydrodynamics of a 1 MW<sub>th</sub> Dual Circulating Fluidized Bed Chemical Looping Gasifier. *Energies* **2023**, *16*, 5630. <https://doi.org/10.3390/en16155630>

Academic Editor: Bartłomiej Iglirski

Received: 20 June 2023

Revised: 13 July 2023

Accepted: 21 July 2023

Published: 26 July 2023



**Copyright:** © 2023 by the authors. Licensee MDPI, Basel, Switzerland. This article is an open access article distributed under the terms and conditions of the Creative Commons Attribution (CC BY) license (<https://creativecommons.org/licenses/by/4.0/>).

**Abstract:** Chemical looping gasification (CLG) is a novel dual-fluidized bed gasification technology that allows for the production of high-calorific syngas from various solid feedstocks (e.g., biomass). Solid circulation between the two coupled fluidized bed reactors, serving the purpose of heat and oxygen transport, is a key parameter for the CLG technology, making system hydrodynamics the backbone of the gasification process. This study serves the purpose to provide holistic insights into the hydrodynamic behavior of the dual-fluidized bed reactor system. Here, special focus is placed on the operational principles of the setup as well as the entrainment from the circulating fluidized bed (CFB) reactors, the latter being the driving force for the solid circulation inside the entire reactor system. Using an elaborate dataset of over 130 operating periods from a cold flow model and 70 operating periods from a 1 MW<sub>th</sub> CLG pilot plant, a holistic set of ground rules for the operation of the reactor setup is presented. Moreover, a novel easily-applicable approach, solely relying on readily-available live data, is presented and validated using data from the 1 MW<sub>th</sub> chemical looping gasifier. Thereby, a straightforward estimation of solid entrainment from any CFB setup is facilitated, thus closing a crucial research gap.

**Keywords:** chemical looping; gasification; hydrodynamics; pilot scale; circulating fluidized bed; dual fluidized bed; cold flow model



## 1. Introduction

The unhalted increase of greenhouse gases (GHG) in the earth's atmosphere, reaching an inglorious record-high concentration of the major GHG CO<sub>2</sub> of 421 ppm in July 2022 on Mauna Loa [1], which was obliterated again in 2023 (424 ppm), show that immediate and unparalleled changes are required to mitigate the impact of man-made climate change to manageable extents in the future. One sector is crucial in terms of climate protection and energy transition, yet not having shown any significant improvement in terms of emitted GHG in recent years [2], is the transport sector. While the electrification of passenger vehicles is in full swing [3] to reduce the footprint of personal transport on the earth's atmosphere, other alternatives are required for other means of transport (e.g., aviation, heavy transport, shipping) [4]. One route under broad consideration is the production of 2nd generation biofuels by converting biogenic residues and wastes into high-calorific syngas, before further treatment and fuel synthesis [5,6].

Amongst others, dual fluidized bed gasification (DFBG) and chemical looping gasification (CLG) are promising gasification technologies. Here, a bed material is transferred between two reactors, transporting heat to the fuel reactor (FR), in which the solid feedstock is converted into a high-calorific syngas, from the air reactor (AR), in which air is used to combust the remaining feedstock. For the CLG technology, illustrated in Figure 1, the utilized bed material is an active bed material, not only transporting sensible heat but also lattice oxygen between the two reactors, allowing for more complete conversion of the feedstock inside the FR. This bed material is thus called an oxygen carrier (OC). Because of the continuous cyclic reduction and oxidation of the OC inside the FR and AR, CLG constitutes an oxygen-driven gasification technology, not relying on a costly air separation unit. On top of that, the CO<sub>2</sub> generated during the autothermal gasification step can be separated efficiently from the N<sub>2</sub>-free FR producer gas in a subsequent syngas cleaning unit. Hence, net negative CO<sub>2</sub> emissions can be realized, when employing CLG in biomass-to-biofuel process chains and utilizing sustainably sourced feedstocks [7–9].

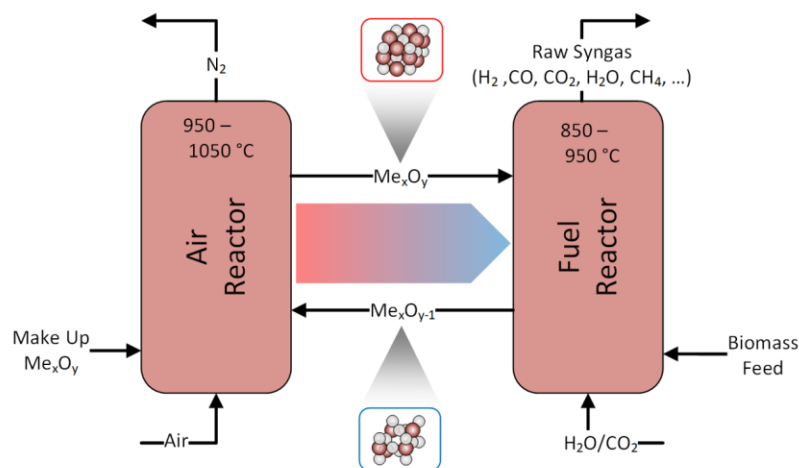


**Figure 1.** Schematic illustration of CLG process.

Although the CLG technology has also been investigated in fixed bed reactors [10,11], generally fluidized bed setups are preferred [12–14], mainly due to their superior heat and mass transfer characteristics. Here, some reactor setups rely on a combination of one bubbling fluidized bed reactor and one circulating fluidized bed reactor (usually the AR) [12,14–17], while others use a dual circulating fluidized bed (CFB) layout [18,19]. While each layout exhibits advantages and disadvantages, they are related to the fact that the solid circulation between the two reactors is facilitated by the entrainment from the CFB(s) [20].

This solid circulation thus forms the backbone of the CLG technology, transporting heat and oxygen between the AR and FR [21,22], thereby allowing for a N<sub>2</sub>-free oxidation of the feedstock inside the FR and the stabilization of FR temperatures at the desired levels (i.e., >800 °C). Consequently, efficient and accurate tailoring of system hydrodynamics is indispensable for efficient CLG operation. In contrast to other CFB applications (e.g., CFB combustion), where strong solid entrainment is undesired [23], maximizing the solid entrainment from the CFB(s) is key in CLG, in order to optimize process conditions (esp. heat transport from AR to FR) [24,25].

The general behavior of bubbling and circulating fluidized bed reactors is well-known and has been studied experimentally in great detail [23]. However, due to the complexity of the heterogeneous gas-solid system, its behavior depending on numerous boundary conditions (e.g., gas velocity and solid flux), the utilized particle system, reactor size, and geometry, etc. [26–31], accurate *a priori* assertions on the system's performance under novel boundary conditions remains a challenge. Although several studies have formulated semi-empirical sets of equations for modeling of fluidized beds [32–38], their application generally is only valid for a given range of boundary conditions. Further complexity originates when considering a coupled fluidized bed system, where two separate reactors, with a sub-set of boundary conditions, interact with each other, making the application of existing modeling approaches to describe the system's behavior impractical. Similitude studies form an alternative to modeling approaches, allowing for the prediction of a given system based on the knowledge gained from a similar system. Here, Glicksman formulated a set of dimensionless parameters (more details see Section 3) applicable for the scaling of fluidized bed reactors [39–41]. In the most general sense, using these scaling relations, one is enabled to devise a simplified experimental setup, from which operation one can thus predict the behavior of the desired fluidized bed layout. The simplified set of Glicksman's dimensionless parameters has widely been used to set up scaled-down cold flow models (i.e., fluidized bed rigs operated at ambient conditions) to successfully predict the behavior of large-scale fluidized beds operated at process conditions. A summary of selected endeavors using Glicksman's scaling approach is given in Table 1. More recent studies show that successful scaling requires the maintaining of all micro-structures of the gas solid conditions inside the CFB, to obtain similar transport properties and hence achieve successful CFB scaling [42], putting an additional requirement on scaling endeavors.

Due to the importance of the hydrodynamic behavior of the fluidized bed system in CLG conditions, the aim of this study is to predict and optimize system hydrodynamics of the 1 MW<sub>th</sub> CLG pilot plant at TU Darmstadt via investigations in a scaled cold flow model. Through the operation of the cold flow model (CFM) with a vast set of scaled boundary conditions, a holistic set of operational rules for the coupled dual-fluidized bed reactor system was derived. Moreover, a clear-cut correlation between the utilized boundary conditions and the solid entrainment from both risers of the reactor system was observed. Based on this dataset, a novel method to estimate the solids entrainment, solely based on temperature and pressure measurements, was developed. Ultimately, the knowledge gained via the operation of the CFM was transferred to the 1 MW<sub>th</sub> CLG unit. Here, it was shown that the operational principles derived at cold conditions allow for stable hydrodynamic operation of the hot gasification system. Consequently, it is inferred that the basic operational rules are also applicable to other reactor setups. Furthermore, the novel method for estimation of the solid entrainment from the CFBs was successfully transferred to the hot conditions in the 1 MW<sub>th</sub> CLG unit, thus allowing for a straightforward estimation of solid circulation between AR and FR, solely using pressure and temperature data.

**Table 1.** Overview of selected scaling approaches using the scaling approach by Glicksman.

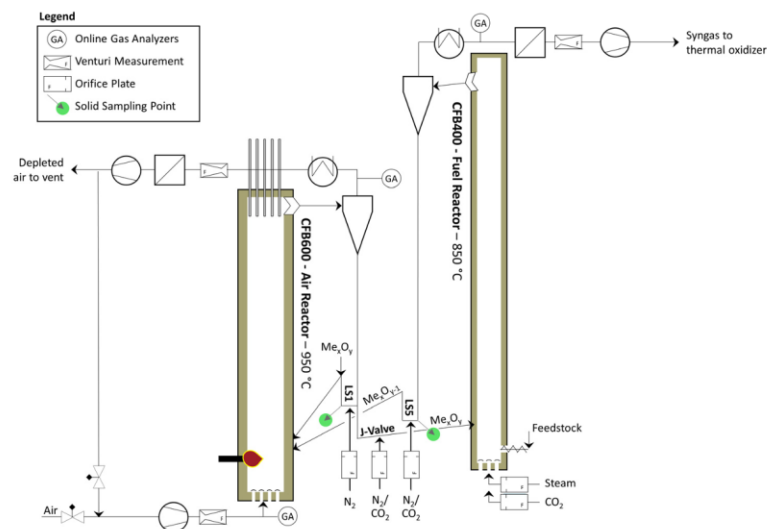
Author(s)	Reactor Setup	Research Focus
Junk et al. [43]	CFB-BFB	<ul style="list-style-type: none"> <li>• Proof-of-concept for novel coupled fluidized bed reactor concept.</li> </ul>
Bischi et al. [44]	CFB-CFB	<ul style="list-style-type: none"> <li>• Validation of validity of coupled fluidized bed reactor setup.</li> </ul>
Masahiko and Hiroshi [45]	CFB	<ul style="list-style-type: none"> <li>• Investigation of effect of main boundary conditions on solid entrainment.</li> </ul>
Djerf et al. [46]	CFB	<ul style="list-style-type: none"> <li>• Investigation of solid flow patterns and entrainment.</li> <li>• Effect of boundary conditions on entrainment and entrainment probability.</li> </ul>
Pröll et al. [20]	CFB-CFB	<ul style="list-style-type: none"> <li>• Proof-of-concept of a reactor system for CLC application.</li> <li>• Effect of boundary conditions on entrainment and solid profiles in CFB.</li> </ul>
Alghamadi et al. [47,48]	CFB-BFB	<ul style="list-style-type: none"> <li>• Effect of boundary conditions on entrainment and entrainment probability.</li> <li>• Derivation of equation for solid holdup in CFB system.</li> </ul>
Markström and Lyngfelt [49]	CFB-BFB	<ul style="list-style-type: none"> <li>• Proof-of-concept of a reactor system for CLC application.</li> <li>• Effect of boundary conditions on hydrodynamic system behavior.</li> </ul>

## 2. Experimental

### 2.1. 1 MW<sub>th</sub> Pilot Plant

#### 2.1.1. Pilot Plant Layout

Marx et al. [18] previously presented a detailed description of the layout of the 1 MW<sub>th</sub> CLG pilot plant, schematically shown in Figure 2. Hence, the subsequent elucidations will be restricted to the most crucial plant components for brevity.

**Figure 2.** Simplified flow diagram of the 1 MW<sub>th</sub> CLG pilot plant.

The CLG reactor system consists of an air reactor (0.59 m inner diameter, 8.66 m height), a fuel reactor (0.4 m inner diameter, 11.35 m height), and three coupling elements (two loop seals and a J-valve). To reduce heat losses and hence allow for autothermal operation (i.e., without electrical heating), the entire system is refractory lined. During CLG operation, the system is filled with 1–1.2 t of OC material. To map the solids distribution in each riser, both risers are equipped with pressure sensors located at different heights (see Table 2). Fluidization of the AR, which has a design temperature of 1050 °C, is possible with air or a mixture of air and recycled flue gas. AR inlet gases can be electrically pre-heated to temperatures up to 375 °C. The gas composition (O<sub>2</sub>, CO<sub>2</sub>) of the AR inlet gases is continuously being measured due to process control reasons [24,25]. Fluidization of the fuel reactor, having a design temperature of 970 °C, can be achieved with air, steam, a mixture of steam and CO<sub>2</sub>, or a mixture of air and CO<sub>2</sub>. Similar to the AR, FR inlet gases can be electrically pre-heated to temperatures up to 450 °C. The AR and FR are each equipped with a cyclone for gas-solid separation and a loop seal to prevent bypassing of gases. By altering fluidization velocities of the J-valve (N<sub>2</sub> or CO<sub>2</sub>), which connects the loop seal (LS) of the AR (LS1) with the fuel reactor, global solid circulation between the two reactors can be adjusted. All entrained material leaving the FR riser is directly transferred into the AR via LS5, which is fluidized with CO<sub>2</sub> or N<sub>2</sub>. On the other hand, the option of internal solid circulation via LS1 fluidized with N<sub>2</sub>, exists for the AR. Each loop seal is equipped with a solid sampling device, allowing for the controlled removal of OC samples during operation (more details on the sampling procedure are provided by Marx et al. [50]). Using an oil-cooled feeding screw, a feedstock input of up to 340 kg/h, corresponding to a thermal power of about 1.7 MW (feedstock: PFR), can be introduced into the dense bed of the FR. Downstream of the cyclone, the FR product gas passes a syngas cooler, where it is cooled to a temperature of approx. 350 °C. At the syngas cooler outlet, the composition (CO, CO<sub>2</sub>, O<sub>2</sub>, H<sub>2</sub>, CH<sub>4</sub>) and the flow rate of the FR product gas are measured online. Before transferring the FR product gas to the stack, it is firstly transferred through a hot gas filter, operated at up to 250 °C, using an induced draft fan. Subsequently, it enters a thermal oxidizer where all hydrocarbon species are fully converted to CO<sub>2</sub> and H<sub>2</sub>O. After online gas sampling (CO, CO<sub>2</sub>, O<sub>2</sub>, SO<sub>2</sub>, NO), the AR product gases are cooled in a heat exchanger to temperatures below 350 °C. Thereafter, particulate matter is removed from the gas stream in a fabric filter. As for the FR, the AR freeboard pressure is controlled with an induced draft fan. Downstream of the induced draft fan, the AR product gases can either be vented to the environment through a stack or can be partly recycled back to the AR airbox via the primary-air fan. Bed material reactor inventories are maintained at the desired levels throughout operation using a make-up feeding system, which allows for the controlled feeding of up to 200 kg/h of ilmenite (ILMf) into the standpipe of LS1 via a dosing screw.

**Table 2.** Pressure sensors of AR and FR risers of 1 MW<sub>th</sub> pilot plant.

AR		FR	
Name	Height [mm]	Name	Height [mm]
AR-CP011	135	FR-CP011	95
AR-CP012	265	FR-CP012	253
AR-CP013	435	FR-CP013	412
AR-CP014	605	FR-CP015	834
AR-CP015	945	FR-CP016	1141
AR-CP016	1105	FR-CP018	2150
AR-CP021	2122	FR-CP021	3392
AR-CP022	3462	FR-CP022	4292
AR-CP031	4615	FR-CP031	5741
AR-CP041	8076	FR-CP038	8161
AR-CP042	8286	FR-CP041	9790
AR-Cy-CP001	Cycl. Outlet	FR-Cy-CP001	Cycl. Outlet

## 2.2. Cold Flow Model

Just like the 1 MW<sub>th</sub> pilot plant, the cold flow model (CFM) consists of two circulating fluidized bed reactors coupled with two loop seals and a J-valve (see Figure 3). Dimensions of the cold flow model are summarized in Table 5, indicating that all dimensions were scaled with a factor of 0.3264 (more details see Section 3). The two cyclones pose an exception to this, having been scaled so that particle separation at similar efficiencies as for 1 MW<sub>th</sub> pilot plant are attainable for the CFM. The FR riser and all coupling elements are made of Plexiglas, allowing for visual observation during operation, whereas the AR riser and both cyclones are made of steel. Fluidization of the two risers is achieved via two air fans, their rotary speeds being controlled via frequency converters. Each primary-air line is equipped with an orifice plate measurement, consisting of two pressure measurements and temperature measurements. An implemented PID controller thus allows for accurate control of the fluidization velocity via the frequency converters. The two loop seals and the J-valve are fluidized with pressurized air, with the inlet flow being adjustable via manual rotary meters. To measure the pressure gradient over the CFM, it is equipped with multiple pressure sensors, being located inside the AR riser, the FR riser (see Table 3), in the three coupling elements, and two at the outlet of the two cyclones.

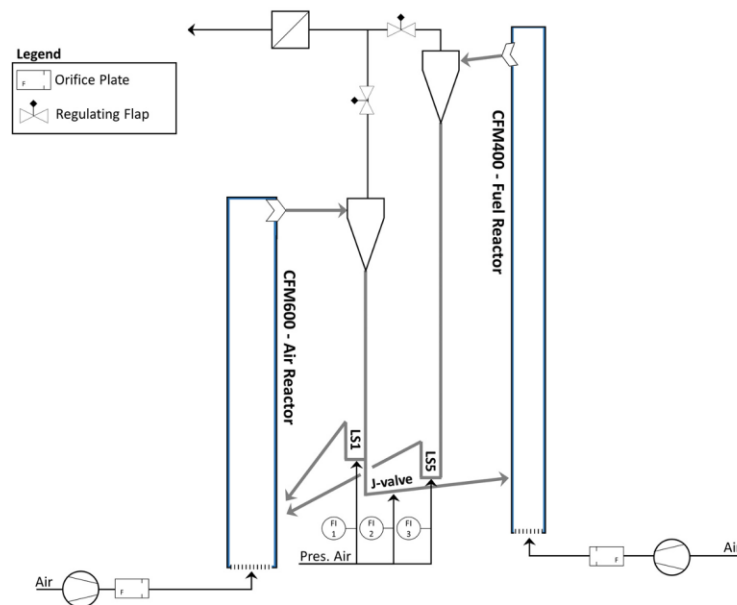


**Figure 3.** Simplified flow diagram of cold flow model (CFM).

At the top of the cyclones of both risers, a duct combines the two streams and transfers the gas into a filter, before venting into the atmosphere. Hence, the CFM is operated at slight overpressures induced by the pressure drop over the duct and filter. To adjust the riser overpressure for the AR and FR independently, two gas flaps are located downstream of the two cyclones.

**Table 3.** Pressure sensors of AR and FR risers of the cold flow model.

AR		FR	
Name	Height [mm]	Name	Height [mm]
AR1	35	FR1	31.6
AR2	50	FR2	89
AR4	73	FR4	223
AR6	120	FR6	378
AR9	269	FR7	569.4
AR11	451	FR8	777.9
AR12	577	FR9	1229
AR13	701	FR10	1556
AR14	761	FR11	1995
AR15	883	FR12	2470.8
AR17	1380	FR13	2961.1
AR18	1655	FR15	3862.5
AR20	2182	Cy2	Cycl. Outlet
AR22	2946		
Cy1	Cycl. Outlet		

### 2.3. Materials

#### 2.3.1. Bed Materials

The ilmenite, which was used as bed material during the 1 MW<sub>th</sub> CLG experiments, was procured from Titania AS (Tellenes, Norway). The same material was previously successfully deployed for chemical looping experiments in the 1 MW<sub>th</sub> pilot [21,51,52]. During material characterization (more details see Section 2.6), a bulk density of 2550 kg/m<sup>3</sup>, a particle density of 4486 kg/m<sup>3</sup>, and a mean particle diameter of 111 μm ( $d_{p,10} = 31$  μm,  $d_{p,90} = 224$  μm) were determined for the fresh OC material. For selected operating periods, a different type of ilmenite from the Norwegian Company Titania AS was used (more details, see Section 2.4.1). This coarser material (ILMc) exhibits a bulk density of 2336 kg/m<sup>3</sup>, a particle density of 4621 kg/m<sup>3</sup>, and a mean particle diameter of 199 μm ( $d_{p,10} = 151$  μm,  $d_{p,90} = 247$  μm) in fresh delivery condition.

Bronze powder from the supplier Makin Metal Powders (Rochdale, UK) was used for the experiments in the scaled cold flow model (see Section 2.2). The fresh powder exhibits a bulk density of 5477 kg/m<sup>3</sup>, a particle density of 8710 kg/m<sup>3</sup>, and a mean particle diameter of 56 μm ( $d_{p,10} = 28$  μm,  $d_{p,90} = 76$  μm).

#### 2.3.2. Feedstocks

Three different biomass feedstocks were used within three dedicated 1 MW<sub>th</sub> CLG test campaigns. During the first test campaign (K1), industrial wood pellets (IWP) conforming to the Norm ENPlus A1, purchased from Eckard GmbH (Lützelbach, Germany), were used. The pellets exhibit a cylindrical shape (l ~10–25 mm, d ~6 mm), a bulk density of 650 kg/m<sup>3</sup>, and a lower heating value of 17.96 MJ/kg. During the second test campaign (K2), pine forest residue pellets (PFR) from AB Torkapparater, Sweden, were used. The pellets also were cylindrical (l ~8–12 mm, d ~6–8 mm), exhibiting a bulk density of 630 kg/m<sup>3</sup> and a lower heating value of 18.3 MJ/kg. For the third test campaign (K3), cylindrical (l ~8–12 mm, d ~6–8 mm), pre-treated wheat straw pellets (WSP), from AB Torkapparater (Stockholm, Sweden), with a bulk density of 504 kg/m<sup>3</sup> and a lower heating value of 16.6 MJ/kg were used. The proximate and ultimate analysis of all pellet types are given in Table 4.

**Table 4.** Proximate and ultimate analysis for industrial wood pellets (IWP), pine forest residue pellets (PFR), and wheat straw pellets (WSP).

Feedstock	IWP	PFR	WSP	Feedstock	IWP	PFR	WSP
Component	wt.-% (d.a.f.)			Component	wt.-% (a.r.)		
C	50.8	48.9	42.50	C-fix	13.3	16.63	16.3
H	6.0	5.8	5.10	Volatiles	79.6	76.77	68.7
O	43.2	38.3	36.70	Ash	0.65	2.20	4.2
N	0.07	0.43	0.10	Moisture	6.5	4.40	10.8
S	0.008	0.024	0.48				
Cl	0.006	0.01	0.071				

## 2.4. Operating Conditions

### 2.4.1. 1 MW<sub>th</sub> Chemical Looping Gasifier

In 2022, the modular 1 MW<sub>th</sub> pilot plant at TU Darmstadt was continuously operated (24 h/day) as an autothermal chemical looping gasifier for approximately 14 days each, in three separate test campaigns, yielding >400 h of chemical looping operation.

Within the first test campaign (K1), approx. 100 h of chemical looping operation were attained, using industrial wood pellets as the feedstock and fine ilmenite (ILMf) as the bed material. To allow for meaningful assessments and exemplifications of crucial trends, thirty operating periods (BP) were selected for analysis. During each BP, the most important boundary conditions, summarized in Table S1 in the Supplementary Material, were kept constant. In-between adaptations of those conditions, the system was left for stabilization, which was usually achieved within 15 min during which the OC inventory undergoes one full cycle through the system [50]. From these 30 operating periods, nine operating periods, during which loop seal samples were collected, are investigated in greater detail. Moreover, all 30 operating periods were split into 20-min intervals, yielding a total of 177 sub-periods for in-depth analysis in Section 4.1.2.

During the second test campaign (K2), the 1 MW<sub>th</sub> pilot plant was operated using pine forest residue pellets as the feedstock, resulting in more than 200 h of successful chemical looping operation. From these 200 h of operation, 35 operating periods, during which the most important boundary conditions were kept constant and loop seal samples were collected, were selected for subsequent analysis (boundary conditions see Table S2 in the Supplementary Material). Throughout the first section of K2, coarse ilmenite (ILMc) was used as the make-up bed material before it was replaced with fine ilmenite (ILMf) in the later stages of the second test campaign. For initial reactor filling at the start of K2, old bed material from K1 was used.

During the third test campaign (K3), the 1 MW<sub>th</sub> pilot plant was operated using pre-treated wheat straw pellets as the feedstock and fine ilmenite (ILMf) as the bed material. (Coarse ilmenite (ILMc) was utilized during system-start up, but was replaced with fine ilmenite (ILMf), before initiation of chemical looping operation). Here, the pilot plant was successfully operated in chemical looping mode for a total of ~80 h, from which five operating periods, during which the most important boundary conditions were kept constant and loop seal samples were collected, were selected for subsequent analysis (boundary conditions see Table S3 in the Supplementary Material).

### 2.4.2. Cold Flow Model

In contrast to the 1 MW<sub>th</sub> pilot plant, the cold flow model (CFM) was operated over short periods (1–6 h), allowing for targeted investigations of individual operating conditions. Prior to the start of the cold flow model, it was filled with the desired amount of bed material. Here, it was safeguarded to sufficiently fill the two loop seals in order to avoid gas bypassing during system startup. Generally, the system was filled with an inventory between 50–120 kg. Subsequently, loop seal fluidization was started for LS1 and LS5 to allow for material transport through both seals before starting AR fluidization.

When solid circulation was observed for the AR, FR and J-valve fluidization were started in quick succession to allow for material transport through the J-valve and entrainment from the FR and hence stable global solid circulation. When all boundary conditions ( $u_{0,AR}$ ,  $u_{0,FR}$  and J-valve fluidization) were set to the target values, the system was left for stabilization for approx. 2–3 min. Thereafter, pressure and temperature signals were recorded for a minimum of 10–15 min, to allow for calculation of mean values for all system variables over a sufficiently long period. After successfully recording one operating period, data recording was terminated without changing the boundary conditions. Subsequently, entrainment was measured using the method described by Pröll et al. [20], i.e., by briefly terminating LS fluidization in one of the loop seals and measuring material accumulation in the LS stand-pipe (see Equation (19)). Following the measurement, LS fluidization was restarted, and the system was left for stabilization before initiating the subsequent entrainment measurement. A minimum of three entrainment measurements was carried out for each operating period for each reactor.

With this approach, a total of 128 operating periods with varying riser gas velocities, J-valve fluidization, and reactor inventories were investigated, yielding a dataset containing data from more than 50 h of CFM operation.

### 2.5. Evaluation Parameters

In this section, the most important evaluation parameters utilized for assessment of the system hydrodynamics in the CFM and 1 MW<sub>th</sub> pilot plant are briefly introduced.

The gas velocity in each riser is calculated by correcting the measured norm volume flow with the average riser temperature ( $T_R$ ) and dividing it by the cross-sectional area of the riser:

$$u_0 = \frac{\dot{V}_n \cdot \frac{T_R}{T_\infty}}{A_R} \quad (1)$$

For the CFM, the norm volume flow was measured via orifice plates located upstream of the reactor inlet, whereas venturi measurements in the AR and FR product gas lines were used to calculate  $\dot{V}$  for the 1 MW<sub>th</sub> pilot plant.

The pressure drop over each riser was defined as the pressure difference between the lowermost (1) and uppermost (N) pressure sensor in each riser (see Tables 2 and 3):

$$\Delta p = p_1 - p_N \quad (2)$$

Using the pressure drop over each riser, the reactor inventory was calculated using the earth's gravity ( $g$ ) and the riser diameter ( $A_R$ ) via:

$$m_{inv.} = \frac{\Delta p \cdot A_R}{g} \quad (3)$$

The solids concentration at any given location inside the riser was calculated by assuming that the pressure drop between two measurement ports is solely induced by the fluidized solids, yielding [23]:

$$\varepsilon_{s,i} = \frac{(p_{i+1} - p_i)}{\rho_p \cdot g \cdot (z_{i+1} - z_i)} \quad (4)$$

The particle Reynolds number is calculated using the gas velocity, particle diameter, and gas data:

$$Re = \frac{u_0 \cdot d_p \cdot \rho_g}{\mu_g} \quad (5)$$

The Archimedes number for each solid-gas system is given by:

$$Ar = \frac{d_p^3 \cdot \rho_g \cdot (\rho_p - \rho_g) \cdot g}{\mu_g^2} \quad (6)$$



To be able to quantify the flow patterns of the particles at the riser outlet, the Stokes number is introduced:

$$Stk = \frac{d_p^2 \cdot \rho_p \cdot u_0}{18 \cdot \mu_g \cdot \frac{D}{2}} \quad (7)$$

Using the dimensionless numbers, the dimensionless particle diameter and velocity can be calculated via [23]:

$$d_p^* = Ar^{\frac{1}{3}} \quad (8)$$

$$u^* = \frac{Re}{Ar^{\frac{1}{3}}} \quad (9)$$

The terminal velocity of the particles inside the riser was calculated via [23]:

$$u_t = \left[ \frac{18}{d_p^{*2}} + \frac{2.335 - 1.744 \cdot \phi_s}{d_p^{*0.5}} \right]^{-1} \cdot \left[ \frac{\rho_g^2}{\mu_g \cdot (\rho_p - \rho_g) \cdot g} \right]^{-\frac{1}{3}}, \quad (10)$$

thus yielding the effective slip velocity of particles suspended in the gas stream [23]:

$$u_p = u_0 - u_t \quad (11)$$

The Reynolds number at minimum fluidization velocity of the ilmenite and bronze particles in the respective fluid was calculated by [23]:

$$Re_{mf} = \begin{cases} (28.7^2 + 0.0494 \cdot Ar)^{0.5} - 28.7, & \text{for } d_p^* < 50 \\ (33.7^2 + 0.0408 \cdot Ar)^{0.5} - 33.7, & \text{for } d_p^* \geq 50 \end{cases} \quad (12)$$

subsequently allowing for a direct calculation of the minimum fluidization velocity  $u_{mf}$  via Equation (5).

As a reference for the experimentally determined values, the saturation carrying capacity is calculated by the approach of Geldart et al. [53,54]:

$$G_s^* = 23.7 \cdot \rho_g \cdot u_0 \cdot e^{-5.4 \cdot \frac{u_t}{u_0}} \quad (13)$$

Furthermore, the approach by Breault et al. [38] is used:

$$G_s^* = 51 \cdot \frac{u_0^{0.19} \cdot d_p^{0.5}}{Ar^{1.2} \cdot D_R^{1.5}} \quad (14)$$

From the values of  $G_s^*$ , calculated via Equations (13) and (14), the solids concentration of a saturated gas stream can be calculated via:

$$\varepsilon_s^* = \frac{G_s^*}{\rho_p \cdot u_p} \quad (15)$$

On the basis of the data collected in the CFM, an equation for the calculation of the entrainment from the riser based on Equation (15), is formulated:

$$G_{s,calc} = \mathbb{P}_{ent} \cdot \varepsilon_{s,e} \cdot \rho_p \cdot u_p \quad (16)$$

Here,  $\mathbb{P}_{ent}$  signifies the entrainment probability of the particles at the top of the riser, either leaving the riser towards the cyclone or traveling back along the riser walls, which is

illustrated in Figure 4. A similar parameter called the backflow ratio ( $k_b$ ), was previously introduced by Pallares and Johnson [35]:

$$\mathbb{P}_{ent.} = \frac{\dot{m}_{oc,ent.}}{\dot{m}_{oc,top}} = \frac{\dot{m}_{oc,ent.}}{\dot{m}_{oc,ent.} + \dot{m}_{oc,back}} = \frac{1}{1 + k_b} \quad (17)$$

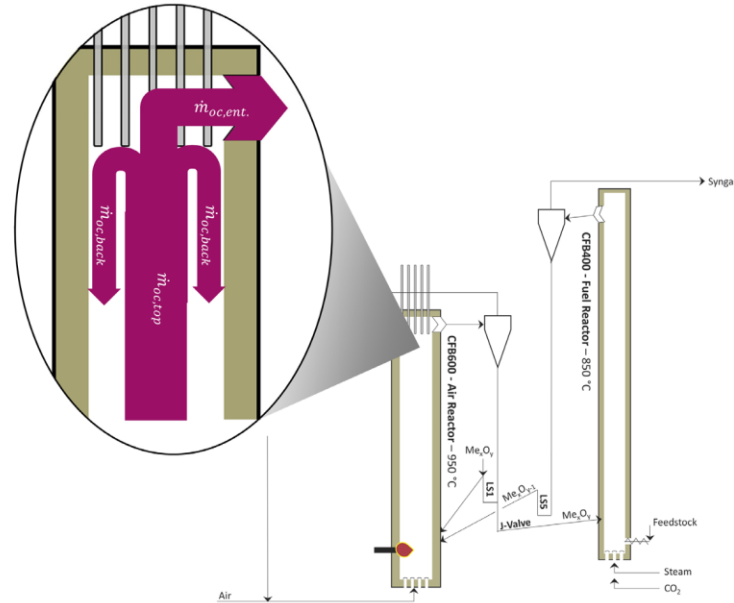


**Figure 4.** Schematic illustration of the path of solid particles at the top of the AR riser with an indication of the most important streams.

Secondly, the solid concentration at the reactor exit ( $\epsilon_{s,e}$ ) is introduced to be able to approximate the solids flow in the riser freeboard:

$$\epsilon_{s,e} = \left( \frac{\delta p}{\delta z} \right)_{FB} \cdot \frac{1}{g \cdot \rho_p} \quad (18)$$

Instead of only using the two uppermost pressure sensors to calculate the pressure gradient over the freeboard via Equation (4),  $\epsilon_{s,e}$  is approximated by calculating the slope of the pressure profile in the freeboard  $\left( \frac{\delta p}{\delta z} \right)_{FB}$  via a linear regression over the three topmost pressure sensors, thereby increasing robustness of the method. This approach thus builds on the findings of Chen et al. [34], who found a positive correlation between the pressure drop in the freeboard and solids entrainment from the riser.

Finally, the actual solid entrainment for the CFM is calculated using the change in height ( $\Delta Z_{meas.}$ ) of the solid bed accumulating inside the loop seal standpipe ( $A_{SP}$ ) during the measurement time ( $t_{meas.}$ ):

$$G_s^c = \frac{\rho_{bulk} \cdot A_{SP} \cdot \Delta Z_{meas.}}{t_{meas.} \cdot A_R} \quad (19)$$

On the other hand, the solid circulation in the 1 MW<sub>th</sub> CLG unit is calculated using the method described by Marx et al. [50], relying on an oxygen balance around the AR and the oxidation degree of solid samples collected from each loop seal:

$$G_s^h = \frac{\dot{m}_{O,in,AR} - \dot{m}_{O,out,AR}}{(X_{S,AR} - X_{S,FR}) \cdot R_{OC} \cdot A_R} \quad (20)$$

From both values, the actual entrainment mass flow can be calculated by:

$$\dot{m}_{ent.} = G_S \cdot A_R \quad (21)$$

## 2.6. Material Characterization

Solid materials collected from both loop seals (see Tables S1–S3 in the Supplementary Material) were analyzed using different lab techniques in order to allow for the subsequent calculation of important evaluation parameters (see Section 2.5).

### 2.6.1. Particle Size Distribution (PSD) and Mean Particle Diameter

The particle size distribution of the fresh materials and solid loop seal samples collected during operation from the 1 MW<sub>th</sub> unit was determined according to the norm DIN66165, using an air jet sieve type LS200-N by the company Hosokawa Alpine AG (Augsburg, Germany). Each PSD was determined singularly. Based on the measured PSD, integral parameters, such as the mean particle diameter, were calculated for each bulk material.

### 2.6.2. Bulk Density

Bulk densities for fresh materials and solid samples were determined using a self-made setup conforming to the norm ISO 697 [55]. Values were determined in triplicates.

### 2.6.3. Particle Density

Particle densities for fresh materials and solid samples were determined according to the norm DIN EN ISO 1183 [56], using water pycnometry in calibrated 25 and 50 mL pycnometers by Carl Roth (Karlsruhe, Germany). Prior to the measurements, the pycnometers were recalibrated using water at room conditions. During pycnometry, water temperatures were measured to account for the impact of changing room temperatures on water densities. All values were determined in duplicates. In case of strong deviations (>15%) for two corresponding values, a third value was determined.

### 2.6.4. Oxidation Degree

In chemical looping, the oxidation degree ( $X_s$ ) of the OC is generally given by [57,58]:

$$X_{s,i} = \frac{m_{OC,i} - m_{OC,red}}{R_{OC} \cdot m_{OC,ox}} \quad (22)$$

Here,  $m_{OC,red}$  and  $m_{OC,ox}$  are the mass of an OC sample in a fully reduced and oxidized state, respectively, while  $m_{OC,i}$  is the mass of the OC sample in its current state.

In the current study, the oxidation degree of the solid samples collected from the 1 MW<sub>th</sub> pilot plant was determined using the method by Marx et al. [50]. Here, the mass of loop seal samples before ( $m_{LS,1}$ ) and after ( $m_{LS,2}$ ) oxidation in a laboratory oven as well as the carbon content ( $w_{C,LS,fine}$ ) determined in an elemental analyzer are used to calculate the oxidation degree of the OC:

$$X_{s,i} = \frac{m_{LS,1} \cdot (1 - w_{C,LS,fine}) - m_{LS,2} \cdot (1 - R_{OC})}{R_{OC} \cdot m_{LS,2}} = 1 - \frac{m_{LS,2} - m_{LS,1} \cdot (1 - w_{C,LS,fine})}{R_{OC} \cdot m_{LS,2}} \quad (23)$$

The calculated values for  $X_s$  can then be utilized to determine the solid circulation via Equation (20).

### 3. Scaling Theory

The cold flow model of the 1 MW<sub>th</sub> pilot plant constitutes a scaled-down version of the 1 MW<sub>th</sub> CLG reactor system [18], with a scaling factor of 0.3624:

$$L_{sc} = \frac{H^c}{H^h} = \frac{D^c}{D^h} \quad (24)$$

To be able to select suitable boundary conditions for scaling, the simplified set of scaling laws by Glicksman et al. [41] was used:

$$\frac{u_0^2}{g \cdot D}, \frac{\rho_p}{\rho_g}, \frac{u_0}{u_{mf}}, \frac{G_s}{u_0 \cdot \rho_p}, \frac{H}{D}, \phi_p, PSD \quad (25)$$

Here, the individual dimensionless numbers signify the Froude number, the solid-gas density ratio, the ratio between gas velocity and minimum fluidization velocity, the dimensionless particle entrainment, the geometrical ratio, the particle sphericity and the particle size distribution, in that order.

To allow for model scaling, the data for the 1 MW<sub>th</sub> CLG unit was firstly compiled. For the particle data, figures for ilmenite used during chemical looping combustion operation were adapted from literature [59,60]. For gas properties (density and viscosity), temperatures and gas composition from estimated heat and mass balances for CLG operation were utilized [24]. Lastly, for the solid circulation, gas velocities, and pressure drops in the 1 MW<sub>th</sub> CLG unit, data from previous CLC experiments conducted in the 1 MW<sub>th</sub> unit were taken as a reference [51,52]. These figures are summarized in Table 5. Subsequently, gas density and viscosity for the CFM were calculated, for ambient pressure and temperature for air. In a last step, a suitable bed material, fulfilling the dimensionless parameters from Equation (25) as closely as possible, had to be determined. Ultimately, bronze powder with an average particle diameter of 57 μm, fulfilling the given criteria to the greatest extent, while also allowing for economically viable and safe operation, was chosen. To calculate the dimensionless groups for the 1 MW<sub>th</sub> CLG unit and the CFM,  $u_0$ ,  $G_s$ , and  $\Delta p$  for the CFM were calculated via:

$$u_0^c = \sqrt{L^{sc}} \cdot u_0^h \quad (26)$$

$$G_s^c = G_s^h \cdot \sqrt{L^{sc}} \cdot \left( \frac{\rho_p^c}{\rho_s^h} \right) \quad (27)$$

$$\Delta p^c = L^{sc} \cdot \Delta p^h \cdot \left( \frac{\rho_p^c}{\rho_s^h} \right) \quad (28)$$

**Table 5.** Design parameters of a cold flow model (°) and 1 MW<sub>th</sub> pilot plant (h).

Parameter	Unit	AR <sup>h</sup>	AR <sup>°</sup>	FR <sup>h</sup>	FR <sup>°</sup>
<i>D</i>	[mm]	590	213	400	144
<i>H</i>	[mm]	8660	4113	11,350	3138
<i>d<sub>p</sub></i>	[μm]	154	56	154	56
<i>ρ<sub>p</sub></i>	[kg/m <sup>3</sup> ]	3710	8710	3710	8710
<i>φ<sub>p</sub>**</i>	[-]	0.7	0.7	0.7	0.7
<i>ρ<sub>g</sub></i>	[kg/m <sup>3</sup> ]	0.297	1.164	0.239	1.164
<i>μ<sub>g</sub></i>	[Pa s]	4.74 × 10 <sup>-5</sup>	1.86 × 10 <sup>-5</sup>	4.34 × 10 <sup>-5</sup>	1.86 × 10 <sup>-5</sup>
<i>u<sub>0</sub></i>	[m/s]	3.0–4.5	1.8–2.7 *	5.0–6.5	3.0–3.9 *
<i>G<sub>s</sub></i>	[kg/s m <sup>2</sup> ]	10.2–14.2	14.2–20.1 *	22.1–30.9	30.9–40.7 *
<i>Δp</i>	[mbar]	50–70	43–60 *	60–100	51–85 *

\* Data for CFM estimated using simplified scaling laws by Glicksman (see Equation (25)). \*\* Sphericity for both particle types estimated.

A derivation for these expressions is provided in Appendix A.

By using the numbers listed in Table 5, one can thus calculate the dimensionless numbers for the 1 MW<sub>th</sub> unit and the CFM, summarized in Table 6. The quotient of the Froude number can be set to unity for both reactors by adjusting the (scaled) gas velocity accordingly. For the quotient of the density ratios, a value of 0.43 is obtained for AR and FR. This deviation can mainly be related to the fact that material selection for the CFM is limited, while the density of air at ambient conditions is significantly higher than that of the AR and FR product gases during CLG operation. For the quotient of the velocity ratio, similar values (i.e., around 0.4) are obtained, which again be related to material selection. (Minimum fluidization velocities were calculated, using solid and gas phase data via Equations (5) and (12)). Values closer to unity would be obtained for a denser material or a material with a larger particle diameter for the given particle density. While the former is not possible for safety and/or economic reasons, the latter would lead to a deviation for other dimensionless parameters listed in Equation (25). However, it was found in the literature that good scaling agreement was obtained even when the density ratio was not considered for CFB scaling [26]. However, it has to be noted that due to the difference in density ratios, the bronze powder falls onto the Geldart A/B transition regime, whereas the ilmenite powder is Type B, increasing overall uncertainty [42]. The quotient for the fourth dimensionless group, the dimensionless entrainment, is equal to one, as it is expected that the entrainment ( $G_s$ ) follows the scaling laws. The geometric similitude is given for both risers, which can be seen when considering the height/diameter ratios listed in Table 6. Finally, another dimensionless group previously used in the literature [20,43], which relates the mean particle and reactor diameter, is also provided in Table 6, as it yields the possibility of quantifying to which extent the PSDs in the hot and cold unit match one another. As visible from the figures presented in Table 6, excellent agreement is also attained for this dimensionless group for the 1 MW<sub>th</sub> unit and the CFM. This can be explained by the fact that the Bronze powder used for experiments in the CFM was selected in such a way that its PSD closely matches that of the ilmenite utilized for CLG operation in the 1 MW<sub>th</sub> unit, which is also visible in Figure 5. (Due to prior experience with chemical looping operation in the 1 MW<sub>th</sub> pilot plant [21,51,52], the effect of continuous operation on the PSD could be considered here, i.e., the PSD of the bronze powder was tuned in such a way that it matches used ilmenite particles, as opposed to the fresh material, subsequently yielding a better comparability of the resulting data).

Upon consideration of the data provided in Table 6, it can thus be summarized that a good agreement between the dimensionless parameters of the 1 MW<sub>th</sub> unit and the cold flow model is attained. Hence, the similitude of the governing hydrodynamic phenomena in the two reactor setups can be assumed. Thus, qualitative and quantitative scaling of the results obtained in the CFM to 1 MW<sub>th</sub> scale is deemed viable.

**Table 6.** Dimensionless groups for cold flow model (<sup>c</sup>) and 1 MW<sub>th</sub> pilot plant (<sup>h</sup>).

Expression	AR <sup>h</sup>	AR <sup>c</sup>	AR <sup>h</sup> /AR <sup>c</sup>	FR <sup>h</sup>	FR <sup>c</sup>	FR <sup>h</sup> /FR <sup>c</sup>
$\frac{u_0^2}{g_s D}$	2.12	2.12	1.00	9.80	9.86	0.99
$\frac{\rho_p}{\rho_g}$	$1.55 \times 10^4$	$3.64 \times 10^4$	0.43	$1.55 \times 10^4$	$3.64 \times 10^4$	0.43
$\frac{u_0}{u_{mf}}$	317.46	835.14	0.38	515.11	1479.39	0.35
$\frac{G_s}{u_0 \rho_p}$	$1.10 \times 10^{-3}$	$1.10 \times 10^{-3}$	1.00	$1.35 \times 10^{-3}$	$1.35 \times 10^{-3}$	1.00
$\frac{H}{D}$	14.15	14.21	1.00	28.38	28.56	0.99
$\frac{D}{d_p}$	3831.2	3750.0	1.02	2597.4	2535.2	1.02

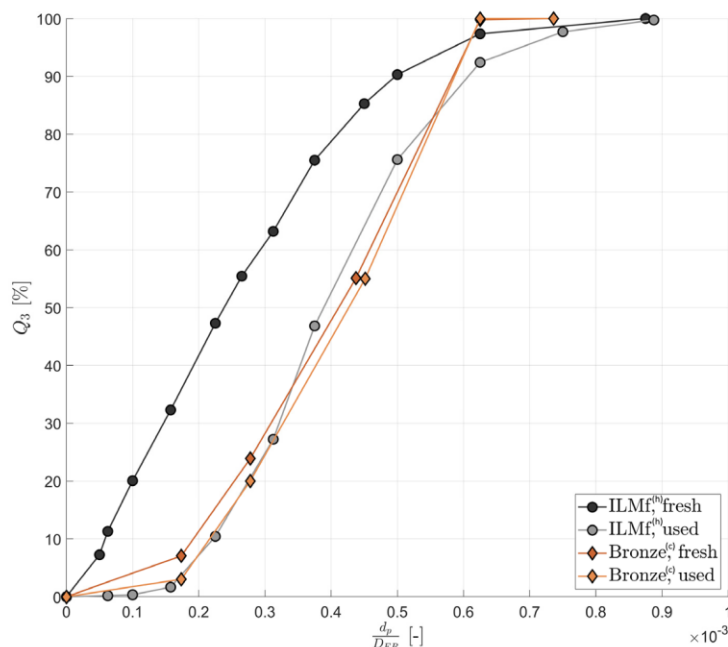


**Figure 5.** Cumulative dimensionless particle size distribution (PSD) for ilmenite <sup>(h)</sup> and bronze <sup>(c)</sup> powder.

#### 4. Results and Discussion

Using data from the cold flow model as well as from the 1 MW<sub>th</sub> pilot plant, the overall hydrodynamic behavior of the coupled dual fluidized system will firstly be evaluated in Section 4.1. Subsequently, the effect of the most important boundary conditions and operating variables on solid entrainment from both reactors in the cold and hot system will be investigated in Section 4.2 before a novel approach to predict solids entrainment solely on pressure and temperature measurements will be presented in Section 4.3.

##### 4.1. Hydrodynamic Behavior of Dual Circulating Fluidized Bed Reactor System

Obtaining a basic understanding of the hydrodynamic behavior of the dual-fluidized bed system is key when attempting to optimize CLG operation. In this Section, the extensive dataset determined in the CFM will first be used to derive a ground set of operating rules for the dual-fluidized bed reactor system in Section 4.1.1 before its applicability in the 1 MW<sub>th</sub> pilot plant will be demonstrated in Section 4.1.2.

##### 4.1.1. Operating Rules for Dual Circulating Fluidized Bed Reactor System

Before launching into the details of the hydrodynamic behavior of the dual-fluidized system, its reactor setup will first be explained in detail in the following, thus allowing for a subsequent in-depth investigation of system hydrodynamics.

As explained in Section 2.1, the AR is equipped with an internal solid recycle (blue color in Figure 6), which means that material entrained from the AR can be directly recycled back to it via LS1, so that changes in the FR hydrodynamics do not require a direct adjustment in hydrodynamic boundary conditions in the AR, thereby stabilizing system hydrodynamics. The material not traveling back to the AR is transported to the FR via the J-valve (green color in Figure 6). Here, the amount of material entering the FR through it can be adjusted by changing the amount of gas (N<sub>2</sub> or CO<sub>2</sub>) used for J-valve fluidization [51]. When considering all solid streams inside the reactor system, it can be

summarized that the entrainment from the AR ( $\dot{m}_{s,AR}$ , purple color in Figure 6) constitutes the baseline for solid circulation, meaning that in order to obtain stable hydrodynamics, material transport through the J-valve ( $\dot{m}_{s,J-Valve}$ ) has to be smaller or equal to it. If not, more material is extracted from LS1 than enters it, and LS1 (slowly) empties. Secondly, the entrainment from the FR ( $\dot{m}_{s,FR}$ ) and the material transport through the J-valve have to be equal so that the reactor inventory of the FR remains constant:

$$\dot{m}_{s,AR} \geq \dot{m}_{s,J-Valve} = \dot{m}_{s,FR} = \dot{m}_{OC} \quad (29)$$

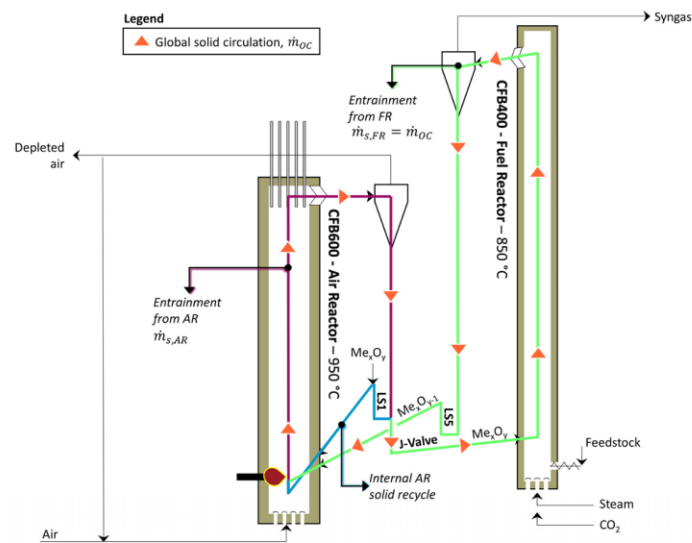


**Figure 6.** The layout of reactor system of the 1 MW<sub>th</sub> pilot plant with an indication of different solid streams cycling through the system.

The most efficient CLG operation is attained when entrainment from the FR is similar to entrainment from the AR, (Due to its smaller cross-sectional area, specific elutriation rates (given in kg/m<sup>2</sup> s) have to be higher for the FR when compared to the AR, which generally means that higher gas velocities are necessary inside the FR). i.e., internal circulation from LS1 to the AR is minimal, as internal material circulation does not contribute positively towards heat or oxygen transport between the AR and FR. While material transport through the J-valve is primarily dependent on the amount of fluidization medium used for its fluidization [51], entrainment from both CFBs positively correlates with two independent operating variables. Firstly, entrainment increases with gas velocity, as more particles are carried with the gas streams at higher gas velocities and hence leave the reactor [27]. Secondly, entrainment was found to increase with increasing reactor inventory. This finding can be explained by the fact that at higher reactor inventories, the height of the dense zone in the CFB increases [27] and hence the distance from the top of the dense zone to the reactor decreases, making it easier for particles to be entrained from the riser. Moreover, even for CFBs with heights greater than the transport disengaging height (TDH), i.e., the height above which the solids concentration does not change with increasing height, entrainment was found to increase, which is attributed to the fact that bubble diameters in the dense bed increase with increasing reactor inventories, favoring solid entrainment [27] (more details see Section 4.2).

This underlying behavior of solid entrainment ultimately leads to a self-stabilization of the hydrodynamic system, which is best illustrated when investigating how it behaves during abrupt changes in the hydrodynamic boundary conditions. Since those are rarely

observed in a large, continuously operated unit, where smooth operation is key, Figure 7 shows the hydrodynamic behavior of the scaled CFM during externally induced transient periods. (Despite the difference in temperature in scale and temperature, the underlying hydrodynamics in the cold flow model and the 1 MW<sub>th</sub> pilot plant are equal. As rapid changes in the boundary conditions are easily realizable in the cold flow unit, it is thus used for the following elucidations).

Firstly, Figure 7a shows how the cold flow model reacts to an abrupt increase in the AR gas velocity. While the reactor pressure drop in the AR decreases, it increases in the FR, which means that a fraction of the reactor inventory is shifted from the AR to the FR. This can be explained by the fact that the solid hold-up in the AR riser decreases with increasing  $u_0$  and, as the total solid inventory of the reactor system is constant, a slight increase in the pressure drop of the FR can be observed. Due to the difference in reactor diameters ( $A_{R,AR} > A_{R,FR}$ ), changes in reactor pressure drop are always more pronounced for the FR than for the AR (see Equation (3)). Apart from the lower solid hold-ups in the AR, larger gas velocities lead to an increase in the entrainment rates for the AR. Yet, as the global solid circulation is only marginally increased, (The increase in global solid circulation arises from the fact that the pressure drop over the J-valve and the inventory in the FR increase, leading to an increase in material throughput through the J-valve and entrainment from the FR, respectively (see Figure 8)). since the fluidization of the J-valve is not altered, the excess entrained from the AR is reintroduced into the AR via LS1, which means that the internal AR circulation rate increases, leading to a stabilization of the overall system. Lastly, as the reactor inventory in the FR increases slightly, while the gas velocity is kept constant, it can be concluded that the global solid circulation rate increases slightly.

The impact of changes in the gas velocity of the FR is illustrated in Figure 7b. Here, a sudden increase in  $u_0$  leads to a rapid decrease in the pressure drop of the FR, whereas the AR pressure drop increases, as more material is entrained from the FR than enters it via the J-valve, leading to lower solid inventories inside the FR. Yet, due to this decrease in the FR inventory, entrainment from the FR decreases, as also observed by Alghamdi et al. [47]. This ultimately results in a stabilization of the system at a higher global circulation rate (i.e.,  $\dot{m}_{s,J-Valve} = \dot{m}_{s,FR}$ ). This also means that solid throughput through the J-valve is increased, which can be attributed to a higher pressure difference from LS1 to the FR bed, resulting in higher material transport rates (more details see Appendix B.1). On the other hand, entrainment from the AR slightly increases, as the reactor inventory increases. Consequently, the internal recycle of the AR tends to decrease slightly as the increase in entrainment from the AR generally is lower than the increase in material throughput via the J-valve. Hence, it has to be safeguarded that solid entrainment from the AR is sufficient, before increasing gas velocities in the FR, to prevent an emptying of LS1 (see also Figure 8).

When fluidization velocities are altered for the J-valve, material transport to the FR is altered, which is shown in Figure 7c. Here, an increase in fluidization of the J-valve, leading to a higher material transport rate to the FR, ultimately results in an increase in  $\Delta p$  for the FR. Due to the larger reactor inventory, the entrainment rate from the FR gradually increases until steady state (i.e.,  $\dot{m}_{s,J-Valve} = \dot{m}_{s,FR}$ ) is reached at a higher global circulation rate. For the AR, an increase in J-valve fluidization results in a decrease in reactor inventory as more material is directed into the FR. Consequently, the entrainment rate from the AR decreases, leading to another reason for the internal recycling of the AR to drop (apart from the higher throughput via the J-valve). Hence, an increase in J-valve fluidization is another measure that can only be carried out without jeopardizing system stability when safeguarding sufficient entrainment from the AR.



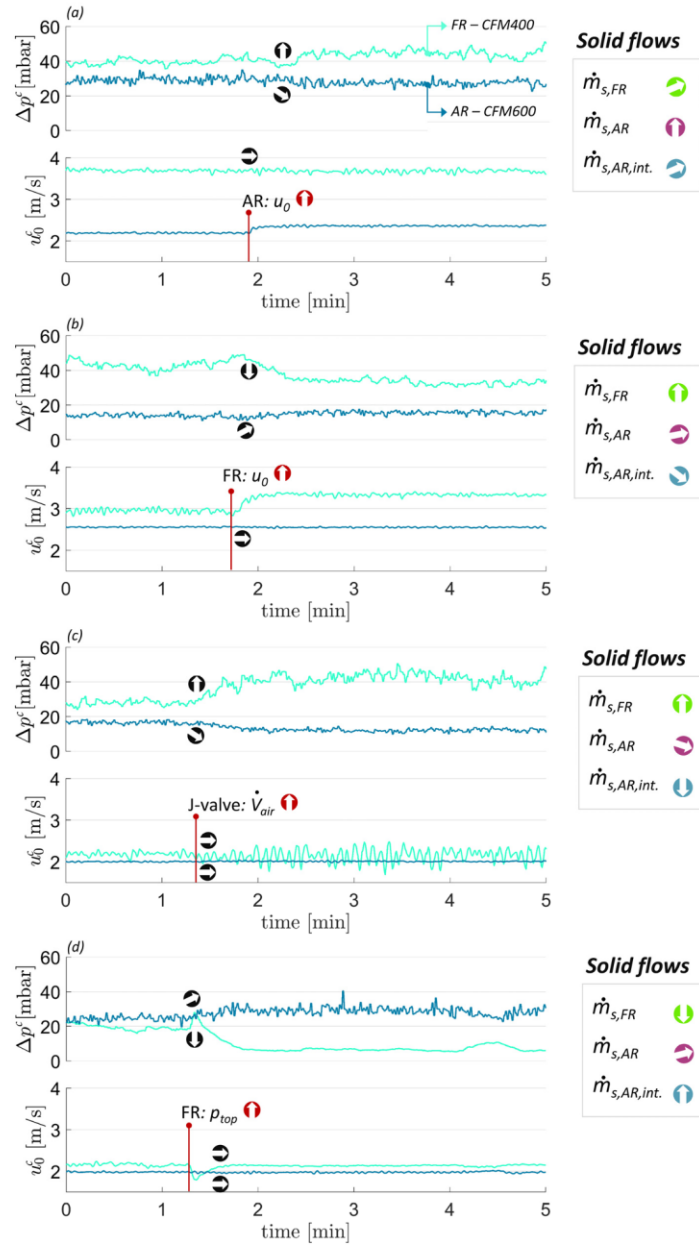


**Figure 7.** Response of dual circulating fluidized bed reactor system to alterations in the hydrodynamic boundary conditions. Time series on the left show the changes in gas velocity and pressure drop for AR and FR of the CFM filled with bronze powder. Illustrations on the right show the change in solid circulation. (a) Increase in AR gas velocity, (b) Increase in FR gas velocity, (c) Increase in J-valve fluidization, and (d) Increase in pressure at the top of FR riser. Colors for the arrows indicating changes in the solid flow rates relate to the coloration of the solid stream in Figure 6.

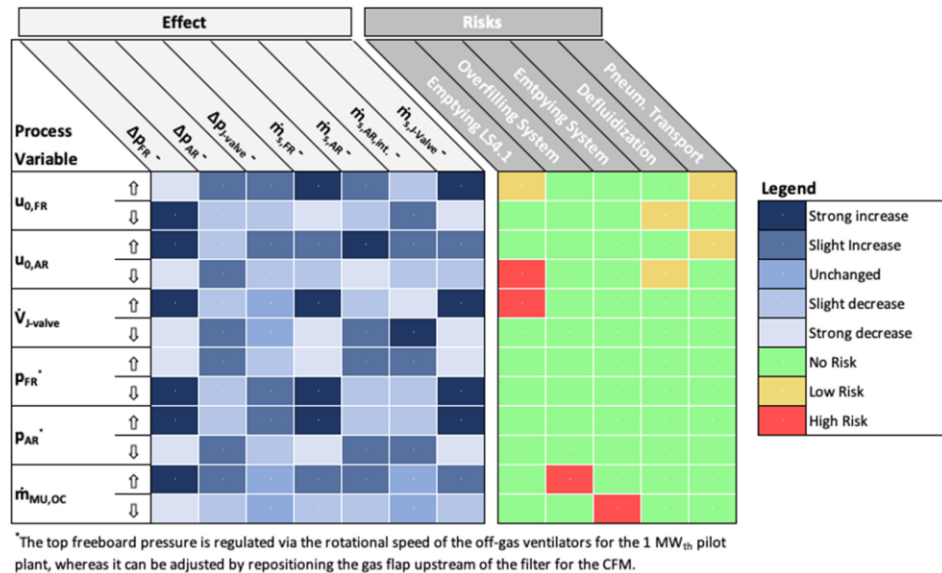


**Figure 8.** Overview of ground-set of rules to adapt hydrodynamic conditions in the dual-circulating fluidized bed reactor system.

Finally, the overhead pressures of the two reactors can be varied independently in the 1 MW<sub>th</sub> pilot plant, (For the CFM, overhead pressures can be adjusted by repositioning the gas flap upstream of the filter). opening the question of how a change in the absolute pressure in one of the reactors alters system hydrodynamics. Figure 7d illustrates how a sudden increase in the overhead pressure of the FR affects hydrodynamics in the CFM. Clearly, FR reactor inventories decrease while AR reactor inventories increase, which can be explained by the fact that the material throughput through the J-valve decreases as the acting pressure over the J-valve is reduced. Consequently, the global solids circulation decreases measurably, while a slight increase in entrainment from the AR entails, thus leading to a significant increase in the internal solids recycled from LS1. Therefore, system hydrodynamics also restrict the extent to which the overhead pressures in the AR and FR can vary, potentially leading to insufficient global solid circulation rates in case of too high FR overhead pressures or an uncontrolled emptying of LS1 towards the FR via the J-valve in case of too high AR overhead pressures.

From the observations explained in detail above, it can thus be summarized that, within given boundaries (e.g., operating range of a CFB), the hydrodynamics of the dual fluidized bed system constitute a self-regulating system. This means that although a change in one variable (e.g.,  $u_{0,FR}$ ) impacts multiple other variables (e.g.,  $\Delta p_{FR}$ ,  $\Delta p_{AR}$ ,  $\dot{m}_{s,FR}$ ), a new stable operating point is found. At this new operating point, circulation rates might be different from before, yet the solid flows entering and leaving the CFB are equal for each of the two CFBs, leading to a stabilization of the system. This behavior is schematically illustrated in Figure 9. Consequently, a free variation of each process variable is possible when considering the following points:

- LS1 must not be emptied, i.e., material entrainment from the AR has to exceed material throughput through the J-valve (see Equation (29)).
- Generally, both reactors have to be operated above the minimum fluidization velocity of the utilized bed material to avoid defluidization. For the given reactor setup, the lower limit for the lower gas velocity is even more stringent, with  $u_0$  having to exceed the terminal velocity of the bed material to attain meaningful solid circulation.

- The gas velocity has to be restricted to prevent complete emptying of the CFB, which would constitute pneumatic transport and hence sub-optimal heat and mass transfer rates inside the CFB.
- The overall reactor inventory should be sufficient to prevent complete emptying of the CFB and should not exceed the maximum holding capacity of the system, which could entail (fluidization) issues during operation.
- The pressure gradient between the overhead pressures should not rise to excessive values, which would lead to disturbances of controlled solid transport between AR and FR and/or pneumatic material transport through the loop seals.

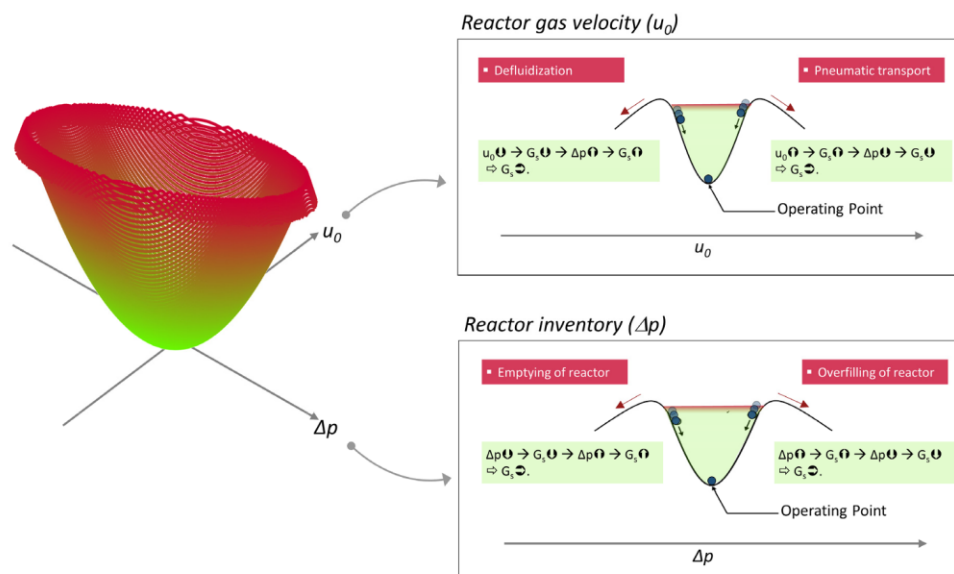


**Figure 9.** Schematic illustration of the self-regulating hydrodynamic system of 1 MW<sub>th</sub> CLG unit. Changes in one variable (e.g.,  $u_0$ ) align with a counter-acting change in another variable (e.g.,  $\Delta p$ ), leading to the finding of a new stable operating point.

Based on the behavior illustrated in Figure 7 and using the insights gathered from the operation of the scaled cold flow model, a ground-set of rules, summarized in Table 6, can thus be deduced for the operation of the dual-fluidized bed reactor system. Here, it becomes obvious that although each operator intervention comes with multiple side effects due to hydrodynamic system entanglement, dedicated measures to freely vary each important hydrodynamic process parameter exist, meaning that targeted and precise operator interventions are possible.

#### 4.1.2. Comparison of Different Operating periods in Cold Flow Model and 1 MW<sub>th</sub> Pilot Plant

Using the basic operating rules developed in Section 4.1.1, 128 stable operating periods with varying boundary conditions were investigated in the CFM (more details see Section 2.4.2). As shown in Figure 10, a clear correlation between gas velocities and reactor pressure drops is visible for the AR. This can be explained by the fact that due to the internal recycling, the AR effectively functions as a solids reservoir. Here, the solid holdup in the riser decreases in case of increased gas velocities as the bed material is moved to the FR and the coupling elements (LS1 and LS5). Moreover, it is visible that in case of higher total reactor inventories, (Here, the total riser inventory  $\text{minv}_{\text{tot}}$  signifies the sum of  $\text{minv}_{\text{AR}}$  and  $\text{minv}_{\text{FR}}$ , i.e., the sum of the mass of the material located inside both risers

for a given operating period. The material located in the loop seals is not considered here), and riser inventories in the AR increase. On the other hand, similarly, clear-cut trends are not observable for the FR. This is related to the fact that the reactor inventory in the FR is not primarily governed by its gas velocity but can be starkly altered via changes in AR hydrodynamics (see Section 4.1.1), thus allowing for both high and low reactor inventories for a given subset of  $u_{0,FR}$  and  $m_{inv,tot}^c$ . Nonetheless, it is clearly visible that similar to the AR, higher riser inventories are attainable inside the FR at higher total inventories, even at high gas velocities. Consequently, the given reactor setup features great flexibility in terms of FR riser inventories, with stable operating points being attainable at pressure drops from 10 to above 70 mbar. In terms of reactor pressure fluctuations, it is visible that standard deviations of the measured pressure drop increase with reactor inventories for both reactors, as bubble coalescence occurs to greater extents [27], thus leading to higher fluctuations in the measured pressure signals upon bursting of the bubbles at the surface of the dense bed.

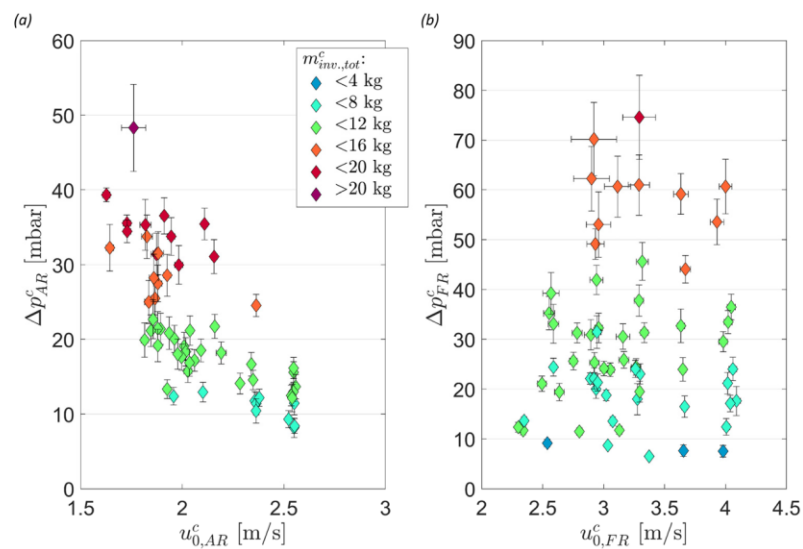


**Figure 10.** Reactor inventory (pressure drop) as a function of the gas velocity for selected operating periods in AR ((a)  $20 \text{ mbar} < \Delta p_{FR} < 40 \text{ mbar}$ ) and FR ((b)  $5 \text{ mbar} < \Delta p_{AR} < 20 \text{ mbar}$ ) from the cold flow model operated with bronze powder (see Table S4).

Due to the similarity of the systems, general trends derived for the cold flow model can also be observed when comparing the hydrodynamic boundary conditions for different stable operating periods obtained in the  $1 \text{ MW}_{th}$  pilot plant. Figure 11 shows the pressure drops for the AR and FR for varying gas velocities for different total riser inventories, attained during the first test campaign (K1). It is clearly visible that for both reactors, the pressure drop decreases for higher gas velocities. As explained before, this can be attributed to the fact that as gas velocities are increased, the solid holdup is decreased, and more material is entrained from the riser. Hence, the reactor inventory decreases until a new steady state is obtained (see Figure 7). As explained above, the coupling of both reactors leads to the fact that a decrease in  $u_0$  in one reactor entails an increase in  $\Delta p$ , whereas  $\Delta p$  behaves inversely for the other reactor, as the overall reactor inventory is maintained constant. Consequently, the riser inventory can be altered in one reactor by changing the gas velocity in the other for a given total reactor inventory. One example of this is the operating periods BP3-1 and BP6-11, marked Figure 11 for which the total riser inventory in both reactors amounts to approx. 170 kg. Although the gas velocities are similar for

both operation points for the AR, reactor inventories vary strongly. This is the case as for BP3-1, gas velocities in the FR are significantly higher than for BP6-11, and hence the solid holdup in the FR is lower for the former. Consequently, riser inventories are higher for BP3-1 in the AR. Another important finding which can be derived from the dataset visualized in Figure 11 is that varying total riser inventories are realizable by changing the total amount of OC present inside the system (e.g., the total reactor inventory can be increased by increasing the OC make-up rates beyond those required to achieve stable reactor inventories for a given period of time). As shown in Figure 11, total riser inventories between 120 and 290 kg were obtained during the test campaign for the operating periods under consideration. When comparing the operating periods BP9-10 and BP10-7, marked in Figure 11, it is visible that for the latter higher riser inventories were obtained at similar gas velocities in both reactors by increasing the total riser inventory from 191 kg to 224 kg. Generally, larger riser inventories are desired, especially in the FR, as they increase solid residence times for a given solid circulation rate and thereby enhance char and volatile conversion [21]. This means that OC make-up rates should be adjusted in such a way that riser inventories do not drop below given threshold values, at which sufficiently long residence times are attained.

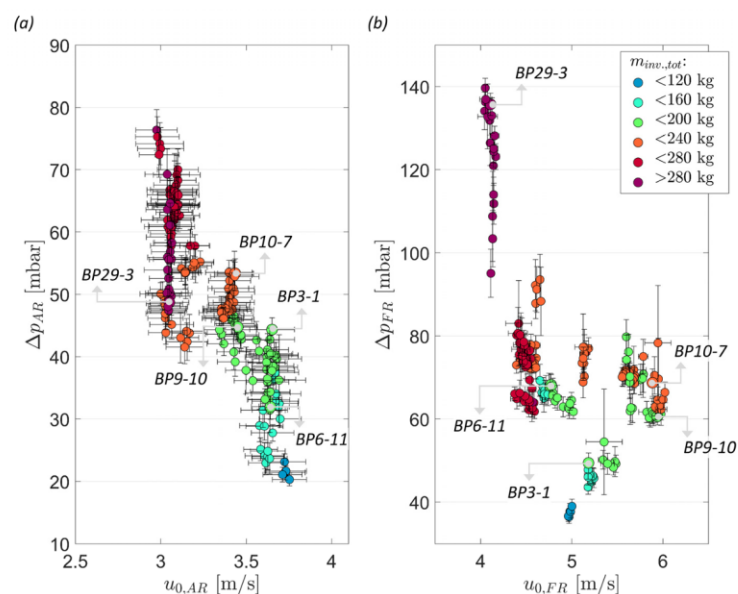


**Figure 11.** Reactor inventory (pressure drop) as a function of the gas velocity in AR (a) and FR (b) for all operating periods from K1 (see Table S1). Grey lines and arrows guide the eye.

For BP29 in K1, a maximization of FR inventories was targeted to boost solid residence times by increasing the total reactor inventory and operating the FR at comparably low gas velocities. One example of this is operating period BP29-3, highlighted in Figure 11. However, during this operating period, it was observed that the FR exhibited strongly fluctuating pressures in the lower sections of the riser. This can be attributed to the fact that due to the stronger coalescence of bubbles in the taller and denser fluidized bed at these high reactor inventories, bubble diameters reach sizes close to the reactor diameter and hence the fluidization regime can switch from turbulent to slugging [44]. Therefore, there exists an upper threshold to which values of the total reactor inventories can be increased while at the same time allowing for stable system hydrodynamics. Moreover, as elaborated before, material throughput through the J-valve decreases as the pressure gradient from AR to FR increases, making attaining high solid circulation rates more difficult at excessively high

FR reactor inventories. (Additionally, it has to be noted that at higher reactor inventories sealing requirements intensify, which can lead to operational issues. One example of this is the solid feeding system of the FR, which has to be pressurized to higher pressures to avoid syngas backflow into the dosing container as FR inventories are increased).

The effect of bed material characteristics on system hydrodynamics can be further evaluated when comparing operating periods from the three different test campaigns, for which particle diameters in the 1 MW<sub>th</sub> unit varied distinctly (for bed material properties please refer to Tables S1–S3 in the Supplementary Material). (For K2 larger OC particle diameters were attained due to the utilization of coarser Ilmenite (ILMc), while for K3 feedstock-related agglomeration led to an increase in average particle size in the CLG system). Figure 12 shows that in the case of larger particle diameters (K2-triangles and K3-squares), the dual fluidized bed system was operated at visibly higher gas velocities, necessary to achieve the required global solid circulation (more details see Section 4.2). Apart from this observation, the data points fall along the previously explained trends, highlighting that the general operational rules apply regardless of the characteristics of the utilized bed material, albeit the exact boundary conditions to reach the desired operational window will vary.

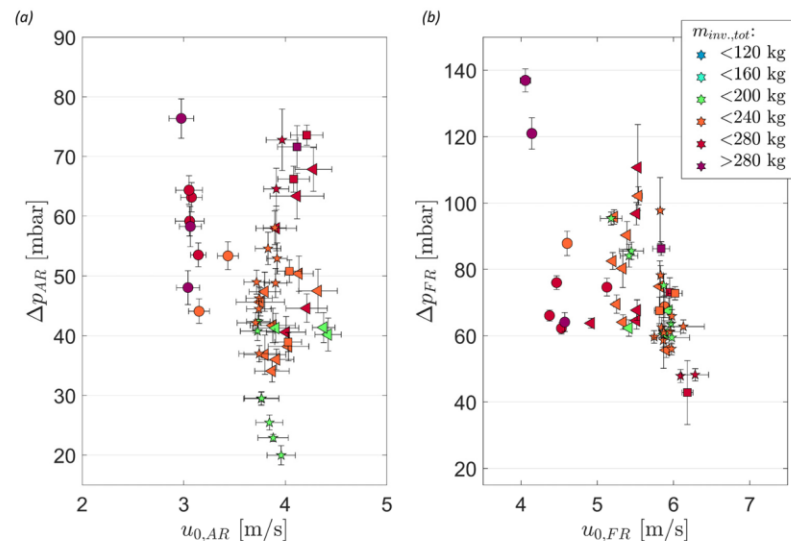


**Figure 12.** Reactor inventory (pressure drop) as a function of the gas velocity in AR (a) and FR (b) for selected 1 MW<sub>th</sub> pilot plant operating periods. K1 (circles, see Table S1), K2 (ILMc-triangles, ILMf-pentagrams, see Table S2), and K3 (squares, see Table S3).

Further insights into system hydrodynamics can be made by in-depth analyses of individual operating periods. One such example is presented in Figure 13, showing pressure profiles for AR and FR for the CFM and the 1 MW<sub>th</sub> pilot plant for two comparable operating periods (see Table 7). For each setup, both reactors show typical CFB pressure profiles, with pressures decaying exponentially with reactor height, as the solid holdup decreases [44]. As shown in Figure 13b, a relatively short, dense bed with a height of approx. 200 mm was obtained for the FR (1 MW<sub>th</sub>) at these boundary conditions, meaning that the feedstock is fed onto the top of the dense bed by the feedings screw, located at a height of around 350 mm. This is related to the fact that relatively high gas velocities (5.5–7 m/s) are necessary in the FR in order to achieve the required solid entrainment from the riser of the CFB. Moreover, the conical shape of the FR in the lower part reinforces this behavior as gas velocities exceeding 10 m/s are attained in the lower reactor sections, further impeding

significant solid holdups in the lower sections for the FR [36]. On the other hand, the dense bed in the AR is higher (see Figure 13a), reaching a height of approx. 500 mm, despite the lower reactor inventory for the AR due to the slower gas velocities in the AR and the purely cylindrical shape of it. Similar observations can be made when considering the profiles obtained for the CFM (see Figure 13c,d), showing a good agreement with the 1 MW<sub>th</sub> data. In terms of freeboard pressures, both reactors show an exponential decay of the solids concentration above the dense bed with only marginally decreasing solid concentrations being obtained above around one-third of their height, signifying the typical behavior for tall CFBs [44]. This consequently allows for a determination of the solids concentration at the reactor outlet ( $\epsilon_{s,e}$ ), via Equation (18) using the three uppermost pressure transmitters in each riser. For the CFM as well as the 1 MW<sub>th</sub> pilot plant values for  $\epsilon_{s,e}$  between 0.005 and 0.007 were obtained for the operating periods under investigation. (As this parameter is dimensionless, scaling is not necessary when transferring between the CFM and the 1 MW<sub>th</sub> pilot plant). Generally, slightly higher values are obtained for the AR than for the FR for both setups, despite the lower gas velocities present inside the AR, showing the effect of reactor height on solids concentration at the reactor outlet. While a good agreement is attained for  $\epsilon_{s,e}$  for the FR for the CFM and the 1 MW<sub>th</sub> pilot plant, the difference in  $\epsilon_{s,e}$  for the AR can be related to the visible discrepancy in (scaled) gas velocities between the two selected operating periods (see Table 7). Nonetheless, the results illustrated in Figure 13 demonstrate that in the case of similar (scaled) operating conditions in the CFM and the 1 MW<sub>th</sub> pilot plant, good comparability between the two datasets is obtained for each reactor, despite slight deviations in Glicksman's dimensionless numbers.

**Table 7.** Comparison of main operating periods for two similar operating periods from CFM and 1 MW<sub>th</sub> pilot plant.

Unit	BP	$u_{0,AR}$ [m/s]	$\Delta p_{AR}$ [mbar]	$u_{0,FR}$ [m/s]	$\Delta p_{FR}$ [mbar]
1 MW <sub>th</sub> pilot	K1-BP10-7	3.43	53.38	5.88	68.78
CFM	BP-97	2.50	36.60	3.27	51.61
CFM (scaled)	BP-97 (scaled)	4.16	43.02	5.42	60.66

#### 4.2. Entrainment and Solid Circulation of the Dual Circulating Fluidized Bed Reactor System

After establishing the hydrodynamic behavior of the dual-fluidized bed system and underlining the importance of solid entrainment from the AR and FR for stable operation and process control, this section will analyze the impact of different operating variables on entrainment from both reactors for the CFM (Section 4.2.1) and the 1 MW<sub>th</sub> pilot plant (Section 4.2.2).

##### 4.2.1. Entrainment from Dual Circulating Fluidized Bed Cold Flow Model

Due to the permanent presence of stable and unvarying boundary conditions (e.g., PSD,  $\rho_p$ ), the achievability of rapid designated alterations of given operating variables, and the possibility to easily measure solid entrainment from both reactors (see Section 2.4.2), the CFM poses ideal conditions to examine the impact of different operating variables on solid entrainment. Subsequently, the impact of riser gas velocity, reactor inventory, and PSD on solid entrainment from the AR and FR will be evaluated. (As elaborated in Section 4.1, J-valve boundary conditions (i.e., gas velocity and acting pressure) also have an important impact on the overall system hydrodynamics. The most important correlations for the behavior of the J-valve are summarized in Appendix B.1).

It is well established that solid entrainment increases with riser gas velocity, with numerous approaches to quantify this impact existing in literature [53,61–63], which are, however, known to be restricted to given boundary conditions (e.g., particle type and properties, reactor layout, boundary conditions) [27]. Moreover, the entrainment determined via these approaches signifies the saturation carrying capacity of the gas in an idealized experimental setup. (Generally, this means that the setup exhibits a smooth reactor exit

( $\mathbb{P}_{ent.}=1$ ) and features a tall CFB riser with  $H > TDH$ . Moreover, the CFB system has to be operated with a fully saturated dense bed with  $\varepsilon_s = \text{const}$  [61]).

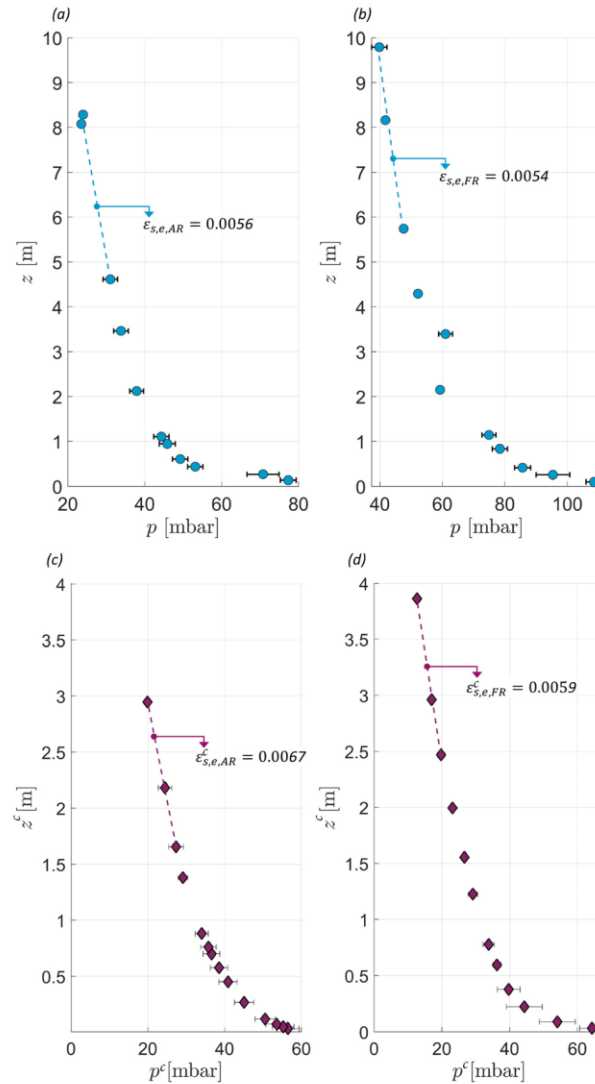


**Figure 13.** Pressure profiles for 1 MW<sub>th</sub> unit (K1, BP10-7) AR (a) and FR (b). Pressure profiles for CFM (BP97) AR (c), FR (d).

The approaches by Tasirin and Geldart [53] and Breault et al. [38], elaborated on in Section 2.5, is given as a reference in Figure 14 (dashed and dotted line, respectively) together with the results determined experimentally in the CFM. It is visible that the experimental values show a similar trend as the values calculated via Equations (13) and (14), with entrainment increasing with increasing gas velocities. However, the following discrepancies can be observed in Figure 14:

- For most operating periods, the calculated values are larger than the experimentally determined ones for both reactors;



- While a distinct impact of the reactor inventory on solids entrainment is visible in the experimental data in Figure 14 (esp. for the FR where the inventory was varied strongly), this is not reflected in the calculated data, as existing calculation approaches, allowing for a direct estimation without further fitting or modeling efforts, do not account for the effect of reactor inventory (see also Equations (8)–(14)).

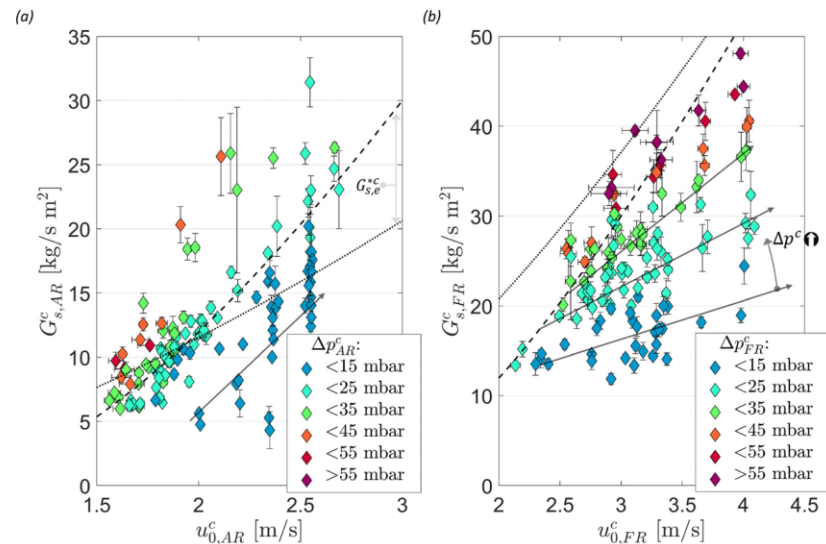


**Figure 14.** Area-specific entrainment for AR (a) and FR (b) as a function of gas velocity for all operating CFM points with bronze power (see Table S4). The black dashed and dotted line illustrate  $G_{s,e}^{*c}$ , calculated via Equations (13) and (14), respectively. Grey arrows to guide the eye.

Apart from the fact that the boundary conditions (e.g., PSD of bed material) in the CFM do not exactly match those used to derive Equations (13) and (14), the former can be explained by the fact that in a real CFB system, entrainment probabilities smaller than one are obtained (i.e., solid material travels back at the top of the riser, intensifying the core-annulus flow, see Figure 4). In order to cast light on the latter, i.e., the effect of reactor inventory on solids entrainment, Figure 15 shows the dataset from Figure 14 with  $\Delta p$  on the abscissa. As well established in literature [23,49], entrainment increases with increasing riser pressure drop, which can be related to two phenomena (albeit only the latter is relevant for tall CFB risers):

- For CFB reactors with heights smaller than the TDH, solid loading decreases continuously with increasing reactor height (i.e., the solid loading does not reach a constant value within the riser). As the reactor inventory is increased, the height of the bottom bed increases, leading to a decrease in the distance from the top of the dense bed and the reactor outlet and hence an increase in solid concentration throughout the entire freeboard. Due to this higher solid concentration in the freeboard, entrainment increases; [27]
- With increasing reactor inventory, bubble coalescence in the bed intensifies, leading to a more pronounced ejection of particles into the freeboard when those larger bubbles reach the top of the dense bed [27]. As particle concentrations in the freeboard increase due to this effect, entrainment intensifies.

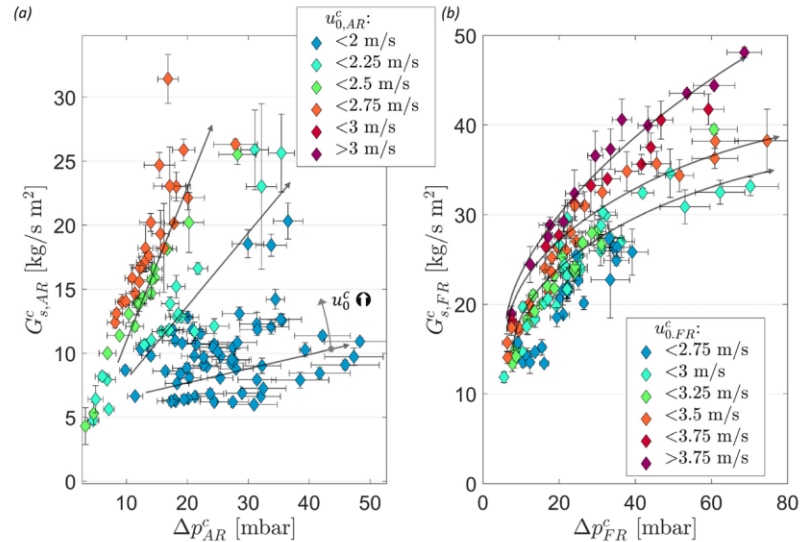


**Figure 15.** Area-specific entrainment for AR (a) and FR (b) as a function of gas reactor pressure drop for all CFM operating periods with bronze power (see Table S4). Grey arrows to guide the eye.

While a continuous linear increase in entrainment with reactor inventory is visible for the AR for a given gas velocity (see Figure 15a), the data follows a logarithmic-like trend for the FR. Another notable finding, visible in Figure 15b, is that the effect of gas velocity on solids entrainment is weaker for the FR (especially fast-circulating at  $\Delta p_{FR} < 20$  mbar). These findings indicate that although both reactors are operated as fluidized beds according to the categorization of Grace [27,28], they behave differently to changes of the underlying boundary conditions. An explanation for this can be obtained when considering the different geometries of the two CFBs. While the FR exhibits a small reactor diameter and a large riser height, resembling the key features of a tall CFB, the opposite is true for the AR. Consequently, changes in reactor inventory lead to the fact that the transport disengaging height reaches the reactor exit region even at low inventories for the AR, as the distance from the top of the dense bed to the reactor exit is comparably small, which is illustrated in the bottom four subplots of Figure 16. Hence, solid entrainment increases with increasing reactor inventory due to (i) and (ii) for the AR and the effect of the reactor inventory on entrainment is pronounced. Moreover, as the TDH increases with gas velocity [64], the effect of gas velocity on entrainment is strong for the AR, as more and more coarse particles (even those with  $u_t > u_0$ ) reach the reactor exit with increasing  $u_0$  for a given reactor inventory. On the other hand, the TDH only reaches the reactor exit zone for large reactor pressure drops ( $\Delta p > 40$  mbar) for the FR, exhibiting tall CFB characteristics (see top subplots in Figure 16). Hence entrainment rates only increase weakly with increasing  $u_0$  for low reactor inventories for the FR. Once the TDH reaches the reactor exit zone (at approx. 40 mbar), the positive impact of  $u_0$  on entrainment rates increases for the FR, as (i) and (ii) come into effect. The strong impact of  $\Delta p$  on entrainment rates for the FR at low reactor inventories ( $\Delta p < 20$  mbar), visible in Figure 15, can be attributed to the formation of a dense bed once the reactor features sufficiently high reactor inventories, thus leading to a pronounced increase in solid entrainment for a given gas velocity [46], due to (ii).

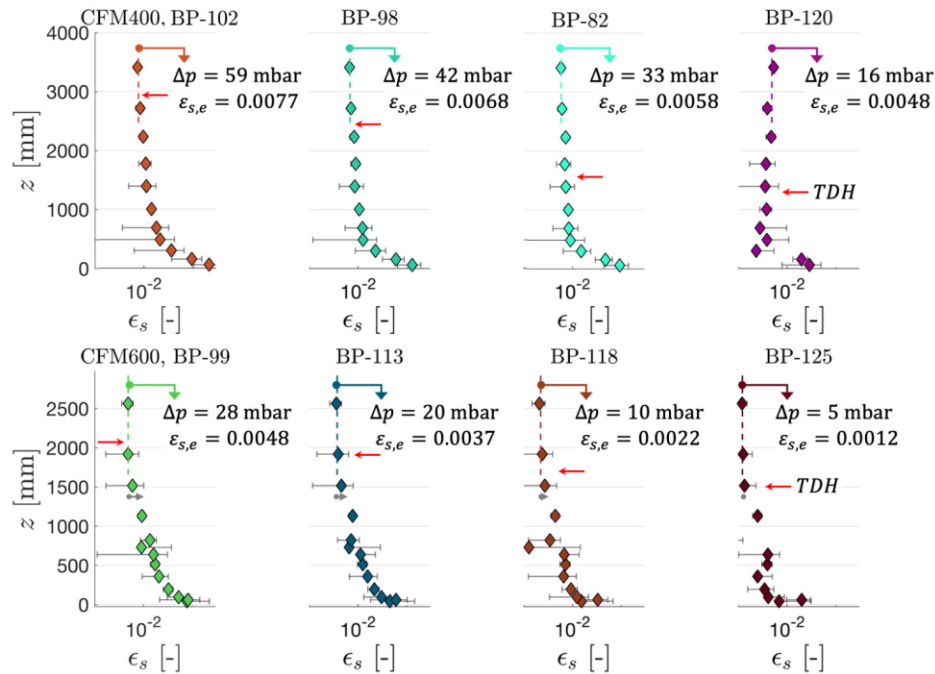


**Figure 16.** Top: FR solid concentration profiles for selected operating periods with constant  $u_{0,FR}$  ( $3.65 \pm 0.05$  m/s) and varying FR solid inventories. Bottom: AR solid concentration profiles for selected operating periods with constant  $u_{0,AR}$  ( $2.3 \pm 0.1$  m/s) and varying AR solid inventories. Red arrows mark the graphically determined TDH.

Another parameter known to affect solid entrainment from a fluidized bed [27], which is prone to changes in a chemical looping setup (e.g., due to attrition, agglomeration, etc.) [57], is the particle size distribution of the bed material cycled through the system. To investigate the impact of this parameter on solid entrainment, the AR of the CFM was operated with the two different ilmenite types (ILMc and ILMf, see Section 2.3) at four different gas velocities. The results of this experimental series are summarized in Figure 17. When comparing the calculated theoretical entrainment velocities (see Equation (10)), for the fine (0.84 m/s) and coarse (1.66 m/s) ilmenite in air ( $\rho_g = 1.225$  kg/m<sup>3</sup>,  $\mu_g = 1.9 \cdot 10^{-5}$  Pa s), it becomes obvious why entrainment was negligible for the lowest investigated gas velocity (approx. 1.3 m/s) for the coarse ilmenite. On the other hand, measurable entrainment was observed for all four investigated gas velocities for the fine material, as the terminal velocities were exceeded for each operating period. Moreover, entrainment rates for the fine ilmenite were approximately four times larger than for the coarse ilmenite for each gas velocity, with the absolute difference in entrainment increasing substantially with increasing  $u_0$  (see also Equation (13)). These findings clearly indicate the effect of particle size on entrainment, highlighting that in case of process-related changes of this parameter, significant impacts on system hydrodynamics, related to changes in the entrainment behavior of the particle system, can be expected. Consequently, exact knowledge of the PSD in the hot system is necessary to be able to adequately scale it in the cold flow model, due to the strong sensitivity of entrainment on the PSD of the particle system. Following this logic, in case of the occurrence of unexpected process-related changes of this parameter during hot operation, results obtained through *a priori* experiments in a scaled cold flow model will become unusable for direct scaling attempts. This means that without prior

knowledge of the impact of the hot process conditions on the bed material's properties (e.g., PSD), adequate scaling in a CFM becomes challenging.

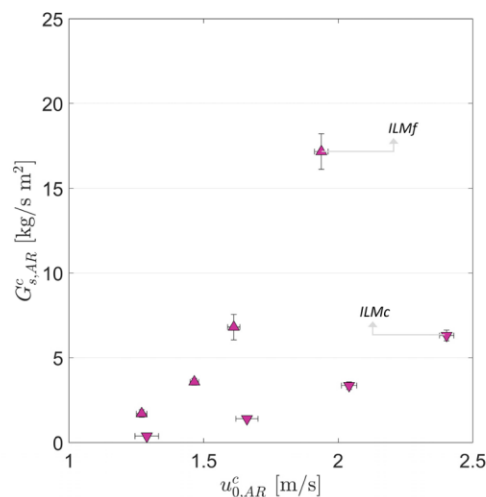


**Figure 17.** Area-specific entrainment for AR as a function of gas velocity for all CFM operating periods operated with ilmenite power (see Table S5).

In summary, the findings regarding entrainment from both risers made in the CFM setup show that for a given reactor setup and particle system, gas velocity and reactor inventory are the main operating variables affecting solids entrainment. For given boundary conditions, changes in the bed material properties (e.g., PSD,  $\rho_p$ ) were demonstrated to significantly alter solid entrainment. Therefore, general trends and approximate values for solid entrainment can be predicted via CFM studies, yet direct extrapolations from the dataset are only viable in case all boundary conditions match the scaled ones in the hot unit. Additionally, correlations not considering the entire state of the CFB system (i.e., particle properties, reactor geometry, gas velocity, and reactor inventory) cannot be expected to yield accurate predictions.

#### 4.2.2. Entrainment from 1 MW<sub>th</sub> DFB Chemical Looping Gasifier

Using the insights regarding entrainment from the CFM, the entrainment behavior of the 1 MW<sub>th</sub> pilot plant is further illuminated in this section. As only the global solid circulation can be determined in the hot unit, using the approach detailed by Marx et al. [50], the subsequent elucidations will be restricted to the entrainment rates from the FR.

Figure 18 summarizes the calculated entrainment from the FR for all three test campaigns in the 1 MW<sub>th</sub> unit. Due to simultaneous occurrence of multiple phenomena and the increased effort necessary to determine values for the solid entrainment when compared to the CFM, a controlled parameter study for the most important hydrodynamic boundary conditions was not possible for the 1 MW<sub>th</sub> unit. Nonetheless, 49 operating periods, for which loop seal samples were collected and boundary conditions were kept constant, exhibiting varying FR gas velocities, reactor inventories, and particle diameters were aggregated. (Albeit other parameters crucial for system hydrodynamics (e.g.,  $\rho_p$ ) were found to vary between operating periods, elaborations are restricted to the three selected variables, having the strongest effect on entrainment, for brevity). When considering the data points shown in Figure 18a, a clear dependence of solid entrainment on gas velocity is visible. Moreover, two distinct regions, one with operating periods for which ilmenite with a mean diameter smaller than 170  $\mu\text{m}$  was used and one with operating periods for which  $d_{p,m} > 170 \mu\text{m}$ , are visible, showing that in order to maintain sufficiently high global solid

circulation rates in the CLG unit, higher gas velocities are necessary when  $d_{p,m}$  increases. This is also visible in Figure 18b, showing that the calculated solid concentration at the reactor exit ( $\epsilon_{s,e}$ ) is significantly lower at higher  $d_{p,m}$  for a given gas velocity, illustrating that transferring larger particles towards the reactor exit requires higher gas velocities (see also Section 4.2.1). In terms of the reactor inventory, clear-cut effects on solids entrainment were not discernable for the 1 MW<sub>th</sub> unit, which is caused by the fact that the number of operating periods for which  $u_0$  and  $d_{p,m}$  are similar, but  $\Delta p$  varies is limited.

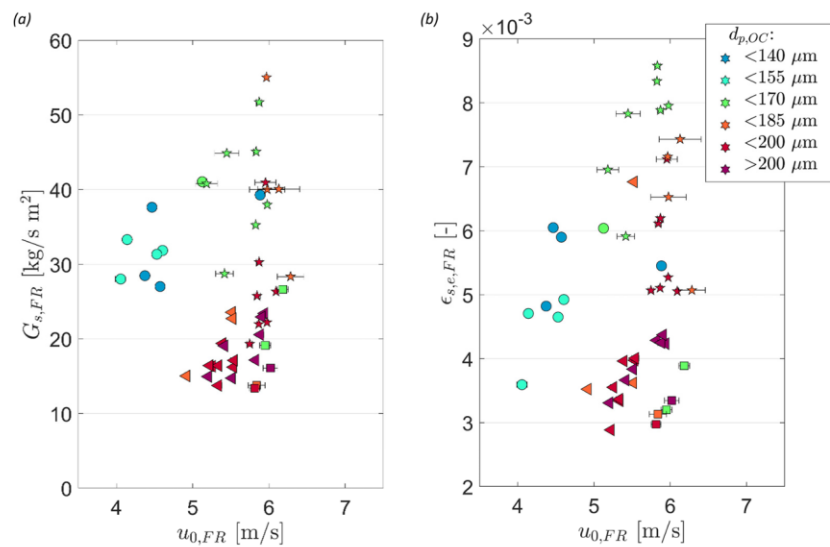


**Figure 18.** (a) Area-specific entrainment for FR as a function of FR gas velocity for 1 MW<sub>th</sub> pilot operating periods. (b) Solids volume concentration at FR riser outlet as a function of FR gas velocity for 1 MW<sub>th</sub> pilot operating periods. K1 (circles, see Table S1), K2 (ILMf-triangles, ILMf-pentagrams, see Table S2), and K3 (squares, see Table 3). Operating periods colored according to the mean particle diameter of the OC.

Therefore, it can be concluded that while some of the general trends regarding solids entrainment, established in the CFM, are also visible in the dataset collected for the 1 MW<sub>th</sub> pilot plant, the increased system complexity of the latter as well as the smaller size of the corresponding dataset make a direct comparison of both datasets for prediction purposes difficult. This will be elaborated in detail in the subsequent Section 4.3 before an alternate approach to purposefully predict the solids entrainment in the 1 MW<sub>th</sub> unit will be introduced.

#### 4.3. Prediction of Entrainment and Solid Circulation of Dual Circulating Fluidized Bed Reactor System

In a first attempt to predict solid entrainment, the data obtained from the CFM is scaled according to Glicksman's simplified scaling laws (see Section 3), in order to assess the promise of the direct scaling approach for entrainment estimation in Section 4.3.1. Thereafter, a novel approach to estimate entrainment from live data measured during CFB operation is derived and applied in Section 4.3.2.

##### 4.3.1. Prediction of Entrainment via Scaling of Data from Dual Circulating Fluidized Bed Cold Flow Model

As it has been shown that the CFM and the 1 MW<sub>th</sub> pilot plant show a good qualitative agreement in terms of their hydrodynamic behavior (see Section 4.1), the merit of CFM data

for a quantitative assessment of riser entrainment in the 1 MW<sub>th</sub> pilot plant is investigated subsequently. In order to do so, CFM data was scaled using Equations (26)–(28), for  $u_0$ ,  $G_s$ , and  $\Delta p$ , respectively. The resulting scaled values (denoted with the superscript  $c \rightarrow h$ ) are given in Figure 19a. Unsurprisingly, the scaled CFM data closely resembles the original CFM data in terms of the governing trends on  $G_s$  (i.e., increase with  $u_0$  and  $\Delta p$ , compare Figure 14b). To allow for meaningful comparisons, the entrainment data from the 1 MW<sub>th</sub> pilot plant (see Figure 18a) was also plotted into the characteristic  $u_0$ - $\Delta p$  map in Figure 19b (again only the system's global solid circulation, i.e., entrainment from the FR is shown here). Upon consideration of the two datasets it becomes clear that while similar general trends are apparent, the following differences are visible:

- For the vast majority of operating periods, reactor inventories were significantly higher in the 1 MW<sub>th</sub> pilot plant, than for the CFM, generally leading to larger entrainment rates for the former (see grey arrow in Figure 19b). Although a wide range of FR reactor inventories was investigated in the CFM, operation in the 1 MW<sub>th</sub> pilot plant was found to be more efficient at even higher inventories than previously deemed suitable during CFM operation (e.g., due to longer solid residence times enhanced feedstock conversions inside the FR [19] and increased entrainment for a given gas velocity). Hence, a direct comparison of the two datasets is only viable for a handful of data points.
- For data points with matching boundary conditions, a decent agreement was obtained (see dotted circle in Figure 19), showing that a direct scaling of CFM data yields good results in the case of well-matched boundary conditions.
- On the other hand, a certain disparity in entrainment rates is visible for several operating periods. Here, lower entrainment rates were obtained for the 1 MW<sub>th</sub> pilot for a given gas velocity and reactor inventory (see dashed circle in Figure 19b). This can be explained by the effect of the average particle diameter, which was larger in K2 (triangles in Figure 19b) due to the utilization of coarse ilmenite, and K3 (squares in Figure 19) because of feedstock-related particle agglomeration, (The PSD of the bronze powder used for CFM experiments was selected in such a fashion that it fulfills Glicksman's scaling laws in case the fine ilmenite (ILMf) is used in the 1 MW<sub>th</sub> pilot in the absence of agglomeration (more details see Section 3)), thus leading to lower solid entrainment for given values of  $u_0$  and  $\Delta p$  than predicated by direct scaling of the CFM data. Here it becomes clear that in case of the occurrence of unexpected process-related changes in bed material properties, direct scaling of the CFM data is no longer possible.

These findings show that while the datasets suggest that a direct scaling of CFM data using Glicksman's simplified scaling set is viable, exact matching of all relevant boundary conditions is a strictly mandatory prerequisite. While this requirement is easily attainable in theory, its practical execution can be elaborate, especially when attempting to predict entrainment rates in a hot unit by preceding CFM studies (as attempted in this study), necessitating an exact prediction of all operating variables and boundary conditions in the hot unit prior to its operation. On the other hand, this is not a problem in case CFM studies are to be utilized to estimate entrainment rates for an existing hydrodynamic dataset from a hot unit, where all boundary conditions and operating variables are known. Nonetheless, due to the limited universality and flexibility of the direct scaling approach, an alternate methodology, allowing for a direct estimation of entrainment rates from readily available process data, would be desirable.

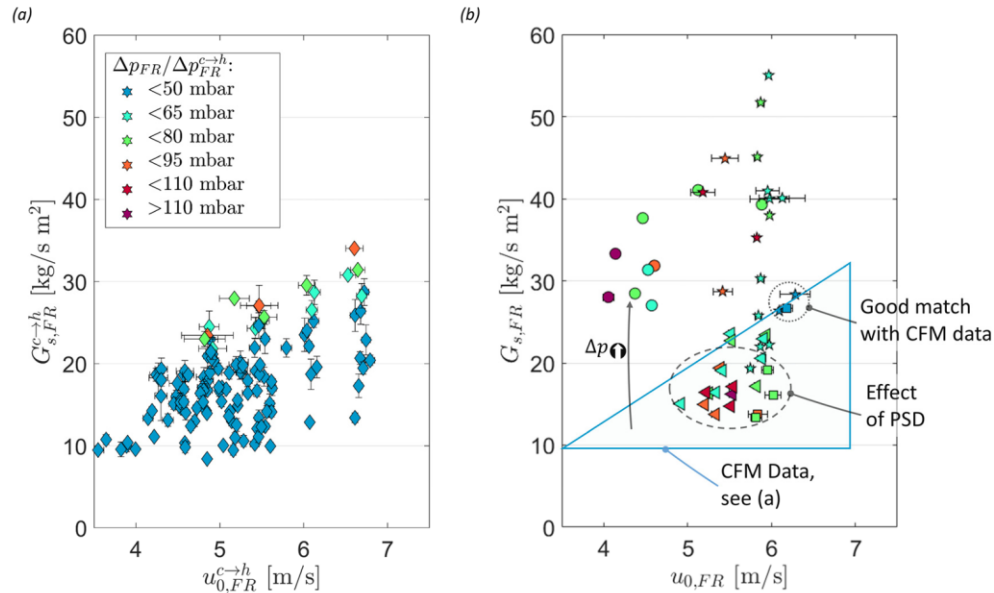


**Figure 19.** (a) Scaled ( $c \rightarrow h$ ) area-specific entrainment for FR as a function riser gas velocity for all CFM operating periods with bronze power (diamonds, operating periods see Table S4). (b) Area-specific entrainment for the FR as a function of riser gas velocity for 1 MW<sub>th</sub> pilot plant for operating periods for which solid samples were collected. K1 (circles, see Table S1), K2 (ILMc-triangles, ILMf-pentagrams, see Table S2), and K3 (squares, see Table S3).

#### 4.3.2. Novel Method for Prediction of Entrainment from Dual Circulating Fluidized Bed Cold Flow Model

In order to establish a more universal approach to calculate entrainment rates from a CFB riser, Equation (15), stating that  $G_s$  is equal to the product of particle velocity ( $u_p$ ), particle density ( $\rho_s$ ), and solids concentration ( $\epsilon_s$ ), is used as a starting point. Here, the estimation of the solids concentration in the gas stream leaving the riser is the most challenging task. As an approximation, the solids concentration at the reactor exit ( $\epsilon_{s,e}$ ), calculated via Equation (18) is used, yielding Equation (16) with an entrainment probability of unity ( $\mathbb{P}_{ent.} = 1$ ).

To firstly assess the merit of Equation (18) to estimate solid concentrations at the reactor exit, Figure 20 shows the calculated values for  $\epsilon_{s,e}$  for all operating periods investigated in the CFM. Clearly, the observable trends for  $\epsilon_{s,e}$  strongly resemble those previously obtained for  $G_s$ , with  $\epsilon_{s,e}$  increasing with gas velocity and reactor inventory. Again, a similar explanation can be provided here, with the gas stream's ability to carry particles increasing with gas velocity and the expulsion rate of particles from the dense bed increasing with reactor inventory (more details see Section 4.2). When comparing the calculated values of  $\epsilon_{s,e}$  with the saturation carrying capacity  $\epsilon_s^*$  (dashed and dotted lines in Figure 20), calculated via Equation (15), it can be seen that the majority of experimentally determined values for  $\epsilon_{s,e}$  exceed the saturation carrying capacity, with sole values obtained for low reactor inventories falling into the proximity of  $\epsilon_s^*$ . Therefore, it can be conjectured that in the case of an infinitely tall riser, for which the effect of the dense bed on particle concentrations at the reactor exit would be negligible, experimentally determined values for  $\epsilon_{s,e}$  would approach the saturation carrying capacity. However, as the effect of particle expulsion from the dense bed on solid concentrations in the CFB freeboard leads to  $\epsilon_{s,e} > \epsilon_s^*$ , the experimentally determined values determined for  $\epsilon_{s,e}$  provide a better estimation of the solids concentration at the top of the riser freeboard than the saturation carrying capacity

$\varepsilon_s^*$ . Moreover, it can be expected that the accuracy of the calculated values for  $\varepsilon_{s,e}$  can be enhanced by increasing the number of pressure measurement points around the reactor exit region.

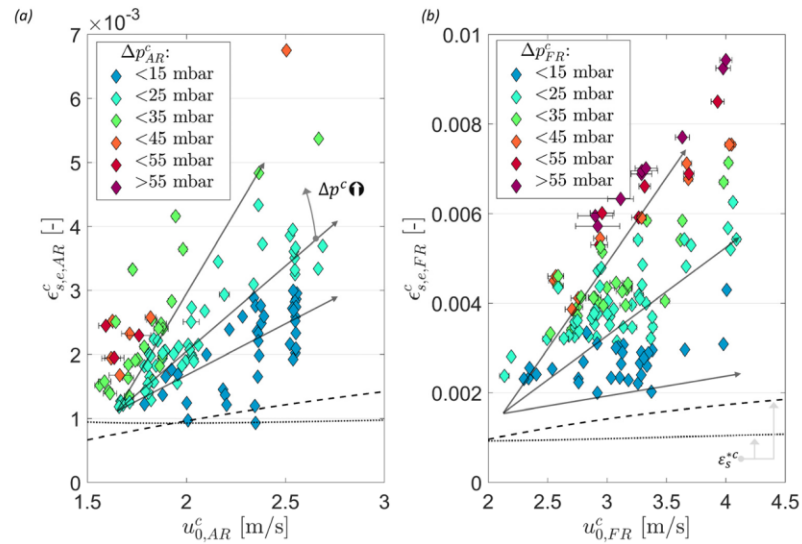


**Figure 20.** Solids volume fraction at reactor outlet for the AR (a) and FR (b) as a function of riser gas velocity for all CFM operating periods with bronze power (see Table S4). Coloring according to reactor pressure drop. The black dashed (Geldat et al. [53]) and dotted (Breault et al. [38]) line illustrates  $\varepsilon_s^*$ , calculated via Equation (15). Grey arrows to guide the eye.

When considering Equations (15) and (16), it becomes clear that a positive correlation between the solids concentration at the reactor outlet and the CFB entrainment rate should be visible as particle entrainment increases at higher solid loadings of the gas stream. This expected positive correlation is illustrated in Figure 21, showing  $\varepsilon_{s,e}$  as a function of the measured solids entrainment for the CFM. Interestingly, a linear correlation between the two variables can be observed for the AR and the FR riser. This finding sparks curiosity, as theoretically, entrainment rates should increase more strongly (i.e., more than linearly) with increasing  $\varepsilon_{s,e}$ , due to the positive impact of  $u_0$  on  $\varepsilon_{s,e}$ , as well as the higher particle velocities obtained at higher gas velocities (see Equation (11)). However, a similar correlation was previously observed by Chen et al. [34] in a cold flow model of a 1.5 MW<sub>th</sub> chemical looping combustion plant, showing a linear correlation between entrainment rates and the pressure drop at the top of the freeboard. (One the one hand, the utilization of  $\varepsilon_{s,e}$  instead of the freeboard pressure drop, as done in this study, represents a more robust approach, as more than two pressure sensors are used, thus reducing the impact of measurement accuracy on the results. Moreover, the application of  $\varepsilon_{s,e}$  allows for further building on this finding, i.e., using  $\varepsilon_{s,e}$  for the direct estimation of G<sub>s</sub>, as done in the following). This shows that another phenomenon, related to the entrainment probability of the particles at the riser exit, is central for achievable entrainment rates, thus limiting the positive effect of  $u_0$  and  $\varepsilon_{s,e}$  on particle elutriation.



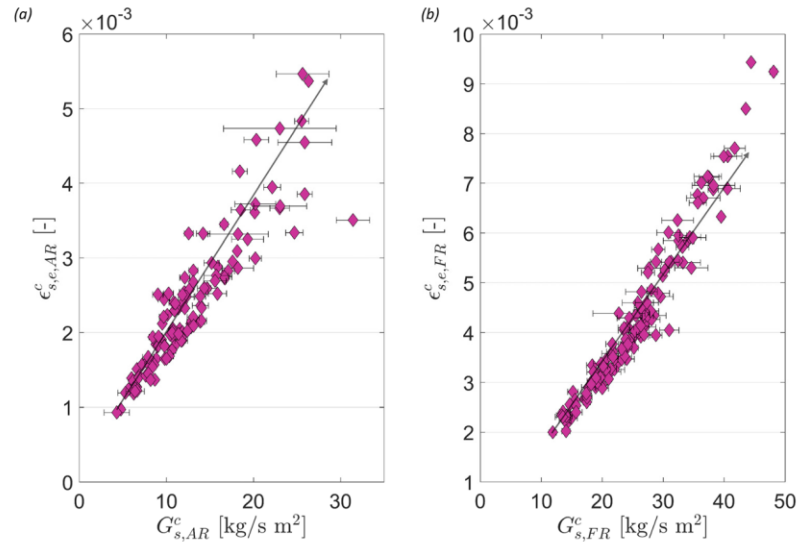


**Figure 21.** Calculated solids volume fraction at reactor outlet for the AR (a) and FR (b) as a function of area-specific solid entrainment for all CFM operating periods with bronze power (see Table S4).

In order to obtain a better understanding of this phenomenon, the maximum entrainment rate from the CFB riser was calculated via the employment of the calculated  $\varepsilon_{s,e}$  values, using Equation (16) and assuming  $\mathbb{P}_{ent} = 1$ . ( $\mathbb{P}_{ent} = 1$ , meaning that all particles suspended in the gas stream inside the riser leave the riser towards the cyclone). The results of this endeavor are illustrated in Figure 22, showing the calculated maximum entrainment rate from the AR and FR of the CFM as a function of the measured entrainment rate. Clearly, the calculated maximum entrainment rates signify an overestimation of the entrainment rate, with calculated values being 2–6 times larger than the measured entrainment rate. This can be explained by the fact that for the calculation of the maximum entrainment rate the entrainment probability was set to one, i.e., all particles traveling with the gas stream were assumed to leave the riser towards the cyclone. Yet, it is known that this is not the case, as a fraction of particles travels back down inside the riser (see also Figure 4), intensifying the well-established core-annulus particle flow inside the CFB [35,46,48]. Additionally, Figure 22 shows that the entrainment probability clearly decreases with increasing solids entrainment for both reactors, as the relative difference between the calculated maximum entrainment rate and measured entrainment rate increases with increasing solids entrainment. This shows that the entrainment probability is not only dependent on reactor geometry and the utilized particle system, but also changes with varying boundary conditions (e.g.,  $u_0$ ,  $G_s$ ), which was also observed by Alghamdi et al. [48]

To assess the effect of boundary conditions on entrainment probability, it was first calculated for all operating periods for the AR and FR of the CFM and then correlated to different boundary conditions (e.g.,  $u_0$ ,  $u_p$ ,  $\Delta p$ , etc.) to find applicable correlations. Apart from the selected boundary conditions, the entrainment probability was also correlated to the Stokes number. This parameter was selected due to the findings made by Djerf et al. [46], who established that  $\mathbb{P}_{ent}$  is closely related to the particle Stokes number, which describes the extent to which particles are able to follow a fluid in the proximity of an obstacle and hence governs the phenomenon of the solid-loaded gas stream bending into the exit duct towards the cyclone. The entire approach is explained in Appendix B.3.

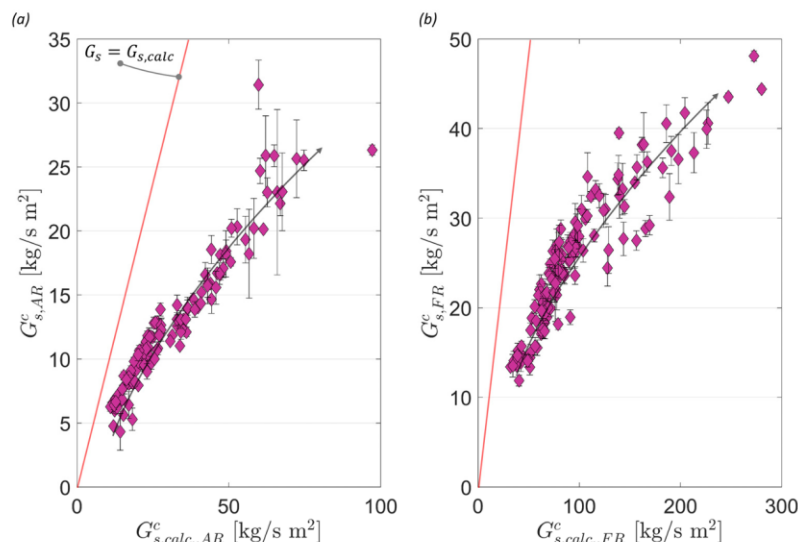


**Figure 22.** Area-specific solid entrainment for the AR (a) and FR (b) as a function of calculated area-specific solid entrainment (via Equation (16) with  $\mathbb{P}_{ent.} = 1$ ) for all CFM operating periods with bronze power (see Table S4). The red angle bisector illustrates the line for which calculated and measured values for  $G_s$  are equal. Grey arrows to guide the eye.

Although several variables yielded a similarly good linear correlation for the entrainment probability in the investigated operating range for both reactors (e.g.,  $u_p$ ), the Stokes number correlation was selected due to the following reasons:

- Acquisition of a good linear fit for AR and FR (albeit with a better linear correlation being obtained for the FR), illustrated in Figure 23;
- The physically sound explanation for the established correlation of entrainment probability and Stokes number and corroborating findings by Djerf et al. [46] (i.e., the low likelihood that the established linear correlation is a random statistical artifact or a peculiarity of the given reactor setup);
- Easy application in the hot unit, not requiring scaling, as the entrainment probability as well as the Stokes number is dimensionless.

The resulting correlations for the entrainment probability are shown in Figure 23, together with the experimentally determined values for  $\mathbb{P}_{ent.}$ . Clearly, an excellent linear correlation was obtained for the FR ( $R^2 = 0.88$ ), whereas a certain skew from the data is visible for the AR ( $R^2 = 0.61$ ). One reason for this could be that the AR was operated at significantly lower Stokes numbers (lower gas velocity, higher riser diameter). Djerf et al. [46] established that at very low Stokes numbers, the entrainment probability is equal to one, whereas it drops to zero for high Stokes numbers, meaning that it has to follow a sigmodal progress. Therefore, a linear correlation can only be expected for Stokes numbers lying in between those extremes, for which the sigmodal curve shape slopes off. Whereas the FR was operated at Stokes numbers falling into this linear regime (see inset in Figure 23b), this was not the case for the AR (see inset in Figure 23a). Nonetheless, the utilized linear correlation also yields a reasonable fit for the AR data. Therefore, both correlations are deemed suitable for subsequent estimation of particle entrainment from the hot unit (more details see below). When comparing the entrainment probabilities obtained for both units with one another, it can be seen that, generally, higher values were obtained for the AR. This can be related to the lower Stokes numbers at which the AR was operated (i.e., boundary conditions that favor that particles follow the path of the fluid stream). Another explanation for this could be the difference in exit geometry for both reactors, which plays a role in

the solid flow pattern at the reactor exit (especially at high solid loads, which is the case in chemical looping configurations) [35], with the AR featuring a smoother cyclone outlet shape (see bottom insets in Figure 23).

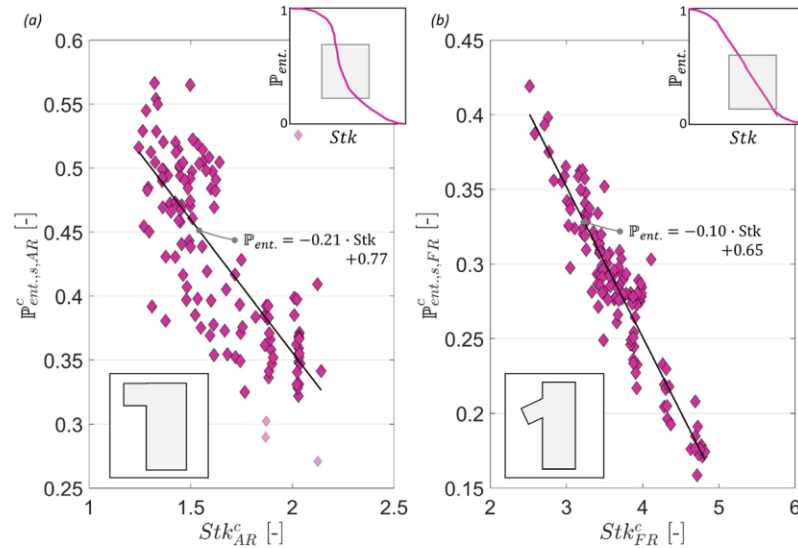


**Figure 23.** Calculated entrainment probability for AR (a) and FR (b) as a function of particle Stokes Number for all CFM operating periods with bronze power (see Table S4). The straight line signifies the linear fit obtained via the approach explained in Appendix B.3. For the AR, certain outliers, paled out in the left subplot, were not used for fitting. The top inset illustrates the location of the dataset on the theoretical sigmodal-shaped curve of the entrainment probability over varying Stokes numbers. The bottom insets illustrate a schematic of the reactor exit geometry for each riser.

Using the correlation for the entrainment probability established in the CFM, the approach described below can be utilized to calculate the entrainment in any hot unit.

- (i) Determination/estimation of particle properties (i.e., PSD,  $\rho_p$ ,  $\varphi_s$ );
- (ii) Determination/estimation of gas properties (i.e.,  $\mu_g$ ,  $\rho_g$ );
- (iii) Calculation of particle terminal velocity and particle slip velocity via Equations (10) and (11);
- (iv) Determination of  $u_0$  (see Equation (1) (The gas volume flow  $V_n$  is determined via a venturi measurement, which per se, is a combination of temperature and pressure measurements)) and  $\varepsilon_{s,c}$  via Equation (18) from temperature and pressure measurements in the hot unit;
- (v) Calculation of Stokes number via Equation (7);
- (vi) Calculation of entrainment probability via linear correlation (see Figure 23);
- (vii) Calculation of riser entrainment for current boundary conditions via Equation (16).

When utilizing this approach, illustrated in Figure 24, the subsequent points have to be considered:

- While all necessary data required for calculation is easily obtainable from live measurements in the hot unit, particle properties for the current operating period (see (i)) can only be obtained via solid sampling. However, when running a continuously operated system with a known bed material, particle properties are unlikely changed dramatically during operation, which means that these parameters can also be treated as constants if the prerequisites are given;
- Generally, the approach can be utilized for any given CFB setup. However, it has to be noted that the entrainment probability was previously found to be dependent on

particle properties and reactor geometry [35]. While the impact of particle properties on entrainment is considered in the given approach, (Whether the given correlation are also valid for a bed material with different properties remains to be investigated in further studies), the latter is only partially (via the riser diameter in Equation (7)). Hence, it can be stated that a suitable correlation for the entrainment probability first has to be established for each riser, e.g., via CFM studies, before allowing for an application of the described method. As indicated in Figure 24, alternatives to determine the entrainment probability are different modeling approaches.

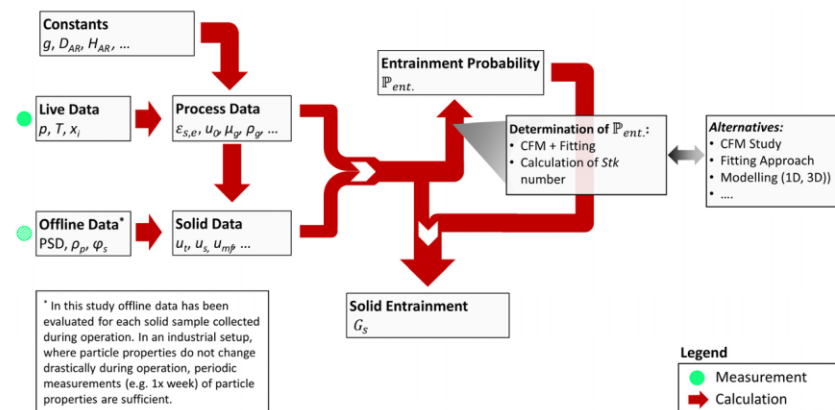


**Figure 24.** Schematic illustration of novel calculation approach for solid entrainment ( $G_s$ ) from the riser of any CFB system.

To investigate the merit of the novel approach for the estimation of solid entrainment, it was applied for the FR of the 1 MW<sub>th</sub> unit, yielding a dataset of calculated values for  $G_s$ . These calculated values ( $G_{s,FR,calc.}$ ) were subsequently compared to the values determined using the method by Marx et al. [50]. The results of this comparison are given in Figure 25. Clearly, a good correlation between the two datasets is obtained, showcasing that the novel approach developed within this study yields reliable values for the solids entrainment from the CFB reactor. When considering the maximum uncertainty of 20% for the values determined via Marx's method [50], a total of 33 from the 49 investigated operating periods show a perfect agreement. This is the case despite the fact that the PSD of the OC varies measurably between the different operating periods, leading to deviations from the scaled operating conditions in the CFM on the basis of which the approach was developed. Hence, the data suggest that the novel approach also features good robustness towards changing boundary conditions, which indicates that a universal application is feasible. (An even higher accuracy of the given approach can be obtained by different measures described in Section 5).

Apart from its simplicity, meaning that besides from live data only knowledge of the particle properties is required, the novel approach also allows for a direct calculation of entrainment from any CFB riser, whereas the approach by Marx et al. [50] requires the transport of an active bed material between two risers. Hence, solid entrainment can be calculated for both risers of the 1 MW<sub>th</sub> unit, as well as for any operating period, as long as particle properties are known. Making use of this thus also allows for a comparison of entrainment rates of the AR and the FR for selected operating periods. Figure 26 shows the calculated solid entrainment rates for AR and FR, using the novel approach. Clearly, entrainment rates for the AR exceed those of the FR for each operating period, meaning that Equation (29) is fulfilled and the reactor system is operated in a stable fashion without emptying LS1. Interestingly, AR entrainment rates are up to three times larger than FR entrainment for the majority of operating periods for which fine ilmenite was

used (circles and pentagrams in Figure 26), suggesting optimization potential in terms of AR fluidization velocities, i.e., significantly lower quantities of fluidization medium could have been utilized for those operating periods without disturbing system hydrodynamics, which would have led to increased CLG process efficiency [24]. On the other hand, AR entrainment rates were closer to FR entrainment rates when operating the CLG unit with coarse ilmenite, which is in line with findings made during the operation, where it was observed that the filling degree of LS1 reacted sensitively to changes in  $u_{0,AR}$  when coarse ilmenite was used. This can be explained by the fact that the AR is operated at lower gas velocities than the FR, and hence AR entrainment rates reacted more sensitively to changes in the PSD, especially so in case a large fraction of particles with  $u_t \approx u_{0,AR}$  were located within the riser.

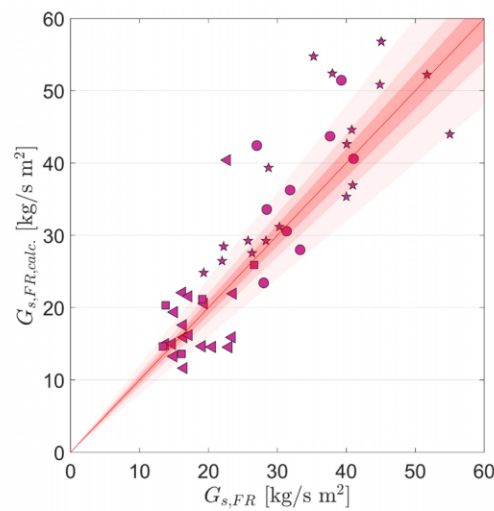


**Figure 25.** Calculated area-specific entrainment for the FR as a function of area-specific entrainment (using the method by Marx et al. [50]) for 1 MW<sub>th</sub> pilot plant for operating periods for which solid samples were collected. K1 (circles, see Table S1), K2 (ILMc-triangles, ILMf-pentagrams, see Table S2), and K3 (squares, see Table S3). The angle bisector denotes the line for which calculated values and the values determined via Marx's [50] method are identical. Red shaded areas denote a relative deviation of 5% (dark), 10% (medium), and 20% (light).

Apart from its advantages, the given method for CFB entrainment prediction exhibits certain limitations and could be refined further. For one, accurate measurement of the pressure in the exit zone of the freeboard is required, making multiple measurement points in this reactor region indispensable. Further, properties of the bed material have to be known accurately (esp.  $d_p$  and  $\rho_p$ ) to allow for precise model predictions. Additional refining of the model could be achieved by only considering particles traveling upwards in the riser in the term  $\varepsilon_{s,e}$  in Equation (16), e.g., by using the approach detailed by Alghamdi et al. [48], thereby improving model predictions. Lastly, the determination of the entrainment probability for each combination of reactor setup, boundary conditions, and bed material remains an arduous task. A more universal approach could potentially be established by correlating  $\mathbb{P}_{ent.}$  with the Stokes number for different boundary conditions and bed materials in varying reactor geometries, thereby greatly improving the range of applicability for the given method.

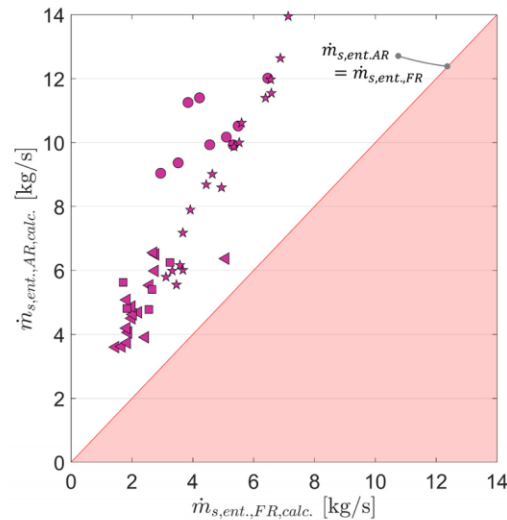


**Figure 26.** Calculated entrainment rates for the AR as a function of calculated entrainment rates for the FR for 1 MW<sub>th</sub> pilot plant for operating periods for which solid samples were collected. K1 (circles, see Table S1), K2 (ILMc-triangles, ILMf-pentagrams, see Table S2), and K3 (squares, see Table S3).

## 5. Conclusions

To describe the hydrodynamics of a dual-fluidized bed system, this study carried out an elaborate parameter study in a scaled cold flow model to comprehend its fundamental hydrodynamic behavior and quantify solids entrainment from both CFB reactors. Thereafter, the results were successfully applied onto the hot 1 MW<sub>th</sub> pilot plant setup. Based on the ensuing results, the following conclusions can be made:

- In the given setup consisting of two CFB reactors, one (the AR) being equipped with an internal solid recycle, the dual-fluidized bed system constitutes a self-regulating system, when operated within a defined stable operating range. This means that individual operating variables can be varied freely without requiring further system adjustments, highlighting the robustness of the given reactor setup.
- Due to the importance of solid circulation and hence CFB solid entrainment on CLG process efficiency, the effect of the most important operating variables and boundary conditions on entrainment were investigated in the cold and hot units. It was found that entrainment correlates positively with increasing riser gas velocity, increasing reactor inventory and decreasing particle diameter, amongst others. Due to the interdependence of entrainment on multiple parameters, existing simplified semi-empirical approaches fail to adequately predict solids entrainment and modeling demands are elaborate.
- An alternative prediction approach is the direct scaling of CFM data to a hot system. It was shown that while this approach is valid in case of exactly matching boundary conditions, it generally suffers from limited universality and flexibility.
- Application of a novel calculation approach, allowing for a straightforward estimation of solid entrainment from any CFB riser, on data gathered during autothermal CLG operation in the 1 MW<sub>th</sub> pilot plant showed good agreement with literature data, proving its suitability any CFB system, if the riser entrainment probability and particle properties are known. A method to derive the former parameter using CFM data, is presented within this study.

In summary, the results presented in this paper provide a comprehensive understanding of the hydrodynamics of the investigated dual-fluidized bed system as well as the dependence of boundary conditions on solid entrainment. The developed ground-set of

operating rules can be utilized to successfully operate different dual-fluidized bed setups and optimize their hydrodynamic performance.

Moreover, the novel approach to calculate solids entrainment from a CFB riser, allows for universal application in different setups. The given approach can be further refined by:

- Optimizing sensor technology in the riser freeboard (i.e., multiple pressure measurements towards the riser exit), thereby increasing method accuracy and robustness.
- Application of the method in given reactor setups with different bed materials to verify its universal applicability regardless of particle characteristics.
- Further investigation of the effect of a wide range of Stoke numbers on riser entrainment probability in different setups in order to establish a universally applicable correlation between the two parameters.

In doing so, the calculation approach can be further extended, ultimately yielding a universal technique to estimate solid entrainment from a wide array of CFB risers operated with different bed materials, thereby closing a crucial research gap.

**Supplementary Materials:** The following supporting information can be downloaded at: <https://www.mdpi.com/article/10.3390/en16155630/s1>, File S1: Boundary conditions for operating points from 1 MW<sub>th</sub> pilot plant (Tables S1–S3); File S2: Boundary conditions for operating points from cold flow model (Tables S4 and S5).

**Author Contributions:** P.D.: Conceptualization, Methodology, Investigation, Data Curation, Writing—Original Draft, Visualization. F.M.: Writing—Review and Editing, Methodology, Investigation, Data Curation. J.S.: Writing—Review and Editing, Supervision, Project Administration, Funding Acquisition. B.E.: Resources, Funding Acquisition. All authors have read and agreed to the published version of the manuscript.

**Funding:** This work has received funding of the European Union’s Horizon 2020-Research and Innovation Framework Programme under grant agreement No. 817841 (Chemical Looping gasification foR sustainAble production of biofuels—CLARA). The content of this work reflects only the author’s view, and the European Commission is not responsible for any use that may be made of the information it contains.

**Data Availability Statement:** All relevant data is contained within the article or supplementary material. Additional data can be made available upon request.

**Acknowledgments:** The authors would like to thank Aichernig Engineering GmbH, Austria, for their support in the design and safety analysis of the 1 MW<sub>th</sub> CLG unit. Moreover, the authors would like to thank AB Torkapparater, Sweden, for the production, storage and shipping of pine forest residue and wheat straw pellets. Lastly, the authors would like to thank Sarah Keller and Bryan Engelen for their efforts during the operation of the CFM as well as Marvin Jost and Levent Aytemiz for their support in the lab analysis of the OC samples.

**Conflicts of Interest:** The authors declare no conflict of interest.

## Nomenclature

### Latin Symbols

$A$	Cross section	$p$	Pressure
$a$	Slope for linear fit	$R_{OC}$	Oxygen transport capability
$Ar$	Archimedes Number	$R^2$	R-squared value
$b$	Y-Intercept for linear fit	$Re$	Reynolds number
$D$	Reactor diameter	$Stk$	Stokes Number
$d_p$	Particle diameter	$T$	Temperature
$g$	Earth’s gravity	$t$	Time
$G_s$	Surface specific solid entrainment	$u_0$	Gas velocity

$H$	Height	$u_p$	Particle velocity
$k_b$	Particle backflow ratio	$u_t$	Terminal velocity
$L_{sc}$	Scaling factor	$V$	Volume
$m_{inv.}$	Mass inventory of riser	$\dot{V}$	Volume flow
$m_i$	Mass of species i	$w_i$	Mass fraction of species i
$\dot{m}_i$	Mass flow of species i	$X_S$	Conversion of Oxygen Carrier
$\mathbb{P}_{ent.}$	Particle entrainment probability	$z_i$	Height of measuring port i

**Greek Symbols**

$\Delta X_s$	Difference in oxidation degree of OC	$\mu$	Dynamic Viscosity
$\Delta p$	Riser pressure drop	$\phi$	Sphericity
$\Delta z$	Change in height	$\rho$	Density
$\varepsilon_s$	Solids volume concentration		

**Acronyms/Abbreviations**

AR	Air Reactor	ILMc	Coarse ilmenite
BFB	Bubbling Fluidized Bed	ILMf	Fine ilmenite
BP	Operating period	IWP	Industrial wood pellets
CFB	Circulating Fluidized Bed Reactor	K1/2/3	Campaign 1/2/3
CFM	Cold Flow Model	LS	Loop Seal
CLG	Chemical Looping Gasification	OC	Oxygen Carrier
CLC	Chemical Looping Combustion	PFR	Pine forest residue
DFBG	Dual Fluidized Bed Gasification	PSD	Particle Size Distribution
DFB	Dual Fluidized Bed	TDH	Transport disengaging height
FR	Fuel Reactor	WSP	Wheat straw pellets
GHG	Greenhouse Gas		

**Indices**

AR	Air Reactor	OC	Oxygen Carrier
back	Backflow in riser	out	Outlet
bulk	Bulk	ox	Oxidized
calc	Calculated	p	Particle
c	Cold Unit—Cold Flow Model	red	Reduced
ent.	Entrained	R	Reactor
e	Exit	s	Solid
FM	Fluidization medium	sp	Stand Pipe
g	Gas	t	terminal
h	Hot Unit—1 MW <sub>th</sub> pilot plant	top	Top of Riser
in	Inlet	tot.	Total
mf	Minimum Fluidization	10	10% of weight cumulative PSD
meas.	Measured	90	90% of weight cumulative PSD
m	mean	-∞	Ambient conditions
n	Norm (at norm conditions)	*	Dimensionless parameter (u/dp)
O	Oxygen		

While the superscripts <sup>c</sup> and <sup>c→h</sup> denote the state in the cold and scaled hot state of the CFM, respectively, variables without a superscript or with the superscript <sup>h</sup> can be associated with the 1 MW<sub>th</sub> pilot plant.

**Appendix A. Further Derivation for Scaling of Fluidized Beds**

Equation (26), relating the gas velocity in the hot and cold fluidized bed, can be derived by assuming a constant Froude number in both units and then inserting Equation (24):

$$\frac{u_0^{h2}}{g \cdot D^h} = \frac{u_0^{c2}}{g \cdot D^c} \quad (A1)$$

For estimation of the solid entrainment, the similitude of the dimensionless entrainment can be used:

$$\frac{G_s^h}{u_0^h \cdot \rho_p^h} = \frac{G_s^c}{u_0^c \cdot \rho_p^c} \quad (A2)$$



Inserting Equation (A1) thus yields Equation (27).

For the pressure drop, it is firstly assumed that it derives solely from the particles inside the riser:

$$\Delta p = \frac{m_{inv,R} \cdot g}{A_R} = \int_0^1 \varepsilon_s(\xi) d\xi \cdot V_R \cdot \rho_p \cdot \frac{g}{A_R} \quad (A3)$$

By then assuming similitude in terms of the solid concentration over the dimensionless height ( $\xi$ ):

$$\int_0^1 \varepsilon_s^h(\xi^h) d\xi^h = \int_0^1 \varepsilon_s^c(\xi^c) d\xi^c, \quad (A4)$$

one obtains:

$$\frac{\Delta p^h}{D^h \cdot \rho_p^h \cdot g} = \frac{\Delta p^c}{D^c \cdot \rho_p^c \cdot g} \quad (A5)$$

Inserting Equation (24) into Equation (A5) finally yields Equation (28).

## Appendix B. Additional Data from Cold Flow Model

### Appendix B.1. Effect of Boundary Conditions on Material Throughput through J-Valve

As global solid circulation in the coupled dual-fluidized bed system is not only dependent on the entrainment from the riser but also the material throughput through the J-valve, it is worthwhile to also highlight the impact of the most important boundary conditions on the latter. (Since material throughput through the J-valve is similar to entrainment for steady-state operating periods, experimentally determined values for  $G_{s,FR}$  are considered for the J-valve in the following). As shown in Figure A1 and as reported in the literature [51], material transport through the J-valve was found to increase with the gas volume flow through the J-valve. This finding can be explained, when considering that material transport in the J-valve resembles pneumatic transport, and the solids carrying capacity of a gas stream increases with gas velocity (see Equations (13)–(15)). Yet, as already briefly mentioned in Section 4.1.1, Figure A1 illustrates that apart from gas velocities, the pressure drop over the J-valve also correlates positively with material transport. Here, it is assumed that as the pressure drop over the J-valve increases, a fraction of the gas used for fluidization of LS1 also travels via the J-valve, thus increasing the effective gas velocity inside the J-valve and hence material transport towards the FR. Consequently, the J-valve throughput is not only influenced by designated alterations of the inlet gas volume flow but also dependent on the pressure profile of the entire dual-fluidized bed system (esp. FR inventory, difference in overhead pressure of AR and FR riser).

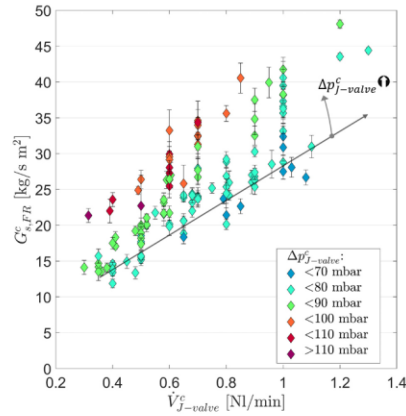


**Figure A1.** Area-specific entrainment for FR as a function of gas flow used for J-valve fluidization for all CFM operating periods with bronze power (see Table S4).

*Appendix B.2. Effect of PSD on Entrainment from Riser*

As elaborated in Section 4.2, entrainment decreases with increasing particle diameter. This can be attributed to the fact that coarser particles have a lower likelihood of being entrained for a given set of boundary conditions, thus leading to lower solids concentration at the reactor outlet for higher particle diameters. The close correlation between entrainment and particle loadings at the reactor outlet, is given in Figure A2. Clearly, both bed material types follow the same trend, showing that the stated correlation exists regardless of particle properties (e.g., PSD). Another interesting trend visible in Figure A2 is that entrainment probabilities equal to one are attained at low entrainment rates (=low Stokes number). Moreover, both bed material types follow a similar trend in terms of entrainment probability, showing that the entrainment probability is governed by similar mechanisms, regardless of particle properties.

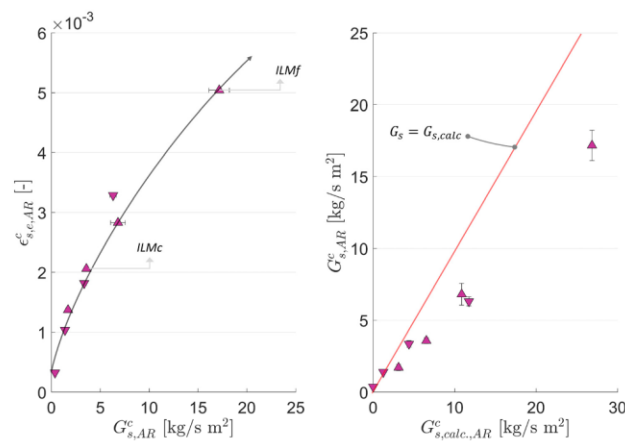


**Figure A2.** Left: Calculated solids concentration at reactor outlet as a function of area-specific power for all CFM operating periods operated with ilmenite power (see Table S5). Right: Area-specific entrainment for AR as a function of calculated area-specific solid entrainment (via Equation (15)) with  $\mathbb{P}_{ent.} = 1$  operating periods operated with ilmenite power (see Table S5).

### Appendix B.3. Correlation for Riser Entrainment Probability for Different Operating Variables

To be able to transfer the findings from made for the CFM to the 1 MW<sub>th</sub> pilot plant, a suitable correlation for the entrainment probability, which was found to change with varying boundary conditions, had to be established. In order to do so, the calculated values for  $\mathbb{P}_{ent.}$  were fitted over all relevant boundary conditions, (Only boundary conditions easily obtainable in a hot CFB setup were used for fitting, to allow for a straightforward application on the 1 MW<sub>th</sub> pilot dataset), using linear, exponential, logarithmic, and polynomial fits, amongst others, using the MATLAB<sup>®</sup> function *fit*. Thereafter, the resulting correlations were compared, using the resulting *R*-squared ( $R^2$ ) values. Finally, the most suitable correlation was selected for subsequent calculations (see Section 4.3.2). As linear fitting yielded the most promising results and allowed for a straightforward application, the subsequent elaborations are limited to the linear fitting approach.

In the first step, the data was fitted in a linear fashion using MATLAB<sup>®</sup>:

$$\mathbb{P}_{ent.} = a \cdot x + b \quad (A6)$$

Subsequently, *R*-squared values were calculated via:

$$R^2 = 1 - \frac{\sum (\mathbb{P}_{ent.,i} - \mathbb{P}_{ent.,fit,i})^2}{\sum (\mathbb{P}_{ent.,i} - \bar{\mathbb{P}}_{ent.})^2} \quad (A7)$$

Here, *i* signifies one data point, the subscript *fit* signifies the fitted value and  $\bar{\mathbb{P}}_{ent.}$  signifies the average entrainment probability for the entire dataset.

Ultimately, the results, summarized in Table A1, were compared to one another and the most suitable correlation was selected. The correlation for the Stokes number was finally selected due to the following reasons:

- Good fit for AR and FR (high *R*-squared values)
- Results by Djerf et al. [46], showing a connection between the entrainment probability and the Stokes number in another cold flow setup.
- Easy application in the hot unit, not requiring scaling, as the entrainment probability as well as the Stokes number are dimensionless.

**Table A1.** Fitting parameters obtained for linear fitting of the calculated entrainment probability over different operating variables.

Operating Variable (x)	AR			FR		
	a	b	R <sup>2</sup>	a	b	R <sup>2</sup>
$u_p$ [m/s]	−0.165	0.674	0.61	−0.119	0.583	0.88
$u_0$ [m/s]	−0.165	0.771	0.61	−0.119	0.653	0.88
$G_{s,calc}$ [kg/m <sup>2</sup> s]	−0.0035	0.533	0.59	−0.0091	0.37	0.69
$\Delta p$ [mbar]	0.0021	0.389	0.09	−0.0012	0.313	0.11
Stk [-]	−0.208	0.771	0.61	−0.101	0.653	0.88
$\varepsilon_{s,e}$ [-]	−49.8	0.549	0.42	−24.6	0.389	0.48

### References

1. Global Monitoring Laboratory (GML); National Oceanic and Atmospheric Administration (NOAA). Monthly Average Mauna Loa CO<sub>2</sub>. Carbon Cycle Greenhouse Gases. Available online: <https://gml.noaa.gov/ccgg/trends/> (accessed on 10 March 2023).
2. European Environmental Agency (EEA). Greenhouse gas emissions from transport in Europe. EEA Indicators. Available online: <https://www.eea.europa.eu/ims/greenhouse-gas-emissions-from-transport> (accessed on 10 March 2023).
3. International Energy Agency (IEA). *Global Electric Vehicle Outlook 2022*; International Energy Agency: Paris, France, 2022.
4. Directive (EU) 2018/2001 of the European Parliament and of the Council of 11 December 2018—On the Promotion of the Use of Energy from Renewable Sources; p. 128. Available online: [https://eur-lex.europa.eu/legal-content/EN/TXT/?uri=uriserv:OJ.L\\_.2018.328.01.0082.01.ENG](https://eur-lex.europa.eu/legal-content/EN/TXT/?uri=uriserv:OJ.L_.2018.328.01.0082.01.ENG) (accessed on 10 March 2023).

5. Atsonios, K.; Nesiadis, A.; Detsios, N.; Koutita, K.; Nikolopoulos, N.; Grammelis, P. Review on dynamic process modeling of gasification based biorefineries and bio-based heat & power plants. *Fuel Process. Technol.* **2020**, *197*, 106188. [\[CrossRef\]](#)
6. Kumar, T.R.; Mattisson, T.; Rydén, M.; Stenberg, V. Process Analysis of Chemical Looping Gasification of Biomass for Fischer-Tropsch Crude Production with Net-Negative CO<sub>2</sub> Emissions: Part 1. *Energy Fuels* **2022**, *36*, 9687–9705. [\[CrossRef\]](#)
7. Nguyen, N.M.; Alobaid, F.; Dieringer, P.; Epple, B. Biomass-Based Chemical Looping Gasification: Overview and Recent Developments. *Appl. Sci.* **2021**, *11*, 7069. [\[CrossRef\]](#)
8. Huang, Z.; Zhang, Y.; Fu, J.; Yu, L.; Chen, M.; Liu, S.; He, F.; Chen, D.; Wei, G.; Zhao, K.; et al. Chemical looping gasification of biomass char using iron ore as an oxygen carrier. *Int. J. Hydrogen Energy* **2016**, *41*, 17871–17883. [\[CrossRef\]](#)
9. Guo, Q.; Cheng, Y.; Liu, Y.; Jia, W.; Ryu, H.-J. Coal Chemical Looping Gasification for Syngas Generation Using an Iron-Based Oxygen Carrier. *Ind. Eng. Chem. Res.* **2014**, *53*, 78–86. [\[CrossRef\]](#)
10. Yan, J.; Sun, R.; Shen, L.; Bai, H.; Jiang, S.; Xiao, Y.; Song, T. Hydrogen-rich syngas production with tar elimination via biomass chemical looping gasification (BCLG) using BaFe<sub>2</sub>O<sub>4</sub>/Al<sub>2</sub>O<sub>3</sub> as oxygen carrier. *Chem. Eng. J.* **2020**, *387*, 124107. [\[CrossRef\]](#)
11. Liu, Q.; Hu, C.; Peng, B.; Liu, C.; Li, Z.; Wu, K.; Zhang, H.; Xiao, R. High H<sub>2</sub>/CO ratio syngas production from chemical looping co-gasification of biomass and polyethylene with CaO/Fe<sub>2</sub>O<sub>3</sub> oxygen carrier. *Energy Convers. Manag.* **2019**, *199*, 111951. [\[CrossRef\]](#)
12. Huseyin, S.; Wei, G.-Q.; Li, H.-B.; He, F.; Huang, Z. Chemical-looping gasification of biomass in a 10 kW<sub>th</sub> interconnected fluidized bed reactor using Fe<sub>2</sub>O<sub>3</sub>/Al<sub>2</sub>O<sub>3</sub> oxygen carrier. *J. Fuel Chem. Technol.* **2014**, *42*, 922–931. [\[CrossRef\]](#)
13. Condori, O.; García-Labiano, F.; de Diego, L.F.; Izquierdo, M.T.; Abad, A.; Adánez, J. Biomass chemical looping gasification for syngas production using LD Slag as oxygen carrier in a 1.5 kW<sub>th</sub> unit. *Fuel Process. Technol.* **2021**, *222*, 106963. [\[CrossRef\]](#)
14. Condori, O.; García-Labiano, F.; de Diego, L.F.; Izquierdo, M.T.; Abad, A.; Adánez, J. Biomass chemical looping gasification for syngas production using ilmenite as oxygen carrier in a 1.5 kW<sub>th</sub> unit. *Chem. Eng. J.* **2021**, *405*, 126679. [\[CrossRef\]](#)
15. Ge, H.; Guo, W.; Shen, L.; Song, T.; Xiao, J. Biomass gasification using chemical looping in a 25 kW<sub>th</sub> reactor with natural hematite as oxygen carrier. *Chem. Eng. J.* **2016**, *286*, 174–183. [\[CrossRef\]](#)
16. Wei, G.; He, F.; Huang, Z.; Zheng, A.; Zhao, K.; Li, H. Continuous Operation of a 10 kW<sub>th</sub> Chemical Looping Integrated Fluidized Bed Reactor for Gasifying Biomass Using an Iron-Based Oxygen Carrier. *Energy Fuels* **2015**, *29*, 233–241. [\[CrossRef\]](#)
17. Pissot, S.; Vilches, T.B.; Maric, J.; Seemann, M. Chemical looping gasification in a 2–4 MW<sub>th</sub> dual fluidized bed gasifier. In Proceedings of the 23rd International Conference on Fluidized Bed Conversion, Seoul, Republic of Korea, 13–17 May 2018; p. 10.
18. Marx, F.; Dieringer, P.; Ströhle, J.; Epple, B. Design of a 1 MW<sub>th</sub> Pilot Plant for Chemical Looping Gasification of Biogenic Residues. *Energies* **2021**, *14*, 2581. [\[CrossRef\]](#)
19. Condori, O.; García-Labiano, F.; de Diego, L.F.; Izquierdo, M.T.; Abad, A.; Adánez, J. Syngas production via Biomass Chemical Looping Gasification (BCLG) in a 50 kW<sub>th</sub> unit using ilmenite as oxygen carrier. *Proc. Fluid. Bed Convers. Conf.* **2022**, *2022*, 10.
20. Pröll, T.; Rupanovits, K.; Kolbitsch, P.; Bolhär-Nordenkamp, J.; Hofbauer, H. Cold Flow Model Study on a Dual Circulating Fluidized Bed (DCFB) System for Chemical Looping Processes. *Chem. Eng. Technol.* **2009**, *32*, 418–424. [\[CrossRef\]](#)
21. Ohlemüller, P.; Busch, J.-P.; Reitz, M.; Ströhle, J.; Epple, B. Chemical-Looping Combustion of Hard Coal: Autothermal Operation of a 1 MW<sub>th</sub> Pilot Plant. *J. Energy Resour. Technol.* **2016**, *138*, 042203. [\[CrossRef\]](#)
22. Pröll, T.; Bolhär-Nordenkamp, J.; Kolbitsch, P.; Hofbauer, H. Syngas and a separate nitrogen/argon stream via chemical looping reforming—A 140kW pilot plant study. *Fuel* **2010**, *89*, 1249–1256. [\[CrossRef\]](#)
23. Kunii, D.; Levenspiel, O. Circulating fluidized-bed reactors. *Chem. Eng. Sci.* **1997**, *52*, 2471–2482. [\[CrossRef\]](#)
24. Dieringer, P.; Marx, F.; Alobaid, F.; Ströhle, J.; Epple, B. Process Control Strategies in Chemical Looping Gasification—A Novel Process for the Production of Biofuels Allowing for Net Negative CO<sub>2</sub> Emissions. *Appl. Sci.* **2020**, *10*, 4271. [\[CrossRef\]](#)
25. Dieringer, P.; Marx, F.; Michel, B.; Ströhle, J.; Epple, B. Design and control concept of a 1 MW<sub>th</sub> chemical looping gasifier allowing for efficient autothermal syngas production. *Int. J. Greenh. Gas Control.* **2023**, *127*, 103929. [\[CrossRef\]](#)
26. Mirek, P. Influence of The Model Scale on Hydrodynamic Scaling in Cfb Boilers. *Braz. J. Chem. Eng.* **2016**, *33*, 885–896. [\[CrossRef\]](#)
27. Kunii, D.; Levenspiel, O. *Fluidization Engineering*, 2nd ed.; Butterworth-Heinemann Series in Chemical Engineering; Butterworth-Heinemann: Boston, MA, USA, 1991.
28. Grace, J.R. Contacting modes and behaviour classification of gas-solid and other two-phase suspensions. *Can. J. Chem. Eng.* **1986**, *64*, 353–363. [\[CrossRef\]](#)
29. Balasubramanian, N.; Srinivasakannan, C.; Basha, C.A. Transition velocities in the riser of a circulating fluidized bed. *Adv. Powder Technol.* **2005**, *16*, 247–260. [\[CrossRef\]](#)
30. Wang, H. Study on Separation Efficiency of Cyclone Separator for 75t/h Circulating Fluidized Bed Boiler. *IOP Conf. Series: Mater. Sci. Eng.* **2020**, *721*, 012037. [\[CrossRef\]](#)
31. Breault, R.W.; Monazam, E.R.; Shadle, L.J.; Rowan, S.; Macfarlan, L.H. The effect of riser end geometry on gas-solid hydrodynamics in a CFB riser operating in the core annular and dilute homogeneous flow regimes. *Powder Technol.* **2017**, *316*, 181–189. [\[CrossRef\]](#)
32. Yang, H.; Yue, G.; Xiao, X.; Lu, J.; Liu, Q. 1D modeling on the material balance in CFB boiler. *Chem. Eng. Sci.* **2005**, *60*, 5603–5611. [\[CrossRef\]](#)
33. Johnsson, F.; Andersson, S.; Leckner, B. Expansion of a freely bubbling fluidized bed. *Powder Technol.* **1991**, *68*, 117–123. [\[CrossRef\]](#)
34. Chen, H.; Li, Z.; Liu, X.; Li, W.; Cai, N.; Bertholin, S.; Tebianian, S.; Yazdanpanah, M.; Zhang, A. Solid Circulation Study in a 1.5 MW<sub>th</sub> Cold Flow Model of Chemical Looping Combustion. *Ind. Eng. Chem. Res.* **2021**, *60*, 2265–2277. [\[CrossRef\]](#)
35. Pallarès, D.; Johnsson, F. Macroscopic modelling of fluid dynamics in large-scale circulating fluidized beds. *Prog. Energy Combust. Sci.* **2006**, *32*, 539–569. [\[CrossRef\]](#)

36. Ohlemüller, P.; Alobaid, F.; Abad, A.; Adanez, J.; Ströhle, J.; Epple, B. Development and validation of a 1D process model with autothermal operation of a 1 MW<sub>th</sub> chemical looping pilot plant. *Int. J. Greenh. Gas Control* **2018**, *73*, 29–41. [CrossRef]
37. Breault, R.W.; Weber, J. Saturation Carrying Capacity for Group A Particles in a Circulating Fluidized Bed. *Energies* **2021**, *14*, 2809. [CrossRef]
38. Breault, R.W.; Weber, J.; Yang, J. Saturation carrying capacity Group B particles in a circulating fluidized bed. *Powder Technol.* **2021**, *384*, 442–451. [CrossRef]
39. Glicksman, L.; Hyre, M.; Farrell, P. Dynamic similarity in fluidization. *Int. J. Multiph. Flow* **1994**, *20*, 331–386. [CrossRef]
40. Glicksman, L.R. Scaling relationships for fluidized beds. *Chem. Eng. Sci.* **1984**, *39*, 1373–1379. [CrossRef]
41. Glicksman, L.; Hyre, M.; Woloshun, K. Simplified scaling relationships for fluidized beds. *Powder Technol.* **1993**, *77*, 177–199. [CrossRef]
42. Breault, R. *Maintaining Microstructure—The Path to Successful Technology Maturation in Fluidized Systems*; Report Number: DOE/NETL-2023/3866; National Energy Technology Laboratory (NETL): Pittsburgh, PA, USA, 2023. Available online: <https://www.osti.gov/biblio/1986293> (accessed on 10 July 2023).
43. Junk, M.; Reitz, M.; Ströhle, J.; Epple, B. Thermodynamic Evaluation and Cold Flow Model Testing of an Indirectly Heated Carbonate Looping Process. *Chem. Eng. Technol.* **2013**, *36*, 1479–1487. [CrossRef]
44. Bischi, A.; Langorgen, Ø.; Morin, J.-X.; Bakken, J.; Ghorbaniyan, M.; Bysveen, M.; Bolland, O. Hydrodynamic viability of chemical looping processes by means of cold flow model investigation. *Appl. Energy* **2012**, *97*, 201–216. [CrossRef]
45. Sato, M.; Itaya, H.; Taguchi, S. A Circulation and Reduction Behavior of Iron Ore in Circulating Fluidized Bed. *ISIJ Int.* **1994**, *34*, 393–400.
46. Djerf, T.; Pallarès, D.; Johnsson, F. Solids flow patterns in large-scale circulating fluidised bed boilers: Experimental evaluation under fluid-dynamically down-scaled conditions. *Chem. Eng. Sci.* **2021**, *231*, 116309. [CrossRef]
47. Alghamdi, Y.; Peng, Z.; Zanganeh, J.; Moghtaderi, B.; Doroodchi, E. Hydrodynamics similarities in cold flow model of chemical looping combustors: An experimental study. *Powder Technol.* **2019**, *343*, 542–550. [CrossRef]
48. Alghamdi, Y.; Peng, Z.; Shah, K.; Moghtaderi, B.; Doroodchi, E. A correlation for predicting solids holdup in the dilute pneumatic conveying flow regime of circulating and interconnected fluidised beds. *Powder Technol.* **2016**, *297*, 357–366. [CrossRef]
49. Markström, P.; Lyngfelt, A. Designing and operating a cold-flow model of a 100 kW chemical-looping combustor. *Powder Technol.* **2012**, *222*, 182–192. [CrossRef]
50. Marx, F.; Dieringer, P.; Ströhle, J.; Epple, B. Solid flux measurement in dual fluidized bed processes based on solid samples. *Fuel* **2023**, *341*, 127589. [CrossRef]
51. Ströhle, J.; Orth, M.; Epple, B. Chemical looping combustion of hard coal in a 1 MW<sub>th</sub> pilot plant using ilmenite as oxygen carrier. *Appl. Energy* **2015**, *157*, 288–294. [CrossRef]
52. Ohlemüller, P.; Ströhle, J.; Epple, B. Chemical looping combustion of hard coal and torrefied biomass in a 1 MW<sub>th</sub> pilot plant. *Int. J. Greenh. Gas Control* **2017**, *65*, 149–159. [CrossRef]
53. Tasirin, S.; Geldart, D. Entrainment of FCC from fluidized beds—A new correlation for the elutriation rate constants  $K_{io}^*$ . *Powder Technol.* **1998**, *95*, 240–247. [CrossRef]
54. Geldart, D.; Cullinan, J.; Georgiades, S.; Gilvray, D.; Pope, D.J. Effect of fines on entrainment from gas fluidized beds. *Trans. Inst. Chem. Eng.* **1979**, *57*, 269–275. Available online: <https://www.osti.gov/etdeweb/biblio/5049007> (accessed on 12 June 2023).
55. ISO 697-1981; Bestimmung der Schüttdichte, Verfahren durch Messen der Masse eines gegebenen Volumens. DIN: Berlin, Germany, 1984.
56. DIN EN ISO 1183-1:2019-09; Kunststoffe—Verfahren zur Bestimmung der Dichte von nicht verschäumte Kunststoffen—Teil 1: Eintauchverfahren, Verfahren mit Flüssigkeitspyknometer und Titrationsverfahren. DIN: Berlin, Germany, 2019.
57. Adanez, J.; Abad, A.; Garcia-Labiano, F.; Gayan, P.; de Diego, L.F. Progress in Chemical-Looping Combustion and Reforming technologies. *Prog. Energy Combust. Sci.* **2012**, *38*, 215–282. [CrossRef]
58. Larsson, A.; Israelsson, M.; Lind, F.; Seemann, M.; Thunman, H. Using Ilmenite to Reduce the Tar Yield in a Dual Fluidized Bed Gasification System. *Energy Fuels* **2014**, *28*, 2632–2644. [CrossRef]
59. Ohlemüller, P.; Alobaid, F.; Gunnarsson, A.; Ströhle, J.; Epple, B. Development of a process model for coal chemical looping combustion and validation against 100 kW<sub>th</sub> tests. *Appl. Energy* **2015**, *157*, 433–448. [CrossRef]
60. Abad, A.; Adanez, J.; Gayán, P.; de Diego, L.F.; García-Labiano, F.; Sprachmann, G. Conceptual design of a 100 MW<sub>th</sub> CLC unit for solid fuel combustion. *Appl. Energy* **2015**, *157*, 462–474. [CrossRef]
61. Bai, D.; Kato, K. Saturation carrying capacity of gas and flow regimes in CFB. *J. Chem. Eng. Jpn.* **1995**, *28*, 179–185. [CrossRef]
62. Colakyan, M.; Levenspiel, O. Elutriation from fluidized beds. *Powder Technol.* **1984**, *38*, 223–232. [CrossRef]
63. Wen, C.Y.; Hashinger, R.F. Elutriation of solid particles from a dense-phase fluidized bed. *AIChE J.* **1960**, *6*, 220–226. [CrossRef]
64. Fournol, A.B.; Bergougnou, M.A.; Baker, C.G.J. Solids entrainment in a large gas fluidized bed. *Can. J. Chem. Eng.* **1973**, *51*, 401–404. [CrossRef]

**Disclaimer/Publisher’s Note:** The statements, opinions and data contained in all publications are solely those of the individual author(s) and contributor(s) and not of MDPI and/or the editor(s). MDPI and/or the editor(s) disclaim responsibility for any injury to people or property resulting from any ideas, methods, instructions or products referred to in the content.

---

*This page is left blank intentionally*

---

**Research Paper V**

---

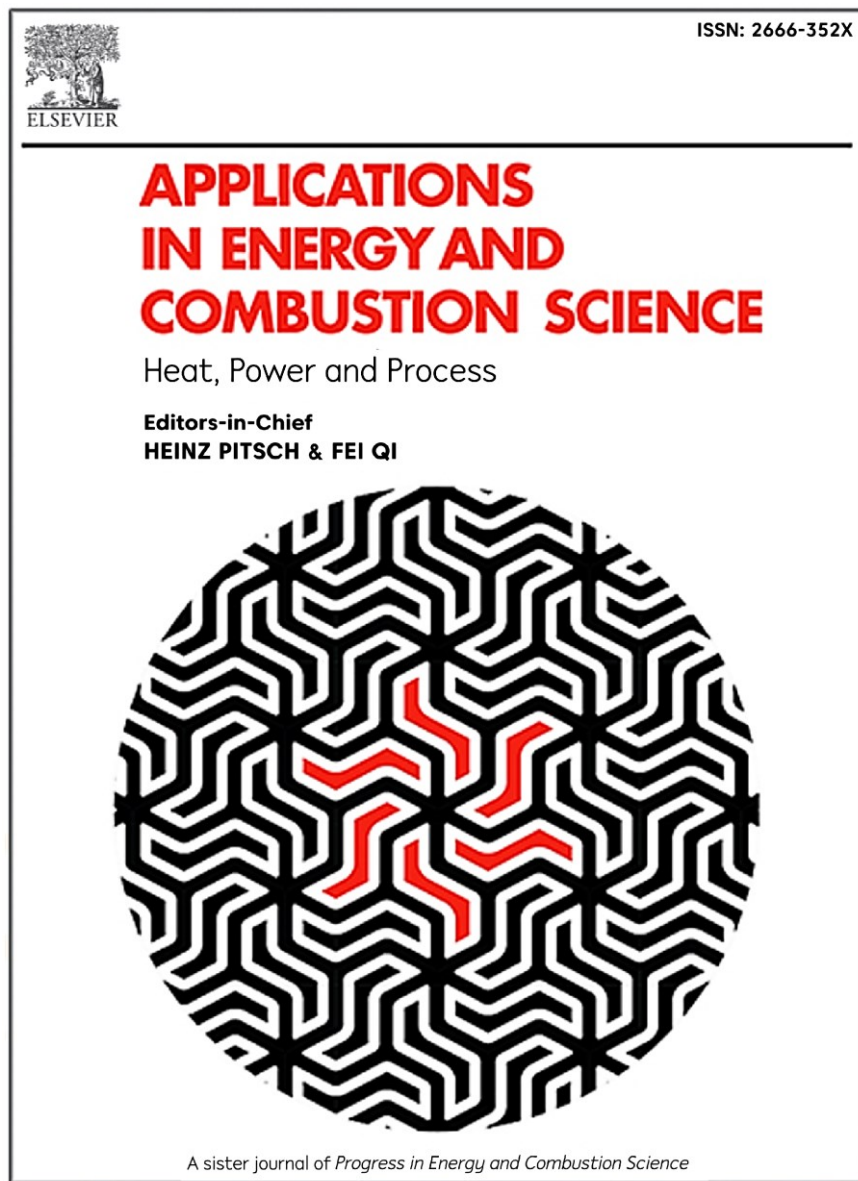
*Fate of Ilmenite as Oxygen Carrier during 1 MW<sub>th</sub> Chemical Looping Gasification of Biogenic Residues*

Paul Dieringer, Falko Marx, Florian Lebendig, Michael Müller, Andrea Di Giuliano, Katia Gallucci, Jochen Ströhle, Bernd Epple

---

**Journal:** Applications in Energy and Combustion Science, Vol. 16  
**Date:** 12/2023  
**DOI:** [10.1016/j.jaecs.2023.10](https://doi.org/10.1016/j.jaecs.2023.10)  
**ISSN:** 2666-352X  
**Copyright:** Open Access License: CC BY 4.0

---



Source: [ScienceDirect](https://www.sciencedirect.com)



## Fate of ilmenite as oxygen carrier during 1 MW<sub>th</sub> chemical looping gasification of biogenic residues

Paul Dieringer<sup>a,\*</sup>, Falko Marx<sup>a</sup>, Florian Lebendig<sup>b</sup>, Michael Müller<sup>b</sup>, Andrea Di Giuliano<sup>c</sup>, Katia Gallucci<sup>c</sup>, Jochen Ströhle<sup>a</sup>, Bernd Epple<sup>a</sup>

<sup>a</sup> Institute for Energy Systems and Technology (EST), Technical University Darmstadt, Otto-Berndt-Str. 2, 64287 Darmstadt, Germany

<sup>b</sup> Forschungszentrum Jülich GmbH, Institute for Energy and Climate Research (IEK-2), Wilhelm-Johnen-Straße, 52428 Jülich, Germany

<sup>c</sup> Department of Industrial and Information Engineering and Economics (DIIIIE), University of L'Aquila, Piazzale E. Pontieri 1, Loc. Monteluco di Roio, 67100 L'Aquila, Italy

### ARTICLE INFO

#### Keywords:

Chemical looping  
Gasification  
Oxygen carrier  
Pilot scale  
Fluidized bed  
Ilmenite  
Biomass

### ABSTRACT

Chemical looping gasification (CLG) is a novel gasification technology, allowing for the efficient conversion of different solid feedstocks (e.g. biogenic residues) into a high-calorific syngas. As in any chemical looping technology, the oxygen carrier (OC), transporting heat and oxygen from the air to the fuel reactor, is crucial in attaining high process efficiencies. To investigate the fate of the OC during CLG in an industrial environment, ilmenite samples, collected during >400 hours of chemical operation in 1 MW<sub>th</sub> scale using three different biomass feedstocks, were analyzed using different lab techniques. In doing so, changes in OC particle morphology and composition induced by CLG operation were determined. Moreover, the most important physical and chemical characteristics of the utilized OC were measured. The ensuing dataset allowed for an in-depth evaluation of the CLG technology in semi-industrial scale in terms of OC lifetime and durability. It was found that in the absence of agglomeration, the cycled OC exhibits an oxygen transport capacity of 2.6 wt.-%, a particle density of 3400 kg/m<sup>3</sup> and particle diameters between 60 and 250 μm in steady-state conditions. Moreover, it was found that OC loss via particle attrition determines the lifetime of the OC inside the 1 MW<sub>th</sub> CLG system. On the other hand, feedstock-related agglomeration, observed during CLG operation with wheat straw, was shown to impede OC circulation between AR and FR and thus prevent efficient CLG operation. In summary, the present study thus not only highlights that generally long-term CLG operation in industry-like conditions is feasible, but also provides important insights into measures to improve OC lifetime and durability inside an industrial chemical looping system, such as an optimization of cyclone efficiency or tailored pre-treatment of the utilized feedstock.

### 1. Introduction

With the global average temperature increase being predicted to exceed the threshold of +1.5°C, within the next four years with great likelihood [1], it is clear that the window for efforts to limit global warming to this critical limit, which was pledged not to be exceeded unilaterally by the world's leaders in the Paris Agreement [2], is closing. Consequently, immediate and unmatched global actions in all sectors are necessary to guarantee the well-being of future generations. One sector for which greenhouse gas (GHG) emissions were not reduced in the past decades [3], despite persistent pledges from industry and politics, is the transport sector. While big advances in electrification of

passenger vehicles were realized in recent years [4], thereby promising a reduction of the future carbon-footprint of personal transport on the earth's atmosphere, alternative approaches are required for other modes of transport (e.g. aviation, heavy transport, shipping) [5]. An auspicious route under consideration for the de-fossilization of those means of transport is the production of 2<sup>nd</sup> generation biofuels. Here, a promising pathway is the thermochemical conversion of biogenic residues into a high-calorific syngas, before further treatment and fuel synthesis [6,7]. Commonly, this is achieved using oxygen-blown gasifiers, in which the feedstock is partially oxidized yielding a high-calorific syngas [8,9]. A novel gasification pathway allowing for an efficient production of synthesis gas from different solid feedstocks is the chemical looping gasification (CLG) technology. Here, an active bed material, called oxygen

\* Corresponding author.

E-mail address: [paul.dieringer@est.tu-darmstadt.de](mailto:paul.dieringer@est.tu-darmstadt.de) (P. Dieringer).

<https://doi.org/10.1016/j.jaecs.2023.100227>

Received 27 July 2023; Received in revised form 30 October 2023; Accepted 15 November 2023

Available online 17 November 2023

2666-352X/© 2023 The Author(s). Published by Elsevier Ltd. This is an open access article under the CC BY license (<http://creativecommons.org/licenses/by/4.0/>).



Nomenclature			
<i>Latin symbols</i>			
$AJI$	attrition index	GHG	greenhouse gas
$c_p$	heat capacity	ILMc	coarse ilmenite
$d_p$	particle diameter	ILMf	fine ilmenite
$h$	height	IWP	industrial wood pellets
$m_{inv.}$	mass inventory of riser	K1/2/3	campaign 1/2/3
$m_i$	mass of species $i$	LS	loop seal
$\dot{m}_i$	mass flow of species $i$	OC	oxygen carrier
$P$	power	PFR	pine forest residue
$p$	pressure	PSD	particle size distribution
$Q_{3,i}$	mass fraction of particles with size $i$	TGA	thermogravimetric analysis
$R_{OC}$	oxygen transport capability	WSP	wheat straw pellets
$T$	temperature	SEM	scanning electron microscopy
$t$	time	EDX	energy dispersive X-ray spectroscopy
$u$	velocity	EDXRF	EDX- fluorescence spectroscopy
$RI$	rate index	XRD	X-ray diffraction
$\dot{Q}$	heat flow		
<i>Greek symbols</i>			
$\Delta m_i$	change in mass of species $i$	<i>Indices</i>	
$\Delta t$	change in time	0	reference state
$\tau_{LT,OC}$	OC lifetime	AR	air reactor
$\eta_{Cyc}$	cyclone separation efficiency	bulk	bulk
$\rho$	density	circ	circulating
$\omega$	mass conversion of OC	exp	experimental
<i>Acronyms/abbreviations</i>		FA	fly ash
AR	air reactor	FR	fuel reactor
BA	bottom ash	finest	finest
CCS/U	carbon capture & storage/utilization	norm	normalized
CFB	circulating fluidized bed reactor	MU	make-up
CLG	chemical looping gasification	m	mean
CLC	chemical looping combustion	mf	minimum fluidization
DFBG	dual fluidized bed gasification	mb	minimum bubbling
FR	fuel reactor	O	oxygen
		OC	oxygen carrier
		ox	oxidized/oxidation
		p	particle
		red	reduced/reduction
		ref	reference
		th	thermal

carrier (OC), is transferred between two reactors. Its purpose is to transport heat and oxygen from the air reactor (AR) to the fuel reactor (FR), in which the solid feedstock is converted into a high-calorific syngas (see Fig. 1). As the OC provides oxygen for the gasification reactions occurring inside the FR, CLG constitutes an oxygen-driven gasification technology. However, as opposed to conventional oxygen-blown gasifiers, CLG does not rely on a costly air separation unit, as the oxygen is selectively taken-up from the inlet air inside the AR by the OC. Another inherent characteristic of the CLG technology is that it facilitates an efficient capturing of the CO<sub>2</sub> formed during the auto-thermal gasification step. For biomass-to-liquid process chains this means that the CO<sub>2</sub> contained in the N<sub>2</sub>-free raw syngas is removed in the downstream syngas purification unit, thus allowing for net negative CO<sub>2</sub> emissions of the process chain, in case it is captured (CCS) or utilized (CCU) in subsequent process steps [6,10].

With novel synthesis pathways for carbon-neutral or carbon-negative fuels being in demand globally, research on the CLG technology has experienced a push in recent years. However, so far its investigation was mainly restricted to lab-scale [11–13] or small pilot-scale [14–16] units, thereby leaving a major research gap, i.e. the advancement of the CLG technology to higher technology readiness levels via pilot-scale investigations in an industrially-relevant environment. By modifying an existing modular 1 MW<sub>th</sub> pilot plant, previously used for carbonate looping [17,18], chemical looping combustion [19,20], and High Temperature Winkler gasification [9,21], for CLG operation [22], the

investigation of the CLG technology in such conditions was facilitated, allowing for in-depth analyses of different phenomena occurring inside a CLG unit in industry-like conditions.

Due to the importance of the OC for chemical looping processes (esp. heat & oxygen transport), one aspect crucial for the up-scaling of the CLG technology is the fate of the OC inside the CLG unit, deciding on process efficiency (e.g. OC activity, material loss) as well as process economics (e.g. material procurement and disposal costs). To cast light onto this subject, early work analyzed the suitability of various OCs in lab scale setups [23]. Generally, ilmenite is considered to be an auspicious OC for chemical looping application, due to its low price, high availability, and advantageous physio-chemical properties (e.g. mechanical rigidity and activity) [24,25]. To investigate the long term effect of chemical looping on ilmenite properties, it was investigated in different lab-scale setups under relevant redox conditions [26–28]. Here, it was found that ilmenite particles undergo characteristic changes during redox cycling, manifesting themselves in an increasing particle porosity, the formation of an iron-rich shell on the particle surface, an overall decrease in their oxygen transport capacity, and a decrease in their attrition resistance. While these findings are universally agreed upon, only limited information on the fate of the OC in real chemical looping setups is available. Generally, this data stems from small lab or pilot plants [11,29–31], giving first insights into the fate of the OC during CLG operation. Apart from confirming general findings made in lab-scale, these studies provide insights into the fate of the OC in real

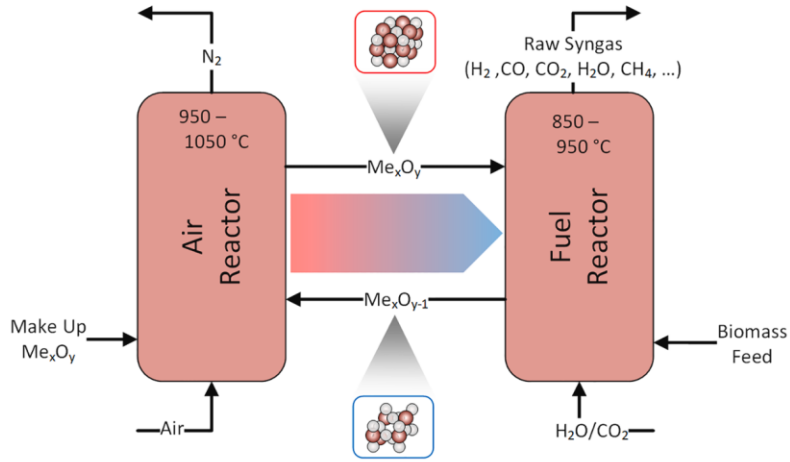


Fig. 1. Schematic illustration of CLG process.

chemical looping systems, with regard to attrition rates, agglomeration behavior, or OC phase composition. However, when striving for reliable information on the performance of OC materials in large-scale setups, the investigation of changes in OC properties occurring during chemical looping operation in an industrially-relevant environment is indispensable.

First and foremost, efficient CLG operation requires sufficiently long oxygen carrier lifetimes, translating in low make-up and material loss rates, which are crucial for operation both technically and economically

[24]. Generally, the OC needs to be replaced due to one (or multiple) of the following reasons [24]:

- Attrition: Due to thermal, chemical, and mechanical strain inside the CLG system, the OC particles in the system can break or abrade leading to a decrease in particle size and ultimately material loss via the cyclone into the downstream filters.
- Agglomeration: In case of thermal (e.g. sintering/melting) or chemical (e.g. ash interactions) influences OC particles can

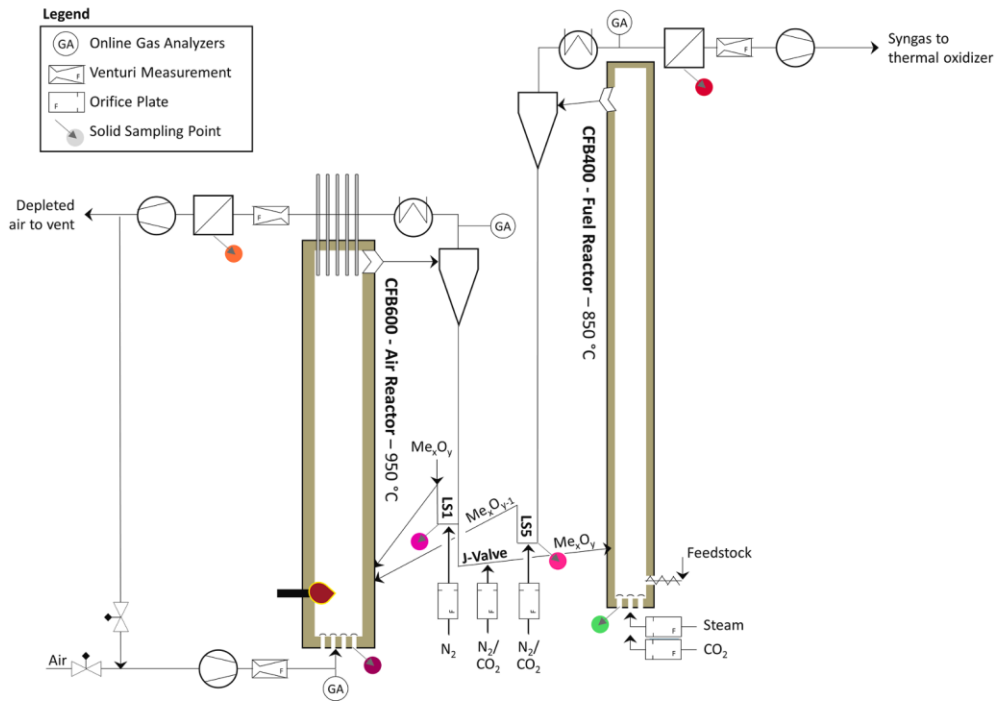


Fig. 2. Simplified flow diagram of the 1 MW<sub>th</sub> CLG pilot plant.

agglomerate, leading to an increase in particle size and hence a decrease in the OC circulation rate within the system. These agglomerates need to be removed from the fluidized bed via sluicing to maintain the desired particle size distribution inside the reactor system.

- Deactivation: Thermal (e.g. sintering/melting) or chemical (e.g. ash interactions) impacts can lead to a decrease in the reactivity of the OC (i.e. lower oxygen carrier capacity or slower oxygen uptake/release kinetics), impairing oxygen transport in the system and ultimately diminishing process efficiency.
- Ash Sluicing: In case feedstocks with high ash-contents are utilized, residual ash needs to be actively removed from the system via ash-sludging, leading to a gradual loss of OC material.

Due to the long-term operation at industry-like conditions, pilot tests inside the 1 MW<sub>th</sub> CLG unit used in this study present ideal conditions to investigate if the mechanisms listed above occur during CLG operation and if so, which one is the most dominant. In order to do so, samples from different positions in the 1 MW<sub>th</sub> pilot plant were collected during operation and subsequently analyzed with regard to their morphology, as well as physical (e.g. particle size and particle density) and chemical (e.g. oxygen transport capacity, redox rates) properties. Moreover, live-data from the process (e.g. OC make-up rates, mass extracted via filters and ash sluicing screws) was utilized to derive insights into the fate of the OC inside the 1 MW<sub>th</sub> CLG unit. Through combination of these unique datasets, this study closes a crucial research gap, thereby further promoting the technology readiness level of chemical looping processes towards market maturity.

## 2. Experimental

### 2.1. 1 MW<sub>th</sub> pilot plant

#### 2.1.1. Pilot plant layout

The layout of the 1 MW<sub>th</sub> CLG pilot plant is described in detail elsewhere [22]. Therefore, only the main features of the pilot, schematically shown in Fig. 2, are elaborated hereinafter for brevity.

The reactor system, consisting of an air reactor (0.59 m inner diameter, 8.66 m height), a fuel reactor (0.4 m inner diameter, 11.35 m height), and three coupling elements (two loop seals and a J-valve), is refractory lined to minimize heat losses, allowing for autothermal operation (i.e. without electrical heating). The AR can be fluidized with air or a mixture of air and recycled flue gas, which can be electrically pre-heated to temperatures up to 375°C. For process control reasons, the inlet gas composition (O<sub>2</sub>, CO<sub>2</sub>) is measured for the AR. The fuel reactor can be fluidized with air, steam, a mixture of steam and CO<sub>2</sub>, or a mixture of air and CO<sub>2</sub>. The FR-fluidization media can be electrically pre-heated to temperatures up to 450°C. Each reactor is equipped with a cyclone for gas solid separation and a loop seal to prevent bypassing of gases. Global solid circulation between the two reactors is achieved with a J-valve, connecting the loop seal (LS) of the AR (LS1) with the fuel reactor. Each loop seal is equipped with a solid sampling facility, allowing for the controlled removal of OC samples during operation. More details on the sampling procedure are provided by Marx et al. [32]. The circulating mass flow between both reactors can be adjusted by changing the fluidization flow of the J-Valve, which can be fluidized with nitrogen or CO<sub>2</sub>. For the fuel reactor, all entrained material leaving the riser is directly transferred into the AR via LS5, which is fluidized with nitrogen or CO<sub>2</sub>. On the other hand, the option of internal solid circulation via LS1, fluidized with nitrogen, exists for the AR. A solid fuel flow up to 340 kg/h corresponding to a thermal power of about 1.7 MW can be introduced into the dense bed of the FR via an oil-cooled feeding screw. The fuel reactor off-gases first pass a syngas cooler, where it is cooled to a temperature of approx. 350°C. Subsequently, the gas composition (CO, CO<sub>2</sub>, O<sub>2</sub>, H<sub>2</sub>, CH<sub>4</sub>) and gas flow is measured online. To allow for safe venting to the environment, the FR product gas is then

transferred through a hot gas filter, operated at up to 250°C, using an induced draft fan, before it enters a thermal oxidizer, required for full conversion of all hydrocarbon species to CO<sub>2</sub> and H<sub>2</sub>O. The FR product gas can also be rerouted to a gas cleaning facility, equipped with a fuel synthesis test rig, if desired. After online gas sampling (CO, CO<sub>2</sub>, O<sub>2</sub>, SO<sub>2</sub>, NO), the off-gases from the AR are cooled in a heat exchanger, to a temperature <250°C. Thereafter, the gas enters a fabric filter for dedusting. Downstream of the induced draft fan controlling the free-board pressure of the AR, the AR flue gases can be vented to the environment through a stack or can be partly recycled back to the AR airbox via the primary-air fan. In order to maintain constant reactor inventories throughout operation, the pilot is equipped with a make-up feeding system, allowing for the controlled introduction of up to 200 kg/h of ilmenite into the standpipe of LS1 via a dosing screw.

### 2.2. Materials

#### 2.2.1. Bed material (1 MW<sub>th</sub> Pilot Plant) - ilmenite

Ilmenite from the Norwegian Company Titania AS, which was successfully deployed during previous chemical looping experiments in the 1 MW<sub>th</sub> pilot [19,20,33], was used for the CLG experiments presented in this study. For the fresh material (ILMf), a bulk density of 2550 kg/m<sup>3</sup>, a particle density of 4486 kg/m<sup>3</sup>, and a mean particle diameter of 111 μm ( $d_{p,10}=31\ \mu\text{m}$ ,  $d_{p,90}=224\ \mu\text{m}$ ) was determined (more details see Section 2.4). For selected operating periods, a different granulation of ilmenite from the Norwegian Company Titania AS, was used. This coarser material (ILMc), exhibits a bulk density of 2336 kg/m<sup>3</sup>, a particle density of 4621 kg/m<sup>3</sup>, and a mean particle diameter of 199 μm ( $d_{p,10}=151\ \mu\text{m}$ ,  $d_{p,90}=247\ \mu\text{m}$ ) in fresh delivery condition.

#### 2.2.2. Feedstocks

For CLG pilot testing in the 1 MW<sub>th</sub> facility, three different feedstocks were used. During the first test campaign (K1), cylindrical industrial wood pellets (IWP) conforming to the Norm ENPlus A1, purchased from Eckard GmbH, Germany, were used. For the second test campaign (K2), cylindrical pine forest residue pellets (PFR) from AB Torkapparater, Sweden were deployed. Throughout the third test campaign (K3), cylindrical pre-treated wheat straw pellets (WSP), from AB Torkapparater, Sweden, were utilized. Proximate and ultimate analysis as well as all pellet dimensions, bulk densities, and lower heating values (LHV) for all pellet types are given in Table 1.

### 2.3. Operating conditions of 1 MW<sub>th</sub> chemical looping gasifier

In 2022, the modular 1 MW<sub>th</sub> pilot plant at TU Darmstadt was continuously operated (24 h/day) as an autothermal chemical looping gasifier for approx. 14 days each in three separate test campaigns, yielding >400 h of chemical looping operation. These intervals of long-term operation allow for in-depth investigations of the fate of the OC during CLG.

Within the first test campaign (K1), the pilot was operated for ~110 h in chemical looping mode, using industrial wood pellets as the feedstock and fine ilmenite (ILMf) as the bed material. During the second test campaign (K2), the 1 MW<sub>th</sub> pilot plant was operated using pine forest residue pellets as the feedstock, resulting in more than 210 h of successful chemical looping operation. Throughout the first section of K2, coarse ilmenite (ILMc) was used as the make-up bed material, before it was replaced with fine ilmenite (ILMf) in the later stages of the second test campaign. For initial reactor filling at the start of K2, old bed material from K1 was used. During the third test campaign (K3), the 1 MW<sub>th</sub> pilot plant was operated using pre-treated wheat straw pellets as the feedstock and fine ilmenite (ILMf) as the bed material.<sup>1</sup> Here, the pilot

<sup>1</sup> Coarse ilmenite (ILMc) was utilized during system-start up, but was replaced with fine ilmenite (ILMf), before initiation of CLG operation.

plant was successfully operated in chemical looping mode for a total of ~80 hours.

#### 2.4. Material characterization

During operation of the 1 MW<sub>th</sub> pilot plant, solid material collected from both loop seals, both filters, and from the ash sluicing screw of both reactors were collected (sampling location see Fig. 2). These materials were analyzed using different lab techniques, in order to allow for the subsequent calculation of important evaluation parameters (see Section 2.5). Using the same methods, the fresh materials (see Section 2.2) as well as agglomerates, retrieved from the reactor after termination of K3 (more details see Section 3.4), were analyzed.

##### 2.4.1. Particle size distribution (PSD) and mean particle diameter

The particle size distribution of the fresh materials and solid loop seal samples was determined according to the norm DIN66165, using an air jet sieve type LS200-N by the company Hosokawa Alpine AG, Germany. Each PSD was determined singularly. Based on the measured PSD, integral parameters, such as the mean particle diameter, were calculated for each bulk material.

##### 2.4.2. Bulk density

Bulk densities for fresh materials and solid samples were determined using a self-made setup, consisting of a pouring device and a collection vessel with known volume, which conforms to the norm ISO 697. Values were determined in triplicates.

##### 2.4.3. Particle density

Particle densities for fresh materials and solid samples were determined using according to the norm DIN EN ISO 1183, using water pycnometry in calibrated 25 and 50 mL pycnometers by Carl Roth, Germany. Prior to the measurements, the pycnometers were recalibrated using water at ambient conditions. During pycnometry, water temperatures were measured to account for the impact of changing room temperatures on water densities. All values were determined in duplicates. In case of strong deviations (>15 %) for two corresponding values, a third value was determined.

##### 2.4.4. Attrition jet cup

Attrition behavior of the OC materials was evaluated using a jet cup according to the setup of Ryden et al. [34]. Inside the jet cup, the material was fluidized with air (600 NL/h), achieving nozzle velocities of approx. 100 m/s. For evaluation, each material was tested for 90 minutes, and the attrition was quantified at 10, 20, 30, 50, 70, and 90 minutes by weighing the filter located at the gas outlet of the jet cup.

##### 2.4.5. Thermogravimetric analysis

Redox behavior as well as the oxygen transport capacity of the OC materials was evaluated via thermogravimetric analysis (TGA). Here, approx. 50 mg of OC material was heated to 950°C under N<sub>2</sub> atmosphere. Subsequently, the OC material was firstly fully oxidized with synthetic air, at a flow rate of 100 mL/min for 20 min. Thereafter, the material was subjected to five redox cycles, using mild reduction and oxidation

conditions (reduction: 20 min, 100 mL/min of 6.5 vol.-% H<sub>2</sub>, 35.5 vol.-% H<sub>2</sub>O in N<sub>2</sub>, oxidation: 20 min, 100 mL/min of synthetic air), to prevent substantial changes in the OC morphology occurring inside the TGA. Finally, the material was cooled down to ambient temperature under N<sub>2</sub> atmosphere.

##### 2.4.6. Pressure fluctuation tests

Using the fresh ilmenite OC (ILMf and ILMc, see Section 2.2.1), as well as ashes of the WSP (see Section 2.2.2), produced by muffle combustion at 700°C for 3 h, pressure fluctuation test were carried out following the method by Di Giuliano et al. [35–37], to evaluate the effect of WSP ashes on fluidization behavior of the utilized OC materials.

Here, ashes from biomass and OC were mixed at constant volumetric ratio (9 ml ash : 90 ml OC), and heated in a fluidized bed quartz reactor up to temperatures in the range 700–1000°C with N<sub>2</sub> as the fluidizing agent. Pressure fluctuation signals were acquired at two and three times the minimum bubbling velocity of the OC at selected temperatures. Subsequent to the pressure fluctuation tests, samples from the fluidized bed were stored for SEM-EDS analyses (see Section 2.4.8).

##### 2.4.7. Feedstock ash melting behavior

Ash of the different feedstocks was produced under gasification-like conditions in N<sub>2</sub>/15 % H<sub>2</sub>O/5 % CO<sub>2</sub> at 550°C. At the beginning, about 5 % O<sub>2</sub> was added to accelerate the carbon conversion until its concentration downstream of the sample, detected by a lambda sensor, increased to ~0.1 %.

The melting behavior of the obtained ash was characterized by hot stage microscopy as described in literature [38,39]. Furthermore, the temperature-dependent melt fraction of the ash under equilibrium conditions was calculated using *FactSage* 8.1 and the *FactPS* (gas) and *FTOXid* (pure solids and SLAGA) databases. All major ash components Al<sub>2</sub>O<sub>3</sub>, CaO, Fe<sub>2</sub>O<sub>3</sub>, K<sub>2</sub>O, MgO, Na<sub>2</sub>O, P<sub>2</sub>O<sub>5</sub> and SiO<sub>2</sub>, recalculated from, were considered.

##### 2.4.8. SEM, SEM-EDX, and SEM EDXRF analysis

Loop seal samples collected during operation of each test campaign, were analyzed via scanning electron microscopy (SEM) and SEM-energy dispersive X-ray spectroscopy (EDX), to determine the distribution of Fe, Ti, Ca, Si, and O on the particle surface. Moreover, micrographs were taken from selected samples and these micrographs were analyzed via SEM-EDX, to map the given elements along the particle diameter.

Additionally, pieces of the agglomerated samples from K3 (more details see Section A.3 in the Supplementary Material) were ground in a mortar and the resulting powder was characterized by EDX- fluorescence spectroscopy (EDXRF) and X-Ray Diffraction (XRD) regarding elemental and mineral composition, respectively. Unground material of the same samples were investigated by SEM-EDX.

Lastly, SEM-EDX analysis of the resulting materials from the pressure fluctuation tests (see Section 2.4.6) was carried out, to visually assess potential changes in particle structure.

**Table 1**

Proximate (as received), ultimate analysis (dry ash free) and other properties for industrial wood pellets (IWP), pine forest residue pellets (PFR), and wheat straw pellets (WSP).

	IWP	PFR	WSP		IWP	PFR	WSP		IWP	PFR	WSP
	Ultimate in wt.-% (d.a.f.)				Proximate in wt.-% (a.r.)				Other Properties		
C	50.8	48.9	42.5	C-fix	13.3	16.63	16.3	d [mm]	6	6 - 8	6 - 8
H	6.0	5.8	5.10	Volatiles	79.6	76.77	68.7	l [mm]	10 -25	8 - 12	8 - 12
O	43.2	38.3	36.7	Ash	0.65	2.20	4.2				
N	0.07	0.43	0.10	Moisture	6.5	4.40	10.8	P <sub>bulk</sub> [kg/m <sup>3</sup> ]	650	630	504
S	0.008	0.02	0.48					LHV [MJ/kg]	17.96	18.3	15.3
Cl	0.006	0.01	0.07								

## 2.5. Evaluation parameters

### 2.5.1. OC oxygen carrying capacity

The oxygen carrying capacity of the OC is calculated by relating the oxidized ( $m_{Ox}$ ) and reduced ( $m_{Red}$ ) masses of the OC [24]. These masses are determined at the end of the oxidation and reduction step inside the TGA (see Section 2.4.5), respectively:

$$R_{OC} = \frac{m_{Ox} - m_{Red}}{m_{Ox}} \quad (1)$$

### 2.5.2. OC redox rate index

To determine the redox reaction rates of different OC samples, the relative weight ( $\omega$ ) of the OC inside the TGA is defined as:

$$\omega(t) = \frac{m(t)}{m_{Ox}} \quad (2)$$

Using this value, the rate index, suggested in literature [23], can be calculated by:

$$RI \text{ [wt. - \% / min]} = 60 \cdot 100 \cdot \left( \frac{d\omega}{dt} \right)_{norm} \quad (3)$$

Here, the last term signifies the normalized relative weight change of the OC ( $d\omega$ ) over time and is calculated by adjusting the weight change determined inside the TGA ( $exp$ ) with reference partial pressures for the reducing or oxidizing gases [27]:

$$\left( \frac{d\omega}{dt} \right)_{norm} = \left( \frac{d\omega}{dt} \right)_{exp} \cdot \frac{P_{ref}}{P_{TGA}} \quad (4)$$

For the oxidation, a reference oxygen partial pressure of 0.1 atm was used, whereas for the reduction a reference hydrogen partial pressure of 0.15 atm was employed [27]. The experimental weight change rate of the OC is calculated via linear regression of the weight vs. time data from the TGA over the first 40 s of reduction and 16 s of oxidation, respectively. In this duration, a relative weight change ( $\Delta\omega$ ) of approx. 0.01 is obtained, for which it was found that OCs generally exhibit fast and constant oxygen release and uptake kinetics [23].

### 2.5.3. OC lifetime

Another important parameter for scale-up of the chemical looping technologies is the OC lifetime. In smaller continuous chemical looping pilots, this parameter relates the fines losses (<40–45  $\mu\text{m}$ ) to the total OC reactor inventory ( $m_{inv}$ ) [29,40]. For the 1 MW<sub>th</sub> CLG system, a similar definition is used. However, in addition to fine losses towards the filters ( $\Delta m_{FA}$ ), the material removed from the AR and FR via ash sluicing ( $\Delta m_{BP}$ ) over a given period of time ( $\Delta t$ ) is also considered here:

$$\tau_{LT,OC} = \frac{m_{inv} \cdot \Delta t}{\Delta m_{FA,AR} + \Delta m_{FA,FR} + \Delta m_{BP,AR} + \Delta m_{BP,FR}} \approx \frac{m_{inv}}{\dot{m}_{MU,OC}} \quad (5)$$

A method to approximate the OC lifetime ( $\tau_{LT,OC}$ ) for the 1 MW<sub>th</sub> CLG plant is by relating the reactor inventory to the OC make-up rate ( $\dot{m}_{MU,OC}$ ), necessary to stabilize the AR and FR reactor inventory.

### 2.5.4. OC attrition index

One factor determining the OC lifetime is its stability towards attrition. Using the jet cup (see Section 2.4.4), the attrition behavior of the OC in a lab environment was analyzed. For further analysis, an attrition index ( $AJI$ ) similar to the one defined by Ryden et al. [34] was defined:

$$AJI \text{ [wt. - \% / h]} = 100 \cdot \frac{m_{fines}(t = 90 \text{ min}) - m_{fines}(t = 30 \text{ min})}{m_{0,OC}} \quad (6)$$

Here,  $m_{0,OC}$  denotes the mass of the OC placed into the jet cup prior to experiment, and  $m_{fines}$  is the mass of fines collected from the filter at the outlet of the jet cup at 90 and 30 minutes.

### 2.5.5. Cyclone efficiency

The cyclone efficiency ( $\eta_{Cyc}$ ) is another important parameter affecting the OC lifetime, as it decides to which extent OC particles can be maintained inside the system. The cyclone efficiency is defined as follows:

$$\eta_{Cyc} = 1 - \frac{\Delta m_{FA}}{\dot{m}_{circ,OC} \cdot \Delta t} \quad (7)$$

Here,  $\Delta m_{FA}$  denotes the fine losses over a given period of time ( $\Delta t$ ), while  $\dot{m}_{circ,OC}$  is the global OC circulation rate, determined via the method of Marx et al. [32].<sup>2</sup>

## 3. Results and discussion

The effect of CLG operation on the OC inside the 1 MW<sub>th</sub> pilot plant will subsequently be analyzed in four dedicated sections. Firstly, characteristic changes in OC morphology and composition arising during chemical looping operation will be discussed in Section 3.1. Subsequently, changes in the physical properties of the OC (e.g. particle size, particle density, etc.) will be analyzed in Section 3.2. Thereafter, changes occurring in the OC's chemical properties during redox cycling in the 1 MW<sub>th</sub> CLG system will be highlighted in Section 3.3. Lastly, the effect of feedstock characteristics on OC properties, observed during operation with wheat straw pellets, will be presented in Section 3.4. In doing so, a holistic overview over the fate of the OC in industry-like CLG conditions will be provided.

### 3.1. Morphological and compositional changes of OC

It is well established that OC particles undergo distinct morphological and compositional changes during chemical looping operation. For one, the particle porosity increases as macro-pores in the range of 50–500 nm are formed within the OC particle [26]. This distinct change in OC morphology was also observed during 1 MW<sub>th</sub> CLG operation, which is not only deducible from the change in particle density (see Section 3.2.2), but is also clearly visible in SEM micrographs of fresh and used OC particles. As visible in Fig. 3, showing micrographs of fresh (Fig. 3a and b) and used (Fig. 3c and d) OC samples, pores form on the inside of the OC during CLG operation, induced through the oxygen migration during the redox activity of the OC inside the FR and AR. This arise of macro-pores inside the OC particle was found to be crucial for OC activation and reactivity [27], making it an important phenomenon in chemical looping operation. The observation of this phenomenon inside the 1 MW<sub>th</sub> CLG unit shows that it occurs regardless of reactor size and operational mode, meaning that it will also occur in an industrial-size CLC/CLG unit. As more porous OC particles generally exhibit weaker mechanical properties [23], it can be inferred that the observed pore formation is one reason why used OC particles from the 1 MW<sub>th</sub> CLG unit exhibit a lower mechanical stability than the fresh OC (see Section A.2 in the Supplementary Material). Moreover, the increased porosity leads to faster oxygen release and uptake by the OC [27], improving the overall redox kinetics (more details see Section 3.3).

Another phenomenon giving rise to the increase in OC particle porosity during chemical looping operation is the well-documented formation of a detached iron-rich layer at the surface of the OC [26–29]. This shell-formation does not only entail the formation of a porous layer between the shell and the core [26,27], which increases particle porosity, but the underlying iron migration was found to lead to cracks inside the OC particle [26,27], also entailing a decrease in particle density. To determine to which extent this behavior occurred

<sup>2</sup> Since the solid entrainment from the AR exceeds the global OC circulation for the given setup of the 1 MW<sub>th</sub> CLG unit, cyclone efficiencies determined for the AR signify minimum values.

during 1 MW<sub>th</sub> CLG operation, selected OC samples were analyzed via SEM-EDX. Micrographs analyzed via SEM-EDX clearly show the formation of a Fe-rich and Ti-depleted shell during CLG operation (see Fig. 4a and c). Further SEM analysis showed the fracturing-off of pieces of the iron-rich shell (see Fig. 4b and c), indicating that the boundary between bulk and shell constitutes a weak point of the OC particle. This means that, as mechanical forces act upon the OC particle inside the CLG system, the shell-layer is easily broken-off and hence is a major reason for particle abrasion. As the growth of the iron-enriched shell was found to increase with increasing redox activity of the particle [26] this finding could explain why lower OC lifetime are reported for CLG when compared to CLC [29], as the OC reaches deeper reduction stages for the former, thus favoring shell-growth and subsequent shell-abrasion.

### 3.2. Change of physical properties of OC during 1 MW<sub>th</sub> pilot testing

It is generally known that physical properties of the OC are of high importance for the operation of chemical looping systems. For example, the OC has to exhibit particle sizes in the right range to achieve sufficient solid circulation and prevent extensive material loss [41]. Moreover, a certain material rigidity is required, to prevent extensive material losses via abrasion and/or fragmentation [24]. Here, ilmenite was found to be a promising material, exhibiting lifetimes >500 h due to its good mechanical stability [25,26]. Moreover, ilmenite was successfully used for chemical looping combustion in 1 MW<sub>th</sub> scale [19,33], underlining its availability in the required particle sizes. Thus, ilmenite is generally considered to be a material well-suited for chemical looping operation [24,25]. Nonetheless, detailed analyses of the physical changes occurring in ilmenite particles in an industry-like chemical looping setup have not been reported in literature, yet.

#### 3.2.1. Particle size distribution, attrition behavior and OC lifetime

A straightforward method to determine the fate of the OC inside the CLG system and evaluate changes of its physical properties during operation is to close the solid mass balance around the CLG system. In literature, OC lifetimes of 1300 and 630 h were reported for ilmenite for continuous CLC and CLG operation in the 1.5 kW<sub>th</sub> range, respectively, by recovering and weighing the fines (<40 μm) collected in the filters during operation [29]. For the 1 MW<sub>th</sub> pilot plant, a similar procedure can be employed, i.e. by continuously weighing the collecting containers from both filters as well as the material removed via ash sluicing during operation (see Eq. (5)). In contrast to smaller units, the OC make-up system is used to stabilize the solids inventory of the 1 MW<sub>th</sub> CLG system during operation (approx. 1200 kg), thus signifying a source of fresh material input into the system. The second solid material fed into the reactor system is the feedstock, which is being introduced inside the FR. Here, feedstock moisture and volatiles leave the FR in a gaseous form. Moreover, the fixed carbon can be assumed to be almost entirely converted into gaseous species inside the reactor system (FR & AR), meaning that only feedstock ash remains in its solid state inside the CLG unit. Consequently, the solid input accumulating in the CLG system constitutes the sum of the fed fresh OC and the ash from the feedstock fed into the FR.

When calculating the total solid input for a five-day period of stable chemical looping operation from K1, a value of approx. 3.6 t is obtained. As shown in Fig. 5, the vast majority of those 3.6 t can be attributed to fresh OC material, since the wood pellets used as feedstock contain only minor amounts of ash (see Table 1). As a basic rule, the bed material can leave the reactor through two pathways: (i) in the form of fines travelling through the cyclones towards the AR or FR filter together with the gas stream, and (ii) from the bottom of the reactor beds through the ash sluicing screws. While the extent of the former pathway is plant- and material-specific and can hardly be impacted by the operating

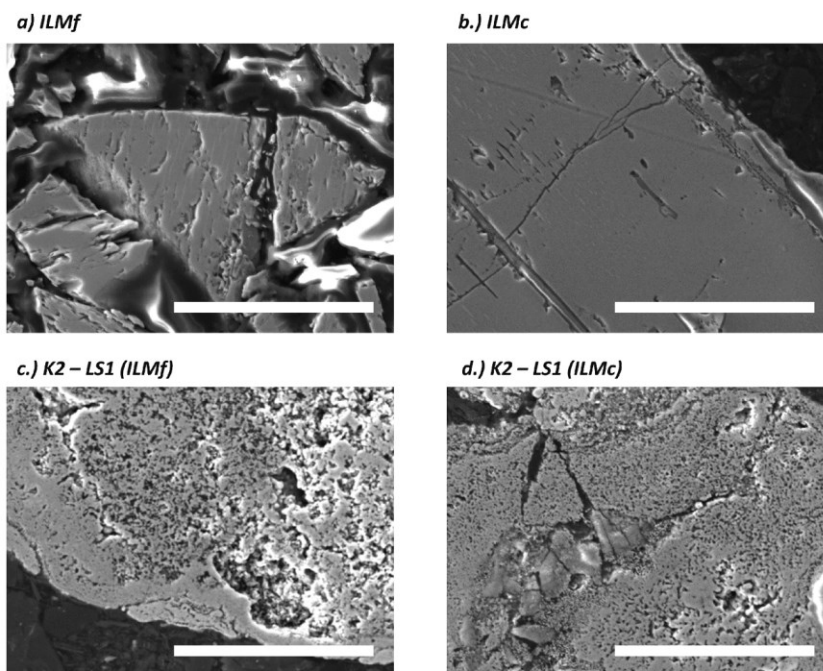
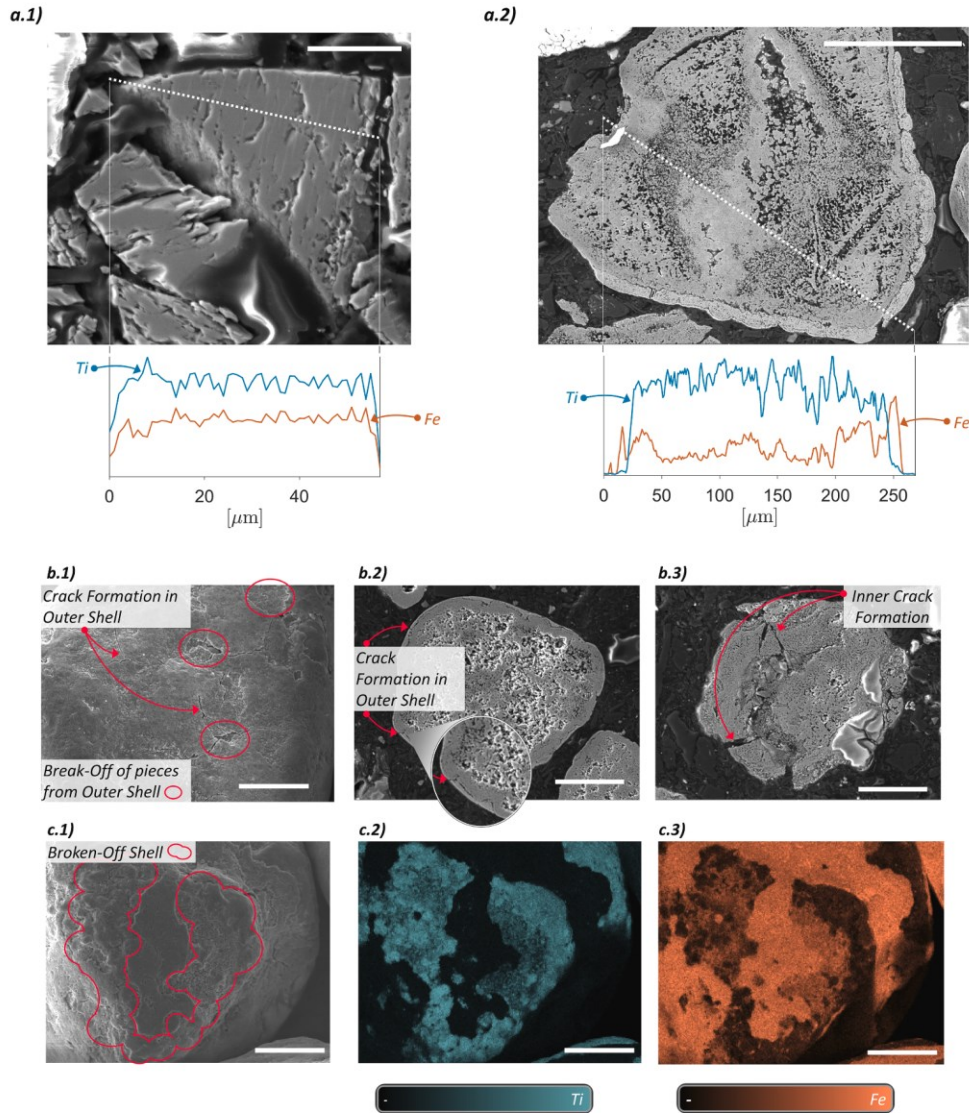


Fig. 3. SEM micrographs of fresh (a+b) and used (c+d) OC from K2. The white bar in the images denotes a length of 50 μm. ILMf and ILMc denote the two different ilmenite granulations (see Section 2.2.1).



**Fig. 4.** SEM/SEM-EDX images and micrographs of OC samples. a.1) SEM micrograph of fresh ILMf with line scan indicating concentration of Fe and Ti (white bar: 20 μm). a.2) SEM micrograph of utilized OC from K2 with line scan indicating concentration of Fe and Ti (white bar: 50 μm). b.1) SEM image of utilized OC from K2 with indications of cracks and broken-off shell (white bar: 50 μm). b.2) SEM micrograph of utilized OC from K2 showing cracks in the outer Fe-rich layer (white bar: 50 μm). b.3) SEM micrograph of utilized OC from K2 showing long cracks reaching into the particle bulk (white bar: 50 μm). c.1–3) SEM-EDX image of utilized OC from K2, with indications of zones where the Fe-rich layer broke off during operation (1), and the respective Ti (2) and Fe (3) content (white bar: 50 μm).

conditions, ash sluicing is a dedicated procedure that only becomes necessary in case changes in the bed material, such as ash accumulation, agglomeration, or deactivation occur to relevant extents. As shown in Fig. 5, this was not the case during pilot testing in the 1 MW<sub>th</sub> scale with industrial wood pellets, as material was not extracted from the reactor system during 125 h of steady state operation. In contrast to that, approx. 3.7 t of material was retrieved from the AR and FR filter, with over 75 % of the material ending up in the FR filter. Similar findings were also made for stable chemical looping operation with the fine

ilmelite (ILMF) during K2, showing that the trends observed for K1 are reproducible (more details see Section A.1 in the Supplementary Material).

To be able to answer why the material is lost in the AR and FR cyclones, a detailed analysis of the solid samples from the 1 MW<sub>th</sub> unit is necessary. One important variable for cyclone efficiencies is the particle size of the material, as depending on the size of the particle surface forces or inertial forces dominate inside the cyclone, leading either to their separation from the gas stream or to their losses towards the filter

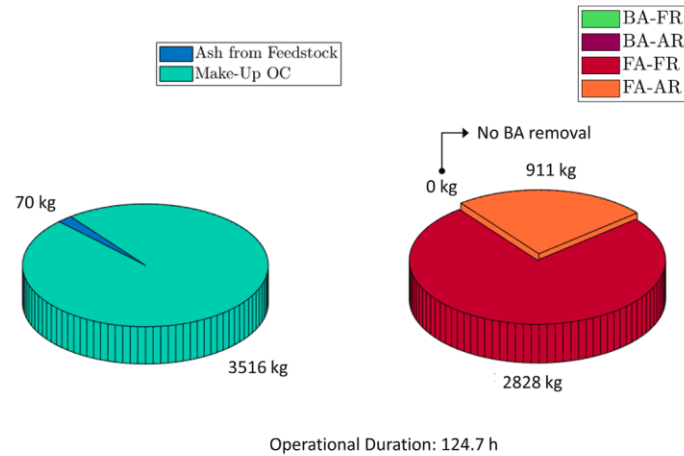


Fig. 5. Solid mass balance around CLG unit for K1 between 9th April 2022 18:00 and 14th April 2022 22:40. Left: Solid material fed into the CLG unit, Right: Solid material extracted from the CLG unit.

[42]. Fig. 6 shows the cumulative particle size distributions (PSD) of the following samples taken during steady state CLG operation from the 1 MW<sub>th</sub> unit:

- BA-FR: Particles from the bottom of the bed of FR,<sup>3</sup>
- BA-AR: Particles from the bottom of the bed of AR,<sup>3</sup>
- LS-FR: Particles from LS5,
- LS-AR: Particles from LS1,
- FA-FR: Particles from the FR Filter,
- FA-AR: Particles from the AR Filter.

It is visible that the material collected from the two filters (AR & FR) exhibits a significantly higher content of fines in comparison to the fresh OC material, whereas the opposite is true for the material extracted from the reactor beds via ash sluicing (i.e. it contains a higher content of coarse particles). The PSDs of the material extracted from both loop seals fall in between those extracted from the filters and from the ash sluicing screws, yet exhibit a lower fraction of fines in comparison to the fresh ilmenite. The resulting mean particle diameter of the material cycling through the CLG system amounts to approx. 130  $\mu\text{m}$ , which is similar to the one previously obtained during CLC operation (=154  $\mu\text{m}$ ) in the 1 MW<sub>th</sub> pilot [19]. These observations can be explained as follows. Ultimately, the fresh OC material fed into the system enters via the stand-pipe of LS1 (see Fig. 2) and is subsequently distributed inside the reactor system. Coarse particles, either from the fresh OC material or agglomerates formed during operation accumulate at the bottom of the reactors and/or the loop seals and are thus primarily found in the samples collected from the bottom beds of both reactors. On the other hand, fine particles which cannot be separated from the gas streams in the cyclones, stemming either from the fresh OC material, from fines formed during attrition of the OC, or from ash compounds from the solid feedstock fed into the FR, leave the reactor system towards the filters and are collected there. Intermediated-size particles in the range of 60–250  $\mu\text{m}$  continuously cycle through the system and are thus found primarily inside the reactor system and hence are being sampled from both loop seals. Apart from these straightforward conclusions, the absence of fine particles <60  $\mu\text{m}$  and the low fraction of particles in the range of 60–100  $\mu\text{m}$  inside the loop seal samples (see Fig. 6), suggest that

<sup>3</sup> Material was extracted via ash sluicing at the end of the experiment (i.e. during system shut-down).

the fine particles are lost during operation. Interestingly, visibly more particles with diameters >60  $\mu\text{m}$  are found in the FR filter compared to the AR filter, suggesting that the FR cyclone exhibits a lower separation efficiency than the AR cyclone, which also explains why significantly more material was lost through the FR filter (see Fig. 5). When considering the PSDs for both fly ash samples in Fig. 6, it is clearly visible that substantial amounts of particles with diameters >40  $\mu\text{m}$  are retrieved in the filters (AR: 14 wt.-%, FR: 37 wt.-%), meaning that for the 1 MW<sub>th</sub> pilot, significantly lower OC lifetimes than for other setups, where only fines with diameters smaller than 40–45  $\mu\text{m}$  are recovered [29,40], can be expected.

Due to the pronounced presence of fine particles inside the fresh OC, the fines collected in the filters stem directly from the fresh material fed into the CLG system to a significant extent. When considering the PSD of the fresh OC it can be stated that approx. 25 wt.-% of the fresh material (<60  $\mu\text{m}$ , see Fig. 6) will be lost rapidly inside the CLG system via the cyclones. The remainder of the fines collected in both filters can be attributed to fine formation through attrition. When considering the entire fines collection of 3739 kg in both filters for the operating period under investigation (see Fig. 5), it can be conjectured that at least 23.5 % (879 kg) of that material directly stems from fine fraction of the fresh OC material fed into the system, which lies below the cut point of the FR cyclone (see grey shading in Fig. 7a). On the other hand, approx. 2141 kg can be directly attributed to attrition of coarser particles into fines, which is illustrated in Fig. 7b. Using this number, an attrition rate of 17.2 kg/h can be calculated for the 1 MW<sub>th</sub> pilot plant for the duration under investigation, which translates into an OC lifetime of 69.8 h (see Eq. (5)).<sup>4</sup>

The most obvious measure to increase OC lifetimes would be an optimization of the FR cyclone to allow for a more efficient removal of fines. When taking into account the average OC circulation rate of 14,974 kg/h, determined using the method of Marx et al. [32], an average separation efficiency (see Eq. (7)) of 99.84 % and 99.95 % can

<sup>4</sup> Feedstock ash and unconverted char escaping via the AR & FR cyclone are not considered here. Through considerations of these solid species, slightly higher OC lifetimes would be obtained, albeit the impact is expected to be minor.



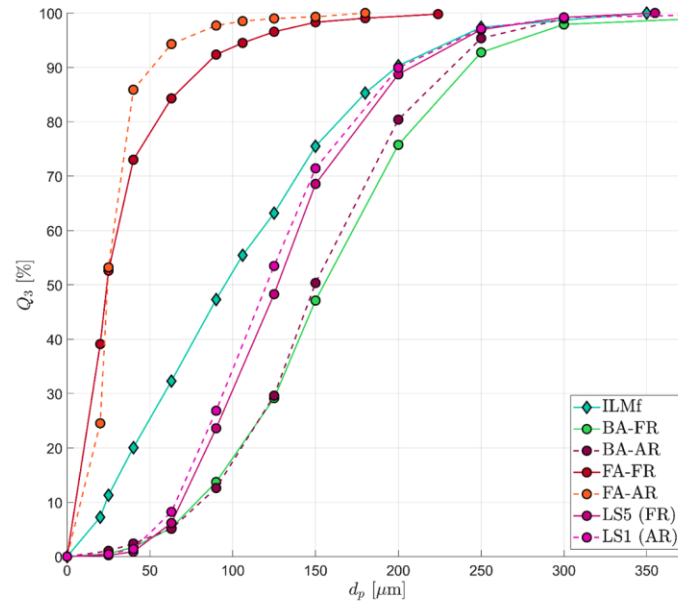


Fig. 6. Cumulative particle size distribution (PSD) of ilmenite samples collected from different positions during operation of the 1 MW<sub>th</sub> pilot. All samples were collected between 14th April 2:30 am and 15th April 11:00 am during CLG operation.

be calculated for the FR and AR cyclone for the operating period under investigation, respectively, leaving room for improvement.<sup>5</sup> As a reference, cyclone efficiencies up to 99.99 % were found to be obtainable by tailoring cyclone inlet geometries for a 8 MW<sub>th</sub> dual fluidized bed gasification (DFBG) system [44], meaning that material losses esp. towards the FR filter could be substantially reduced. For example, material losses via the cyclones would decrease by 26.5 %, in case the cut points for both cyclones were shifted to 40 μm, meaning that OC lifetimes up to 95.0 h would be achieved. Another potential measure to reduce material consumption in the 1 MW<sub>th</sub> unit would be to tailor the PSD of the fresh OC (e.g. via sieving), to prevent direct material losses of the fines contained in the fresh material. In an attempt to reduce material consumption, old bed material from K1 and coarse Ilmenite (ILMc) was used during K2. Here, it was found that material losses were drastically reduced, yielding OC lifetimes of up to 170 h.<sup>6</sup> On the one hand, this was related to the fact that fine losses from the fresh material were completely eliminated. Moreover, as the average particle diameter of the coarse ilmenite (=199 μm) lies further away from the cut-point of the FR cyclone, attrition of the larger OC particles does not lead to a direct loss of those via the cyclone (more details see Section A.1 in the Supplementary Material).

However, even when tailoring the fresh OC PSD and optimizing cyclone geometries, substantially lower OC lifetimes (<500 h) than reported for smaller units in literature are expected to be obtained in the 1 MW<sub>th</sub> unit. A comparison of SEM images of OC samples from both loop seals, shown in Fig. 8, suggests that attrition follows a similar mechanism as observed in smaller units. Here, it was found that particle rounding and detachment of outer particle layers drive attrition rates, as

opposed to particle fragmentation [26,28], which is also suggested by the recorded SEM images (more details see Section 3.3). The obvious similarity in the governing mechanism leaves the question why attrition rates observed in the 1 MW<sub>th</sub> unit exceed those previously reported in literature.

On the one hand, this could be related to greater mechanical stresses in the 1 MW<sub>th</sub> pilot plant, leading to a more severe mechanical strain on the OC particles. In terms of acting mechanical forces, reactor geometry and configuration play an important role in chemical looping systems [45]. For fluidized bed configurations it is known that jet and cyclonic attrition effects dominate particle attrition, with both factors increasing in effect with increasing gas velocity [28]. As gas velocities ( $u_0$ ) up to 7 m/s in the FR are necessary to achieve the required solid circulation in the 1 MW<sub>th</sub> unit [46], it becomes obvious that larger mechanical stresses act on the OC inside the given CLG system, when compared to smaller pilots where generally lower gas velocities are employed (impact forces scale with  $u_0^2$ , frictional Stoke forces with  $u_0$ ). Additionally, the inner refractory lining of the riser, cyclone, loop seals and stand-pipe of the 1 MW<sub>th</sub> unit exhibits a rougher and more uneven surface than their steel counterparts used in smaller setups [29,47,48]. On the one side, this leads to increased wall-particle friction, while it also decreases smoothness in the particle trajectory, thus making particle-particle impacts more likely. Consequently, it can be stated that due to the combination of those boundary conditions, the mechanical strain on the OC particles is larger for the 1 MW<sub>th</sub> unit in comparison to smaller pilots, for which OC lifetimes >500 h were determined [29].

Another factor playing into the OC lifetime are the chemical stresses acting on the OC during redox cycling. It is generally accepted, that the particle's attrition resistance decreases through the intrinsic morphological changes induced through redox cycling [26,28,45,49-51] (see also Section 3.1). This was also shown for the 1 MW<sub>th</sub> CLG unit, with samples exposed to longer redox cycling durations showing higher attrition rates in the jet cup (see Section A.2 in the Supplementary Material). With deeper OC reduction stages being obtained for CLG when compared to CLC [52] it was found that OC lifetimes decrease for

<sup>5</sup> The comparably high separation efficiencies can be attributed to the high solid loadings in the gas streams leaving the AR and FR, which are known to enhance cyclone separation efficiencies [43].

<sup>6</sup> However, utilization of ILMc led to sub-optimal CLG efficiency, mainly related to insufficient solid circulation rates between the AR and FR, making its utilization in the 1 MW<sub>th</sub> CLG system unbeneficial.

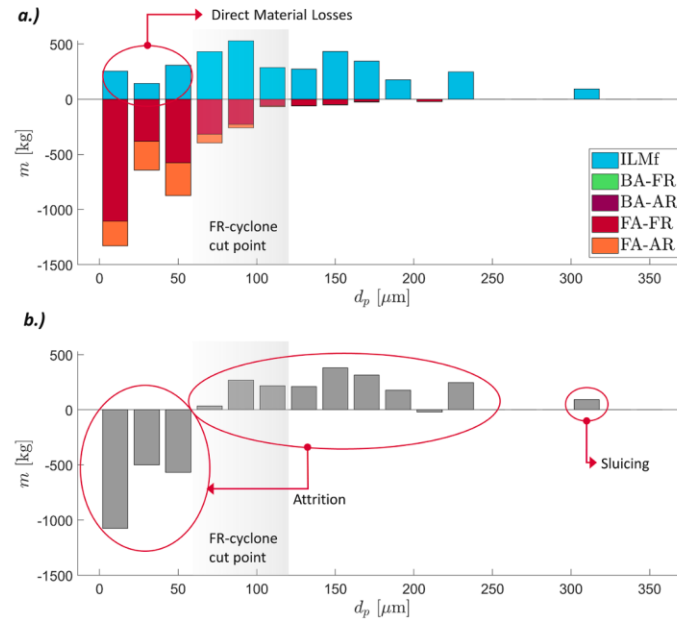


Fig. 7. a) Particle specific input (+) and output (-) of solids from 1 MW<sub>th</sub> pilot between 9th April 2022 18:00 and 14th April 2022 22:40. b) Net particle specific solid in-/output between 9th April 2022 18:00 and 14th April 2022 22:40.

the former [29]. However, as the chemical stress in the 1 MW<sub>th</sub> unit is not different to that in smaller setups, it has to be summarized that the comparably shorter OC lifetimes observed in the 1 MW<sub>th</sub> CLG unit cannot be attributed to it.

Lastly, the thermal strain on the OC in the 1 MW<sub>th</sub> CLG unit could potentially lead to increased attrition rates. The amplifying effect of temperatures on OC attrition is reported in literature [28,50]. While all CLC/CLG systems are operated at elevated temperatures leading to a certain thermal strain on the OC particles, they are exposed to additional thermal stresses in an autothermal CLG setup such as the 1 MW<sub>th</sub> unit, due to the temperature difference between AR and FR. This temperature difference means that the OC particles are rapidly cooled down upon entering the FR and are heated up again upon entering the AR. With temperature differences in the range of 100 K being observed in autothermal systems [32,52], the repeated temperature increase/decrease could lead to substantial weakening of the OC structure. Another factor which needs to be considered is that because of this temperature difference between AR and FR, the OC is generally exposed to higher maximum temperatures in an autothermal setup.<sup>7</sup> This factor becomes of an even greater relevance, when considering the results by Nelson et al. [28], who found that ilmenite attrition rates increase sharply between 895 and 970 °C from 0.9 wt.-%/h to 3.2 wt.-%/h in a modified air-jet setup.<sup>8</sup> This finding suggests that there exists a critical temperature threshold above which OC attrition increases sharply and due to the intrinsic properties of the CLC/CLG process, the exceeding of this threshold is more likely in an autothermal setup.

In summary, it can thus be stated that the relatively low OC lifetimes observed for the 1 MW<sub>th</sub> CLG pilot plant result from an interplay

comparably low (FR) cyclone efficiency and the PSD of the fresh OC material, increased mechanical stresses induced through harsher process conditions (e.g.  $u_0$ ) and reactor materials, and increased thermal stresses due to inherent peculiarities of the autothermal CLG process.

### 3.2.2. Bulk and particle density

Apart from particle size and attrition rate, particle density is a crucial property of any material used in fluidized beds [53]. Fig. 9 shows that in contrast to the average particle diameter, which rapidly reaches a constant unchanged value inside the CLG system (see Fig. 9a), particle as well bulk densities of the OC material cycling through the system change gradually with increasing operating time. Clearly, all values determined for LS samples during operation lie distinctly below the ones determined for the fresh material. Moreover, it is visible that particle densities decrease with increasing operating time, indicating an increasing particle porosity, induced through redox cycling [26] (more details see Section 3.1). Similarly, bulk densities also decrease with increasing operating time, with changing particle porosity and shape. Both decreasing trends are interrupted by a phase of increased make-up feeding on 11th April, where reactor inventories were increased by the plant operators (see Fig. 9d). Here the effect of the large quantities of freshly fed material on the both densities is clearly visible, shifting the average particle and bulk density towards the properties of the fresh OC (see red arrows in Fig. 9b and c). On the other hand, the average particle diameter is unaffected by the increased make-up rates, underlining the hypothesis that the fines from the make-up material are rapidly lost during operation (more details see Section 3.2.1). Subsequent to the feeding of the fresh material on April 11<sup>th</sup>, the decreasing trend in both densities continues, underlining the continued occurrence of morphological changes in the OC particles during CLG operation. These changes in particle morphology were also observed during chemical looping combustion operation and were found to go in hand with a decrease in particle rigidity [26]. Consequently, it can be summarized that for the given make-up rates and in the absence of bed material sludging, densities of the OC particle decrease continuously, indicating ongoing

<sup>7</sup> E.g. for a FR temperature of 875 °C, the max. system temperature in an externally heated setup amounts to 875-900 °C, while it amounts to 975-1000 °C in an autothermal setup.

<sup>8</sup> An attrition rate of 3.2 wt.-%/h would translate into an OC lifetime of approx. 31 h, falling into the same range as observed in the 1 MW<sub>th</sub> CLG unit.

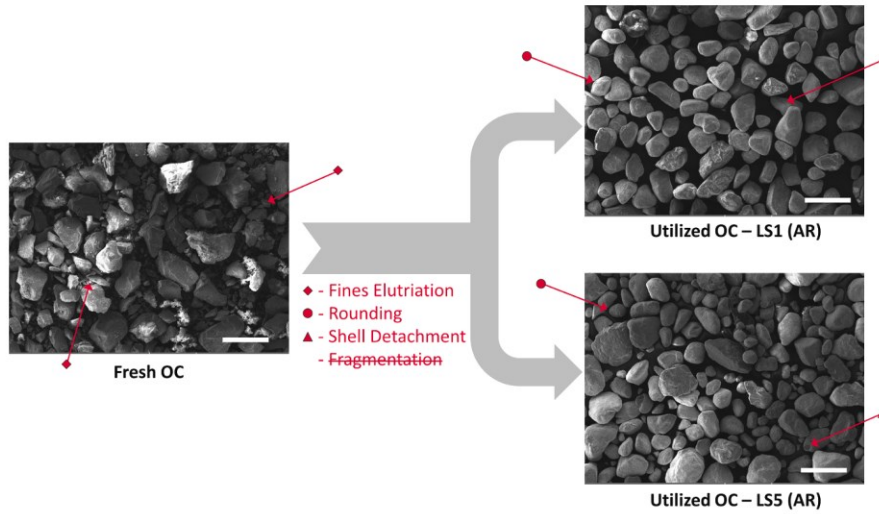


Fig. 8. SEM images of fresh (left) and utilized (right) OC material from K1. Arrows with diamonds at the end indicate fines in the fresh material no longer present in the utilized OC, arrows with circles indicate rounded OC particles and arrows with triangles indicate particles with a broken-off or cracked shell.

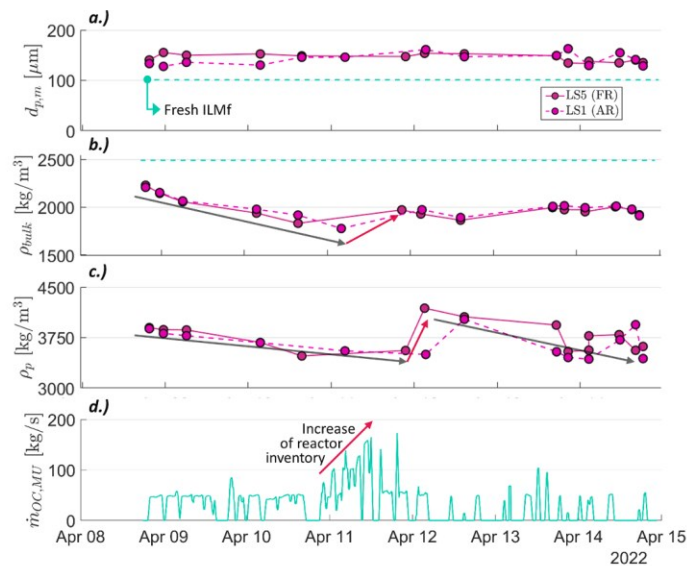


Fig. 9. Change of particle properties from LS1 and LS5 between 8th April 2022 18:00 and 14th April 2022 22:40 (K1). Dashed blue line indicates the properties of fresh ilmenite - a) Average particle diameter, b) bulk density, c) particle density. d) Make-up feed of ilmenite into 1 MW<sub>th</sub> pilot between 8th April 2022 18:00 and 14th April 2022 22:40.

morphological changes inside the OC particles. For the given operating times, fully constant values for bulk and particle densities were not obtained in the 1 MW<sub>th</sub> unit. However, upon consideration of Fig. 9 it can be stated that a bulk density of ~1800 kg/m<sup>3</sup> and a particle density of ~3400–3500 kg/m<sup>3</sup> can be expected for the OC bed material during continuous CLG operation.

### 3.2.3. Summary

Based on the observations of the mechanical properties of the OC

particles during CLG operation, it can be summarized that mechanical and chemical strains lead to a decrease in particle diameter, particle density, and bulk density with elapsing operating time. When woody biomasses (IWP and PFR) were used as the feedstock, material deactivation or agglomeration do not determine the lifetime of the OC inside the 1 MW<sub>th</sub> unit. Rather, material losses through the cyclones defined the necessary make-up rates, with OC lifetimes observed in the 1 MW<sub>th</sub> pilot plant being significantly lower than those observed in smaller pilots.

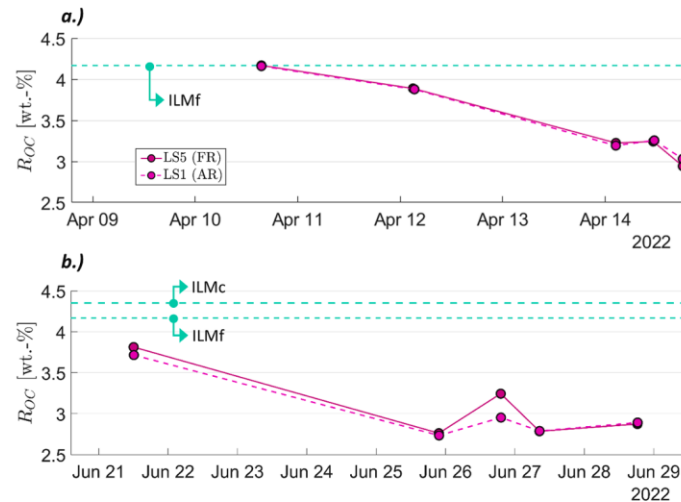


Fig. 10. a.) Change of oxygen carrying capacity of samples from LS1 and LS5 between 8th April 2022 19:00 and 14th April 2022 12:40 (K1). b.) Change of oxygen carrying capacity of samples from LS1 and LS5 between 20th June 2022 10:00 and 29th June 2022 12:00 (K2). Dashed blue line indicates the properties of fresh ilmenite (ILMc, ILMf).

On the one hand, the comparably low OC lifetimes can be attributed to peculiarities of the 1 MW<sub>th</sub> pilot, such as the high gas velocities required in the FR in order to attain the necessary OC circulation rates or the low separation efficiency of the FR cyclone. On the other hand, reactor materials (refractory lining) and process conditions (e.g.  $\Delta T$  between AR and FR), present in any industry-like or industry CLG setup such as 1 MW<sub>th</sub> pilot plant, are expected to lead to decreased OC lifetimes, when compared to smaller pilots.

To optimize OC lifetimes in a full-scale setup, the following measures are therefore suggested:

- Optimization of cyclone geometries to minimize losses of particles  $>40 \mu\text{m}$ ,
- Tailoring of PSD of fresh OC (e.g. removal of all fines with  $d_p < 30\text{--}40 \mu\text{m}$ ) to minimize direct losses of fresh material,
- Equipment of the CLG system with a secondary solid removal unit operation downstream of the cyclone, to remove the coarser fraction of the fines and allow for its subsequent reintroduction into the CLG unit.<sup>9</sup>

All in all, it is believed that by implementing those approaches, OC lifetimes could be increased beyond 300 h for a full-scale CLG unit, meaning that procurement and waste removal costs should not pose a substantial barrier for implementation from a technical or economic perspective [56].

### 3.3. Change of chemical properties of OC during 1 MW<sub>th</sub> pilot testing

Apart from the physical changes the OC particle undergoes in a

<sup>9</sup> One such option, which has been successfully utilized in DFBG units, is the separation of particles in a filter equipped with an automatic recycling route back to the gasifier, to reduce fresh material consumption and convert entrained char [54,55]. Another viable approach would be the utilization of a widened U-turn in a vertically-aligned two-stage gas cooler, in which particles settle down and can then be removed (e.g. via a rotary valve) and recycled. Alternatively, a second cyclone could be used to enhance the overall solid separation from the gas stream.

chemical looping system, which were detailed in Section 3.2, the chemical strain induced on the OC during redox cycling also entails changes in the chemical properties of the OC. The impact of CLG operation on the OC oxygen transport capacity is elaborated on in Section 3.3.1, before the impact on redox reaction rates is highlighted in Section 3.3.2.

#### 3.3.1. Oxygen transport capacity of OC

To assess the oxygen transport capacity of the OC samples, its weight change inside the TGA was assessed over five redox cycles (more details see Section 2.4.5). Here it was found that all samples exhibit stable oxygen transport capacities over five cycles,<sup>10</sup> thus signifying the oxygen transport capacity of the OC materials inside the 1 MW<sub>th</sub> CLG unit.

When considering the progression of the oxygen carrying capacity of the OC ( $R_{OC}$ ) over time, Fig. 10 shows that it decreases visibly during CLG operation. While  $R_{OC}$  values close to that of fresh ilmenite were determined for LS samples collected shortly after the start of chemical looping operation (K1: 10th April 2022, K2: 21st June 2022), the oxygen transport capacity of the OC decreased to below 3% for K1 within four days of operation, despite continuous make-up feeding. A similar behavior was observed during redox cycling in different setups [26,27], with the OC's oxygen carrying capacity decreasing continuously over up to 100 cycles [27]. This behavior was attributed to the formation of  $\text{Fe}_2\text{O}_3$  at the expense of  $\text{Fe}_2\text{TiO}_5$  inside the OC particle during redox cycling, with the former exhibiting a lower oxygen transport capacity than the latter [27]. This change in particle chemistry can be related to the compositional changes taking place inside the OC during chemical looping operation, i.e. the iron migration inside OC particles (more details see Section 3.1). Another factor contributing to the decreasing  $R_{OC}$  with time, is the abrasion of the Fe-rich outer layer of the OC particles (see Section 3.1), leading to a selective removal of the active OC phase from the system. For K2, stable  $R_{OC}$  values in the range of 2.7–3.2% were obtained after approx. five days of chemical looping operation, showing that in case of continuous make-up feeding, the oxygen transport capacity of the OC inside the CLG system stabilizes if sufficiently

<sup>10</sup> Selected samples were analyzed for up to 50 cycles, exhibiting stable  $R_{OC}$  values for the entire TGA experiment.

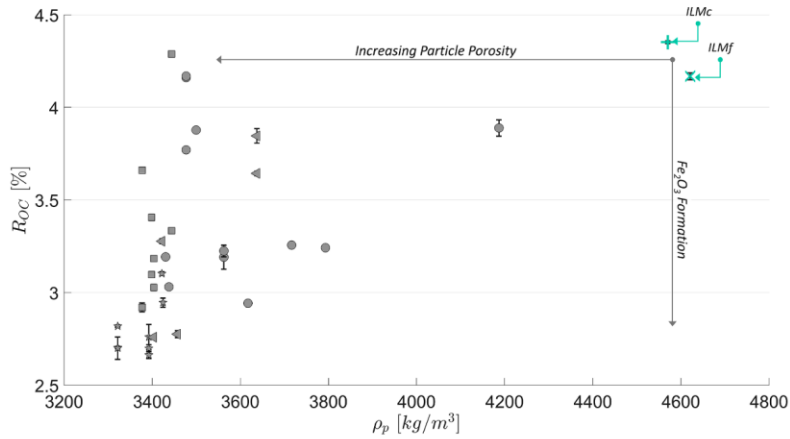


Fig. 11. Oxygen transport capacity of OC as a function of particle density for different loop seal samples from 1 MW<sub>th</sub> pilot plant (circles: K1, triangles: K2-ILMc, pentagrams: K2-ILMf, squares – K3). Values for fresh OC materials are given as a reference (plus: ILMc, cross: ILMf).

long operation durations are provided.

While this decrease in  $R_{OC}$  is of great relevance for CLC operation, where high oxygen transport rates to the FR are essential for process efficiency [24,27], it does not pose a major issue for CLG operation, where oxygen transport from the FR to the AR has to be restricted to maximize process efficiency [16,52]. With minimum values of approx. 2.6 % being determined for  $R_{OC}$  for samples collected from the 1 MW<sub>th</sub> CLG unit, it can thus be summarized that the observed decrease in oxygen transport capacity does not pose a critical issue for operation, as oxygen fluxes up to 365 kg/h would still be obtainable in the 1 MW<sub>th</sub> unit.<sup>11</sup> This oxygen release would yield a maximum attainable oxygen-to-fuel equivalence ratio of 0.87,<sup>12</sup> well above  $\lambda=0.3-0.35$ , required for autothermal CLG operation [52,57], meaning that even for lower values of  $R_{OC}$  oxygen release by the OC inside the FR would still need to be limited via process control [52].

Fig. 11 relates the particle density of the OC, giving an indication of the physical changes it has undergone (see Section 3.2), with the oxygen transport capacity of the OC sample, signifying its chemical ageing. Here it becomes obvious that while the density of the majority of OC particles lies within a relatively narrow range of 3300 to 3700 kg/m<sup>3</sup> (fresh OC: 4600 kg/m<sup>3</sup>), the variation in  $R_{OC}$  is much bigger, ranging from 2.5 to 4.0 % (fresh OC: 4.2 %). This finding suggests that the increase in particle porosity because of thermal, mechanical, and chemical strain inside the CLG is a comparably fast process, yielding particle densities <3700 kg/m<sup>3</sup> within a few hours. On the other hand, the chemical ageing of the OC inside the CLG unit seems to occur over a longer duration, leading to decreasing  $R_{OC}$  values with each redox cycle. Another interesting finding which can be inferred from Fig. 11 is that the lowest oxygen transport capacities were obtained when fine ilmenite was used during K2 (pentagrams in Fig. 11). For this operational period, the cold gas efficiency of the CLG unit was maximized by restricting the oxygen transport to the FR. This approach thus led to the OC being highly reduced in the FR [29, 58], i.e. the chemical strain on the OC was intensified. This explains why lower oxygen transport capacities were obtained for this operational period, as it is established, that iron migration to the OC surface is accelerated in more reducing environments [28].

<sup>11</sup> Assuming an OC circulation rate of 14 t/h.

<sup>12</sup> For a thermal load of 1.2 MW<sub>th</sub> (industrial wood pellets as the feedstock) and assuming full reduction and oxidation of the OC inside the FR and AR, respectively.

### 3.3.2. Redox reaction rates of OC

In contrast to the oxygen carrying capacity of the OC, its oxygen release rate plays a crucial role in CLG, determining how deeply the OC is reduced inside the FR [29,52]. The shrinking core model, widely used to describe the oxygen release by the OC inside the chemical looping system in literature [59,60], states the oxygen release rate of the OC decreases with decreasing  $R_{OC}$ , since the OC's propensity to release oxygen decreases as it is further reduced. However, Adanez et al. [27] found that contrary to this explanation, stable OC oxygen release rates can be observed during redox cycling. This was attributed to the increase in particle porosity incurring during redox cycling (see also Section 3.1), enhancing the oxygen release of the OC and hence countering the negative effect of decreasing  $R_{OC}$  values on redox kinetics. To assess to which extent oxygen release and uptake rates of the OC change during redox cycling inside the 1 MW<sub>th</sub> CLG system, the rate index of different loop seal samples collected during operation were determined via TGA (see Section 2.4.5). The reduction rate indices ( $RI_{red}$ ) determined for the OC samples for the reduction step are shown in Fig. 12a.1–c.1. Upon consideration of the data, the following observations can be made:

- The reduction rates for the fresh OC remain relatively constant for each redox cycle, confirming findings made by Adanez et al. [27];
- On the other hand, the reduction rates of the utilized OC samples decrease from the first to the third redox cycle, before reaching a relatively stable value from the fourth cycle onwards;<sup>13</sup>
- For the first TGA cycle, used OC samples exhibit significantly higher reduction rates than the fresh OC material;
- For the fifth redox cycle, reduction rates of the utilized samples lie within the range of the reduction rates of the fresh OC material (2.5–4.5 wt.-%/min). These reduction rates are similar to values reported in literature [27].

When considering the first redox cycle (see Fig. 12a.1), where the OC samples still exhibit the same characteristics as in the 1 MW<sub>th</sub> unit, the high reduction rates when compared to the fresh OC underline that oxygen release kinetics in the FR are not deteriorating during CLG operation. This can be explained by the increased particle porosity of the

<sup>13</sup> By investigating different samples for 25 redox cycles inside the TGA, it was found that rate indices reach an entirely constant value after 7-10 TGA redox cycles, with samples exhibiting a sharper decrease in reaction rates during the first three cycles requiring more cycles for stabilization.

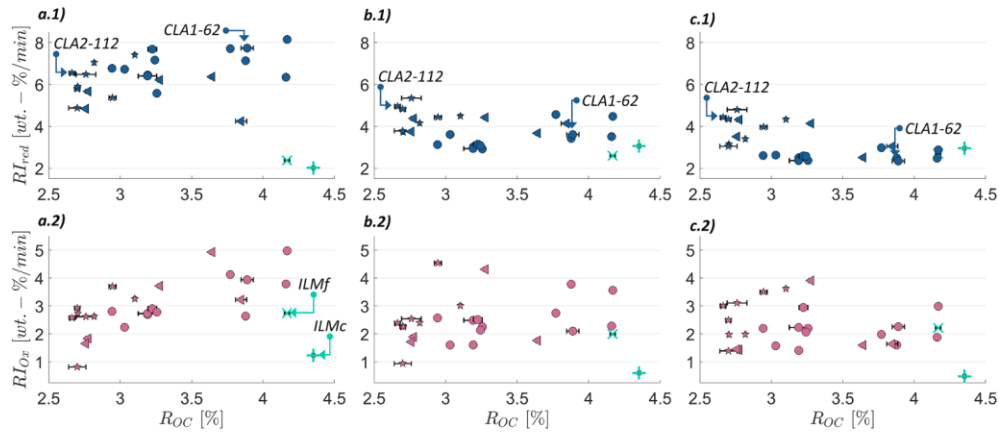


Fig. 12. Reduction (1) and oxidation (2) rate index for different loop seal samples from 1 MW<sub>th</sub> pilot plant for first (a), third (b) and fifth (c) TGA cycle, (circles: K1, triangles: K2-ILMc, pentagrams: K2-ILMf). Values for fresh OC materials are given as a reference (plus: ILMc, cross: ILMf).

utilized OC samples, induced through thermal, chemical, and mechanical strain (see also Section 3.2.2). Overall, the data from the first redox cycle in the TGA thus suggests that the effect of increased particle porosity on oxygen release rates dominates the effect of decreasing oxygen transport capacities for the OC samples from the 1 MW<sub>th</sub> unit, thus leading to larger  $RI_{red}$  values for the utilized materials than those of the fresh OC material. Moreover, the highest oxygen release rates are obtained for utilized OC samples exhibiting relatively high  $ROC$  values (>3.0 %). This again supports the hypothesis that mechanical ageing of the OC particles inside the CLG unit is a faster process than chemical ageing (see also Section 3.3.1). This means that particles located inside the system for several hours still exhibit a comparably high oxygen transport capacity, as iron migration to the surface has only occurred to limited extents, yet their porosity has already increased substantially. This consequently leads to high rate indices (>7 wt.-%/min) for those samples.

To explain why the rate indices of the utilized OC materials decrease during redox cycling inside the TGA, the differences between different samples provide insights into potential mechanics of the occurring processes. As the fresh OC materials do not exhibit a decrease in reduction rate indices during redox cycling (see Fig. 12a.1–c.1), it can be postulated that a characteristic of the utilized OC particles crucial for oxygen release rates is altered during TGA cycling. As  $ROC$  values remain unchanged for all samples for each TGA cycle (see Section 3.3.1), it can thus be presumed that the particle porosity of the utilized OC materials is decreased with each TGA cycle. Here, one hypothesis is that in the absence of mechanical and thermal stress inside the TGA, small cracks and defects formed because of those strains inside the 1 MW<sub>th</sub> CLG unit, are “healed” as oxygen migrates through the lattice structure, leading to its restructuring.<sup>14</sup> Another hypothesis is that the surface of the OC is restructured during oxidation inside the TGA, owing to the strongly exothermic reaction and ensuing high surface temperatures. These hypotheses would also explain why the extent of decrease in reduction rate indices with each cycle varies between different OC samples. While for samples with high  $ROC$  values (indicating minor chemical ageing), a drop

in  $RI_{red}$  values by more than two thirds can be observed (see sample CLA1–62 in Fig. 12a.1–c.1), the decrease is more moderate for samples with lower oxygen transport capacities (see sample CLA2–112 in Fig. 12a.1–c.1). This means that the observed restructuring occurs more pronouncedly inside the TGA for OC samples exhibiting only minor defects induced through short-term mechanical and thermal strain (CLA1–62), whereas larger defects arisen through longer CLG durations cannot be healed to the same extent inside the TGA (CLA2–112). By investigating selected samples after 1, 2, 4, and 8 TGA cycles via SEM, it was validated that porosity in the particle bulk, the distribution of Iron and Titanium along the particle diameter, as well as the morphology of the OC surface change with increasing cycling duration inside the TGA. This shows that TGA cycling changes OC properties. Thus, the rate indices measured during the first TGA cycle are representing the state of the OC inside the CLG system most accurately.

Consideration of the rate indices determined for the oxidation step, shown in Fig. 12a.2–c.2, shows that the utilized OC samples exhibit similar oxidation rates as the fresh OC material. In contrast to the reduction step, distinct impacts in terms of OC particle properties or TGA cycle number on oxidation rate indices cannot be observed. This suggests that due to the relatively high partial pressure of oxygen used inside the TGA (0.21 atm), leading to fast oxygen take-up rates by the OC, other factors (e.g. bulk diffusion) govern the oxidation kinetics for the given boundary conditions.

All in all, these results show that TGA redox cycling affects OC properties differently than redox cycling in a real chemical looping setup. Depending on the state of the sample used inside the TGA and the boundary conditions used during redox cycling, the incurring effects on particle morphology and composition vary. Hence, TGA studies provide fundamental insights into the general mechanics of the impact on redox cycling on OC particle characteristics, yet do not provide a holistic picture of the chemical properties of the OC inside a CLG system, e.g. due to the absence of mechanical and thermal stresses inside a TGA setup. Nonetheless, TGA studies can be utilized to assess the redox behavior of OC samples. In the current study, the utilized OC samples were found to exhibit a higher reduction rate than the fresh material, which was attributed to the changes in morphology the OC undergoes during chemical looping operation. On the other hand, oxidation rates were found to be unaffected by OC morphology, indicating a kinetic limitation independent of particle morphology (e.g. bulk diffusion).

### 3.3.3. Summary

Thermogravimetric analysis of loop seal samples collected during 1

<sup>14</sup> The absence of any decreasing trend of  $ROC$  even during long-term redox cycling inside the TGA (50 cycles), also indicates that in contrast to other studies [27], the redox conditions used for TGA cycling in this study did not promote any major changes in chemical composition of the OC. This shows that due to the moderate redox conditions used inside the TGA, the OC was given sufficiently long times for homogeneous chemical restructuring.

$MW_{th}$  operation revealed that changes in the OC chemistry, induced through redox cycling (see Section 3.1), lead to a reduction in the OC's ability to transport oxygen from the AR to the FR. However, this drop-off in  $R_{OC}$  is not crucial for CLG operation, where oxygen transport to the FR is of lesser importance than the heat transport facilitated by the circulating OC [52,57]. Additionally, it was shown that oxygen uptake and release rates of the utilized OC are generally higher than those of fresh, activated ilmenite. This was attributed to the increase in particle porosity the OC incurs during redox cycling inside the CLG system. Consequently, the chemical properties of the OC do not determine the lifetime of the OC inside the 1  $MW_{th}$  CLG system, which means that generally, replacement of the OC inventory via sluicing from the reactor system was not required. Hence, it can be inferred that active OC replacement due to chemical deactivation should also not be necessary in an industrial CLG unit.

### 3.4. Effect of feedstock properties on OC during 1 $MW_{th}$ pilot testing

In terms of feedstock interactions, ilmenite is known to be an attractive oxygen carrier, which is not prone to excessive feedstock-related carbon deposition or deactivation phenomena [26]. These findings were validated in 1  $MW_{th}$  pilot scale, as the utilized ilmenite materials did not exhibit any significant deactivation phenomena, indicating blocking or poisoning of active sites for any of the three utilized feedstocks (see also Section 3.3). However, these properties do not prevent operational issues related to the combination of high reactor temperatures and potential low-melting ash components in biomass chemical looping. While these are of lower importance for woody biomasses, generally exhibiting low ash contents and ashes with sufficiently high melting points, it becomes a relevant issue for herbaceous or agricultural biomasses (e.g. rice husk or wheat straw) [61]. Apart from the higher ash content of these biomasses, this can be related to their ash chemistry, rich in silicates and alkali salts [61], which are known to increase the risk of formation of low-melting eutectic phases [38,62,63].

These general findings regarding ash melting were also observed during pilot testing in 1  $MW_{th}$  pilot scale. While agglomeration was not observed to any extent during CLG operation with the woody feedstocks IWP and PFR, excessive agglomeration was detected during CLG

operation with WSP in K3, within a single day of chemical looping operation (see Fig. 13). Maintaining fluidization in both reactors despite the occurrence of agglomeration was not an issue. However, the continuous growth of the OC particles led to a decrease in entrainment from both reactors, which is an issue also discussed in literature [64]. With the decrease in entrainment rates from both reactors, OC circulation rates dropped, leading to increasing temperature differences ( $\Delta T$ ) between AR and FR with increased operating time, as less heat was transported between AR and FR by the OC, ultimately leading to low CLG process efficiencies [58]:

$$\dot{Q}_{OC} = \dot{m}_{OC} \cdot c_{p,OC} \cdot (T_{AR} - T_{FR}) = \dot{m}_{OC} \cdot c_{p,OC} \cdot \Delta T \quad (8)$$

This underlines, that the pronounced occurrence of feedstock related agglomeration poses an issue requiring further attention when striving for the upscaling of the CLG technology. The observed operational issues are of an increased concern as the WSP used during K3 were pre-treated, using a pre-treatment concept developed using different modeling and experimental techniques [36,39,65], which led to stable CLG operation with wheat straw pellets in 20  $kW_{th}$  scale [14]. This poses the question why agglomeration occurred inside the 1  $MW_{th}$  pilot to the observed extents. In the following sections it will thus be attempted to provide an explanation for the observed behavior by providing insights gathered during inspection of the CLG unit after operation with WSP (Section 3.4.1), further analysis of the raw materials used during pilot testing (Section 3.4.2), and subsequent analysis of samples collected during pilot testing (Section 3.4.3). Finally, a summary of the results and a strategy to prevent this behavior are presented in Section 3.4.4.

#### 3.4.1. Inspection of 1 $MW_{th}$ CLG unit after operation with WSP

Subsequent to the shut-down of the CLG unit after K3, all relevant components of the cooled-down 1  $MW_{th}$  pilot plant were inspected, to be able to locate the main reaction regions in which agglomeration had occurred during CLG operation (more details see Table A 1 in the Supplementary Material). Here, it was found that the majority of agglomerates as well as the agglomerates with the greatest dimensions were found inside the AR, which is illustrated in Fig. 14. Interestingly, very large zones of coherent agglomerates were recovered towards the top of the AR riser, as well as the AR cyclone, and LS1 incl. its standpipe.

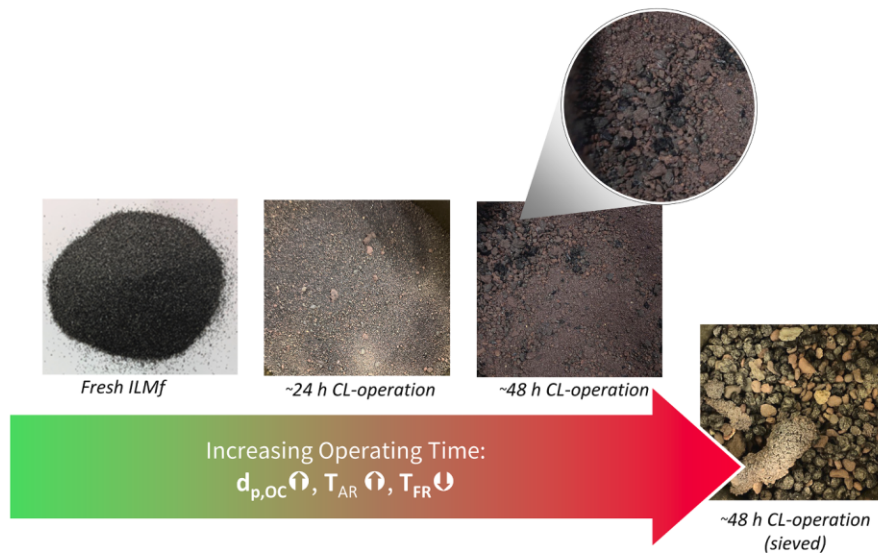


Fig. 13. Images of OC at start of experiment (left), during CLC operation (28th Aug.) and CLG operation (29th August).

Images of those agglomerates are shown in the insets in Fig. 14.<sup>15</sup> Upon closer inspection of the removed parts, it was noticed that the slabs exhibit a layered, porous structure, suggesting that they had been formed continuously over time. Moreover, the retrieved junks exhibited certain mechanical stability despite their porosity, yet could be broken down manually, without the need of additional tools, due to their brittleness (see Fig. 15).

On the FR side of the CLG unit (i.e. FR and LS5), only small agglomerates were found (located on the nozzle grid of the FR and LS5), suggesting that agglomeration did not occur to substantial extents inside the FR. Therefore, it can be postulated that in the 1 MW<sub>th</sub> pilot agglomeration was mainly driven by temperature (being higher inside the AR) and not by reaction atmosphere, which are both known to play a critical role in agglomeration phenomena<sup>16</sup> [61]. Moreover, it can be assumed that as the feedstock pellets entered the AR and were fully converted with the inlet oxygen. This resulted in particles solely consisting of ash components, also favoring the occurrence of ash melting and ultimately agglomeration. When considering the reactor locations from which large agglomerates were retrieved, it becomes obvious that these exhibit zones where the following conditions were met during CLG operation:

- Temperatures > 900°C,
- Oxidizing atmosphere, leading to full char conversion,
- Low gas velocity/low turbulence.

Consequently, it is postulated that in zones exhibiting low turbulence, molten ash particles, formed at hot and oxidizing conditions inside the AR according to the melt-induced agglomeration mechanism [61,66], were able to stick to the reactor lining (see Fig. 16c). Subsequently, the circulating oxygen carrier adhered to this sticky surface (Fig. 16d), leading to a steady growth in the size of the agglomerated layer (Fig. 16e) until the fully formed slab was continuously formed (Fig. 16d). Growth of the slab into more central zones of the AR riser, where gas velocities and gas solid loadings are higher, was prevented by attrition through the by-passing OC particles, removing protruding parts. Following a similar mechanism (i.e. via molten ash particles forming inside the AR), smaller agglomerates were formed inside the AR, as OC particles collided with the molten ash. Yet, in contrast to the larger agglomerate slabs, these agglomerates were maintained in a fluidized state inside the fluidized bed, preventing their continuous growth via attrition (see also Fig. 24). Hence, smaller particle agglomerates could be recovered from the AR via ash sluicing.

While the proposed mechanism, illustrated in Fig. 16, explains the formation of agglomerates retrieved from the AR during operation and inspection of the CLG unit, the root cause for the occurrence of agglomeration inside the 1 MW<sub>th</sub> pilot plant, whereas stable long-term operation without observation of any agglomerates was feasible by pre-treated wheat straw pellets in the 20 kW<sub>th</sub> scale [14,48], remains unclear. In order to answer this question, an in-depth analysis of the fresh materials utilized during 1 MW<sub>th</sub> pilot testing (Section 3.4.2) as well as of samples collected from different parts of the CLG unit during operation and inspection (Section 3.4.3), was carried out and is presented below.

<sup>15</sup> For removal of the agglomerates from the reactor system, they had to be manually crushed to the smaller pieces shown in Fig. 14.

<sup>16</sup> Generally, it is known that ash melting occurs earlier (i.e. at lower temperatures) in reducing atmospheres [61]. As only minor amounts of agglomerates were retrieved from the FR, it can be concluded that FR temperatures were too low to lead to ash melting, despite the fact that a reducing atmosphere was present.

#### 3.4.2. Characterization of fresh materials utilized during 1 MW<sub>th</sub> CLG operation with WSP

In a first attempt to explain why agglomeration had occurred during 1 MW<sub>th</sub> pilot testing in the observed extent, the fresh materials were analyzed to assess whether it is possible to predict the agglomerating tendency of the feedstock. For one, the ash of the pre-treated wheat straw pellets was analyzed regarding its elemental composition. Based on the resulting data (see Table A 6 in the Supplementary Material), the ash melting behavior of the wheat straw pellets was modelled using the software FactSage, via the approach detailed by Lebendig et al. [38]. As shown in Fig. 17, it was found that the pre-treated wheat straw pellets (WSP) used during 1 MW<sub>th</sub> pilot testing generally exhibit a significantly higher melt fraction than the other two feedstocks used during pilot testing. At the maximum AR temperature experienced during K3 (1025°C), WSP exhibit almost 80 wt.-% slag content, indicating pronounced melt formation at the relevant reactor temperatures, whereas IWP and PFR only exhibit 30 and 18 wt.-%, respectively. For comparison, the pre-treated additivated wheat straw pellets used during CLG operation in 20 kW<sub>th</sub> scale by Condori et al. [14] are also shown in Fig. 17, displaying a slag amount approx. 20 wt.-% lower than that of WSP at this temperature. Another factor probably having prevented extensive slag formation during 20 kW<sub>th</sub> testing is the absence of a significant temperature difference between AR and FR for externally heated units (more details see Section 3.2.1), generally leading to lower AR temperatures in the 20 kW<sub>th</sub> setup.

These findings were validated by hot stage microscopy (see Section 2.4.7), showing that ash melting commences at 920°C and intensifies around 1000°C for the WSP, whereas IWP and PFR feedstock used during K1 and K2 do not show any signs of deformation before 1200°C (see Fig. 18). This behavior can be related to the relatively high amount of K and a relatively low amount of Si present in the ashes of the WSP, which can be considered to be a first indicator for a lower melting point (more details see Section A.2.1 in the Supplementary Material).

To further assess the agglomeration tendency of the WSP with the two utilized ilmenite types (coarse: ILMc & fine: ILMf) in a relevant environment (i.e. a fluidized bed), their fluidizing behavior in N<sub>2</sub> at temperatures between 700 and 1000°C was investigated (see Section 2.4.6). Through this approach, previously used to determine the suitability of different feedstocks for CLG [35], it was assessed whether the agglomerating behavior of the raw materials used during 1 MW<sub>th</sub> pilot testing could be replicated in a lab setup. It was found that in terms of the fluidization behavior, the presence of WSP-ashes did not significantly alter the fluidization behavior of the two utilized ilmenite types (more details see Section A.2.2 in the Supplementary Material).<sup>17</sup> However, subsequent SEM analysis of the tested samples showed agglomeration had occurred to some extent inside the fluidized bed quartz reactor (see Fig. 19, more details see Section A.2.3 in the Supplementary Material). Therefore, it can be concluded that similar melting phenomena also occurred in the 1 MW<sub>th</sub> pilot. Hence, it can be postulated that the combination of the significantly longer duration of

<sup>17</sup> Although the utilized ilmenite did not exhibit any fluidization issues inside the 1 MW<sub>th</sub> unit, neither during CLG pilot testing nor in previous CLC test campaigns, the laboratory-scale evaluations by Pressure Fluctuation Tests of the ILMf and ILMc samples investigated in this work showed that both samples develop some recalcitrance towards fluidization at the high temperatures (>900 °C), identified by the overpressure peaks preceding fluidization in "pressure drop vs. superficial velocity" experimental curves (not shown). This behavior occurred more pronouncedly for ILMf, with the extreme consequence of the absence of its bubbling fluidization at 1000 °C, whereas ILMc remained fluidizable by bubbling fluidization also at 1000 °C. The development of more pronounced adhesion forces between finer particles and with quartz reactor walls is a possible explanation. Other coarse ilmenite samples, previously studied by the same method elsewhere [35–37], usually showed bubbling fluidization in the presence of ashes at three times their minimum bubbling velocity.



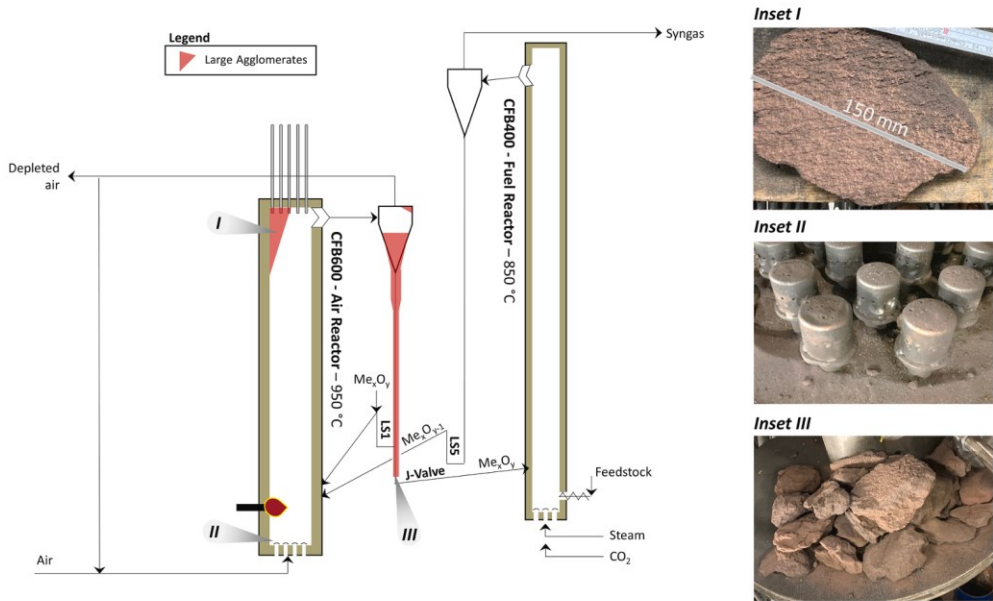


Fig. 14. Layout of reactor system of the 1 MW<sub>th</sub> pilot plant with indication of zones of large agglomerates found after opening of the reactor. Insets: Agglomerates found in riser (Inset I), on nozzle grid (Inset II) and in stand-pipe of LS1 (Inset III).

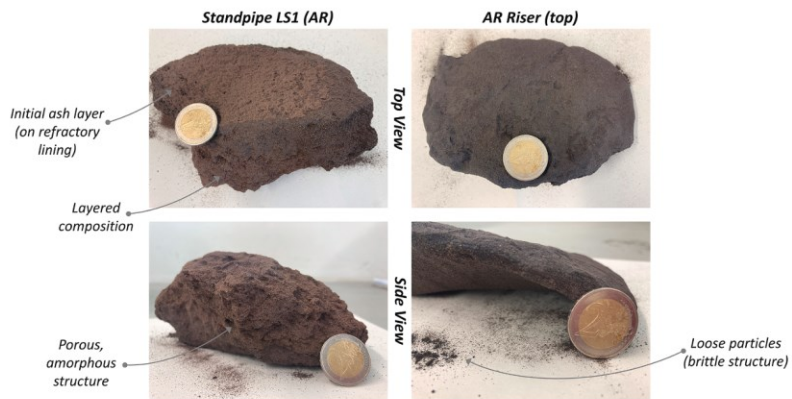


Fig. 15. Close-up images of large agglomerate slabs collected from the standpipe of LS1 (left) and AR riser (right).

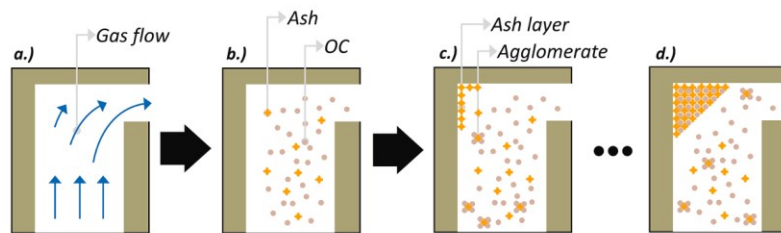


Fig. 16. Postulated mechanism for formation of large agglomerate slabs inside AR. a.) Empty AR with indication of gas flow, b.) AR with ilmenite and ash particles, c.) formation of first agglomerates and sticky ash layer on AR refractory lining in zones of low turbulence & adherence of ilmenite particles on ash layer, d.) growth of ash/OC layer on refractory lining, yielding fully formed agglomerate slabs.

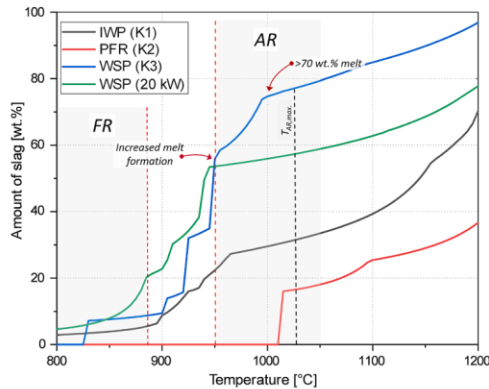


Fig. 17. Modelled melt fraction of selected feedstock ashes considering all major ash components. Grey shaded areas denote the FR and AR temperature range experienced in the 1 MW<sub>th</sub> pilot plant.

the pilot experiments and the exposure of the OC bed material to more feedstock ashes inside the 1 MW<sub>th</sub> CLG unit consequently led to the formation of larger agglomerates inside the reactor system, leading to an increase in the average particle size of the OC as well as the formation of large agglomerates in zones of low turbulence.

### 3.4.3. Characterization of different samples collected during 1 MW<sub>th</sub> CLG operation with WSP

After determining that agglomeration also occurs in lab-scale setups and hence must be related to the properties of the raw materials, rather than the setup of the 1 MW<sub>th</sub> pilot plant, samples collected during 1 MW<sub>th</sub> CLG testing were analyzed to obtain a better understanding of the occurring mechanism. These samples included samples collected from the six sampling locations of the 1 MW<sub>th</sub> pilot plant (see Fig. 2) during

pilot testing, as well as samples collected from the pilot during inspection after plant shut-down (see Fig. 14).

The solid samples collected during operation were analyzed via SEM-EDX and their particle size distributions were determined to quantify the extent to which agglomeration had occurred.

Upon consideration of Fig. 20, it can be postulated that agglomeration had already started to occur shortly after the start of CLG operation, as particles with diameters larger than 350 μm were recovered from the loop seals and bottom ash (K3). Clearly, those particles cannot stem from the fresh OC materials, exhibiting maximum particle diameters of 300 μm. Moreover, the PSD of the loop seal samples from K3, is clearly shifted towards the right when compared to K1 and K2, evidencing the occurrence of agglomeration during operation with wheat straw pellets. Upon consideration of the PSD from the AR bed material collected during CLG operation in K3 (see Fig. 20), it can be seen that the coarse fraction of the OC inside the riser of the AR exceeds that found inside the loop seals. Hence, it cannot only be summarized that agglomeration had occurred, but also that due to this, the formed agglomerates accumulated at their origin (AR) and only partially participated in OC circulation. That means, the formed agglomerates can be expected to reduce the attainable global solid circulation of the CLG system, as their entrainment is significantly lower than for the raw OC [64]. Still, judging from the recorded PSDs shown in Fig. 20, some agglomerates ( $d_p > 300 \mu\text{m}$ ) were also recovered from both loop seals, meaning that they are either transported there from their origin of formation or that agglomerates form inside the cyclones/stand-pipes before accumulating inside the loop seals. When considering the observations made during inspection of the pilot plant subsequent to CLG operation (see Section 3.4.1), the former hypothesis seems to be the more convincing one for LS5, as the AR and LS1 were found to be the main origin for agglomerates, yet particles larger 350 μm are recovered in LS5. Due to the high temperatures present in LS1, it can be assumed that agglomeration also occurred between the AR outlet and LS1 (see also Section 3.4.1). This is also validated by Fig. 20 showing that more agglomerates were found inside LS1 than in LS5. Consequently, it can be summarized that agglomerated particles with diameters up to 400 μm still participated in

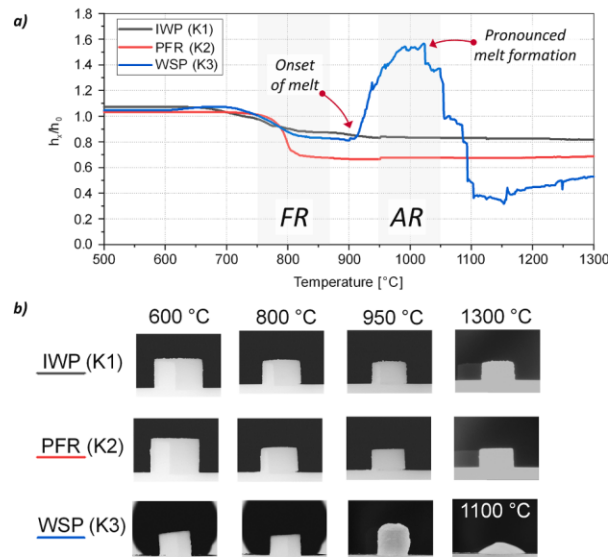


Fig. 18. Sintering and melting behavior of selected feedstock ashes investigated by hot stage microscopy. a.) Change in relative height during hot stage microscopy. Grey shaded areas denote the FR and AR temperature range experienced in the 1 MW<sub>th</sub> pilot plant. b.) Images of ash samples recorded during hot stage microscopy for selected temperatures. Results for IWP and PFR adapted from [38].

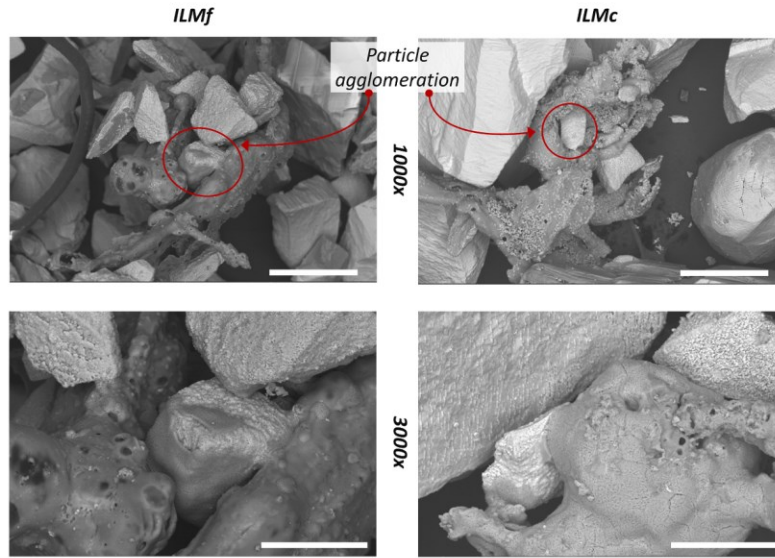


Fig. 19. SEM micrographs of ILMf+WSP-ash (left) and ILMc+WSP-ash (right) after fluidization with N<sub>2</sub> at 1000°C, magnified at: 1000x (top) and 3000x (bottom). Red circles indicate detection of particle agglomeration. The white bar denotes a length of 100 μm (top) and 40 μm (bottom).

solid circulation, leading to their dispersal in the entire CLG unit, yet due to their impaired mobility inside the CLG system, they accumulated at their origin of formation. Apart from the agglomerate-related effects, the PSDs of materials sampled from the 1 MW<sub>th</sub> pilot plant, shows similar trends as for K1, with the fine fraction of the OC being recovered in the AR and FR filter (more details see Section 3.2).

When considering the PSDs of the bed material samples collected from the AR (i.e. at the postulated source of the found agglomerates) for different operating times, further information on the progression of agglomeration formation inside the 1 MW<sub>th</sub> CLG unit can be derived. Shortly after completion of system start up (= termination of OC-aided combustion operation at 0 h), the PSD still largely resembled the PSD of

coarse ilmenite, used during this operational period (see 5 h in Fig. 21). This indicates that agglomeration had not occurred to substantial extents before initiating chemical looping operation. Subsequently, the coarse ilmenite inside the CLG system was slowly replaced with fresh fine ilmenite between 5 h and 24 h, as chemical looping operation was commenced and boundary conditions were optimized. However, despite this bed material replacement, which should have entailed a drop in OC particle sizes, the average PSD inside the AR clearly shifted to the right, with particles >350 μm making up more than 25 wt.-% of the AR inventory and the median particle diameter increasing to 235 μm after 24 h chemical looping operation. The only viable explanation for this observation is that the pronounced occurrence of agglomeration inside

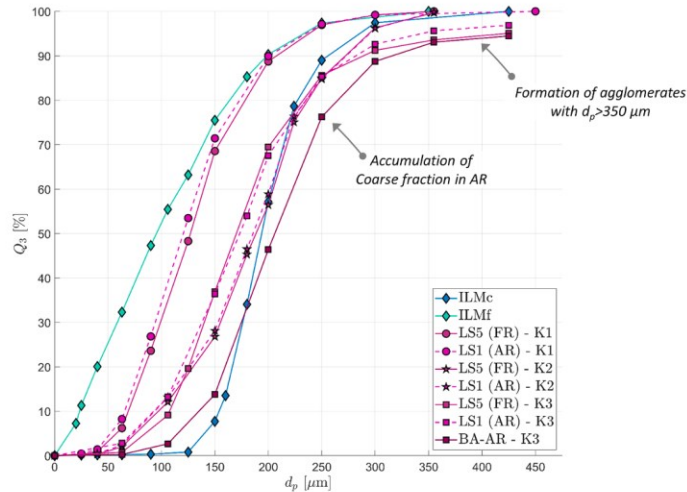


Fig. 20. Cumulative particle size distribution (PSD) of ilmenite samples collected from LS1 and LS5 for test campaigns K1, K2, and K3. PSD of fresh OC materials are given as a reference.

the AR during chemical looping operation. As the used ilmenite inside the system was replaced with fresh fine ilmenite to large extents after agglomeration was detected by the plant operators between 50 and 55 h, the PSD of the AR clearly shifted to smaller particle diameters. This intervention led to significantly improved system hydrodynamics as the average particle size of the OC decreased, allowing for larger solid circulation rates between AR and FR [46]. However, as shown in Fig. 21, the positive effect was short-lived, as the PSD subsequently deteriorated dramatically from 55 h over 89 h and 90 h, until the median particle diameter inside the AR reached 560  $\mu\text{m}$  before system shut down (93 h).

The findings made via PSD analysis are also supported when considering the SEM images of loop seal samples from K1 and K3, shown in Fig. 22. While for K1, the most notable observation is the change in shape of the OC particles to a more round form, which can mainly be attributed to abrasion [67,68] (see also Section 3.3), samples from K3 clearly show large agglomerates composed of multiple OC particles. Moreover, visibly more agglomerates are found in LS1 than in LS5, supporting the hypothesis that the AR is the origin of the agglomerates and those large particles are only found in LS5 after entrainment from the AR and FR. In terms of the formation mechanism of the agglomerates, the SEM image for K3 in LS1 shows agglomerates of multiple sizes, supporting the hypothesis, illustrated in Fig. 16, that molten WSP ash functions as a glue binding particles and agglomerates together, according to the melt-induced agglomeration mechanism, which was found to be dominant in chemical looping systems [61], thereby leading to an increase in particle size with increasing operating time.

Further analysis of a sub-set of solid samples collected after shut-down of the CLG unit (see Table A 2 and Figure A 4 in the Supplementary Material) was carried out to explain the formation of agglomerates in the cm-range (see Section 3.4.1). These samples were analyzed via EDXRF and XRD analysis, thereby determining elemental and mineral composition, respectively, as well as via SEM-EDX. SEM-EDX analysis showed that the agglomerates retrieved from the air reactor (CLA-S-75, photograph see Fig. 23a) consist of individually distinguishable particles sticking together (see Fig. 23b,c and Figure A 5 and in the

Supplementary Material), supporting previous findings. By means of EDX analysis, these agglomerated particles were identified as oxygen carrier material (mainly consisting of Ti, Fe and O) and ash particles (mainly consisting of Si, K, Ca and O). As indicated by the chemical analysis, the samples contain a high amount of the oxygen carrier ilmenite, which not only consists of the mineral phase Ilmenite ( $\text{FeTiO}_3$ ) but also Hematite ( $\text{Fe}_2\text{O}_3$ ) and Pseudobrookite ( $\text{Fe}_2\text{TiO}_5$ ). The latter two phases contain  $\text{Fe}^{3+}$ , indicating that the oxygen carrier was - even inside the FR - far from being completely reduced. Furthermore, Titanite ( $\text{CaTi}(\text{SiO}_4)\text{O}$ ) and Hollandite ( $\text{K}_{1.5}\text{Ti}_{7.2}\text{Fe}_{0.8}\text{O}_{16}$ ) are present inside the samples, which are both reaction products of ilmenite and ash, indicating a certain chemical interaction between the WSP ashes and the OC, also reported in literature [69]. This finding hints at a potential poisoning of the active phases of the OC due to contaminant mineral matter in the feedstock, as reported by Lebendig et al. [38]. The amorphous phase, which was found to “bridge” the OC particles inside the agglomerates, most certainly constitutes the melt at operation temperature. Correspondingly, amorphous phases mainly consisting of the major ash elements K, Si, Ca, and O were found to be located in between the individual OC particles in the (agglomerate) samples from K3 via SEM-EDX (more details see Section A.3 in the Supplementary Material). As illustrated in Fig. 23d, these amorphous phases are molten at operation temperature and therefore act as “glue”, sticking individual OC particles together and promoting the unhindered growth of agglomerates. Non-agglomerated particles contained significantly lower amounts of amorphous phase. Here, the amount of melt was not (yet) sufficient in case of these particles to glue them together and form bigger agglomerates.

In terms of the mechanical rigidity of the agglomerated particles, investigation of the samples in the jet cup (see Section 2.4.4), confirmed the general findings made during inspection of the 1 MW<sub>th</sub> CLG pilot plant (i.e. agglomerates are brittle, more details see Section 3.4.1). While for the fresh ilmenite materials (Fig. 24a and b), as well as loop seal samples from K1 (Fig. 24c and d) no significant shift in PSD was visible inside the jet cup, loop seal samples from K3 (Fig. 24e and f)

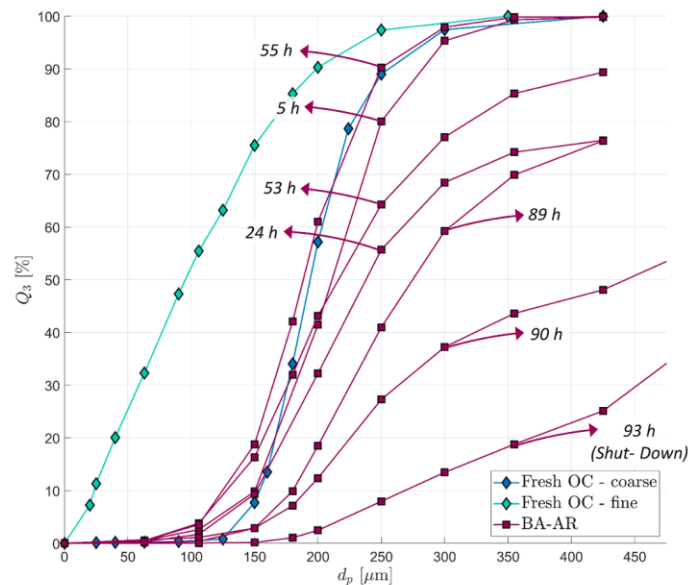


Fig. 21. Cumulative particle size distribution (PSD) of ilmenite samples collected from the AR via ash sluicing for the third test campaign (K3). PSD of fresh OC materials are given as a reference. After 9 hours of OC-aided compustion operation, chemical looping operation was initiated on 26th August 2022. This point in time is used as the reference time (0 h).

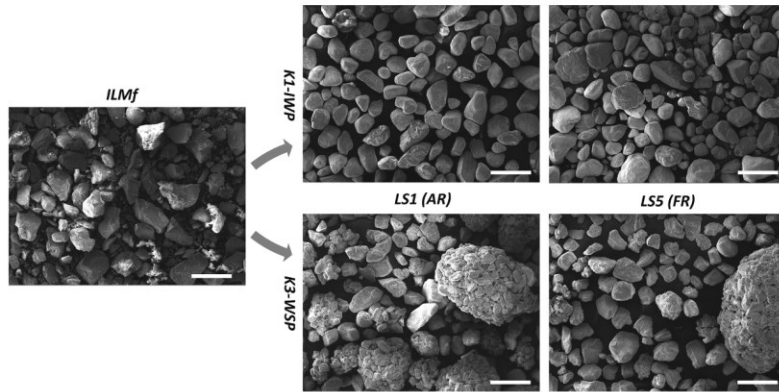


Fig. 22. SEM images of fresh ilmenite (ILMf, left), samples collected from LS1 and LS5 during K1 (top) and K3 (bottom) at 70x magnification. The white bar denotes a length of and 500  $\mu\text{m}$ .

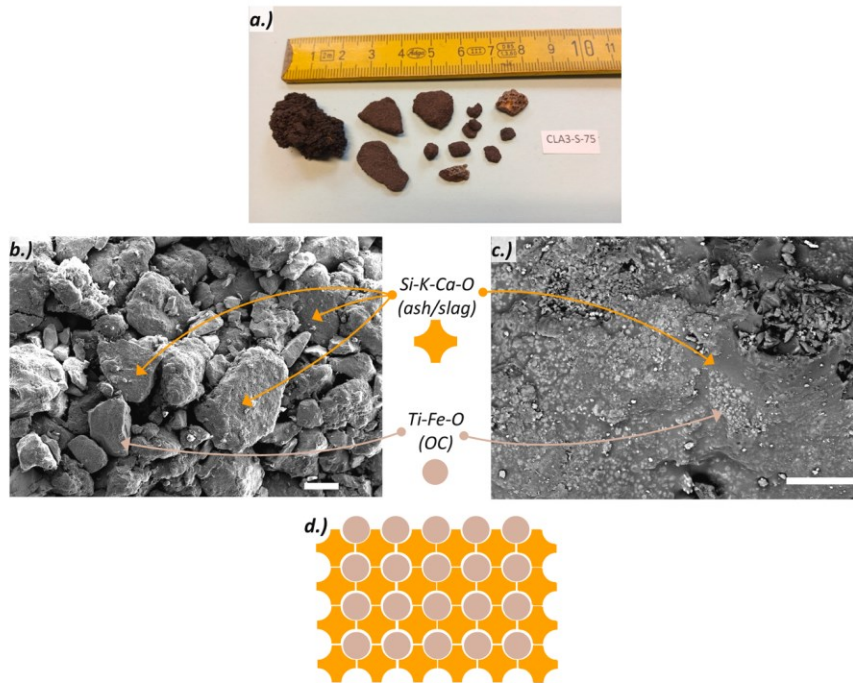


Fig. 23. a) Photograph of solid sample CLA3-S-75, b) SEM image of sample CLA3-S-75 (magnification 300x) with indication of zones of OC and slag, c) SEM image of sample CLA3-S-75 (magnification 1500x) with indication of zones of OC and slag, d) Simplified illustration of composition of agglomerates formed during 1 MW<sub>th</sub> CLG operation. The white bar denotes a length of 100  $\mu\text{m}$  (b.) and 10  $\mu\text{m}$  (c.).

showed a decrease in average particle size during the attrition experiments. As visible in Fig. 24e especially larger agglomerates retrieved from LS1 broke into smaller particles inside the jet cup. This again underlines that agglomerates do not exhibit a uniform, stable structure, but rather consist of multiple particles being attached to one another via an amorphous ash phase. It can therefore be postulated that when mechanical force is applied, the agglomerates break along those binding ash “bridges” between the individual OC particles. This finding also explains why the amount of large (>1 cm) agglomerates retrieved from the AR riser was limited, as the formation of larger agglomerates are

prevented inside the turbulent gas-solid flow inside the riser. On the other hand, mechanical forces inside the lower region of the cyclone, as well as the LS1 stand-pipe were insufficient to break formed agglomerates apart, leading to a continuous agglomerate growth.

### 3.4.4. Summary and outlook on suggested agglomeration mitigation strategies

Based on the results from pilot testing, plant inspection, and subsequent lab-scale experiments, a mechanism explaining the occurrence of OC agglomeration in the CLG unit during K3 was derived. Here, the

origin of agglomeration was found to be the low ash melting point of the WSP ashes, which can mainly be related to their high potassium and low silica content. The molten ashes, formed mainly inside the AR where temperatures are generally higher than in the FR and where full conversion of the pellets is achieved, act as a “glue” binding OC particles together, according to the melt-induced agglomeration mechanism [66]. Consequently, the size of agglomerates increases with time, as more particles get attached to one another via an amorphous molten phase mainly composed of Calcium, Potassium, and Silicate. Moreover, the formed agglomerates were found to also be able to stick to reactor walls, especially in regions of low turbulence (e.g. stand-pipe), where the resistance to material build-up and attrition forces are low, leading to the formation of large agglomerate slabs (>15 cm).

Due to this mechanism, the average particle size inside the CLG unit increased from approx. 111  $\mu\text{m}$  (fresh ilmenite) to beyond 500  $\mu\text{m}$ , preventing sufficient solid circulation between AR and FR. Moreover, large, brittle slabs of agglomerates formed inside the top of the AR riser as well as the standpipe of LS1, posing another obstacle to circulating solid particles. Consequently, system hydrodynamics were significantly impaired during CLG operation with WSP, resulting in insufficient heat and oxygen transport from the AR to the FR. To counter the ensuing effects of this on the CLG process (esp. too low FR temperatures), operators first adjusted hydrodynamic boundary conditions to the maximum extent (i.e. increase in fluidization velocities) before opting to boost FR temperatures via an increase in thermal load.<sup>18</sup> Yet, while this approach generally leads to an increase in system temperatures for CLG operation, it resulted in a much stronger increase in AR temperatures when compared to FR temperatures for operation with the WSP due to the agglomeration-related limitations in heat and oxygen transport to the FR.<sup>19</sup> Consequently, the tendency towards agglomeration inside the AR increased further, thus again entailing an increase in the mean particle diameter of the OC, which ultimately led to another decrease in solid circulation rates and FR temperatures. The explained vicious cycle, leading to the extensive agglomeration behavior observed during K3, is illustrated in Fig. 25. As indicated in Fig. 25, the only way to break this cycle is the wide-ranging replacement of bed inventory with fresh OC material, resulting in a decrease in the average particle diameter and thus an increase in solid circulation rate. However, it is clear that the effect of material replacement is only of a temporary nature, as agglomeration occurs continuously.

Therefore, it can be concluded that continuous bed material replacement is required in case agglomeration occurs in considerable fashion inside the CLG unit. Depending on the extent of agglomeration occurring, the ash sluicing and make-up rates have to be adjusted by the operators, to prevent an uncontrolled increase in the average OC particle diameter with elapsed time, leading to impaired system hydrodynamics. For the 1 MW<sub>th</sub> CLG unit, the make-up rate to achieve a temporary alleviation of agglomeration-related issues was approx. three times higher than in the absence of agglomeration (K1 & K2), leading to drastically reduced OC lifetimes. An option to decrease procurement and disposal costs in a full-scale unit would be post processing of the discharged bed material from the AR and FR using a sieving apparatus, to remove agglomerates (>300  $\mu\text{m}$ ) and allow for a reintroduction of the remaining material via the make-up system. However, the prevention of the occurrence of agglomeration inside the CLG unit clearly would be the more preferential solution, especially when aiming to prevent the formation of larger agglomerates inside the CLG system, which can

hinder material transport to significant extents.

To prevent the occurrence of agglomeration inside the CLG system for any feedstock of choice, the raw feedstock firstly has to be analyzed (esp. regarding its ash composition). Based on this analysis, an optimized biomass pre-treatment concept can be derived using a methodology comprised of simulation and experimental efforts [35]. Final analysis of the ensuing pre-treated feedstock, based on simulative and experimental investigations, can then be used to predict the risk of bed agglomeration in a CLG environment. For feedstocks with a low agglomeration tendency, addition of substances such as CaCO<sub>3</sub> during pelletization can be sufficient [14,48], while more problematic feedstocks require additional pre-treatment steps, such as washing, which was found to be beneficial for the removal of components tending toward ash agglomeration (e.g. potassium) [38,39,61,65]. Ultimately, this shows that technical solutions for the prevention of agglomeration inside the CLG system exist, allowing for sufficiently long OC lifetimes, regardless of the utilized raw feedstock.

#### 4. Conclusions

In the modular 1 MW<sub>th</sub> pilot plant over 300 h of chemical looping operation were achieved, using three different biomasses as the feedstock. Within this study, OC samples from different locations of the 1 MW<sub>th</sub> pilot were analyzed regarding their morphology, composition, as well as physical and chemical properties. The main conclusions from these analyses are:

- As reported in other studies, the OC undergoes several changes during chemical looping operation, which can be related to mechanical, thermal, and chemical strains acting inside the CLG system. Here, the most important ones are iron-migration to the particle surface, an increase in particle porosity, and particle abrasion.
- For one, these changes entail particle loss in the form of fines. Moreover, a decrease in the oxygen transport capacity of the OC was observed, while oxygen uptake and release kinetics improve during operation due to the larger porosity of the utilized OC particles.
- In the absence of agglomeration, OC loss via particle attrition determines the lifetime of the OC inside the 1 MW<sub>th</sub> CLG system. Here, OC lifetimes of approx. 70 h were determined during operation with industrial wood pellets and pine forest residue. On the one hand, these relatively low lifetimes can be related to peculiarities of the 1 MW<sub>th</sub> system (e.g. low cyclone separation efficiencies). On the other hand, the data suggests that due to the thermal, mechanical, and chemical stresses acting in an industrial CLG setup, lower lifetimes (200–300 h) than in lab configurations (>500 h) can be realized. To further explore how OC lifetimes can be optimized, a quantification of the effect of those different stresses under industry-like conditions as well as their interplay should be carried out in future studies.
- During operation with wheat straw pellets, particle agglomeration, impeding OC circulation between AR and FR and thus preventing efficient CLG operation, was observed. The occurrence of agglomeration was related to the feedstock's ash chemistry, leading to particle agglomeration following the melt-induced agglomeration mechanism. Subsequent lab analyses showed that the agglomeration tendency of different feedstocks is predictable, allowing for the conceptualization of tailored pre-treatment concepts, facilitating the utilization of a wide array of feedstocks for CLG.

In summary, the results show that CLG operation in industry-like conditions is feasible, meaning that long-term operation in representative boundary conditions can be attained using ilmenite as the bed material. Moreover, the most important characteristics of the utilized OC particles were determined, providing value insights into the fate of the OC during CLG in semi-industrial scale. On the basis of the elucidations provided in this study, process efficiency of pilot and industrial plants can thus be optimized, thereby providing an important reference

<sup>18</sup> When trying to increase FR temperatures in case of stable hydrodynamics (i.e. in the absence of agglomeration), an alternative to changing the solid circulation rate is increasing the thermal load of the CLG unit, which results in an overall increase in system temperatures (i.e. FR and AR temperatures increase) [58].

<sup>19</sup> In some cases the propane load was increased instead of the thermal load of the solid feedstock, making the effect even more drastic.

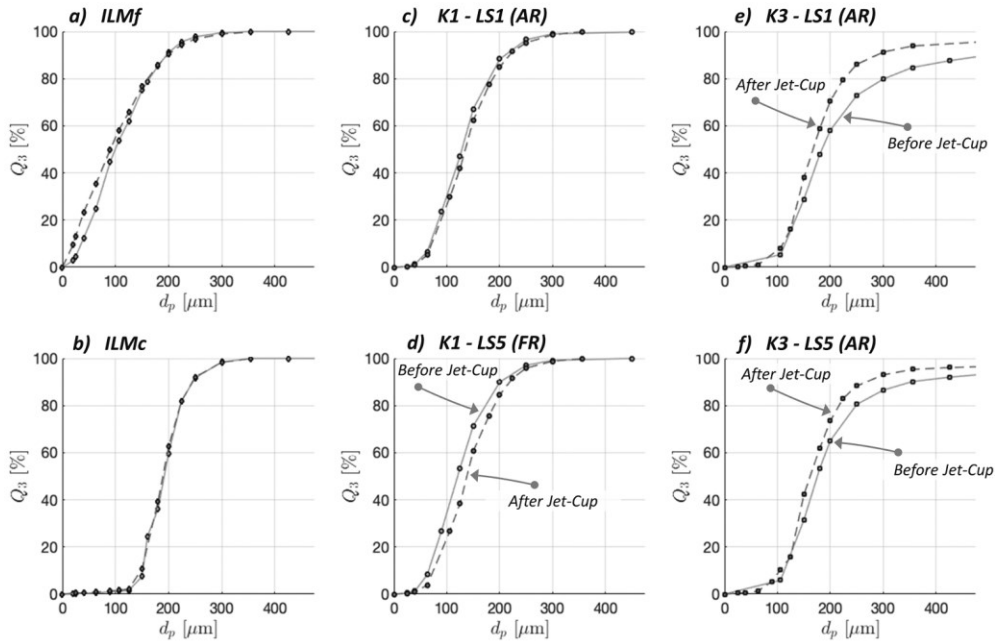


Fig. 24. PSD of OC before (-) and after (-) attrition tests in jet cup. a), b) fresh ilmenite; c), d) loop seal samples from K1; e), f) loop seal samples from K3.

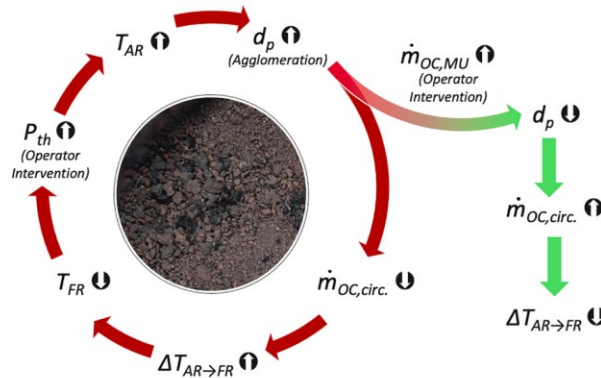


Fig. 25. Schematic illustration of proposed vicious cycle of agglomeration (red arrows), as observed during 1 MW<sub>th</sub> CLG operation with WSP. Green arrows indicate the approach to break cycle during operation.

for future scale-up endeavors.

**Funding**

This work has received funding of the European Union’s Horizon 2020-Research and Innovation Framework Programme under grant agreement No. 817841 (Chemical Looping gasification foR sustainAble production of biofuels-CLARA).

The content of this work reflects only the author’s view, and the European Commission is not responsible for any use that may be made of

the information it contains.

**CRedit authorship contribution statement**

**Paul Dieringer:** Conceptualization, Methodology, Investigation, Data curation, Writing – original draft, Visualization. **Falko Marx:** Writing – review & editing, Methodology, Investigation, Data curation. **Florian Lebendig:** Methodology, Investigation. **Michael Müller:** Methodology, Investigation, Writing – original draft, Funding acquisition. **Andrea Di Giuliano:** Methodology, Investigation, Writing –

original draft, Funding acquisition. **Katia Gallucci:** Methodology, Investigation, Writing – original draft, Funding acquisition. **Jochen Ströhle:** Writing – review & editing, Supervision, Project administration, Funding acquisition. **Bernd Eppe:** Resources, Funding acquisition.

#### Declaration of Competing Interest

The authors declare that they have no known competing financial interests or personal relationships that could have appeared to influence the work reported in this paper.

#### Data availability

Data will be made available on request.

#### Acknowledgments

The authors would like to thank Aichernig Engineering GmbH, Austria for their support in the design and safety analysis of the 1 MW<sub>th</sub> CLG unit. Moreover, the authors would like to thank AB Torkapparater, Sweden for the production, storage and shipping of pine forest residue and wheat straw pellets. Lastly, the authors would like to thank Egbert Wessel, Mirko Ziegner, Marvin Jost, Levent Aytemiz, and Niklas Engering for their support in lab analysis of the OC samples.

#### Supplementary materials

Supplementary material associated with this article can be found, in the online version, at [doi:10.1016/j.jaecs.2023.100227](https://doi.org/10.1016/j.jaecs.2023.100227).

#### References

- [1] World Meteorological Organization (WMO). WMO global annual to decadal climate update (target years: 2023-2027). World Meteorological Organization (WMO); 2023 [Online]. Available: [https://library.wmo.int/index.php?lvl=notice\\_display&id=22272#.ZG5HPS2l0Wo](https://library.wmo.int/index.php?lvl=notice_display&id=22272#.ZG5HPS2l0Wo).
- [2] Horowitz CA. Paris agreement. Int Leg Mater 2016;55(4):740–55. <https://doi.org/10.1017/S0020782900004253>.
- [3] European Environmental Agency (EEA). “Greenhouse gas emissions from transport in Europe,” *EEA Indicators*. <https://www.eea.europa.eu/ims/greenhouse-gas-emissions-from-transport> (accessed Mar. 10, 2023).
- [4] International Energy Agency (IEA). Global electric vehicle outlook 2022. 2022.
- [5] Directive (EU) 2018/2001 of the European Parliament and of the Council - of 11 December 2018 - on the promotion of the use of energy from renewable sources. Off J Eur Union 2018;L28.
- [6] Atsonios K, Nesiadis A, Detsios N, Koutita K, Nikolopoulos N, Grammelis P. Review on dynamic process modeling of gasification based biorefineries and bio-based heat & power plants. Fuel Process Technol 2020;197:106188. <https://doi.org/10.1016/j.fuproc.2019.106188>.
- [7] Roshan Kumar T, Mattisson T, Rydén M, Stenberg V. Process analysis of chemical looping gasification of biomass for Fischer–Tropsch crude production with net-negative CO<sub>2</sub> emissions: part 1. Energy Fuel 2022. <https://doi.org/10.1021/acs.energyfuels.2c00819>.
- [8] Higman C. Gasification. Combustion engineering issues for solid fuel systems. Elsevier; 2008. p. 423–68. <https://doi.org/10.1016/B978-0-12-373611-6.00011-2>.
- [9] Langner E, Kaltenmorgen J, Heinze C, Ströhle J, Eppe B. Fluidized bed gasification of solid recovered fuels in a 500 kW<sub>th</sub> pilot plant. Fuel 2023;344:127901. <https://doi.org/10.1016/j.fuel.2023.127901>.
- [10] Nguyen NM, Alobaid F, Dieringer P, Eppe B. Biomass-based chemical looping gasification: overview and recent developments. Appl Sci 2021;11(15):7069. <https://doi.org/10.3390/app11157069>.
- [11] Condiri O, García-Labiano F, de Diego LF, Izquierdo MT, Abad A, Adánez J. Biomass chemical looping gasification for syngas production using LD Slag as oxygen carrier in a 1.5 kW<sub>th</sub> unit. Fuel Process Technol 2021;222:106963. <https://doi.org/10.1016/j.fuproc.2021.106963>.
- [12] Hedayati A, Soleimanisalam AH, Linderholm CJ, Mattisson T, Lyngfelt A. Experimental evaluation of manganese ores for chemical looping conversion of synthetic biomass volatiles in a 300 W reactor system. J Environ Chem Eng 2021; 105112. <https://doi.org/10.1016/j.jece.2021.105112>.
- [13] Huang Z, et al. Biomass char direct chemical looping gasification using NiO-modified iron ore as an oxygen carrier. Energy Fuel 2014;28(1):183–91. <https://doi.org/10.1021/ef401528k>.
- [14] Condiri O, Abad A, Izquierdo MT, de Diego LF, García-Labiano F, Adánez J. Assessment of the chemical looping gasification of wheat straw pellets at the 20 kW<sub>th</sub> scale. Fuel 2023;344:128059. <https://doi.org/10.1016/j.fuel.2023.128059>.
- [15] Huseyin S, Wei G, Li H, He F, Huang Z. Chemical-looping gasification of biomass in a 10 kW<sub>th</sub> interconnected fluidized bed reactor using Fe<sub>2</sub>O<sub>3</sub>/Al<sub>2</sub>O<sub>3</sub> oxygen carrier. J Fuel Chem Technol 2014;42(8):922–31. [https://doi.org/10.1016/S1872-5813\(14\)60039-6](https://doi.org/10.1016/S1872-5813(14)60039-6).
- [16] Ge H, Guo W, Shen L, Song T, Xiao J. Biomass gasification using chemical looping in a 25 kW<sub>th</sub> reactor with natural hematite as oxygen carrier. Chem Eng J 2016; 286:174–83. <https://doi.org/10.1016/j.cej.2015.10.092>.
- [17] Hilz J, Helbig M, Haaf M, Daikeler A, Ströhle J, Eppe B. Investigation of the fuel influence on the carbonate looping process in 1 MW<sub>th</sub> scale. Fuel Process Technol 2018;169:170–7. <https://doi.org/10.1016/j.fuproc.2017.09.016>.
- [18] Hilz J, Helbig M, Haaf M, Daikeler A, Ströhle J, Eppe B. Long-term pilot testing of the carbonate looping process in 1 MW<sub>th</sub> scale. Fuel 2017;210:892–9. <https://doi.org/10.1016/j.fuel.2017.08.105>.
- [19] Ohlemüller P, Ströhle J, Eppe B. Chemical looping combustion of hard coal and torrefied biomass in a 1 MW<sub>th</sub> pilot plant. Int J Greenhouse Gas Control 2017;65: 149–59. <https://doi.org/10.1016/j.ijggc.2017.08.013>.
- [20] Ohlemüller P, Busch J-P, Reitz M, Ströhle J, Eppe B. Chemical-looping combustion of hard coal: autothermal operation of a 1 MW<sub>th</sub> pilot plant. J Energy Res Technol 2016;138(4):042203. <https://doi.org/10.1115/1.4032357>.
- [21] Heinze C, May J, Langner E, Ströhle J, Eppe B. High temperature Winkler gasification of Rhenish lignite in an optimized 500 kW<sub>th</sub> pilot plant. Fuel 2023; 333:126289. <https://doi.org/10.1016/j.fuel.2022.126289>.
- [22] Marx F, Dieringer P, Ströhle J, Eppe B. Design of a 1 MW<sub>th</sub> pilot plant for chemical looping gasification of biogenic residues. Energies 2021;14(9):2581. <https://doi.org/10.3390/en14092581>.
- [23] Johansson M, Mattisson T, Lyngfelt A. Comparison of oxygen carriers for chemical-looping combustion. Therm sci 2006;10(3):93–107. <https://doi.org/10.2298/TSCI0603093J>.
- [24] Adanez J, Abad A, Garcia-Labiano F, Gayán P, de Diego LF. Progress in chemical-looping combustion and reforming technologies. Prog Energy Combust Sci 2012;38 (2):215–82. <https://doi.org/10.1016/j.pecs.2011.09.001>.
- [25] Leon H, Lyngfelt A, Johansson M, Jerndal E, Mattisson T. The use of ilmenite as an oxygen carrier in chemical-looping combustion. Chem Eng Res Des 2008;86(9): 1017–26. <https://doi.org/10.1016/j.cherd.2008.03.019>.
- [26] Cuadrat A, Abad A, Adánez J, de Diego LF, García-Labiano F, Gayán P. Behavior of ilmenite as oxygen carrier in chemical-looping combustion. Fuel Process Technol 2012;94(1):101–12. <https://doi.org/10.1016/j.fuproc.2011.10.020>.
- [27] Adánez J, Cuadrat A, Abad A, Gayán P, de Diego LF, García-Labiano F. Ilmenite activation during consecutive redox cycles in chemical-looping combustion. Energy Fuels 2010;24(2):1402–13. <https://doi.org/10.1021/ef900856d>.
- [28] Nelson T, Van Der Watt JG, Laudal D, Feilen H, Mann M, Srinivasachar S. Reactive jet and cyclonic attrition analysis of ilmenite in chemical looping combustion systems. Int J Greenh Gas Control 2019;91:102837. <https://doi.org/10.1016/j.ijggc.2019.102837>.
- [29] Condiri O, García-Labiano F, de Diego LF, Izquierdo MT, Abad A, Adánez J. Biomass chemical looping gasification for syngas production using ilmenite as oxygen carrier in a 1.5 kW<sub>th</sub> unit. Chem Eng J 2021;405:126679. <https://doi.org/10.1016/j.cej.2020.126679>.
- [30] Wei G, He F, Huang Z, Zheng A, Zhao K, Li H. Continuous operation of a 10 kW<sub>th</sub> chemical looping integrated fluidized bed reactor for gasifying biomass using an iron-based oxygen carrier. Energy Fuel 2015;29(1):233–41. <https://doi.org/10.1021/ef5021457>.
- [31] Huang Z, et al. Chemical looping gasification of biomass char using iron ore as an oxygen carrier. Int J Hydrog Energy 2016;41(40):17871–83. <https://doi.org/10.1016/j.ijhydene.2016.07.089>.
- [32] Marx F, Dieringer P, Ströhle J, Eppe B. Solid flux measurement in dual fluidized bed processes based on solid samples. Fuel 2023;341:127589. <https://doi.org/10.1016/j.fuel.2023.127589>.
- [33] Ströhle J, Orth M, Eppe B. Chemical looping combustion of hard coal in a 1 MW<sub>th</sub> pilot plant using ilmenite as oxygen carrier. Appl Energy 2015;157:288–94. <https://doi.org/10.1016/j.apenergy.2015.06.035>.
- [34] Rydén M, Moldenhauer P, Lindqvist S, Mattisson T, Lyngfelt A. Measuring attrition resistance of oxygen carrier particles for chemical looping combustion with a customized jet cup. Powder Technol 2014;256:75–86. <https://doi.org/10.1016/j.powtec.2014.01.085>.
- [35] Di Giuliano A, Funcia I, Pérez-Vega R, Gil J, Gallucci K. Novel application of pretreatment and diagnostic method using dynamic pressure fluctuations to resolve and detect issues related to biogenic residue ash in chemical looping gasification. Processes 2020;8(9):1137. <https://doi.org/10.3390/pr8091137>.
- [36] Di Giuliano A, Malsegna B, Lucantonio S, Gallucci K. Experimental assessments of pyrolytic and fluid-dynamic interactions between pretreated residual biomasses and fluidized beds made up of oxygen carriers for chemical looping gasification. Adv Powder Technol 2023;34(5):104010. <https://doi.org/10.1016/j.apt.2023.104010>.
- [37] Di Giuliano A, Lucantonio S, Malsegna B, Gallucci K. Pretreated residual biomasses in fluidized beds for chemical looping gasification: experimental devolatilizations and characterization of ashes behavior. Bioresour Technol 2022;345:126514. <https://doi.org/10.1016/j.biortech.2021.126514>.
- [38] Lebendig F, Funcia I, Pérez-Vega R, Müller M. Investigations on the effect of pre-treatment of Wheat Straw on ash-related issues in chemical looping gasification (CLG) in comparison with woody biomass. Energies 2022;15(9):3422. <https://doi.org/10.3390/en15093422>.
- [39] Lebendig F, Müller M. Effect of pre-treatment of herbaceous feedstocks on behavior of inorganic constituents under chemical looping gasification (CLG) conditions. Green Chem 2022;24(24):9643–58. <https://doi.org/10.1039/D2GC02906E>.



- [40] Lyngfelt A, Thunman H. Construction and 100 h of operational experience of a 10-kW chemical-looping combustor. Carbon dioxide capture for storage in deep geologic formations. Elsevier; 2005. p. 625–45. <https://doi.org/10.1016/B978-008044570-0/50122-7>.
- [41] L.-S. Fan, "Chemical looping systems for fossil energy conversions," p. 437.
- [42] Marinuc M, Rus F. The effect of particle size and input velocity on cyclone separation process. Bull Transilv Univ Bras II: For Wood Ind Agric Food Eng 2011; 117–22.
- [43] Wang H. Study on separation efficiency of cyclone separator for 75t/h circulating fluidized bed boiler. IOP Conf Ser: Mater Sci Eng 2020;721(1):012037. <https://doi.org/10.1088/1757-899X/721/1/012037>.
- [44] Bolhar-Nordenkamp M, et al. Scale-up of a 100kWth pilot FICFB-gasifier to a 8 MWth FICFB-gasifier demonstration plant in Güssing (Austria). In: presented at the Proc. 1st International Ukrainian Conference on Biomass For Energy; 2002.
- [45] Chung C, Qin L, Shah V, Fan L-S. Chemically and physically robust, commercially-viable iron-based composite oxygen carriers sustainable over 3000 redox cycles at high temperatures for chemical looping applications. Energy Environ Sci 2017;10(11):2318–23. <https://doi.org/10.1039/C7EE02657A>.
- [46] Dieringer P, Marx F, Ströhle J, Epple B. System hydrodynamics of a 1 MWth dual circulating fluidized bed chemical looping gasifier. Energies 2023;16(15):5630. <https://doi.org/10.3390/en16155630>.
- [47] Markström P, Linderholm C, Lyngfelt A. Chemical-looping combustion of solid fuels – Design and operation of a 100 kW unit with bituminous coal. Int J Greenh Gas Control 2013;15:150–62. <https://doi.org/10.1016/j.ijggc.2013.01.048>.
- [48] Condori O, García-Labiano F, de Diego LF, Izquierdo MT, Abad A, Adánez J. Syngas production via Biomass Chemical Looping Gasification (BCLG) in a 50 kWth unit using ilmenite as oxygen carrier. In: Proceedings of the Fluidized Bed Conversion Conference 2022; 2022. p. 10.
- [49] Corcoran A, Knutsson P, Lind F, Thunman H. Comparing the structural development of sand and rock ilmenite during long-term exposure in a biomass fired 12 MWth CFB-boiler. Fuel Process Technol 2018;171:39–44. <https://doi.org/10.1016/j.fuproc.2017.11.004>.
- [50] De Diego LF, et al. Development of Cu-based oxygen carriers for chemical-looping combustion. Fuel 2004;83(13):1749–57. <https://doi.org/10.1016/j.fuel.2004.03.003>.
- [51] Li H, Sun Z, Tian L, Gao L, Xu Y, Cao Y. The investigation on the attrition of hematite oxygen carrier particles in a fluidization-based chemical looping system. Fuel Process Technol 2022;236:107441. <https://doi.org/10.1016/j.fuproc.2022.107441>.
- [52] Dieringer P, Marx F, Alobaid F, Ströhle J, Epple B. Process control strategies in chemical looping gasification—a novel process for the production of biofuels allowing for net negative CO<sub>2</sub> emissions. Appl Sci 2020;10(12):4271. <https://doi.org/10.3390/app10124271>.
- [53] Kunii D, Levenspiel O. Fluidization engineering. Butterworth-Heinemann series in chemical engineering. 2 ed. Boston: Butterworth-Heinemann; 1991.
- [54] Bolhar-Nordenkamp M, Rauch R, Bosch K, Aichernig C. Biomass CHP plant Güssing – using gasification for power generation. In: Proceeding of the 2nd Regional Conference on Energy Technology Towards a Clean Environment; 2003. p. 7.
- [55] H. Hermann, R. Reinhard, B. Klaus, K. Reinhard, and A. Christian, "Biomass CHP plant Güssing – a success story," p. 13.
- [56] Gogulancea V, et al. Technoeconomic and environmental assessment of biomass chemical looping gasification for advanced biofuel production. Int J Energy Res 2023;2023:1–17. <https://doi.org/10.1155/2023/6101270>.
- [57] Samprón I, de Diego LF, García-Labiano F, Izquierdo MT. Optimization of synthesis gas production in the biomass chemical looping gasification process operating under auto-thermal conditions. Energy 2021;226:120317. <https://doi.org/10.1016/j.energy.2021.120317>.
- [58] Dieringer P, Marx F, Michel B, Ströhle J, Epple B. Design and control concept of a 1 MWth chemical looping gasifier allowing for efficient autothermal syngas production. Int J Greenh Gas Control 2023;127:103929. <https://doi.org/10.1016/j.ijggc.2023.103929>.
- [59] Abad A, Adánez J, Cuadrat A, García-Labiano F, Gayán P, de Diego LF. Kinetics of redox reactions of ilmenite for chemical-looping combustion. Chem Eng Sci 2011; 66(4):689–702. <https://doi.org/10.1016/j.ces.2010.11.010>.
- [60] Abad A, Adánez J, García-Labiano F, de Diego LF, Gayán P, Celaya J. Mapping of the range of operational conditions for Cu-, Fe-, and Ni-based oxygen carriers in chemical-looping combustion. Chem Eng Sci 2007;62(1–2):533–49. <https://doi.org/10.1016/j.ces.2006.09.019>.
- [61] Miao Z, Jiang E, Hu Z. Review of agglomeration in biomass chemical looping technology. Fuel 2022;309:122199. <https://doi.org/10.1016/j.fuel.2021.122199>.
- [62] Lindström E, Öhman M, Backman R, Boström D. Influence of sand contamination on slag formation during combustion of wood derived fuels. Energy Fuels 2008;22(4):2216–20. <https://doi.org/10.1021/ef700772q>.
- [63] Mlonka-Mędrala A, Magdziarz A, Gajek M, Nowińska K, Nowak W. Alkali metals association in biomass and their impact on ash melting behaviour. Fuel 2020;261:116421. <https://doi.org/10.1016/j.fuel.2019.116421>.
- [64] Bénoni D, Briens CL, Baron T, Duchesne E, Knowlton TM. A procedure to determine particle agglomeration in a fluidized bed and its effect on entrainment. Powder Technol 1994;78(1):33–42. [https://doi.org/10.1016/0032-5910\(93\)02780-E](https://doi.org/10.1016/0032-5910(93)02780-E).
- [65] Lucantonio S, Di Giuliano A, Gallucci K. Influences of the pretreatments of residual biomass on gasification processes: experimental devolatilizations study in a fluidized bed. Appl Sci 2021;11(12):5722. <https://doi.org/10.3390/app11125722>.
- [66] Morris JD, Daood SS, Chilton S, Nimmo W. Mechanisms and mitigation of agglomeration during fluidized bed combustion of biomass: A review. Fuel 2018; 230:452–73. <https://doi.org/10.1016/j.fuel.2018.04.098>.
- [67] de Diego LF, García-Labiano F, Gayán P, Celaya J, Palacios JM, Adánez J. Operation of a 10kWth chemical-looping combustor during 200 h with a CuO–Al<sub>2</sub>O<sub>3</sub> oxygen carrier. Fuel 2007;86(7–8):1036–45. <https://doi.org/10.1016/j.fuel.2006.10.004>.
- [68] Huang Z, et al. Synthesis gas production through biomass direct chemical looping conversion with natural hematite as an oxygen carrier. Bioresour Technol 2013; 140:138–45. <https://doi.org/10.1016/j.biortech.2013.04.055>.
- [69] Öhman M, Nordin A, Skrifvars B-J, Backman R, Hupa M. Bed agglomeration characteristics during fluidized bed combustion of biomass fuels. Energy Fuels 2000;14(1):169–78. <https://doi.org/10.1021/ef990107b>.